VISCOELASTICITY: FROM INDIVIDUAL CELL BEHAVIOR TO COLLECTIVE TISSUE REMODELING

EDITED BY: Ivana Dusan Pajic-Lijakovic, Karine Guevorkian, Jose J. Munoz and Elias H. Barriga

PUBLISHED IN: Frontiers in Physics and Frontiers in Physiology

frontiers Research Topics

ISSN 1664-8714
ISBN 978-2-88971-695-1
DOI 10.3389/978-2-88971-695-1

About Frontiers

Frontiers is more than just an open-access publisher of scholarly articles: it is a pioneering approach to the world of academia, radically improving the way scholarly research is managed. The grand vision of Frontiers is a world where all people have an equal opportunity to seek, share and generate knowledge. Frontiers provides immediate and permanent online open access to all its publications, but this alone is not enough to realize our grand goals.

Frontiers Journal Series

The Frontiers Journal Series is a multi-tier and interdisciplinary set of open-access, online journals, promising a paradigm shift from the current review, selection and dissemination processes in academic publishing. All Frontiers journals are driven by researchers for researchers; therefore, they constitute a service to the scholarly community. At the same time, the Frontiers Journal Series operates on a revolutionary invention, the tiered publishing system, initially addressing specific communities of scholars, and gradually climbing up to broader public understanding, thus serving the interests of the lay society, too.

Dedication to Quality

Each Frontiers article is a landmark of the highest quality, thanks to genuinely collaborative interactions between authors and review editors, who include some of the world's best academicians. Research must be certified by peers before entering a stream of knowledge that may eventually reach the public - and shape society; therefore, Frontiers only applies the most rigorous and unbiased reviews.
Frontiers revolutionizes research publishing by freely delivering the most outstanding research, evaluated with no bias from both the academic and social point of view. By applying the most advanced information technologies, Frontiers is catapulting scholarly publishing into a new generation.

What are Frontiers Research Topics?

Frontiers Research Topics are very popular trademarks of the Frontiers Journals Series: they are collections of at least ten articles, all centered on a particular subject. With their unique mix of varied contributions from Original Research to Review Articles, Frontiers Research Topics unify the most influential researchers, the latest key findings and historical advances in a hot research area! Find out more on how to host your own Frontiers Research Topic or contribute to one as an author by contacting the Frontiers Editorial Office: frontiersin.org/about/contact

VISCOELASTICITY: FROM INDIVIDUAL CELL BEHAVIOR TO COLLECTIVE TISSUE REMODELING

Topic Editors:
Ivana Dusan Pajic-Lijakovic, University of Belgrade, Serbia
Karine Guevorkian, UMR168 Unite physico-chimie Curie (PCC), France
Jose J. Munoz, Universitat Politecnica de Catalunya, Spain
Elias H. Barriga, Gulbenkian Institute of Science (IGC), Portugal

Citation: Pajic-Lijakovic, I. D., Guevorkian, K., Munoz, J. J., Barriga, E. H., eds. (2021). Viscoelasticity: From Individual Cell Behavior to Collective Tissue Remodeling. Lausanne: Frontiers Media SA. doi: 10.3389/978-2-88971-695-1

Table of Contents

frontiers in Physics

EDITORIAL
published: 29 September 2021
doi: 10.3389/fphy.2021.773096

Editorial: Viscoelasticity: From Individual Cell Behavior to Collective Tissue Remodeling

Ivana D. Pajic-Lijakovic[1]*, *Karine Guevorkian*[2], *Elias H. Barriga*[3] and *Jose J. Muñoz*[4,5,6]

[1]Department of Chemical Engineering, Faculty of Technology and Metallurgy, University of Belgrade, Belgrade, Serbia, [2]Institut Curie, Université PSL, Sorbonne Université, CNRS UMR168, Laboratoire Physico Chimie Curie, Paris, France, [3]Mechanisms of Morphogenesis Laboratory, Gulbenkian Institute of Science (IGC), Oeiras, Portugal, [4]Universitat Politecnica de Catalunya, Barcelona, Spain, [5]Centre Internacional de Mètodes Numèrics en Enginyeria (CIMNE), Barcelona, Spain, [6]Institut de Matemàtiques de la UPC-BarcelonaTech (IMTech), Barcelona, Spain

Keywords: viscoelasticity of multicellular systems, collective cell rearrangement, multi scale mathematical modeling, elastography, cell jamming state transition, active elastic turbulence

Editorial on the Research Topic

Viscoelasticity: From Individual Cell Behavior to Collective Tissue Remodeling

This issue gathers exciting multi-disciplinary work relating viscoelasticity and collective cell remodeling within various biological processes such as morphogenesis, tumorigenesis, and wound healing. Viscoelasticity is influenced by energy transfer and dissipation during cell rearrangement at various time and space scales. Cumulative structural changes at a subcellular level have effects on viscoelasticity at a supracellular level. Established configurations of migrating cells and the rate of their change, which significantly regulate viscoelasticity at a supracellular level, have the impact on the cohesiveness inhomogeneity and various mechanical and biochemical processes at a subcellular level. This Research Topic aims to connect the macroscopic viscoelastic parameters with the individual and collective cell response. Consideration of biochemical, biophysical and bio-mechanical aspects responsible for tissue remodeling, intercalation, and migration were discussed on various multicellular systems under *in vivo* and *in vitro* conditions.

Thus in this Research Topic we aim to provide a state-of-the-art view about the current knowledge related to viscoelasticity caused by collective cell remodeling and adhesive contractile properties, covering a plethora of phenomena such as: 1) single cell response under stretched monolayers modeled with an improved Vertex model, 2) adhesion percolation within a tissue as an important factor which influences its viscoelasticity, 3) the active turbulence caused by collective cell migration accompanied with the generation of mechanical waves, 4) cell jamming state transitions, and 5) viscoelastic response characterization in liver diseases. Alternative techniques to measure and control cell rearrangement under various experimental conditions are also considered, including atomic force microscopy measurements and various elastography techniques.

OPEN ACCESS

Edited and reviewed by:
Ralf Metzler,
University of Potsdam, Germany

***Correspondence:**
Ivana D. Pajic-Lijakovic
iva@tmf.bg.ac.rs

Specialty section:
This article was submitted to Biophysics, a section of the journal Frontiers in Physics

Received: *09 September 2021*
Accepted: *15 September 2021*
Published: *29 September 2021*

Citation:
Pajic-Lijakovic ID, Guevorkian K, Barriga EH and Muñoz JJ (2021) Editorial: Viscoelasticity: From Individual Cell Behavior to Collective Tissue Remodeling. Front. Phys. 9:773096. doi: 10.3389/fphy.2021.773096

This Research Topic provides an overview of the current understanding of various: biological, biochemical, biophysical and mechanical aspects of cell remodeling. The inter-relation between cell remodeling and tissue viscoelasticity was discussed by emphasizing the relevant rheological parameters, the way of their measurement under *in vivo*/*in vitro* conditions, and the strategy of multi-scale constitutive modeling.

AUTHOR CONTRIBUTIONS

All authors listed have made a substantial, direct, and intellectual contribution to the work and approved it for publication.

Conflict of Interest: The authors declare that the research was conducted in the absence of any commercial or financial relationships that could be construed as a potential conflict of interest.

frontiers in Physics

REVIEW
published: 06 November 2020
doi: 10.3389/fphy.2020.585681

Mechanical Oscillations in 2D Collective Cell Migration: The Elastic Turbulence

Ivana Pajic-Lijakovic and Milan Milivojevic*

Department of Chemical Engineering, Faculty of Technology and Metallurgy, University of Belgrade, Belgrade, Serbia

Various types of mechanical waves, such as propagative waves and standing waves, are observed during 2D collective cell migration. Propagative waves are generated during monolayer free expansion, whereas standing waves are generated during swirling motion of a confluent monolayer. Significant attempts have been made to describe the main characteristics of mechanical waves obtained within various experimental systems. However, much less attention is paid to correlate the viscoelasticity with the generated oscillatory instabilities. Mechanical waves have recognized during flow of various viscoelastic systems under low Reynolds number and called "the elastic turbulence." In addition to Reynolds number, Weissenberg number is needed for characterizing the elastic turbulence. The viscoelastic resistive force generated during collective cell migration caused by a residual stress accumulation is capable of inducing apparent inertial effects by balancing with other forces such as the surface tension force, the traction force, and the resultant force responsible for cell migration. The resultant force represents a product of various biochemical processes such as cell signaling and gene expression. The force balance induces (1) forward flow and backward flow in the direction of cell migration as characteristics of the propagative waves and (2) inflow and outflow perpendicular to the direction of migration as characteristics of the standing waves. The apparent inertial effects are essential for appearing the elastic turbulence and represent the characteristic of (1) the backward flow during the monolayer free expansion and (2) the inflow during the cell swirling motion within a confluent monolayer.

Keywords: multi scale nature of viscoelasticity of multicellular system, collective cell migration, apparent inertia effects, the elastic turbulence, rheological behavior of extracellular matrix

OPEN ACCESS

Edited by:
Aljaz Godec,
Max Planck Institute for Biophysical Chemistry, Germany

Reviewed by:
Claudia Tanja Mierke,
Leipzig University, Germany
Andrew Clark,
Institut Curie, France

****Correspondence:***
Ivana Pajic-Lijakovic
iva@tmf.bg.ac.rs

Specialty section:
This article was submitted to Biophysics, a section of the journal Frontiers in Physics

Received: *21 July 2020*
Accepted: *14 September 2020*
Published: *06 November 2020*

Citation:
Pajic-Lijakovic I and Milivojevic M (2020) Mechanical Oscillations in 2D Collective Cell Migration: The Elastic Turbulence. Front. Phys. 8:585681. doi: 10.3389/fphy.2020.585681

INTRODUCTION

Collective cell migration within a monolayer induces spontaneous generation of mechanical waves [1–5]. A more comprehensive account of oscillatory patterns generation is essential for a wide range of biological processes such as morphogenesis, wound healing, regeneration, and cancer invasion [6–9]. Specifically, in this review, we concentrate on mechanical oscillations, a term we use to identify all periodical fluctuations of mechanical parameters, such as cell velocity, the resulting strain, substrate tractions, and stresses. These oscillations can be divided into two major categories: (1) standing waves generated in a confined environment [3, 5, 10–12] and (2) propagative waves generated during monolayer free expansion that travel through the system [2, 5, 13]. The standing waves represent a characteristic of local cell rearrangement, which leads to swirling motion [3]. Propagative waves have been observed during wound healing [2]. This monolayer expansion

induces fluctuations of cell packing density [13]. Tlili et al. [13] reported that the frequency of velocity weaves depends only on cell packing density at the moving forward. Both types of waves induce a periodical softening and stiffening of multicellular domains [2, 3, 5]. It is necessary to correlate cell packing density with cell strains and residual stress accumulation.

Oscillator, wave-like motion of multicellular systems has been related to long-time effective inertia [3, 11]. The effective inertia is induced by generated cellular stress during long-time rearrangement. Notbohm et al. [3] considered a cell stress generation as a product of a chemical coupling where cellular stress results in increased contractility, which has a feedback impact to the effective inertia. The effective inertia, together with cellular elasticity, supports the oscillatory waves of motion [3]. Serra-Picamal et al. [2] assumed a biphasic stress response of single cells as a product of cytoskeletal reinforcement and fluidization. They also neglected long-time inertial effects. Banerjee et al. [14] coupled local strain with contractility and impose a turnover time for contractile elements, resulting in effective inertia and viscoelasticity based on the formulated continuum model. They did not take into consideration stress relaxation and residual stress accumulation caused by collective cell migration. Murray et al. [15] related cell packing density with cell stress. They also neglected inertial effects. Various approaches have been applied. Notbohm et al. [3] proposed a continuum model formulated in terms of a few coarse-grained fields such as traction and velocity, measured directly in the experiments. Murray et al. [15] proposed a continuum model presented as a system of equations capable for describing interrelation between variables such as (1) cell packing density, (2) matrix density, and (3) matrix viscoelasticity. Serra-Picamal et al. [2] and Deforet et al. [11] formulated stochastic particle-based simulations. Serra-Picamal et al. [2] balanced active propulsion force with cell elastic force and cell–matrix friction force. Deforet et al. [11] accounted for the force of inertia and balanced it with friction, intercellular adhesions, and active propulsion.

Significant attempts have been made to describe the main characteristics of mechanical waves by considering various types of experimental systems. The main characteristics of standing waves are (1) the radial velocity and cell tractions are uncorrelated; (2) radial stress component σ_{crr} and the corresponding strain rate $\dot{\boldsymbol{\varepsilon}}_{\boldsymbol{crr}}$ are uncorrelated; (3) radial stress component is simultaneously tensional and compressional; and (4) time derivative of the stress component is in a phase with the corresponding strain rate [3]. The main characteristics of propagative waves are that (1) normal stress component σ_{cxx} and corresponding strain rate $\dot{\boldsymbol{\varepsilon}}_{\boldsymbol{cxx}}$ are in phase quadrature, (2) normal stress component is always tensional, and (3) velocity and cell tractions are uncorrelated [2]. Even though the most studied model is Madin-Darbvy canine kidney cells (MDCK), other types have been employed, and despite the intrinsic variability between them, all reports seem to agree on the typical times and space scale: mechanical oscillations happen with a periodicity of ∼0.5–1 mm and ∼3–6 h [2, 3, 5]. The effective velocity of transmission of mechanical signals, whether traveling or standing waves, is 0.2–1 μm/min [2, 3]. These cooperative motions are driven by active cellular forces, but the physical nature of these forces and how they generate elastic waves remain poorly understood. However, it is well-known that generation of waves and their transfer strongly depends on the state of cell–cell junctions and contractility [2, 3, 16, 17]. Most of the works on generation of mechanical waves within cell monolayers have been carried out on fibroblasts, which develop weaker cell–cell adhesions [5]. The knowledge obtained on these cell types is difficult to transfer on epithelial cells, which develop strong cell–cell junctions. However, various confluent multicellular systems under *in vivo* conditions are capable of generating the cell swirling motion and on that base mechanical waves, which have been experimentally confirmed [18, 19]. Additional experimental work is necessary to correlate the state of cell–cell adhesion contacts and the characteristics of mechanical waves. Until now, little is reported about influence of the monolayer viscoelasticity on propagation of mechanical waves. Tambe et al. [1], Serra-Picamal et al. [2], and Notbohm et al. [3] treated a monolayer as homogeneous, isotropic, and elastic. On that basis, they neglected inertial effects during collective cell migration. Viscoelastic relaxation is expected to result in long-time-scale stress accumulation and consequently give rise to oscillations through the effective inertia. The stress accumulation can induce local stiffening and on that basis perturb established cell migrated pattern. In general, inertial effects have been discussed in the context of turbulence and quantified by dimensionless Reynolds number $R_e = \frac{vL\rho}{\eta}$ (where v is the velocity, L is the characteristic length, ρ is the density, and η is the viscosity). The turbulence of Newtonian liquids is induced at large R_e number, i.e., high velocity and low viscosity. However, viscoelastic systems have a few properties that distinguish them from Newtonian fluids [20, 21]. The stress field in viscoelastic systems is not uniquely defined by the current rate of strain, but rather depends on the flow history, with characteristic relaxation times for stress and strain-rate [20]. To the contrary of the turbulence generated within the Newtonian liquids, the so-called "elastic turbulence" appears during flow of viscoelastic liquids such as solutions of flexible long-chain polymers under low Reynolds number $R_e \rightarrow 0$, i.e., low velocity and high viscosity [22, 23]. The elastic turbulence represents a consequence of the system viscoelastic nature and is quantified by Weissenberg number $W_i = \frac{v}{L}\tau_R$ (τ_R is the stress relaxation time). For the case of polymer solutions, this elastic turbulence is accompanied by stretching of polymer chains resulting in significant system stiffening. The system stiffening is caused by residual stress accumulation, which leads to sharp growth of the flow resistance. Groisman and Steinberg [23] proposed the dimensionless elastic parameter $X = \frac{W_i}{R_e}$ for characterization of the elastic turbulence rather than R_e number. Steinberg [24] pointed out that the elastic turbulence of polymer solutions represents the characteristic of large $W_i > 1$ and vanishingly small $R_e \ll 1$ number. Larson et al. [25] physically described the elastic parameter X as the ratio between the stress relaxation time τ_R and the viscous diffusion time t_v, i.e., $X = \frac{\tau_R}{t_v}$ (where $t_v = \frac{L^2\rho}{\eta}$). Groisman and Steinberg [26] considered Couette-Taylor (CT) flow of viscoelastic polymer solutions and pointed out that the flow can become unstable when the stress relaxation time is large enough. They considered the oscillatory instabilities generation in highly elastic polymeric

liquids. The rheological response of these systems corresponds to the case when the centrifugal force is totally suppressed by the elastic hoop stress. At those conditions, the flow instabilities in the form of swirls appear as a consequence of this hoop stress. Swirling flow induces inflow and outflow in radial direction driven by action of centrifugal force against elastic force [22]. This important result points out that apparent inertial effects are caused by the system simultaneous stiffening and softening occurring when $R_e \rightarrow 0$ which lead to inflow and outflow. The inflow for $v_r < 0$ (where v_r is the radial velocity component) corresponds to the compression and the outflow for $v_r > 0$ corresponds to extension. Multicellular systems are much complex than polymer solutions, but their viscoelastic nature significantly influences cell rearrangement and should not be neglected [8, 9]. Flow instabilities generated during collective cell migration show similar rheological properties as ones recognized for other viscoelastic systems. However, cellular systems have not been considered in the context of the elastic turbulence yet. Murray et al. [15], Serra-Picamal et al. [2], Tambe et al. [1], and Notbohm et al. [3] neglected inertial effects during collective migration of cell monolayers. This assumption has been supported by low R_e number flow. However, apparent inertial effects could represent a consequence of inflow during cell swirling motion and backward flow during monolayer expansion caused by residual stress accumulation. The aim of this work is to relate viscoelastic nature of cell monolayer during collective cell migration with generated standing and propagative mechanical waves. Consequently, it is necessary to (1) postulate viscoelastic constitutive model for cell monolayer and extracellular matrix; (2) describe cell packing density change, matrix density change, and their interrelation (needed for the description of volume force balance); and (3) formulate the volume force balance that drives cell rearrangement by accounting for two time scales, i.e., a time scale of minutes (for the stress relaxation) and time scale of hours (for collective cell migration, strain change, and residual stress accumulation).

VISCOELASTICITY OF CELL MONOLAYER CAUSED BY COLLECTIVE CELL MIGRATION: THE DIMENSIONLESS CRITERIA

Flow of viscoelastic systems should be characterized by two dimensionless numbers: (1) Reynolds number R_e and Weissenberg number W_i as well as (2) their ratio X [23]. The oscillatory instabilities in the flow, the so-called elastic turbulence, represent the characteristic of large $W_i > 1$ and vanishingly small $R_e \rightarrow 0$ number [24]. The underlying mechanism of this oscillatory phenomenon is related to the coupling of the collective cell migration with the viscoelastic force, which resists the movement. The viscoelastic force arises as a consequence of the residual stress accumulation. While stress relaxation time corresponds to a time scale of minutes, the residual stress accumulation corresponds to a time scale of hours [8, 9, 27]. The parameters R_e and W_i can be estimated based on experimental data from the literature such as (1) the cell velocity $v_x \sim 0.5\ \frac{\mu m}{\min}$ [2]; (2) the characteristic length $L = v_x \Delta\tau$ (where $\Delta\tau$ is the period of oscillation equal to $\Delta\tau \approx 4 - 6\ h$, [2]); (3) the density of cells could be close to the density of water, i.e., $\rho \sim 1\ \frac{g}{cm^3}$; (4) the viscosity of epithelium $\eta = 4.4 \times 10^5\ Pas$ [27]; (5) the stress relaxation time $\tau_R = 3 - 14$ min [24]; and (6) the characteristic time of residual stress accumulation corresponds to the period of mechanical oscillations $\Delta\tau$ [2, 3]. Instead of W_i, we formulated the effective value of the Weissenberg number, which accounts for the characteristic time for the residual stress accumulation equal to $W_{i\,eff} = W_i \frac{\Delta\tau}{\tau_R}$. Corresponding dimensionless numbers are $R_e \sim 10^{-15}$, $W_{i\,eff} \sim 0.3$, while $X \sim 10^{14}$. Groisman and Steinberg [23] distinguished critical experimental conditions for the appearance of oscillatory instabilities during flow of polyacrylamide in viscous sugar syrup as a consequence of stress relaxation. They pointed out that critical parameters are $R_e = 0.3$ and $W_i = 3.5$. Generation of oscillatory instabilities in 2D collective cell migration has been experimentally confirmed [2, 3]. For deeply understanding of this complex phenomenon, it is necessary to consider the viscoelasticity of multicellular systems.

CELL LONG-TIME REARRANGEMENT DURING COLLECTIVE CELL MIGRATION: MODELING CONSIDERATION

Cell long-time rearrangement caused by collective cell migration should be discussed based on formulated interrelations between various variables such as (1) cell velocity $\vec{\boldsymbol{v}}_c$ as a function of matrix viscoelasticity $\tilde{\boldsymbol{\sigma}}_m = \tilde{\boldsymbol{\sigma}}_m(\tilde{\boldsymbol{\varepsilon}}_m)$, cell viscoelasticity $\tilde{\boldsymbol{\sigma}}_c = \tilde{\boldsymbol{\sigma}}_c(\tilde{\boldsymbol{\varepsilon}}_c)$, and cell surface tension γ_{st} and (2) cell packing density n as a function of cell velocity, matrix density ρ, and matrix viscoelasticity (where $\tilde{\boldsymbol{\sigma}}_c$ is the cell stress, $\tilde{\boldsymbol{\varepsilon}}_c$ is the cell strain, $\tilde{\boldsymbol{\sigma}}_m$ is the matrix stress, and $\tilde{\boldsymbol{\varepsilon}}_m$ is the matrix strain). The interrelations between various variables are shown in **Figure 1**.

Consequently, the modeling consideration accounts for the following steps: (1) the expression of cell velocity $\vec{\boldsymbol{v}}_c$ as the rate of change the cell displacement field, i.e., $\frac{d\vec{\boldsymbol{u}}_c}{d\tau}$ (where $\vec{\boldsymbol{u}}_c$ is the cell displacement field) [8, 9]; (2) the formulation of local cell shear and volumetric strains $\tilde{\boldsymbol{\varepsilon}}_{cS}$ and $\tilde{\boldsymbol{\varepsilon}}_{cv}$, respectively, as a function of the cell displacement field [8, 9]; (3) the introduction of a constitutive viscoelastic model for cells $\tilde{\boldsymbol{\sigma}}_c = \tilde{\boldsymbol{\sigma}}_c(\tilde{\varepsilon}_c)$ (where $\tilde{\boldsymbol{\sigma}}_c$ is the cell stress and $\tilde{\boldsymbol{\varepsilon}}_c$ is the cell strain) [28, 29]; (4) the formulation of the rate of change the matrix displacement field $\frac{d\vec{\boldsymbol{u}}_m}{d\tau}$ as a function of $\frac{d\vec{\boldsymbol{u}}_c}{d\tau}$ [29, 30], (5) the formulation of local matrix shear and volumetric strains $\tilde{\boldsymbol{\varepsilon}}_{mS}$, $\tilde{\boldsymbol{\varepsilon}}_{mv}$, respectively, as a function of the matrix displacement field [29, 30]; (6) the discussion of the rheological behaviors of various matrix applied as a substrate for 2D collective cell migration $\tilde{\boldsymbol{\sigma}}_m = \tilde{\boldsymbol{\sigma}}_m\left(\tilde{\boldsymbol{\varepsilon}}_m\right)$ (where $\tilde{\boldsymbol{\sigma}}_m$ is the matrix stress and $\tilde{\boldsymbol{\varepsilon}}_m$ is the matrix strain) [2, 3, 30]; (7) the formulation of changing the cell packing density $n(r, \tau)$ as function of various fluxes, such as cell convective flux, conductive flux, durotaxis flux, haptotaxis flux, and galvanotaxis flux [15]; (8) the expression of matrix density change $\frac{\partial\rho}{\partial\tau}$ as a function of matrix convective flux [15]; (9) the formulation of forces that influences cell long-time rearrangement such

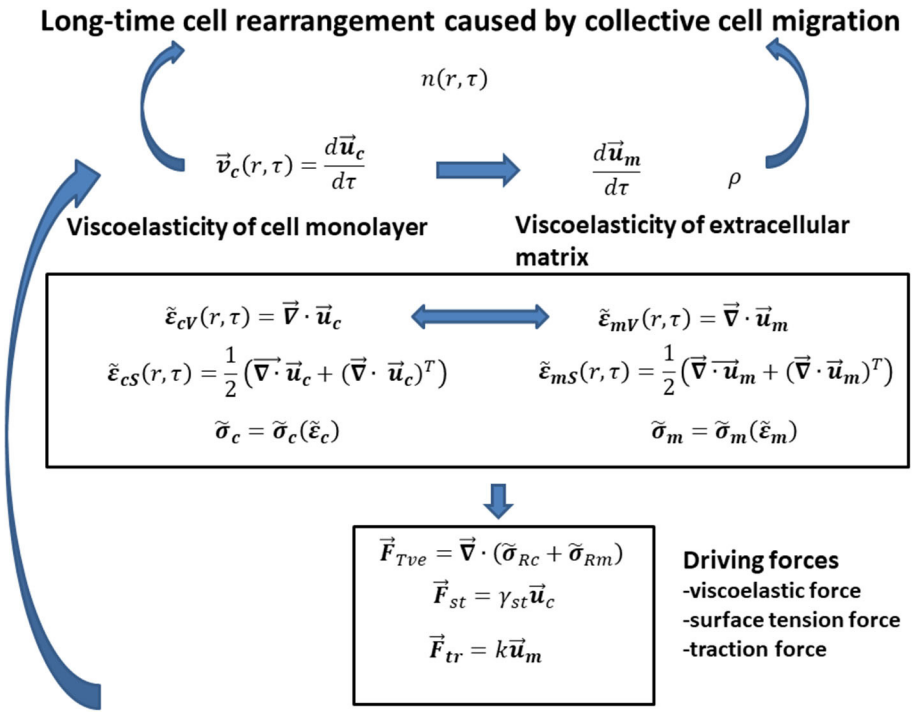

FIGURE 1 | The schematic representation of interrelations between main model parameters that influence the generation of mechanical waves during (1) monolayer free expansion and (2) cell swirling motion within a confluent monolayer.

as the viscoelastic force, the traction force, and the surface tension force based on modified model proposed by Murray et al. [15]; and (10) the formulation of the interrelation between the cell velocity $\vec{v}_c$ and the forces that influences generation of propagative waves and standing wave based on the corresponding momentum balance. Discussion of cell long-time rearrangement in the context of the elastic turbulence proposed by Groisman and Steinberg [23] is the main goal of this paper.

Viscoelasticity of Multicellular Systems

Viscoelasticity of multicellular systems caused by collective cell migration has been considered on two time scales [8, 9]. The stress relaxation happens at a short-time scale t, whereas the long time scale τ is important for tracking the strain change and the residual stress accumulation as shown in **Figures 2A,B** for (A), a monolayer free expansion inspired by Serra-Picamal et al. [2], and (B), swirling motion of a confluent monolayer inspired by Notbohm et al. [3].

Stress relaxation is primarily induced by adaptation of adhesion contacts and cell shapes [16, 31], which occur at time scale of minutes. However, the local change of strain caused by collective cell migration is slower and occurs at time scale of hours. This long time scale corresponds to collective cell migration, which accounts for cumulative effects of various biochemical processes such as cell signaling and gene expression [6, 32].

Cell velocity $\vec{v}_c$ can be expressed as follows:

$$\vec{v}_c(r,\tau)=\frac{d\vec{u}_c}{d\tau} \tag{1}$$

where $\vec{u}_c$ is the cell displacement field. The cell local velocity is influenced by various forces such as the viscoelastic force, the traction force, and the surface tension force. Detailed description of the forces and formulation of the force balance is necessary for understanding the mechanical waves. Corresponding cell local volumetric and shear strains depend on $\vec{u}_c$ and can be expressed as follows [8, 9]:

$$\begin{aligned}\tilde{\varepsilon}_{cV}(r,\tau) &= \left(\vec{\nabla}\cdot\vec{u}_c\right)\tilde{I}\\ \tilde{\varepsilon}_{cS}(r,\tau) &= \frac{1}{2}\left(\vec{\nabla}\vec{u}_c+(\vec{\nabla}\vec{u}_c)^T\right)\end{aligned} \tag{2}$$

where $\tilde{I}$ is the identity tensor, $\tilde{\varepsilon}_{cV}(r,\tau)$ is the cell volumetric strain, and $\tilde{\varepsilon}_{cS}(r,\tau)$ is the cell shear strain. Strains induce generation of stress within a cell monolayer. Collective cell migration induces inhomogeneous distribution of stress [9]. Tambe et al. [1] considered long-time residual stress distribution within collective migrated epithelial cell monolayers. Consequently, stress relaxation phenomena have not been reconstructed from their data. Maximum stress accumulation corresponds to 100–150 Pa [1]. However, Marmottant et al. [27] considered stress relaxation of cellular aggregate under constant strain (i.e., the aggregate shape) condition caused by

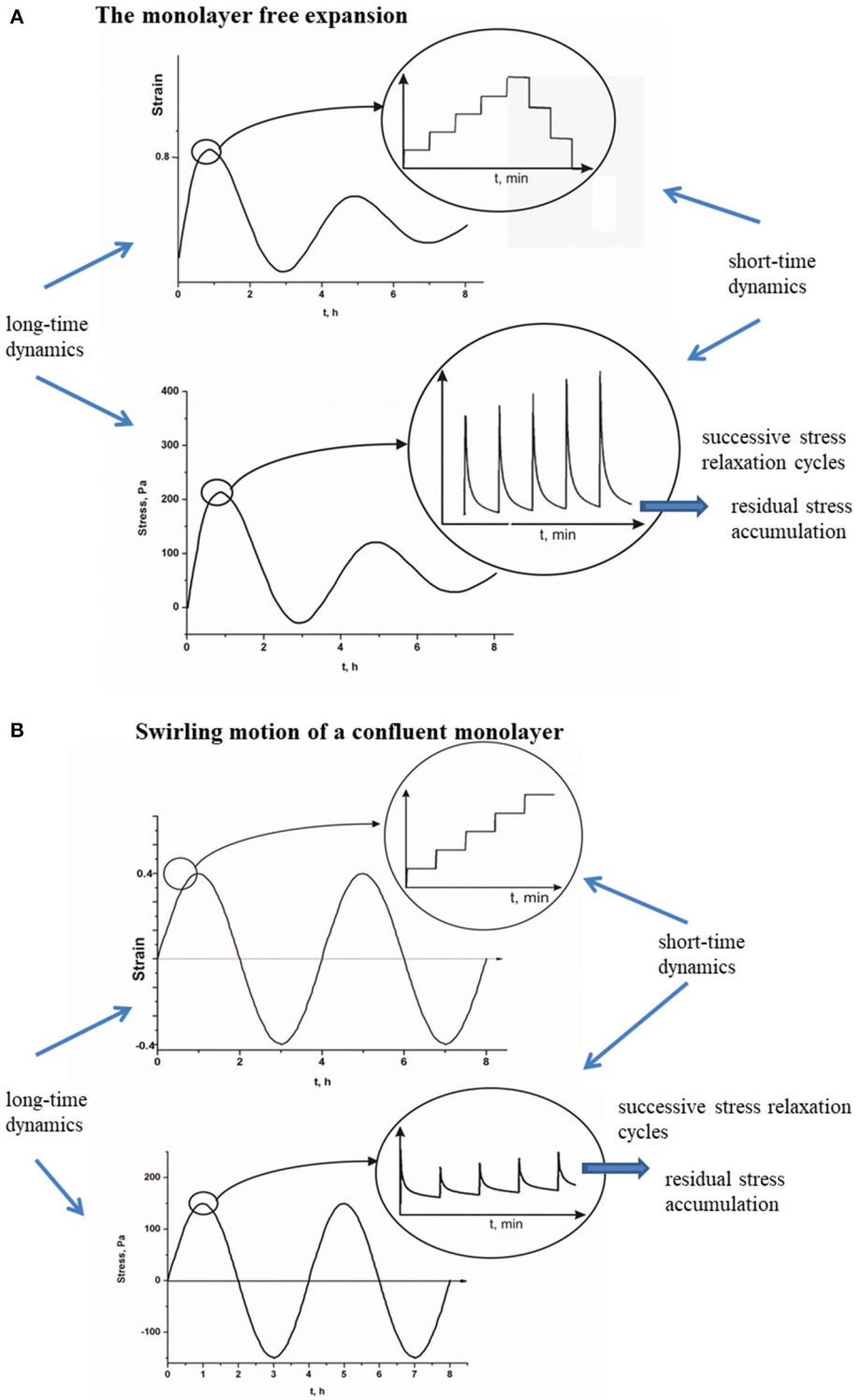

FIGURE 2 | (A,B) Short-time relaxation cycles of cell stress and long-time residual stress accumulation for propagative and standing waves.

the aggregate uniaxial compression between parallel plates. The stress decreases exponentially with the relaxation time equal to 3–14 min up to equilibrium value. Stress relaxes from ∼27 Pa to the residual stress value equal to ∼17 Pa during 25 min [27]. This time period corresponds to a short-time cycle. On the other hand, the strain is constant during the short-time cycle and changes

from one stress cycle to another. Maximum average strain rate in x-direction during monolayer free expansion is $\dot{\varepsilon}_{xx} \approx 0.29\ h^{-1}$ [2], while the corresponding period of oscillation is 4–6 h [2, 3].

Stress relaxation ability under constant strain condition represents the characteristic of the viscoelastic solid rather than viscoelastic liquid. The Maxwell model suitable for viscoelastic liquid describes stress relaxation under constant strain rate [20]. However, in the case we considered, the strain change was much slower than the stress relaxation [8, 9]. Accordingly, stress relaxes under constant strain per short-time cycle. Cell stress at a supracellular level accounts for cumulative effects of cell–cell and cell–matrix interactions [17, 33]. Cell–cell interactions influence generation of active forces as a product of the contractility of actomyosin cytoskeleton and cell's protrusions in the polarization direction. Passive forces accounts for deformation of cells during their migration. Cumulative effects of cell–cell and cell–matrix frictions influence energy dissipation obtained at a long time scale. The cell stress accounts for normal stress and shear stress contributions [9]. Normal and shear stresses consist of elastic and viscous parts and can be expressed as follows: $\tilde{\boldsymbol{\sigma}}_{cV} = \tilde{\boldsymbol{\sigma}}_{cVe} + \tilde{\boldsymbol{\sigma}}_{cVvis}$ for volumetric stress and $\tilde{\boldsymbol{\sigma}}_{cS} = \tilde{\boldsymbol{\sigma}}_{cSe} + \tilde{\boldsymbol{\sigma}}_{cSvis}$ for shear stress (where $\tilde{\boldsymbol{\sigma}}_{cVe}$ and $\tilde{\boldsymbol{\sigma}}_{cSe}$ are elastic contributions, while $\tilde{\boldsymbol{\sigma}}_{cVvis}$ and $\tilde{\boldsymbol{\sigma}}_{cSvis}$ are viscous contributions, respectively), similarly as was formulated by Murray et al. [15] for viscoelastic systems. The simplest constitutive model for a viscoelastic solid capable to describe stress relaxation is the Zener model [28]. The Zener model is expressed as follows:

$$\tilde{\boldsymbol{\sigma}}_c + \tau_R \dot{\tilde{\boldsymbol{\sigma}}}_c = G\tilde{\boldsymbol{\varepsilon}}_c + \eta\dot{\tilde{\boldsymbol{\varepsilon}}}_c \tag{3}$$

where $\dot{\tilde{\boldsymbol{\sigma}}}_c = \frac{d\tilde{\boldsymbol{\sigma}}_c}{d\tau}$, $\dot{\tilde{\boldsymbol{\varepsilon}}}_c = \frac{d\tilde{\boldsymbol{\varepsilon}}_c}{d\tau}$, G_c is the elastic modulus, and η is the viscosity. The relaxation of stress under constant strain condition $\tilde{\boldsymbol{\varepsilon}}_{c0}(r,\tau)$ is as follows:

$$\tilde{\boldsymbol{\sigma}}_c(r,t,\tau) = \tilde{\boldsymbol{\sigma}}_{c0}\, e^{-\frac{t}{\tau_R}} + \tilde{\boldsymbol{\sigma}}_{cR}(r,\tau)\left(1 - e^{-\frac{t}{\tau_R}}\right) \tag{4}$$

where t is the short-time scale, τ is the long time scale, $\tilde{\boldsymbol{\sigma}}_{c0}(\tau)$ is the initial value of the stress for single short-time relaxation cycle, and the stress relaxation time is $\tau_R = \frac{\eta}{G_c}$. The residual stress $\tilde{\boldsymbol{\sigma}}_{cR}(r,\tau)$ is equal to

$$\tilde{\boldsymbol{\sigma}}_{cR}(r,\tau) = G_c\, \tilde{\boldsymbol{\varepsilon}}_{c0}(r,\tau) \tag{5}$$

Notbohm et al. [3] considered 2D cell swirling motion within a confluent monolayer by monitoring long-time change of stress radial component σ_{crrR}. They pointed out that the long-time change of residual stress $\frac{d\sigma_{crrR}}{d\tau}$ correlated well with the long-time strain change $\frac{d\varepsilon_{crr}}{d\tau}$ during the time period of 24 h. This result indicates that the Zener model could be suitable for describing the viscoelasticity of cell monolayers because it accounts for experimentally obtained correlations between $\frac{d\sigma_{crrR}}{d\tau}$ and $\frac{d\varepsilon_{crr}}{d\tau}$ and describes the stress relaxation. The residual stress accumulation represents the consequence of generated strain and its long-time change [9, 34]. This cause–consequence relation is expressed by the constitutive model (Equations 1–5). The residual stress accumulation induces local stiffening of the monolayer, which is responsible for generation of flow instabilities. Pajic-Lijakovic and Milivojevic [8, 9, 34] pointed out that the residual stress accumulation can suppress cell migration by decreasing cell velocity and local strain. On that basis, this stress accumulation is a main cause of the generation of apparent inertial effects, which results in the elastic turbulence. For deeper insight into the influence of cell viscoelasticity on the cell velocity in the form of apparent inertial effects, it is necessary to formulate a force balance for (1) monolayer free expansion and (2) cell swirling motion within a confluent monolayer. Besides the viscoelasticity of cells, the viscoelasticity of a supracellular matrix significantly influences cell long-time rearrangement in the context of durotaxes, haptotaxis, and galvanotaxes [15].

Viscoelasticity of an Extracellular Matrix

Various hydrogel matrices have been used as a substrate for cell migration. The rheological behavior of hydrogels frequently corresponds to a poroviscoelasticity [35]. The matrix stress relaxation phenomena caused by cell tractions include (1) the hydrogel viscoelastic relaxation and (2) poroelastic relaxation caused by solvent diffusion. Polyacrylamide gel coated by collagen has been a widely used matrix for 2D cellular systems [1–3]. Hydrogels of natural origins are basement membrane–based gel preparations; some examples include fibrin gel, collagen gel, alginate gel, chitosan gel, and Matrigel [15, 30, 35, 36]. Matrigel is a commercially available basement membrane based gel. These cell–matrix systems are suitable for considering collective cell migration in 2D and 3D. Chaudhuri et al. [37] considered the influence of Ca-alginate viscoelasticity on cell spreading. Chaudhuri et al. [37] and Pajic-Lijakovic et al. [30] proposed the Burgers model for describing the viscoelasticity of Ca-alginate hydrogel. Various hydrogel matrices have been treated as elastic [1–3], while the others have been treated as a viscoelastic [26, 36]. Murray et al. [15] proposed the Kelvin-Voigt model for describing the viscoelasticity of fibrous extracellular matrices. Pajic-Lijakovic et al. [29] described the long-time change of the matrix displacement field $\frac{d\vec{\boldsymbol{u}}_m}{d\tau}$ by cell action as follows:

$$\frac{d\vec{\boldsymbol{u}}_m(r,\tau)}{d\tau} = \frac{\delta F_m}{\delta \vec{\boldsymbol{u}}_m} + \frac{d\vec{\boldsymbol{u}}_c(r,\tau)}{d\tau} \tag{6}$$

where F_m is the free energy function that accounts for cell–matrix mechanical and electrostatic interactions, and $\vec{\boldsymbol{u}}_c(r,\tau)$ is the cell displacement field. The first term of the right-hand side of Equation (6) accounts for the rheological response of a matrix caused by its structural changes, whereas the second one represents the driving force for the matrix displacement field fluctuations. The corresponding matrix volumetric and shear strains are equal to

$$\begin{aligned} \tilde{\boldsymbol{\varepsilon}}_{mV}(r,\tau) &= (\vec{\nabla} \cdot \vec{\boldsymbol{u}}_m)\tilde{\boldsymbol{I}} \\ \tilde{\boldsymbol{\varepsilon}}_{mS}(r,\tau) &= \frac{1}{2}\left(\vec{\nabla}\vec{\boldsymbol{u}}_m + (\vec{\nabla}\vec{\boldsymbol{u}}_m)^T\right) \end{aligned} \tag{7}$$

where $\tilde{\boldsymbol{\varepsilon}}_{mV}(r,\tau)$ is the matrix volumetric strain and $\tilde{\boldsymbol{\varepsilon}}_{mS}(r,\tau)$ is the matrix shear strain. Corresponding matrix stress-strain constitutive model $\tilde{\boldsymbol{\sigma}}_m = \tilde{\boldsymbol{\sigma}}_m(\tilde{\boldsymbol{\varepsilon}}_m)$ depends on the choice of the

matrix and the type of cells (where $\tilde{\boldsymbol{\sigma}}_m$ is the matrix stress). Cell traction force depends on the matrix displacement field and was expressed as $\overrightarrow{\boldsymbol{F}}_{tr} = k\overrightarrow{\boldsymbol{u}}_m$ (where k is an elastic constant) [15]. Pajic-Lijakovic et al. [30] considered residual stress accumulation $\tilde{\boldsymbol{\sigma}}_{Rm}$ within Ca-alginate hydrogel matrix without cells. It is useful in order to estimate cell–matrix interactions. They pointed out that the increase in the residual stress within the Ca-alginate matrix was significant (∼7 kPa) after 10 repeated cycles, even under a low externally induced compression strain of 2% per cycle.

Cell migration speed, cell packing density, and correlation of cell migration depend on cell–matrix mechanical and electrostatic interactions, which influence the state of cell–matrix adhesion contacts and on that basis the state of single cells. Viscoelasticity of matrix influences accumulated stress within a monolayer and on that basis the correlation of cell migration [38]. Intensive cell stress accumulation can perturb and even suppress cell migration. This cause–consequence relation was to be discussed based on (1) the rate of change the cell packing density [15] and (2) the force balance formulated by modified the model proposed by Murray et al. [15]. The cell speed has been correlated with the matrix stiffness. The speed of migrating cells is lower at softer matrices due to weak traction and cell slipping [39]. However, high matrix stiffness leads to a decrease in the migration speed caused by cell–matrix adhesion strengthening. Thus, medium matrix stiffness is suitable for cell migration. The relation between matrix stiffness and cell spreading can be expressed in the form of durotaxis flux $\overrightarrow{J}_d$ [15] as follows:

$$\overrightarrow{J}_d = k_d n \overrightarrow{\nabla} G_{sm} \tag{8}$$

where k_d represents a measure of cell–matrix mechanical interactions, which influence the matrix displacement field $\overrightarrow{\mathbf{u}}_m$ and the state of cell–matrix adhesion contacts, $n(r,\tau)$ is the packing density of cells, and G_{sm} is the elastic shear modulus of a matrix. Besides of the matrix viscoelasticity, the matrix density is also influenced by cell–matrix interaction. Long-time change of the matrix density has the feedback impact on the packing density of cells as well. The phenomenon can be expressed in the form of haptotaxis flux [15] as follows:

$$\overrightarrow{J}_h = k_h n \overrightarrow{\nabla} \rho \tag{9}$$

where k_h is the measure of cell–matrix interactions which influences the matrix density ρ. Change of the matrix density ρ caused by cell tractions has been described by Murray et al. [15] in the form of matrix convective flux as:

$$\frac{\partial \rho}{\partial \tau} = -\overrightarrow{\nabla} \cdot \left(\rho \frac{d\overrightarrow{\mathbf{u}}_m}{d\tau} \right) \tag{10}$$

where $\frac{d\overrightarrow{\mathbf{u}}_m}{d\tau}$ is the matrix displacement field change expressed by Equation (6). Cell tractions induce water outflow from the hydrogel by changing its density as well as the rheological behavior. Polyelectrolyte nature of matrix influences cell–matrix electrostatic interactions as well as the state of cell–matrix adhesion contacts. The good example is Ca-alginate hydrogel matrix [30]. Electrostatic interchain and intrachain interactions caused by cell tractions influence the residual stress accumulation within a matrix $\tilde{\boldsymbol{\sigma}}_{mR}$, which has the feedback impact to the matrix local stiffness. The phenomenon can be expressed in the form of galvanotaxis flux [15] as follows:

$$\overrightarrow{J}_g = k_g n \overrightarrow{\nabla} \phi_e \tag{11}$$

where k_g is the measure of cell–matrix electrostatic interactions, and ϕ_e is the local electrostatic potential.

Long-Time Change of Cell Packing Density

Cell packing density change $\frac{\partial n(r,\tau)}{\partial \tau}$ is a product of cell–cell and cell–matrix interactions. It is self-regulated property due to the contact inhibition during collective cell migration and force-induced cell repolarization [17, 39]. Several processes have been accounted for such behaviors as follows: (1) contact inhibition of locomotion (CIL), (2) contact following of locomotion, and (3) contact enhancement of locomotion [17]. Cell packing density change during collective cell migration is expressed as follows [15]:

$$\frac{\partial n(r,\tau)}{\partial \tau} = -\overrightarrow{\nabla} \cdot \overrightarrow{J} \tag{12}$$

where $\overrightarrow{J}$ is the flux of cells equal to $\overrightarrow{J} = \overrightarrow{J}_{conv} + \overrightarrow{J}_{cond} + \sum_i \overrightarrow{J}_i$, such that $\overrightarrow{J}_{conv} = n\overrightarrow{v}_c$ is the convective flux, $\overrightarrow{v}_c$ is cell velocity (Equation 1), $\overrightarrow{J}_{cond} = -D_{eff}\overrightarrow{\nabla} n$ is the conductive flux, D_{eff} is the effective diffusion coefficient, and $\overrightarrow{J}_i = k_i n \overrightarrow{\nabla} \phi_i$, are haptotaxis, durotaxis, plitotaxis, galvanotaxis, and chemotaxis fluxes such that $\phi \equiv \rho$ is the matrix density for the haptotaxis, $\phi \equiv \phi_e$ is the electrostatic potential for the galvanotaxis, $\phi \equiv c$ is the concentration of nutrients for the chemotaxis, $\phi \equiv G_{sm}$ is the local shear modulus of a matrix for the durotaxis, $\phi \equiv G_{sc}$ is the local shear modulus of cells for plitotaxis, whereas k_i is the model parameter that accounts for various types of interactions such as mechanical, electrostatic, or chemical. Conductive flux accounts for cell response to a local variation of cell density. Haptotaxis, durotaxis, and galvanotaxis fluxes account for cell–matrix mechanical and electrostatic interactions. The tractions exerted by cells on the matrix generate gradients in (1) the matrix density and correspondingly the haptotaxis flux, (2) the electrostatic potential and the galvanotaxis flux, and (3) the matrix stiffness and the durotaxis flux [15]. Chemotaxis flux accounts for cell response to a concentration of nutrients [15]. Plitotaxis flux represents the consequence of cell–cell mechanical interactions, which leads to the establishing of gradients in cell shear modulus. Cell mitosis is neglected at this time scale. Rieu et al. [40] reported that diffusion coefficient for collectively migrated endodermal cells is $D_{eff} = 0.45 \pm 0.2\ \frac{\mu m^2}{\min}$, whereas for ectodermal cells the diffusion coefficient is $D_{eff} = 1.05 \pm 0.4\ \frac{\mu m^2}{\min}$. If the conductive mechanism is dominant, the model Equation (12) becomes the second Fick's law. In this case, the solution for the density is oscillatory in space. If the convective mechanism is dominant, the oscillatory change of the cell packing density

can be induced only by oscillatory change of the cell velocity. At this step of consideration, it is necessary to determine which mechanism is dominant convective or conductive during 2D cell migration. To do so, we postulated following condition:

1. if $L_{\max} \leq \sqrt{t_C D_{eff}}$, the conductive mechanism is dominant, and
2. if $L_{\max} \gg \sqrt{t_C D_{eff}}$, the convective mechanism is dominant.

where t_C is the period of long-time oscillations equal to $t_C \approx 4-6\ h$ [2, 3], and $L_{\max}$ is the maximum velocity correlation length. As the cell packing density increases and cells become more dense and slow down their movement, the correlation length first increases to ∼10-cell lengths or $L_{\max} \sim 150\ \mu m$ and later decreases [41, 42]. The result of this simple calculation points out that the convective mechanism dominantly influences the cell packing density change, while the conductive mechanism can be neglected. This finding indicates that oscillatory changes of cell packing density come primarily from the oscillatory change of cell velocity.

Cell long-time rearrangement is described by interrelation between the following variables such as (1) the displacement of cells $\vec{\boldsymbol{u}}_c$ (Equation 1) and corresponding cell volumetric and shear strains, (2) the displacement of matrix $\vec{\mathbf{u}}_m$ (Equation 6) and corresponding matrix volumetric and shear strains, (3) the cell packing density n (Equation 12), and (4) the matrix density ρ (Equation 10). Displacement fields of cells and matrix induce generation of strains. The strains lead to generation of the corresponding stresses based on the proposed constitutive models for cells and for a matrix. Oscillatory change of one variable induces oscillatory changes of the others. For deeper understanding of this oscillatory dynamic, it is necessary to formulate the force balance for (1) monolayer expansion and (2) cell swirling motion within a confluent monolayer.

THE FORCE BALANCE

The force balance is responsible for oscillatory patterning the cell long-time rearrangement. Murray et al. [15] formulated the momentum balance by neglecting inertia effects as $\sum_i \vec{\boldsymbol{F}}_i = \mathbf{0}$. They supported this assumption by pointing out the fact that the corresponding R_e number is low. The force balance proposed by Murray et al. [15] should be expanded by accounting for the additional surface tension force $\vec{\boldsymbol{F}}_{st}$ which significantly influences the monolayer free expansion [43]. The surface tension has been recognized as one of the key parameters, which influences cell aggregate rounding after uniaxial compression [27]. The aggregate rounding occurs via collective cell migration [27]. The resulted force balance can be expressed as follows:

$$\sum_i \vec{\boldsymbol{F}}_i = \rho \vec{\boldsymbol{F}}_{tr} - \vec{\boldsymbol{F}}_{Tve} - n\vec{\boldsymbol{F}}_{st} \tag{13}$$

where $\vec{\boldsymbol{F}}_{tr} = k\vec{\boldsymbol{u}}_m$ is the cell traction force, k is an elastic constant [15], $\vec{\boldsymbol{F}}_{st} = \gamma_{st}\vec{\boldsymbol{u}}_c$ is the surface tension force, γ_{st} is the surface tension, $\vec{\boldsymbol{u}}_c$ is the cell displacement field, $\vec{\boldsymbol{F}}_{Tve}$ is the viscoelastic force per unit volume equal to $\vec{\boldsymbol{F}}_{Tve} = \vec{\nabla} \cdot (\tilde{\boldsymbol{\sigma}}_{Rc} - \tilde{\boldsymbol{\sigma}}_{Rm})$, $\tilde{\boldsymbol{\sigma}}_{\boldsymbol{Rc}}$ is the cell residual stress (Equation 5), and $\tilde{\boldsymbol{\sigma}}_{Rm}$ is the matrix residual stress. Consequently, the viscoelastic force accounts for cell and matrix contributions. The $\vec{\boldsymbol{F}}_{Tve}$ is the resistive force directed always opposite to the direction of migration. The surface tension force $\boldsymbol{n}\vec{\boldsymbol{F}}_{st}$ always acts in order to decrease a surface and on that basis to decrease a surface free energy. When cells undergo the forward flow during monolayer expansion, both forces $\vec{\boldsymbol{F}}_{Tve}$ and $n\vec{\boldsymbol{F}}_{st}$ act in the direction opposite of migration in order to resist this movement. However, when cells undergo the backward flow driven by the surface tension force $n\vec{\boldsymbol{F}}_{st}$, the viscoelastic force $\vec{\boldsymbol{F}}_{Tve}$ acts in the direction opposite of backward flow. The traction force $\boldsymbol{\rho}\vec{\boldsymbol{F}}_{tr}$ acts in the direction of cell migration and influences the rate of cell expansion depending on the rheological behavior of a matrix [3, 15, 30]. The force balance is established and perturbed many times during collective cell migration. These perturbations are primarily induced by accumulation of the residual stress within a multicellular system [8, 9] and by cell adaptation under stress conditions [16]. In order to completely understand this complex dynamic of cell long-time rearrangement, it is necessary to distinguish (1) equilibrium regimens for which $\sum_i \vec{\boldsymbol{F}}_i = 0$ and (2) perturbed regimens for which $\sum_i \vec{\boldsymbol{F}}_i \neq 0$ in various experimental conditions. Every perturbation induces change of cell velocity $\vec{\boldsymbol{v}}_c$ and corresponding strain rates $\dot{\tilde{\boldsymbol{\varepsilon}}}_{cV}$ and $\dot{\tilde{\boldsymbol{\varepsilon}}}_{cS}$, and on that basis provokes the cell rheological response, which can lead to a local softening or stiffening of monolayer parts. Local stiffening represents a consequence of the cell residual stress $\tilde{\sigma}_{Rc}$ accumulation [9]. Consequently, the momentum balance can be expressed in the form of inertial wave equation:

$$\boldsymbol{n}\frac{D\vec{\boldsymbol{v}}_c}{D\tau} = \rho\vec{\boldsymbol{F}}_{tr} - \vec{\boldsymbol{F}}_{Tve} - n\vec{\boldsymbol{F}}_{st} \tag{14}$$

where $\frac{D\vec{\boldsymbol{v}}_c}{D\tau} = \frac{\partial\vec{\boldsymbol{v}}_c}{\partial\tau} + (\vec{\boldsymbol{v}}_c \cdot \vec{\nabla})\vec{\boldsymbol{v}}_c$ is the material derivative [44]. The left-hand side of Equation (14) corresponds to the resultant force. Inertial waves, i.e., inertial oscillations, are a type of mechanical waves. The perturbations of the force balance, caused by cell viscoelasticity, represent the main cause for generation of (1) propagative waves during monolayer free expansion and (2) standing waves during collective cell migration within a confluent monolayer. Consequently, various types of perturbations were to be elaborated in more details.

Propagative Waves Generation in a Freely Expanded Monolayer: Modeling Consideration

The free expansion of a cell monolayer has been considered in 2D by using Cartesian coordinates such that $\vec{\boldsymbol{v}}_c = \vec{\boldsymbol{v}}_c(v_{cx}, v_{cy})$ (where v_x and v_y are the velocity components) [2]. The corresponding momentum balance can be expressed as follows:

For x-direction:

$$n\left(\frac{\partial v_{cx}}{\partial\tau} + v_x\frac{\partial v_{cx}}{\partial x} + v_y\frac{\partial v_{cx}}{\partial y}\right) = \rho F_{tr\,x} - F_{Tve\,x} - nF_{st\,x} \tag{15}$$

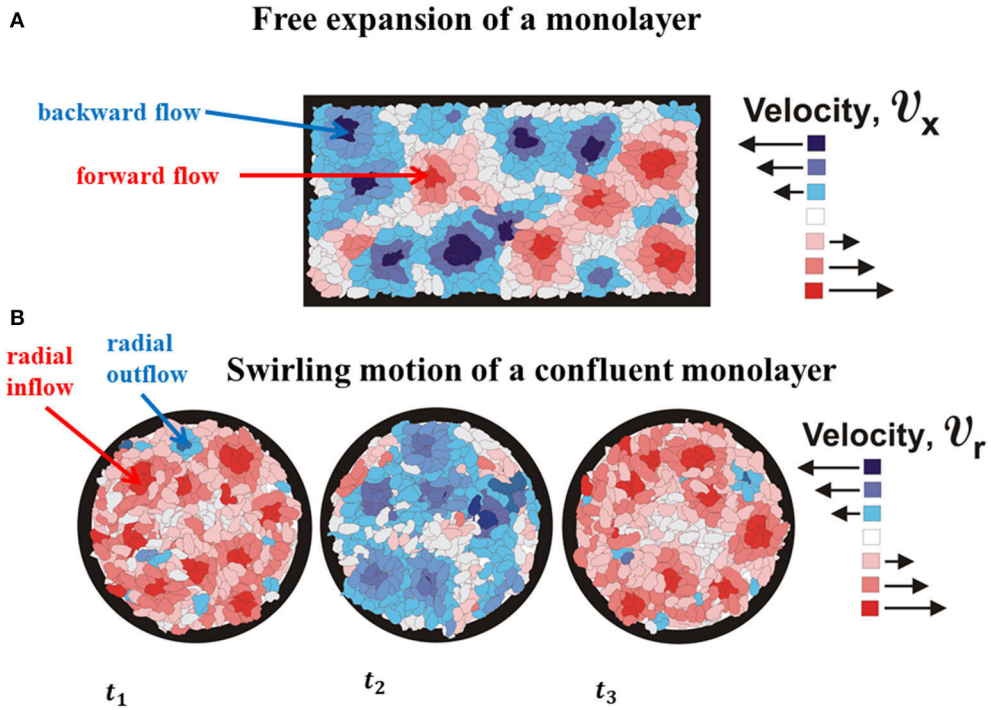

FIGURE 3 | The schematic presentation of **(A)** cell forward and backward flows as the characteristics of propagative waves and **(B)** cell outflow and inflow as the characteristics of standing waves.

For y-direction:

$$n\left(\frac{\partial v_{cy}}{\partial \tau}+v_x\frac{\partial v_{cy}}{\partial x}+v_y\frac{\partial v_{cy}}{\partial y}\right)=\rho F_{tr\,y}-F_{Tve\,y}-nF_{st\,y}$$

The monolayer expansion occurs in two opposite directions, i.e., $x \in (0, L(\tau))$ and $x \in (0, -L(\tau))$. The main characteristic of propagative waves is that (1) normal stress component σ_{cxx} and corresponding strain rate $\dot{\boldsymbol{\varepsilon}}_{cxx}$ are in phase quadrature; (2) normal stress component is always tensional; and (3) velocity and cell tractions are uncorrelated [2, 5]. These periodic extensions of multicellular domains lead to alternate softening and stiffening of cell monolayer. The periodic change of the rheological behavior is connected to the forward flow and backward flow, which is experimentally confirmed by Serra-Picamal et al. [2]. These forward flow and backward flow were shown schematically in **Figure 3**.

Serra-Picamal et al. [2] considered a free expansion of Madin-Darbvy canine kidney type II cells on polyacrylamide gels. Cellular domains that undergo forward flow can be divided into two regimens: (1) initial, unlimited cell migration, which corresponds to the condition that cell velocity increases with x, i.e., $\dot{\boldsymbol{\varepsilon}}_{cxx} > 0$; and (2) final limited cell migration, which corresponds to the condition that cell velocity decreases with x, i.e., $\dot{\boldsymbol{\varepsilon}}_{cxx} < 0$ (where $\dot{\boldsymbol{\varepsilon}}_{cxx}$ is the volumetric strain rate in x-direction equal to $\dot{\boldsymbol{\varepsilon}}_{cxx} = \frac{\partial v_{cx}}{\partial x}$ and v_{cx} is the x-component of cell velocity) [2]. Maximum velocity for the forward flow is $v_{cx}^{\max} \approx 1 \frac{\mu m}{\min}$ [2]. The characteristic of the domains with maximum cell velocity is the intensive normal and shear residual stresses accumulation up to $\sim$ 400 Pa [2]. Cellular domains that undergo backward flow are unstable primarily due to collisions with surrounding cell domains, which undergo the forward flow. These collisions additionally reduce the cell velocity within surrounding domains under forward flow. The lifetime of domains under backward flow is shorter than the period of oscillations due to (1) domain collisions and (2) rapid decrease in the surface tension force, which drives the backward flow. The phenomenon will be explained in detail in a few steps.

The initial unlimited forward flow of cellular domains leads to their extension. When the extension becomes significant, it induces (1) an increase in the resistive force $\vec{\boldsymbol{F}}_{Tve}$ caused by accumulation of the residual stress, which leads to the monolayer local stiffening; and (2) an increase in the surface tension force $n\vec{\boldsymbol{F}}_{st}$. Both forces act to suppress the cell forward flow (**Figure 4A**).

This state corresponds to the limited forward flow. Cell domains that correspond to the unlimited forward flow conditions are softer than those related to the limited forward flow conditions due to an accumulation of the cell residual stress. The local stiffening of the monolayer, which corresponds to the limited forward flow regime, is induced by the extension of adhesion contacts and force-induced repolarization (FIR) [17]. When the cell velocity tends to zero $\vec{\boldsymbol{v}}_c \rightarrow 0$ and the surface tension force $n\vec{\boldsymbol{F}}_{st}$ becomes large enough, they induce onset of the backward flow by decreasing the displacement $\vec{\boldsymbol{u}}_c$ (thus reducing the surface tension force $n\vec{\boldsymbol{F}}_{st}$ itself), which leads to

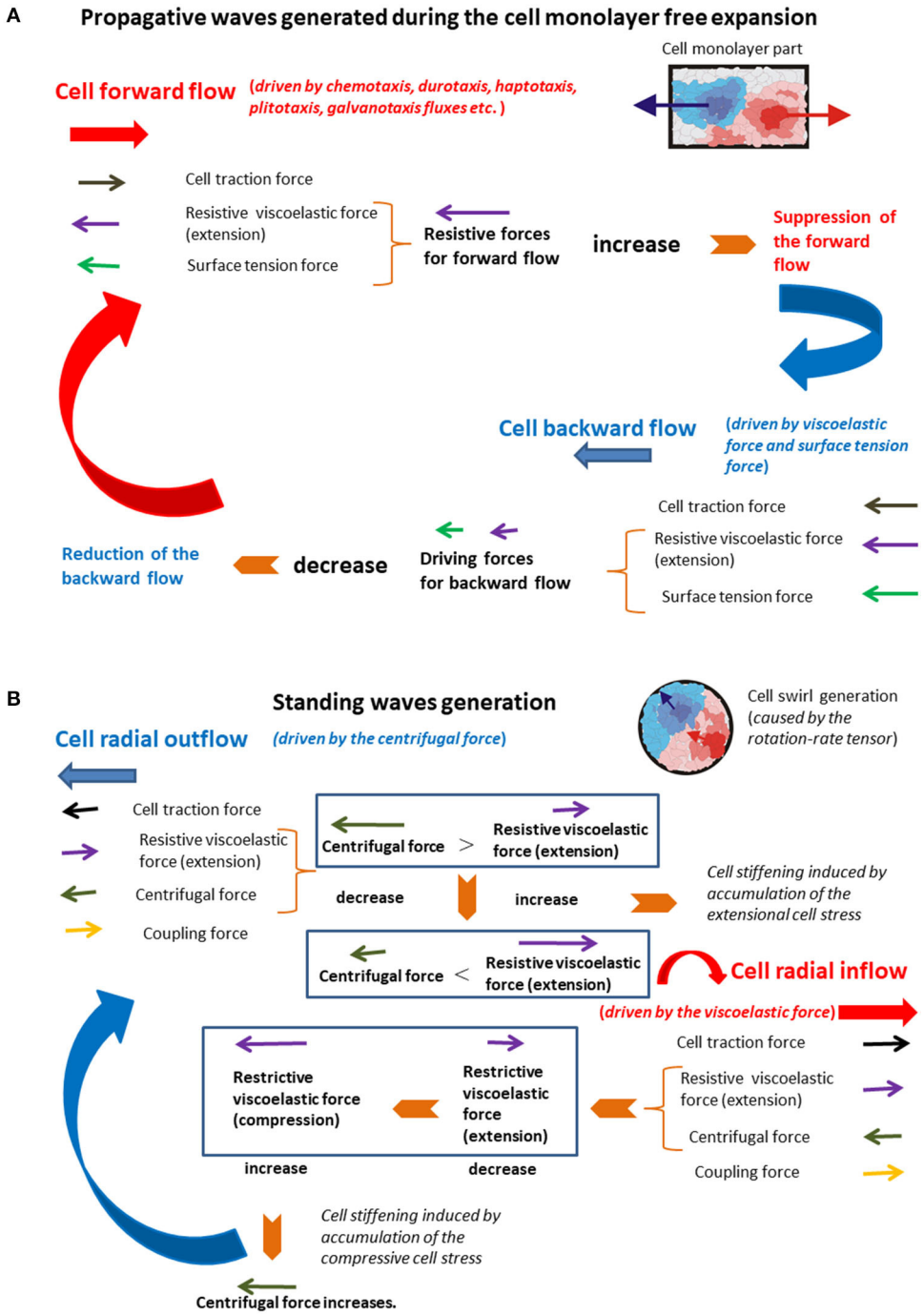

FIGURE 4 | (A,B) The schematic presentation of the force balance for the generation of **(A)** propagative waves and **(B)** standing waves.

rapid reduction of the backward flow. Collision of backward flow domains with surrounding domains under forward flow additionally suppresses the backward flow. This backward flow leads to the monolayer local softening and decreases in both forces $\vec{F}_{Tve}$ and $n\vec{F}_{st}$, which establishes the unlimited forward flow again. The action of the viscoelastic force to forward flow and backward flow is not symmetric and induce delay effects. The action of viscoelastic force and the surface tension force in order to suppress the forward flow and generate the backward flow are responsible for periodical extension of the monolayer in the form of propagative waves. Stiffer domains, which correspond to the limited forward flow regimen, form some kind of supracellular network within a monolayer. This supracellular network has a main role in keeping cellular integrity

during the monolayer free expansion. The supracellular network formation is experimentally confirmed by Serra-Picamal et al. [2]. After consideration of the standing waves generation, the comparative analysis of the main characteristics of both types of waves was to be performed from the standpoint of single cells.

Standing Waves Generation in Confluent Cell Monolayers

Collective cell migration within a confluent monolayer leads to cell swirling motion [3]. The prerequisite of cell swirl appearing is the reduction of cell polarity alignment (LA) and strong CIL as reported by Lin et al. [45]. Weak LA and strong CIL can be established under confluent environment. Collective cell migration induces a gradient of velocity field during shear flow. The gradient of the velocity field $\vec{\nabla}\vec{v}_c = \frac{1}{2}\left(\dot{\tilde{\varepsilon}}_{cS} + \dot{\tilde{\omega}}_c\right)$ can be decomposed into its symmetric and antisymmetric parts [where $\dot{\tilde{\varepsilon}}_{cS}$ is the symmetric shear-rate tensor equal to $\tilde{\dot{\varepsilon}}_{cS} = \frac{1}{2}\left(\vec{\nabla}\vec{v}_c + \left(\vec{\nabla}\vec{v}_c\right)^T\right)$ and $\dot{\tilde{\omega}}_c$ is the antisymmetric rotation-rate tensor equal to $\dot{\tilde{\omega}}_c = \frac{1}{2}\left(\vec{\nabla}\vec{v}_c - \left(\vec{\nabla}\vec{v}_c\right)^T\right)$]. The tensor $\dot{\tilde{\omega}}_c$ is responsible for the cell swirling motion if the conditions of weak LA and strong CIL are satisfied [45]. Cell swirling motion within a confluent monolayer has been considered in 2D by using cylindrical coordinates, i.e., $\vec{v}_c = \vec{v}_c(v_{cr}, v_{c\theta})$ (where v_{cr} is the radial component and $v_{c\theta}$ is the azimuthal component of velocity) [3]. A circular cell motion induces the generation of internal centrifugal force equal to $F_C = n\frac{v_{c\theta}^2}{r}$ responsible for radial extension of the swirl parts and local radial outflow such that $v_{cr} > 0$. The centrifugal force decreases with an increase in r. Consequently, the action of the centrifugal force is more intensive in the swirl core region in comparison with the peripheral region. The viscoelastic force $\vec{F}_{Tve}$ is the resistive force and acts against centrifugal force in order to suppress cell migration. The traction force $\rho\vec{F}_{tr}$ acts in the direction of cell migration and influences the rate of cell spreading depending on the rheological behavior of a matrix [3, 15, 30]. The surface tension force $n\vec{F}_{st}$ can be neglected during collective cell migration within a confluent monolayer.

The corresponding momentum balance can be expressed as follows:

For r-direction:

$$n\left(\frac{\partial v_{cr}}{\partial \tau} + v_r\frac{\partial v_{cr}}{\partial r} + \frac{v_{c\theta}}{r}\frac{\partial v_{cr}}{\partial \theta} - \frac{v_{c\theta}^2}{r}\right) = \rho F_{tr\,r} - F_{Tve\,r} \quad (16)$$

For θ-direction:

$$n\left(\frac{\partial v_{c\theta}}{\partial \tau} + v_{cr}\frac{\partial v_{c\theta}}{\partial r} + \frac{v_{c\theta}}{r}\frac{\partial v_{c\theta}}{\partial \theta} + \frac{v_{cr}v_{c\theta}}{r}\right) = \rho F_{tr\,\theta} - F_{Tve\,\theta}$$

where the internal centrifugal is equal to $F_C = n\frac{v_{c\theta}^2}{r}$, and the force that accounts for coupling between radial elongation (or compression) with azimuthal shear flow is expressed as $F_{CL} = n\frac{v_{cr}v_{c\theta}}{r}$. The coupling force F_{CL} acts to reinforce the radial flow [22].

The standing waves represent a characteristic of local cell rearrangement, which leads to swirling motion. The main characteristics of standing waves are (1) the radial velocity and cell tractions are uncorrelated, (2) normal stress component σ_{crr} and the corresponding strain rate $\dot{\boldsymbol{\varepsilon}}_{crr}$ are uncorrelated, (3) normal stress component is simultaneously tensional and compressional, and (4) time derivative of the stress component is in phase with the corresponding strain rate component [3]. Coordinated motion of close-packed cell monolayer with confining border leads to local swirling. Critical diameter of swirls is $\sim$ 250 μm, above which global rotation is substituted by smaller vortices and transient coordinated flow. This value of the critical diameter is expected if we have in mind that the velocity correlation length is $\sim$ 150 μm [5].

Notbohm et al. [3] considered confluent migration of Madin-Darbvy canine kidney type II cells on polyacrylamide gels. They reported that radial component of velocity v_{cr} simultaneously changes a direction every $\sim$ $4to6$ h. The velocity v_{cr} is approximately constant within domains $\Delta r \sim 30to40\ \mu m$ during the time period $\Delta\tau \sim 1to2\ h$ and fluctuates in the same direction within a time period of $\sim 4to6\ h$ [3]. The corresponding local strain rate is $\dot{\boldsymbol{\varepsilon}}_{crr} \approx 0$ during the time period $\Delta\tau \sim 1to2\ h$. If the $\dot{\boldsymbol{\varepsilon}}_{crr} \approx 0$, it means that the corresponding strain component is $\varepsilon_{crr} \approx const$. The maximum radial velocity is equal to $v_{cr}^{\max} \approx 0.25\ \frac{\mu m}{\min}$, while the maximum normal residual stress is $\sim 300\ Pa$ for extension and $\sim -300\ Pa$ for compression. The swirling motion of the viscoelastic multicellular system induces generation of the standing waves. This type of waves will be considered in the context of cell inflow and outflow within a swirl (**Figure 3**). Presence of inflow and outflow during a cell swirling motion is recognized experimentally by Notbohm et al. [3]. These inflow and outflow are shown schematically in **Figure 4B**.

Radial extension of swirl parts (the cell outflow for $v_{cr} > 0$ and $\frac{\partial v_{cr}}{\partial \tau} \approx 0$ during $\Delta\tau$, [3]) caused by the action of the centrifugal force induces intensive coupling between radial elongation flow and azimuthal shear flow and an increase in the viscoelastic force $\vec{F}_{Tve}$, which leads to the local system stiffening. The system stiffening leads to a decrease in the cell velocity component $v_{c\theta}$, as well as a decrease in the centrifugal force, which causes the cell radial inflow and consequently the local compression of swirl parts. The inflow is characterized by the radial component of velocity such that $v_{cr} < 0$ and $\frac{\partial v_{cr}}{\partial \tau} \approx 0$ during $\Delta\tau$ [3]. The inflow induces change of the viscoelastic force direction from extension to compression, which results in the increase in the centrifugal force. Consequently, the viscoelastic (elongation) force resists the outflow, while the viscoelastic (compressive) force resists the inflow. The increase in the centrifugal force leads to the system outflow again characterized by the radial component of velocity $v_{cr} > 0$. The centrifugal force is larger in the swirl core region in comparison with the peripheral region. Consequently, the inflow and outflow events are more intensive in the core region as was experimentally observed by Notbohm et al. [3]. The action of the viscoelastic force to the inflow and outflow is not symmetric

and induces delay effects [22]. These delay effects can induce time shift between inflow and outflow. This time shift induces perturbations of inflow–outflow dynamic, which leads to altered extension and compression of the swirl parts. These long-time cycles correspond to standing waves. Differences between these two types of mechanical waves were to be discussed from the standpoint of single cells.

RESULTS AND DISCUSSION

The aim of this theoretical consideration is to emphasize the role of viscoelasticity in provoking apparent inertial effects and generating the oscillatory mechanical instabilities in the form of standing waves and propagative waves within multicellular systems caused by collective cell migration. The propagative waves are generated during monolayer expansion, while the standing waves are generated during the cell swirling motion within a confluent monolayer. These flow instabilities represent a characteristic of the elastic turbulence that occurs under low R_e number. The phenomenon has been experimentally confirmed during flow of various viscoelastic systems such as polymer liquids [23, 25], and it has been recognized in experiments of 2D collective cell migration but has not been explained properly yet [1–3]. The elastic turbulence is induced primarily by viscoelastic force, which acts against a movement of the system constituents. The system viscoelastic response under migration is a product of the energy storage and energy dissipation caused by its structural ordering. The structural ordering accounts for orientation and deformation of the system constituents in the direction of flow, which can induce significant accumulation of residual stress and the system stiffening. The system stiffening changes the characteristic of flow, which has the feedback impact to its rheological behavior. This cause–consequence cycle can be understood in the form of apparent inertial effects, which leads to generation of mechanical waves [22].

Multicellular systems are much complex than polymer liquids, but their viscoelastic nature significantly influences characteristics of collective cell migration [8, 9]. In this case, the system structural ordering accounts for cumulative effects of various interrelated processes at cellular and supracellular levels. Processes at cellular level are cell activation, polarization, signaling, and changes the state of cell–cell and cell–matrix adhesion contacts [16, 20, 32, 46]. Processes at the supracellular level account for cumulative effects of processes at the cellular level. These are polarity alignment, polarity-flow alignment, contact regulation of locomotion, and FIR [17, 33, 47].

Generation of mechanical waves caused by collective cell migration accounts for cause–consequence relations between (1) cell packing density $n(r,\tau)$ change (Equation 12) as the result of cell–cell and cell–matrix interactions described by convective, conductive, haptotaxis, durotaxis, galvanotaxis, plitotaxis, and chemotaxis fluxes; (2) matrix density $\rho(r,\tau)$ change (Equation 10) as the result of cell–matrix interactions described by convective flux caused by cell tractions; (3) force balance equation (Equation 14), which relates cell velocity with viscoelasticity of multicellular system; viscoelasticity of a matrix; cell surface tension; cell tractions; cell packing density; and matrix density.

A long-time cell rearrangement during monolayer expansion is accomplished by local forward flow and backward flow. The forward flow is divided into two regimens unlimited forward flow and limited forward flow. The limitations come from the action of the viscoelastic force against migration. The forward flow induces an accumulation of the extensional residual stress and an increase in the resistive viscoelastic force, which leads to the stiffening of monolayer parts and suppresses cell migration. The forward flow also induces an increase in cell displacement field and on that basis an increase in the surface tension force. Once the forward flow is suppressed, the surface tension force induces the backward flow, which leads to (1) a decrease in the surface tension force itself and (2) the softening of the monolayer part. The backward flow decreases rapidly because of (1) a decrease in the surface tension force and (2) collisions with surrounding domains under forward flow. This softening results in a decrease in the viscoelastic force. Lower values of the viscoelastic force as well as the surface tension force induce forward flow of the monolayer again. Those long-time cycles repeat many times in the form of the propagative waves [2].

A long-time cell rearrangement during the cell swirling motion (within a confluent monolayer) should be considered in the context of cell radial inflow and outflow. The confluence induces reduction of cell polarity alignment, which is essential for appearing cell swirls [45]. The inflow and outflow are induced by action of the centrifugal force against the viscoelastic force. The centrifugal force leads to radial extension of swirl parts, which results in the cell outflow. This radial extension causes an increase in the viscoelastic force, which leads to the system local stiffening. The viscoelastic force suppresses cell migration by increasing the residual stress accumulation, which results in a decrease in the centrifugal force. The consequence of the centrifugal force decrease is the radial cell inflow, which leads to the softening of swirl parts. This softening causes a decrease in the viscoelastic force and consequently the increase in the centrifugal force responsible for the cell outflow again. Those long-time cycles repeat many times in the form of the standing waves [3].

Both types of waves represent a consequence of apparent inertial effects. The apparent inertial effects are related to the periodic generation of (1) the backward flow during monolayer expansion and (2) the inflow during a cell swirling motion. The maximum velocity for (1) inflow and outflow is $\sim$ 0.25 $\frac{\mu m}{\min}$, and (2) forward flow and backward flow is $\sim$ 1 $\frac{\mu m}{\min}$. The maximum extensional stress accumulated during (1) forward flow is $\sim$ 300 *Pa* and (2) outflow is $\sim$ 400 *Pa*. It would be interesting to calculate maximum extensional stress necessary to break cell–cell adherens junction (AJs). AJs are cadherin–catenin complexes linked to actin filaments. Cadherins are transmembrane glycoproteins containing an extracellular domain that mediates cell–cell adhesion via homophilic or heterophilic interactions and an intracellular domain that controls signaling cascades involved in a variety of cellular processes, including polarity, gene expression, etc. [7]. E-cadherin bond breakage requires the force of $\sim$200 nN, while the

maximum area of single AJ is $\sim 100\ \mu m^2$ [48]. It corresponds to the extensional stress equal to $\sim 2\ kPa$. This result means that forward flow and backward flow and inflow and outflow are not capable to perturb the integrity of multicellular system.

The main difference between propagative waves generated during monolayer expansion and standing waves generated during cell swirling motion within a confluent monolayer is related to oscillatory stress change. Generated propagative waves induce damped oscillatory change of the extensional residual stress, whereas the compressive stress is not generated based on the experimental data by Serra-Picamal et al. [2] (**Figure 2A**). To the contrary with the propagative waves, the generation of standing waves induces altered extension and compression [3] (**Figure 2B**). Corresponding stress oscillations were not damped during time period of 24 h. This difference can be discussed in the context of two cellular processes: (1) contact regulation of locomotion (CRL) and (2) FIR. The CRL depends strongly on the cell–cell collision angle [15, 36]. While the forward flow and backward flow act parallel to the direction of migration, the inflow and outflow act perpendicular to the direction of migration. The forward flow and backward flow intensify cell head-to-tail interactions and induce periodic cell repolarization in the direction of flow by keeping the strong of AJs [39]. Reinforced AJs are capable to resist strain and reduce residual stress accumulation [49]. Consequently, the backward flow induces a decrease in the extensional stress rather than to create cell compression. The inflow and outflow intensify cell side-to-side interactions, which can induce cell depolarization and weakening of AJs [16]. Consequently, the inflow can lead to the accumulation of compressive residual stress.

Model developed can be applied to describe generation of mechanical waves within 3D multicellular systems. Standing waves as a characteristic of the cell swirling motion (1) can be generated during migration of strongly connected cell clusters through dense environment made by cells in passive (resting) state during a tissue development [9] and (2) have been observed during migration of the internal cell group within a Neural crest supracell caused by contractions of an actin cable [18, 19]. Propagative waves could be generated during collective cell migration of stratified epithelium under *in vivo* conditions [18].

The rheological behavior of a matrix influences cell–cell and cell–matrix interactions and through the viscoelastic force influences the rate of cell spreading, as well as characteristics of generated mechanical waves.

CONCLUSION

Oscillatory instabilities in the form of mechanical waves are generated during collective cell migration such as propagative waves and standing waves. The propagative waves are generated during monolayer free expansion, whereas standing waves are generated during cell swirling motion of a confluent monolayer. Significant attempts have been made to describe the main characteristics of mechanic waves. The main characteristics of standing waves are (1) the radial velocity and cell tractions are uncorrelated; (2) radial stress component σ_{crr} and the corresponding strain rate $\dot{\boldsymbol{\varepsilon}}_{crr}$ are uncorrelated; (3) radial stress component is simultaneously tensional and compressional; and (4) time derivative of the stress component is in a phase with the corresponding strain rate. The main characteristic of propagative waves is that (1) normal stress component σ_{cxx} and corresponding strain rate $\dot{\boldsymbol{\varepsilon}}_{cxx}$ are in phase quadrature; (2) normal stress component is always tensional; and (3) velocity and cell tractions are uncorrelated. However, a little is reported about the influence of the monolayer viscoelasticity on generation of mechanical waves. Mechanical waves have recognized during flow of various viscoelastic systems under low R_e number. The phenomenon is called the elastic turbulence. The elastic turbulence has been quantified by the ratio between two dimensionless parameters such Weissenberg number and Reynolds number. These oscillatory flow instabilities have also been monitored experimentally during 2D collective cell migration.

Propagative waves represent the consequence of cell forward flow and cell backward flow during monolayer expansion driven by interrelation between forces such as the viscoelastic force, the traction force, and the surface tension force. These forces influence the rate of change of momentum and lead to periodic extensions in the direction of flow. Standing waves represent the consequence of cell radial inflow and outflow during swirling motion driven by the interrelation between the centrifugal force, the viscoelastic force, and the traction force, while the influence of the surface tension force can be neglected. This force balance leads to the periodic extension and compression in the direction perpendicular to flow. The apparent inertial effects represent the characteristic of (1) the backward flow during monolayer free expansion and (2) the inflow during the cell swirling motion within a confluent monolayer.

Additional experiments are necessary in order to determine a long-time constitutive model for 2D multicellular systems caused by collective cell migration and correlate the migrating patterns with the residual stress distribution and the rate of its change. Cell long-time rearrangement can be controlled by matrix viscoelasticity. This theoretical consideration could help in deeper understanding of various biological processes by which an organism develops its shape and heals wounds in the context of the mechanism underpinning the epithelial expansion.

AUTHOR CONTRIBUTIONS

IP-L: conceptualization, methodology, and writing—original draft preparation. MM: illustrations and writing—review and editing. All authors contributed to the article and approved the submitted version.

FUNDING

This work was supported by the Ministry of Education, Science and Technological Development of the Republic of Serbia (Contract No. 451-03-68/2020-14/200135).

ACKNOWLEDGMENTS

Authors would like to thank Dr. Giovanni Cappello for useful discussion which inspired this work.

REFERENCES

1. Tambe DT, Croutelle U, Trepat X, Park CY, Kim JH, Millet E, et al. Monolayer stress microscopy: limitations, artifacts, and accuracy of recovered intercellular stresses. *PLoS ONE.* (2013) 8:e551721-13. doi: 10.1371/journal.pone.0055172
2. Serra-Picamal X, Conte V, Vincent R, Anon E, Tambe DT, Bazellieres E, et al. Mechanical waves during tissue expansion. *Nat Phys.* (2012) 8:628–34. doi: 10.1038/nphys2355
3. Notbohm J, Banerjee S, Utuje KJC, Gweon B, Jang H, Park Y, et al. Cellular contraction and polarization drive collective cellular motion. *Biophys J.* (2016) 110:2729–38. doi: 10.1016/j.bpj.2016.05.019
4. Peyret G, Mueller R, Alessandro J, Begnaud S, Marcq P, Me'ge RM, et al. Sustained oscillations of epithelial cell sheets. *Biophys J.* (2019) 117:464–78. doi: 10.1016/j.bpj.2019.06.013
5. Petrolli V, Boudou T, Balland M, Cappello G. Oscillations in collective cell migration. In: Pajic-Lijakovic I, Barriga E, editors. *Viscoelasticity Collective Cell Migration.* Elsevier (2020). Available online at: https://www.elsevier.com/books/viscoelasticity-and-collective-cell-migration/pajic-lijakovic/978-0-12-820310-1
6. Blanchard GB, Fletcher AG, Schumacher LJ. The devil is in the mesoscale: mechanical and behavioural heterogeneity in collective cell movement. *Sem Cell Dev Biol.* (2019) 93:46–54. doi: 10.1016/j.semcdb.2018.06.003
7. Barriga EH, Mayor R. Adjustable viscoelasticity allows for efficient collective cell migration. *Sem Cell Dev Biol.* (2019) 93:55–68. doi: 10.1016/j.semcdb.2018.05.027
8. Pajic-Lijakovic I, Milivojevic M. Long-time viscoelasticity of multicellular surfaces caused by collective cell migration – multi-scale modeling considerations. *Sem Cell Dev Biol.* (2019) 93:87–96. doi: 10.1016/j.semcdb.2018.08.002
9. Pajic-Lijakovic I, Milivojevic M. Collective cell migration and residual stress accumulation: rheological consideration. *J Biomech.* (2020) 108:109898. doi: 10.1016/j.jbiomech.2020.109898
10. Doxzen K, Vedula SRK, Leong MC, Hirata H, Gov NS, Kabla AJ, et al. Guidance of collective migration by substrate geometry. *Integr Biol.* (2013) 5:1026–35. doi: 10.1039/c3ib40054a
11. Deforet M, Hakim V, Yevick H, Duclos G, Silberzan P. Emergence of collective modes and tri-dimensional structures from epithelial confinement. *Nat Comm.* (2014) 5:3747. doi: 10.1038/ncomms4747
12. Kocgozlu L, Saw TB, Le AP, Yow I, Shagirov M, Wong E, et al. Epithelial cell packing induces distinct modes of cell extrusions. *Curr Biol.* (2016) 26:2942–50. doi: 10.1016/j.cub.2016.08.057
13. Tlili S, Gauquelin E, Li B, Cardoso O, Ladoux B, Delanoë-Ayari H, et al. Collective cell migration without proliferation: density determines cell velocity and wave velocity. *R Soc Open Sci.* (2018) 5:172421. doi: 10.1098/rsos.172421
14. Banerjee S, Utuje KJC, Marchetti MC. Propagating stress waves during epithelial expansion. *Phys Rev Lett.* (2015) 114:228101. doi: 10.1103/PhysRevLett.114.228101
15. Murray JD, Maini PK, Tranquillo RT. Mechanochemical models for generating biological pattern and form in development. *Phys Rep.* (1988) 171:59–84. doi: 10.1016/0370-1573(88)90003-8
16. Iyer KV, Gomez RP, Paijmans J, Julicher F, Eaton S. Epithelial viscoelasticity is regulated by mechanosensitive e-cadherin turnover. *Curr Biol.* (2019) 29:578–91.e5. doi: 10.1016/j.cub.2019.01.021
17. Alert R Trepat X. Physical models of collective cell migration. *Annu Rev Condens Matter Phys.* (2020) 11:77–101. doi: 10.1146/annurev-conmatphys-031218-013516
18. Shellard A, Mayor R. Supracellular migration – beyond collective cell migration. *J Cell Sci.* (2019) 132:jcs226142. doi: 10.1242/jcs.226142
19. Shellard A, Mayor R. Rules of collective migration: from the wildebeest to the neural crest. *Phil Trans R Soc B.* (2020) 375:20190387. doi: 10.1098/rstb.2019.0387
20. Pajic-Lijakovic I, Milivojevic M. Viscoelasticity of multicellular surfaces. *J Biomech.* (2017) 60:1–8. doi: 10.1016/j.jbiomech.2017.06.035
21. Pajic-Lijakovic I. The basic concept of viscoelasticity. In: Pajic-Lijakovic I, Barriga E, editors. *Viscoelasticity Collective Cell Migration*. Elsevier (2020). Available online at: https://www.elsevier.com/books/viscoelasticity-and-collective-cell-migration/pajic-lijakovic/978-0-12-820310-1
22. Groisman A, Steinberg V. Mechanism of elastic instability in Couette flow of polymer solutions. *Exp Phys Fluids.* (1998) 10:2451–63. doi: 10.1063/1.869764
23. Groisman A, Steinberg V. Elastic turbulence in a polymer solution flow. *Nature.* (2000) 405:53–5. doi: 10.1038/35011019
24. Steinberg V. Scaling relations in elastic turbulence. *Phys Rev Lett.* (2019) 123:234501. doi: 10.1103/PhysRevLett.123.234501
25. Larson RG. Flow-induced mixing, demixing, and phase transitions in polymeric fluids. *Rheol Acta*. (1992) 31:497–520. doi: 10.1007/BF00367006
26. Groisman A, Steinberg V. Couette-taylor flow in a dilute polymer solution. *Phys Rev Lett.* (1996) 77:1480–3. doi: 10.1103/PhysRevLett.77.1480
27. Marmottant P, Mgharbel A, Kafer J, Audren B, Rieu JP, Vial JC, et al. The role of fluctuations and stress on the effective viscosity of cell aggregates. *Proc Natl Acad Sci USA*. (2009) 106:17271–5. doi: 10.1073/pnas.0902085106
28. Pajic-Lijakovic I, Milivojevic M. Jamming state transition and collective cell migration. *J Biol Eng.* (2019) 13:73. doi: 10.1186/s13036-019-0201-4
29. Pajic-Lijakovic I, Levic S, Nedovic V, Bugarski B. Biointerface dynamics-multi scale modeling considerations. *Col Surf B Biointerf.* (2015) 132:236–45. doi: 10.1016/j.colsurfb.2015.05.013
30. Pajic-Lijakovic I, Milivojevic M, Levic S, Trifkovic K, Stevanovic-Dajic Z, Radosevic R, et al. Matrix resistance stress: a key parameter for immobilized cell growth regulation. *Proc Biochem.* (2017) 52:30–43. doi: 10.1016/j.procbio.2016.10.017
31. Friedl P, Alexander S. Cancer invasion and the microenvironment: plasticity and reciprocity. *Cell.* (2011) 147:992–1009. doi: 10.1016/j.cell.2011.11.016
32. Petrungaro G, Morelli L, Uriu K. Information flow in the presence of cell mixing and signaling delays during embryonic development. *Sem Cell Dev Biol.* (2019) 93:26–35. doi: 10.1016/j.semcdb.2018.09.008
33. Koride S, Loza AJ, Sun SX. Epithelial vertex models with active biochemical regulation of contractility can explain organized collective cell motility. *APL Bioeng.* (2018) 2:031906. doi: 10.1063/1.5023410
34. Pajic-Lijakovic I, Milivojevic M. Viscoelasticity of multicellular systems caused by collective cell migration: dynamics at the biointerface. *Europ Biophys J.* (2020) 49:253–265. doi: 10.1007/s00249-020-01431-2
35. Kane KIW, Moreno EL, Lehr CM, Hachi S, Dannert R, Sanctuary R, et al. Determination of the rheological properties of Matrigel for optimum seeding conditions in microfluidic cell cultures. *AIP Advances.* (2018) 8:125332. doi: 10.1063/1.5067382
36. Chaudhuri O, Gu L, Darnell M, Klumpers D, Bencherif SA, Weaver JC, et al. Substrate stress regulates cell spreading. *Nat Commun.* (2015) 6:6364. doi: 10.1038/ncomms7365
37. Zhao X, Huebsch N, Mooney DJ, Suo Z. Stress-relaxation behaviour in gels with ionic and covalent crosslinks. *J App Phys.* (2010) 107:063509 1–5. doi: 10.1063/1.3343265
38. Murrell M, Kamm R, Matsudaira P. Substrate viscosity enhances correlation in epithelial sheet movement. *Biophys J.* (2011) 101:297–306. doi: 10.1016/j.bpj.2011.05.048
39. Pathak A, Kumar S. Independent regulation of tumor cell migration by matrix stiffness and confinement. *Proc Natl Acad Sci USA*. (2012) 109:10334–9. doi: 10.1073/pnas.1118073109
40. Rieu JP, Upadhyaya A, Glazier JA, Ouchi NB, Sawada Y. Diffusion and deformations of single hydra cells in cellular aggregates. *Biophys J.* (2000) 79:1903–14. doi: 10.1016/S0006-3495(00)76440-X
41. Petitjean L, Reffay M, Grasland-Mongrain E, Poujade M, Ladoux B, Buguin A, et al. Velocity fields in a collectively migrating epithelium. *Biophys J.* (2010) 98:1790–800. doi: 10.1016/j.bpj.2010.01.030
42. Puliafito A, Hufnagel L, Neveu P, Streichan S, Sigal A, Fygenson DK, et al. Collective and single cell behavior in epithelial contact inhibition. *Proc Natl Acad Sci USA.* (2012) 109:739–44. doi: 10.1073/pnas.1007809109
43. Zhao T, Zhang Y, Wei Q, Shi X, Zhao P, Chen LQ, et al. Active cell-matrix coupling regulates cellular force landscapes of cohesive epithelial

monolayers. *NPJ Comp Mat*. (2018) 10:1–6. doi: 10.1038/s41524-018-0069-8
44. Bird RB, Stewart WE, Lightfoot EN. *Transport Phenomena*. New York, NY: John Wiley & Sons INC (1960).
45. Lin SZ, Ye S, Xu GK, Li B, Feng XQ. Dynamic migration modes of collective cells. *Biophys J*. (2018) 115:1826–35. doi: 10.1016/j.bpj.2018.09.010
46. Zemel A, Rehfeldt F, Brown ACX, Disher DE, Safran SA. Optimal matrix rigidity for stress fiber polarization in stem cells. *Nat Phys*. (2010) 6:468–73. doi: 10.1038/nphys1613
47. George M, Bullo F, Campàs O. Connecting individual to collective cell migration. *Sci Rep*. (2017) 7:9720. doi: 10.1038/s41598-017-10069-8
48. Pinheiro D, Bellaiche Y. Mechanical force-driven adherens junction remodeling and epithelial dynamics. *Dev Cell*. (2018) 47:3–19. doi: 10.1016/j.devcel.2018.09.014
49. Liu Z, Tan JL, Cohen DM, Yang MT, Saidecki NJ, Ruiz SA, et al. Mechanical tugging force regulates the size of cell–cell junctions. *Proc Natl Acad Sci USA*. (2010) 107:9944–9. doi: 10.1073/pnas.0914547107

Conflict of Interest: The authors declare that the research was conducted in the absence of any commercial or financial relationships that could be construed as a potential conflict of interest.

frontiers in Physics

REVIEW
published: 04 June 2021
doi: 10.3389/fphy.2021.670571

Existing and Potential Applications of Elastography for Measuring the Viscoelasticity of Biological Tissues *In Vivo*

Kaiwen Zhang[1,2], *Min Zhu*[1,2], *Evan Thomas*[2], *Sevan Hopyan*[2,3,4]* *and Yu Sun*[1,5,6]*

[1]Department of Mechanical and Industrial Engineering, University of Toronto, Toronto, ON, Canada, [2]Program in Developmental and Stem Cell Biology, Research Institute, The Hospital for Sick Children, University of Toronto, Toronto, ON, Canada, [3]Department of Molecular Genetics, University of Toronto, Toronto, ON, Canada, [4]Division of Orthopaedic Surgery, The Hospital for Sick Children and University of Toronto, Toronto, ON, Canada, [5]Institute of Biomedical Engineering, University of Toronto, Toronto, ON, Canada, [6]Department of Electrical and Computer Engineering, University of Toronto, Toronto, ON, Canada

Mechanical tissue properties contribute to tissue shape change during development. Emerging evidence suggests that gradients of viscoelasticity correspond to cell movement and gene expression patterns. To accurately define mechanisms of morphogenesis, a combination of precise empirical measurements and theoretical approaches are required. Here, we review elastography as a method to characterize viscoelastic properties of tissue *in vivo*. We discuss its current clinical applications in mature tissues and its potential for characterizing embryonic tissues.

Keywords: elastography, viscoelasticity, *in vivo* measurement, morphogenesis, embryo

OPEN ACCESS

Edited by:
Ivana Dusan Pajic-Lijakovic, University of Belgrade, Serbia

Reviewed by:
Philip Wijesinghe, University of St Andrews, United Kingdom
Kirill Larin, University of Houston, United States
Yanping Cao, Tsinghua University, China

***Correspondence:**
Yu Sun
sun@mie.utoronto.ca
Sevan Hopyan
sevan.hopyan@sickkids.ca

Specialty section:
This article was submitted to Biophysics, a section of the journal Frontiers in Physics

Received: *21 February 2021*
Accepted: *10 May 2021*
Published: *04 June 2021*

Citation:
Zhang K, Zhu M, Thomas E, Hopyan S and Sun Y (2021) Existing and Potential Applications of Elastography for Measuring the Viscoelasticity of Biological Tissues In Vivo. *Front. Phys. 9:670571. doi: 10.3389/fphy.2021.670571*

INTRODUCTION

Viscoelasticity, among other mechanical properties, is intrinsic to biological tissue. The term implies that tissue exhibits time-dependent responses to an applied force [1–3]. Characterization of the viscoelastic behavior of biological tissue has been performed *in vitro* [4, 5], *ex vivo* [6], and *in vivo* [7, 8] to gain insight into tissue stiffness and fluidity. *In vivo* assessment is preferable to determine tissue properties in their native environment, and elastography has the advantage of minimally disturbing that environment. In brief, elastography introduces a disturbance to displace specific regions within a tissue, which is subsequently imaged and analyzed to determine the local viscoelastic response.

It is worth noting that elastography was not originally developed for the purpose of measuring viscoelastic properties. As the name indicates, in its earlier development, only elasticity (in terms of Young's modulus) was at the center of attention, lacking viscosity information (coefficient of viscosity) [9, 10]. However, as the properties of biological tissue were progressively understood, a variety of theoretical frameworks were developed and integrated with earlier elastography techniques. In recent years, although the name of elastography remains largely unchanged (some studies have adopted the term "viscoelastography" [11, 12]), it has become more common that quantitative values of various moduli, as we will discuss in detail in later sections, include information of material viscoelasticity.

In clinical settings, elastography techniques for measuring the viscoelastic properties of mature tissues have been well established *in vivo* to diagnose and distinguish among different pathologies [7, 13–16]. The motivation of shifting from measuring elasticity information to viscoelasticity information lies within the fact that as mature tissues exhibit varying degrees of viscoelastic behavior, the sufficiency and validity of solely relying on elasticity information have been

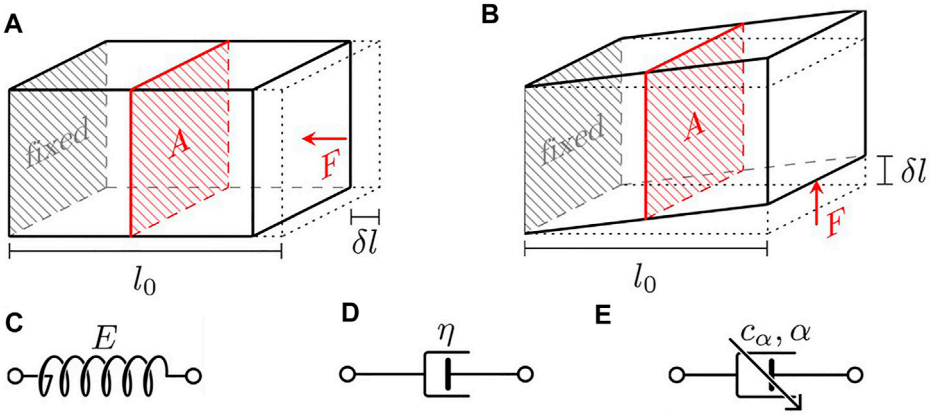

FIGURE 1 | Illustration of the definition of stress and schematics of the basic rheological elements. **(A)** Normal stress, **(B)** shear stress, **(C)** Hookean spring, **(D)** Newtonian dashpot, and **(E)** fractional springpot.

questioned [17]. For instance, elastography-based studies on assessing hepatic tumor malignancy [15, 18], benign/normal breast tissues [19], and the efficacy of cornea disease treatment [20] have reported a more prominent effect by using viscosity as the differentiator rather than elasticity. Thus, assessing the viscoelastic behavior of mature tissues is necessary to provide more accurate *in vivo* measurements and characterization, subsequently improving tumor diagnostic accuracy.

In studies of embryonic tissues, it is increasingly understood how forces generated by cells can coordinate morphogenesis [21–23]. In response to forces, embryonic tissues, which are both liquid- and solid-like, exhibit viscoelastic behavior [3, 24]. Cells have receptors that can sense physical forces as well as chemical cues. For example, cadherin molecules have both mechanical and sensory properties which are applied for adhesion and signaling, respectively [24]. It is currently challenging to perform loss and gain of function experiments of mechanical cues to define their roles *in vivo* as one can with chemical cues. Although increasingly precise tools are being developed to characterize the mechanical and viscoelastic properties of embryonic tissues [25], data supporting their efficacy are currently sparse. Albeit less explicitly discussed, the motivation to study viscoelasticity in the context of developmental biology is twofold. At the single-cell level, various membrane-enclosed and membrane-less organelles exhibit viscoelastic behavior to different degrees. The latter can take on the form of liquid droplets that undergo controlled dissolution and condensation *via* phase separation [26, 27]. The occurrence of irreversible aggregation promotes further transition of some condensates from liquid-like to solid-like [28], underlying the pathologies in many neurodegenerative diseases [29]. Thus, probing viscoelasticity at the single-cell level would potentially facilitate our understanding of how changes in compartmental viscoelasticities correlate to the phase change in condensates and overall cell behavior. At the multicell level within an embryonic tissue, gradients of stiffness measured by the Young's modulus were discovered as a cue that potentially guides cell migration by a process called durotaxis [30]. However, due to the omission of the viscous properties of ECM, durotaxis may need to be reexamined in the context of viscoelasticity to incorporate the potential role of viscosity in impeding the migratory speed. *Viscoelasticity and Developmental Biology* is dedicated to the in-depth discussion of existing and potential roles of viscoelasticity in the context of developmental biology.

TABLE 1 | Glossary of parameters.

Parameter	Symbol	SI (Derived) Unit
Elastic stress	σ	*Pa*
Shear stress	τ	*Pa*
(Complex) Creep compliance	$(J^*)\,J$	Pa^{-1}
(Complex) Relaxation modulus	$(F^*)\,F$	*Pa*
Strain	ε	Dimensionless
(Complex) Young's modulus	$(E^*)\,E$	*Pa*
Strain rate	$\dot{\varepsilon}$	s^{-1}
Coefficient of viscosity	η	*Pa s*
Complex modulus	Y^*	*Pa*
Storage modulus	Y'	*Pa*
Loss modulus	Y''	*Pa*
Angular frequency	ω	$rad\ s^{-1}$
Phase delay; loss angle	δ	*rad*
Magnitude of complex modulus	$\lvert Y\rvert$	*Pa*
Coefficient of springpot	c_α	$Pa\ s^\alpha$
Fractional exponent	α	Dimensionless
Gamma function	$\Gamma(\,)$	N/A
Amplitude of wave	A	*m*
(Complex) Angular wave number	$(k^*)\,k$	m^{-1}
Poisson's ratio	ν	Dimensionless
Propagation speed of compressional wave	c_c	$m\ s^{-1}$
Propagation speed of shear wave	c_s	$m\ s^{-1}$
(Complex) Shear modulus	$(G^*)\,G$	*Pa*
Density of medium	ρ	$kg\ m^{-3}$
Propagation speed of surface wave	c_{sf}	$m\ s^{-1}$

For the purpose of this review, the common assumption made in elastography techniques, that is, biological tissues are isotropic and homogenous, is also assumed. The definitions of elastic stress (σ), whether compressive or tensile, and shear stress (τ) are illustrated in **Figures 1A,B**, respectively. A glossary of the

major parameters discussed throughout this review, in order of appearance, is given in **Table 1**. Here, the basics of rheological models and properties of waves necessary to understand elastography (*Estimation of Material Moduli* and *Wave Properties and Parameters*), as well as the classification of existing elastography techniques used to characterize material viscoelastic properties (*Viscoelasticity Measurement with Elastography*) have been discussed. The role of viscoelasticity in the context of developmental biology (*Viscoelasticity and Developmental Biology*), the clinical applications on mature tissues and potential extension to embryonic tissues (*Current Applications of Elastography*), and an outlook to future directions (*Challenge and Outlook*) have been outlined.

ESTIMATION OF MATERIAL MODULI

The classical approach to estimating moduli that reflect the viscoelastic properties of a material is implemented by performing one of the following three canonical tests: creep, stress relaxation, and oscillatory loading. Once the data obtained from the tests, whether time-dependent or frequency-dependent, is fitted with the constitutive equation of a selected rheological model, the coefficient of each parameter within the model can be determined as an approximate representation of the viscoelastic properties of the material. Alternatively, if the constitutive equation is solved in the time domain, the Fourier transform can be taken to derive the solution in the frequency domain [31].

Classical Rheological Models

A common approach to the study of material viscoelasticity is to derive the expression of creep compliance, relaxation modulus, or their complex forms, from the constitutive equation of a linear theoretical framework. Depending on the properties of the material, differently structured rheological models can generate different levels of fit. Expressions of the creep compliance (J) and relaxation modulus (F) are commonly derived in the time domain *via* creep and stress relaxation tests. If their frequency-dependent complex forms, (J^*) and (F^*), need to be determined, oscillatory tests are conducted.

Elements of Rheological Models

Classical linear rheological models consist of various combinations of different numbers of Hookean springs, which model elastic behavior, and Newtonian dashpots, which model viscous behavior. Schematics of a Hookean spring and a Newtonian dashpot are shown in **Figures 1C,D**, respectively. Upon an applied elastic stress (σ), a Hookean spring exhibits linear elastic behavior and immediately produces an elastic strain (ε). The elasticity can be quantitatively represented by the Young's modulus (E), which determines the stiffness of the material (with units of **Pa**), *via* Hooke's law as follows:

$$E = \frac{\sigma}{\varepsilon}. \tag{1}$$

A Newtonian dashpot exhibits a viscous behavior that is proportional to the strain rate ($\dot{\varepsilon}$), which represents the change in strain with respect to time. The viscous behavior is representative of the material fluidity and is expressed (with units of **Pa s**) *via* the coefficient of viscosity (η) as follows:

$$\eta = \frac{\sigma}{\dot{\varepsilon}}. \tag{2}$$

Common two-element rheological models include the Maxwell model and the Kelvin–Voigt model. The Maxwell model consists of a Hookean spring of Young's modulus E in series with a Newtonian dashpot of coefficient of viscosity η. The Kelvin–Voigt model consists of a Hookean spring E and a Newtonian dashpot η in parallel. Models with three elements were also developed to more realistically characterize the creep-recovery and stress relaxation behavior of a viscoelastic material. These include notably the standard linear solid model, also known as the Zener model, which consists of two Hookean springs and one Newtonian dashpot arranged in one of the two equivalent configurations. The schematics of the above rheological models are illustrated in **Figures 2A–C**.

Creep and Stress Relaxation

There are two one-dimensional tests that utilize the application of a step input to examine material viscoelasticity, namely, creep and stress relaxation. The creep test assesses the time-dependent change in material strain, $\varepsilon(t)$, upon the introduction of a step stress. A stress relaxation (or relaxation) response is the time-dependent change in material stress, $\sigma(t)$, after a step strain is introduced. Data from the creep and relaxation tests are often acquired and analyzed in the time domain. For a linear viscoelastic material, the stress response to a step strain input of ε_0 is defined as follows:

$$\sigma(t) = F(t)\varepsilon_0. \tag{3}$$

Here, $F(t)$ is a monotonically decreasing function of time defined as the relaxation modulus. Similarly, if a step input of stress, σ_0, is introduced, the corresponding creep response is given as follows:

$$\varepsilon(t) = J(t)\sigma_0. \tag{4}$$

Here, $J(t)$ is a monotonically increasing function of time defined as the creep compliance. The mathematical representation of creep compliance and relaxation modulus of the three classical rheological models is summarized in **Table 2**.

Oscillatory Loading

In an oscillatory loading test, an oscillatory excitation, instead of a step input, is used to disturb the material. The material can be loaded in a time-varying manner such that the response can be examined over a range of frequencies. The complex modulus of the material, Y^*, can be determined using dynamic mechanical analysis (DMA) on the data collected with dynamic mechanical analyzers and rheometers [4, 32]. The complex modulus [33] consists of a real component, the storage modulus Y', which is the slope of the loading curve that characterizes the elastic behavior and measures the stored energy, and an imaginary component, the loss modulus Y'', which is the area bounded by the loading and unloading curves that characterizes the viscous

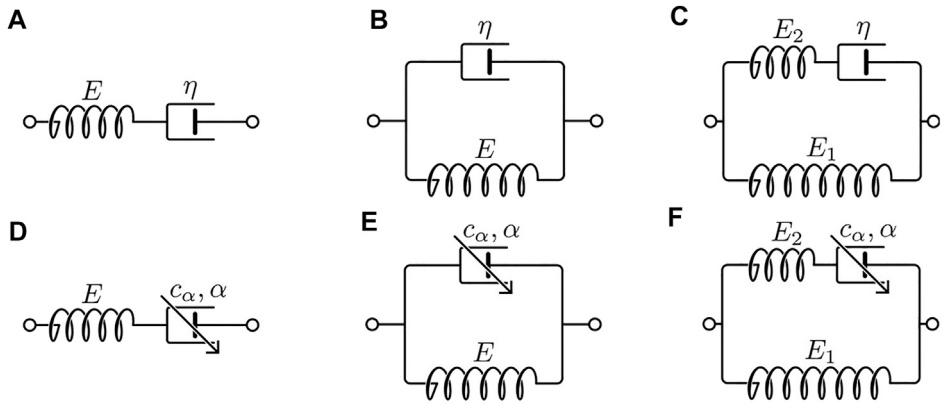

FIGURE 2 | Schematics of the classical rheological models and their fractional analogs. **(A)** Maxwell, **(B)** Kelvin–Voigt, **(C)** Zener, **(D)** fractional Maxwell, **(E)** fractional Kelvin–Voigt, and **(F)** fractional Zener.

TABLE 2 | Summary of equations of the classical rheological models.

Model name	Maxwell	Kelvin–Voigt	Zener
Constitutive equation	$\sigma + \frac{\eta}{E}\dot{\sigma} = \eta\dot{\varepsilon}$	$\sigma = E\varepsilon + \eta\dot{\varepsilon}$	$\sigma + \frac{\eta}{E_2}\dot{\sigma} = E_1\varepsilon + \eta\dot{\varepsilon} + \frac{\eta E_1}{E_2}\dot{\varepsilon}$
Step input			
Creep compliance $\boldsymbol{J(t)}$	$J(t) = \frac{1}{E} + \frac{1}{\eta}t$	$J(t) = \frac{1}{E}\left(1 - e^{-\frac{E}{\eta}t}\right)$	$J(t) = \frac{1}{E_1 + E_2} + \left(\frac{1}{E_1} - \frac{1}{E_1 + E_2}\right)\left(1 - e^{-\frac{E_1 E_2}{\eta(E_1 + E_2)}t}\right)$
Relaxation modulus $\boldsymbol{F(t)}$	$F(t) = Ee^{-\frac{E}{\eta}t}$	$F(t) = E + \eta\delta(t)$	$F(t) = E_1 + E_2 e^{-\frac{E_2}{\eta}t}$
Oscillatory input			
Complex modulus $\boldsymbol{Y^*(\omega) = Y'(\omega) + iY''(\omega)}$	$Y^*(\omega) = \frac{\omega^2\eta^2 E}{\omega^2\eta^2 + E^2} + i\frac{\omega\eta E^2}{\omega^2\eta^2 + E^2}$	$Y^*(\omega) = E + i\omega\eta$	$Y^*(\omega) = \frac{\omega^2\eta^2(E_1 + E_2) + E_1 E_2^2}{\omega^2\eta^2 + E_2^2} + i\frac{\omega\eta E_2^2}{\omega^2\eta^2 + E_2^2}$

behavior and measures the energy loss. The repetitive depiction of the stress–strain relationship allows for individual estimation of the frequency-dependent storage and loss moduli.

If an oscillatory strain input with an amplitude of ε_0 is applied to a linear material, following the Euler's formula, its time-dependent form can be written as an exponential:

$$\varepsilon(t) = \varepsilon_0 e^{i\omega t}. \tag{5}$$

The corresponding stress response will also be oscillatory with an amplitude of σ_0, but out of phase by δ with the strain input as follows:

$$\sigma(t) = \sigma_0 e^{i(\omega t + \delta)}. \tag{6}$$

This phase delay, δ, is referred to as the loss angle of the material and reflects to what degree the material is viscoelastic. If the stress and strain curves are completely in phase, the loss angle is at its minimum value of 0 and the material is considered purely elastic. If, however, completely out of phase, the loss angle maximizes at $\pi/2$ and the material is purely viscous. The material is considered viscoelastic when the phase delay is away from the boundary limits.

The complex modulus, Y^*, is calculated from the ratio of oscillatory stress to strain, in a similar fashion as how the creep compliance and the relaxation modulus were defined. The storage and loss moduli are directly equated to the real and imaginary components of the ratio as follows:

$$Y^* = \frac{\sigma(t)}{\varepsilon(t)} = \frac{\sigma_0}{\varepsilon_0}\ e^{i\delta} = \frac{\sigma_0}{\varepsilon_0}(\cos\delta + i\sin\delta) = Y' + iY''. \tag{7}$$

The tangent of the loss angle, $\tan\delta$, as well as the magnitude of the complex modulus, $|Y|$, are alternative ways to characterize the complex modulus as follows:

$$\tan\delta = \frac{Y''}{Y'}, \tag{8a}$$

$$|Y| = \sqrt{Y'^2 + Y''^2}. \tag{8b}$$

Similarly, if an oscillatory stress is applied such that $\sigma(t) = \sigma_0 e^{i\omega t}$, the ratio of oscillatory strain to stress is defined as the complex compliance J^* that is also composed of a real storage compliance (J') and an imaginary loss compliance (J'') [33]. The complex compliance is used less often due to the practical difficulty to apply and control an oscillatory stress in comparison to an oscillatory strain.

As the oscillatory loading test is often conducted in the frequency domain, the expression of the complex modulus is more often a function of frequency ($Y^*(\omega)$). Once fitted to a rheological model, the coefficients of each parameter within the model can be determined at a given frequency. The expressions of

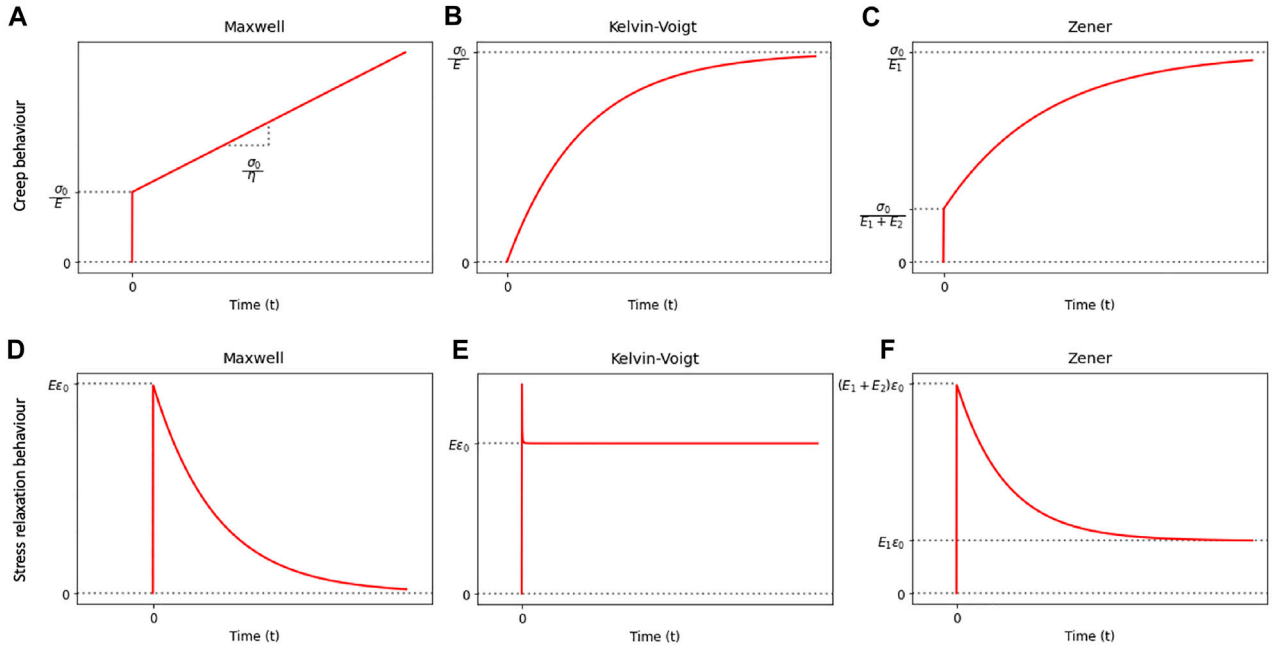

FIGURE 3 | Illustration of the creep and stress relaxation behaviors of the classical rheological models.

the complex moduli derived from the constitutive equations of classical rheological models are summarized in **Table 2**.

Limitation of Classical Rheological Models

Although classical rheological models serve as a foundational theoretical basis for the characterization of material viscoelastic behavior, they are limited by modeling accuracy. The creep and stress relaxation behaviors of the three classical rheological models are shown in **Figures 3A–F**. When an assumed Maxwell material is subjected to a step stress input of σ_0, the creep response follows a linear relationship as a function of time, which fails to realistically represent the "creeping" behavior as should be observed in a viscoelastic material (**Figure 3A**). The Kelvin–Voigt model, in comparison, can predict the creep response of a viscoelastic material more realistically as an assumed Kelvin–Voigt material creeps following an increasing exponential decay (**Figure 3B**). However, it is limited in the ability to model the relaxation response of a viscoelastic material since an impulse at $\mathbf{t} = 0$ is only idealistic (**Figure 3E**). As models of more elements were developed, including the three-element Zener model and the more generalized Maxwell and Kelvin models, the modeling accuracy was consequently improved. However, as the constitutive equations of multielement models became more complex, the analysis of model parameters became more computationally expensive.

In fact, studies using generalized models have revealed that the viscoelastic response of several biological tissues [34–37], such as the epithelial tissue, the kidney, and the liver, follows a distinctive power law behavior such that the stress–time, strain–time, and complex modulus–frequency relationships are approximately linear on a log–log scale [31, 38]. For the purpose of modeling the viscoelastic behavior of biological tissues in the common elastography frequency range of 40–1,000 Hz [31], studies have shown that the incorporation of fractional calculus into classical rheology bears modeling advantages [31, 38, 39].

Fractional Models

In fractional models, a fractional derivative element, the fractional springpot (**Figure 1E**), is introduced. The springpot is defined by its coefficient, c_α, similar to E for a Hookean spring and η for a Newtonian dashpot. The stress–strain relation as defined by a springpot [38] is given as follows:

$$\sigma(t) = c_\alpha \frac{d^\alpha \varepsilon(t)}{dt^\alpha}, \ \alpha \in [0, 1]. \tag{9}$$

Conceptually, a springpot is a generalization of the classical viscoelastic components. At the two limiting conditions, one such that the fractional exponent $\alpha = 0$, the springpot reduces to a Hookean spring and its coefficient c_α becomes E, whereas when $\alpha = 1$, the springpot reduces to a Newtonian dashpot and its coefficient becomes η. Naturally, a springpot of varying α can exhaustively represent any intermediate viscoelastic behavior bounded by the limiting conditions.

The creep and relaxation behaviors as defined in **Eqs 3**, **4** can now be characterized by the fractional creep compliance and the relaxation modulus, respectively [38], as follows:

$$J(t) = \frac{1}{c_\alpha \Gamma(1+\alpha)} t^\alpha, \tag{10a}$$

$$F(t) = \frac{c_\alpha}{\Gamma(1-\alpha)} t^{-\alpha}. \tag{10b}$$

The creep and relaxation behaviors of the springpot have been adapted to assess the viscoelastic response of a single cell alongside its subcompartments [40–42].

TABLE 3 | Summary of equations of the fractional models.

Model name	Fractional Maxwell	Fractional Kelvin–Voigt	Fractional Zener
Constitutive equation	$\sigma + \frac{c_\alpha}{E}\frac{d^\alpha \sigma}{dt^\alpha} = c_\alpha \frac{d^\alpha \varepsilon}{dt^\alpha}$	$\sigma = E\varepsilon + c_\alpha \frac{d^\alpha \varepsilon}{dt^\alpha}$	$\sigma + \frac{c_\alpha}{E_2}\frac{d^\alpha \sigma}{dt^\alpha} = E_1\varepsilon + c_\alpha \frac{d^\alpha \varepsilon}{dt^\alpha} + \frac{c_\alpha E_1}{E_2}\frac{d^\alpha \varepsilon}{dt^\alpha}$
Step input			
Creep compliance $J(t)$	$J(t) = \frac{1}{E} + \frac{1}{c_\alpha \Gamma(1+\alpha)} t^\alpha$	$J(t) = \frac{t^\alpha}{c_\alpha} E_{\alpha,1+\alpha}\left(-\frac{E}{c_\alpha} t^\alpha\right)$	$J(t) = \frac{1}{E_1 + E_2} + \frac{1}{E_1} - \frac{1}{E_1} E_{\alpha,1}\left(-\frac{E_1 E_2}{c_\alpha (E_1 + E_2)} t^\alpha\right)$
Relaxation modulus[a] $F(t)$	$F(t) = EE_{\alpha,1}\left(-\frac{E}{c_\alpha} t^\alpha\right)$	$F(t) = E + \frac{c_\alpha}{\Gamma(1-\alpha)} t^{-\alpha}$	$F(t) = E_1 + E_2 E_{\alpha,1}\left(-\frac{E_2}{c_\alpha} t^\alpha\right)$
Oscillatory input			
Complex modulus $Y^*(\omega) = Y'(\omega) + iY''(\omega)$	$Y^*(\omega) = \frac{(E\cos(\frac{\pi}{2}\alpha) + c_\alpha \omega^\alpha) E c_\alpha \omega^\alpha}{(c_\alpha \omega^\alpha)^2 + E^2 + 2E c_\alpha \omega^\alpha \cos(\frac{\pi}{2}\alpha)} + i\frac{E^2 c_\alpha \omega^\alpha \sin(\frac{\pi}{2}\alpha)}{(c_\alpha \omega^\alpha)^2 + E^2 + 2E c_\alpha \omega^\alpha \cos(\frac{\pi}{2}\alpha)}$	$Y^*(\omega) = E + c_\alpha \omega^\alpha \cos\left(\frac{\pi}{2}\alpha\right) + ic_\alpha \omega^\alpha \sin\left(\frac{\pi}{2}\alpha\right)$	$Y^*(\omega) = E_1 + \frac{E_2^2 c_\alpha \omega^\alpha \cos(\frac{\pi}{2}\alpha) + E_2 (c_\alpha \omega^\alpha)^2}{(c_\alpha \omega^\alpha)^2 + E_2^2 + 2E_2 c_\alpha \omega^\alpha \cos(\frac{\pi}{2}\alpha)} + i\frac{E_2^2 c_\alpha \omega^\alpha \sin(\frac{\pi}{2}\alpha)}{(c_\alpha \omega^\alpha)^2 + E_2^2 + 2E_2 c_\alpha \omega^\alpha \cos(\frac{\pi}{2}\alpha)}$

[a]$E_{\alpha,\beta}(t)$: *Mittag-Leffler function [173].*

Under an oscillatory input, the complex modulus of a springpot, following the definition from **Eq. 7**, can be expressed as follows:

$$Y^* = c_\alpha \omega^\alpha e^{i\delta} = c_\alpha \omega^\alpha (\cos\delta + i\sin\delta) = Y' + iY'',\ \delta = \frac{\pi}{2}\alpha. \quad (11)$$

Fractional models can be constructed from the classical models by replacing the Newtonian dashpot(s) within the original models with springpot(s). Common fractional analogs of the classical models include the fractional Maxwell model, the fractional Kelvin–Voigt model, and the fractional Zener model. Schematics of the fractional analogs are shown in **Figures 2D–F**. Expressions [38, 43] of the moduli derived based on these fractional models are summarized in **Table 3**. The creep and relaxation behaviors exhibited by the fractional models with selective values of the fractional exponent are qualitatively illustrated in **Figures 4A–F**. When α=0, η, as shown in **Figures 4A–F**, is simply replaced by an E of a different value. Furthermore, a generalized fractional model can be constructed by replacing all model elements with springpots. For an elaborated list of fractional models, analytical expressions of moduli, and illustrative behaviors, please refer to reference [38].

WAVE PROPERTIES AND PARAMETERS

This section includes the relevant wave equations that are necessary in facilitating our understanding of how a sample medium can be excited by the propagating waves and how wave parameters can be derived and used to quantify viscoelasticity of the medium. In the context of wave-based elastography techniques, the assumption of one-dimensional, time-harmonic waves that propagate rightward along the $+x$ direction in an unbounded biological medium is sufficient. We, first, restrict our discussion to pure elastic waves that propagate with no energy loss, before expanding to consider wave attenuation in a viscoelastic medium.

Wave Propagation in a Purely Elastic Medium

For a one-dimensional, time-harmonic wave that propagates rightward along the $+x$ direction in an unbounded biological medium, several equations **(Eqs 12)**–b**(16b)** have been adapted from [31, 33, 44] to demonstrate the derivation of relevant wave parameters. The displacement of particles along x at time t can be defined as follows:

$$u(x,t) = Ae^{i(\omega t - kx)}. \quad (12)$$

Here, A is the wave amplitude, and k is the wave number which is given as follows:

$$k = \frac{\omega}{c}. \quad (13)$$

In an elastic medium with known values of Poisson's ratio (ν) and the Young's modulus (E), the propagation speed of compressional wave (c_c) is as follows:

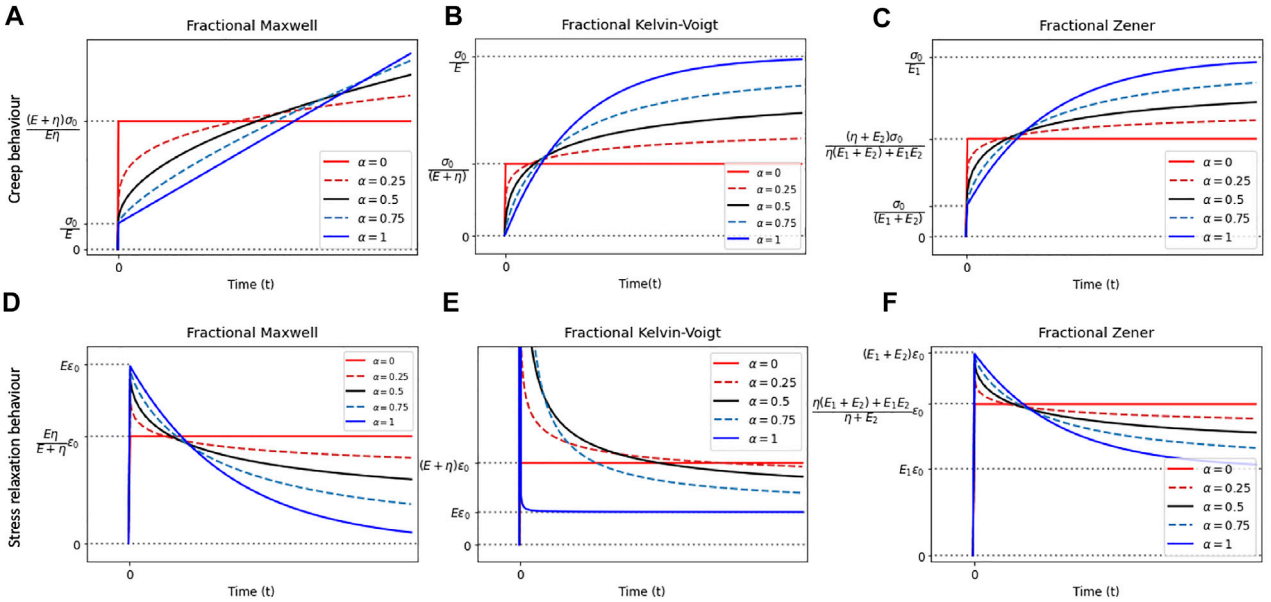

FIGURE 4 | Illustration of the creep and stress relaxation behaviors of the fractional rheological models with selective values of α.

$$c_c = \sqrt{\frac{E(1-\nu)}{\rho(1+\nu)(1-2\nu)}}. \tag{14}$$

The propagation speed of shear wave (c_s) in an elastic medium is related to the shear modulus (G) of the medium, medium density (ρ), angular frequency (ω), phase delay (δ), and displacement between two points that the wave propagated through (Δx), which is given as follows:

$$c_s = \frac{\omega \Delta x}{\delta}, \tag{15a}$$

$$c_s = \sqrt{\frac{G}{\rho}}. \tag{15b}$$

The shear modulus (G) can be inferred from the angular frequency (ω) and wave number (k), or known values of Poisson's ratio (ν) and the Young's modulus (E), which is given as follows:

$$G = \rho c_s^2 = \rho \frac{\omega^2}{k^2}, \tag{16a}$$

$$G = \frac{E}{2(1+\nu)}. \tag{16b}$$

Another important parameter is the propagation speed of surface acoustic waves (c_{sf}), which can be related to c_s if evaluated in an elastic medium [45, 46], and is given as follows:

$$c_{sf} = c_s \frac{0.87 + 1.12\nu}{1+\nu} = \sqrt{\frac{G}{\rho}} \frac{0.87 + 1.12\nu}{1+\nu} = \sqrt{\frac{E}{2\rho(1+\nu)}} \frac{0.87 + 1.12\nu}{1+\nu}. \tag{17}$$

For nearly incompressible medium, the Poisson's ratio is approximately 0.5, allowing **Eqs 14**, **16b**, **17** to be further simplified.

Wave Propagation in a Viscoelastic Medium

When waves propagate in a viscoelastic medium, hysteresis occurs due to its viscous nature such that the waves attenuate as they propagate, dissipating energy [31, 47]. In comparison to a purely elastic medium, the stress–strain relationship of a viscoelastic medium is no longer linear. Instead of an instantaneous response to a step input, a complex response is characterized by the complex modulus Y^*, as mentioned in *Estimation of Material Moduli*. The storage modulus is determined by the restoration of energy due to the elastic property of the medium, while the loss modulus is related to its ability to dissipate energy [33]. The fraction of stored-to-dissipated energy determines whether the medium behaves more like a viscoelastic solid or viscoelastic liquid.

Depending on whether compressional (longitudinal) waves or shear (transverse) waves are propagated, the notation of the generalized complex modulus Y^* takes on E^* or G^*, respectively. The equations of the propagation speed of various wave types subsequently reflect the change in medium property. If shear wave propagation is used as an example, **Eq. 15b** becomes as follows:

$$c_s = \sqrt{\frac{G' + iG''}{\rho}}. \tag{18}$$

The wave number also takes a complex form of k^*. **Eq. 16a** becomes as follows:

$$G' + iG'' = \rho \frac{\omega^2}{(k' + ik'')^2}. \tag{19}$$

Equating the real and imaginary components of G^*, expressions of the storage and loss moduli can be individually obtained [47], which is given as follows:

$$G' = \rho\omega^2 \frac{k'^2 - k''^2}{\left(k'^2 + k''^2\right)^2}, \tag{20a}$$

$$G'' = -2\rho\omega^2 \frac{k'k''}{\left(k'^2 + k''^2\right)^2}. \tag{20b}$$

Equation 12 can be rewritten to reflect the added influence of attenuation as follows:

$$u(x,t) = Ae^{i\left(\omega t - \left(k' + ik''\right)x\right)} = Ae^{k''x}e^{i\left(\omega t - k'x\right)}, \tag{21}$$

The real component of the complex wave number, k', remains in the same form as **Eq. 13**. Combining with **Eq. 15a**, k' can be related with the 1D gradient of the phase delay as follows:

$$k' = \frac{\omega}{c_s} = \frac{\delta}{\Delta x}. \tag{22}$$

The term $e^{k''x}$ describes an exponential decay along the $+x$ direction, of which the attenuation coefficient k'' has a leading term relating to the first power of frequency [31] as follows:

$$k'' = -\left(\omega\sqrt{\frac{\rho}{|G|}}\right)\left(\frac{1}{2}\left(1 - \frac{G'}{|G|}\right)\right)^{\frac{1}{2}}. \tag{23}$$

For biological tissues that exhibit a power law viscoelastic behavior, the wave attenuation may also follow a power law behavior such that ω is replaced with ω^α. The significance and inclusion of these equations will become clear as we move into the details of how elastography techniques are built upon various actuation methods.

VISCOELASTICITY MEASUREMENT WITH ELASTOGRAPHY

Palpation has long been a principal method to externally examine tissue stiffness. Although it is still commonly used as a preliminary assessment method to detect abnormal tissue, it is unable to provide quantifiable data. With an increasing interest in probing properties deeper within the tissue, the concept of elastography was brought to attention by Ophir et al. in 1991 [9]. Elastography techniques first require a method of actuation that introduces disturbance to the tissue, which is then assessed with an imaging tool, most commonly including ultrasound, magnetic resonance imaging (MRI), optical coherence tomography (OCT), alongside photoacoustic (PA) imaging, and Brillouin spectroscopy (BS). In combination with an actuation method, these form the measuring basis for the earliest ultrasound elastography (USE) [9], magnetic resonance elastography (MRE) [48], optical coherence elastography (OCE) [49], photoacoustic elastography (PAE) [50], and Brillouin Microscopy (BM) [51], respectively. Elastography techniques can often output quantitative values of the storage and loss moduli and/or parameters of a fitted rheological model. In this section, we provide a classification of the types of elastography that have been used on biological tissues and how viscoelasticity can be measured through each method of actuation.

The actuation methods are conceptually illustrated in **Figure 5**. Mechanical, acoustic, optical, and magnetic means of actuation have been principally developed. They could be quasi-static, transient, or oscillatory. Data gathered through elastography techniques based on oscillatory input are usually analyzed in the frequency domain, and the others in the time domain. In the case of optical actuation, the disturbance is caused by photon absorption or scattering within the tissue, whereas the other methods result in mechanical deformation. A summary of the elastography techniques discussed in this section is provided in **Table 4**.

Mechanical Actuation

The mechanical load can be quasi-static (**Figure 5A**) or dynamic (**Figure 5B**). Elastography was first developed on the basis of quasi-static mechanical actuation to assess only the elasticity of a sample [9]. In the experimental setup, a compression plate was placed onto the sample surface to alter the local strain within the sample. An ultrasonic transducer was used to send echo signals into the sample. By cross-correlating the pre- and post-compression curves of the echo amplitude, the time delay between two segments of A-lines was determined at the point where the maximum correlation value occurred. From a series of time delays estimated from the cross-correlation of multiple A-line pairs, the axial displacements, a strain profile $\varepsilon(x)$, and a Young's modulus profile $E(x)$, if the applied compressional stress is known, as a function of depth (x) can be estimated. In combination with ultrasonic imaging, this technique is referred to as quasi-static elasticity imaging or strain elastography. Cross-correlation became a fundamental analytical method in strain elastography and was later used to evaluate the viscoelastic behavior of a sample. Once the data gathered through cross-correlation were fitted to a rheological model [52], the Young's modulus and coefficient of viscosity of the model elements could then be calculated using the constitutive equation of the fitted model. The ease of implementation and cost efficiency in computation have allowed quasi-static compression to be combined with other imaging modalities besides ultrasound. For instance, OCT and MRI have been used in the development of compression OCE [53, 54] and compression MRE [55], respectively. Similarly, upon a quasi-static load or strain, a time-dependent creep or relaxation profile can be obtained *via* the corresponding imaging modality and used to derive the parameter coefficients once fitted to a rheological model.

Dynamic mechanical actuation requires the placement of a mechanical vibrator onto the sample surface (**Figure 5B**). The vibrator can produce transient impulses or oscillatory waves that propagate deeper into the sample along the $+x$ direction. If the actuation is induced transiently, a single cycle of sinusoidal wave at low frequency (~50 **Hz**) is typically applied to the sample surface, generating both compressional and shear waves that propagate spherically into the sample with distinguishable wave properties [56]. In particular, the propagation speed (c_s) and attenuation (k'') of the shear wave as functions of depth (x)

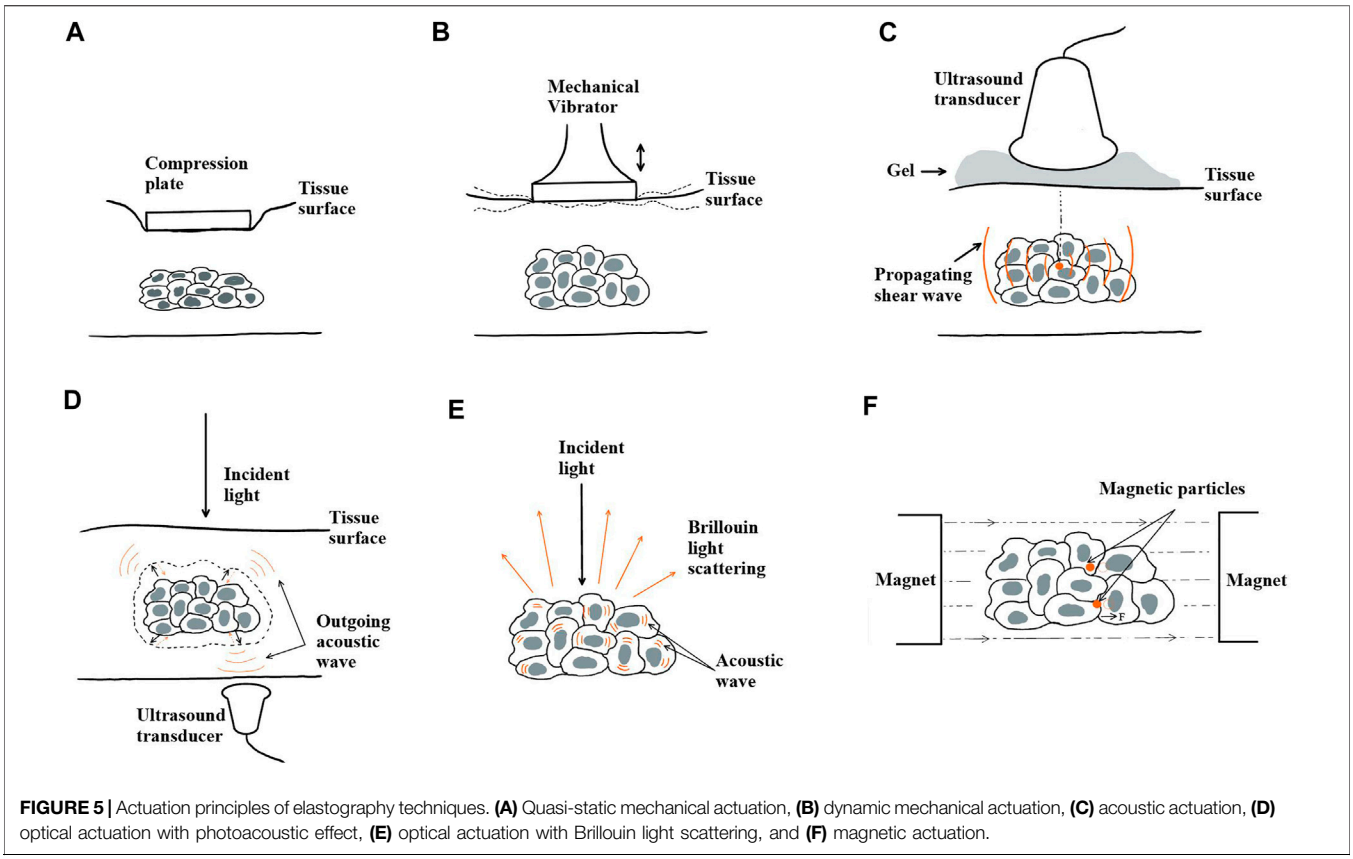

FIGURE 5 | Actuation principles of elastography techniques. **(A)** Quasi-static mechanical actuation, **(B)** dynamic mechanical actuation, **(C)** acoustic actuation, **(D)** optical actuation with photoacoustic effect, **(E)** optical actuation with Brillouin light scattering, and **(F)** magnetic actuation.

can be deduced if combined with an appropriate imaging modality of a frame rate in the kHz range [57]. Once fitted to a rheological model, the coefficients of model parameters can be determined [58–60]. Combined with ultrasound-based imaging techniques, this technique is referred to as compression transient elastography [56]. The earlier OCE was also coupled with a transient stepwise mechanical pulse [49].

Sonoelastography is an ultrasound-based elastography technique that applies continuous mechanical vibration to produce low amplitude (less than 0.1 mm) and low frequency (less than 1 kHz) harmonic shear waves [61–63]. Parameters from the vibration patterns at various input frequencies, including the propagation speed of shear wave (c_s) and phase delay (δ), are analyzed from the Doppler shift and fitted into a rheological model to obtain coefficients of viscoelasticity [64]. Using MRI, one of the first viscoelasticity studies was performed by Muthupillai et al. in 1995 in conjunction with dynamic mechanical actuation [48]. This combination was termed dynamic compression MRE, where harmonic mechanical waves of frequency on the lower spectrum (less than 1 kHz) were propagated to induce shear stress. The three-dimensional displacement fields, including $u(x,t)$, and the phase delay extracted from MRI with harmonic motion-sensitizing gradient waveforms were then used to either reconstruct the viscoelastic parameters by inversion of the Helmholtz equation [7, 13], or directly calculate the frequency-dependent complex shear storage $G'(\omega)$ and loss moduli $G''(\omega)$ of the sample [13, 15]. In the latter case, a rheological model is needed to further determine the shear modulus and coefficient of viscosity of the model elements. Some OCE studies have also been coupled with dynamic compression, including a branch of shear wave OCE that is actuated by direct contact [65–68]. The complex wave number and shear wave speed can be extracted and used to derive the complex shear modulus. A rheological model is necessary if coefficients of viscoelasticity need to be quantified. Spectroscopic OCE (S-OCE) [69] is another representative of dynamic compression OCE. A frequency sweep (0–1,000 Hz) allows the frequency-dependent viscoelastic behavior of the sample to be examined within a range of frequencies. The raw OCT data often undergo several steps of processing to eventually arrive at relationships that can depict the complex viscoelastic response of the sample. A complex OCT signal is first obtained by sampling in the k-space and filtered to minimize phase noise, from which the phase difference, frequency-dependent complex displacement, modulus, and strain rate can be estimated [69, 70]. If the complex modulus is further fitted with a rheological model, individual coefficient of the components within the model can be determined.

Acoustic Actuation

Acoustic actuation relies on focused ultrasound beams produced by an ultrasound transducer to propagate acoustic waves within the tissue sample (**Figure 5C**). The displacement fields and properties of the propagating acoustic waves can be obtained through the coupled imaging tool to further characterize the viscoelastic behavior of the sample.

TABLE 4 | Summary of elastography techniques.

Actuation		Imaging		Technique	Qualitative/ quantitative
Principle	**Comment**	**Modality**	**Comment**		
Mechanical	Quasi-static external compression on the tissue surface	Ultrasound	First developed to measure strain, later developments can measure quantitative viscoelastic parameters	Strain elastography	Qualitative; Quantitative if applied stress is known
		OCT		Compression optical coherence elastography	
		PACT		Compression photoacoustic elastography	
		MRI		Compression magnetic resonance elastography	
	Harmonic external vibration on the tissue surface	OCT	Measure displacement to calculate phase delay	Dynamic optical coherence elastography	Qualitative; Quantitative
		Doppler ultrasound-based techniques	Measure propagation speed of shear wave	Sonoelastography	
		MRI	Analyze displacement patterns	Dynamic magnetic resonance elastography	
	Transient external pulse on the tissue surface	Ultrasound-based motion tracking techniques	Measure time shift between two consecutive signals	Transient elastography	Quantitative
		OCT	Measure propagation speed of shear wave	Transient shear wave optical coherence elastography	
Acoustic	Induce acoustic radiation force within a ROI to generate shear wave	Ultrasound-based techniques	Measure displacement at the focal point	Acoustic radiation force impulse imaging	Qualitative
		Ultrasound-based techniques	Measure parameters of the propagating shear wave	Shear wave elastography imaging	Quantitative
	Focus the acoustic radiation force at various depths to generate conical shear wave	Ultrasound-based techniques	Allow real-time tracking of shear wave propagation	Supersonic shear imaging	Quantitative
	Induce acoustic radiation force impulse remotely; can be air-pulsed	OCT	Measure surface shear wave propagation speed or bulk shear wave propagation speed	Acoustic shear wave optical coherence elastography	Quantitative
Optical	Laser	Photoacoustic imaging	Measure phase difference between the photoacoustic signal and References signal	Photoacoustic viscoelasticity imaging	Qualitative
	Laser (and mechanical compression)	PACT	Measure parameters of the emitted acoustic wave	Photoacoustic elastography	Qualitative Quantitative
	Laser	Brillouin spectrometer or spectroscopy	Measure longitudinal modulus and Brillouin shift	Brillouin microscopy	Quantitative
	Photonic force	OCT	Measure oscillation amplitude of beads embedded in the sample	Photonic force optical coherence elastography	Quantitative
	Laser	OCT	Measure elastic wave propagation speed as induced by the photonic force by light absorption	Pulse laser optical coherence elastography	Quantitative
Magnetic	External magnetic field displaces predeposited magnetic particles	OCT	Measure displacement of individual magnetic particle	Magnetomotive optical coherence elastography	Quantitative

A technique referred to as acoustic radiation force impulse (ARFI) imaging developed by Nightingale et al. combined contactless transient acoustic actuation with ultrasound-based imaging [71, 72]. ARFI relies on focused ultrasound beams to deliver a high-intensity burst that generates acoustic radiation force, deforming the sample within a specific region of interest (ROI). The spatiotemporal relaxation behavior of the sample at the focal point is then recorded by the same transducer, and the resulting time-dependent tissue displacements are mapped. By fitting the relaxation behavior to a rheological model, the viscous and elastic parameters of the model may be determined [73].

Another type of acoustic actuation used is based on the properties of acoustic shear wave. A technique that utilizes oscillatory shear waves induced by and propagating in the orthogonal direction of the acoustic actuation is shear wave elasticity imaging (SWEI) [74]. SWEI offers a quantitative assessment of local material viscoelasticity in terms of shear storage modulus ($G^{'}$) and shear loss modulus ($G^{''}$) derived from the propagation speed of shear wave (c_s) and phase delay (δ). The quantification of sample viscoelasticity is typically carried out by fitting to appropriate rheological models [75]; however, model-independent methods have also been developed

[12, 76, 77]. To allow for an extended imaging region and an increased data acquisition speed (~5,000 fps), supersonic shear imaging (SSI) [78] was developed with the added ability to focus the impulses at multiple focal depths such that conical shear waves can be generated [14, 79]. Another popular coupling modality is OCT, upon which surface acoustic wave OCE (SAW-OCE), acoustic radiation force OCE (ARF-OCE), and shear wave OCE (SW-OCE) have been developed. In SAW-OCE, the phase velocity of the propagating surface wave (c_{sf}) laterally across the surface of the sample and its dispersion curve can be determined from the phase delay *via* OCT. Values of the parameters can then be fitted into the Rayleigh wave dispersion equation [80] or a rheological model [81] to extract the viscoelastic parameters. A subset of SAW-OCE termed air-coupled OCE utilizes contactless air puffs to generate SAW, under the influence of which the sample's time-dependent deformation can be mapped with OCT [45, 80, 82]. The slope and area bounded by the hysteresis curve can be calculated to derive the loss in energy that corresponds to the viscous behavior and storage modulus to the elastic behavior [82]. A rheological model can be used to derive numerical values of the Young's modulus and coefficient of viscosity. In ARF-OCE, similar to ARFI, an ultrasound transducer is used to propagate pulsed ARF to remotely initiate local sample displacements [83]. The phase delay between adjacent A-lines can be obtained under OCT and used to estimate time-dependent axial displacements and strain. When model-dependent, further estimation of the parameter coefficients can be achieved. ARF-OCE can also be model-independent where the complex shear modulus can be estimated from a direct measurement of the propagation speed of surface wave [83]. Acoustically actuated SW-OCE can sometimes be induced by ARF [84], where the propagation speed of bulk shear waves is used to derive model parameters once fitted.

Optical Actuation

Optical actuation is enabled by the optical properties of biological tissues including absorption and scattering. For example, photoacoustic imaging (**Figure 5D**) was developed based on the photoacoustic effect by which a sample of biological tissue absorbs the energy from optical beams and releases it in the form of acoustic waves. A technique referred to as photoacoustic viscoelasticity (PAVE) imaging was developed by Gao et al., using intensity-modulated laser beams emitted toward the tissue sample [85]. Developed based on the photoacoustic effect as well, the tissue absorbs incoming light waves and undergoes thermal expansion. The viscoelastic nature of biological tissues introduces a phase delay (δ) in the detected photoacoustic signal, which relates to the viscosity–elasticity ratio (η/E) of the tissue and the modulation frequency (ω) [85], which is given as follows:

$$\delta = \arctan\left(\frac{\eta\omega}{E}\right), \tag{24}$$

thus providing a qualitative comparison between the viscous and elastic behavior of the tissue sample. Recent advances have demonstrated the feasibility of quantifying the Young's modulus by establishing a photoacoustic shear wave model [86]. The viscosity parameter can be subsequently determined *via* **Eq. 24**.

Using a combination of optical beams, an external vibration source, and a measurement technique based on photoacoustic computed tomography (PACT), photoacoustic elastography (PAE) has emerged in recent years, attempting to measure strain concurrently with the functional parameters of a tissue sample [50, 87, 88]. A strain profile can be obtained from cross-correlating A-line pairs using photoacoustic imaging. If the stress applied by the external vibrator is known, a model can be fitted to quantify the elasticity of the sample. Although only quantitative values of the Young's modulus have been demonstrated, an extension to viscosity may be achieved if the strain profile can be obtained as a function of time, in a way that is similar to how strain elastography can be used to quantify viscoelastic parameters.

Another optically actuated elastography technique, Brillouin microscopy, uses inelastic Brillouin light scattering as a contrast mechanism to measure properties of biological tissues (**Figure 5E**). The incident light interacts with the inherent acoustic phonons within the tissue sample. A frequency shift, referred to as the Brillouin shift, is then introduced to the outgoing light. This change in frequency can be directly related to the mechanical properties of the sample by calculating the complex longitudinal modulus containing a real and an imaginary part [51]. The real part yields a measurable frequency shift (ν_B), which can be used to derive the longitudinal modulus of the tissue that characterizes its elastic properties [89], whereas the imaginary part is related to the spectral width ($\mathbf{\Gamma}_B$) that can be further used to determine the longitudinal coefficient of viscosity of the material [51, 90].

In combination with OCT, several optically actuated OCE techniques are worth mentioning, namely, photonic force OCE (PH-OCE) and pulse laser OCE. PH-OCE offers a contactless method that induces a harmonically modulated ultra–low radiation pressure force generated by a low-numerical aperture beam [91, 92]. The radiation pressure force subsequently causes sub-nanometer oscillations of predeposited microbeads in a sample. A linear model is used to decouple the mechanical and photothermal responses of the sample to the incoming radiation pressure such that the mechanical response can be isolated. The oscillation amplitude of a microbead can then be captured under OCT and estimated, as it is a function of the input radiation pressure force and radius of the microbead. The oscillation amplitude is also directly related to the complex shear modulus of the sample from which further extraction of viscoelastic parameters can be achieved depending on the choice of a suitable rheological model. In pulse laser OCE [93], wave generation is achieved by focusing pulsed laser irradiation toward the sample. By absorption of the light and localized thermal expansion within the sample, the irradiation is converted into compressional and shear waves that further propagate within the sample. The propagation of the laser-induced elastic waves can be profiled and the local time-dependent displacements can be mapped. A derivation of pulse laser OCE uses dye-loaded perfluorocarbon nanodroplets [94]. When excited by the laser

pulse, the nanodroplets undergo rapid liquid–gas phase transition, inducing elastic waves.

Magnetic Actuation

Magnetic actuation introduces a disturbance to the sample using a magnetomotive force generated by an external magnetic field. First, magnetic nanoparticles (MNPs) are predeposited into the sample that is placed within the external magnetic field (**Figure 5F**). The magnitude and direction of the magnetomotive force can be controlled by adjusting gradients of the magnetic field. The viscoelastic behavior of the surrounding microenvironment of the MNPs in response to the disturbance can be inferred by analyzing the time-dependent displacement of the MNPs. One common imaging modality that magnetic actuation, whether static or dynamic, can be implemented with is OCT. Collectively, this technique is referred to as magnetomotive OCE (MM-OCE) [95–97]. MM-OCE allows for contactless manipulation, through which local MNP displacement in the sub-nanometer range can be detected. Static MM-OCE typically uses OCT to map the time-dependent phase variation in response to a step stress, from which the nanoscale time-dependent local displacements, amplitude with decay, and resonant frequency can be deduced. A rheological model can be fitted to determine the elastic modulus and coefficient of viscosity of the model parameters. Swept-frequency loading techniques have also been implemented in dynamic MM-OCE studies to determine the frequency-dependent viscoelastic behavior of the tissue [97].

VISCOELASTICITY AND DEVELOPMENTAL BIOLOGY

Physical forces, whether externally applied or internally generated, drive tissue shape changes during embryogenesis [24]. For instance, anisotropic tensional stress orients ectodermal remodeling in the early mouse limb bud [98], anteroposterior (AP) tensile force mediates *Drosophila* germ band extension [22, 99], contractile force of an actin cable initiates *Drosophila* dorsal closure [100], tensile convergence force drives *Xenopus* blastopore closure [23], and the formation of head fold in a chick embryo is driven by a mechanical force that is likely associated with neurulation [101].

Since embryonic tissues exhibit both solid- and liquid-like characteristics, they undergo viscoelastic changes under an applied force [3]. Substrates with various storage-to-loss moduli ratios can be artificially manufactured to mimic properties of the extracellular environment. It has been demonstrated that cells are sensitive to both elasticity and viscosity, resulting in morphological changes, proliferation, spreading, stiffening, softening, migration, and differentiation of cells [102–104]. Changes in the viscoelastic properties of extracellular matrix (ECM) have been shown to affect the functional and migratory behaviors of cells [105]. In an *in vivo* study of the *Drosophila* embryo during morphogenesis, myosin II pulses were used to assess how viscous dissipation in response to transient forces can stabilize local cell deformation [106]. Thus, to understand how physical forces regulate morphogenetic movements, characterization of the viscoelastic response within an embryo at both the cellular and tissue scales is necessary. In this section, emphasis is placed on the phase separation and transition of the intracellular membrane-less organelles, durotaxis and viscotaxis, respectively, along with the capability of existing techniques to examine viscoelastic properties at cellular and tissue scales.

Liquid–Liquid Phase Separation and Liquid–Solid Phase Transition

Intracellular mechanics have been shown to directly correlate with intracellular rheology and mechanotransduction [107]. Many intracellular compartments such as subcompartments within the nucleus, stress granules, germ cell granules, actin bodies, and other ribonucleoprotein (RNP) bodies are membrane-less and exhibit liquid-like behavior [108–110]. At the subcellular level, thermodynamic force drives intracellular compartmentalization toward a more energy-favorable state, sequestering molecules that assemble into phase-separated liquid droplets [26, 111]. The process by which condensates form is referred to as liquid–liquid phase separation (LLPS) [112]. During the dynamic dissolution and condensation of intracellular condensates, a cell will likely exhibit any combination of elastic and viscous behaviors as its properties reflect the collective properties of membrane-less and membrane-bound intracellular compartments. *In vivo* studies have suggested that some condensates, such as the fibrillarin (FIB1) protein, exhibit viscoelastic behavior [27, 108]. As many of the condensates reside within the nucleus and are constituted by RNP bodies [113], the assembly and disassembly of intracellular condensates will likely have an effect on the protein concentration [27, 108, 114] and subsequently the rate at which the condensates contribute to genetic activities that regulate the functional behavior of a cell [113]. For instance, it has been demonstrated *in vitro* that an increase in the concentration of the RNA LAF-1 within RNP bodies can decrease their viscosity [114]. However, there have been rather limited studies on the mechanical properties of intracellular condensates. Thus, a deeper look into the viscoelastic properties of intracellular and, especially, intranucleolar condensates will likely refine our understanding of the role viscoelasticity plays in nuclear and cellular activities.

During LLPS, liquid droplets can, often undesirably and irreversibly, undergo further liquid–solid phase transition (LSPT) during which compartments progress to a more viscoelastic or even solid-like state [26, 27, 112]. In studies of neurodegenerative diseases, LSPT has been proposed as an explanation for undesirable stiffening and inhibited molecular dynamics [26] due to protein aggregation. For example, LSPT involving a mutant FUS protein is believed to contribute to the progression of ALS [115]. Hence, a shift on the viscoelastic spectrum exhibited by a condensate that is normally fluid-like toward a more solid-like state can suggest a pathological tendency. The protein aggregation driven by LSPT is often

irreversible, suggesting it is of value to investigate the exact phase boundary where liquid droplets become solid-like *in vivo* [116]. The long-term motivation is to detect the onset and monitor the progression of neurodegenerative diseases to assess the adequacy of medical intervention.

Durotaxis and Viscotaxis

Durotaxis was proposed in the early 2000s by Lo et al. as a mechanism by which cells migrate collectively toward greater substrate stiffness [117]. Despite the fact that biological tissues are intrinsically viscoelastic, pioneering *in vitro* studies in which stiffness gradients were artificially generated to mimic the ECM environment were often conducted on purely elastic substrates [118, 119]. Later studies identified stiffness gradients *in vivo* during embryogenesis, where the stiffness is commonly quantified using elastic (Young's or shear) modulus. For example, the apparent elastic modulus of *Xenopus* cranial mesoderm was measured using atomic force microscopy (AFM), revealing that the collective migration of neural crest cells is triggered by mesodermal stiffening [120]. Also using AFM, it was shown that axonal growth, while not strictly durotaxis, is guided by a stiffness gradient in the brain of the *Xenopus* embryo [121]. Magnetic tweezers were used to uncover a mesodermal stiffness gradient along which cells migrate within the early mouse limb bud [122].

As the stiffness of ECM is sometimes attributed to the abundance of collagen [123], which can be realistically modeled as a viscoelastic material with quantifiable storage and loss moduli [124], cell-matrix interactions and resulting cell migration thus exhibit dynamic time-dependent mechanical responses [105]. Paths of migration and areas that cells migrate toward are likely of different viscosity in addition to higher elasticity, thereby impacting the timescale of the responses of migrating cells to stiffness gradients [125]. To elucidate the effect of ECM viscosity on cell movements, several *in vitro* studies have either isolated the effects of the viscosity of substrates or implemented tunable storage-to-loss moduli ratios of substrates. An increase in the substrate loss modulus can lead to viscous drag and cell-matrix energy dissipation that impedes the migratory speed of cells [104, 105, 126–130]. In a separate study using viscoelastic substrates, it was proposed that within a viscous environment, greater migratory speed corresponds to greater apparent modulus [131]. Therefore, the empirically measured Young's moduli for characterizing local tissue stiffness may differ from the theoretical values in the absence of ECM viscosity considerations. A more recent study constructed a substrate with gradients of viscosity while keeping the elasticity constant, and demonstrated that human mesenchymal stem cells migrate along a viscosity gradient [132]. Viscosity-dependent cell migration has been given the name "viscotaxis" in some studies [132, 133].

To further test the validity of these *in vitro* observations and to more physiologically evaluate how mechanical cues correlate with cell migration patterns, we believe there is sufficient motivation to examine the role of viscoelasticity gradients *in vivo*. Results obtained from studies of stiffness, viscosity, and viscoelasticity gradients should be compared to more rigorously delineate the collective migratory behavior of cells in response to mechanical cues.

Existing Techniques for Measuring Embryonic Tissue Viscoelasticity

A handful of methods have been applied to measure the viscoelastic properties of embryonic tissues, including, predominantly, AFM (**Figure 6A**), magnetic tweezers using magnetic particles or ferrofluid droplets (**Figure 6B**), and micropipette aspiration (**Figure 6C**). AFM has been used to quantify the viscoelastic properties of embryonic tissues by indenting the tissue surface and analyzing the approach–retraction hysteresis using rheological models [134, 135]. For instance, AFM has been applied to quantify the elasticity and viscosity of the mouse mandibular arch *in vivo* [136]. Magnetic tweezers have been used to probe tissue viscoelastic behavior in the early mouse limb bud [122], mouse mandibular arch [137], and *Drosophila* embryo during cellularization [138]. Other magnetically actuated systems to measure viscoelasticity include ferrofluid oil droplets deployed in the zebrafish tailbud [139] and the *Drosophila* embryo [140, 141]. Confocal imaging has been combined with computer-aided cell tracking to calculate local tissue strain rate (a measurement of viscosity) during *Drosophila* germ band extension [22, 99]. Micropipette aspiration, which applies a known suction force to deform a region of interest, has been applied to determine the local viscoelastic response of a tissue or a single cell [142, 143]. For the purpose of measuring the viscoelastic properties of intracellular condensates, microrheology techniques have also been used to quantify the viscosity of the condensates through the Stokes–Einstein relation by assuming the condensates behave as equilibrium Newtonian liquids [112, 114]. For other intracellular structures such as the nuclear actin network, microrheology has also been used to probe the viscoelastic creep response [144]. Magnetic micron-size wires in combination with rotational magnetic spectroscopy have been adapted to measure the shear viscoelasticity of cytoplasm and to quantify the shear modulus and coefficient of viscosity [145]. At the single-cell level, a rheometer has been used *in vitro* to estimate the time-dependent power law creep function [40], relaxation behavior, and frequency-dependent complex modulus [146].

However, existing *in vivo* measurement techniques either require direct contact, are invasive, lack cellular spatial resolution, lack adequate throughput, or are unable to retrieve depth information. A limitation of AFM is that only two-dimensional surface measurements can be reliably taken. Deeper tissue assessment by AFM either requires dissection for exposure or model-based derivation [135, 136], both of which are suboptimal. Magnetic devices allow measurements within a bulk tissue sample but require the injection of magnetic particles or fluids by skilled individuals. Although the use of magnetic particles allows for the simultaneous assessment of multiple locations within a 3D sample, existing magnetic techniques lack broad spatial coverage within an embryo. To define mechanisms of cell migration in 3D, ECM properties and cellular behaviors need to be considered, and

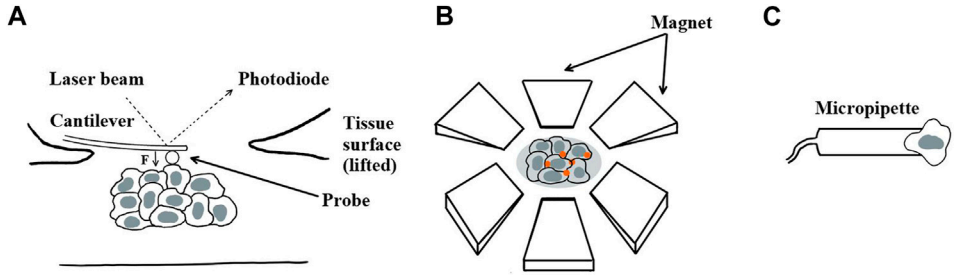

FIGURE 6 | Existing techniques for measuring the viscoelasticity of embryonic tissues. **(A)** Atomic force microscopy, **(B)** magnetic tweezers, and **(C)** micropipette aspiration.

techniques that provide noninvasive, continuous, volumetric, and spatially resolved measurements without sacrificing acquisition speed would be ideal.

CURRENT APPLICATIONS OF ELASTOGRAPHY

Since quantitative measurements of viscoelasticity have been clinically realized *in vivo* on a variety of mature tissue types, we selectively list examples of *in vivo* clinical elastography applications. In comparison, the *in vivo* application of elastography on embryonic tissues is far less developed. Several examples of using elastography techniques on embryonic animal tissues *in vivo* are discussed. The challenge in advancing current techniques is discussed in *Challenge and Outlook*.

Adult Tissue

Transient elastography has been used *in vivo* for the detection and mapping of aggregated breast tumors within surrounding soft tissues [57], the assessment of stages of liver fibrosis [60], and the quantification of properties of blood clots [59]. Dynamic mechanical actuation has been adapted in compression MRE on assessing a variety of adult tissues such as liver fibrosis [15], breast lesions [7, 147], gray and white matter within the brain [13], and glioblastoma [148]. In the case of liver fibrosis, for instance, the purpose is usually to diagnose and classify stages of fibrosis. Among breast lesions, it is mainly for detecting and distinguishing between malignant and benign tumors. In glioblastoma, viscoelastic measurements are for the purpose of presurgical evaluation. More recently, dynamic compression MRE has been used to assess the differences of subcortical gray matter among adults in different age-groups [149].

SWEI-based elastography has been used to probe the viscoelastic properties of a healthy liver [150], a posttransplant liver [77], liver fibrosis [75], and normal breast tissue [151]. Sonoelastography has been used to assess the shear modulus and viscosity of healthy skeletal muscle [16]. During contraction, an increase in both shear modulus and viscosity has been observed in comparison to the relaxed state [16]. *In vivo* applications of supersonic shear imaging (SSI) include assessment of the complex shear modulus of breast lesions [79], measuring the viscoelastic and anisotropic properties of muscle tissue [14], and liver tissue [152].

OCE (compression, ARF based, and shear wave.) is extensively used to assess the viscoelastic properties of the human cornea *in vivo* as the superior submicron scale resolution of OCT can capture subtle changes in wave properties [153] and tissue properties, making it suitable for the detection of early-onset disease such as keratoconus [154]. In addition, *in vivo* dynamic OCE has been performed on human skin to assess its mechanical properties [155]. BM has, in recent years, been used in noncontact assessment of corneal biomechanics with and without keratoconus [156]. Although the current BM application focuses only on extracting the elastic information in terms of the longitudinal modulus, it is capable of decoupling the viscous component if needed [157].

Embryonic Tissue

Elastography has emerged to measure the viscoelastic properties of embryonic tissues. Most applications have been optically actuated due to the intricate nature of light's ability to achieve subcellular spatial resolution. The attenuation of light in embryonic tissues is also less of a concern since the tissue can be considered as homogenous and isotropic, such that there is a minimal difference in the refractive indices of different parts of the embryo. Recent advances in OCE have acknowledged its potential for facilitating our understanding of the viscoelastic properties of embryonic tissues [53, 158, 159]. For instance, transient-compression OCE was used for the quantification of viscoelasticity of a living chicken embryo *in vivo* [160]. BM was used to quantify the longitudinal modulus and viscosity of spinal cord tissue [161], and ECM [162] *in vivo* in a zebrafish larva. For the purpose of examining the viscoelastic properties of intracellular condensates within a developing cell, a form of magnetic actuation has been used in combination with optical imaging [144].

CHALLENGE AND OUTLOOK

Elastography techniques for assessing the viscoelasticity of mature tissues have been established, and future considerations may include tissue anisotropy and heterogeneity to improve measurement accuracy.

Substantial instrument development is still necessary to facilitate further application of the aforementioned elastography techniques to embryonic tissues *in vivo*. For elastography actuated by quasi-static compression, quantification of the elastic modulus cannot be achieved without known values of the applied stress. Moreover, coupling of the stress applied to the embryo surface requires additional attention and may vary case by case. USE- and MRE-based techniques, regardless of the coupled actuation method, have spatial resolutions of 100–200 μm at best, and therefore generally cannot achieve a spatiotemporal resolution sufficient for capturing the viscoelastic behavior of embryonic tissues [163–165]. Acoustically actuated elastography often requires additional time gain compensation as it suffers from the trade-off between spatial resolution, which increases with increasing frequency of the incoming wave, and attenuation of the wave intensity as the wave travels deeper into the tissue, which also increases with higher frequency. Actuating magnetically, as previously mentioned, requires the deposition of foreign particles into the tissue sample and can only provide measurements at a limited number of locations within a volume. Optical actuation methods are thermally induced. Overabsorption of light energy by the tissue may lead to phototoxicity and tissue damage. In addition, the advantageous cellular resolution offered by OCT is achieved at the sacrifice of depth penetration, although this may be insignificant as the depth of embryonic tissues may be up to several millimeters at most. A unified consideration, therefore, leaves the potential advancements of BS- and OCE-based elastography techniques in the spotlight.

However, there are some limitations. A pitfall of implementing BM on embryonic tissues is that a standardized systematic approach is not yet formulated. The biophysical basis on which the measurements and relationships were derived as well as the appropriateness of applying high frequencies (in GHz range) on biological tissues remain contentious [51, 166]. Furthermore, to be able to quantify the longitudinal modulus, known numerical values of the optical properties of the tissue, including the local refractive index and tissue density, are prerequisites [51]. The complex longitudinal modulus, a parameter also used to characterize viscoelastic behavior, differs from the complex modulus (Young's or shear) used in existing elastography techniques. The lack of a universal correlation between complex moduli may require additional calibration.

A crucial issue hampering the assessment of mechanisms of morphogenesis is the lack of an appropriate approach for mapping viscoelastic properties *in vivo*. Despite current drawbacks, BM and OCE are among the few techniques that have the ability to generate 3D *in vivo* quantitative viscoelasticity data for an embryonic sample. BM can achieve submicron-scale spatial resolution [25, 167], which is sufficient for visualizing subcellular structures. A recent study used BM to reveal a liquid–solid phase transition in intracellular stress granules by measuring the elastic longitudinal modulus [168]. Although no direct measurement was made on the viscoelastic properties, it demonstrated the feasibility of probing intracellular compartments with BM. OCT enables rapid 3D imaging within seconds with millimeter-scale depth penetration [169], can achieve a spatial resolution of 1–10 μm [170, 171], and is able to resolve local displacements at the nanometer scale [172]. Therefore, it may be a fit for more embryonic animal models and possibly human embryos.

To advance the applicability of elastography techniques for assessing embryonic tissue properties, an ideal derivative of current methods would entail an actuation approach that is contactless, or at the minimum, easy to couple, noninvasive, and nondestructive. The technique should neither disturb the surrounding environment of the embryo nor interfere with its natural development. In addition, nontoxicity, which is a property that most optically actuated techniques lack, needs to be considered and carefully calibrated. The imaging method should provide adequate contrast, signal-to-noise ratio, data acquisition speed, and spatial resolution (submicron scale) to capture time-dependent movement of individual cells during a substantive developmental interval. During the next few years, we hope to witness the emergence of such elastography techniques and their applications to developmental biology.

AUTHOR CONTRIBUTIONS

KZ drafted the manuscript. MZ, ET, SH, and YS edited the manuscript.

FUNDING

This work was supported by a project grant from the Canadian Institutes of Health Research (#168992).

REFERENCES

1. Fung YC. *Biomechanics: Mechanical Properties of Living Tissues*. New York, NY: Springer-Verlag (1981).
2. Sasaki N. "Viscoelastic Properties of Biological Materials", in *Viscoelasticity – From Theory to Biological Applications*. Editor J. de Vicente IntechOpen (2012).
3. Forgacs G, Foty RA, Shafrir Y, and Steinberg MS. Viscoelastic Properties of Living Embryonic Tissues: a Quantitative Study. *Biophys J* (1998) 74(5): 2227–34. doi:10.1016/S0006-3495(98)77932-9
4. Kiss MZ, Varghese T, and Hall TJ. Viscoelastic Characterization of *In Vitro* Canine Tissue. *Phys Med Biol* (2004) 49(18):4207–18. doi:10.1088/0031-9155/49/18/002
5. Pan L, Zan L, and Foster FS. Ultrasonic and Viscoelastic Properties of Skin Under Transverse Mechanical Stress *In Vitro*. *Ultrasound Med Biol* (1998) 24(7):995–1007. doi:10.1016/S0301-5629(98)00071-4
6. Guertler CA, Okamoto RJ, Schmidt JL, Badachhape AA, Johnson CL, and Bayly PV. Mechanical Properties of Porcine Brain Tissue *In Vivo* and *Ex Vivo* Estimated by MR Elastography. *J Biomech* (2018) 69:10–8. doi:10.1016/j.jbiomech.2018.01.016
7. Sinkus R, Tanter M, Xydeas T, Catheline S, Bercoff J, and Fink M. Viscoelastic Shear Properties of *In Vivo* Breast Lesions Measured by

MR Elastography. *Magn Reson Imaging* (2005) 23(2):159–65. doi:10.1016/j.mri.2004.11.060
8. Nava A, Mazza E, Furrer M, Villiger P, and Reinhart WH. *In Vivo* Mechanical Characterization of Human Liver. *Med Image Anal* (2008) 12(2):203–16. doi:10.1016/j.media.2007.10.001
9. Ophir J, Céspedes I, Ponnekanti H, Yazdi Y, and Li X. Elastography: A Quantitative Method for Imaging the Elasticity of Biological Tissues. *Ultrason Imaging* (1991) 13(2):111–34. doi:10.1177/016173469101300201
10. Sarvazyan AP, Skovoroda AR, Emelianov SY, Fowlkes JB, Pipe JG, Adler RS, et al. "Biophysical Bases of Elasticity Imaging," in *Acoustical Imaging*. Editor J. P. Jones Boston, MA: Springer (1995), 223–40. doi:10.1007/978-1-4615-1943-0_23
11. Pitre JJ, Jr, Koziol LB, Kruger GH, Vollmer A, Ophir J, Ammann J-J, et al. Design and Testing of a Single-Element Ultrasound Viscoelastography System for Point-of-Care Edema Quantification. *Ultrasound Med Biol* (2016) 42(9):2209–19. doi:10.1016/j.ultrasmedbio.2016.04.013
12. Kazemirad S, Bernard S, Hybois S, Tang A, and Cloutier G. Ultrasound Shear Wave Viscoelastography: Model-Independent Quantification of the Complex Shear Modulus. *IEEE Trans Ultrason Ferroelectr Freq Control* (2016) 63(9):1399–408. doi:10.1109/TUFFC.2016.2583785
13. Green MA, Bilston LE, and Sinkus R. *In Vivo* Brain Viscoelastic Properties Measured by Magnetic Resonance Elastography. *NMR Biomed* (2008) 21(7):755–64. doi:10.1002/nbm.1254
14. Gennisson JL, Deffieux T, Macé E, Montaldo G, Fink M, and Tanter M. Viscoelastic and Anisotropic Mechanical Properties of *In Vivo* Muscle Tissue Assessed by Supersonic Shear Imaging. *Ultrasound Med Biol* (2010) 36(5):789–801. doi:10.1016/j.ultrasmedbio.2010.02.013
15. Garteiser P, Doblas S, Daire J-L, Wagner M, Leitao H, Vilgrain V, et al. MR Elastography of Liver Tumours: Value of Viscoelastic Properties for Tumour Characterisation. *Eur Radiol* (2012) 22:2169–77. doi:10.1007/s00330-012-2474-6
16. Hoyt K, Kneezel T, Castaneda B, and Parker KJ. Quantitative Sonoelastography for the *In Vivo* assessment of Skeletal Muscle Viscoelasticity. *Phys Med Biol* (2008) 53(15):4063–80. doi:10.1088/0031-9155/53/15/004
17. Rus G, Faris IH, Torres J, Callejas A, and Melchor J. Why are Viscosity and Nonlinearity Bound to Make an Impact in Clinical Elastographic Diagnosis? *Sensors* (2020) 20(8):2379. doi:10.3390/s20082379
18. Doblas S, Garteiser P, Haddad N, Daire J, Wagner M, Leitão H, et al. Magnetic Resonance Elastography Measurements of Viscosity: A Novel Biomarker for Human Hepatic Tumor Malignancy?. Proc Int Soc Magn Reson Med ISMRM, Canada (2011) 19:389.
19. Kumar V, Denis M, Gregory A, Bayat M, Mehrmohammadi M, Fazzio R, et al. Viscoelastic Parameters as Discriminators of Breast Masses: Initial Human Study Results. *PLoS One* (2018) 13(10):e0205717. doi:10.1371/journal.pone.0205717
20. Han Z, Aglyamov SR, Li J, Singh M, Wang S, Vantipalli S, et al. Quantitative Assessment of Corneal Viscoelasticity Using Optical Coherence Elastography and a Modified Rayleigh-Lamb Equation. *J Biomed Opt* (2015) 20(2):020501. doi:10.1117/1.JBO.20.2.020501
21. Krieg M, Arboleda-Estudillo Y, Puech P-H, Käfer J, Graner F, Müller DJ, et al. Tensile Forces Govern Germ-Layer Organization in Zebrafish. *Nat Cell Biol* (2008) 10:429–36. doi:10.1038/ncb1705
22. Butler LC, Blanchard GB, Kabla AJ, Lawrence NJ, Welchman DP, Mahadevan L, et al. Cell Shape Changes Indicate a Role for Extrinsic Tensile Forces in Drosophila Germ-Band Extension. *Nat Cell Biol* (2009) 11:859–64. doi:10.1038/ncb1894
23. Shook DR, Kasprowicz EM, Davidson LA, and Keller R. Large, Long Range Tensile Forces Drive Convergence During Xenopus Blastopore Closure and Body axis Elongation. *Elife* (2018) 7:e26944. doi:10.7554/eLife.26944
24. Keller R. Physical Biology Returns to Morphogenesis. *Science* (2012) 338(6014):201–3. doi:10.1126/science.1230718
25. Sánchez-Iranzo H, Bevilacqua C, Diz-Muñoz A, and Prevedel R. A 3D Brillouin Microscopy Dataset of the *In-Vivo* Zebrafish Eye. *Data Brief* (2020) 30:105427. doi:10.1016/j.dib.2020.105427
26. Alberti S, Gladfelter A, and Mittag T. Considerations and Challenges in Studying Liquid-Liquid Phase Separation and Biomolecular Condensates. *Cell* (2019) 176(3):419–34. doi:10.1016/j.cell.2018.12.035
27. Weber SC. Sequence-Encoded Material Properties Dictate the Structure and Function of Nuclear Bodies. *Curr Opin Cell Biol* (2017) 46:62–71. doi:10.1016/j.ceb.2017.03.003
28. Mongera A, Rowghanian P, Gustafson HJ, Shelton E, Kealhofer DA, Carn EK, et al. A Fluid-to-Solid Jamming Transition Underlies Vertebrate Body Axis Elongation. *Nature* (2018) 561:401–5. doi:10.1038/s41586-018-0479-2
29. Patel A, Lee HO, Jawerth L, Maharana S, Jahnel M, Hein MY, et al. A Liquid-to-Solid Phase Transition of the ALS Protein FUS Accelerated by Disease Mutation. *Cell* (2015) 162(5):1066–77. doi:10.1016/j.cell.2015.07.047
30. Sunyer R, and Trepat X. Durotaxis. *Curr Biol* (2020) 30(9):R383–7. doi:10.1016/j.cub.2020.03.051
31. Parker KJ, Szabo T, and Holm S. Towards a Consensus on Rheological Models for Elastography in Soft Tissues. *Phys Med Biol* (2019) 64(21):215012. doi:10.1088/1361-6560/ab453d
32. Zhu Y, Zhang X, Zheng Y, Chen X, Shen Y, Lin H, et al. Quantitative Analysis of Liver Fibrosis in Rats with Shearwave Dispersion Ultrasound Vibrometry: Comparison with Dynamic Mechanical Analysis. *Med Eng Phys* (2014) 36(11):1401–7. doi:10.1016/j.medengphy.2014.04.002
33. Bland DR. *The Theory of Linear Viscoelasticity*. Mineola, NY: Dover Publications (2016).
34. Sack I, Jöhrens K, Würfel J, and Braun J. Structure-Sensitive Elastography: On the Viscoelastic Powerlaw Behavior of *In Vivo* Human Tissue in Health and Disease. *Soft Matter* (2013) 9(24):5672–80. doi:10.1039/C3SM50552A
35. Khalilgharibi N, Fouchard J, Asadipour N, Barrientos R, Duda M, Bonfanti A, et al. Stress Relaxation in Epithelial Monolayers is Controlled by the Actomyosin Cortex. *Nat Phys* (2019) 15:839–47. doi:10.1038/s41567-019-0516-6
36. Nicolle S, Vezin P, and Palierne J-F. A Strain-Hardening Bi-Power Law for the Nonlinear Behaviour of Biological Soft Tissues. *J Biomech* (2010) 43(5):927–32. doi:10.1016/j.jbiomech.2009.11.002
37. Fabry B, Maksym GN, Butler JP, Glogauer M, Navajas D, and Fredberg JJ. Scaling the Microrheology of Living Cells. *Phys Rev Lett* (2001) 87:148102. doi:10.1103/PhysRevLett.87.148102
38. Bonfanti A, Kaplan JL, Charras G, and Kabla A. Fractional Viscoelastic Models for Power-Law Materials. *Soft Matter* (2020) 16(26):6002–20. doi:10.1039/d0sm00354a
39. Taylor LS, Lerner AL, Rubens DJ, and Parker KJ. "A Kelvin-Voight Fractional Derivative Model for Viscoelastic Characterization of Liver Tissue", in Proceedings of the ASME 2002 International Mechanical Engineering Congress and Exposition. Advances in Bioengineering, November 17–22, 2002, New Orleans, LA, 447–8.
40. Desprat N, Richert A, Simeon J, and Asnacios A. Creep Function of a Single Living Cell. *Biophys J* (2005) 88(3):2224–33. doi:10.1529/biophysj.104.050278
41. Zhou EH, Quek ST, and Lim CT. Power-Law Rheology Analysis of Cells Undergoing Micropipette Aspiration. *Biomech Model Mechanobiol* (2010) 9:563–72. doi:10.1007/s10237-010-0197-7
42. Pullarkat P, Fernandez P, and Ott A. Rheological Properties of the Eukaryotic Cell Cytoskeleton. *Phys Rep* (2007) 449(1–3):29–53. doi:10.1016/j.physrep.2007.03.002
43. Mainardi F, and Spada G. Creep, Relaxation and Viscosity Properties for Basic Fractional Models in Rheology. *Eur Phys J Spec Top* (2011) 193(1):133–60. doi:10.1140/epjst/e2011-01387-1
44. Truell R, Elbaum C, and Chick BB. *Ultrasonic Methods in Solid State Physics*. Cambridge, MA: Academic Press (2013).
45. Wang S, Li J, Manapuram RK, Menodiado FM, Ingram DR, Twa MD, et al. Noncontact Measurement of Elasticity for the Detection of Soft-Tissue Tumors Using Phase-Sensitive Optical Coherence Tomography Combined with a Focused Air-Puff System. *Opt Lett* (2012) 37(24):5184–6. doi:10.1364/OL.37.005184
46. Kirkpatrick SJ, Duncan DD, and Fang L. Low-Frequency Surface Wave Propagation and the Viscoelastic Behavior of Porcine Skin. *J Biomed Opt* (2004) 9(6):1311. doi:10.1117/1.1803843
47. Vappou J, Maleke C, and Konofagou EE. Quantitative Viscoelastic Parameters Measured by Harmonic Motion Imaging. *Phys Med Biol* (2009) 54(11):3579–94. doi:10.1088/0031-9155/54/11/020
48. Muthupillai R, Lomas D, Rossman P, Greenleaf J, Manduca A, and Ehman R. Magnetic Resonance Elastography by Direct Visualization of Propagating

Acoustic Strain Waves. *Science* (1995) 269(5232):1854–7. doi:10.1126/science.7569924
49. Schmitt JM. OCT Elastography: Imaging Microscopic Deformation and Strain of Tissue. *Opt Express* (1998) 3(6):199–211. doi:10.1364/OE.3.000199
50. Hai P, Yao J, Li G, Li C, and Wang LV. Photoacoustic Elastography. *Opt Lett* (2016) 41(4):725–8. doi:10.1364/OL.41.000725
51. Prevedel R, Diz-Muñoz A, Ruocco G, and Antonacci G. Brillouin Microscopy: An Emerging Tool for Mechanobiology. *Nat Methods* (2019) 16:969–77. doi:10.1038/s41592-019-0543-3
52. Sridhar M, and Insana MF. Ultrasonic Measurements of Breast Viscoelasticity. *Med Phys* (2007) 34(12):4757–67. doi:10.1118/1.2805258
53. Kennedy BF, Wijesinghe P, and Sampson DD. The Emergence of Optical Elastography in Biomedicine. *Nat Photon* (2017) 11:215–21. doi:10.1038/nphoton.2017.6
54. Wijesinghe P, Mclaughlin RA, Sampson DD, and Kennedy BF. Parametric Imaging of Viscoelasticity Using Optical Coherence Elastography. *Phys Med Biol* (2015) 60(6):2293–307. doi:10.1088/0031-9155/60/6/2293
55. Clarke EC, Cheng S, Green M, Sinkus R, and Bilston LE. Using Static Preload with Magnetic Resonance Elastography to Estimate Large Strain Viscoelastic Properties of Bovine Liver. *J Biomech* (2011) 44(13):2461–5. doi:10.1016/j.jbiomech.2011.06.023
56. Gennisson J-L, Deffieux T, Fink M, and Tanter M. Ultrasound Elastography: Principles and Techniques. *Diagn Interv Imaging* (2013) 94(5):487–95. doi:10.1016/j.diii.2013.01.022
57. Bercoff J, Chaffai S, Tanter M, Sandrin L, Catheline S, Fink M, et al. *In Vivo* Breast Tumor Detection Using Transient Elastography. *Ultrasound Med Biol* (2003) 29(10):1387–96. doi:10.1016/S0301-5629(03)00978-5
58. Catheline S, Gennisson J-L, Delon G, Fink M, Sinkus R, Abouelkaram S, et al. Measurement of Viscoelastic Properties of Homogeneous Soft Solid Using Transient Elastography: An Inverse Problem Approach. *J Acoust Soc Am* (2004) 116(6):3734–41. doi:10.1121/1.1815075
59. Gennisson J-L, Lerouge S, and Cloutier G. Assessment by Transient Elastography of the Viscoelastic Properties of Blood During Clotting. *Ultrasound Med Biol* (2006) 32(10):1529–37. doi:10.1016/j.ultrasmedbio.2006.06.008
60. Zhao J, Zhai F, Cheng J, He Q, Luo J, Yang X, et al. Evaluating the Significance of Viscoelasticity in Diagnosing Early-Stage Liver Fibrosis with Transient Elastography. *PLoS One* (2017) 12(1):e0170073. doi:10.1371/journal.pone.0170073
61. Lerner RM, Parker KJ, Holen J, Gramiak R, and Waag RC. Sono-Elasticity: Medical Elasticity Images Derived from Ultrasound Signals in Mechanically Vibrated Targets. *Acoust Imaging* (1988) 16:317–27. doi:10.1007/978-1-4613-0725-9_31
62. Lerner RM, Huang SR, and Parker KJ. "Sonoelasticity" Images Derived from Ultrasound Signals in Mechanically Vibrated Tissues. *Ultrasound Med Biol* (1990) 16(3):231–9. doi:10.1016/0301-5629(90)90002-t
63. Taylor LS, Porter BC, Rubens DJ, and Parker KJ. Three-Dimensional Sonoelastography: Principles and Practices. *Phys Med Biol* (2000) 45(6):1477–94. doi:10.1088/0031-9155/45/6/306
64. Cortes DH, Suydam SM, Silbernagel KG, Buchanan TS, and Elliott DM. Continuous Shear Wave Elastography: A New Method to Measure Viscoelastic Properties of Tendons *In Vivo*. *Ultrasound Med Biol* (2015) 41(6):1518–29. doi:10.1016/j.ultrasmedbio.2015.02.001
65. Ramier A, Tavakol B, and Yun SH. Measuring Mechanical Wave Speed, Dispersion, and Viscoelastic Modulus of the Cornea Using Optical Coherence Elastography. *Opt Express* (2019) 27(12):16635–49. doi:10.1364/OE.27.016635
66. Nguyen TM, Song S, Arnal B, Wong EY, Huang Z, Wang RK, et al. Shear Wave Pulse Compression for Dynamic Elastography Using Phase-Sensitive Optical Coherence Tomography. *J Biomed Opt* (2014) 19(1):016013. doi:10.1117/1.JBO.19.1.016013
67. Kearney SP, Khan A, Dai Z, and Royston TJ. Dynamic Viscoelastic Models of Human Skin Using Optical Elastography. *Phys Med Biol* (2015) 60(17):6975–90. doi:10.1088/0031-9155/60/17/6975
68. Jin Z, Zhou Y, Shen M, Wang Y, Lu F, and Zhu D. Assessment of Corneal Viscoelasticity Using Elastic Wave Optical Coherence Elastography. *J Biophotonics* (2019) 13(1):e201960074. doi:10.1002/jbio.201960074
69. Adie SG, Liang X, Kennedy BF, John R, Sampson DD, and Boppart SA. Spectroscopic Optical Coherence Elastography. *Opt Express* (2010) 18(25):25519–34. doi:10.1364/OE.18.025519
70. Liang X, Adie SG, John R, and Boppart SA. Dynamic Spectral-Domain Optical Coherence Elastography for Tissue Characterization. *Opt Express* (2010) 18(13):14183. doi:10.1364/OE.18.014183
71. Nightingale KR, Palmeri ML, Nightingale RW, and Trahey GE. On the Feasibility of Remote Palpation Using Acoustic Radiation Force. *J Acoust Soc Am* (2001) 110(1):625–34. doi:10.1121/1.1378344
72. Nightingale K, Soo MS, Nightingale R, and Trahey G. Acoustic Radiation Force Impulse Imaging: *In Vivo* Demonstration of Clinical Feasibility. *Ultrasound Med Biol* (2002) 28(2):227–35. doi:10.1016/s0301-5629(01)00499-9
73. Walker WF, Fernandez FJ, and Negron LA. A Method of Imaging Viscoelastic Parameters with Acoustic Radiation Force. *Phys Med Biol* (2000) 45(6):1437–47. doi:10.1088/0031-9155/45/6/303
74. Sarvazyan AP, Rudenko OV, Swanson SD, Fowlkes JB, and Emelianov SY. Shear Wave Elasticity Imaging: a New Ultrasonic Technology of Medical Diagnostics. *Ultrasound Med Biol* (1998) 24(9):1419–35. doi:10.1016/S0301-5629(98)00110-0
75. Chen S, Sanchez W, Callstrom MR, Gorman B, Lewis JT, Sanderson SO, et al. Assessment of Liver Viscoelasticity by Using Shear Waves Induced by Ultrasound Radiation Force. *Radiology* (2013) 266(3):964–70. doi:10.1148/radiol.12120837
76. Amador C, Urban MW, Chen S, and Greenleaf JF. Loss Tangent and Complex Modulus Estimated by Acoustic Radiation Force Creep and Shear Wave Dispersion. *Phys Med Biol* (2012) 57(5):1263–82. doi:10.1088/0031-9155/57/5/1263
77. Nenadic IZ, Urban MW, Heng Zhao H, Sanchez W, Morgan PE, Greenleaf JF, et al. "Application of Attenuation Measuring Ultrasound Shearwave Elastography in 8 Post-Transplant Liver Patients", in IEEE International Ultrasonics Symposium, Chicago, IL, September 3–4, 2014, 987–90. (2014). doi:10.1109/ULTSYM.2014.0242
78. Bercoff J, Tanter M, and Fink M. Supersonic Shear Imaging: A New Technique for Soft Tissue Elasticity Mapping. *IEEE Trans Ultrason Ferroelect Freq Contr* (2004) 51(4):396–409. doi:10.1109/TUFFC.2004.1295425
79. Tanter M, Bercoff J, Athanasiou A, Deffieux T, Gennisson J-L, Montaldo G, et al. Quantitative Assessment of Breast Lesion Viscoelasticity: Initial Clinical Results Using Supersonic Shear Imaging. *Ultrasound Med Biol* (2008) 34(9):1373–86. doi:10.1016/j.ultrasmedbio.2008.02.002
80. Han Z, Singh M, Aglyamov SR, Liu C-H, Nair A, Raghunathan R, et al. Quantifying Tissue Viscoelasticity Using Optical Coherence Elastography and the Rayleigh Wave Model. *J Biomed Opt* (2016) 21(9):090504. doi:10.1117/1.JBO.21.9.090504
81. Zvietcovich F, Rolland JP, and Parker KJ. An Approach to Viscoelastic Characterization of Dispersive Media by Inversion of a General Wave Propagation Model. *J Innov Opt Health Sci* (2017) 10(6):1742008. doi:10.1142/S1793545817420081
82. Maczynska E, Karnowski K, Szulzycki K, Malinowska M, Dolezyczek H, Cichanski A, et al. Assessment of the Influence of Viscoelasticity of Cornea in Animal *Ex Vivo* Model Using Air-Puff Optical Coherence Tomography and Corneal Hysteresis. *J Biophotonics* (2018) 12(2):e201800154. doi:10.1002/jbio.201800154
83. Leartprapun N, Iyer R, and Adie SG. "Model-Independent Quantification of Soft Tissue Viscoelasticity with Dynamic Optical Coherence Elastography. *Opt Coherence Tomogr Coherence Domain Opt Methods Biomed* (2017) XXI:1005322. doi:10.1117/12.2251626
84. Zhu J, Qi L, Miao Y, Ma T, Dai C, Qu Y, et al. 3D Mapping of Elastic Modulus Using Shear Wave Optical Micro-Elastography. *Sci Rep* (2016) 6(1):1–9. doi:10.1038/srep35499
85. Gao G, Yang S, and Xing D. Viscoelasticity Imaging of Biological Tissues with Phase-Resolved Photoacoustic Measurement. *Opt Lett* (2011) 36(17):3341–3. doi:10.1364/OL.36.003341
86. Wang Q, Shi Y, Yang F, and Yang S. Quantitative Photoacoustic Elasticity and Viscosity Imaging for Cirrhosis Detection. *Appl Phys Lett* (2018) 112:211902. doi:10.1063/1.5021675
87. Wang LV, and Hu S. Photoacoustic Tomography: *In Vivo* Imaging from Organelles to Organs. *Science* (2012) 335(6075):1458–62. doi:10.1126/science.1216210
88. Singh MS, and Thomas A. Photoacoustic Elastography Imaging: A Review. *J Biomed Opt* (2019) 24(4):040902. doi:10.1117/1.JBO.24.4.040902
89. Elsayad K, Werner S, Gallemi M, Kong J, Sanchez Guajardo ER, Zhang L, et al. Mapping the Subcellular Mechanical Properties of Live Cells in Tissues

with Fluorescence Emission-Brillouin Imaging. *Sci Signal* (2016) 9(435):rs5. doi:10.1126/scisignal.aaf6326
90. Mattana S, Caponi S, Tamagnini F, Fioretto D, and Palombo F. Viscoelasticity of Amyloid Plaques in Transgenic Mouse Brain Studied by Brillouin Microspectroscopy and Correlative Raman Analysis. *J Innov Opt Health Sci* (2017) 10(6):1742001. doi:10.1142/s1793545817420019
91. Leartprapun N, Iyer RR, Untracht GR, Mulligan JA, and Adie SG. Photonic Force Optical Coherence Elastography for Three-Dimensional Mechanical Microscopy. *Nat Commun* (2018) 9:2079. doi:10.1038/s41467-018-04357-8
92. Leartprapun N, Lin Y, and Adie SG. Microrheological Quantification of Viscoelastic Properties with Photonic Force Optical Coherence Elastography. *Opt Express* (2019) 27:22615. doi:10.1364/oe.27.022615
93. Das S, Schill A, Liu C-H, Aglyamov S, and Larin KV. Laser-Induced Elastic Wave Classification: Thermoelastic Versus Ablative Regimes for All-Optical Elastography Applications. *J Biomed Opt* (2020) 25:1–13. doi:10.1117/1.jbo.25.3.035004
94. Liu CH, Nevozhay D, Sokolov KV, and Larin KV. "Tissue Biomechanics with Nanobomb Optical Coherence Elastography", in Biophotonics Congress: Biomed Optics Congress, Hollywood, FL, April 3–6, 2018 (2018).
95. Huang PC, Iyer RR, Liu YZ, and Boppart SA. Single-Shot Two-Dimensional Spectroscopic Magnetomotive Optical Coherence Elastography with Graphics Processing Unit Acceleration. *Opt Lett* (2020) 45(15):4124. doi:10.1364/OL.397900
96. Crecea V, Oldenburg AL, Liang X, Ralston TS, and Boppart SA. Magnetomotive Nanoparticle Transducers for Optical Rheology of Viscoelastic Materials. *Opt Express* (2009) 17(25):23114. doi:10.1364/OE.17.023114
97. Oldenburg AL, and Boppart SA. Resonant Acoustic Spectroscopy of Soft Tissues Using Embedded Magnetomotive Nanotransducers and Optical Coherence Tomography. *Phys Med Biol* (2010) 55(4):1189–201. doi:10.1088/0031-9155/55/4/019
98. Lau K, Tao H, Liu H, Wen J, Sturgeon K, Sorfazlian N, et al. Anisotropic Stress Orients Remodelling of Mammalian Limb Bud Ectoderm. *Nat Cell Biol* (2015) 17:569–79. doi:10.1038/ncb3156
99. Blanchard GB, Kabla AJ, Schultz NL, Butler LC, Sanson B, Gorfinkiel N, et al. Tissue Tectonics: Morphogenetic Strain Rates, Cell Shape Change and Intercalation. *Nat Methods* (2009) 6:458–64. doi:10.1038/nmeth.1327
100. Solon J, Kaya-Çopur A, Colombelli J, and Brunner D. Pulsed Forces Timed by a Ratchet-Like Mechanism Drive Directed Tissue Movement During Dorsal Closure. *Cell* (2009) 137(7):1331–42. doi:10.1016/j.cell.2009.03.050
101. Varner VD, Voronov DA, and Taber LA. Mechanics of Head Fold Formation: Investigating Tissue-Level Forces During Early Development. *Development* (2010) 137:3801–11. doi:10.1242/dev.054387
102. Charrier EE, Pogoda K, Wells RG, and Janmey PA. Control of Cell Morphology and Differentiation by Substrates with Independently Tunable Elasticity and Viscous Dissipation. *Nat Commun* (2018) 9:449. doi:10.1038/s41467-018-02906-9
103. Barriga EH, and Mayor R. Adjustable Viscoelasticity Allows for Efficient Collective Cell Migration. *Semin Cell Dev Biol* (2019) 93:55–68. doi:10.1016/j.semcdb.2018.05.027
104. Cameron AR, Frith JE, and Cooper-White JJ. The Influence of Substrate Creep on Mesenchymal Stem Cell Behaviour and Phenotype. *Biomaterials* (2011) 32:5979–93. doi:10.1016/j.biomaterials.2011.04.003
105. Chaudhuri O, Cooper-White J, Janmey PA, Mooney DJ, and Shenoy VB. Effects of Extracellular Matrix Viscoelasticity on Cellular Behaviour. *Nature* (2020) 584:535–46. doi:10.1038/s41586-020-2612-2
106. Clément R, Dehapiot B, Collinet C, Lecuit T, and Lenne P-F. Viscoelastic Dissipation Stabilizes Cell Shape Changes during Tissue Morphogenesis. *Curr Biol* (2017) 27(20):3132–42. doi:10.1016/j.cub.2017.09.005
107. Mathieu S, and Manneville J-B. Intracellular Mechanics: Connecting Rheology and Mechanotransduction. *Curr Opin Cell Biol* (2019) 56:34–44. doi:10.1016/j.ceb.2018.08.007
108. Feric M, Vaidya N, Harmon TS, Mitrea DM, Zhu L, Richardson TM, et al. Coexisting Liquid Phases Underlie Nucleolar Subcompartments. *Cell* (2016) 165:1686–97. doi:10.1016/j.cell.2016.04.047
109. Hyman AA, Weber CA, and Jülicher F. Liquid-Liquid Phase Separation in Biology. *Annu Rev Cell Dev Biol* (2014) 30:39–58. doi:10.1146/annurev-cellbio-100913-013325
110. Malinovska L, Kroschwald S, and Alberti S. Protein Disorder, Prion Propensities, and Self-Organizing Macromolecular Collectives. *Biochim Biophys Acta* (2013) 1834(5):918–31. doi:10.1016/j.bbapap.2013.01.003
111. Banani SF, Lee HO, Hyman AA, and Rosen MK. Biomolecular Condensates: Organizers of Cellular Biochemistry. *Nat Rev Mol Cell Biol* (2017) 18:285–98. doi:10.1038/nrm.2017.7
112. Brangwynne CP, Eckmann CR, Courson DS, Rybarska A, Hoege C, Gharakhani J, et al. Germline P Granules are Liquid Droplets that Localize by Controlled Dissolution/Condensation. *Science* (2009) 324(5935):1729–32. doi:10.1126/science.1172046
113. Shin Y, Chang Y-C, Lee DSW, Berry J, Sanders DW, Ronceray P, et al. Liquid Nuclear Condensates Mechanically Sense and Restructure the Genome. *Cell* (2019) 176:1518. doi:10.1016/j.cell.2019.02.025
114. Elbaum-Garfinkle S, Kim Y, Szczepaniak K, Chen CC, Eckmann CR, Myong S, et al.The Disordered P Granule Protein LAF-1 Drives Phase Separation into Droplets with Tunable Viscosity and Dynamics. *Proc Natl Acad Sci USA* (2015) 112(23):7189-94. doi:10.1073/pnas.1504822112
115. Li YR, King OD, Shorter J, and Gitler AD. Stress Granules as Crucibles of ALS Pathogenesis. *J Cell Biol* (2013) 201(3):361–72. doi:10.1083/jcb.201302044
116. Loewe B, Chiang M, Marenduzzo D, and Marchetti MC. Solid-Liquid Transition of Deformable and Overlapping Active Particles. *Phys Rev Lett* (2020) 125(3):038003. doi:10.1103/PhysRevLett.125.038003
117. Lo CM, Wang HB, Dembo M, and Wang Y. Cell Movement is Guided by the Rigidity of the Substrate. *Biophys J* (2000) 79(1):144–52. doi:10.1016/S0006-3495(00)76279-5
118. Hartman CD, Isenberg BC, Chua SG, and Wong JY. Vascular Smooth Muscle Cell Durotaxis Depends on Extracellular Matrix Composition. *Proc Natl Acad Sci USA* (2016) 113(40):11190–5. doi:10.1073/pnas.1611324113
119. Sunyer R, Conte V, Escribano J, Elosegui-Artola A, Labernadie A, Valon L, et al. Collective Cell Durotaxis Emerges from Long-Range Intercellular Force Transmission. *Science* (2016) 353(6304):1157–61. doi:10.1126/science.aaf7119
120. Barriga EH, Franze K, Charras G, and Mayor R. Tissue Stiffening Coordinates Morphogenesis by Triggering Collective Cell Migration *In Vivo*. *Nature* (2018) 554:523–7. doi:10.1038/nature25742
121. Koser DE, Thompson AJ, Foster SK, Dwivedy A, Pillai EK, Sheridan GK, et al. Mechanosensing is Critical for Axon Growth in the Developing Brain. *Nat Neurosci* (2016) 19(12):1592–8. doi:10.1038/nn.4394
122. Zhu M, Tao H, Samani M, Luo M, Wang X, Hopyan S, et al. Spatial Mapping of Tissue Properties *In Vivo* Reveals a 3D Stiffness Gradient in the Mouse Limb Bud. *Proc Natl Acad Sci USA* (2020). 117(9):4781–91. doi:10.1073/pnas.1912656117
123. Clément B. "Extracellular Matrix Remodelling and Matrix Metalloproteinases in the Liver", in *Matrix Metalloproteinases in Tissue Remodelling and Inflammation*. Editors V Lagente and E. Boichot Birkhäuser Basel (2008). doi:10.1007/978-3-7643-8585-9_9
124. Forgacs G, Newman SA, Hinner B, Maier CW, and Sackmann E. Assembly of Collagen Matrices as a Phase Transition Revealed by Structural and Rheologic Studies. *Biophysical J* (2003) 84:1272–80. doi:10.1016/s0006-3495(03)74942-x
125. Collinet C, and Lecuit T. Programmed and Self-Organized Flow of Information during Morphogenesis. *Nat Rev Mol Cell Biol* (2021) 22:245–65. doi:10.1038/s41580-020-00318-6
126. Cai D, Dai W, Prasad M, Luo J, Gov NS, and Montell DJ. Modeling and Analysis of Collective Cell Migration in an In Vivo Three-dimensional Environment. *Proc Natl Acad Sci USA* (2016) 113(15):E2134–41. doi:10.1073/pnas.1522656113
127. Müller C, Müller A, and Pompe T. Dissipative Interactions in Cell-Matrix Adhesion. *Soft Matter* (2013) 9:6207. doi:10.1039/c3sm50803j
128. Schultz KM, Kyburz KA, and Anseth KS. Measuring Dynamic Cell-Material Interactions and Remodeling During 3D Human Mesenchymal Stem Cell Migration in Hydrogels. *Proc Natl Acad Sci USA* (2015) 112:E3757–E3764. doi:10.1073/pnas.1511304112
129. Murrell M, Kamm R, and Matsudaira P. Substrate Viscosity Enhances Correlation in Epithelial Sheet Movement. *Biophys J* (2011) 101:297–306. doi:10.1016/j.bpj.2011.05.048
130. Charrier EE, Pogoda K, Li R, Wells RG, and Janmey PA. Elasticity-Dependent Response of Malignant Cells to Viscous Dissipation. *Biomech Model Mechanobiol* (2020) 20:145–54. doi:10.1007/s10237-020-01374-9

131. Martinez JS, Lehaf AM, Schlenoff JB, and Keller TCS. Cell Durotaxis on Polyelectrolyte Multilayers with Photogenerated Gradients of Modulus. *Biomacromolecules* (2013) 14:1311–20. doi:10.1021/bm301863a
132. Shirke PU, Goswami H, Kumar V, Shah D, Das S, Bellare J, et al. "Viscotaxis"-Directed Migration of Mesenchymal Stem Cells in Response to Loss Modulus Gradient. *bioRxiv* (2020) 804492. doi:10.1101/804492
133. Liebchen B, Monderkamp P, ten Hagen B, and Löwen H. Viscotaxis : Microswimmer Navigation in Viscosity Gradients. *Phys Rev Lett* (2018) 120:120. doi:10.1103/physrevlett.120.208002
134. Krieg M, Fläschner G, Alsteens D, Gaub BM, Roos WH, Wuite GJL, et al. Atomic Force Microscopy-Based Mechanobiology. *Nat Rev Phys* (2019) 1: 41–57. doi:10.1038/s42254-018-0001-7
135. Efremov YM, Wang W-H, Hardy SD, Geahlen RL, and Raman A. Measuring Nanoscale Viscoelastic Parameters of Cells Directly from AFM Force-Displacement Curves. *Sci Rep* (2017) 7:1541. doi:10.1038/s41598-017-01784-3
136. Tao H, Zhu M, Lau K, Whitley OKW, Samani M, Xiao X, et al. Oscillatory Cortical Forces Promote Three Dimensional Cell Intercalations that Shape the Murine Mandibular Arch. *Nat Commun* (2019) 10:1703. doi:10.1038/s41467-019-09540-z
137. Zhu M, Zhang K, Tao H, Hopyan S, and Sun Y. Magnetic Micromanipulation for *In Vivo* Measurement of Stiffness Heterogeneity and Anisotropy in the Mouse Mandibular Arch. *Research* (2020) 2020:7914074. doi:10.34133/2020/7914074
138. D'Angelo A, Dierkes K, Carolis C, Salbreux G, and Solon J. *In Vivo* Force Application Reveals a Fast Tissue Softening and External Friction Increase during Early Embryogenesis. *Curr Biol* (2019) 29(9):1564–71. doi:10.1016/j.cub.2019.04.010
139. Serwane F, Mongera A, Rowghanian P, Kealhofer DA, Lucio AA, Hockenbery ZM, et al. *In Vivo* quantification of Spatially Varying Mechanical Properties in Developing Tissues. *Nat Methods* (2017) 14:181–6. doi:10.1038/nmeth.4101
140. He B, Doubrovinski K, Polyakov O, and Wieschaus E. Apical Constriction Drives Tissue-Scale Hydrodynamic Flow to Mediate Cell Elongation. *Nature* (2014) 508(7496):392–6. doi:10.1038/nature13070
141. Doubrovinski K, Swan M, Polyakov O, and Wieschaus EF. Measurement of Cortical Elasticity inDrosophila Melanogasterembryos Using Ferrofluids. *Proc Natl Acad Sci USA* (2017) 114(5):1051–6. doi:10.1073/pnas.1616659114
142. Dassow MV, Strother JA, and Davidson LA. Surprisingly Simple Mechanical Behavior of a Complex Embryonic Tissue. *PLoS One* (2010) 5:e15359. doi:10.1371/journal.pone.0015359
143. Guevorkian K, Gonzalez-Rodriguez D, Carlier C, Dufour S, and Brochard-Wyart F. Mechanosensitive Shivering of Model Tissues Under Controlled Aspiration. *Proc Natl Acad Sci* (2011) 108:13387–92. doi:10.1073/pnas.1105741108
144. Feric M, Broedersz CP, and Brangwynne CP. Soft Viscoelastic Properties of Nuclear Actin Age Oocytes Due to Gravitational Creep. *Sci Rep* (2015) 5: 16607. doi:10.1038/srep16607
145. Berret J-F. Local Viscoelasticity of Living Cells Measured by Rotational Magnetic Spectroscopy. *Nat Commun* (2016) 7:10134. doi:10.1038/ncomms10134
146. Desprat N, Guiroy A, and Asnacios A. Microplates-Based Rheometer for a Single Living Cell. *Rev Scientific Instr* (2006) 77(5):055111. doi:10.1063/1.2202921
147. Sinkus R, Siegmann K, Xydeas T, Tanter M, Claussen C, and Fink M. MR Elastography of Breast Lesions: Understanding the Solid/liquid Duality Can Improve the Specificity of Contrast-Enhanced MR Mammography. *Magn Reson Med* (2007) 58(6):1135–44. doi:10.1002/mrm.21404
148. Streitberger K-J, Reiss-Zimmermann M, Freimann FB, Bayerl S, Guo J, Arlt F, et al. High-Resolution Mechanical Imaging of Glioblastoma by Multifrequency Magnetic Resonance Elastography. *PLoS One* (2014) 9: e110588. doi:10.1371/journal.pone.0110588
149. Hiscox LV, Johnson CL, McGarry MDJ, Perrins M, Littlejohn A, van Beek EJR, et al. High-Resolution Magnetic Resonance Elastography Reveals Differences in Subcortical Gray Matter Viscoelasticity between Young and Healthy Older Adults. *Neurobiol Aging* (2018) 65:158–67. doi:10.1016/j.neurobiolaging.2018.01.010
150. Amador Carrascal C, Chen S, Urban MW, and Greenleaf JF. Acoustic Radiation Force-Induced Creep-Recovery (ARFICR): A Noninvasive Method to Characterize Tissue Viscoelasticity. *IEEE Trans Ultrason Ferroelectr Freq Control* (2018) 65:3–13. doi:10.1109/tuffc.2017.2768184
151. Rzymski P, Skórzewska A, Skibińska-Zielińska M, and Opala T. Factors Influencing Breast Elasticity Measured by the Ultrasound Shear Wave Elastography - Preliminary Results. *Arch Med Sci* (2011) 7(1):127–33. doi:10.5114/aoms.2011.20617
152. Muller M, Gennisson J-L, Deffieux T, Tanter M, and Fink M. Quantitative Viscoelasticity Mapping of Human Liver Using Supersonic Shear Imaging: Preliminary *In Vivo* Feasability Study. *Ultrasound Med Biol* (2009) 35(2): 219–29. doi:10.1016/j.ultrasmedbio.2008.08.018
153. Lan G, Aglyamov SR, Larin KV, and Twa MD. *In Vivo* Human Corneal Shear-Wave Optical Coherence Elastography. *Optom Vis Sci* (2021) 98(1): 58–63. doi:10.1097/OPX.0000000000001633
154. Ramier A, Eltony AM, Chen Y, Clouser F, Birkenfeld JS, Watts A, et al. *In Vivo* Measurement of Shear Modulus of the Human Cornea Using Optical Coherence Elastography. *Sci Rep* (2020) 10:10. doi:10.1038/s41598-020-74383-4
155. Kennedy BF, Hillman TR, Mclaughlin RA, Quirk BC, and Sampson DD. *In Vivo* Dynamic Optical Coherence Elastography Using a Ring Actuator. *Opt Express* (2009) 17(24):21762–72. doi:10.1364/OE.17.021762
156. Yun SH, and Chernyak D. Brillouin Microscopy. *Curr Opin Ophthalmol* (2018) 29(4):299–305. doi:10.1097/ICU.0000000000000489
157. Bailey M, Alunni-Cardinali M, Correa N, Caponi S, Holsgrove T, Barr H, et al. Viscoelastic Properties of Biopolymer Hydrogels Determined by Brillouin Spectroscopy: A Probe of Tissue Micromechanics. *Sci Adv* (2020) 6:eabc1937. doi:10.1126/sciadv.abc1937
158. Wang S, and Larin KV. Optical Coherence Elastography for Tissue Characterization: a Review. *J Biophoton* (2015) 8(4):279–302. doi:10.1002/jbio.201400108
159. Larin KV, and Sampson DD. Optical Coherence Elastography - OCT at Work in Tissue Biomechanics [Invited]. *Biomed Opt Express* (2017) 8(2):1172–202. doi:10.1364/BOE.8.001172
160. Marrese M, Antonovaite N, Nelemans BKA, Smit TH, and Iannuzzi D. Micro-Indentation and Optical Coherence Tomography for the Mechanical Characterization of Embryos: Experimental Setup and Measurements on Chicken Embryos. *Acta Biomater* (2019) 97:524–34. doi:10.1016/j.actbio.2019.07.056
161. Schlüßler R, Möllmert S, Abuhattum S, Cojoc G, Müller P, Kim K, et al. Mechanical Mapping of Spinal Cord Growth and Repair in Living Zebrafish Larvae by Brillouin Imaging. *Biophys J* (2018) 115(5):911–23. doi:10.1016/j.bpj.2018.07.027
162. Bevilacqua C, Sánchez-Iranzo H, Richter D, Diz-Muñoz A, and Prevedel R. Imaging Mechanical Properties of Sub-Micron ECM in Live Zebrafish Using Brillouin Microscopy. *Biomed Opt Express* (2019) 10:1420. doi:10.1364/boe.10.001420
163. Qian X, Ma T, Yu M, Chen X, Shung KK, and Zhou Q. Multi-Functional Ultrasonic Micro-Elastography Imaging System. *Sci Rep* (2017) 7:1230. doi:10.1038/s41598-017-01210-8
164. Braun J, Tzschätzsch H, Körting C, Ariza de Schellenberger A, Jenderka M, Drießle T, et al. A Compact 0.5 T MR Elastography Device and its Application for Studying Viscoelasticity Changes in Biological Tissues during Progressive Formalin Fixation. *Magn Reson Med* (2017) 79(1): 470–8. doi:10.1002/mrm.26659
165. Bigot M, Chauveau F, Beuf O, and Lambert SA. Magnetic Resonance Elastography of Rodent Brain. *Front Neurol* (2018) 9:1010. doi:10.3389/fneur.2018.01010
166. Wu P-J, Kabakova IV, Ruberti JW, Sherwood JM, Dunlop IE, Paterson C, et al. Water Content, Not Stiffness, Dominates Brillouin Spectroscopy Measurements in Hydrated Materials. *Nat Methods* (2018) 15:561–2. doi:10.1038/s41592-018-0076-1
167. Raghunathan R, Zhang J, Wu C, Rippy J, Singh M, Larin KV, et al. Evaluating Biomechanical Properties of Murine Embryos Using Brillouin Microscopy and Optical Coherence Tomography. *J Biomed Opt* (2017) 22(8):086013. doi:10.1117/1.JBO.22.8.086013

168. Antonacci G, and Braakman S. Erratum: Corrigendum: Biomechanics of Subcellular Structures by Non-Invasive Brillouin Microscopy. *Sci Rep* (2017) 7:46789. doi:10.1038/srep46789
169. Kennedy BF, Kennedy KM, and Sampson DD. A Review of Optical Coherence Elastography: Fundamentals, Techniques and Prospects. *IEEE J Sel Top Quan Electron* (2014) 20(2):272–88. doi:10.1109/JSTQE.2013.2291445
170. Sun C, Standish B, and Yang VXD. Optical Coherence Elastography: Current Status and Future Applications. *J Biomed Opt* (2011) 16(4):043001. doi:10.1117/1.3560294
171. Curatolo A, Villiger M, Lorenser D, Wijesinghe P, Fritz A, Kennedy BF, et al. Ultrahigh-Resolution Optical Coherence Elastography. *Opt Lett* (2016) 41(1): 21–4. doi:10.1364/OL.41.000021
172. Wang RK, Kirkpatrick S, and Hinds M. Phase-Sensitive Optical Coherence Elastography for Mapping Tissue Microstrains in Real Time. *Appl Phys Lett* (2007) 90(16):164105. doi:10.1063/1.2724920
173. Mainardi F. On Some Properties of the Mittag-Leffler Function E_α $(-t^\alpha)$, Completely Monotone for $t > 0$ with $0 < \alpha < 1$. *Discrete Continuous Dynamical Syst* (2014) 19(7):2267–78. doi:10.3934/dcdsb.2014.19.2267

Conflict of Interest: The authors declare that the research was conducted in the absence of any commercial or financial relationships that could be construed as a potential conflict of interest.

frontiers in Physics

ORIGINAL RESEARCH
published: 09 June 2021
doi: 10.3389/fphy.2021.649821

Activity-Induced Fluidization and Arrested Coalescence in Fusion of Cellular Aggregates

*Steven Ongenae, Maxim Cuvelier, Jef Vangheel, Herman Ramon and Bart Smeets**

MeBioS, KU Leuven, Leuven, Belgium

At long time scales, tissue spheroids may flow or appear solid depending on their capacity to reorganize their internal structure. Understanding the relationship between intrinsic mechanical properties at the single cell level, and the tissue spheroids dynamics at the long-time scale is key for artificial tissue constructs, which are assembled from multiple tissue spheroids that over time fuse to form coherent structures. The dynamics of this fusion process are frequently analyzed in the framework of liquid theory, wherein the time scale of coalescence of two droplets is governed by its radius, viscosity and surface tension. In this work, we extend this framework to glassy or jammed cell behavior which can be observed in spheroid fusion. Using simulations of an individual-cell based model, we demonstrate how the spheroid fusion process can be steered from liquid to arrested by varying active cell motility and repulsive energy as established by cortical tension. The divergence of visco-elastic relaxation times indicates glassy relaxation near the transition toward arrested coalescence. Finally, we investigate the role of cell growth in spheroid fusion dynamics. We show that the presence of cell division introduces plasticity in the material and thereby increases coalescence during fusion.

Keywords: spheroid fusion, arrested coalescence, tissue rheology, visco-elastic model, individual cell-based model, glass transition, tissue engineering, organoids

OPEN ACCESS

Edited by:
Karine Guevorkian, UMR168 Unite Physico-Chimie Curie (PCC), France

Reviewed by:
Jens Elgeti, Helmholtz-Verband Deutscher Forschungszentren (HZ), Germany
Andrej Vilfan, Max Planck Society (MPG), Germany

****Correspondence:***
Bart Smeets
bart.smeets@kuleuven.be

Specialty section:
This article was submitted to Biophysics, a section of the journal Frontiers in Physics

Received: *05 January 2021*
Accepted: *21 May 2021*
Published: *09 June 2021*

Citation:
Ongenae S, Cuvelier M, Vangheel J, Ramon H and Smeets B (2021) Activity-Induced Fluidization and Arrested Coalescence in Fusion of Cellular Aggregates. Front. Phys. 9:649821. doi: 10.3389/fphy.2021.649821

1 INTRODUCTION

A general understanding of the rheological properties of multicellular tissues is important to gain insight into the physics of morphogenetic processes during development. Furthermore, robust models of these materials allow for the design and characterization of generic unit operations, such as aggregation, dispersion, and fusion, which are used for the production of artificial tissues. Given its analogy to the merging of two liquid droplets, the fusion of tissue spheroids has received considerable interest as a model for soft tissue rheology. An analytical expression of the onset of coalescence of two equal viscous droplets under influence of their surface tension was first derived by Frenkel [1] and was improved and extended upon so that the dynamics of complete coalescence could be accurately modeled [2, 3]. Furthermore, various extensions to this framework have been proposed to take into account specific properties of multicellular materials, for example differences in spheroid size [4], and the presence of biological processes such as proliferation, differentiation and apoptosis, which may conflict with the assumption of conservation of mass [4, 5].

However, the liquid model cannot consistently reproduce *in vitro* tissue behavior. For instance, Kosheleva et al. showed that fusion dynamics did not correspond to liquid model predictions based on nano-indentation surface tension measurements [6]. Furthermore, arrested fusion has been observed between spheroids treated with Rho-kinase inhibitor affecting acto-myosin contractility [7,

8]. Arrested fusion was shown to be controlled by cancer cell activity in tumors [9]. To explain these observations, Oriola et al. recently proposed to model spheroids during fusion as visco-elastic materials instead of simple liquid droplets [10]. Such an approach has already been applied to parallel plate compression [11], micro-pipette aspiration [12], and tissue-detachment/fracture assays [13]. In general, a tissue may behave like an elastic solid at short time scales and like a liquid at longer time scales [14]. However, they can also appear solid-like at long time scales. This may occur when tissues change from a fluid-like to a solid-like state by undergoing a jamming transition [15]. In the jammed state, individual cells are caged by their neighbors preventing the cells from rearranging, resulting in glassy rheology, whereas in the unjammed state cells are able to move freely, resembling a fluid-like state.

Multiple computational approaches such as phase field models [16], Monte Carlo based models [17–19], and individual cell-based models [4, 10, 18–22], allow for the characterization of tissue-scale rheological behavior as a function of cell-scale mechanical properties or to simulate fusion of spheroids in more complex geometries. Schötz et al. calibrated an individual cell-based model to better describe the random motion of cells in tissues close to a glass transition. Nevertheless, when investigating fusion with that model, it could still be described by a liquid model. On the other hand, simulations that resulted in a solidification during spheroid fusion have already been mentioned by Kosztin et al. [20]. This observation was attributed to high levels of cell adhesion, but was not further analyzed. Recently, using individual cell-based computational models, it was demonstrated that a divergence of the visco-elastic relaxation time can be observed within a transition region of arrested fusion, indicative of a jammed system [10]. The existence of arrested fusion could thus be traced back to the build up of elastic energy during fusion.

In this work, we derive a simplified analytical expression for the coalescence of visco-elastic tissue spheroids on the basis of elasticity caused by internal structure of the droplet [23, 24]. Doings so we obtain similar results to [10]. We demonstrate the applicability of this expression by using an individual-cell based model approach to simulate the fusion process and, using this expression, we are able to compare the relaxation dynamics of fusion to the characteristic timescales involved in the preceding aggregation (or compaction) process in which the individual tissue spheroids have been formed. Finally, we extend this simulation framework to include a morphological model of the cell cycle. In analogy to active motility, cell division and growth may introduce excitation that may induce fluidization, as was observed in other systems [25–28]. Here, we investigate whether, in spheroid fusion, there is an additional active contribution of cell division beyond a mere correction for the increase in volume, and assess to what extent this contribution may unjam the cellular material [4, 5] and recover tissue coalescence.

2 MATERIALS AND METHODS

2.1 Individual Cell-Based Model

We follow an individual cell-based model approach as described in detail in Smeets et al. [29, 30]. This model has already been used to study cell aggregation and compaction dynamics. In this paper we extend the model by taking into account cell proliferation. All details of the individual cell based model can be found in **Supplementary Section S1**. In brief, the model is based on a simulation framework introduced by Delile et al. [31], in which cells are simulated as self-propelled particles. Conservative active forces are exchanged between neighboring cells, similar to [10]. The connectivity network is based on a Delaunay triangulation of the cell center coordinates. For the edges of this network, a symmetric central potential is calculated, which is parameterized by adhesion w_a and cortical tension w_r. Protrusive active forces are responsible for active migration with velocity v_t. These forces are calculated in the direction of the cell's polarization which is randomly diffusing with rotational diffusivity D_r. Hence, activity from cell motility may be parameterized as $D_{\text{eff}} := v_t^2/(2D_r)$. Overdamped equations of motion are integrated to evolve the system over time. Finally, cells are able to grow and multiply based on a cell cycle model, which is explained in **Supplementary Section S1.2**. The model parameters are listed in tables in **Supplementary Tables S1, S2**.

2.2 Simulation Setup

The simulation pipeline is shown in **Figure 1** and follows a sequence of generic unit operations to form a small tissue via fusion. In the first step we simulate the seeding and spontaneous aggregation of two aggregates for 24 h, each in their own micro-well, similar to [30]. This guarantees that the shape of each spheroid is consistent with respect to its underlying mechanical properties. It should be noted that, depending on the mechanical properties that govern the aggregation process, this relaxed configuration may have a highly irregular shape. Any (few) remaining cells that did not get incorporated in the main aggregates, are removed from the simulation in analogy to a real fusion experiment. In the second step, the two aggregates are transferred to a larger micro-well and are brought into contact with each other, simulating another 50 h during which the fusion process naturally progresses. In the final step, we extract the spheroid contours and fit two circles to compute the contact angle θ for each simulation, as explained in (**Supplementary Section S2**). Each realization of a simulated fused spheroid is initialized independently. To calculate the average fusion dynamics, i.e., the average of $\sin[\theta(t)]^2$ across all repeats, we take into account that not all spheroids start fusing at the same time, because the initial contact between the spheroids can be weak. To account for this, we define the time at which fusion starts as the last time at which we observe two distinct objects in the extracted contours. For further analysis, the extracted shape measures are shifted in time using this offset.

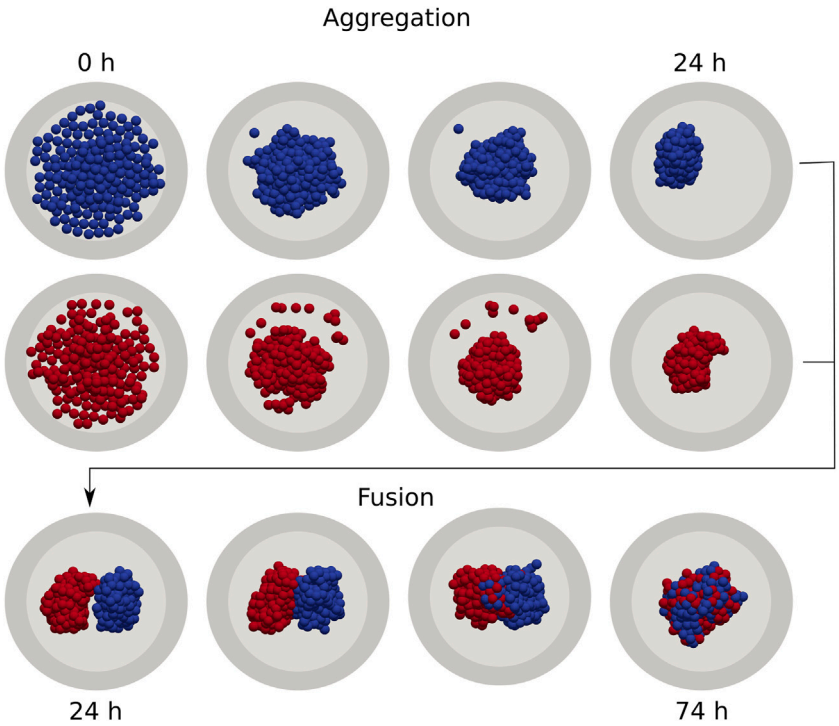

FIGURE 1 | Individual cell-based model of cell aggregation and spheroid fusion. First, gravitationally deposited cells aggregate in independent cylindrical wells for 24 h **(top)**. Next, two aggregates are extracted and combined in a single fusion simulation, which continues for a further 50 h **(bottom)**.

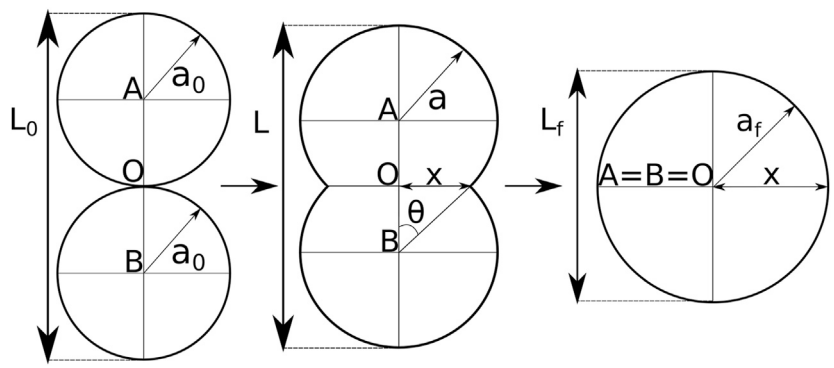

FIGURE 2 | Shape evolution during spheroid fusion adapted from [3]. The shape is described by two intersecting circles with equal radius *a*, and center *A* and *B*. *O* marks the center of the axis system, and depicts the initial contact point. Based on the intersections one defines the neck radius *x* and the angle θ. During fusion the centers *A* and *B* gradually move toward point *O*, the radius *a* increases and the doublet length *L* decreases. a_0 and a_f is the radius of the spheroids before, and after complete fusion, respectively. L_0 and L_f is the length of the spheroid doublet before, and after complete fusion, respectively.

2.3 Visco-Elastic Approximation of the Fusion Process

The fusion dynamics of two equal visco-elastic spheres can be approximated by the differential equation

$$\dot{\theta} = \frac{\Gamma}{2a_0\eta}\cot(\theta) - \frac{G'}{8\eta}\sin(\theta) = \frac{\cot(\theta)}{2\tau_\Gamma} - \frac{\sin(\theta)}{2\tau_\varepsilon} \qquad (1)$$

as derived in (**Supplementary Section S3**). Here, θ is the angle as shown in **Figure 2**, and is influenced by the surface tension Γ, the radius of the spheroid before fusion a_0, the apparent viscosity of the tissue η and the shear modulus of the tissue G'. We combine these parameters into two characteristic time constants; $\tau_\Gamma := a_0\eta/\Gamma$ is the visco-capillary time, and $\tau_\varepsilon := 4\eta/G'$ is the visco-elastic time. The analytical solution of **Eq. 1** is

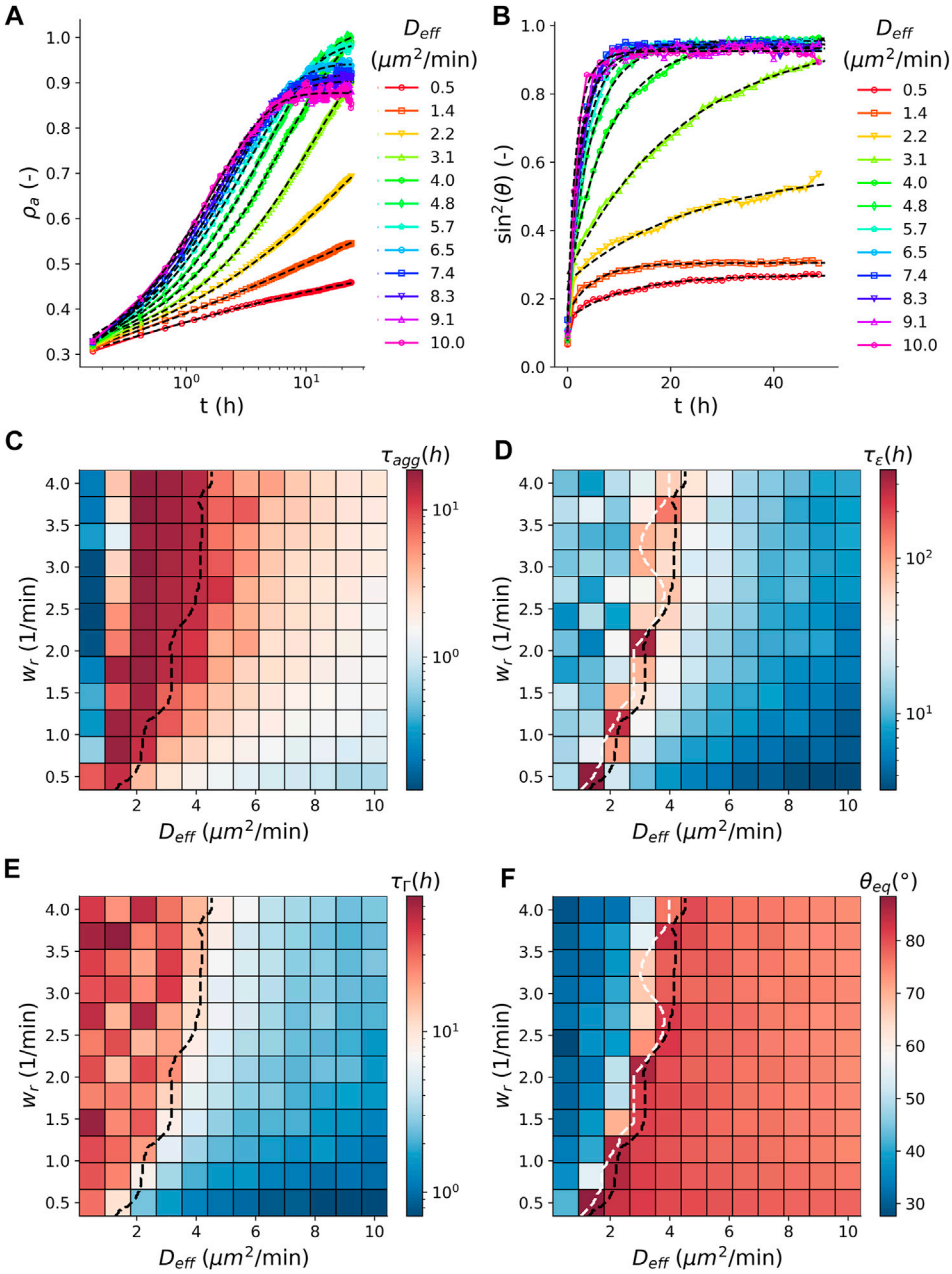

FIGURE 3 | Comparison between aggregation and fusion. **(A)** Time evolution of the average ($N = 100$) apparent density ρ_a for varying activity D_{eff} at constant level of cell repulsion $w_r = 2.09\,\text{min}^{-1}$. The fits of the KWW law **Eq. 5**, are shown as black dashed lines. **(B)** Average ($N = 50$) fusion dynamics, represented as $\sin^2(\theta)$, for varying cell activity D_{eff} at constant level of cell repulsion $w_r = 2.09\,\text{min}^{-1}$. Based on the fusion dynamics equation **Eqs. 2**, **3**, the simulated data is fitted in the form $\sin^2(\theta)$. These fits are shown as black dashed lines. **(C)** Estimated values of τ_{agg} based on KWW law **Eq. 5** during aggregation for varying cell repulsion w_r and cell activity D_{eff}. The black dashed line shows the separation of arrested versus complete fusion based on θ_{eq}. A similar trend between this black dashed line and the divergence in τ_{agg} can be observed. **(D–F)** Estimated values of the visco-elastic time constant τ_ε, the visco-capillary time constant τ_Γ based on fitting fusion dynamics in $\sin^2(\theta)$ using **Eqs. 2**, **3**, and the equilibrium angle θ_{eq} calculated using **Eq. 4**. The black dashed line shows the separation of arrested versus complete fusion based on θ_{eq}. The white dashed line represents the separation between two regions of low τ_ε. Both lines are obtained by performing a watershed segmentation on the images of θ_{eq} and $\log(\theta_\varepsilon)$, respectively, and show a similar trend.

$$\cos(\theta) = -\frac{\tau_\varepsilon}{2\tau_\Gamma} + \sqrt{\frac{\tau_\varepsilon^2}{4\tau_\Gamma^2} + 1} \times \tanh\left(\frac{\sqrt{4\tau_\Gamma^2 + \tau_\varepsilon^2}}{4\tau_\Gamma\tau_\varepsilon}(t + C)\right) \quad (2)$$

in which the complex number C (**Supplementary Section S3**) can be obtained from the initial conditions $\theta(t = 0) = \theta_0$

$$C = \frac{4\tau_\Gamma\tau_\varepsilon}{\sqrt{4\tau_\Gamma^2 + \tau_\varepsilon^2}} \operatorname{arctanh}\left(\frac{2\tau_\Gamma\cos(\theta_0) + \tau_\varepsilon}{\sqrt{4\tau_\Gamma^2 + \tau_\varepsilon^2}}\right) \quad (3)$$

In analogy to previous studies on spheroid fusion, the fusion dynamics are reported as $\sin^2(\theta) = (x/a)^2$ with a the radius of the spheroid and x the contact radius which both vary in time [4, 10, 18, 20, 21]. Other studies perform the analysis based on $(x/a_0)^2$ [5, 6, 17, 19], but this is less consistent with the underlying theory (see **Supplementary Section S4**). **Eq. 2** is used to calculate $\sin^2(\theta)$. When fitting, we use this equation with free variables: τ_Γ, τ_ε and θ_0. In order to compare simulated fusion experiments, θ_0 is retained as a free variable since the discrete initial adhesion between the first contacting cell pair will permit a rapid relaxation toward a non-zero initial angle, θ_0. Based on the fitted values, the predicted equilibrium angle θ_{eq} can be obtained as

$$\cos(\theta_{eq}) = -\frac{\tau_\varepsilon}{2\tau_\Gamma} + \sqrt{\frac{\tau_\varepsilon^2}{4\tau_\Gamma^2} + 1} = -\frac{2\Gamma}{Ga_0} + \sqrt{\frac{4\Gamma^2}{G^2a_0^2} + 1} \quad (4)$$

3 RESULTS

3.1 Arrested Coalescence Dynamics

The average dynamics of simulated tissue spheroid fusion are consistent with the derived visco-elastic material model, expressed in the time evolution of contact angle θ, **Eq. 1**, as shown in **Figure 3B** where we varied the cell activity D_{eff}. At sufficiently low D_{eff}, coalescence appears arrested and complete fusion is not attained. Given the correspondence to the visco-elastic model, the parameters τ_Γ and τ_ε can be interpreted as characteristic timescales of the multi-cellular visco-elastic material. From the fit of τ_Γ, τ_ε and the instantaneous initial angle θ_0, we are able to calculate the equilibrium fusion angle, θ_{eq}, using **Eq. 4**. When varying the cell activity D_{eff} and the repulsive energy w_{r}, two distinct regions can be recognized based on θ_{eq}, **Figure 3F**. For low activity (D_{eff}) fusion is arrested, while at higher activities fusion is complete. Higher levels of repulsion w_{r} require more cell activity to fluidize the material and hence to attain complete fusion. Similarly, the characteristic visco-capillary time τ_Γ increases when cell activity decreases and when cell repulsion increases, **Figure 3E**. When reducing cell activity within the fluidized region, the visco-elastic time τ_ε gradually increases and displays a divergence near the transition line toward arrested coalescence. This divergence of elastic relaxation time is indicative of an underlying glass transition, as was already pointed out in [10], although based on somewhat different analytical and computational models. The transition from arrested to complete fusion as characterized by θ_{eq}, coincides with the glass transition as characterized by the divergence of τ_ε, as shown in **Figure 3D**. Since this computational model is based on the same individual cell-based framework that was used to simulate the aggregate formation process, we are able to make a direct comparison between dynamics of aggregation and dynamics of tissue spheroid fusion. At sufficient cell activity, the aggregation process is consistent with the dewetting of a liquid film from a surface, as was demonstrated in [30]. Upon decrease in activity, this correspondence is lost. Instead, the aggregate density ρ_a follows the dynamics of granular compaction, characterized by stretched exponential relaxation (KWW law):

$$\rho_a(t) = \rho_f - (\rho_f - \rho_0)\exp\left[-\left(t/\tau_{\text{agg}}\right)^\beta\right] \quad (5)$$

with initial density ρ_0, final density ρ_f, exponent β and characteristic timescale τ_{agg}, see **Figure 3A**. In this equation the apparent packing density is expressed by $\rho_a = 3V_a/(4\pi R_a^3)$ Here, V_a is the apparent volume of the spheroid approximated as the sum of cell volumes using an average cell radius. R_a is the radius of the spheroid, which is obtained based on the projected area on the bottom of the micro-well, assuming a circular geometry. During compaction, a similar glass transition as observed during the fusion process can be recognized from the divergence of τ_{agg} [30]. For the same underlying cell properties D_{eff} and w_{r}, these two transitions closely align, as demonstrated in **Figure 3B**, although the transition in the fusion process consistently occurs at higher values of cell activity. We hypothesize that this discrepancy is due to the additional constraints in cell movement imposed by the geometry of the spheroid during the fusion process, compared to the loose network connectivity that characterizes the aggregation phase. Due to the sequential simulation of aggregation and fusion, which mimics the experimental procedure, additional compaction may occur during fusion, particularly at low activity when compaction proceeds slowly. We verified that the effect of this additional compaction on the predicted equilibrium angle θ_{eq} is minor, as shown in **Supplementary Figure S7**, where we compare fusion of self-assembled aggregates to artificially compacted spheroid structures.

3.2 Increase of Coalescence Due to Cell Division

Next, we turn to the role of cell division in the arrest of coalescence. For this, we simulated the fusion dynamics in the presence of cell proliferation, see (**Supplementary Section S1.2**) Although cell proliferation is not explicitly accounted for in the derivation of our analytical model, **Eq. 1** still fits the fusion dynamics of our simulated spheroid fusion in the presence of cell division well, **Figure 4A**. **Figures 4B,C** compares the characteristic visco-elastic time constant τ_ε and the predicted equilibrium angle θ_{eq} without ($k_{\text{div}} = 2 \times 10^{-8}\,\text{h}^{-1}$) and with ($k_{\text{div}} = 0.06\,\text{h}^{-1}$) cell division, when varying cell motility D_{eff} at repulsive energy $w_{\text{r}} = 2.09\,\text{min}^{-1}$. This enables us to evaluate the effect of cell growth/division as an additional source of biological excitation compared to active cell motility. The simulated cell division rate corresponds to a cell cycle period

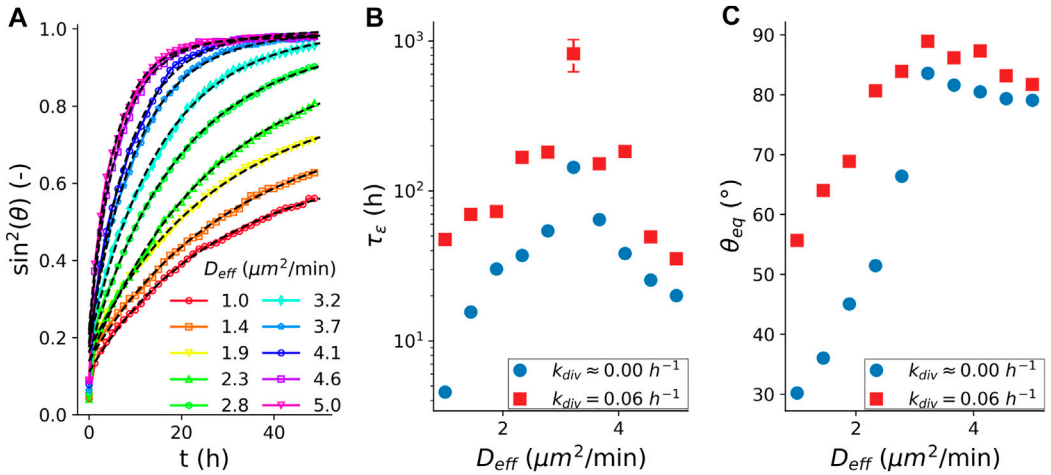

FIGURE 4 | Fusion characteristics in the presence of cell division. **(A)** Average (N = 100) fusion dynamics with simulated cell cycle, quantified as $\sin^2(\theta)$, during 50 h for varying cell activity D_{eff} at constant $w_r = 2.09\,\mathrm{min}^{-1}$ and $k_{div} = 0.06\,\mathrm{h}^{-1}$. The simulated data is fitted by calculating $\sin^2(\theta)$ based on the solution for θ **Eqs. 2**, **3**. Although cell division is not taken into account in the fusion dynamics model, it still fits the data well. Fitting results of have to be interpret as effective parameters. **(B–C)** Comparison of fusion dynamics characteristics in presence and in absence of cell division, as a function of cell activity D_{eff} at a constant $w_r = 2.09\,\mathrm{min}^{-1}$. The estimated values for the visco-elastic time constant τ_ε are based on fitting the average fusion dynamics in $\sin^2(\theta)$ using **Eqs. 2**, **3**, the predicted equilibrium angle θ_{eq} calculated by **Eq. 4**. The error bars for τ_ε correspond to two times the standard error obtained from the fits. In these graphs, the error bars are only one time larger than the marker. These graphs show that cell division promotes spheroid fusion, although the system remains arrested at low levels of cell activity.

of approximately 16.7 h, which is lower than many commonly used cell lines which are used for spheroid fusion. Yet, even at this relatively high division rate, we do not see a strong shift in critical activity beyond which the material appears fluid-like, as indicated by the coincidence of the peak in τ_ε for varying D_{eff} with and without cell division (**Figure 4B**). However, we do observe that the presence of cell division greatly increases the overall visco-elastic relaxation time, indicating a decrease in the apparent elasticity of the multi-cellular material. Furthermore, cell division markedly increases the equilibrium angle θ_{eq} in the arrested fusion region. Hence, in the simulated configuration, cell division appears to recover coalescence by increasing the plasticity of the tissue. However, it has no strong influence on the location of the fluidization transition.

4 DISCUSSION

In this work, we derived an expression for the arrested coalescence of tissue spheroid fusion, based on visco-elastic material properties. Simulations of a minimal individual cell-based model of the fusion process showed that this expression is able to describe the transition of liquid-like to arrested coalescence dynamics. Furthermore, a divergence in the visco-elastic relaxation time indicates the presence of jammed or glassy relaxation behavior near the transition toward arrested coalescence. These findings are highly similar to recent work from Oriola et al. [10], hence a brief comparison between these contemporary results is appropriate. First, the analytical expressions for the dynamics of θ (**Eq. 1** in [10], compared to **Eq. 1**) are based on somewhat different assumptions. Our model is an extension of the model of Pokluda [3] by adding an elastic energy term in the equation which was suggested by [23, 24]. This has the advantage that in the absence of elasticity, the model of Pokluda is retrieved. The downside of our approach is that this leads to an inconsistency in the strain and strain rate for viscous energy dissipation rate and the elastic energy rate (we note this difference as ε and ε). For the viscous dissipation term, we have, according to Pokluda [3] $\dot{\varepsilon} = (1/a)(\mathrm{d}/\mathrm{d}t)[a(\theta)\cos(\theta)]$. On the other hand, the strain in arrested coalescence is suggested to be $\varepsilon = 1 - a(\theta)(1 + \cos(\theta)/(2a_0))$ [23, 24]. Therefore the strain rate is $\dot{\varepsilon} = -(1/2a_0)(\mathrm{d}/\mathrm{d}t)[a(\theta)(1 + \cos(\theta))]$. These expressions are equivalent in magnitude only for the onset of fusion i.e. $\theta \approx 0$ and $a(\theta) = a_0$. In contrast to our hybrid model, Oriola et al. [10] consistently use the strain rate as suggested for arrested coalescence [23, 24]. Furthermore, they introduce elasticity by considering the spheroid as an incompressible Kelvin-Voigt material, instead of adding a separate elastic energy term, hence obtaining a critical value for the Young's modulus for which fusion is inhibited. Moreover, whereas they include a "pre-strain" to account for the initial fusion onset, we allow for an instantaneous initial angle θ_0. Still, both models are parameterized by two essential characteristic timescales: the visco-capillary timescale τ_Γ and the visco-elastic timescale τ_ε. Secondly, one key difference between the individual cell-based model in this work and the one in [10] is the implementation of the active cell motility. Their model is based on "protrusions" defined on the level of cell-cell bonds, and effectuates persistence by means of a protrusion lifetime per bond. Our model is based on a polarization direction defined for each cell which diffuses over time. Nonetheless, the similarity of the main results underpins that the transition of liquid-like to arrested coalescence is a generic phenomenon that is not dependent on the precise assumptions of the visco-elastic description, nor on

the implementation details of the individual cell-based model. Additionally, because arrested fusion is the main discrepancy for fusion of the jammed tissue, the simulation of shötz et al. [22] of cells close to the jamming transition can still adequately be described by a liquid model.

The glassy relaxation dynamics during fusion mirror the dynamics of the aggregation process during which the initial tissue spheroids are formed. A direct comparison between these two unit processes shows that there is a clear correspondence between, on the one hand, the transition from granular compaction to liquid dewetting during the aggregation phase, and on the other hand, the transition from arrested coalescence to liquid behavior during the fusion phase. However, this transition occurs for slightly smaller values of cell activity in the case of aggregate formation. Experimental confirmation of this correspondence can be found in studies involving Rho kinase inhibitor, which has been observed to cause arrested dynamics during aggregate formation of human periosteum-derived cells [30], as well as inhibit fusion of spheroids from human mesenchymal stem cells [8] and of embryonal chicken organoids [7]. The role of cell activity in fluidization has been experimentally shown [9]. They related cell activity as obtained from cell tracking to the outcome of fusion. The fusion of low cell activity tumor spheroids appears like a jammed tissue and results in arrested coalescence, while in high cell activity tumor spheroids, fusion is completed. They also noted that the dynamics of this arrested fusion process could not be captured with the classical model. The equation, as derived in this paper will therefore contribute to a better understanding of spheroid fusion in general.

In addition, we considered the effect of cell division on the dynamics of the fusion process. In the framework of arrested coalescence, we showed that the presence of cell division may recover coalescence of fusion. Other studies on the role of cell growth in biological active matter systems, for example in simulations of two-dimensional epithelial tissues [27], or in growing 3D cell aggregates [25], observed an increase of fluidization induced by cell division. More generally, an overview of the role of cell division in tissue rheology and mechanics is provided in [32]. However, in our simulations, the effect of cell division on the location of the fluidization transition was limited, at least for realistic cell division rates compared to the timescale of fusion. Instead, cell division appeared to increase plasticity of the glassy material and thereby improves coalescence in the arrested phase. However, it should be noted that the absence of fluidization as a result of cell division in simulations could be partly due to the minimal representation of cell shape, which introduces artificial energy barriers and thereby overly penalizes neighbor exchanges. This shortcoming could be addressed in more detailed tissue models, such as vertex models [33] or deformable cell models [34, 35]. On the other hand, our representation of the cell cycle was limited to cell growth and cell division, while fluidization is often investigated in the presence of apoptosis when the number of cells is stationary or at a homeostatic pressure [28]. We expect that including apoptosis will further fluidize the tissue as this creates random vacancies around caged cells, offering a low energy route for local relaxation. Additional complexities on fusion dynamics could arise as cells enter a pressure-dependent dormant state, increasing tissue heterogeneity. For example, the increased pressure in the core of tumor spheroids results in a jammed stage with dormant cells, while cells at the periphery grow and motility is super-diffusive [36].

In practice, technologies that involve the production of artificial tissues frequently incorporate subsequent steps of micro-aggregation and tissue assembly, where the latter often relies on the (partial) fusion of spheroids to create larger tissue constructs [37]. To complicate matters, all these steps are typically accompanied by biological processes such as cell division, production of extracellular matrix, cell differentiation or apoptosis. However, since the physical description of the underlying aggregation and fusion dynamics is highly generic, each of these steps may be parameterized in terms of its characteristic material properties, allowing for the comparison within and between different culture conditions and production formats. As such, continued efforts toward the characterization of structure, rheology and mechanics of these artificial tissues will become indispensable.

DATA AVAILABILITY STATEMENT

The datasets presented in this study can be found in online repositories. The names of the Zenodo repository/repositories and accession number(s) can be found in the article/**Supplementary Material**.

AUTHOR CONTRIBUTIONS

BS and HR conceived the project, SO and BS designed and conducted the simulations, SO performed the mathematical analysis, SO performed data analysis. SO, MC, JV, and BS wrote the manuscript. All authors commented on the manuscript.

FUNDING

This work is part of Prometheus, the KU Leuven R&D Division for Skeletal Tissue Engineering. SO acknowledges support from KU Leuven internal funding C14/18/055. MC acknowledges support form the Research Foundation Flanders (FWO), grant 1S46817N. BS acknowledges support from the Research Foundation Flanders (FWO) grant 12Z6118N.

ACKNOWLEDGMENTS

We thank Jiří Pešek for proofreading the derivations.

SUPPLEMENTARY MATERIAL

The Supplementary Material for this article can be found online at: https://www.frontiersin.org/articles/10.3389/fphy.2021.649821/full#supplementary-material

REFERENCES

1. Frenkel JJ. Viscous Flow of Crystalline Bodies under the Action of Surface Tension. *J Phys* (1945) 9:385. doi:10.1007/BF03398399
2. Eshelby J. Discussion,' in a.J. Shuler, 'seminar on the Kinetics of Sintering'. *Met Trans* (1949) 185:806.
3. Pokluda O, Bellehumeur CT, and Vlachopoulos J. Modification of Frenkel's Model for Sintering. *Aiche J* (1997) 43:3253–6. doi:10.1002/aic.690431213
4. McCune M, Shafiee A, Forgacs G, and Kosztin I. Predictive Modeling of post Bioprinting Structure Formation. *Soft matter* (2014) 10:1790–800. doi:10.1039/c3sm52806e
5. Dechristé G, Fehrenbach J, Griseti E, Lobjois V, and Poignard C. Viscoelastic Modeling of the Fusion of Multicellular Tumor Spheroids in Growth Phase. *J Theor Biol* 454 (2018) 102 – 9. doi:10.1016/j.jtbi.2018.05.005
6. Kosheleva NV, Efremov YM, Shavkuta BS, Zurina IM, Zhang D, Zhang Y, et al. Cell Spheroid Fusion: beyond Liquid Drops Model. *Sci Rep* (2020) 10:12614. doi:10.1038/s41598-020-69540-8
7. Pierzchalska M, Panek M, and Grabacka M. The Migration and Fusion Events Related to Rock Activity Strongly Influence the Morphology of Chicken Embryo Intestinal Organoids. *Protoplasma* (2019) 256:575–81. doi:10.1007/s00709-018-1312-3
8. Tsai A-C, Liu Y, Yuan X, and Ma T. Compaction, Fusion, and Functional Activation of Three-Dimensional Human Mesenchymal Stem Cell Aggregate. *Tissue Eng Part APart A* (2015) 21:1705–19. doi:10.1089/ten.TEA.2014.0314
9. Grosser S, Lippoldt J, Oswald L, Merkel M, Sussman DM, Renner F, et al. Cell and Nucleus Shape as an Indicator of Tissue Fluidity in Carcinoma. *Phys Rev X* (2021) 11:011033. doi:10.1103/physrevx.11.011033
10. Oriola D, Marin-Riera M, Aalderink G, Anlas K, Gritti N, Sharpe J, et al. *Arrested Coalescence of Multicellular Aggregates* (2020) *arXiv:2012.01455*.
11. Yu M, Mahtabfar A, Beelen P, Demiryurek Y, Shreiber DI, Zahn JD, et al. Coherent Timescales and Mechanical Structure of Multicellular Aggregates. *Biophysical J* 114 (2018) 2703 – 16. doi:10.1016/j.bpj.2018.04.025
12. Guevorkian K, Colbert M-J, Durth M, Dufour S, and Brochard-Wyart F, Aspiration of Biological Viscoelastic Drops. *Phys Rev Lett* (2010) 104:218101. doi:10.1103/PhysRevLett.104.218101
13. Gonzalez-Rodriguez D, Bonnemay L, Elgeti J, Dufour S, Cuvelier D, and Brochard-Wyart F. Detachment and Fracture of Cellular Aggregates. *Soft Matter* (2013) 9:2282–90. doi:10.1039/C2SM26648B
14. Forgacs G, Foty RA, Shafrir Y, and Steinberg MS. Viscoelastic Properties of Living Embryonic Tissues: a Quantitative Study. *Biophysical J* 74 (1998) 2227–34. doi:10.1016/S0006-3495(98)77932-9
15. Mongera A, Rowghanian P, Gustafson HJ, Shelton E, Kealhofer DA, Carn EK, et al. A Fluid-To-Solid Jamming Transition Underlies Vertebrate Body axis Elongation. *Nature* (2018) 561:401–5. doi:10.1038/s41586-018-0479-2
16. Yang X, Mironov V, and Wang Q. Modeling Fusion of Cellular Aggregates in Biofabrication Using Phase Field Theories. *J Theor Biol* 303 (2012) 110–8. doi:10.1016/j.jtbi.2012.03.003
17. Fleming PA, Argraves WS, Gentile C, Neagu A, Forgacs G, and Drake CJ. Fusion of Uniluminal Vascular Spheroids: A Model for Assembly of Blood Vessels. *Dev Dyn* (2010) 239:398–406. doi:10.1002/dvdy.22161
18. Flenner E, Janosi L, Barz B, Neagu A, Forgacs G, and Kosztin I. Kinetic Monte Carlo and Cellular Particle Dynamics Simulations of Multicellular Systems. *Phys Rev E* (2012) 85:031907. doi:10.1103/PhysRevE.85.031907
19. Flenner E, Marga F, Neagu A, Kosztin I, and Forgacs G. Relating Biophysical Properties across Scales. Schnell S, Maini PK, Newman SA, and Newman TJ, editors. *Relating Biophysical Properties across Scales. Multiscale Modeling of Developmental SystemsCurrent Topics in Developmental Biology*, 81. Academic Press (2008). p. 461–83. doi:10.1016/S0070-2153(07)81016-7
20. Kosztin I, Vunjak-Novakovic G, and Forgacs G. Colloquium: Modeling the Dynamics of Multicellular Systems: Application to Tissue Engineering. *Rev Mod Phys* (2012) 84:1791–805. doi:10.1103/RevModPhys.84.1791
21. Shafiee A, McCune M, Forgacs G, and Kosztin I. Post-deposition Bioink Self-Assembly: a Quantitative Study. *Biofabrication* (2015) 7:045005. doi:10.1088/1758-5090/7/4/045005
22. Schötz E-M, Lanio M, Talbot JA, and Manning ML. Glassy Dynamics in Three-Dimensional Embryonic Tissues. *J R Soc Interf* (2013) 10:20130726. doi:10.1098/rsif.2013.0726
23. Pawar AB, Caggioni M, Hartel RW, and Spicer PT. Arrested Coalescence of Viscoelastic Droplets with Internal Microstructure. *Faraday Discuss* (2012) 158:341–35. doi:10.1039/c2fd20029e
24. Dahiya P, Caggioni M, and Spicer PT. Arrested Coalescence of Viscoelastic Droplets: Polydisperse Doublets. *Phil Trans R Soc A* (2016) 374:20150132. doi:10.1098/rsta.2015.0132
25. Ranft J, Basan M, Elgeti J, Joanny J-F, Prost J, and Jülicher F. Fluidization of Tissues by Cell Division and Apoptosis. *Proc Natl Acad Sci* (2010) 107:20863–8. doi:10.1073/pnas.1011086107
26. Malmi-Kakkada AN, Li X, Samanta HS, Sinha S, and Thirumalai D. Cell Growth Rate Dictates the Onset of Glass to Fluidlike Transition and Long Time Superdiffusion in an Evolving Cell colony. *Phys Rev X* (2018) 8:021025. doi:10.1103/PhysRevX.8.021025
27. Matoz-Fernandez DA, Martens K, Sknepnek R, Barrat JL, and Henkes S. Cell Division and Death Inhibit Glassy Behaviour of Confluent Tissues. *Soft Matter* (2017) 13:3205–12. doi:10.1039/C6SM02580C
28. Basan M, Prost J, Joanny J-F, and Elgeti J. Dissipative Particle Dynamics Simulations for Biological Tissues: Rheology and Competition. *Phys Biol* (2011) 8:026014. doi:10.1088/1478-3975/8/2/026014
29. Smeets B, Pešek J, Deckers T, Hall GN, Cuvelier M, Ongenae S, et al. Compaction Dynamics during Progenitor Cell Self-Assembly Reveal Granular Mechanics. *Matter* 2 (2020) 1283 – 95. doi:10.1016/j.matt.2020.02.016
30. Smeets B, Pešek J, Deckers T, Hall GN, Cuvelier M, Ongenae S, et al. Compaction Dynamics during Progenitor Cell Self-Assembly Reveal Granular Mechanics. *Matter* 2 (2020) 1283 – 95. doi:10.1016/j.matt.2020.02.016
31. Delile J, Herrmann M, Peyriéras N, and Doursat R. A Cell-Based Computational Model of Early Embryogenesis Coupling Mechanical Behaviour and Gene Regulation. *Nat Commun* (2017) 8:13929. doi:10.1038/ncomms13929
32. Godard BG, and Heisenberg C-P. Cell Division and Tissue Mechanics. *Curr Opin Cel Biol* 60 (2019) 114 – 20. doi:10.1016/j.ceb.2019.05.007
33. Krajnc M, Dasgupta S, Ziherl P, and Prost J. Fluidization of Epithelial Sheets by Active Cell Rearrangements. *Phys Rev E* (2018) 98:022409. doi:10.1103/PhysRevE.98.022409
34. Van Liedekerke P, Neitsch J, Johann T, Alessandri K, Nassoy P, and Drasdo D. Quantitative Cell-Based Model Predicts Mechanical Stress Response of Growing Tumor Spheroids over Various Growth Conditions and Cell Lines. *Plos Comput Biol* (2019) 15:e1006273. doi:10.1371/journal.pcbi.1006273
35. Smeets B, Cuvelier M, Pešek J, and Ramon H. The Effect of Cortical Elasticity and Active Tension on Cell Adhesion Mechanics. *Biophysical J* (2019) 116:930–7. doi:10.1016/j.bpj.2019.01.015
36. Sinha S, Malmi-Kakkada AN, Li X, Samanta HS, and Thirumalai D. Spatially Heterogeneous Dynamics of Cells in a Growing Tumor Spheroid: Comparison between Theory and Experiments. *Soft Matter* (2020) 16:5294–304. doi:10.1039/C9SM02277E
37. De Moor L, Fernandez S, Vercruysse C, Tytgat L, Asadian M, De Geyter N, et al. Hybrid Bioprinting of Chondrogenically Induced Human Mesenchymal Stem Cell Spheroids. *Front Bioeng Biotechnol* (2020) 8:484. doi:10.3389/fbioe.2020.00484
38. Ongenae S, Cuvelier M, Vangheel J, Ramon H, and Smeets B. *mpacts_arrested_coalescence-master* (2021) doi:10.5281/zenodo.4745560 CrossRef Full Text

Conflict of Interest: The authors declare that the research was conducted in the absence of any commercial or financial relationships that could be construed as a potential conflict of interest.

frontiers in Physics

REVIEW
published: 09 June 2021
doi: 10.3389/fphy.2021.666916

Viscoelastic Networks: Forming Cells and Tissues

Bernat Corominas-Murtra[1] *and Nicoletta I. Petridou*[2]*

[1]Institute of Biology, Karl-Franzens-University Graz, Graz, Austria, [2]European Molecular Biology Laboratory, Heidelberg, Germany

Spatiotemporal changes in viscoelasticity are a key component of the morphogenesis of living systems. Experimental and theoretical findings suggest that cellular- and tissue-scale viscoelasticity can be understood as a collective property emerging from macromolecular and cellular interactions, respectively. Linking the changes in the structural or material properties of cells and tissues, such as material phase transitions, to the microscopic interactions of their constituents, is still a challenge both at the experimental and theoretical level. In this review, we summarize work on the viscoelastic nature of cytoskeletal, extracellular and cellular networks. We then conceptualize viscoelasticity as a network theory problem and discuss its applications in several biological contexts. We propose that the statistical mechanics of networks can be used in the future as a powerful framework to uncover quantitatively the biomechanical basis of viscoelasticity across scales.

Keywords: viscoelasticity, percolation theory, network, morphogenesis, rigidity

OPEN ACCESS

Edited by:
Elias H. Barriga, Gulbenkian Institute of Science (IGC), Portugal

Reviewed by:
Melissa Turan, University College London, United Kingdom
Ana Patricia Ramos, Gulbenkian Institute of Science (IGC), Portugal

***Correspondence:**
Nicoletta I. Petridou
nicoletta.petridou@embl.de

Specialty section:
This article was submitted to Biophysics, a section of the journal Frontiers in Physics

Received: *11 February 2021*
Accepted: *19 May 2021*
Published: *09 June 2021*

Citation:
Corominas-Murtra B and Petridou NI (2021) Viscoelastic Networks: Forming Cells and Tissues. Front. Phys. 9:666916. doi: 10.3389/fphy.2021.666916

INTRODUCTION

The viscoelastic or material properties of cells and tissues are key regulators of cell and tissue growth, motion, and homeostasis [1–5]. Viscoelasticity allows living systems to preserve a basic architecture due to their solid-like characteristics, but also at the same time to dynamically reorganize in different shapes and patterns due to their viscous-like characteristics [4, 6–8]. Cellular-scale viscoelasticity influences several single-cell functions such a shape, division, and motility, and it is predominantly determined by the physical properties of the underlying cytoskeletal networks [8]. Tissue-scale viscoelasticity was shown to be important in collective morphogenetic processes such as tissue folding, spreading, wound healing and migration, and it is mainly determined by the interplay of cell-cell and/or cell-extracellular space interactions [2, 4, 5]. Advances in biophysical tools measuring viscoelasticity [4, 9, 10] have revealed an essential and physiologically relevant link between material properties and morphogenesis [11–13], opening the challenge to now understand how emergent viscoelasticity is regulated by, and in turn, regulates the mechanochemistry of living systems.

A material is *viscoelastic* if it displays both viscous and elastic behavior [14]. Our knowledge of viscoelasticity mainly comes from material sciences, where certain physical parameters are well-defined for non-living materials such as glasses, rubbers, metals and polymers [14, 15]. Viscoelasticity of such materials is evaluated from the degree of deformation upon constant force application and release, an experimental procedure called creep and recovery test (**Figure 1A**). Solid-like objects deform shortly and reversibly under constant force, whereas fluid-like objects irreversibly increase their deformation as long as a force is exerted. Viscoelastic materials exhibit characteristics of both solids and fluids: at short time scales they deform elastically and, at long timescales, they behave as viscous fluids. On the theoretical level, viscoelasticity was independently modelled by Maxwell and Kelvin in the 19th century [14]. Both models abstract a viscoelastic system as a composite structure containing an elastic spring connected to a dashpot

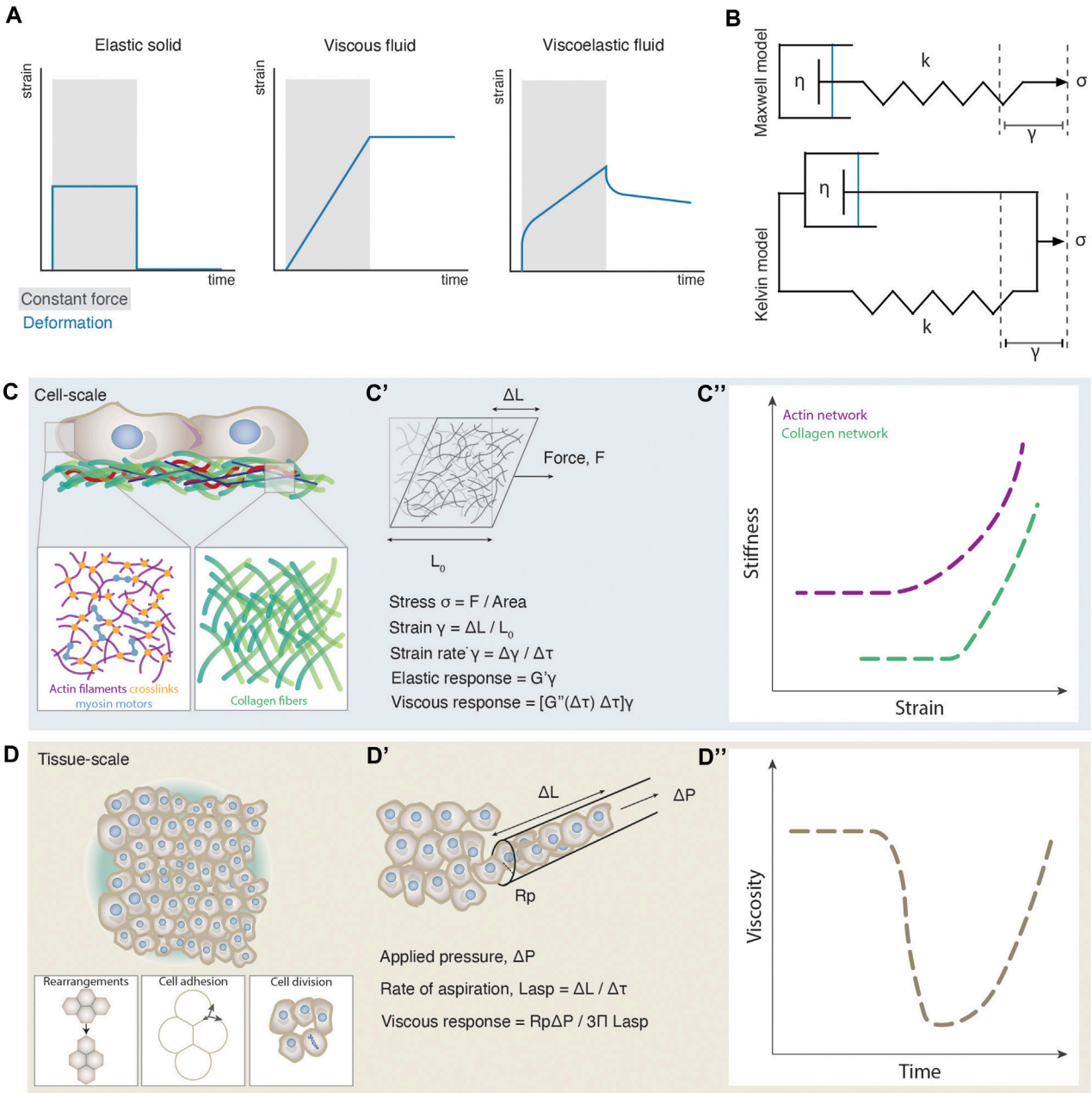

FIGURE 1 | Emergence of cell and tissue viscoelasticity. **(A)** Strain plots as a function of time for different materials during constant force application (grey shaded box) and release. **(B)** Schematic illustrations of the Maxwell and Kelvin viscoelastic models. In the Maxwell model (top) the spring and dashpot are connected in series and account for the behaviour of viscoelastic fluid materials. In the Kelvin model (bottom) the spring and dashpot are connected in parallel and account for the behaviour of viscoelastic solid materials. Stress σ is applied along the axis of the spring triggering a strain γ. k is the spring constant and η is the viscosity of the fluid. **(C)** Cellular-scale viscoelasticity is defined by the cytoskeletal network and extracellular matrix. The close ups illustrate an exemplary composition of an actin and collagen network. **(C')** Schematic illustration of an experimentally induced deformation of a cytoskeletal network and a paradigm of how viscoelastic properties can be computed from such experiments. **(C")** Stiffness-strain plots of actin and collagen networks exhibiting a non-linear increase of their elastic modulus, or a stress-stiffening response. The plot was adapted from [71, 141]. **(D)** Tissue-scale viscoelasticity is determined by several cellular processes such as cell rearrangements, cell-cell adhesion and cell division. **(D')** Schematic illustration of an experimentally induced deformation of an embryonic tissue using micropipette aspiration and a paradigm of how viscoelastic properties can be computed from such experiments. **(D")** Plot of the nonlinear decrease of tissue viscosity as observed during zebrafish morphogenesis. F, Force; σ, stress; γ, strain; G', elastic modulus; G'', viscous modulus; ΔP, applied pressure; ΔL, deformation length; R_p, pipette radius.

BOX 1 | Terminology.

Affine deformation: Deformation of a body in which the macroscopic strain is translated uniformly to all microscopic parts of the material.
Bulk modulus: Denoted by K, describes the material's response to isotropic hydrostatic pressure.
Cell contact network: A network where the nodes are cells and links represent active contacts between neighbouring cells.
Contour length: In a polymer chain, the contour length, l_c, *is the distance between the two extremes of the filament if the polymer is fully unfolded.*
Critical point: Magnitude of the control parameter that triggers a phase transition. At the critical point, a discontinuity on some macroscopic observable is expected, and specific statistical patterns, such as power-laws, often largely independent of system's details, are observed. Formally, the functional dependence of the order parameter on the control parameter shows a singularity in some of its derivatives at the critical point.
Cytoskeleton: A network of biopolymer fibres that extends throughout a cell. It is the main determinant of the material response of the cell under deformations and stress.
ECM network: The extracellular matrix (ECM) is a non-cellular component providing the material backbone for the cellular constituents. Beyond its structural character, it plays a key, active role in morphogenesis, differentiation and homeostasis.
Elastic modulus: Also known as Young's modulus, E, quantifies the strain response to uniaxial stress in the direction of this stress in the linear regime.
Enthalpic elasticity: In a polymer network where $l_p/l_c \gg 1$ filaments are considered stiff, and deformation comes from the stretching or compression of them. The main energetic costs come from changes of the enthalpy of the system. Systems in the enthalpic regime show in general small deformations under stress.
Entropic elasticity: In a polymer network where $l_p/l_c \ll 1$ filaments are rugged and fluctuate due to thermal agitation. In these systems, the elastic response against deformation is due to the unfolding of these filaments towards the axis of the stress. This unfolding results in a decrease of the entropy of the system. The materials in these regimes are usually elastic and deformations can be in general big, and recover the initial configurations when the stress is released
Interstitial fluid: space between the cells of a nonconfluent tissue.
Isostatic point: A system is at the isostatic point when the degrees of freedom of its constituents are absorbed by the constraints imposed by the structure in a non-redundant way. In the theory of rigidity, the isostatic point is marked by the critical value of connectivity in which the system becomes rigid, e.g., the lowest value of connectivity that leaves no degrees of freedom within the internal constituents of the system.
Jamming: Divergence of the viscosity of a material with increasing particle density
Micro/macro mapping: The mapping between microscopic dynamics, often containing a great number of degrees of freedom to a single, often scalar microscopic observable. The most common example is the microscopic motion of particles in a gas giving rise to the macroscopic observable of temperature.
Network rigidity: A topological concept where a network structure (or part of it) made of nodes and connecting links is considered to be generically rigid if no independent (geometric) movement of the nodes is possible without stretching/compressing a link.
Percolation: A network is in the *percolating regime* if a significant part of its nodes define a connected cluster, that is, for any pair of nodes of this cluster, there is a path that connects them. In a random network, the emergence of the percolating cluster is an abrupt event, and has all the properties of a high order phase transition as described in statistical mechanics. Many different classes of percolation transitions can be defined, depending on the attributes one expects to observe in the emerging cluster when the average connectivity increases.
Persistence length: In a polymer chain, the persistence length, l_p, quantifies the length scale at which significant bending fluctuations occur. Formally, it is the length at which the polymer chain appears straight in the presence of Brownian forces.
Phase transition: Macroscopic change in the properties of a system (order parameter) when a parameter crosses a certain critical value (control parameter), also called critical point.
Rigidity percolation: A high order phase transition triggered by increasing the average number of links per node in a network, leading to the sudden emergence of a rigid region that spans almost the whole network, the Giant Rigid Cluster (GRC). The term rigidity percolation comes from the fact that almost any two nodes of the graph are connected through a path that is entirely inside the same rigid cluster.
Shear modulus: Denoted by G, quantifies the material's response to shear stress.
Strain: Denoted by γ, quantifies the deformation of a body. It quantifies relative displacements of parts of the body other than the ones that can be attributed to rigid body motions.
Strain softening response: Non-linear response of many biological materials consisting on the decrease of the stiffness along the increase of strain.
Strain stiffening response: Non-linear response of many biological materials consisting on the increase of the stiffness along the increase of strain.
Vertex models: Tissue models represented by tilling of the space (in general, over 2D surfaces) in which the energetic contributions come from geometric considerations on the cell shape and cell-cell contact regions (vertices).
Viscosity: Denoted by η, quantifies the material's flow at a given velocity upon stress
T1 transition: Relative movement of cells in a tissue occurring when an edge between two cells shrinks to a point and a new edge arises between two neighbouring cells. The outcome of this process is a net change of neighbouring cells and, in consequence, a relative movement, with respect to the other cells, of at least one cell within the tissue.

containing a viscous fluid (**Figure 1B**). The difference between Maxwell's and Kelvin's approaches comes from the disposition of the system: In Maxwell's model, the dashpot and the spring are connected in series, whereas in Kelvin's model, the two components are connected in parallel. As a result, when force is applied on the system, in the former, the deformation of the spring will drag the dashpot, describing the deformation of a *viscoelastic fluid*; whereas when force is applied in the latter, the dashpot response is restricted by the deformation of the spring, describing thus the deformation of a *viscoelastic solid* [16]. Although biological materials display characteristics of viscoelastic materials, due to their heterogeneous composition and dynamic nature, fitting such models and frameworks from material science, is conceptually and technically still difficult [16, 17]. For instance, during experimental measurements of cell and tissue viscoelasticity, typically an external force is applied to the system such as via a micropipette, or a magnetic field [13, 18, 19] for a certain time window, during which its deformation is monitored (**Figure 1C'**). From such measurements, parameters such as *elastic modulus*, *viscosity*, and *yield stress* can be extrapolated (**Box 1**) [16, 20, 21]. However, whether such measurements are relevant to the time window of morphogenesis still needs to be addressed, since such measurements show how a tissue deforms when applying an exogenous force for a certain time. How these features compare to the magnitude and duration of the endogenously exerted forces is still unclear [9, 22, 23]. In addition, during such experimental measurements, the applied force typically triggers a large

deformation of the material (nonlinear regime). In contrast however, most theoretical frameworks predicting viscoelasticity upon deformation, are based on forces triggering infinitesimal deformations (linear regime) [24]. Last, similar to the viscoelasticity of non-living materials, viscoelasticity of cells and tissues is a property arising from their underlying structure, defined by the way macromolecules and cells interact [1, 8, 15, 25–29]. Several theoretical frameworks have for long been used in non-living materials to link the *microscopic* structure to the *macroscopic* viscoelastic properties (**Box 1**), showing that viscoelasticity may behave as an emergent property [27–32], in the same way, e.g., temperature arises non-trivially from microscopic particle motion in statistical mechanics [14]. How macroscopic viscoelasticity can be predicted by the interactions of the microscopic constituents of living cells and tissues is an open question at the interface of statistical and soft matter physics with molecular and cell biology, and the main topic of this review.

An intriguing empirical observation is that the material properties of the microscale components of cell and tissue viscoelasticity, such as the cytoskeletal elements and the cells, respectively, usually do not match the macroscale material properties of cells and tissues [15, 29, 33]. Macroscopic viscoelasticity frequently exhibits nonlinear changes that are not observed at the microscopic level. Such examples have been experimentally detected such as the *strain-stiffening* response of the *cytoskeleton* networks [26, 30, 34], *phase transitions* in the energetic costs of cell movements [12] or abrupt changes in tissue viscosity [13] (**Box 1**, **Figures 1C",D"**). In the above cases, the mechanical resilience of the individual microscopic components to forces falls short in explaining the macroscopic viscoelastic changes, and thus probing the pattern of interactions between the components instead, is key.

Such nonlinear phenomena set a number of challenges to the theoretical understanding of cell and tissue dynamics. Theoretical analyses of cell and tissue material properties are typically addressed from the biopolymer or cell level, respectively. In the first theoretical approach, the microscopic basis is the mechanical properties of the biopolymer filaments building the cytoskeleton [35] and the macroscopic viscoelastic features are derived from the network geometry and local topology of the filaments [26]. Nonlinear phenomena such as strain-stiffening of cytoskeletal networks have been probed with such models. In the second theoretical approach, the microscopic basis is the tiling patterns of the constituents, such as the cells forming a tissue. In such modeling frameworks, mainly represented by the *vertex models* (**Box 1**) [25, 36, 37], rheological properties such as rigidity and fluidity are inferred from the energetic costs for cells to independently move through the tissue [27, 28, 38–41]. This viewpoint comes from the fundamental observation that material deformation can only take place through cell-cell rearrangements. Nonlinear phenomena such as *jamming* transitions (**Box 1**) have been predicted with such frameworks [27, 28, 40–42]. A third theoretical approach that is not as frequently applied in active viscoelastic systems, but has been used so far to probe material properties across scales, is network theory [29, 31, 43, 44]. In this framework, the starting point is the topology of the network, e.g., how the system's constituents are connected between them. Of particular relevance for these approaches is the concept of *percolation* (**Box 1**). Percolation refers to a wide range of phenomena where a sudden shift in the macroscopic properties of a system made of microscopic, interacting units, is observed when a certain threshold of connectivity at the microscopic scale is overcome [45]. In material sciences, percolation transitions underlie many sudden, qualitative changes in the behavior/response of the material, including, among other, shifts in rigidity and force transmission properties [46–54]. A paradigmatic example of the role of percolation theory in explaining material properties is found in the exploration of the emergence of cracks when the material is under stress. In this context, the length and width of cracks emerging in the material increase dramatically when the system approaches the critical point of *rigidity* percolation [55, 56] (**Box 1**). Several forms of percolation theory have been applied to cytoskeletal networks, fiber networks and, recently, to "cellular" networks - tissues - to map material properties [29, 31, 43, 44]. As is the case with inanimate materials, the structure of interactions at the microscopic level --and the potential nonlinear shifts arising from small changes in them-- are supposed to underlie and, ultimately, explain, the emergence of macroscopic material properties like viscoelasticity.

In this review we summarize and discuss experimental and theoretical work probing cell and tissue viscoelasticity as an emergent property. We will first introduce experimental findings on how viscoelasticity emerges in cytoskeletal networks, extracellular matrix fiber networks and tissues. We will then summarize and classify theoretical frameworks supporting such experimental findings that address cell and tissue material properties. Finally, we will discuss the potential of applying network theory to predict viscoelasticity, and speculate how such an approach could impact our biophysical understanding of the material properties of living systems and their morphogenesis.

VISCOELASTICITY AS AN EMERGENT PROPERTY: EXPERIMENTAL OBSERVATIONS

Cellular Viscoelasticity

Changes in cellular-scale viscoelasticity are key for cell physiology [57]. Both the cytosol and cytoskeleton contribute to cellular-scale viscoelasticity, with cytoplasmic viscosity dominating processes of macromolecular movement [58] and cytoskeletal viscoelasticity influencing cell morphology, motility and division [8, 57]. Given that experimental work suggests that the cytoskeleton is the major determinant of cellular viscoelasticity [59, 60], we focus here on its viscoelastic properties. The cytoskeleton is the underlying biopolymer scaffold of living cells, and its viscoelasticity offers a balance between dynamic reorganization and maintenance of the cell body. Cytoskeletal

viscoelasticity is a complex phenomenon, since it arises from the mechanical properties and interactions of at least three different biopolymers: actin, microtubules and intermediate filaments. These fiber structures further self-organize into filaments and heterogeneous networks through mechanisms of entanglement, branching, crosslinking and bundling (**Figure 1C**) [61–64]. Such mechanisms involve several types of linkers, such as cross-linking/bundling proteins a-actinin and fascin, and motor proteins like myosin and kinesin [65]. In general, the mechanical properties of the cytoskeleton depend on the physical properties of the individual filaments, the pattern of linkages between the filaments, and the geometry of the filament arrangement [66, 67]. Although cell viscoelasticity is a result of the heterogeneous mechanical properties of all cytoskeletal elements together, our understanding of this process comes mostly from studying each type of element separately (for extensive reviews see [1, 3, 8]).

At the single-filament level, each cytoskeletal biopolymer displays different physical properties, assessed by the ratio of its *persistence length* (l_p) over its *contour length* (l_c) (**Box 1**). When $l_c > l_p$, the polymers are flexible, and this is the case for the intermediate filaments, which display the shortest l_p (from 200 nm to ~1 μm) and are the softest among the cytoskeletal elements [68, 69]. Actin filaments have a higher l_p (from 3 to 17 μm) and are semiflexible and microtubules exhibit the highest l_p (>1 mm) and are stiff polymers [70]. Already at the single filament level, semiflexible polymers such as actin and vimentin, display a nonlinear increase of their *shear modulus* at different *strain* amplitudes [71] (**Box 1**). This nonlinear force-extension relationship becomes more apparent at the network level, where new material properties emerge that are absent at the single filament level. Cytoskeletal elements build networks via various forms of filament interactions that influence the viscoelastic behavior of the whole network. For example, transient and non-covalent interactions with crosslinks turn the network into a viscoelastic material, whereas covalent interactions turn the network into an elastic material [3]. Experimental measurements of reconstituted cytoskeletal networks (**Figure 1C'**) revealed nonlinear force-extension relationships such as stress-stiffening in the presence of tensile load (**Figure 1C"**) but also *stress-softening* in the presence of compressive load [5, 30, 33, 62, 71, 72] (**Box 1**). Actin and intermediate filament networks are highly strain-sensitive, with 10–100 times stiffening appearing at very low strains [71, 73]. Experimental work suggests that depending on the density and interactions in the network e.g. dense vs sparse, the macroscopic material properties change following a well-defined phase diagram [30]. Gardel and colleagues have shown that the addition of crosslinkers results in the formation of rigid solid networks, with elastic modulus several orders of magnitude greater [30]. Even when using flexible crosslinkers like filamin, the network displays nonlinear increases of the elastic modulus when increasing strain, reaching values that match the elastic moduli of cells [34]. Similarly, addition of molecular motors to reconstituted actin networks, such as myosin II, leads to a sharp increase of the elastic modulus [74, 75]. Microtubules on the other hand, and also weakly cross linked actin networks, decrease their modulus as the applied stress is increasing displaying a stress-softening response [30, 76–78]. In conclusion, experimental work shows a very rich collection of nonlinear macroscopic viscoelastic behaviors of the cytoskeleton that represent a challenge for theoretical understanding at the microscopic level.

Extracellular Matrix Viscoelasticity

Besides the emergence of material properties in intracellular cytoskeletal networks, similar behaviors are observed in networks of the extracellular matrix (ECM), the non-cellular material backbone spanning cells and tissues. ECM viscoelasticity is fundamental in cell migration, tissue morphogenesis, organ development, and cancer progression [5, 79, 80]. The ECM is a heterogeneous network composed by several biopolymer filaments, such as fibronectin, laminin, and collagen, that exhibit various persistence lengths. This can range from the 4–8 nm persistence length l_p of flexible hyaluronan biopolymers to a few millimeters' persistence length l_p of stiff collagen fibers [81, 82]. Given that the ECM is composed of various proteins, enzymes and polysaccharides, probing its viscoelasticity becomes highly complex. Due to its covalent nature of crosslinking, in contrast to the cytoskeletal networks, the ECM is considered an elastic-like network [83]. Collagen networks also display a strain-stiffening response that is in this case emerging from the network level and specifically its connectivity [73, 84, 85] (**Figures 1C, C"**). In this case, the nonlinear behaviour emerges for strain of only 10% increase where stiffness increases by 100x before network rupture [44] (**Figure 1C"**).

Tissue Viscoelasticity

Similarly, tissue-scale viscoelasticity has been recently experimentally measured to undergo nonlinear changes [11–13, 86–89] resembling phase transitions [90–92]. Direct measurements of viscoelastic features such as yield stress and viscosity have been performed in embryonic tissues and spatial and/or temporal drastic changes have been observed [12, 13]. In the case of the early zebrafish blastoderm, for example, tissue viscosity was found to abruptly drop by more than an order of magnitude within a few minutes at the onset of morphogenesis [13] (**Figures 1D', D"**). In addition, comparison of the yield stress between two neighboring tissues along the zebrafish body axis, the presomitic mesoderm and the progenitor zone, has revealed the presence of solid-like and fluid-like tissues, respectively [12]. However, does cell viscoelasticity scale in such cases with tissue viscoelasticity? Although --to our knowledge-- no simultaneous analysis has been performed yet on measuring both cell and tissue scale viscoelasticity under different conditions to quantitatively assess their relationship, several lines of evidence point at the hypothesis that tissue-scale viscoelasticity critically depends on the interaction patterns between cells. Along these lines, it was reported that inhibition of myosin cytoskeletal motors in zebrafish, that is expected to decrease cell-scale viscoelasticity, had no effect on tissue viscosity [29]. Similarly, pharmacological treatments of the zebrafish tailbud with blebbistatin (a

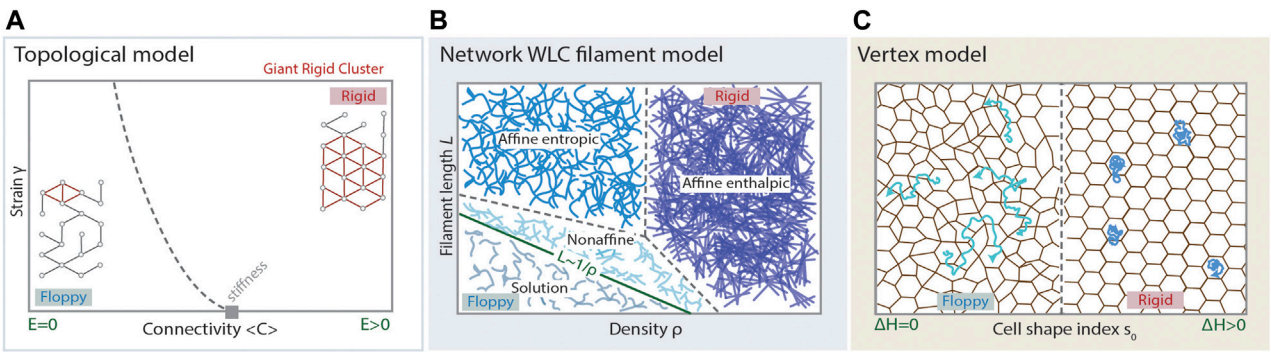

FIGURE 2 | Modelling cell and tissue viscoelasticity. **(A)** Phase diagram of the regimes arising in a topological model for rigidity, such as stiffness percolation, predicting a floppy to rigid transition at a critical point of average connectivity of the underlying network (grey rectangle). A random network displaying average connectivity below the isostatic point (critical point), has a small Giant Rigid Cluster (red) and the whole network is floppy, displaying Young's modulus $E = 0$. The same network, exhibiting connectivity above the critical point forms a big Giant Rigid Cluster making the whole network rigid, hence displaying $E > 0$. Figure adapted from [31, 138]. **(B)** Phase diagram of the network of WLC filaments' model showing strain-stiffening response of semiflexible biopolymer networks. At low density and low filament length, the network is in solution and in a floppy regime. The solid line indicates the rigidity percolation transition where the network gains stability above a critical density and length, and can be approximated by $L \sim 1/\rho$. At intermediate density but longer lengths, the network displays an affine elastic deformation due to the entropic stretching of the filaments. At higher density the network displays an affine elastic deformation dominated by the enthalpic stretching and bending of the network and is in a rigid regime. Figure adapted from [26]. **(C)** Phase diagram of a vertex model predicting a floppy to rigid phase transition in simulated confluent tissues. Below a critical point of a cell shape index s_0 (defined by cell-cell adhesion and cell contractility) cells are free to move and display high mean squared displacement (long cell trajectories) and the tissue is fluid-like, thanks that the increase of energy due to cell-cell rearrangements $\Delta H = 0$. Above the critical point cells acquire a hexagonal shape and display caged limited motion (short cell trajectories), and cell-cell rearrangements have a positive energy penalty $\Delta H > 0$. Figure adapted from [27, 28].

pharmacological myosin II inhibitor), which lowers cytoskeletal elasticity, had surprisingly inverse results on the tissue-scale material properties, where the tissue yield stress in treated embryos it is almost double than the control embryos [12]. In contrast, changes in cell rearrangements, cell-cell adhesion, contractility and cell division rates were shown to trigger changes in the tissue scale material properties (**Figure 1D**) [11–13, 86–88, 93]. This agrees with extensive theoretical work inferring tissue material phase transitions based on certain cell parameters such as cell motility and adhesion [27, 28, 32, 41], and quantitatively linking tissue rigidity to cell-cell connectivity and adhesion [29], but not directly to the rigidity of individual cells.

Overall, experimental measurements of several viscoelastic characteristics in cells and tissues have revealed nonlinear changes at the macroscale, e.g., viscosity, yield-stress, elastic modulus that do not trivially match similar changes at the microscale, e.g., individual cell and filaments material properties, strongly supporting that viscoelasticity of living systems is an emergent property.

VISCOELASTICITY AS AN EMERGENT PROPERTY: THEORETICAL MODELS

Several theoretical frameworks have been developed to establish a micro-macro link that can explain cell and tissue viscoelasticity. Numerous models exist in describing complex viscoelastic behaviors in chemical polymers where we recommend to the reader for a more specialized relevant literature [94–96]. Here however, we will summarize experimentally-based models belonging to three categories, based on the abstraction used to represent the biological system: In *cytoskeleton networks*, the building blocks are the biopolymer filaments and their mechanical properties, in *vertex models*, the geometrical properties of individual cells tilling the tissue and finally, in the *topological models*, the local topological arrangements of e.g., cell-cell contacts.

Modeling Viscoelasticity in Cytoskeleton Networks

The theoretical modeling of filament networks must account for the particular rheological phenomena these systems show, such as the strain stiffening response, stiffening tunability, and recoverable network fluidization [8, 15, 26, 30, 33, 71, 77, 97–99]. These models consider, at the microscopic level, filament properties like stiffness or length, and the local geometric and topological patterns of cross-linking, which project to the macroscopic level as material properties. Given these parameters, qualitative shifts in the response of the network are expected while increasing the density of filaments: First, beyond a certain threshold of density, the phenomenon of *geometric percolation* is observed, usually referred to simply as percolation, purely based on the network topology (**Box 1**). At higher filament density, another qualitative shift in the properties of the network is observed, when the *stiffness percolation* threshold is overcome (**Figure 2A**). Beyond this filament density threshold, any stress applied at any point of the network will propagate throughout the whole system, meaning that the Young modulus, E, transits from $E = 0$ to $E > 0$ [26, 100]. Stiffness percolation is related to *rigidity percolation* (**Box 1**), where stresses are no longer absorbed locally, but rather globally. Rigidity percolation, however, only refers to the topological structure [48, 101], whereas, in the case of

filament networks, further parameters are considered, as discussed below.

A well accepted model describing the phase space of filament viscoelasticity defined by the parameters of filament density and individual filament properties is the Worm-like Chain (WLC) model [15, 102]. In the WCL model, biopolymers are considered as elastic rods or fibers with finite resistance to bending. Geometrically, such fibers are depicted by an inextensible curve with an energy penalty for bending. Let $r(s, t)$ denote the path the curve takes in space (and time), parameterized by s, the arc length along the curve and χ the bending modulus. The functional accounting for the energy costs of fiber deformation will be given by:

$$H = \frac{\chi}{2} \int_0^{l_c} \left| \frac{d^2 r}{ds^2} \right|^2 ds$$

The second derivative accounts for the local curvature of the filament. The bending modulus χ has units of energy times length. The above energy function is penalizing any increase of the filament curvature and χ gives us the scale of such energy penalties. Thermal fluctuations play an important role here, due to the microscopic size of the filaments. As it is standard in statistical mechanics [103], non-zero temperature regimes imply the presence of stochastic, brownian fluctuations whose scale is $k_B T$, where T is the room temperature and k_B is the Boltzmann constant. Knowing the scale of the local stochasticity due to temperature enables the definition of a characteristic length for the system, as:

$$l_p = \frac{\chi}{k_B T}$$

which corresponds to the persistence length l_p(**Box 1**). Together with the contour length l_c (**Box 1**), the filaments are classified according to their stiffness as flexible, semi-flexible and stiff. If $l_p/l_c \ll 1$, the filament is *flexible* and thermal agitation can induce traverse fluctuations. In this regime, entropic elasticity (**Box 1**) dominates the dynamics, such as during cytoskeleton stretching [30, 71, 75, 104]. In the case where $l_p/l_c \gg 1$, filaments are considered *stiff* and no fluctuations induced by thermal agitation are allowed. In this regime, enthalpic elasticity (**Box 1**) dominates the deformations of the filament, such as during cytoskeleton bending or buckling observed in branched actin networks in the cell lamellipodia [77, 105]. Finally, when $l_p/l_c \approx 1$, filaments are considered semi-flexible and transverse undulations due to thermal fluctuations are possible, although attenuated. Whereas both the flexible and rigid regime show linear response to strain, the response in the semiflexible regime is nonlinear. To characterize the phase space, we observe that the system can transit between different regimes by changing the filament density ρ (proportional to $1/l_c$) and filament length L playing the role of l_p (proportional to the chain's molecular weight). Taking these two parameters as the coordinates of a phase diagram, one can identify four regimes: *Affine* entropic, affine enthalpic, non-affine, solution [15, 26, 33] (**Figure 2B**, **Box 1**). In this phase diagram, the phase transition from a fluid regime to a rigid regime is found at the border between the solution and the non-affine regime (**Figure 2B**), whose functional shape can be approximated as:

$$L \sim \rho^{-1}$$

Experimental work on reconstituted F-actin networks, revealed that linear and nonlinear strain-stress relationships can be explained by entropic and enthalpic models, respectively. In the absence of crosslinkers, actin networks generally form weak elastic gels mimicking the elastic nature of the filaments [106, 107]. At the entropic regime, elasticity comes from the resistance of each polymer/filament against stretching [33, 107]. At the enthalpic regime, while increasing strain, filaments first bend, reorganize along the direction of shear strain and the network deformation arises from the enthalpic stretching of the aligned filaments [108–110]. Further work showed that by decreasing the concentration of cross-linkers the network transits from affine to non-affine [74, 75]. In conclusion, the modeling of biopolymer networks within this framework has proven powerful enough to account for the special viscoelastic properties of these systems.

Modeling Viscoelasticity in Tissues

Cell-Based and Energy Minimization in Vertex models

When modelling tissue viscoelasticity, the fundamental units, cells, are considered to exhibit certain properties [25, 111–117] (**Box 1**) arising from the cell cytoskeleton [118]. Parameters, such as departure from an ideal cell shape and active fluctuations condense the material response of the cell and its effect to the tissue architecture under stress. There are several abstractions, depending on where the emphasis is placed concerning the energetic cost of the tissue deformations or configurations. Here, we will briefly mention Cellular Potts models and Centroid models, and focus more on the *Vertex models* (**Box 1**) which provide a widely applicable framework to the understanding of biological tissue properties.

Cellular Potts models idealize the tissue architecture as a mesh in which each point can be in several states and, accordingly, can represent a part of the cell, a contact point, or a free space. Each state of the mesh point has a particular contribution to the overall energy of the system, and may depend critically on the state of its neighbors [116]. Cellular Potts models may be considered within the much broader family of network models. In turn, centroid models base the analysis on the assumption that cells can be represented by their centroid position within the geometry of the tissue. Energetic contributions are based on geometrical considerations between centroids, such as distance between them [117, 119, 120]. The source of energetic contributions can be considered somehow complementary or even opposed [120] to the one considered in vertex models and the energetic costs associated with different configurations can be associated with material properties of the modeled tissue.

Vertex models have recently received a lot of attention due to their potential in describing a wide range of tissue properties [25, 27, 36, 111–115, 117–119, 121–123]. Moreover, the accurate

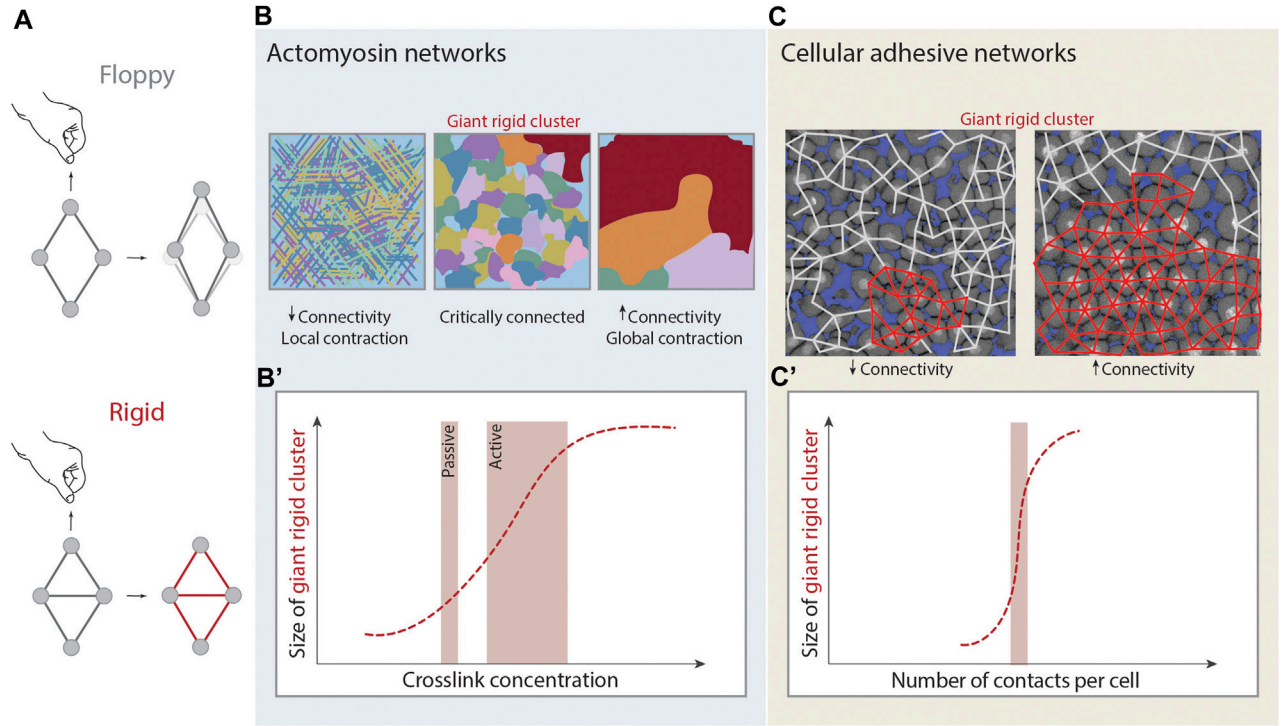

FIGURE 3 | Rigidity percolation in living systems. **(A)** Schematic illustration of rigidity. A rhombus cluster of four nodes and four links deforms in the presence of a deformation force. Just by the addition of one link that absorbs the remaining degrees of freedom of the central nodes, under the same deformation force it does not deform and it is considered rigid. **(B,B')** Rigidity percolation transition in actomyosin crosslinked networks. **(B)** At low connectivity (left) or low crosslinker concentration the network is mostly disconnected and displays local contractions. At intermediate connectivity (middle) and intermediate crosslinker concentration the network is critically connected. At higher connectivity (right) and high crosslinker concentration the network is fully connected, the Giant Rigid Cluster (GRC, red) emerges and the network displays global contractions and signs of fracture. **(B')** Plot of the size of the GRC as a function of crosslinker concentration and thus average connectivity. Depending on the absence or presence of contractility the system can be considered as passive or active respectively, and this changes the transition point. Figure adapted from [43]. **(C,C')** Rigidity percolation transition in cellular networks - tissues - of the zebrafish embryonic blastoderm. **(C)** At low average connectivity (~3.5 contacts per cell) the GRC (red) is small and the blastoderm is fluidized whereas at higher connectivity (>4 contacts per cell) the GRC is big, occupies almost the whole network and the tissue displays experimentally high viscosity. **(C')** Plot of the size of the GRC as a function of cell connectivity. Note that the GRC is emerging sharply at the critical point of connectivity (2/3 of maximum potential connectivity). Figure adapted from [29].

study of their mathematical properties revealed a plethora of interesting physical properties [27, 28], such as second order rigidity [121], that could play a relevant role in the modeling of biological tissues. Importantly, these properties may imply an interesting departure from the framework proposed by inanimate material science, and proposes a theoretical framework that extends to biological materials. In principle, vertex models have been postulated to model confluent tissues, with recent approaches extending the framework to non-confluent tissues [32]. The essential problem vertex models try to answer is: what are the energetic costs for cell migration within a tissue? In that framework, fluid states are those by which the movement of cells can happen at almost no cost, and rigid states will correspond to those states by which moving a cell - in particular, performing a T1 transition - implies a positive energy penalty, to be paid either in the form of external work or by the cells themselves (**Figure 2C**). Arguably, the response to an external stress will be, at least partially, driven by the possibility of cell rearrangements which, in turn, depend on the ease of movements of cells within the tissue. The energetic contributions that configure the overall energy of the tissue come from the resistance against compression and the departure from some preferred shape in cells which, in most cases, is introduced as the preferred relation perimeter/area in 2D projections [27, 113, 121, 122]. Having N cells, the functional accounting for the energy of the (2D) system reads:

$$H = \sum_j^N K_{Aj}\left(A_j - A_{0j}\right)^2 + K_{Pj}\left(P_j - P_{0j}\right)^2 \qquad (1)$$

where A_j and A_{0j} are the actual and preferred areas of cell j; P_j and P_{0j} are the actual and preferred perimeter of cell j. K_{Aj} and K_{Pj} are the area and perimeter moduli, respectively. The first term models volume incompressibility and the second term models the active contractility of the actomyosin subcellular cortex. As shown, the underlying complex properties of the filament network which are themselves the outcome of a multidimensional problem have been absorbed by the scalar parameters K_{Aj} and K_{Pj}. The above equation can be non-dimensionalized in length if we divide it by $\sqrt{A_0}$, resulting in an effective shape index s_0:

$$s_0 = \frac{P_0}{\sqrt{A_0}}$$

s_0 will act as the control parameter in the different phase transitions between the material regimes of the tissue (**Figure 2C**). The study of the energetic costs of motility within the tissue is performed through the analysis of the energy barriers arising when a T1 transition occurs (**Box 1**). The energy barrier corresponding to a T1 transition can, in consequence, be computed as the energy difference, based on **Eq. 1**, associated to the reduction of the length of an edge to 0 [124, 125]:

$$\Delta H = H(l) - H(0)$$

If a T1 transition can be performed at no energy cost, the tissue is in a fluid configuration. Otherwise, the tissue is considered rigid. Remarkably, one can observe a well-defined phase transition from $\Delta H = 0$to $\Delta H > 0$ as a function of s_0. In particular, for values $s_0 < 3.81$, the energy imbalance is no longer zero, meaning that T1 transitions happen at a finite energy cost. Interestingly, in disordered systems, the shear modulus vanishes at $s_0 < 3.81$ [25, 27]. Given the composition of tissues, any deformation must involve rearrangement of cells and, therefore T1 transitions. Consistently, one would expect that the shear modulus goes hand in hand with the energy barriers. Remarkably, this is not the case, and for values $3.71 < s_0 < 3.81$, the tissue has zero linear response but non-zero high-order response [121]. In consequence, this phenomenon has been called "second order rigidity" and the material regime has been named "soft solid" regime [126]. In spite of the numerical evidence that the emergence in the linear regime of the shear modulus coincides with the emergence of theoretical energy barriers in disordered systems, it is currently still unclear what is the theoretical background that could explain the emergence of viscoelastic properties from the theoretical framework of vertex models. Finally, an extension of this vertex model has been developed for non-confluent tissues where stochastic fluctuations in cell surface tensions, density and cell rearrangements control rigid-to-fluid transitions [32]. This contribution detaches the framework of vertex models from the structural constraints that confluency imposes, hence broadening their application in biological tissues.

Topological Models Based on Cell Contact Networks

The presence of *interstitial fluid* (**Box 1**) in non-confluent tissues, such as embryonic tissues and tumors [12, 13, 127], opens the possibility to apply even simpler theoretical frameworks to study their viscoelasticity [29]. The reason is that abandoning confluence liberates the system from a lot of implicit constraints at the structural level. Within non-confluent tissues, the range of potential structural patterns increases enormously and topological models can exploit this potential heterogeneity. Here we discuss how topological models can be connected to the rheological properties of non-confluent tissues.

Topological models consider only the structural pattern of connections as the source of the material properties of the tissues. When the system is abstracted at the topological level, its structure is represented by a network defined by nodes and connections among them (**Figure 2A**). It is important to stress that, at first approximation, no other component, such as link properties or geometric embedding, is considered. The topological analysis, therefore, distills the structure of the system at the level of microscopic minimal components and combinatorial relations among them. In that sense, the basic observables of these models are, for example, the number of links connecting a given node to other nodes of the network, or the existence of paths, within the graph, between a given pair of them. In general, the approximation of a random network, in which the number of connections per node fluctuates stochastically according to some general constraint, quite accurately describes the behavior of real systems --given a suitable choice of constraints [92, 128–131]. For example, in the case that a network is representing the contacts of cells in epithelial (2D) tissues, it must belong to the class of *planar* networks, namely, those networks that can be extended in a 2D surface without displaying any link overlap [131]. In spite of the apparent simplicity of the approach, the study of networks at the topological level displays a wide range of non-linear phenomena, such as phase transitions or self-organized criticality [92, 129–131]. Particularly relevant is the phenomenon of *percolation* [91, 92, 128, 129], briefly mentioned in previous sections (**Box 1**). We will focus on the emergence of the so-called *rigid cluster percolation* (**Box 1**), due to its important implications in cells and tissue material properties.

Rigid cluster percolation is based on *generic* rigidity theory. Given a graph of N nodes and N_L links, a graph is rigid if none of its nodes can be moved independently without constraining or stretching a link (**Figure 3A**). Despite that the informal definition provided above for rigidity percolation appeals to material deformations e.g., stretching, compressing links, it turns out that the identification of rigid regions in a graph is a purely topological problem: it relies on the identification of actual degrees of freedom remaining in the network through application of the pebble game algorithm [47] based on a theorem considering only the topology of the network [101] (see **Figure 3A**). A natural question arises: what are the conditions leading to rigidity in a network? The answer is based on Maxwell's constraint counting [48, 132], where very large networks made of N nodes and N_L links are considered, the links acting as pairwise constraints, limiting the possibilities of independent motion of the nodes connected by the link. For simplicity, a random triangular lattice is considered (e.g., networks in **Figure 2A**) where the probability that a link exists is p_e. If $p_e = 1$, all the links are present and the average connectivity $\langle c \rangle$, the average number of links per node, is $\langle c_M \rangle = 6$ --recall we are considering very large networks where the boundary effects are negligible. In consequence, the number of links of this network will be fairly approximated by:

$$N_L = \frac{p_e}{2} N \langle c_M \rangle \quad (2)$$

A network will be rigid if the constraints absorb all the degrees of freedom for the motion of nodes (**Figure 3A**). Considering a triangular lattice embedded in a 2D plane, each node has, a priori, $d = 2$ degrees of freedom (position x and y). The number of degrees of freedom remaining in the network or *Floppy* modes, F, will be approximated by:

$$F = dN - N_L$$

Note that here we consider that all links are responsible for an independent constraint. We must notice that this is an important simplification [51, 132] of the problem, but has proven useful in terms of both simplicity and predictive power. Starting from $p_e = 0$, the number of floppy modes is expected to decrease as long as p_e grows. The key question is to identify the p_e by which $F = 0$ and, thus, the whole network is expected to be rigid. This is known as the *isostatic point* (**Box 1**) and, using the expression for E found in **Eq. 2**, and setting $F = 0$, we obtain:

$$dN = \frac{p_e}{2} N \langle c_M \rangle$$

that lead us to:

$$p_e = \frac{2d}{\langle c_M \rangle} = \frac{2}{3} \tag{3}$$

which, in terms of average network connectivity, implies $\langle c \rangle = 4$. That is, if the probability of link existence is $p_e > 2/3$, one expects the network to be rigid, and no independent movements could, in principle, be performed without imposing work over the system. Nevertheless, the emergence of rigidity is a much more complex phenomenon. In the case that $p_e < 2/3$, for example, there are constraints already acting in the system, so one would expect to see rigid regions within the network. At the same time, the probabilistic nature of the reasoning for finding the isostatic point may induce one to think that some regions of the network may remain floppy even for $p_e > 2/3$ The answer is that, in very large systems, the relative size of rigid regions at $p_e < 2/3$, is negligible and that, for $p_e > 2/3$ one observes the emergence of the giant rigid cluster (GRC) spanning almost all the network (**Figure 2A**). The emergence of the GRC is abrupt and has all the features of high order phase transitions. Therefore, the isostatic point $p_e = 2/3$ is the critical point of a phase transition called generic rigidity percolation, or simply, rigidity percolation [47, 51].

In order to connect rigidity and topology with the material properties, the mechanics of the links, considered as springs, should also be considered. In that context, $p_e < 2/3$ (subcritical regime) implies that one can perform a differential deformation over the network at no cost. On the contrary, if $p_e > 2/3$, any deformation implies an energetic cost in the form of external work performed over the network, as some spring will have to be unavoidably stretched or compressed. Therefore, in the case of very large systems, the first natural consequence of the emergence of the rigid cluster is that the Young modulus E will be $E = 0$ in the subcritical regime and $E > 0$ in the supercritical regime. In consequence, the topological phase transition that results into the emergence of the GRC projects into the material properties, implying a qualitative shift in the material response of the system under deformations. How does it project specifically into the viscoelastic behavior of the network? To understand that, a minimal ingredient of viscoelastic behavior should be introduced within the springs. This is performed by considering that each spring may update its rest length at random [29, 133]. Specifically, in the simplest approach, the spring updates its rest length at random at every time unit step with probability $p = \frac{1}{\tau}$. Formally, if at time t the rest length is $l(t)$ and the actual length, due to some external stress, is $l(t) + \Delta l(t)$, then:

$$p\left(l(t+1) \rightarrow l(t) + \Delta l(t)\right) = \frac{1}{\tau}$$

In **Box 2** we show how the microscopic dynamics of energy dissipation gives rise to macroscopic viscosity. In particular, if E is the Young modulus of the network, each link has the same spring constant k, and all such springs update their rest length at random with probability $p = \frac{1}{\tau}$ at every time step, one is led to:

$$\frac{d\gamma}{dt} = \frac{1}{E}\left(\frac{d\sigma}{dt} + \frac{\sigma}{\tau}\right) \tag{4}$$

where γ, is the strain and σ, the applied stress (**Figure 1B**). **Eq. 4** is a constitutive equation for a Maxwellian viscoelastic material [14] (**Figure 1B**). The above equation enables us to identify:

$$\eta = E\tau \tag{5}$$

as the viscosity of the system. What is relevant here is that we have a direct relation between the Young's modulus of the system, E, and the viscosity of the material, η, up to a constant that is the average lifetime of springs: The faster the update of the spring rest length is, the more fluid the behavior of the material will be. On the contrary, in the limit of no updating, the material is only elastic. Moreover, it is established above that the emergence of a finite Young's modulus depends critically on the rigidity regime of the network. In conclusion, non-zero viscosity will emerge as the consequence of the emergence of the GRC, at least at the linear level. The phase transition observed for the emergence of the rigid cluster must therefore leave a footprint in the viscoelastic behavior of the network at the critical point.

The above framework is able to bridge, in spite of its simplicity, microscopic topological patterns to macro-structural properties [47, 51], without a priori reference to the mechanical properties of the constituents. These patterns, in turn, can be formally mapped to macroscopic material observables, such as viscoelasticity, hence demonstrating a potentially widely applicable framework to quantitatively link microscopic interactions to macroscopic viscoelasticity across scales.

RIGIDITY PERCOLATION PROBING VISCOELASTICITY ACROSS SCALES

Recent experimental work indicates that analysis at the purely topological level has the potential to indeed probe viscoelastic

BOX 2 | Viscosity of a network of springs.

We sketch here, in a very simplified way, the connection between viscoelasticity and the topological property of generic rigidity. We present a version of the Maxwell's model for viscoelasticity (see **Figure 1B**), where the particularity comes from the conceptualization of the dashpot, whose role is absorbed by a stochastic resetting of the rest-lengths of the springs forming a network that, in turn, models the structure of the material. This modelization enables the linking of Maxwell's network rigidity to Maxwell's theory of viscoelasticity.

Let us consider a network of springs, each with elastic constant k. Each spring updates its rest length at random with probability $p = 1/\tau$ at every time step. If, at time t the rest length is $l(t)$ and the actual length, due to some external stress, is $l(t) + \Delta(t)$, with probability $p = 1/\tau$, the rest length at time $t + 1$ will be updated as:

$$l(t+1) \rightarrow l(t) + \Delta l(t).$$

The whole network has Young's modulus E. We consider a random lattice arranged in a rectangular form, in a way that the bottom layer is attached to the ground and the upper layer receives the stress $\sigma(t)$ uniformly —is pulled up. To study the strain $\gamma(t)$, the elastic contribution, $\gamma_e(t)$ and the contribution of the energy dissipation due to rest-length resetting, $\gamma_u(t)$ must be considered. The overall strain will thus read:

$$\gamma(t) = \gamma_e(t) + \gamma_u(t).$$

We first consider the elastic component, e.g.:

$$\gamma_e(t) = \frac{\sigma(t)}{E}.$$

To compute $\gamma_u(t)$, we observe that, in a mean-field approximation, a fraction of $1/\tau$ of springs of the network will update their rest length per time step. Since the elastic deformation for the applied stress is $\gamma_e(t)$, the equation for $\gamma_u(t)$ is:

$$\delta\gamma_u(t) \approx \frac{\gamma_e(t)}{\tau}.$$

Using the expression for $\gamma_e(t)$, and applying the continuous approximation, this leads to:

$$\frac{d\gamma_u}{dt} = \frac{\sigma}{\tau E}.$$

Considering the two contributions, the overall strain evolves according to the following equation:

$$\frac{d\gamma}{dt} = \frac{1}{E}\left(\frac{d\sigma}{dt} + \frac{\sigma}{t}\right),$$

Which is a constitutive equation for a Maxwellian viscoelastic material [14]. The above equation enables us to identify the viscosity as:

$$\eta = E\tau.$$

In consequence, qualitative changes in the Young's modulus of the network will project into qualitative changes in the viscoelastic behaviour of the system. If $k = 0$, as it happens in spring networks whose connectivity is in the rigidity subcritical regime, one expects that, at the linear level, $\eta = 0$. On the contrary, if the network is in the supercritical rigidity regime, $k > 0$ and, in consequence, $\eta > 0$.

To grasp the physical role of τ, we consider the simple scenario where we perform an instantaneous, small deformation over the network by pushing the upper layer a distance d, under the assumption that $k > 0$. In this case, the constitutive equation can be rewritten as:

$$\frac{d\sigma}{dt} + \frac{\sigma}{t} = 0,$$

since the strain is 0. The solution of the above equation is given by $\sigma(t) = \sigma_0 e^{-t/\tau}$, that is a dissipation of energy in as system with characteristic scale τ.

properties across scales. These models have been applied to several forms of biological networks, such as the cytoskeleton, ECM and cellular networks–tissues, to probe their material properties [29, 31, 44].

In the case of the cytoskeleton, both experimental and theoretical studies have shown that network connectivity is an essential parameter for cytoskeletal network mechanics [26]. If the actomyosin cytoskeleton is considered as a passive system, then rigidity percolation can predict the elastic modulus of the system based solely on its connectivity. In fact, a phase transition is proposed to occur in such networks, where mechanical rigidity emerges at the isostatic point --see **Eq. 3** [31] (**Figures 3B,B'**). Such a framework can be expanded to active systems, where network connectivity together with motor activity can be further used as parameters to predict the contractile behavior of the actin cytoskeleton. Experiments on actin gels, where connectivity is regulated by the density of fascin crosslinkers and the motor activity by the density of myosin, showed characteristics of a rigidity percolation transition [43]. Briefly, weakly crosslinked networks (low connectivity) showed local contractions, medially crosslinked networks (higher connectivity) formed distinct contractile clusters within the network with a certain rigid cluster size distribution and, strongly crosslinked networks (highest connectivity) exhibited global network contraction associated with network fracture [43] (**Figure 3B**). The authors further propose that the motors have the ability to reduce connectivity via forcing the crosslinkers to unbind, in order to avoid network fracture and thus the interplay of motor activity and crosslinking drives active gels to a critically connected state that can balance between local and global contractions [43].

Rigidity properties of ECM networks and, in particular, type I collagen fiber networks, have also been well-described by rigidity percolation theory [134]. Studies combining experiments and theory suggest that the shear modulus of collagen fibers shows a strong correlation with the collagen volume fraction, and that these networks display connectivity near the percolation threshold [134–138]. Further experimental work however, has revealed that collagen networks with connectivity slightly below the isostatic threshold, can also become rigid in the presence of large deformation instead, thus in such cases passive rigidity percolation may not be sufficient to explain ECM rigidity [44, 85]. In particular, increasing shear deformation in sub-isostatic networks leads to nonlinear increase of the elastic modulus of such networks along different connectivity values, an observation highlighting the possibility of incorporating the active nature of such systems when applying rigidity percolation theory [139].

Recently, the concept of rigidity percolation has been applied in non-confluent embryonic tissues to map tissue rigidity/viscosity (**Box 2**). Although tissues do not form physically crosslinked networks as the cytoskeleton or ECM, they can be approached as "cellular networks", where the nodes are the cells and the connecting links the adherens-junctions (**Figure 3C**) [140]. This theory was applied to the zebrafish blastoderm which undergoes an abrupt and dramatic loss in viscosity at the onset of morphogenesis [13, 29]. These changes in blastoderm viscosity were probed via rigidity percolation analysis over cell contact networks of the blastoderm. The size of the GRC was analyzed as a function of connectivity, and it was found that the GRC size correlates with the experimentally observed changes in tissue viscosity [29] (**Figure 3C**). The emergence and disappearance of the GRC around the critical point matched the empirical observations where embryos whose cell contact network displays an average connectivity below the critical point, display a small GRC and are fluidized, whereas embryos whose network displays an average connectivity above the critical point display a big GRC and are rigid (**Figure 3C**). This work further traced hallmarks of phase transitions, such as the diverge of macroscopic observables and its critical exponents at criticality, showing that rigidity percolation theory can be applied in embryonic tissues *in vivo* to link macroscopic tissue rigidity to the microscopic cell connectivity of these tissues [13, 29].

DISCUSSION AND OUTLOOK

Living cells and tissues behave like viscoelastic materials [20, 141], a long-standing observation that has only recently been linked to cell and tissue physiology [2–5]. Spatiotemporal regulation of viscoelasticity has been shown to influence essential biological processes, such as cell motility, proliferation, wound healing and the morphogenetic processes of body axis elongation and tissue spreading during embryonic development [11–13, 86, 88, 142–144]. Tracing the microscopic regulators of viscoelasticity is, however, a challenging task: typically, the mechanical properties of these microscopic building blocks do not match trivially the emerging viscoelastic behavior of cells and tissues at the macroscopic scale. Among many examples, we find the nonlinear increase of the elastic modulus of cytoskeletal and fiber networks in response to strain, or abrupt drastic changes in tissue viscosity without associated mechanical changes at the cellular level [12, 29, 30, 33]. Given that the mechanical properties of tissues are regulated at the microscopic level, e.g., from the properties of the microscopic building blocks and their interactions, quantitatively bridging the microscale to macroscale is fundamental in order to understand the emergence of viscoelasticity [145]. Several theoretical approaches shed light on the biological mechanisms by which viscoelasticity can emerge in a system. However, the application of such theories is still far from comprehensive, given several challenges --such as the active, non-equilibrium nature of living systems.

At the cellular scale, the viscoelasticity of networked biopolymer filaments forming the cytoskeleton and ECM is most frequently modeled based on the mechanics, geometric alignment and local topology of the biopolymer fibers. It is worth mentioning that most of the research activity was performed in networks composed of actin or microtubules or intermediate filaments. In fact, biopolymer networks show a much wider heterogeneity, since the cytoskeleton is a dynamic mixture of all the cytoskeletal elements, interacting with each

other, and these interactions were shown to affect their mechanical properties. Percolating networks of actin and vimentin for example, display synergistic effects in the elastic modulus, which becomes much greater than the sum of the elastic moduli of the two networks alone [146]. Another synergistic effect on actin and IFs networks is the recently reported phenomenon of super-elasticity, observed during epithelial morphogenesis [147]. Similarly, actin and MTs composite networks were shown to exhibit reinforcement against compression and mechanical enhancement [148–150], and a similar phenomenon was also observed when compressing composite ECM networks of collagen and hyaluronan [151, 152]. Future experimental and theoretical work on composite networks is expected to provide a more complete understanding of cell and ECM viscoelasticity.

At the tissue scale, the vertex models are widely used to represent tissue viscoelasticity and have the special advantage of collapsing the emergence of macroscopic properties on a single cellular parameter, such as cell shape, and its associated scalar parameters, such as compressibility or departure from preferred area/perimeter [27, 28]. Since, in a tilling of cells, deformation can only arise through cell-cell rearrangements, vertex models mostly focus the analysis on the study of the energy penalties associated with these cell-cell rearrangements. Such rearrangements can for example be induced by differences in cell-cell adhesion and cortical tension or active tension fluctuations [27, 28, 32, 125]. It is implicitly postulated that the results at that level of abstraction will project into the material properties of the system. Even though numerical approaches are coherent with the predictions of the models, a direct bridge between micro and macro scales in tissue viscoelasticity has yet to be clearly described. The recent application of rigidity percolation in tissues however, provides a quantitative link between the topological patterns of cell-cell contacts and tissue rigidity regime (quantified by the size of the GRC). In the case of the zebrafish blastoderm, the topological approach of rigidity percolation was sufficient to capture the floppy and rigid regimes of the tissue by one single (microscopic) measurable parameter, the average number of cell-cell contacts in different cell types and, as a result, match the observed (macroscopic) changes in viscoelasticity [29]. Cell connectivity was further shown to be defined by the biophysics of cell-cell contacts and specifically the cell-cell interfacial tension at the contact. In this biological context, experimental testing of the phase transition parameters revealed that changes in connectivity and cell-cell adhesion were driven by cell division, and not by cell rearrangements, cell shape or active tension fluctuations [29]. Since cell-cell adhesion is key in tissue rigidity theoretical frameworks so far, we speculate that some parameters may be common, such as cell-cell adhesion strength [29, 32, 118, 123], and some others may be context-specific such as cell division and rearrangements. Future experimental work has the potential to disentangle the physiological role of several cellular parameters in rigidity transitions.

In all of the above models, incorporating detailed dynamic analyses of the microscopic parameters that can account for local heterogeneities, such as in adhesion strength (between the cells and with their environment), shape differences or heterogeneous motility patterns, will increase their potential to model absolute viscosity values and provide a more accurate and representative image of tissue viscoelasticity. A key challenge is the choice of the viscoelastic model relevant to the biological system. Here, we have extensively described how Maxwell viscoelasticity has the potential to be linked to Maxwell rigidity. However, other biological systems may be better described with different models. For example, the Kelvin model was recently used to describe the phenomenon of arrested coalescence in multicellular aggregates from the adherent and contractile protrusion interactions between the cells [153]. In addition, both Maxwell and Kelvin viscoelastic models can describe different viscoelastic regimes during density/packing dependent collective cell migration [154]. Another important challenge is to understand if and how the timescale of a biological process taking place at the microscale is relevant to the timescale of a biological process taking place at the macroscale when bridging scales in viscoelasticity. For example, how macromolecular motion within the cytoskeleton (milliseconds to seconds) influences cell shape changes driven by the mechanics of the cytoskeleton (seconds to minutes), or how cellular motion within a tissue (minutes) influences tissue-scale fluidization (minutes) and spreading (hours)? Several theoretical and experimental frameworks should be developed do bridge scales in time and space [142, 155].

Disentangling the connection between microscale behavior and emerging, macroscopic properties is not a novel goal: it has been the long-sought target of statistical mechanics in order to connect thermodynamics to a solid microscopic basis [156]. Moving towards a broader conception of statistical mechanics encompassing the living phenomena requires the introduction of the microscopic role of the biological building blocks - which are far more complex than gas particles, for example. Nevertheless, establishing the critical point in the microscopic dynamics of the building blocks that would trigger a macroscopic phase transition would create a rich toolbox for biology, regardless of the theoretical approach being used. Phase diagrams or morphospaces, accounting for what is possible in the relations between tissue organization and material properties, can be defined that will allow further exploration for the different regimes the system can occupy and their grounding. In the case of the zebrafish blastoderm, for example, it was experimentally possible to position the system in the vicinity of criticality. Hallmarks of criticality, such as divergence of macroscopic observables with associated power laws, were determined experimentally in the living embryo, showing that tissue morphogenesis in vertebrates may start close to a critical point of a rigidity transition. This indicates that embryonic tissues may be at optimal fitness [157] since they are able to easily switch between rigid and floppy regimes by slightly changing their connectivity at almost zero energetic cost [29]. Through this lens, one can explore fundamental questions concerning morphogenesis. How do local heterogeneities in the microscopic parameters influence the emergence of macroscopic viscoelasticity? How do noisy biological systems [158–160]

guarantee stability during development when they are poised at criticality?

Networked systems and criticality have been for long used to understand an extremely rich palette of macroscopic phenomena occurring in the natural world [92, 131, 161, 162], that now include the viscoelastic characteristics of biological systems, from the nanometer scale of the cytoskeleton to the micrometer scale of tissues and embryos. Such observations indicate that an efficient organizing strategy of complex biological systems may be to behave as networked systems close to criticality.

AUTHOR CONTRIBUTIONS

BC-M and NP designed, drafted, revised and finalised the work.

ACKNOWLEDGMENTS

We thank Preeti Sahu and Edouard Hannezo for critical discussion on the topic and Anna Erzberger and Gautam Dey for feedback on the manuscript.

REFERENCES

1. Huber F, Schnauß J, Rönicke S, Rauch P, Müller K, and Fütterer C. Emergent Complexity of the Cytoskeleton: from Single Filaments to Tissue. *Adv Phys* (2013) 62(1):1–112. doi:10.1080/00018732.2013.771509
2. Barriga EH, and Mayor R. Adjustable Viscoelasticity Allows for Efficient Collective Cell Migration. *Semin Cell Dev Biol* (2019) 93:55–68. doi:10.1016/j.semcdb.2018.05.027
3. Burla F, Mulla Y, Vos BE, Aufderhorst-Roberts A, and Koenderink GH. From Mechanical Resilience to Active Material Properties in Biopolymer Networks. *Nat Rev Phys* (2019) 1(4):249–63. doi:10.1038/s42254-019-0036-4
4. Petridou NI, and Heisenberg CP. Tissue Rheology in Embryonic Organization. *EMBO J* (2019) 38(20):e102497. doi:10.15252/embj.2019102497
5. Chaudhuri O, Cooper-White J, Janmey PA, Mooney DJ, and Shenoy VB. Effects of Extracellular Matrix Viscoelasticity on Cellular Behaviour. *Nature* (2020) 584(7822):535–46. doi:10.1038/s41586-020-2612-2
6. Lecuit T, Lenne P-F, and Munro E. Force Generation, Transmission, and Integration during Cell and Tissue Morphogenesis. *Annu Rev Cell Dev Biol* (2011) 27:157–84. doi:10.1146/annurev-cellbio-100109-104027
7. Clément R, Dehapiot B, Collinet C, Lecuit T, and Lenne P-F. Viscoelastic Dissipation Stabilizes Cell Shape Changes during Tissue Morphogenesis. *Curr Biol* (2017) 27(20):3132–42.e3134. doi:10.1016/j.cub.2017.09.005
8. Pegoraro AF, Janmey P, and Weitz DA. Mechanical Properties of the Cytoskeleton and Cells. *Cold Spring Harb Perspect Biol* (2017) 9(11):a022038. doi:10.1101/cshperspect.a022038
9. Campàs O. A Toolbox to Explore the Mechanics of Living Embryonic Tissues. *Semin Cell Dev Biol* (2016) 55:119–30. doi:10.1016/j.semcdb.2016.03.011
10. Gómez-González M, Latorre E, Arroyo M, and Trepat X. Measuring Mechanical Stress in Living Tissues. *Nat Rev Phys* (2020) 2(6):300–17. doi:10.1038/s42254-020-0184-6
11. Barriga EH, Franze K, Charras G, and Mayor R. Tissue Stiffening Coordinates Morphogenesis by Triggering Collective Cell Migration In Vivo. *Nature* (2018) 554(7693):523–7. doi:10.1038/nature25742
12. Mongera A, Rowghanian P, Gustafson HJ, Shelton E, Kealhofer DA, and Carn EK. A Fluid-To-Solid Jamming Transition Underlies Vertebrate Body axis Elongation. *Nature* (2018) 561(7723):401–5. doi:10.1038/s41586-018-0479-2
13. Petridou NI, Grigolon S, Salbreux G, Hannezo E, and Heisenberg C-P. Fluidization-mediated Tissue Spreading by Mitotic Cell Rounding and Non-canonical Wnt Signalling. *Nat Cell Biol* (2019) 21(2):169–78. doi:10.1038/s41556-018-0247-4
14. Findley WN, Lai JS, and Onaran K. *Creep and Relaxation of Nonlinear Viscoelastic Materials*. Amsterdam: Elsevier (1989).
15. Broedersz CP, and MacKintosh FC. Modeling Semiflexible Polymer Networks. *Rev Mod Phys* (2014) 86(3):995–1036. doi:10.1103/RevModPhys.86.995
16. Özkaya N, and Nordin M. Mechanical Properties of Biological Tissues. Editor Nordin M. In: *Fundamentals of Biomechanics*. New York: Springer (1999).
17. Gutierrez-Lemini D. *Engineering Viscoelasticity*. New York: Springer (2014). doi:10.1007/978-1-4614-8139-3
18. Serwane F, Mongera A, Rowghanian P, Kealhofer DA, Lucio AA, and Hockenbery ZM. In Vivo quantification of Spatially Varying Mechanical Properties in Developing Tissues. *Nat Methods* (2017) 14(2):181–6. doi:10.1038/nmeth.4101
19. D'Angelo A, Dierkes K, Carolis C, Salbreux G, and Solon J. In Vivo Force Application Reveals a Fast Tissue Softening and External Friction Increase during Early Embryogenesis. *Curr Biol* (2019) 29(9):1564–71.e6. doi:10.1016/j.cub.2019.04.010
20. Forgacs G, Foty RA, Shafrir Y, and Steinberg MS. Viscoelastic Properties of Living Embryonic Tissues: a Quantitative Study. *Biophysical J* (1998) 74(5):2227–34. doi:10.1016/S0006-3495(98)77932-9
21. Bonn D, Denn MM, Berthier L, Divoux T, and Manneville S. Yield Stress Materials in Soft Condensed Matter. *Rev Mod Phys* (2017) 89(3):035005. doi:10.1103/RevModPhys.89.035005
22. Davidson LA. Embryo Mechanics. *Curr Top Dev Biol* (2011) 95:215–41. doi:10.1016/b978-0-12-385065-2.00007-4
23. Mongera A, Pochitaloff M, Gustafson HJ, Stooke-Vaughan GA, Rowghanian P, and Campàs O. Mechanics of the Cellular Microenvironment as Perceived by Cells In Vivo</em&gt. *bioRxiv* (2021). 2021.2001.2004.425259. doi:10.1101/2021.01.04.425259
24. Kollmannsberger P, and Fabry B. Linear and Nonlinear Rheology of Living Cells. *Annu Rev Mater Res* (2011) 41(1):75–97. doi:10.1146/annurev-matsci-062910-100351
25. Farhadifar R, Röper J-C, Aigouy B, Eaton S, and Jülicher F. The Influence of Cell Mechanics, Cell-Cell Interactions, and Proliferation on Epithelial Packing. *Curr Biol* (2007) 17(24):2095–104. doi:10.1016/j.cub.2007.11.049
26. Pritchard RH, Shery Huang YY, and Terentjev EM. Mechanics of Biological Networks: from the Cell Cytoskeleton to Connective Tissue. *Soft Matter* (2014) 10(12):1864–84. doi:10.1039/C3SM52769G
27. Bi D, Lopez JH, Schwarz JM, and Manning ML. A Density-independent Rigidity Transition in Biological Tissues. *Nat Phys* (2015) 11(12):1074–9. doi:10.1038/nphys3471
28. Bi D, Yang X, Marchetti MC, and Manning ML. Motility-driven Glass and Jamming Transitions in Biological Tissues. *Phys Rev X* (2016) 6(2). doi:10.1103/PhysRevX.6.021011
29. Petridou NI, Corominas-Murtra B, Heisenberg C-P, and Hannezo E. Rigidity Percolation Uncovers a Structural Basis for Embryonic Tissue Phase Transitions. *Cell* (2021) 184(7):1914–28.e19. doi:10.1016/j.cell.2021.02.017
30. Gardel ML, Shin JH, MacKintosh FC, Mahadevan L, Matsudaira P, and Weitz DA. Elastic Behavior of Cross-Linked and Bundled Actin Networks. *Science* (2004) 304(5675):1301–5. doi:10.1126/science.1095087
31. Alvarado J, Sheinman M, Sharma A, MacKintosh FC, and Koenderink GH. Force Percolation of Contractile Active Gels. *Soft Matter* (2017) 13(34):5624–44. doi:10.1039/c7sm00834a
32. Kim S, Pochitaloff M, Stooke-Vaughan GA, and Campàs O. Embryonic Tissues as Active Foams. *Nat Phys* (2021). doi:10.1038/s41567-021-01215-1
33. MacKintosh FC, Käs J, and Janmey PA. Elasticity of Semiflexible Biopolymer Networks. *Phys Rev Lett* (1995) 75(24):4425–8. doi:10.1103/PhysRevLett.75.4425
34. Gardel ML, Nakamura F, Hartwig JH, Crocker JC, Stossel TP, and Weitz DA. Prestressed F-Actin Networks Cross-Linked by Hinged Filamins Replicate Mechanical Properties of Cells. *Proc Natl Acad Sci* (2006) 103(6):1762–7. doi:10.1073/pnas.0504777103
35. Wen Q, and Janmey PA. Polymer Physics of the Cytoskeleton. *Curr Opin Solid State Mater Sci* (2011) 15(5):177–82. doi:10.1016/j.cossms.2011.05.002
36. Fletcher AG, Osterfield M, Baker RE, and Shvartsman SY. Vertex Models of Epithelial Morphogenesis. *Biophysical J* (2014) 106(11):2291–304. doi:10.1016/j.bpj.2013.11.4498

37. Alt S, Ganguly P, and Salbreux G. Vertex Models: from Cell Mechanics to Tissue Morphogenesis. *Phil Trans R Soc B* (2017) 372:20150520. doi:10.1098/rstb.2015.0520
38. Angelini TE, Hannezo E, Trepat X, Marquez M, Fredberg JJ, and Weitz DA. Glass-like Dynamics of Collective Cell Migration. *Proc Natl Acad Sci* (2011) 108(12):4714–9. doi:10.1073/pnas.1010059108
39. Sadati M, Taheri Qazvini N, Krishnan R, Park CY, and Fredberg JJ. Collective Migration and Cell Jamming. *Differentiation* (2013) 86(3):121–5. doi:10.1016/j.diff.2013.02.005
40. Park J-A, Kim JH, Bi D, Mitchel JA, Qazvini NT, and Tantisira K. Unjamming and Cell Shape in the Asthmatic Airway Epithelium. *Nat Mater* (2015) 14(10):1040–8. doi:10.1038/nmat4357
41. Merkel M, and Manning ML. A Geometrically Controlled Rigidity Transition in a Model for Confluent 3D Tissues. *New J Phys* (2018) 20(2):022002. doi:10.1088/1367-2630/aaaa13
42. Atia L, Bi D, Sharma Y, Mitchel JA, Gweon B, and A. Koehler S. Geometric Constraints during Epithelial Jamming. *Nat Phys* (2018) 14:613–20. doi:10.1038/s41567-018-0089-9
43. Alvarado J, Sheinman M, Sharma A, MacKintosh FC, and Koenderink GH. Molecular Motors Robustly Drive Active Gels to a Critically Connected State. *Nat Phys* (2013) 9(9):591–7. doi:10.1038/nphys2715
44. Sharma A, Licup AJ, Jansen KA, Rens R, Sheinman M, and Koenderink GH. Strain-controlled Criticality Governs the Nonlinear Mechanics of Fibre Networks. *Nat Phys* (2016) 12(6):584–7. doi:10.1038/nphys3628
45. Hunt A, Ewing R, and Ghanbarian B. *Percolation Theory: Topology and Structure*. Cham: Springer (2014). doi:10.1007/978-3-319-03771-4
46. Thorpe MF. Continuous Deformations in Random Networks. *J Non-Crystalline Sol* (1983) 57(3):355–70. doi:10.1016/0022-3093(83)90424-6
47. Jacobs DJ, and Thorpe MF. Generic Rigidity Percolation: The Pebble Game. *Phys Rev Lett* (1995) 75(22):4051–4. doi:10.1103/PhysRevLett.75.4051
48. Jacobs DJ, and Thorpe MF. Generic Rigidity Percolation in Two Dimensions. *Phys Rev E* (1996) 53(4):3682–93. doi:10.1103/PhysRevE.53.3682
49. Alexander S. Amorphous Solids: Their Structure, Lattice Dynamics and Elasticity. *Phys Rep* (1998) 296(2):65–236. doi:10.1016/S0370-1573(97)00069-0
50. Thorpe MF, Jacobs DJ, Chubynsky MV, and Phillips JC. Self-organization in Network Glasses. *J Non-Crystalline Sol* (2000) 266-269:859–66. doi:10.1016/S0022-3093(99)00856-X
51. Chubynsky MV, and Thorpe MF. Algorithms for Three-Dimensional Rigidity Analysis and a First-Order Percolation Transition. *Phys Rev E* (2007) 76(4). doi:10.1103/PhysRevE.76.041135
52. Wyart M, Liang H, Kabla A, and Mahadevan L. Elasticity of Floppy and Stiff Random Networks. *Phys Rev Lett* (2008) 101(21):215501. doi:10.1103/PhysRevLett.101.215501
53. Broedersz CP, Depken M, Yao NY, Pollak MR, Weitz DA, and MacKintosh FC. Cross-link-governed Dynamics of Biopolymer Networks. *Phys Rev Lett* (2010) 105(23):238101. doi:10.1103/PhysRevLett.105.238101
54. Tighe BP. Relaxations and Rheology Near Jamming. *Phys Rev Lett* (2011) 107(15):158303. doi:10.1103/PhysRevLett.107.158303
55. Driscoll MM, Chen BG-g., Beuman TH, Ulrich S, Nagel SR, and Vitelli V. The Role of Rigidity in Controlling Material Failure. *Proc Natl Acad Sci USA* (2016) 113(39):10813–7. doi:10.1073/pnas.1501169113
56. Bouzid M, and Del Gado E. Network Topology in Soft Gels: Hardening and Softening Materials. *Langmuir* (2018) 34(3):773–81. doi:10.1021/acs.langmuir.7b02944
57. Fletcher DA, and Mullins RD. Cell Mechanics and the Cytoskeleton. *Nature* (2010) 463(7280):485–92. doi:10.1038/nature08908
58. Shamipour S, Caballero-Mancebo S, and Heisenberg C-P. Cytoplasm's Got Moves. *Dev Cell* (2021) 56(2):213–26. doi:10.1016/j.devcel.2020.12.002
59. Trickey WR, Vail TP, and Guilak F. The Role of the Cytoskeleton in the Viscoelastic Properties of Human Articular Chondrocytes. *J Orthop Res* (2004) 22(1):131–9. doi:10.1016/s0736-0266(03)00150-510.1016/s0736-0266(03)0150-5
60. Bonakdar N, Gerum R, Kuhn M, Spörrer M, Lippert A, and Schneider W. Mechanical Plasticity of Cells. *Nat Mater* (2016) 15(10):1090–4. doi:10.1038/nmat4689
61. de Gennes PG. Reptation of a Polymer Chain in the Presence of Fixed Obstacles. *J Chem Phys* (1971) 55(2):572–9. doi:10.1063/1.1675789
62. Lin Y-C, Broedersz CP, Rowat AC, Wedig T, Herrmann H, and MacKintosh FC. Divalent Cations Crosslink Vimentin Intermediate Filament Tail Domains to Regulate Network Mechanics. *J Mol Biol* (2010) 399(4):637–44. doi:10.1016/j.jmb.2010.04.054
63. Blanchoin L, Boujemaa-Paterski R, Sykes C, and Plastino J. Actin Dynamics, Architecture, and Mechanics in Cell Motility. *Physiol Rev* (2014) 94(1):235–63. doi:10.1152/physrev.00018.2013
64. Basnet N, Nedozralova H, Crevenna AH, Bodakuntla S, Schlichthaerle T, and Taschner M. Direct Induction of Microtubule Branching by Microtubule Nucleation Factor SSNA1. *Nat Cell Biol* (2018) 20(10):1172–80. doi:10.1038/s41556-018-0199-8
65. Lieleg O, Claessens MMAE, and Bausch AR. Structure and Dynamics of Cross-Linked Actin Networks. *Soft Matter* (2010) 6(2):218–25. doi:10.1039/B912163N
66. Fabry B, Maksym GN, Butler JP, Glogauer M, Navajas D, and Fredberg JJ. Scaling the Microrheology of Living Cells. *Phys Rev Lett* (2001) 87(14):148102. doi:10.1103/PhysRevLett.87.148102
67. Chen DTN, Wen Q, Janmey PA, Crocker JC, and Yodh AG. Rheology of Soft Materials. *Annu Rev Condens Matter Phys* (2010) 1(1):301–22. doi:10.1146/annurev-conmatphys-070909-104120
68. Schopferer M, Bär H, Hochstein B, Sharma S, Mücke N, and Herrmann H. Desmin and Vimentin Intermediate Filament Networks: Their Viscoelastic Properties Investigated by Mechanical Rheometry. *J Mol Biol* (2009) 388(1):133–43. doi:10.1016/j.jmb.2009.03.005
69. Beck R, Deek J, Choi MC, Ikawa T, Watanabe O, and Frey E. Unconventional Salt Trend from Soft to Stiff in Single Neurofilament Biopolymers. *Langmuir* (2010) 26(24):18595–9. doi:10.1021/la103655x
70. Gittes F, Mickey B, Nettleton J, and Howard J. Flexural Rigidity of Microtubules and Actin Filaments Measured from thermal Fluctuations in Shape. *J Cell Biol* (1993) 120(4):923–34. doi:10.1083/jcb.120.4.923
71. Storm C, Pastore JJ, MacKintosh FC, Lubensky TC, and Janmey PA. Nonlinear Elasticity in Biological Gels. *Nature* (2005) 435(7039):191–4. doi:10.1038/nature03521
72. van Oosten ASG, Vahabi M, Licup AJ, Sharma A, Galie PA, and MacKintosh FC. Uncoupling Shear and Uniaxial Elastic Moduli of Semiflexible Biopolymer Networks: Compression-Softening and Stretch-Stiffening. *Sci Rep* (2016) 6(1):19270. doi:10.1038/srep19270
73. Wen Q, and Janmey PA. Effects of Non-linearity on Cell-ECM Interactions. *Exp Cell Res* (2013) 319(16):2481–9. doi:10.1016/j.yexcr.2013.05.017
74. Mizuno D, Tardin C, Schmidt CF, and MacKintosh FC. Nonequilibrium Mechanics of Active Cytoskeletal Networks. *Science* (2007) 315(5810):370–3. doi:10.1126/science.1134404
75. Koenderink GH, Dogic Z, Nakamura F, Bendix PM, MacKintosh FC, and Hartwig JH. An Active Biopolymer Network Controlled by Molecular Motors. *Proc Natl Acad Sci* (2009) 106(36):15192–7. doi:10.1073/pnas.0903974106
76. Xu S, and W. Reinhardt H. Crack Extension Resistance and Fracture Properties of Quasi-Brittle Softening Materials like Concrete Based on the Complete Process of Fracture. *Int J Fracture* (1998) 92(1):71–99. doi:10.1023/A:1007553012684
77. Chaudhuri O, Parekh SH, and Fletcher DA. Reversible Stress Softening of Actin Networks. *Nature* (2007) 445(7125):295–8. doi:10.1038/nature05459
78. Lin Y-C, Koenderink GH, MacKintosh FC, and Weitz DA. Viscoelastic Properties of Microtubule Networks. *Macromolecules* (2007) 40(21):7714–20. doi:10.1021/ma070862l
79. Rozario T, Dzamba B, Weber GF, Davidson LA, and DeSimone DW. The Physical State of Fibronectin Matrix Differentially Regulates Morphogenetic Movements In Vivo. *Dev Biol* (2009) 327(2):386–98. doi:10.1016/j.ydbio.2008.12.025
80. Rozario T, and DeSimone DW. The Extracellular Matrix in Development and Morphogenesis: a Dynamic View. *Dev Biol* (2010) 341(1):126–40. doi:10.1016/j.ydbio.2009.10.026
81. Licup AJ, Münster S, Sharma A, Sheinman M, Jawerth LM, and Fabry B. Stress Controls the Mechanics of Collagen Networks. *Proc Natl Acad Sci USA* (2015) 112(31):9573–8. doi:10.1073/pnas.1504258112
82. Berezney JP, and Saleh OA. Electrostatic Effects on the Conformation and Elasticity of Hyaluronic Acid, a Moderately Flexible Polyelectrolyte. *Macromolecules* (2017) 50(3):1085–9. doi:10.1021/acs.macromol.6b02166
83. Muiznieks LD, and Keeley FW. Molecular Assembly and Mechanical Properties of the Extracellular Matrix: A Fibrous Protein Perspective.

Biochim Biophys Acta (Bba) - Mol Basis Dis (2013) 1832(7):866–75. doi:10.1016/j.bbadis.2012.11.022
84. Han YL, Ronceray P, Xu G, Malandrino A, Kamm RD, and Lenz M. Cell Contraction Induces Long-Ranged Stress Stiffening in the Extracellular Matrix. *Proc Natl Acad Sci USA* (2018) 115(16):4075–80. doi:10.1073/pnas.1722619115
85. Jansen KA, Licup AJ, Sharma A, Rens R, MacKintosh FC, and Koenderink GH. The Role of Network Architecture in Collagen Mechanics. *Biophysical J* (2018) 114(11):2665–78. doi:10.1016/j.bpj.2018.04.043
86. Iyer KV, Piscitello-Gómez R, Paijmans J, Jülicher F, and Eaton S. Epithelial Viscoelasticity Is Regulated by Mechanosensitive E-Cadherin Turnover. *Curr Biol* (2019) 29(4):578–91.e575. doi:10.1016/j.cub.2019.01.021
87. Khalilgharibi N, Fouchard J, Asadipour N, Barrientos R, Duda M, and Bonfanti A. Stress Relaxation in Epithelial Monolayers Is Controlled by the Actomyosin Cortex. *Nat Phys* (2019) 15(8):839–47. doi:10.1038/s41567-019-0516-6
88. Tetley RJ, Staddon MF, Heller D, Hoppe A, Banerjee S, and Mao Y. Tissue Fluidity Promotes Epithelial Wound Healing. *Nat Phys* (2019) 15(11): 1195–203. doi:10.1038/s41567-019-0618-1
89. Cavanaugh KE, Staddon MF, Banerjee S, and Gardel ML. Adaptive Viscoelasticity of Epithelial Cell Junctions: from Models to Methods. *Curr Opin Genet Dev* (2020) 63:86–94. doi:10.1016/j.gde.2020.05.018
90. Stanley HE. *Introduction to Phase Transitions and Critical Phenomena*. New York: Oxford University Press (1971).
91. Domb C, and Green MS. *Phase Transitions and Critical Phenomena*. London: Academic Press (1972).
92. Solé R. *Phase Transitions*. Princeton, NJ: Princeton University Press (2011). doi:10.1515/9781400838929
93. Jain A, Ulman V, Mukherjee A, Prakash M, Cuenca MB, and Pimpale LG. Regionalized Tissue Fluidization Is Required for Epithelial gap Closure during Insect Gastrulation. *Nat Commun* (2020) 11(1):5604. doi:10.1038/s41467-020-19356-x
94. Rubinstein M, Colby RH, Dobrynin AV, and Joanny J-F. Elastic Modulus and Equilibrium Swelling of Polyelectrolyte Gels. *Macromolecules* (1996) 29(1): 398–406. doi:10.1021/ma9511917
95. Gurtovenko AA, and Gotlib YY. Dynamics of Inhomogeneous Cross-Linked Polymers Consisting of Domains of Different Sizes. *J Chem Phys* (2001) 115(14):6785–93. doi:10.1063/1.1401819
96. Müller P. Critical Behaviour of the Rouse Model for Gelling Polymers. *J Phys A: Math Gen* (2003) 36(42):10443–50. doi:10.1088/0305-4470/36/42/002
97. Janmey PA, McCormick ME, Rammensee S, Leight JL, Georges PC, and MacKintosh FC. Negative normal Stress in Semiflexible Biopolymer Gels. *Nat Mater* (2007) 6(1):48–51. doi:10.1038/nmat1810
98. Lieleg O, and Bausch AR. Cross-Linker Unbinding and Self-Similarity in Bundled Cytoskeletal Networks. *Phys Rev Lett* (2007) 99(15):158105. doi:10.1103/PhysRevLett.99.158105
99. Trepat X, Deng L, An SS, Navajas D, Tschumperlin DJ, and Gerthoffer WT. Universal Physical Responses to Stretch in the Living Cell. *Nature* (2007) 447(7144):592–5. doi:10.1038/nature05824
100. Zaccone A, and Scossa-Romano E. Approximate Analytical Description of the Nonaffine Response of Amorphous Solids. *Phys Rev B* (2011) 83(18): 184205. doi:10.1103/PhysRevB.83.184205
101. Laman G. On Graphs and Rigidity of Plane Skeletal Structures. *J Eng Math* (1970) 4(4):331–40. doi:10.1007/BF01534980
102. Kratky O, and Porod G. Röntgenuntersuchung Gelöster Fadenmoleküle. *Recl Trav Chim Pays-bas* (1949) 68(12):1106–22. doi:10.1002/recl.19490681203
103. Pathria RK, and Beale PD. *Statistical Mechanics*. Oxford: Oxford University Press (2002).
104. Tharmann R, Claessens MMAE, and Bausch AR. Viscoelasticity of Isotropically Cross-Linked Actin Networks. *Phys Rev Lett* (2007) 98(8): 088103. doi:10.1103/PhysRevLett.98.088103
105. Wagner B, Tharmann R, Haase I, Fischer M, and Bausch AR. Cytoskeletal Polymer Networks: The Molecular Structure of Cross-Linkers Determines Macroscopic Properties. *Proc Natl Acad Sci* (2006) 103(38):13974–8. doi:10.1073/pnas.0510190103
106. Janmey PA, Peetermans J, Zaner KS, Stossel TP, and Tanaka T. Structure and Mobility of Actin Filaments as Measured by Quasielastic Light Scattering, Viscometry, and Electron Microscopy. *J Biol Chem* (1986) 261(18):8357–62. doi:10.1016/s0021-9258(19)83920-0
107. Hinner B, Tempel M, Sackmann E, Kroy K, and Frey E. Entanglement, Elasticity, and Viscous Relaxation of Actin Solutions. *Phys Rev Lett* (1998) 81(12):2614–7. doi:10.1103/PhysRevLett.81.2614
108. Onck PR, Koeman T, van Dillen T, and van der Giessen E. Alternative Explanation of Stiffening in Cross-Linked Semiflexible Networks. *Phys Rev Lett* (2005) 95(17):178102. doi:10.1103/PhysRevLett.95.178102
109. van Dillen T, Onck PR, and Van der Giessen E. Models for Stiffening in Cross-Linked Biopolymer Networks: A Comparative Study. *J Mech Phys Sol* (2008) 56(6):2240–64. doi:10.1016/j.jmps.2008.01.007
110. Žagar G, Onck PR, and Van der Giessen E. Elasticity of Rigidly Cross-Linked Networks of Athermal Filaments. *Macromolecules* (2011) 44(17):7026–33. doi:10.1021/ma201257v
111. Nagai T, and Honda H. A Dynamic Cell Model for the Formation of Epithelial Tissues. *Philosophical Mag B* (2001) 81(7):699–719. doi:10.1080/13642810108205772
112. Hilgenfeldt S, Erisken S, and Carthew RW. Physical Modeling of Cell Geometric Order in an Epithelial Tissue. *Proc Natl Acad Sci* (2008) 105(3):907–11. doi:10.1073/pnas.0711077105
113. Staple DB, Farhadifar R, Röper J-C, Aigouy B, Eaton S, and Jülicher F. Mechanics and Remodelling of Cell Packings in Epithelia. *Eur Phys J E* (2010) 33(2):117–27. doi:10.1140/epje/i2010-10677-0
114. Chiou KK, Hufnagel L, and Shraiman BI. Mechanical Stress Inference for Two Dimensional Cell Arrays. *PLoS Comput Biol* (2012) 8(5):e1002512. doi:10.1371/journal.pcbi.1002512
115. Wang G, Manning ML, and Amack JD. Regional Cell Shape Changes Control Form and Function of Kupffer's Vesicle in the Zebrafish Embryo. *Dev Biol* (2012) 370(1):52–62. doi:10.1016/j.ydbio.2012.07.019
116. Vroomans RMA, Hogeweg P, and ten Tusscher KHWJ. Segment-Specific Adhesion as a Driver of Convergent Extension. *PLoS Comput Biol* (2015) 11(2):e1004092. doi:10.1371/journal.pcbi.1004092
117. Marin-Riera M, Brun-Usan M, Zimm R, Välikangas T, and Salazar-Ciudad I. Computational Modeling of Development by Epithelia, Mesenchyme and Their Interactions: a Unified Model. *Bioinformatics* (2016) 32(2):219–25. doi:10.1093/bioinformatics/btv527
118. Manning ML, Foty RA, Steinberg MS, and Schoetz E-M. Coaction of Intercellular Adhesion and Cortical Tension Specifies Tissue Surface Tension. *Proc Natl Acad Sci USA* (2010) 107(28):12517–22. doi:10.1073/pnas.1003743107
119. Delile J, Herrmann M, Peyriéras N, and Doursat R. A Cell-Based Computational Model of Early Embryogenesis Coupling Mechanical Behaviour and Gene Regulation. *Nat Commun* (2017) 8(1):13929. doi:10.1038/ncomms13929
120. Sharpe J. Computer Modeling in Developmental Biology: Growing Today, Essential Tomorrow. *Development* (2017) 144(23):4214–25. doi:10.1242/dev.151274
121. Sahu P, Sussman DM, Rübsam M, Mertz AF, Horsley V, and Dufresne ER. Small-scale Demixing in Confluent Biological Tissues. *Soft Matter* (2020) 16(13):3325–37. doi:10.1039/C9SM01084J
122. Wang X, Merkel M, Sutter LB, Erdemci-Tandogan G, Manning ML, and Kasza KE. Anisotropy Links Cell Shapes to Tissue Flow during Convergent Extension. *Proc Natl Acad Sci USA* (2020) 117(24):13541–51. doi:10.1073/pnas.1916418117
123. Lawson-Keister E, and Manning ML. Jamming and Arrest of Cell Motion in Biological Tissues arXiv (2021).
124. Weaire DL, and Hutzler S. *The Physics of Foams*. Oxford: Oxford University Press (1999).
125. Bi D, Lopez JH, Schwarz JM, and Manning ML. Energy Barriers and Cell Migration in Densely Packed Tissues. *Soft Matter* (2014) 10(12):1885–90. doi:10.1039/C3SM52893F
126. Moshe M, Bowick MJ, and Marchetti MC. Geometric Frustration and Solid-Solid Transitions in Model 2D Tissue. *Phys Rev Lett* (2018) 120(26):268105. doi:10.1103/PhysRevLett.120.268105
127. Douezan S, Guevorkian K, Naouar R, Dufour S, Cuvelier D, and Brochard-Wyart F. Spreading Dynamics and Wetting Transition of Cellular Aggregates. *Proc Natl Acad Sci* (2011) 108(18):7315–20. doi:10.1073/pnas.1018057108
128. Bollobas B. *Modern Graph Theory*. US: Springer (1998). doi:10.1007/978-1-4612-0619-4
129. Newman MEJ, Strogatz SH, and Watts DJ. Random Graphs with Arbitrary Degree Distributions and Their Applications. *Phys Rev E* (2001) 64(2): 026118. doi:10.1103/PhysRevE.64.026118

130. Dorogovtsev SN, and Mendes JFF. *Evolution of Networks: From Biological Nets to the Internet and WWW*. Oxford: Oxford University Press (2003). doi:10.1093/acprof:oso/9780198515906.001.0001
131. Newman M. *Networks: An Introduction*. Oxford: Oxford University Press (2010). doi:10.1093/acprof:oso/9780199206650.001.0001
132. Maxwell JC. I.-On Reciprocal Figures, Frames, and Diagrams of Forces. *Trans R Soc Edinb* (1870) 26(1):1–40. doi:10.1017/S0080456800026351
133. Muñoz JJ, and Albo S. Physiology-based Model of Cell Viscoelasticity. *Phys Rev E* (2013) 88(1):012708. doi:10.1103/PhysRevE.88.012708
134. Silverberg JL, Barrett AR, Das M, Petersen PB, Bonassar LJ, and Cohen I. Structure-Function Relations and Rigidity Percolation in the Shear Properties of Articular Cartilage. *Biophysical J* (2014) 107(7):1721–30. doi:10.1016/j.bpj.2014.08.011
135. Poole AR, Pidoux I, and Rosenberg L. Role of Proteoglycans in Endochondral Ossification: Immunofluorescent Localization of Link Protein and Proteoglycan Monomer in Bovine Fetal Epiphyseal Growth Plate. *J Cell Biol* (1982) 92(2):249–60. doi:10.1083/jcb.92.2.249
136. Forgacs G, Newman SA, Hinner B, Maier CW, and Sackmann E. Assembly of Collagen Matrices as a Phase Transition Revealed by Structural and Rheologic Studies. *Biophysical J* (2003) 84(2 Pt 1):1272–80. doi:10.1016/s0006-3495(03)74942-x
137. Yadavalli VK, Svintradze DV, and Pidaparti RM. Nanoscale Measurements of the Assembly of Collagen to Fibrils. *Int J Biol Macromolecules* (2010) 46(4): 458–64. doi:10.1016/j.ijbiomac.2010.02.012
138. Shivers JL, Arzash S, Sharma A, and MacKintosh FC. Scaling Theory for Mechanical Critical Behavior in Fiber Networks. *Phys Rev Lett* (2019) 122(18):188003. doi:10.1103/PhysRevLett.122.188003
139. Iravani A, Thambyah A, and Burrowes KS. A Viscoelastic Two-Dimensional Network Model of the Lung Extracellular Matrix. *Biomech Model Mechanobiol* (2020) 19(6):2241–53. doi:10.1007/s10237-020-01336-1
140. Pinheiro D, and Bellaïche Y. Mechanical Force-Driven Adherens Junction Remodeling and Epithelial Dynamics. *Dev Cell* (2018) 47(1):3–19. doi:10.1016/j.devcel.2018.09.014
141. Kasza KE, Rowat AC, Liu J, Angelini TE, Brangwynne CP, and Koenderink GH. The Cell as a Material. *Curr Opin Cell Biol* (2007) 19(1):101–7. doi:10.1016/j.ceb.2006.12.002
142. Ranft J, Basan M, Elgeti J, Joanny J-F, Prost J, and Jülicher F. Fluidization of Tissues by Cell Division and Apoptosis. *Proc Natl Acad Sci* (2010) 107(49): 20863–8. doi:10.1073/pnas.1011086107
143. Saadaoui M, Rocancourt D, Roussel J, Corson F, and Gros J. A Tensile Ring Drives Tissue Flows to Shape the Gastrulating Amniote Embryo. *Science* (2020) 367(6476):453–8. doi:10.1126/science.aaw1965
144. Zhu M, Tao H, Samani M, Luo M, Wang X, and Hopyan S. Spatial Mapping of Tissue Properties In Vivo Reveals a 3D Stiffness Gradient in the Mouse Limb Bud. *Proc Natl Acad Sci USA* (2020) 117(9):4781–91. doi:10.1073/pnas.1912656117
145. Barber DL, and Trepat X. Editorial Overview: Cell Dynamics: Integrating Cell Dynamics across Scales. *Curr Opin Cell Biol* (2020) 66:130–2. doi:10.1016/j.ceb.2020.06.003
146. van Doorn JM, Lageschaar L, Sprakel J, and van der Gucht J. Criticality and Mechanical Enhancement in Composite Fiber Networks. *Phys Rev E* (2017) 95(4):042503. doi:10.1103/PhysRevE.95.042503
147. Latorre E, Kale S, Casares L, Gómez-González M, Uroz M, and Valon L. Active Superelasticity in Three-Dimensional Epithelia of Controlled Shape. *Nature* (2018) 563(7730):203–8. doi:10.1038/s41586-018-0671-4
148. Brangwynne CP, MacKintosh FC, Kumar S, Geisse NA, Talbot J, and Mahadevan L. Microtubules Can bear Enhanced Compressive Loads in Living Cells Because of Lateral Reinforcement. *J Cell Biol* (2006) 173(5): 733–41. doi:10.1083/jcb.200601060
149. Das M, and MacKintosh FC. Poisson's Ratio in Composite Elastic Media with Rigid Rods. *Phys Rev Lett* (2010) 105(13):138102. doi:10.1103/PhysRevLett.105.138102
150. Huisman EM, Heussinger C, Storm C, and Barkema GT. Semiflexible Filamentous Composites. *Phys Rev Lett* (2010) 105(11):118101. doi:10.1103/PhysRevLett.105.118101
151. Lai VK, Nedrelow DS, Lake SP, Kim B, Weiss EM, and Tranquillo RT. Swelling of Collagen-Hyaluronic Acid Co-gels: An In Vitro Residual Stress Model. *Ann Biomed Eng* (2016) 44(10):2984–93. doi:10.1007/s10439-016-1636-0
152. Burla F, Tauber J, Dussi S, van der Gucht J, and Koenderink GH. Stress Management in Composite Biopolymer Networks. *Nat Phys* (2019) 15(6): 549–53. doi:10.1038/s41567-019-0443-6
153. Oriola D, Marin-Riera M, Aalderink G, Anlas K, Gritti N, and Sharpe J (2020). Arrested Coalescence of Multicellular Aggregates. arXiv.2012.01455.
154. Pajic-Lijakovic I, and Milivojevic M. Viscoelasticity and Cell Jamming State Transition. *bioRxiv* (2021) 436195, 2021. 2021.2003.2019. doi:10.1101/2021.03.19.436195
155. Pajic-Lijakovic I, and Milivojevic M. Multiscale Nature of Cell Rearrangement Caused by Collective Cell Migration. *Eur Biophys J* (2021) 50(1):1–14. doi:10.1007/s00249-021-01496-7
156. Sklar L. *Physics and Chance: Philosophical Issues in the Foundations of Statistical Mechanics*. Cambridge: Cambridge University Press (1993). doi:10.1017/cbo9780511624933
157. Hidalgo J, Grilli J, Suweis S, Muñoz MA, Banavar JR, and Maritan A. Information-based Fitness and the Emergence of Criticality in Living Systems. *Proc Natl Acad Sci* (2014) 111(28):10095–100. doi:10.1073/pnas.1319166111
158. Arias AM, and Hayward P. Filtering Transcriptional Noise during Development: Concepts and Mechanisms. *Nat Rev Genet* (2006) 7(1):34–44. doi:10.1038/nrg1750
159. Mateus AM, Gorfinkiel N, and Arias AM. Origin and Function of Fluctuations in Cell Behaviour and the Emergence of Patterns. *Semin Cell Dev Biol* (2009) 20(7):877–84. doi:10.1016/j.semcdb.2009.07.009
160. Garcia-Ojalvo J, and Martinez Arias A. Towards a Statistical Mechanics of Cell Fate Decisions. *Curr Opin Genet Dev* (2012) 22(6):619–26. doi:10.1016/j.gde.2012.10.004
161. Newman M, Barabasi A-L, and Watts DJ. *The Structure and Dynamics of Networks*. Princeton: Princeton University Press (2006).
162. Muñoz MA. Colloquium: Criticality and Dynamical Scaling in Living Systems. *Rev Mod Phys* (2018) 90(3):031001. doi:10.1103/RevModPhys.90.031001

Conflict of Interest: The authors declare that the research was conducted in the absence of any commercial or financial relationships that could be construed as a potential conflict of interest.

frontiers in Physics

REVIEW
published: 21 June 2021
doi: 10.3389/fphy.2021.666192

Viscoelasticity Imaging of Biological Tissues and Single Cells Using Shear Wave Propagation

Hongliang Li[1,2†], *Guillaume Flé*[1,2†], *Manish Bhatt*[1], *Zhen Qu*[1], *Sajad Ghazavi*[1,2], *Ladan Yazdani*[1,2], *Guillaume Bosio*[1,2], *Iman Rafati*[1,2] *and Guy Cloutier*[1,2,3*]

[1]*Laboratory of Biorheology and Medical Ultrasonics, University of Montreal Hospital Research Center, Montreal, QC, Canada,* [2]*Institute of Biomedical Engineering, University of Montreal, Montreal, QC, Canada,* [3]*Department of Radiology, Radio-Oncology and Nuclear Medicine, University of Montreal, Montreal, QC, Canada*

Changes in biomechanical properties of biological soft tissues are often associated with physiological dysfunctions. Since biological soft tissues are hydrated, viscoelasticity is likely suitable to represent its solid-like behavior using elasticity and fluid-like behavior using viscosity. Shear wave elastography is a non-invasive imaging technology invented for clinical applications that has shown promise to characterize various tissue viscoelasticity. It is based on measuring and analyzing velocities and attenuations of propagated shear waves. In this review, principles and technical developments of shear wave elastography for viscoelasticity characterization from organ to cellular levels are presented, and different imaging modalities used to track shear wave propagation are described. At a macroscopic scale, techniques for inducing shear waves using an external mechanical vibration, an acoustic radiation pressure or a Lorentz force are reviewed along with imaging approaches proposed to track shear wave propagation, namely ultrasound, magnetic resonance, optical, and photoacoustic means. Then, approaches for theoretical modeling and tracking of shear waves are detailed. Following it, some examples of applications to characterize the viscoelasticity of various organs are given. At a microscopic scale, a novel cellular shear wave elastography method using an external vibration and optical microscopy is illustrated. Finally, current limitations and future directions in shear wave elastography are presented.

Keywords: viscoelasticity (linear), elastography, mechanical shear waves, ultrasound imaging, magnetic resonance imaging, optical imaging, optical coherence tomography, photoacoustic imaging

OPEN ACCESS

Edited by:
Ivana Dusan Pajic-Lijakovic, University of Belgrade, Serbia

Reviewed by:
Ivan Pelivanov, University of Washington, United States
Simon Chatelin, de l'Informatique et de l'Imagerie (ICube), France

****Correspondence:***
Guy Cloutier
guy.cloutier@umontreal.ca

†These authors share first authorship

Specialty section:
This article was submitted to Biophysics, a section of the journal Frontiers in Physics

Received: *09 February 2021*
Accepted: *04 June 2021*
Published: *21 June 2021*

Citation:
Li H, Flé G, Bhatt M, Qu Z, Ghazavi S, Yazdani L, Bosio G, Rafati I and Cloutier G (2021) Viscoelasticity Imaging of Biological Tissues and Single Cells Using Shear Wave Propagation. Front. Phys. 9:666192. doi: 10.3389/fphy.2021.666192

INTRODUCTION

Changes in mechanical properties of biological soft tissues are often associated with physiological dysfunctions. Viscoelasticity is an important mechanical biomarker to characterize structural changes and/or constituents of tissues. However, the assessment of elasticity through imaging has been more often exploited than viscosity, and an historical perspective of development has been to replace manual palpation by physicians and to answer an ultimate and natural question: 'is the region hard or soft?' The elasticity, represented by the Young's modulus E, is able to characterize tissue deformation by using a linear relationship between stress σ and strain ε as $E = \sigma/\varepsilon$. The rationale behind the elasticity

assessment of biological soft tissues is that Young's moduli of different types of human tissues differ by a few orders of magnitude [1], and are affected by the presence of a pathology.

Since biological soft tissues are hydrated, they are not only represented by their solid-like behavior using elasticity, but also by their fluid-like behavior using viscosity. Viscosity represents the hysteretic effect between stress and strain applied on a tissue. It is becoming an important biomarker of pathological changes in biological tissues. Mechanical test is the most basic method to measure the viscosity of *ex vivo* soft tissues. To this end, a constant strain is applied to a test specimen. The stress relaxation with time is used to characterize the viscosity of the tissue. Another way of mechanical test is dynamic mechanical analysis. Periodic strain or stress is imposed on a specimen. The dynamic responses in terms of different incentive frequencies are associated with tissue viscoelasticity. Relevant works on mechanical testing of biological soft tissues can be found in [2–9]. Alternatively, imaging-based approaches are becoming more popular for *in vivo* viscoelasticity assessment. These approaches exploit tissue deformations in acoustic, magnetic or optical fields to characterize viscoelasticity in a non-invasively manner. Soft tissues can maintain their function during the measurement avoiding destructive testing [10]. Based on a clinical perspective, the *in situ* and localized assessment of tissue viscoelasticity through imaging had major impacts on diagnosis (e.g., cancers, liver fibrosis, musculoskeletal disorders, cardiovascular diseases, etc. . .). Since biological tissues consist of cells, extracellular matrices, and structural proteins, a recent field of development has been to study sub-cellular biomechanical properties associated with pathological processes through imaging. This finding encouraged researchers to impel bio-elasticity research further into a microscopic scale.

This review aims to provide a state-of-the-art summary of developments made in the field of shear wave elastography, which concerns elasticity and viscosity imaging through mechanical shear wave analysis. This technology requires a shear wave source, the tracking of shear wave propagation through imaging, and the processing of the shear wave propagation characteristics through physical models or image processing algorithms. Shear waves can be generated by external or internal vibrating sources. An external mechanical actuator in physical contact with an organ or cell is a common way to induce shear wave propagation from the surface to the core, whereas acoustic radiation or Lorentz forces can be used as internal *in situ* localized shear wave sources. The detection of the shear wave propagation is usually performed using ultrasound (US), magnetic resonance (MR), optical or photoacoustic imaging methods. Elasticity and viscosity can be obtained from estimations of shear storage and loss moduli, which require the determination of the shear wave velocity and attenuation into the interrogated medium. In the following sections, the generation and tracking of shear waves are described. Determining elasticity and viscosity maps through the solution of an inverse problem based on elastic wave propagation equations and underlying assumptions are also addressed throughout the text. Note that this review is not intended to detail artifacts and confounders of shear wave imaging because these are organ, tissue structure, and tissue pathology specific. Nevertheless, such information is presented briefly in some sections.

BIOMECHANICAL PRINCIPLES OF SHEAR WAVE ELASTOGRAPHY

General Concepts in Shear Wave Elastography

The major approach since the early steps of elastography imaging has been to approximate the tissue as isotropic and purely elastic. This situation has been widely described so the main constitutive relations essential to shear wave elastography (SWE) understanding are recalled here. The relationship between the applied stress and the strain response of the solicited tissue is given by Hook's law:

$$T_{ij}(\boldsymbol{r},t) = c_{ijkl}(\boldsymbol{r},t)S_{kl}(\boldsymbol{r},t) \tag{1}$$

where T and S are the stress and strain tensors, respectively, and c_{ijkl} contain the elastic parameters of interest. Under the assumption of small deformations, the strain tensor is given by:

$$S_{kl}(\boldsymbol{r},t) = \frac{1}{2}\left(\nabla \boldsymbol{u} + (\nabla \boldsymbol{u})^T\right) \tag{2}$$

where $\boldsymbol{u}$ is the 3-dimensional motion field in unit of (m) induced by stressing the tissue. The time domain wave equation describing the propagation of local displacements is obtained using Newton's second law:

$$\rho \frac{\partial^2 \boldsymbol{u}(\boldsymbol{r},t)}{\partial t^2} = \nabla \cdot \boldsymbol{T}(\boldsymbol{r},t) + \boldsymbol{f}(\boldsymbol{r},t) \tag{3}$$

where ρ is the material's density in [kg/m^3] and $\boldsymbol{f}$ [Nm^{-3}] is the source term. After Fourier transform into the frequency domain, **Eqs 1–3** are expressed as:

$$\tilde{T}_{ij}(\boldsymbol{r},\omega) = c^*_{ijkl}(\boldsymbol{r},\omega)\tilde{S}_{kl}(\boldsymbol{r},\omega) \tag{4}$$

$$\tilde{S}_{kl}(\boldsymbol{r},\omega) = \frac{1}{2}\left(\nabla \tilde{\boldsymbol{u}} + (\nabla \tilde{\boldsymbol{u}})^T\right) \tag{5}$$

$$-\rho\omega^2 \tilde{\boldsymbol{u}}(\boldsymbol{r},\omega) = \nabla \cdot \tilde{\boldsymbol{T}}(\boldsymbol{r},\omega) + \tilde{\boldsymbol{f}}(\boldsymbol{r},\omega) \tag{6}$$

where $\omega = 2\pi f$ with f the frequency, and the tilde (~) and star (*) notations refer to complex numbers. Full development of **Eq. 3** (available in Ref. [11]) leads to the governing equation of motion propagation in elastic solids known as the Navier's equation:

$$\rho \frac{\partial^2 \boldsymbol{u}}{\partial t^2} = \mu \nabla^2 \boldsymbol{u} + (\lambda + \mu)\nabla(\nabla \cdot \boldsymbol{u}) \tag{7}$$

where μ is the shear modulus in (Pa) reflecting the amount of energy the tissue can store as elastic deformation, and λ is the first Lamé coefficient in (Pa) reflecting the tissue's compressibility. The Navier's equation does not rely on rheological models and conveys an approximation of the material's natural properties based on physical assumptions. The same development applied to **Eq. 6** leads to:

$$-\rho\omega^2 \tilde{\boldsymbol{u}} = G^* \nabla^2 \tilde{\boldsymbol{u}} + (\lambda^* + G^*)\nabla(\nabla \cdot \tilde{\boldsymbol{u}}) \tag{8}$$

where $G^* = G' + jG''$ is the general notation of the complex shear modulus in the frequency domain of Navier's equation, G' is the shear storage modulus that reflects the amount of mechanical energy stored as shear deformation in the solid, and G'' is the shear loss modulus reflecting the amount of mechanical energy dissipated due to shear viscosity. Similarly, $\lambda^* = \lambda' + \lambda''$ is the complex Lamé coefficient, where λ' and λ'' are the compression storage and loss moduli, respectively, reflecting the amount of energy stored and lost in the solid due to compression deformation and compressional viscosity. In purely elastic solids, the wave field does not dissipate and shows an instantaneous response to load. In such cases, the loss moduli equal zero, and $G^* = G' = \mu$ and $\lambda^* = \lambda$. The Young's modulus E, characterizing the solid's resistance to deformation under loading, and the Poisson's ratio ν characterizing the tissue's compressibility, are defined by:

$$E = \frac{\mu(3\lambda + 2\mu)}{\lambda + \mu}, \tag{9}$$

and

$$\nu = \frac{\lambda}{2(\lambda + \mu)} \tag{10}$$

The motion field $\boldsymbol{u}$ propagates as compression and shear waves of which velocities v_c and v_s are, respectively, given by (see Ref. [11] for details):

$$v_c = \sqrt{\frac{\lambda + 2\mu}{\rho}} \tag{11}$$

and

$$v_s = \sqrt{\frac{\mu}{\rho}} \tag{12}$$

The large difference between the two velocities observed in biological tissues (typically v_c is around 1,540 ms^{-1} and v_s is found around 1–10 ms^{-1}) suggests that λ is much greater than μ, thus allowing for the following approximation often used to report SWE measurements:

$$E \approx 3\mu \tag{13}$$

This observation is directly linked to the tissue incompressibility assumption, which causes λ to approach infinity [12]. Additionally, λ was shown to vary slightly as opposed to μ, which spans a few orders of magnitude in biological tissues [13]. Consequently, the shear modulus or the Young's modulus is the mechanical parameter considered in elastography reconstruction processes.

Another approach much less often used to reconstruct material mechanical properties in SWE is to model the solid as isotropic and viscoelastic instead of purely elastic. Here, the response of the loaded tissue shows a delay with respect to actuation and elastic waves attenuate due to energy dissipation in the solid, which is specific to viscous materials. Attenuation may be accounted for in the time-domain Navier's equation by introducing a damping term, and linking it to viscosity using rheological models such as the generalized Maxwell, standard linear solid, or Kelvin-Voigt, which are further discussed in the next section. The following **Table 1** presents the stress-strain relationships used to derive wave equations from Newton's second law for the three aforementioned rheological models [14].

A different option to integrate viscoelastic properties into the description of the material is to formulate the problem in the frequency domain, provided a harmonic actuation. In this case, the complex shear modulus, as described in **Eq. 8**, has a non-zero imaginary part accounting for shear wave dissipation due to the material's shear viscosity. Relating G'' values to actual viscosity values depends on rheological modeling, as discussed in the next section. For instance, in the case of a solid described by the Kelvin-Voigt model, the complex shear modulus is given by $G(\boldsymbol{r})^* = G(\boldsymbol{r})' + jG(\boldsymbol{r})' = \mu(\boldsymbol{r}) + j\eta(\boldsymbol{r})\omega$, where $\eta(\boldsymbol{r})$ is the local shear viscosity.

For G' and G'' estimation, the displacement field $\tilde{\boldsymbol{u}}$ may be used as the solution to the Navier's equation in direct or iterative inversion, or the shear wave velocity at frequency $\frac{\omega}{2\pi}$ may be measured. Here, the complex wave number is noted as $k = k' + jk'' = \frac{\omega}{\sqrt{G^*/\rho}}$, in analogy with the complex shear modulus notation, and the dispersion relation is given by $k' = \frac{\omega}{v_p}$, where v_p is the phase velocity of the shear wave at the frequency $\frac{\omega}{2\pi}$. Considering a plane wave decomposition of the wave field, the ith component has the form $U_i(r_i, t) = Ae^{-j(k_i r_i - \omega t)} = Ae^{-j(k_i' r_i - \omega t) - k_i'' r_i}$. The imaginary number k'' is often noted α and is the shear wave attenuation coefficient (m^{-1}). Thus, a linear system of two equations may be raised and independent experimental evaluations of v_p and α from the displacement field allows assessing G' and G''. Also, the Young's modulus becomes complex-valued in viscoelastic models. However, most viscoelasticity reconstruction processes stick to the evaluation of G' and G''. Finally, it is to be noted that the equivalence between longitudinal and compression waves on one hand, and transverse and shear waves on the other hand, is true for plane waves only.

To date, isotropic elastic and viscoelastic characterization of soft matters have mostly been considered in shear wave elastography, owing to the availability of various inversion schemes. However, the anisotropic and poroelastic nature of certain biological tissues, such as the brain, has long been acknowledged. In poroelasticity, the medium is modeled as a porous solid matrix crossed by flowing fluid, and thus contains two separate phases, as opposed to more common models containing one phase. Consequently, the motion field measured in imaging protocols is not only due to the solid tissue deformation but also to the pressure gradient in fluid pores. Although poroelasticity was early studied using quasi-static deformations [15], implementation in shear wave elastography imaging remains in its infancy. Oscillatory deformations in poroelasticity have first been described by Biot [16, 17], and later by [18]. Assuming a viscous fluid flow, fluid saturation in pores, and a compressible linearly elastic solid, poroelasticity equations of propagation are given by:

TABLE 1 | Stress-strain relationships for three common rheological models accounting for the viscoelastic behavior of soft tissues. Details about these models are reported in the next section. *T, S, c* and η are the stress, strain, elasticity and viscosity tensors respectively, E, E_1, and E_2 are Young's moduli specific to the Maxwell and standard linear solid models.

Model	Stress-strain relationship
Kelvin-Voigt	$T = cS + \eta\frac{dS}{dt}$
Maxwell	$\eta\frac{dT}{dt} + E\,T = E\eta\frac{dS}{dt}$
Standard linear solid	$(E_1 + E_2)T + \eta\frac{dS}{dt} = E_1E_2S + E_1\eta\frac{dS}{dt}$

$$\nabla \cdot \mu\nabla u + \nabla\left(\lambda + \mu\right)\left(\nabla \cdot u\right) - \left(1 - \beta\right)\nabla p = -\omega^2\left(\rho - \beta\rho_f\right)u, \quad (14)$$

$$\frac{\omega^2\rho_f\left(1 - \beta\right)}{\beta}\left(\nabla \cdot u\right) + \nabla^2 p = 0, \quad (15)$$

$$\beta = \frac{\omega\phi_p^2\rho_f\kappa}{i\phi_p^2 + \omega\kappa\left(\rho_a + \phi_p\rho_f\right)}, \quad (16)$$

where μ is the shear modulus, λ the first Lamé's parameter, u the complex time harmonic displacement field, β the effective stress coefficient (dimensionless), p the complex time harmonic pressure field, ω the actuation frequency, ρ the bulk density, ρ_f the pore fluid density, ϕ_p the material porosity, κ the hydraulic conductivity, and ρ_a the apparent mass density.

Finally, anisotropy has been considered for biomechanical modeling in the context of shear wave elastography. In such cases, the material's mechanical response (strain) is dependent on the direction in which it is solicited (stress). Full derivation of relevant mechanical parameters under different symmetry assumptions is beyond the scope of this review, and the interested reader is referred to the excellent pedagogical development in [19]. Briefly, Hooke's law describes the relationship between applied stress and material strain:

$$\sigma_{ij} = \sum_{k,l=1}^{3} C_{ijkl}\epsilon_{ij} \quad (17)$$

where σ and ϵ are the stress and strain tensors, respectively. In isotropic materials, the tensor C_{ijkl} is fully described by two parameters, E and ν. In anisotropic materials, more constants are needed to account for the direction dependance of ϵ. The most used anisotropic model is transverse isotropy, which is particularly used to characterize fibrous tissues (*e.g.*, muscles). Transversely isotropic materials are organized in layers where in-plane mechanical properties are isotropic, and out-of-plane ones are anisotropic. In such cases, 5 parameters are necessary to describe C_{ijkl}. Two of them, μ_{13} and μ_{12}, characterize the shear motion along and perpendicular to the fiber axis, respectively. The other three, E_1, E_2, and E_3 characterize the compression motion along, perpendicular in-plane, and perpendicular out-of-plane to the fiber axis, respectively. Injection of the Hooke's law into Newton's second equation allows to derive equations of shear wave propagation along directions of dependency the same way as to derive the Navier's equation of elasticity. Other anisotropic models exist, such as the orthotropic one which shows a lower level of symmetry (three perpendicular planes) than the transverse isotropy model. The orthotropic model has been used to develop waveguide elastography, which describes the propagation of the different polarizations of shear waves along separate directions. The orthotropic tensor along with equations of polarized wave propagation are described in detail in [20].

Characterization of Tissue Viscoelasticity

Most soft bio-tissues contain more than 70-w% of water, thus they can be considered as fluid-like solids, which means these materials have characteristics of both solids and fluids [1]. Elasticity refers to the solid property that describes the ability of a material to return to its original shape after a stress is removed [21]. The fluid property is given by the viscosity (η) that describes the ability of a material to resist to its deformation due to a tensile stress or shear stress [21]. Three categories of properties are often used to characterize the viscoelasticity of a soft material: its compressibility, which is usually measured by the bulk modulus (K) and the Poisson's ratio (ν); its tension, which mainly refers to the Young's modulus (E); and shear properties, described by the second Lamé coefficient (μ) and the complex shear modulus (G^*).

The complex shear modulus (see **Eq. 8** and accompanied description) is self-sufficient to describe the viscoelasticity of biological tissues. In general, the storage modulus G' reflects the shear elastic property while the loss modulus G'' reflects the viscous response of the material. Alternatively, rheological models were considered to relate experimental measurements to elastic and viscous properties of tissues. Mathematically, the Kelvin-Voigt and Maxwell models have been considered most frequently to describe viscoelastic tissues [22–24], i.e., quantifying the shear elasticity and viscosity. The two models are represented by a purely elastic spring connected to a purely viscous dashpot in parallel (Kelvin-Voigt) or in series (Maxwell), respectively. A material with only elasticity is called a purely elastic material (only a spring), while a material with only viscosity (only a dashpot) is called a Newtonian fluid [25]. A soft tissue or soft tissue-like material falls between these two extreme conditions and can be called as a viscoelastic material [26]. Other material models are used less frequently, while most of them are constructed with different combinations of single/multiple spring(s) and dashpot(s) in more complicated arrangements, such as the Zener model, generalized Maxwell model, and generalized Kelvin-Voigt model [27–29].

Note that in the field of SWE, the complex shear modulus G^* may be sometimes confused with the storage modulus G' and the second Lamé coefficient μ (also known as the shear modulus). Although the storage modulus reflects the tissue elasticity, they are not rigorously the same. For sake of clarity, in this review, the elasticity is denoted by $|\mu|$, *i.e.* the real component of the second Lamé coefficient. Therefore, for incompressible soft tissues (*i.e.*, for a Poisson ratio close to 0.5) with a negligible viscous component, it can be assumed that such a tissue is a purely elastic material so that G^* solely represents the real shear elasticity and so $G^* = G' = |\mu|$ [30, 31]. Otherwise, the calculation of elasticity (as well as the viscosity) is rheological model dependent.

Mathematical relations between tissue excitation and response [32] may be divided into two groups according to the temporal difference of the excitation [30, 33]: namely quasi-static measurements and dynamic measurements [also termed shear wave (SW) measurements]. The quasi-static measurement methods mainly analyze the stress-strain behavior. On the other hand, SW measurement methods determine

the complex shear modulus by tracing and analyzing a propagated SW in the specimen.

During the past years, studies in the field of SWE measurements were often targeting absolute values of elasticity $|\mu|$ and viscosity η. To do so, rheological models of the material are needed to derive those parameters. For instance, when the Kelvin-Voigt model or Maxwell model is considered, the complex shear modulus can be written as follows [28, 34, 35]:

$$G_{KV} = |\mu| + j\omega_S\eta, \tag{18a}$$

$$G_M = \frac{j\omega_S\eta|\mu|}{|\mu| + j\omega_S\eta}, \tag{18b}$$

where G_{KV} represents G^* of the Kelvin-Voigt model, and G_M is that for the Maxwell model, both satisfy $G^* = G' + jG''$. In **Eq. 18**, ω_S is the angular frequency of the SW. Alternatively, by solving the wave equation in **Eq. 8**, a general solution of G' and G'' without considering a rheological model can be obtained, as in [28]:

$$G' = \rho\omega_S^2 v_S^2 \cdot \frac{\omega_S^2 - \alpha_S^2 v_S^2}{\left(\omega_S^2 + \alpha_S^2 v_S^2\right)^2}, \tag{19}$$

$$G'' = 2\rho\omega_S^2 v_S^2 \cdot \frac{\omega_S \cdot \alpha_S \cdot v_S}{\left(\omega_S^2 + \alpha_S^2 v_S^2\right)^2}. \tag{20}$$

Here, as synergized with **Eq. 18**, one can see that both $|\mu|$ and η are functions of v_S, α_S, and ω_S. Since v_S and α_S can be experimentally measured at certain ω_S, $|\mu|$ and η, in a specified rheological model, can be thereafter calculated.

In common practice, when the viscosity η is taken into account for tissue characterization, it can be determined either directly using both v_S and α_S with knowing the corresponding ω_S, or alternatively by evaluating the dispersion of v_S with respect to ω_S without determining the value of α_S, *i.e.*, by knowing multiple pairs of v_S and ω_S [27, 36, 37]. However, one should also notice that the viscoelastic property of biological tissues are rather complex, depend on the tissue type, and on the presence of a pathological condition, so that there is not simply a best, or a most appropriate material model for all tissues. Furthermore, pathological changes with time of a tissue could also lead to a major change of its viscoelastic property, thus a certain material model may no longer be suitable for the tissue when it becomes abnormal and progresses toward a more severe pathological state. Meanwhile, the derivation of elasticity $|\mu|$, and viscosity η, are rather different among different material models. That means, using different models with same measures (such as v_S and α_S) would lead to different results [28], and hence would be meaningless to clinical studies. Therefore, nowadays it is always suggested that no rheological model is assumed, and instead of that, directly access the shear storage G' and loss G'' moduli would be not only more rigorous and appropriate, but also mathematically convenient to describe tissue viscoelastic properties [28, 37].

ULTRASOUND SHEAR WAVE ELASTOGRAPHY

Generation and Detection of Shear Waves

A shear wave, also called a transverse wave, is a moving mechanical wave that consists of particle oscillations occurring perpendicular to the direction of the energy transfer [38]. As briefly introduced, SWs in ultrasound imaging can be generated either from an external vibration source (such as a mechanical vibrator/shaker) [39–42], or internally by an acoustic radiation force (ARF) [13, 44–51], as illustrated in **Figure 1**. The control of the SW amplitude and frequency of the ARF is considered in [13]. In terms of waveforms, the SW can also be generated as continuous waves [39, 40, 42, 44–46] or impulse waves [41, 47–51], as can be seen in the examples of **Figure 2**. In ultrasound imaging, the probe fires longitudinal pressures and detects particle displacements along the axial direction, therefore only SWs that propagate along the lateral direction of the ultrasound beam, or SW components whose displacements occurred on the axial direction, can be detected.

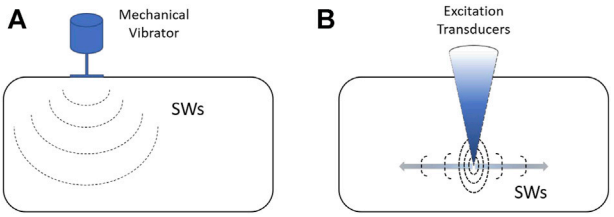

FIGURE 1 | Shear wave generation sources: **(A)** an external vibration source, and **(B)** am internal acoustic radiation force.

Many remarkable techniques were invented over the past 30 years based upon different combinations of external or internal SW sources, and continuous or impulse SWs. In 1988, Lerner et al. proposed a method to map the propagation of low frequency SWs with a Doppler ultrasound displacement detection technique to assess tissue stiffness [39]. Later in 1990, Yamakoshi et al. proposed a dynamic measurement method to determine the SW speed v_S using an external mechanical vibration source [40], as seen in **Figure 2A**. The parameter v_S was determined by analyzing the wavelength of a continuously propagated SW using the Doppler ultrasound technique. Catheline et al. developed in 1999 an impulse SW measurement method [41]. In this method, an ultrasonic probe was located at one side of the specimen to capture the propagation of the impulse SW generated by a mechanical vibrator located at the other side of the specimen. A plane wave ultrasound system was used, enabling a high frame rate in detection mode, then the parameter v_S was determined through the time-of-flight (TOF) technique applied on successive images. See below for more information on the TOF method. Since such a method used an impulse SW, it is also called transient SW imaging, or transient elastography (TE). Nowadays, the largely used clinical device Fibroscan [52, 53] is based on TE. In 2004, a method using two external SW sources to generate continuous SWs toward each other with slightly different SW frequencies was proposed [42]. Due to the frequency difference, interfered SW patterns termed as "crawling waves" moved with a much slower speed than the expected v_S, This allowed the observation of propagated crawling waves with a conventional low frame rate B-mode imaging system. Once the speed of the crawling wave is obtained, v_S could be derived.

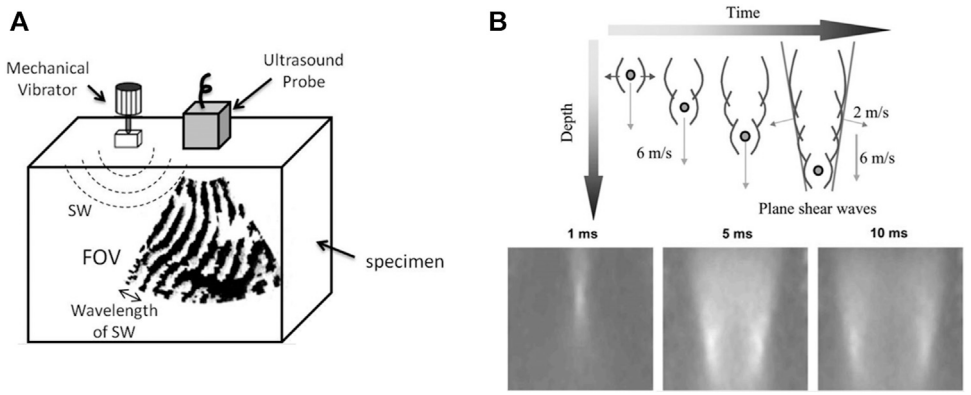

FIGURE 2 | Examples of the generation of **(A)** continuous shear waves, adapted from [40] copyright 1990 IEEE, and **(B)** impulse shear waves, reproduced with permission from [47] copyright 2004 IEEE.

In 1998, Sarvazyan et al. developed a SW measurement method, termed shear wave elasticity imaging (SWEI), by using a SW remotely generated by an ARF of a focused ultrasound beam [13]. In this method, a transient SW pulse was firstly produced at the focus of the ultrasound beam and propagated along sideways. Then, imaging transducers were used to trace the moving of SW fronts and viscoelastic parameters were derived thereafter. The same year, Fatemi and Greenleaf developed a method to produce an oscillatory ARF by mixing two ultrasound beams with different frequencies [44]. A short period of harmonic (continuous) or tone-burst SWs was generated and propagated along sideways, which made the SW narrow-band (while the SW generated by Sarvazyan's method was broadband) and then v_S could be determined by finding the phase difference of the SW at two apart locations [45]. By repeating the measurement with continuous SWs at different frequencies, or retrieving different frequency components of a tone-burst SW, both G' and η could be derived. This method is termed as SW dispersion ultrasound vibrometry (SDUV). Later in 2004, based on the combination of Catheline's impulse SW method [41] and the ARF technique [13], Bercoff et al. developed an advanced SW measurement method known as supersonic shear imaging (SSI) [47]. With this method, an ultra-high-speed scanner is used, then multiple ARF impulses are triggered consecutively and very quickly at different depths. Each impulse produces a SW point-like source then all these SWs are interfering constructively and result in two SW planes propagating in opposite directions, as can be seen in **Figure 2B**. A two-dimensional v_S image is obtained with this method. Moreover, since this technique is creating broadband SWs, tissue viscosity can also be estimated through the v_S dispersion method (using the same principle as SDUV). In 2012, Song et al. developed a SW method, which also used multiple lateral ARFs as in [48]; the method was termed as comb-push ultrasound shear elastography (CUSE) [49]. It firstly generates multiple ARF excitations at different spatial locations to produce multiple impulse SWs by using the push mode of the ultrasound probe, and then quickly switches to the scanning mode of the probe to detect the SW propagation. Therefore, v_S could be measured through the TOF technique by tracing the movement of the SW front from each SW source. The use of the comb-push excitation provided multiple SW sources in the specimen so that such method is effectively compensating for the worse signal-to-noise ratio (SNR) due to the SW attenuation at the location far away from a given SW source.

Knowing that $v_S = \lambda_S \times f_S$, one may like to measure v_S through the TOF technique, or instead to determine λ_S in the spatial domain. For most biological tissues, v_S travels at a few m/s, which means it only takes a couple of ms for a SW to travel through the entire field of view (FOV) of a common ultrasound probe. Physically, a focused ultrasound system triggers transducer elements sequentially from one edge to another to complete a B-mode scan, as a result the frame rate is typically less than 100 frames/sec in such a system, which is not fast enough to measure the TOF without a particular modification of the experimental setup [42]. Therefore, measuring λ_S becomes the realistic option. In this scenario, the spatial resolution is determined and limited by λ_S. Although increasing f_S is reducing λ_S, and so is improved the resolution, one should also notice that a higher frequency would cause a quick attenuation of the SW propagation. Thus, empirically f_S is usually adjusted to a few hundreds of Hz, which leads the lateral resolution of elastography images to a sub-centimeter level with using standard focused ultrasound beamforming. On the other hand, a plane wave system can trigger all transducer elements of the probe at the same time to emit a plane compression wave, enabling it to have a very high frame rate in B-mode (up to 10,000 frames/sec) [47]. Thus, in this scenario, the TOF technique is applicable, and theoretically the distance that a SW travels within two consecutive frames could be as short as a few-tenth of mm. Since the distance is comparable to the physical interval of two adjacent transducer elements in a common ultrasound array probe, the lateral spatial resolution of SWE with using a plane wave system is approximately the same as that of B-mode imaging [54]. It is also worth noting that, when tissue boundaries/layers exist under the FOV, and a propagating SW passes through those interfaces, physical phenomena such as reflection, refraction, diffraction, and mode conversion could

occur at the interfaces and cause artifacts. Although directional filters are usually applied to mitigate those effects [55, 56], practically it is still difficult to remove all the unwanted waves. Therefore, the v_S measured within approximately one λ_S from the interfaces are usually considered unreliable, which to some extent would downgrade the spatial resolution at those areas [57].

Viscoelasticity Reconstruction

As introduced earlier, ultrasound SWE contributed to the non-invasive assessment of mechanical properties of soft tissues [58–62]. One method largely used clinically is transient elastography (TE) [63–67], which utilizes a dynamic compression generated by the vibration of the transducer on the skin to produce shear waves. No structural imaging is provided with this method to guide the measure. Moreover, in some patients with morbid obesity and ascites, the attenuation of shear waves travelling from the surface of the body to the organ of interest (typically the liver) may avoid reliable measurements [68, 69]. The acoustic radiation force impulse (ARFI) [60, 70] and supersonic shear imaging (SSI) [47, 71, 72] methods use a radiation pressure to locally induce shear waves within the organ of interest. TE, ARFI and SSI are assessing tissue elasticity (no viscosity) based on the measurement of the shear wave speed [73]. The Young's modulus is estimated and displayed as an image using $E = 3|\mu| = \rho v_s^2$. Alternatively, different approaches have been developed to retrieve and display the viscous component of a tissue [50, 51, 74, 75]. Such approaches have not yet been validated on large clinical cohorts, nor implemented on clinical scanners. Details on technologies proposed to determine tissue viscoelasticity are given next.

Most studies utilized a rheological model, which has been introduced earlier, e.g., the Kelvin-Voigt model, to find the viscosity after the reconstruction of elasticity [45, 76–78]. The complex shear modulus $G^* = G' + jG''$ was also estimated using different approaches, such as measuring the acoustic radiation force-induced creep [74], solving the Navier's wave equation numerically [79], inverting analytically the solution of the shear wave scattering from a mechanical inclusion [80–82], and using a finite-element based method [83]. Note that a torsional SW source was used in the latter method, as originally proposed in [84].

Kazemirad et al. [50] developed a method for the quantitative measurement of viscoelastic parameters G' and G'' at various frequencies, based on the assumption of a cylindrical shear wave front produced by a radiation pressure, allowing to avoid wave diffraction effects. Other studies have also used the same geometrical assumption for quantitative viscoelastic measurements [75, 85, 86]. Notice that the cylindrical wave front assumption would not necessarily hold when considering inhomogeneous media, such as a tissue embedding a tumor. A recent method for estimating tissue viscosity without geometrical assumption on the wave front was proposed by [51], which utilized the shear wave velocity v_S and attenuation α_S computed by the frequency shift method [87]. Recently, [88] performed a study to characterize viscoelastic properties of oil-in-gel viscoelastic phantoms and *in vivo* human livers. They found that the shear wave dispersion and attenuation were linked together and related to the tissue viscosity. As reviewed above, the shear wave speed and attenuation are widely used for reconstructing viscoelastic properties. Experimental methods to obtain those shear wave properties are separately described below.

Shear Wave Speed

One of the widely used methods implemented on clinical scanners is the group velocity [89–92] that assumes the tissue as elastic, homogeneous, isotropic, linear, and of infinite dimension with respect to the wavelength. The group velocity is estimated using time-of-flight (TOF)-based algorithms for particle displacement or particle velocity assessments in the time domain [72, 93]. TOF–based algorithms are usually based on cross-correlation (CC) [94] and time-to-peak (TTP) methods [90]. Basically, the CC provides a moving average estimate of the shear wave speed using all sample points, and performs multiple cross-correlations along the direction of the wave propagation, which may result in artifacts for periodic shear wave patterns, whereas TTP estimates the velocity based on the tracking of the movement of one point on the waveform [90]. Although group velocity estimation methods are considered robust [91], they are theoretically applicable to strictly elastic materials thus requiring resorting to other techniques for the evaluation of the viscous behavior [95].

The variation of the shear wave velocity with frequency refers to the wave dispersion happening in a viscoelastic medium [45]. Some methods have used this phenomenon to evaluate viscoelastic properties of tissues [45, 96]. Measuring shear wave velocities at specific frequencies is known as phase velocity estimation [45]. Beside the viscoelastic property of a tissue, its finite thickness can also affect the dispersion due to reflections during propagation, which may result in wave mode conversion [97–99]. The phase velocity and the group velocity are not equal in the presence of dispersion. It was shown that the phase velocity has a lower value by a factor of 8–9% compared with the group velocity in soft tissues [100].

One technique to measure the phase velocity is the phase gradient approach, which estimates the velocity using the phase difference evaluated at different spatial locations for specific frequencies [45, 85, 96]. An alternative method to estimate the shear wave phase velocity is performed by two-dimensional Fourier transform (2D-F) analysis, which converts spatiotemporal data to a wavenumber in the frequency domain, and uses the peak magnitude distribution to estimate the phase velocity [101, 102]. The dispersion either from the phase gradient or 2D-F can be fitted to rheological models to quantify viscoelastic parameters of the medium [45, 103]. The attenuating nature of a tissue is the cause of the dispersion of the phase velocity. The shear wave dispersion and attenuation can be estimated by the computation of a power law coefficient, with the assumption of a power law rheological model for the tissue [100, 104].

Local phase velocity imaging (LPVI) [105, 106] is another method that can produce a phase velocity map. The LPVI

requires applying bandpass filters to obtain the maximal frequency range for the phase velocity. Although this method demonstrates good reconstructions of 2D shear wave phase velocity, results are sensitive to the frequency range selected, and they may change when using different transducers, focal configurations, and focal depths [78].

Shear Wave Attenuation

The dependency of the wave amplitude with distance is attributed to geometrical spreading of the wave energy and to viscoelastic attenuation. Wave diffraction by geometrical spreading can be reduced by using the method of [50] that is considering cylindrical shear waves produced by a supersonic radiation pressure source. Other methods including this assumption were based on a 2-D Fourier transform and the computation of the spectral width to assess the frequency dependent attenuation [75, 107, 108]. A robust method assuming a cylindrical wavefront and no rheological model is the attenuation-measuring ultrasound shear wave elastography (AMUSE) algorithm [107]. This method, however, does not provide any attenuation map since the computation requires all datasets within the selected region-of-interest. Since biological tissues such as the kidney, muscles, and tendons are anisotropic, and because the wave produced by a linear SW front may no longer be cylindrical in those media; then, abovementioned algorithms may lead to inaccurate results [96, 109–112].

Frequency-shift methods used for compression and seismic wave analyses [113–115] inspired the field of shear wave elastography to assess tissue viscosity. Frequency-shift methods are not based on wave amplitude, so the dependency of these methods to geometrical wave spreading is released [113]. Bernard et al. developed such a frequency-shift method for shear wave attenuation by model-fitting of the amplitude spectrum [87]. This method made a few assumptions, which may not hold in all viscoelastic media such as fatty liver. A two-point frequency-shift method was later proposed by Kijanka and Urban to soften assumptions made by Bernard et al.; in their report, they considered a varying shape parameter of the gamma distribution used to fit the shear wave amplitude spectrum [116]. This technique used only two spatial points instead of all points along the propagation path, as in [87], to estimate the attenuation coefficient [116]. Using only two spatial points reduces the computation time but may affect robustness in cases of noisy shear wave displacement maps. Viscosity maps based on the cylindrical wavefront assumption of [50] or frequency-shift method of [87] can be found in [51].

Applications

A few examples of ultrasound shear wave viscoelasticity imaging applications are presented next. The reader may refer to recent review papers on this subject for other examples [117–119]. The focus below is on the liver and breast as those organs were largely investigated in clinical studies using SWE.

Liver

Liver fibrosis occurs when an abnormal large amount of liver tissue becomes scarred. It can lead to cirrhosis, its long-term sequel, and further evolve as hepatocellular carcinoma [120]. Liver fibrosis can be differentiated into 5 categories, from F0 for a normal liver to F4 for cirrhosis; these categories have been obtained by biopsy intervention, which is the gold standard for liver classification. However, liver biopsy is invasive, could lead to bleeding or worse outcomes, and even death [121], and because a small amount of tissues is taken, it is not always representative of the full liver due to sampling errors [118, 122]. Fibrosis is one pathology known to increase liver stiffness [69, 123–126] along with inflammation, edema, congestion and extra hepatic cholestasis [64, 127, 128]. Shear wave elastography was mainly used to classify fibrosis based on liver elasticity using different cutoff values. This imaging method is accurate to assess liver fibrosis of stage 2 and higher [69, 123, 129–131], has a good repeatability [132], and may allow to diminish the number of biopsy [133]. Yet the impact of steatosis on liver stiffness is uncertain [88, 134–136]. To overcome this, some teams proposed investigating viscous properties. If no clear consensus is reached yet, a few studies showed promising results based on shear wave dispersion and attenuation to assess steatosis stages [88, 137] or necroinflammation [138, 139]. Shear wave elastography presents some limitations for liver imaging, such as difficult measurements in obese patients, and confounding impact of factors such as inflammation, which can increase liver stiffness or change the liver stiffness threshold for classification. In addition to fibrosis assessment and classification, SWE was also proven useful to follow patients with chronic liver disease [65]. An example of a liver SWE image is given in **Figure 3**.

Breast

Shear wave elastography is used to help identify breast cancers, since it has been shown that malignant tissues appear stiffer than its healthy counterpart [140–142]. X-ray mammography, MR imaging and ultrasonography are used to detect tissue lesions or to classify suspicious masses into different categories, typically classification 0 for incomplete data to 6 for histologically proven malignancy. Nonetheless, excluding the expensive MR imaging method, these approaches have poor specificity and mammography often find false negative results in dense breasts [143]. Category 4, which corresponds to suspicion for malignant tissues, has a degree of certainty varying from 2 to 95% to assess malignancy proven by biopsy, and has a cancer detection rate of 10–30% [144]. Shear wave elastography allowed improving breast lesion characterization [145–148], and reducing the number of unnecessary invasive biopsy due to the improvement in specificity [148–150]. Elasticity parameters such as the maximum or mean Young modulus E within the lesion, and in surrounding tissues, are used to separate benign from malignant masses. Recent works investigated viscosity behavior using the shear viscosity [151], linear dispersion slope [152], and storage and loss moduli [153] to differentiate malignant from benign tissues. Ultrasound data on the viscous behavior of breast lesions are scarce but may prove to be of clinical value in the future. Some studies investigated the use of SWE as a tool to monitor cancer treatment performance [154],

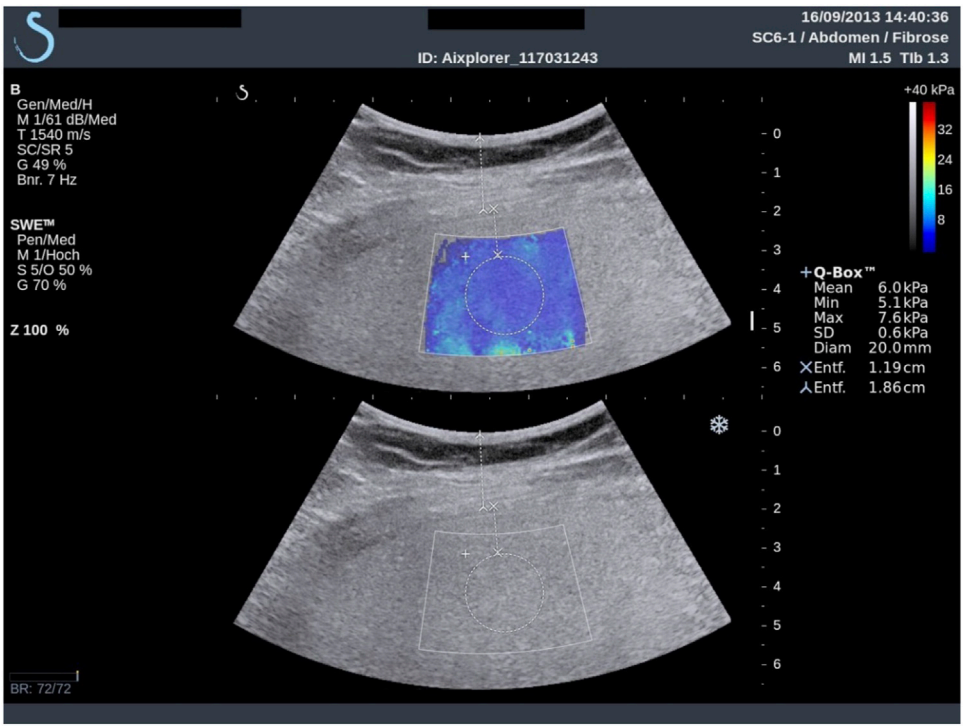

FIGURE 3 | Example of superimposing the shear wave elastogram on the corresponding B-scan in a 34-years-old man with histologic F1 fibrosis. The dynamic range of Young moduli was set between 0 and 40 kPa during the clinical exam, which was sufficient to cover the range of values expected for the four stages of liver fibrosis. Reproduced with permission from [69]. Copyright 2015, Elsevier.

with a decrease in malignant mass elasticity during treatment, or for early prediction of therapy successes [155, 156], with a better treatment response for softer tumors. **Figure 4** gives examples of Young's modulus elasticity maps of breast lesions.

Other Applications

Although SWE has targeted mainly the liver and breast, other organs and techniques have been developed. Prostate cancers [158], thyroid cancer nodules [159], and blood clot characterization [160] have been investigated, to name a few examples, with the Young's modulus as the descriptive mechanical parameter. If the assumption of an isotropic medium is generally accepted for most organs, it is not the case for muscles and tendons. Anisotropic and transversely isotropic models using shear waves have been recently investigated [24, 161, 162], some other teams explored viscoelastic properties using different probe orientations [109, 163–165]. A non-exhaustive list of SWE clinical applications can be found in **Table 2**.

MAGNETIC RESONANCE ELASTOGRAPHY

Magnetic resonance elastography (MRE) is another non-invasive imaging technology for assessment of mechanical properties of soft tissues. Since its first description by Muthupillai et al. in 1995 [166], MRE has been integrated into clinical routines for liver disease detection, and has shown great potential for other organs, notably the brain, of which only MRE can assess the *in-vivo* viscoelastic components without surgical intervention. Principles of MRE investigation are similar to those of any SWE method (**Figure 5**). A major feature of MRE resides in its ability to measure 3D displacement fields by simply changing the axes of encoding gradients, which is an advantage over other imaging devices operating elastography. The main drawback may be found in the longer scan times relative to ultrasound elastography for instance. MRE has a poor temporal resolution and relies on a stroboscopic-like recording arrangement to generate time resolved images, as opposed to ultrasound SWE where burst measurements are performed at a high acquisition rate. Typically, MRE data contain 4 to 8 images per harmonic actuation cycle. Spatially, MRE is sometimes referred to as a super resolution imaging modality as measured displacement amplitudes are much smaller than the image pixel size (tens of microns versus one to 3 mm). We review in this section the main three steps in MRE investigation, namely motion generation strategies, motion encoding techniques, and inversion methods. Finally, applications to the liver and brain are discussed. These organs were subjectively chosen as liver disease diagnosis is the only MRE protocol clinically established, and non-invasive *in-vivo* brain mechanics assessment is not enabled by any elastography techniques other than MRE.

Generation of Acoustic Waves in MRE

In MRE, most applications involve the generation of time-harmonic wave fields using external surface actuators. These

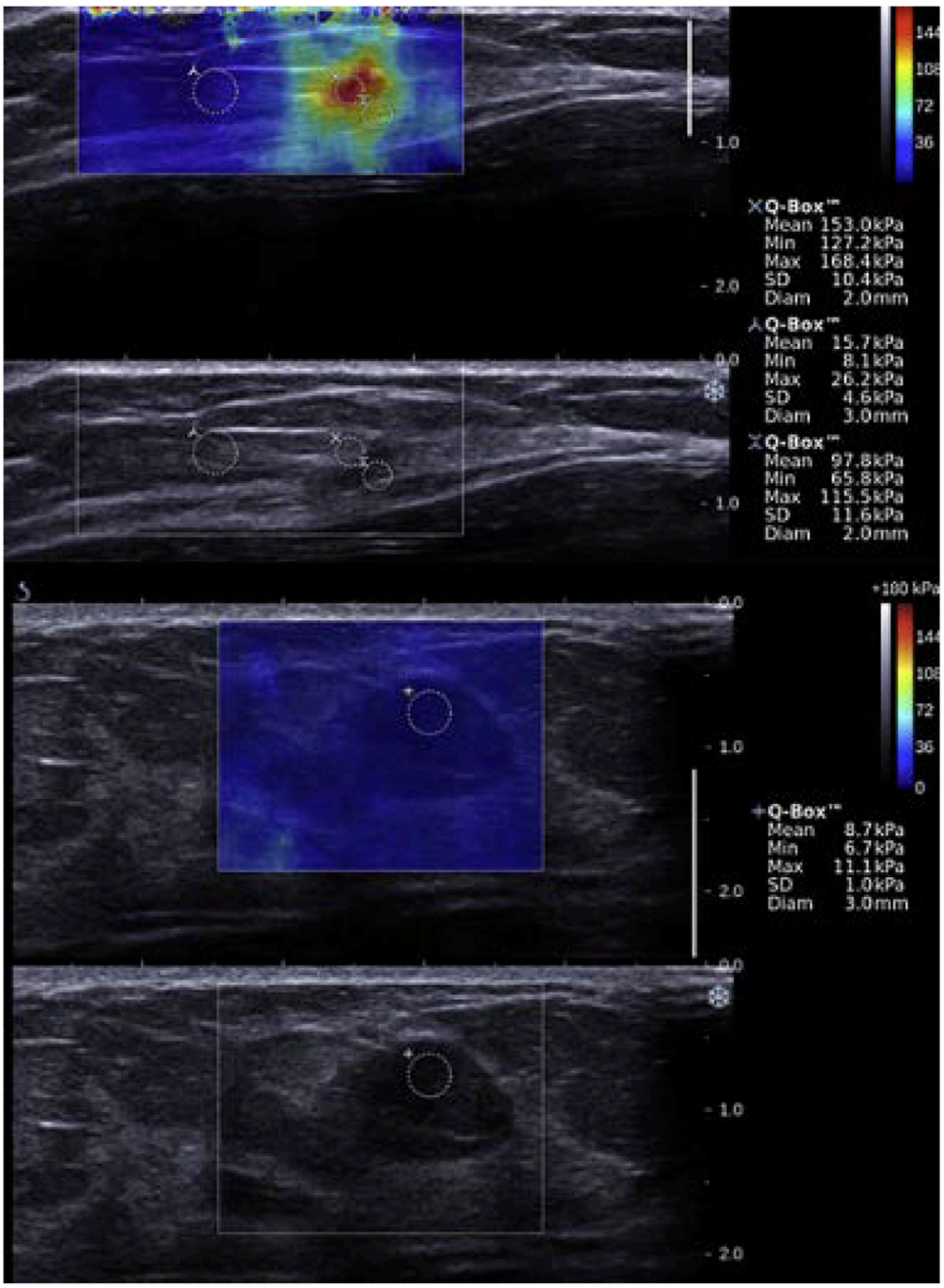

FIGURE 4 | Examples of shear wave elastography images of breast tissues. (Top two panels): A 50-year-old woman with an abnormality in her left breast on screening mammography is presented. Biopsy was made on the red region (high Young's modulus), and concluded that the lesion was an invasive carcinoma (pT1a, pN0). The first panel gives the SWE map superimposed on the B-mode image, whereas the bottom panel is the B-mode image. (Bottom two panels): A 48-year-old woman who presented with an abnormality in her left breast on screening ultrasound is presented. Biopsy was made on the suspicious region, and concluded that the lesion was a fibroadenoma (benign tumor). The blue color on the shear wave elastography image indicates a low Young's modulus. The third panel gives the SWE map superimposed on the B-mode image, whereas the bottom panel is the B-mode image. The range of Young's moduli on the colorbar is from 0 to 180 kPa. Reproduced with permission from [157]. Copyright 2015, Elsevier.

actuators must meet the requirements imposed by magnetic resonance safety rules, in other words they must be made of non-magnetic materials and be adaptable to fit into the experimental or clinical magnet bore of the scanner. Design of actuators has been shown to be application dependent; we review in this section the main techniques to induce motion in soft tissues in the context of MRE. Loudspeakers have been widely used to transmit motion to tissues and may be divided into pneumatic and rigid categories. In the pneumatic one, air pulses are transmitted from the loudspeaker pulsing

membrane to the investigated tissue by means of a wave guide (plastic tube). The tube is connected to an interface attached to the surface of the tissue. Plastic pads with a soft membrane and air cushions are the main examples of such interfaces. Main advantages are versatility allowing for applications to various organs [167–176], and the electricity-free transmission system (pneumatic) requiring no electrical current inside the magnetic resonance imaging (MRI) room. The main drawback may reside in the limitation to simple mono-frequency waveforms only. In the rigid category, loudspeakers transmit motion to tissues via a rigid rod attached to the membrane on one end, and to the patient on the other end. This configuration is also versatile [177–184] and handles arbitrary waveforms but requires the loudspeaker to be inside the MRI room. Lorentz-coil actuators have also been used to generate motion in various organs [185–192], and rely on the coupling of the MRI magnetic field $\boldsymbol{B_0}$ with an electrical current injected into the coil. These actuators must

TABLE 2 | An overview of main applications and viscoelastic properties in ultrasound SWE.

	Generation of SW			Viscoelastic parameters							Rheological model
	Mechanical pushes	Focused acoustic beams		Elasticity (Young's modulus)	Viscosity	Shear modulus	Shear wave speed		Shear wave dispersion	Shear wave attenuation	
	TE	ARFI	SSI				Group velocity	Phase velocity			
Liver	[61, 65] [69, 118] [125, 127] [126, 137] [135, 416] [131, 133] [128] [64] [124]	[69, 118] [126, 130] [61, 416] [131, 135] [129]	[69, 88] [132, 138] [61, 416] [135, 152] [134, 139]	[125, 127] [130, 132] [126, 416] [133, 135] [128, 134] [64, 65]	[139]		[88, 126] [416] [135] [129]	[88] [118] [137] [138] [152] [139]	[88] [137] [138] [152] [139]	[88]	[88] [138] [152] [139]
Breast	[140]	[146] [151] [157]	[152, 157] [147, 154] [145, 156] [142, 148] [149, 150] [155, 417] [418]	[140, 152] [146, 157] [147, 154] [145, 156] [142, 148] [149, 150] [155, 417]	[151]	[151]	[140] [146] [147] [142] [148] [418] [157]	[152] [151]	[152]		[152] (power law) [151]
Thyroid		[419, 420] [159, 421] [422, 423]	[159, 424] [367, 425] [426, 427] [428, 429] [430]	[419, 421] [423, 424] [367, 425] [426, 427] [429, 430]		[428]	[420] [159] [422] [429]				
Muscle		[163]	[109, 164] [431, 432]			[109, 164] [431, 432]	[109] [164, 431] [432]	[163] [109]			[109]
Tendon	[434]		[435] [436] [165]	[435] [436]			[435] [436] [165]	[434]			[434]
Blood clot	[66] [438]	[81]	[439] [440]	[439] [440]	[66] [81]	[438] [81]	[439] [440]	[66] [81]		[66]	[66] [438] [81]
Prostate		[441]	[442–445] [446, 447]	[442, 443] [445, 446] [447]		[444]	[441, 442] [443, 444] [445, 446] [447]				

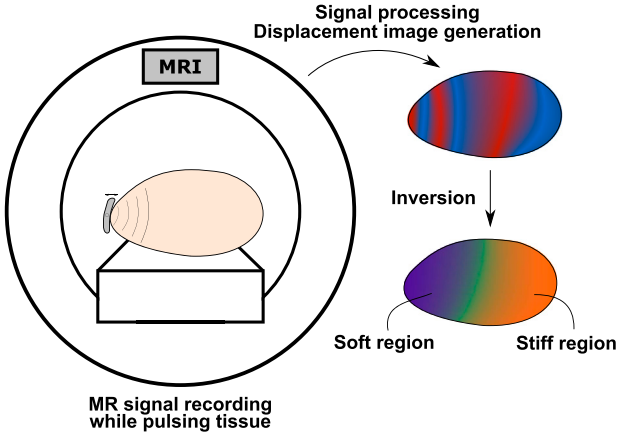

FIGURE 5 | Workflow in MRE investigation. Small time harmonic deformations are generated in the scanned tissue using an external actuator or natural body pulsation. These small deformations are recorded by the MR scanner using tailored acquisition sequences to produce time series propagation images. The complex MR signal is then processed to extract the motion field data, which is finally used as an entry to physical modeling allowing for calculation of mechanical parameters.

be designed according to the targeted organ as they are placed relative to $\boldsymbol{B_0}$. Piezoelectric drivers allow to deliver arbitrary waveform pulses to tissues while avoiding the constraint of positioning relative to $\boldsymbol{B_0}$. Significant displacement fields could be obtained using this technique in various conditions (human abdomen [193, 194], human brain [195, 196], human breast [197], and mouse brain [198, 199]).

A major bottleneck in generating sufficiently high motion deflection in tissues is the decrease of the motion amplitude with increasing excitation frequencies. Using a wide range of mechanical excitation finds its application in the analysis of frequency dependent mechanical behavior of soft tissues [8, 178, 191, 198, 200–203]. The more frequencies, the more valuable is the information. Centrifugal force based MRE drivers have been proposed to circumvent this limitation at high frequencies. The centrifugal force allows to maintain the displacement amplitude high regardless of the frequency [204]. The "air-ball" actuator and "gravitational actuator" are the first examples of the centrifugal force implementation. The "air-ball" actuator [205] consists in a ball circulating in a circular chamber under injection of compressed air. The revolution speed of the ball is imposed by the pressured air of which the pressure determines the actuator vibration frequency. The "gravitational transducer" is made of a mass attached to an axis and rotating around this axis. The rotation speed is driven by the rotating axis connected to a motor [206]. All the aforementioned techniques consist in shaking the surface of the probed tissue, which implies that elastic waves propagate to the region of interest with sufficient amplitude. This can be an issue if the imaged domain is deep under the surface thus increasing the risk of high attenuation. Producing a wave field *in situ* may be an alternative way to ensure that a sufficient amount of displacement remains in the region of interest. In that regard, focused ultrasounds have been used to generate shear waves along with an MR scanner for motion detection [207]. This technique requires a heavy experimental setup compatible with the MR environment and has not been, to date, more than a proof of concept. Instead of using external devices to produce motion at chosen locations, the concept of intrinsic actuation taking advantage of natural internal vibrations has gained interest. This method consists in encoding motion induced in organs by the natural pulsation of the heart and arteries, and presents the significant advantage of not requiring any additional equipment. Tailored MRE protocols must be adopted to adapt to the low frequency characteristics of natural pulsations (around 1 Hz). For now, intrinsic actuation has been applied to the brain [208–211].

Acoustic Wave Detection

Whereas most magnetic resonance imaging protocols attempt to reduce or compensate for motion, MR elastography seeks to take advantage of small vibrations in the scanned tissue. Numerous MRE specific pulse sequences [chronologically sorted application of radiofrequency (RF)-pulses and magnetic gradients to generate and manipulate the MR signal] have been designed to acquire driven or natural motion in biological tissues, while maintaining reasonable scan times and image quality. We review, in this section, the main concepts of MR elastography pulse sequences allowing for detecting acoustic wave propagation. More specific details and theory, along with fast acquisition strategies are available elsewhere [19, 212]. Motion encoding principles in MRI were first introduced by measuring sea-water velocity [213], and further applied in the context of angiography to measure blood flow [214]. The proof consisted in relying spin velocities to the phase shift spins experienced when space and time varying bipolar magnetic fields are applied. A similar concept, leading to MRE, was developed in which motion of spins around their position at rest is encoded in the phase of the complex MR signal using magnetic-field gradients, named motion encoding gradients (MEGs) [166]. The accumulated net phase of moving spins varies according to their trajectory while a time dependent MEG is applied. This net phase thus allows to track local motion of tissue eventually providing the displacement maps required for retrieving mechanical parameters. MRE sequences are generally based on existing MR encoding outfitted with MEGs. Not only are their setting key to be compatible with the characteristics of the induced motion but so are other inherent MR imaging parameters, leading to a broad variety of MRE sequences.

The timing of the chosen MR based-sequence rises a certain amount of constraints regarding scan time, motion sensitivity, and image quality. The MR sequence design and underlying physics are beyond the scope of the present review, thus only the main concepts relevant to overall MRE understanding is briefly discussed. For in-depth details, see [19, 215]. When a tissue is placed in the strong static magnetic field $\boldsymbol{B_0}$ of an MR scanner, a net magnetization aligned with the magnetic field is produced from the contribution of each uncoupled individual nuclear spin (those of hydrogen nuclei in clinical scanners) [215]. The key concept in MR signal generation consists in

tipping the net magnetization of the desired portion of the scanned tissue out of its resting state using some excitation radiofrequency pulses tuned at the Larmor frequency of the spins in the scanner [216]. Magnetization enters a precession motion about the $\boldsymbol{B_0}$ axis under the effect of this RF-pulse. Once excited, the magnetization is no longer aligned with $\boldsymbol{B_0}$ and tends to realign and reach its resting state back again. This process called relaxation occurs at a certain time rate dictated by the interactions between spins themselves and with their environment. The time constant T_1 characterizes the exponential regrowth of the magnetization parallel to $\boldsymbol{B_0}$ (longitudinal component of the magnetization) due to spin-lattice interactions. Time constants T_2 and T_{2^*} characterize the exponential decay of the transverse magnetization component (perpendicular to the longitudinal one) due to spin-spin interactions and magnetic field inhomogeneity (combined with the spin-spin interaction), respectively.

Timewise, $T_{2^*} < T_2 < T_1$ and decay rates are given by $R_{2^*} = 1/T_{2^*}$ and $R_2 = 1/T_2$, where $R_{2^*} > R_2$. The time evolution of the MR signal immediately following the RF-pulse excitation is named free induction decay (FID) and is governed by T_{2^*} effects. Receive coils are used to monitor relaxation by measuring the voltage induced by the precessing magnetization according to Faraday's law. Manipulation of the magnetization allows to generate MR signal peaks at adjustable delays after the application of the excitation RF-pulse, i.e., during the FID, or later when the signal appears to have vanished. MR sequences may be divided into two main categories of mechanisms leading to different timing for data acquisition. Spin echo (SE) sequences employ a second RF-pulse called refocusing RF-pulse, occurring after the FID, and allowing for compensation of T_{2^*} effects (magnetic field inhomogeneity). Some of the MR signal can thus be recovered after the FID. In this case, the limiting time constant becomes $T_2 > T_{2^*}$. Passed the exponential decay due to T_2 effects, the MR signal can no longer be recovered. The peak of the recovered MR signal, the echo, occurs at the "echo time" *TE* after the application of the RF-pulse excitation. Gradient recalled echo (GRE) sequences, however, typically operate within the FID (occurring immediately after the RF-pulse excitation) and do not allow for magnetic field inhomogeneity effects compensation. The operating window in such sequences is thus limited by the T_{2^*} weighted decay, and thus leads to much faster acquisition protocols. Magnetic field gradients are used, instead of a second RF-pulse, to manipulate the magnetization and generate a signal echo at *TE*. As aforementioned, MRE sequences usually consist in incorporating motion encoding gradients into an MR based-sequence. This modification is consequently subjected to timing limits of the base-sequence. The short timing of gradient echo type sequences presents a narrower time slot for the MEGs to operate than that of spin echo type sequences. The impact of such inherent characteristics is discussed below.

The first descriptions of the motion encoding mechanism in MRE were reported in Refs. [166, 217]. As aforementioned, a spin moving in the presence of a magnetic-field gradient $\boldsymbol{G}$ experiences a phase shift ϕ:

$$\phi(\tau) = \gamma \int_0^\tau \boldsymbol{G}(t) \cdot \boldsymbol{r}(t) dt \tag{21}$$

where γ is the gyromagnetic ratio of the material [rad s^{-1} T^{-1}] and $\boldsymbol{r}$ is the time-dependent position vector of the spin. From this equation appears that the phase shift depends on both the spin trajectory $\boldsymbol{r}$ and the applied $\boldsymbol{G}$. Consequently, a given arbitrary spin motion results in different accumulated phases depending on the magnetic gradient waveform. Hence, the remaining definition of $\boldsymbol{G}$ sets the type of motion the encoding process is sensitive to. Since the inherent function of magnetic field gradients is to add a controlled space-dependency to the static and homogeneous magnetic field $\boldsymbol{B_0}$, even static spins experience a space dependent phase accumulation while MEGs are switched on. In order to cancel this unwanted phase accumulation, $\boldsymbol{G}$ can be set to oscillate in time allowing the phase accumulated during the first half of the gradient oscillation period to be compensated during the second half. This technique is called zeroth moment nulling [19]. Non-oscillating MEGs are called unbalanced gradients and are thus rarely used in conventional MRE sequences. Additionally, the effect of constant velocity and constant acceleration background components in moving spins may also need to be cancelled. This can be achieved by applying first and second moment nulling, respectively [19]. Both consist in adjusting the MEGs oscillation profile so that the accumulated phase in **Eq. 21** goes to zero for unwanted spin motion.

Many MRE applications have resorted to full wave encoding (MEGs tuned to the same frequency as that of the motion oscillation) with zeroth [188, 197, 198, 218–221] and first moment nulling [166, 172, 173, 175, 181, 203]. For all types of oscillating gradients, the area under the curve of MEGs over the operation time must equal zero for proper motion encoding. Early in MRE, several examples of motion encoding strategies were derived in the case of time-harmonic excitation, leading to time-harmonic spin trajectories and involving full-wave encoding [217]. Spin trajectories $\boldsymbol{r}$ can then be written as:

$$\boldsymbol{r}(t) = r_0 + \xi_0 cos(\boldsymbol{k} \cdot \boldsymbol{r} - \omega t + \theta), \tag{22}$$

where r_0 is the position vector of spins at rest, ξ_0 is the spins displacement amplitude, $\boldsymbol{k}$ the wave vector, $\boldsymbol{r}$ the position vector, ω the oscillation frequency, and θ some initial phase offset. Solving **Eq. 21** using **Eq. 22** and the MEG temporal profile allows to quantify the encoding efficiency, which is defined as the amount of phase shift in the signal per displacement unit. Encoding efficiency formulas for common MEG waveforms are available in Refs. [19, 212].

Full wave encoding scheme ensures a good motion sensitivity but compels the minimum achievable value of the echo time dependent on the driver actuation period. GRE sequence short timing due to T_{2^*} effects is well suited to high actuation frequencies (short time slot for MEGs to operate); however, it limits the applicable number of MEG cycles [166, 188, 197, 220, 222, 223]. The optimal setting resides at the trade-off between the SNR increase permitted by short *TEs* and the higher motion

sensitivity permitted by multiple MEG cycles. A similar conclusion can be drawn with regards to SE sequences, which present a more flexible timing enabled by their inherent longer echo and repetition times [215, 224]. Multiple MEG cycles can thus be incorporated into the sequence while maintaining the echo intensity sufficiently high. SE sequences are often implemented with fast readout strategies, for instance echo planar imaging (EPI) necessitating only one or few combinations of excitation- and refocusing-RF pulses to generate a whole image, which allows to circumvent the use of many long repetition times (*TRs*) [172, 175, 181, 203].

So far, single actuation frequency cases have been presented. Full-wave encoding can also be used to extract a frequency of interest from a multi-frequency oscillating wave field by selecting proper MEG profile (frequency and number of cycles) [177, 222, 225]. This configuration presents little interest in cases where the actuation frequency is chosen by the user. The only way of performing multi-frequency acquisitions using full-wave encoding is to repeat the encoding for each frequency separately [188, 191, 198, 201, 219, 223, 226], which has an impact on the acquisition time. However, multiple frequency components can be simultaneously encoded in a single acquisition using wide band MEGs, and manually selected using a temporal Fourier transform [177, 178, 180, 182, 210, 227–230]. The main advantage of simultaneous multi-frequency encoding is the time saving making them more suited to *in vivo* studies compared with repeated single frequency acquisitions over a given frequency range. The main drawback is the overall lower motion amplitude at each frequency of the multi-frequency actuation compared with the repeated acquisition scheme, due to total energy deposition divided into the total number of frequencies.

The wideband property of MEGs has been further extended to fractional encoding where the frequency of the mechanical oscillation is smaller than that of MEGs, and the mechanical time period is larger or equal to the repetition time [186]. With shorter MEG time periods, scan duration can be reduced and higher SNR can be obtained by shortening the echo time accordingly [190]. A major advantage of this approach is found in measurement of low frequency induced motion, such as heart pulsation driven actuation (around 1 Hz), where full-wave encoding would lead to unpractical echo times [208, 209, 211, 231]. Despite the lower motion sensitivity in fractional encoding, this method has proven successful using fast acquisition protocols (spoiled GRE and GRE/SE equipped with EPI readout strategy) [169, 170, 179, 190–192, 201, 209, 232–234]. Besides multi-frequency acquisitions, reduced *TE* and *TR* permitted by fractional encoding have also been exploited in balanced steady state free precession MRE [186, 235, 236], despite the original development circumventing the use of MEGs [237]. Although high phase-to-noise ratios were reported, this sequence type presents significant timing constraints (actuation frequency linked to *TR*), and non-linear phase accumulation between consecutive *TRs* leading to additional signal post-processing steps. It has consequently been used only sporadically [19, 190, 212].

Inverse Problem in MRE

The previous section reviewed some acquisition approaches to measure motion induced in the tissue of interest. The last essential step in elastography consists in relying these displacements to mechanical parameters using physical models. This section addresses the most reported inversion schemes employed in MRE. More specific information about processing times and modeling details can be found in Refs. [238, 239]. A major strength of magnetic resonance is the capacity of encoding motion in the three directions of space, allowing for full 3D inversion of the Navier equation. This strength comes at the cost of overall longer scan times for which alternatives have been discussed above. Despite the availability of fast 3D MRE sequences, all mechanical parameter reconstruction methods do not make use of complete displacement data sets and take advantage of physical assumptions allowing for processing of reduced dimension displacement data. We propose to classify inversion schemes into two categories. The direct approach consists in formulating the inverse problem with the mechanical parameters as unknowns. Experimentally obtained displacement data are inserted into the equations of elasticity, and quantities of interest are extracted through direct inversion. The iterative approach consists in iteratively solving the forward problem for displacements starting from an initial set of guessed mechanical parameters. These mechanical parameters are iteratively updated to minimize the difference between experimental displacement data and computed displacement solution. The final solution is the set of mechanical parameters that makes that difference converge to a global minimum.

Direct Methods

The first reported inversion method in the context of MRE, assuming isotropy, local homogeneity, no attenuation, and incompressibility, consisted in estimating the local wavelength of the measured wave field. This technique is termed LFE (local frequency estimation). Briefly, pairs of filters centred on spatial frequencies usually separated by one octave are applied to the wave field. The ratio of displacements filtered by each filter of one pair equals the local wavelength [240]. To ensure that local spatial frequency is included in the bandwidth of the filter pair, the process is repeated over a certain range of frequencies. From the evaluated wavelength (inverse of spatial frequency), the magnitude of the shear modulus $|\mu|$ is retrieved using $|\mu| = \rho v_s^2 = \rho(\lambda_s f)^2$, where λs is the local wavelength and f is the temporal actuation frequency. We recall here that ρ is the tissue density, vs the shear wave speed, and that such assessment assumes a purely elastic tissue (no viscosity). The original publication describing LFE [225] employed log-normal quadrature filters but other functions have been studied [241, 242]. This method has been widely used in all types of study [166, 169, 171, 174, 175, 221, 223], as it is fast and only requires a single component of the displacement field. LFE has also proven a certain robustness against noise as it does not directly compute spatial derivative of the image, thus circumventing noise enhancement. To date, LFE is the only reconstruction method used and marketed for routine clinical practice. Although the LFE in itself provides no insight into the viscous behavior of the

investigated tissue, this method has been combined with an attenuation model to estimate both G' and G'', thus avoiding calculation of 2nd or 3rd order derivatives [223]. Phase gradient methods allow for simple estimation of the wave number k, similarly to LFE, which is used to quantify elasticity only. They have been sporadically used given their insensitivity to wave attenuation and their dependency on planar waves [243].

Early in MRE were also reported direct methods assuming viscoelastic materials, as described in *General Concepts in Shear Wave Elastography*, and using the strong formulation of the Helmholtz equation [198, 220, 244]. The underlying assumptions of isotropy, local homogeneity, and incompressibility are used to neglect the stiffness gradient across the tissue, and to decouple motion components in the equation system. From there, a single motion component can be used to retrieve the complex-valued shear modulus ($G^* = G' + jG''$). Planar assumption allows to consider the 2D curvature of the wave field instead of its 3D, which further decreases the required amount of data to solve the inverse problem. This method has also been widely used [177, 178, 182, 219, 227–229, 243, 245] given its simplicity and low computational cost but strongly depends on data filtering and evaluation of second derivatives [244, 246]. Using this scheme, stiffness reconstruction was shown to be altered by the neglected first Lamé parameter (**Eq. 8**) [247]. Applying the Helmholtz decomposition to the wave field allows to separate divergence-free (shear) from irrotational (compressional) components. Taking the curl of the Helmholtz equation increases the differentiation order but physically isolates the shear component of interest. This approach has become prominent when the Helmholtz equation is employed to retrieve storage and loss moduli [172, 187, 189, 190, 198, 199, 232, 247, 248]. To improve resolution and stabilize the direct inversion of the mono-frequency Helmholtz equation, a multi-frequency approach named MDEV (multi-frequency dual elasto visco inversion) was introduced [200]. A multi-frequency wave field is built upon data sets of individual different frequencies, ignoring the dispersion of mechanical parameters with respect to frequency, reducing the risk of nodes due to standing waves and stabilizing the equation system by adding equations with same unknown. Various studies have resorted to inversion schemes based on this method [8, 193, 194]. As an alternative to the 2nd order derivative assessment required by MDEV, a phase-gradient based method termed k-MDEV was proposed. It consists in evaluating the complex wave number k of a plane wave (see *General Concepts in Shear Wave Elastography*), which can then be related to both phase velocity for elastic modulus estimation and attenuation for viscous behavior quantification [194].

A finite-element (FE) based inversion method was recently proposed, also assuming local homogeneity, for storage and loss moduli assessment. It takes advantage of the weak form of the equations of motion to reduce the differentiation order, and exploits divergence-free test functions to lower the impact of the compression field [249]. So far, most of the discussed approaches have in common the assumption of local homogeneity, neglecting the gradient of mechanical parameters across the tissue, and incompressibility, invoked to neglect terms involving the divergence of displacements (unless the curl operator is applied). The local homogeneity assumption was shown to alter the reconstructed mechanical parameters in regions where the latter are not constant [218], that is in most clinical cases and notably tumorous tissues. Direct methods, still employing the strong form of the Navier equation and neglecting the divergence of the wave field, were proposed to consider heterogeneity using single [250] and multifrequency (HMDI–heterogeneous multifrequency direct inversion) [251] approaches. To address the compression aspect in nearly incompressible materials, which was shown to lead to artefacts and inaccuracies [252, 253] when disregarded [253] or processed using displacement formulation only [254, 255], direct FE formulations of the inverse problem have been proposed using curl-based [256] and mixed displacement-pressure [253, 256, 257] schemes.

Iterative Methods

Overall, iterative methods make less restrictive assumptions on tissue mechanical properties than direct ones relying on the algebraic strong formulation of the elasticity equations, and have been reported to solve for more unknowns than FE-based direct methods by adjusting the number of parameters to update in the minimization process. From a computational standpoint, solving forward problems, that is, mapping data information (i.e., displacement field) from source information (i.e., elasticity distribution) is a smoothing process. On the contrary, inverse problem consisting in mapping source information (i.e., elasticity distribution) from data information (i.e., displacement field) is a noise-enhancing process [258]. Consequently, iterative approaches tend to be more robust against noise than direct ones. Following FE discretization approaches, similar to direct FE ones, iterative schemes have been developed [259–261]. Near incompressibility is often assumed and requires to modify the formulation of elasticity equations in order to solve for pressure in addition to displacements (aforementioned mixed "pressure-displacement" formulation), and material heterogeneity is mostly considered [257, 262]. In MRE, the subzone technique has gained significant interest amongst iterative processes [263]. It consists in dividing the imaged domain into overlapping subdomains termed subzones, and solving iteratively the forward problem for displacements in each subdomain parallelly [197]. Once the solution in each subzone has converged, subzones are randomly redistributed over the domain and the iterative solution calculation is performed again. Retrieved mechanical parameter distributions, corresponding to each subzone distribution, are finally averaged to form the final solution. This reconstruction method has been applied to phantoms, brain [176, 203, 264, 265] and breast [266, 267] data, and has proven its capacity to reconstruct multiple variables at various actuation frequencies using elastic and viscoelastic physical models (compressible elastic [268], compressible viscoelastic [269], and nearly incompressible viscoelastic [176, 184, 203, 231, 264–266, 268, 270–272]). Additionally, poroelastic models have been introduced for accurate consideration of the biphasic nature

of entangled solid-liquid structures in biological tissues [168, 184, 211, 270, 271, 273]).

Applications

Liver

MRE can be applied to virtually any organ provided sufficient displacement data quality and suitable inversion scheme. We mainly restrict our discussion to liver applications due to the clinical availability of the technique, and to brain of which *in-vivo* mechanical properties have yet only been non-invasively accessible using this elastography method. MRE in clinics has so far been restricted to liver scanning for fibrosis, and diagnosis of chronic liver diseases using purely elastic models, i.e., assessing the shear modulus only and ignoring the tissue's viscous behavior. Under these assumptions, meta-analyses over the past few years on liver MRE have highlighted the high performance of the method in distinguishing liver fibrosis stages in non-alcoholic fatty liver disease, and cirrhosis considering the stiffness increase under this condition [274, 275]. Viscoelastic parameters in human liver diseases have also been early investigated using multi-frequency MRE to assess the frequency dispersion of storage and loss moduli (G' and G'') in healthy and fibrotic patients [180]. Results showed an increase in both G' and G'' in fibrotic with respect to healthy livers. Evaluation of the elastic modulus and viscosity using a standard linear solid model in healthy and fibrotic human livers led to a similar conclusion, where both elasticity and viscosity increased in pathological liver tissues [178]. This trend was also reported in [276], and in a performance study of MRE in the detection of fibrotic livers [277]. Overall, stiffness only or both stiffness and viscosity increases have been observed against the fibrotic stage. Interestingly, a case of liver steatosis in rats where only viscosity varied while stiffness remained unchanged has been reported in [278]. Despite these findings, the storage modulus was found to correlate much better with stages of liver fibrosis than viscosity [279]. Additionally, measurement of wave damping for viscosity characterisation is influenced by reflections off boundaries and renders its measurement troublesome. To date, stiffness variations for estimation of liver fibrosis severity has been mostly investigated.

Brain

MRE has also been proven successful and robust in the brain [280]. Its high water content and the observed shear wave attenuation in MRE acquisitions suggest that restriction to purely elastic models may lack of accuracy. The healthy brain's viscoelastic behavior has been highlighted by evaluating the dispersion of reconstructed mechanical parameters at varying frequencies in humans [8] and rats [198]. Both storage and loss moduli tended to increase with frequency. Additionally, cerebral viscoelasticity was shown to follow a frequency power law, where all reconstructed parameters vary independently [203]. These reconstructions suggested that the falx cerebri's viscous behavior is singular in comparison with other brain regions. Along similar lines in healthy brain characterization, viscoelasticity changes due to physiological aging have been considered [227, 229, 281]. From these studies appear that the brain softens but sees its relative viscous-to-elastic behavior unchanged over time. Such investigations along with MRE of neurological diseases have underlined the high potential of this technique in detecting neurodegenerative pathologies [282]. Non-invasive differentiation of natural structures of the brain based on their mechanical response to stimulus imparts MRE a significant advantage. For instance, the cerebellum has been shown to be softer and tends to be less viscous than the cerebrum [189].

High resolution mapping of stiffness and dispersion effects have suggested that cortical white matter is stiffer and more viscous than grey matter [191]. MRE has also been used to quantify the viscoelastic changes of altered brains. Notably, Alzheimer's disease was shown to reduce the brain's stiffness (elasticity only) [181]. Glioblastoma has been shown to take lower stiffness and viscosity values using multi-frequency MRE in humans [201], and mono-frequency MRE in a rat model [283]. A similar softening trend was observed in multiple sclerosis [182, 228, 284], where viscoelasticity was assessed using a global parameter. On the other hand, normal pressure hydrocephalus appears to trigger the opposite effect [175, 211]. Recent research on brain viscoelasticity has opened new avenues in the understanding of connexions between cerebral functions and tissue mechanical behavior. For instance, joint investigation of hippocampus viscoelasticity (shear stiffness and damping ratio), and relational memory has allowed to correlate hippocampal viscoelastic variations to performance in completion of spatial reconstruction tasks [285]. Viscoelasticity was characterised using an adjusted damping ratio that indicates the dominant tissue behavior between elasticity and viscosity. Results showed that better relational memory performance correlated with a rather elastic mechanical behavior of the hippocampus. This constituted the first observation of the kind.

The same principle was applied to assess the correlation between cardiovascular health through aerobic fitness exercises, relational memory performance through spatial reconstruction tasks, and hippocampal viscoelasticity using MRE. The study showed that better memory performance was associated with higher values of the adjusted damping ratio, which was itself associated with better aerobic fitness performance [286]. Light fitness exercise has also been shown to have a potential impact on hippocampal viscoelasticity and associated cerebral functions in multi-sclerosis patients [287]. These investigations laid the first stone for the characterisation of relationships between physical and cerebral functional behaviors, and brain viscoelasticity [288–291].

Brain Anisotropy and Poroelasticity

Finally, most advanced improvements in viscoelasticity characterisation embed tissue anisotropy, which is particularly relevant in the brain given its fibrous structure. As a deviation from brain applications: the first use of anisotropy in MRE was proposed for breast tumor detection through the evaluation of an assumed symmetrical stiffness tensor [292]. Results suggested that carcinoma have an anisotropic structure revealing a preferred orientation, certainly due to vascularisation, and suggesting transverse isotropy. Breast cancer was then also characterized assuming a transversely isotropic model leading

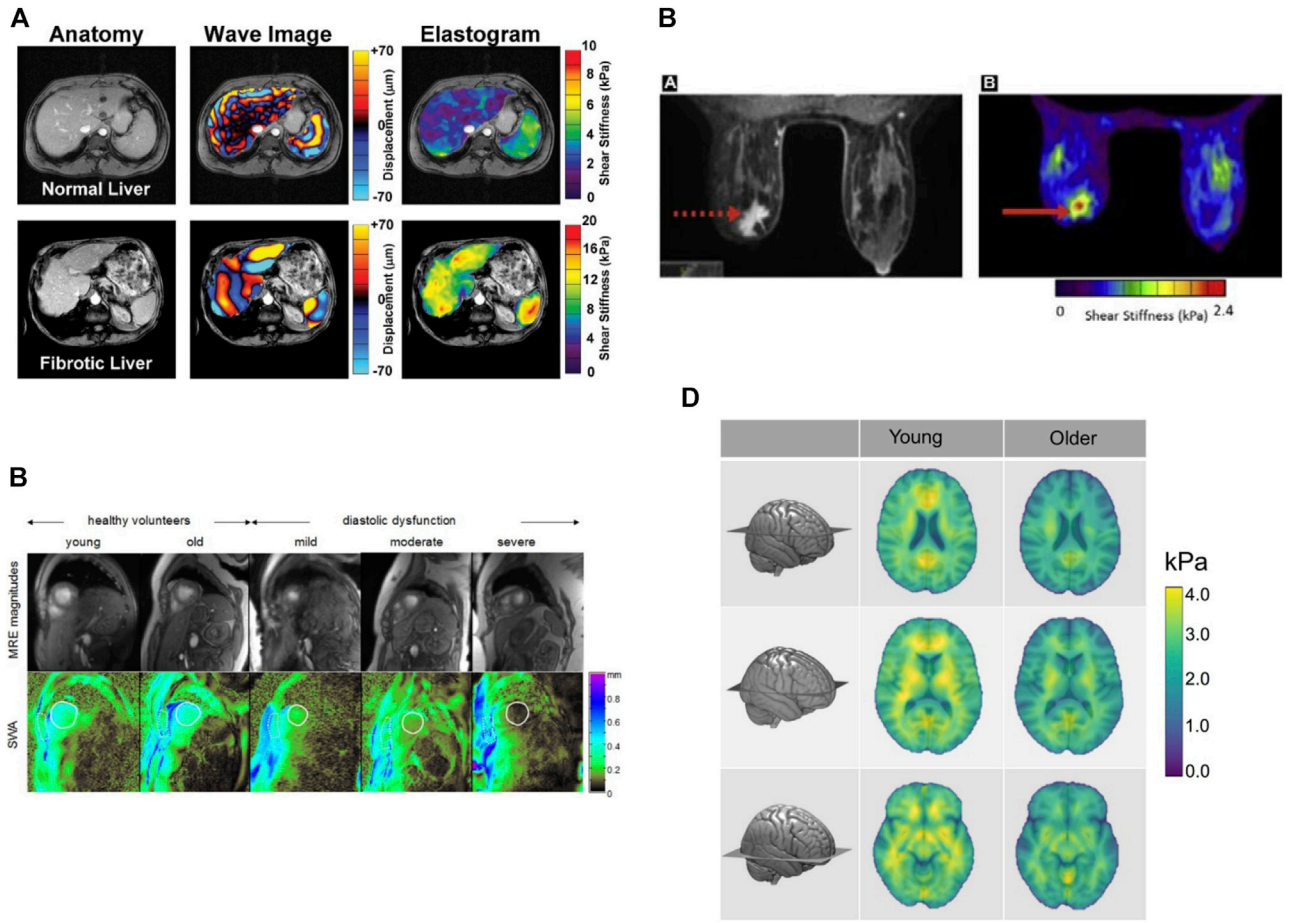

FIGURE 6 | (A) MRE of the liver. Anatomic images, displacement and shear stiffness maps of healthy and stage 4 fibrotic livers. Reproduced with permission from [296]. Copyright 2007 AGA Institute. **(B)** MRE of the breast. Anatomic image and shear stiffness map of a biopsy-proven invasive ductal carcinoma. Reproduced with permission from [297]. Copyright 2020 Elsevier. **(C)** MRE of the heart. Shear wave amplitude maps of a healthy heart versus hearts with diastolic dysfunction. Reproduced with permission from [234]. Copyright 2014 RSNA. **(D)** Mean shear stiffness of the cerebrum in young and older adults. Reproduced with permission from [281]. Copyright 2018, Elsevier.

to a 5-parameter reconstruction [247]. Again, results showed a preferred orientation in the tumor structure. Transversely isotropic mechanical property recovery was experimentally validated in fibrous tissues using MRE and diffusion tensor imaging (DTI) [293]. *In-vivo* brain anisotropic stiffness assessment in humans assuming separately orthotropy and transverse isotropy suggested that white matter exhibits a transverse isotropy structure [20]. Shear wave speed analysis was performed from prior knowledge of fiber orientation using DTI. Two shear wave modes were then observed, a faster longitudinal mode relatively to a slower transverse mode. The transverse anisotropy of white matter was later nuanced in favor of a mild only anisotropy in a study on *ex-vivo* porcine brain, where a purely transverse shear wave mode was generated and used to estimate three isotropic parameters in the absence of longitudinal modes [294]. Human brain anisotropy was also highlighted using variations in reconstructed stiffness distribution depending on actuation direction [176]. This constitutes a direct measurement of the anisotropy impact in isotropic models. Such observation was quantified using a finite element formulation of a heterogeneous, nearly incompressible, and transverse isotropic model providing benchmark displacement fields for inversion testing [265].

In addition to the significant research effort in evaluating and understanding cerebral viscoelasticity, the high water content of the brain has motivated to consider it as poroelastic, i.e., made of two, solid and liquid, entangled phases. The impact of poroelasticity versus viscoelasticity on reconstruction has been shown to be relevant at low frequencies (a few Hertz) using the forward problem formulation in the harmonic regime, and the aforementioned subzone iterative scheme [184]. At higher frequencies, viscoelasticity seems to remain a more suitable model than poroelasticity. Overall, poroelasticity and low frequency intrinsic actuation thus constitute an interesting and original package in MRE investigation. This setup circumventing resorting to pulsing equipment has been used in a few studies, and holds promise for more accurate detection of brain pathologies [208, 211]. Another approach to highlight brain poroelasticity

TABLE 3 | An overview of main applications and technical developments in MRE.

	Sequence type		Moment nulling		Encoding		Actuation				Inversion	
	SE	GRE	0^{th}	1^{st}	Fractional/ multifrequency	Full wave	Loudspeaker (pulsed air and solid rod)	Electro-magnetic	Piezoelectric	Intrinsic	Direct	Iterative
Brain	[8, 172, 175–177, 181–184, 191, 195, 198, 201, 203, 209, 219, 227–229]	[184, 208, 210, 211, 223]	[8, 177, 182, 184, 198, 203, 208, 210, 211, 219, 227–229]	[8, 172, 175, 176, 181, 183, 191, 195, 201, 209, 223]	[8, 177, 182, 184, 191, 195, 201, 209, 210, 227–229]	[172, 175, 176, 181, 183, 184, 198, 203, 219, 223]	[172, 175–177, 181–184, 209, 223, 227–229]	[191]	[8, 195, 198, 201, 203, 219]	[208–211]	[8, 172, 175, 177, 181, 182, 191, 195, 198, 201, 209, 210, 219, 223, 227–229]	[176, 183, 184, 203, 208, 211]
Muscle		[174]	[174]			[174]	[174]				[174]	
Liver	[8, 171, 178, 180, 190, 194]	[188, 190, 448]	[8, 178, 180, 188, 190]	[8, 171, 194, 448]	[8, 178, 180, 190, 194, 448]	[171, 188]	[171, 178, 180, 448]	[188, 190]	[8, 194]		[8, 171, 178, 180, 188, 190, 194, 448]	
Prostate	[248]	[192]	[192]	[248]	[192]	[248]		[192]	[248]		[192, 248]	
Kidney	[173]			[173]		[173]	[173]				[173]	
Heart		[170, 179, 233, 234]	[179, 233, 234]	[170]	[170, 179, 233, 234]		[170, 179, 233, 234]				[170, 179]	
Breast	[185]	[197]	[185, 197]			[185, 197]		[185]	[197]		[185]	[197]
Spleen	[193, 194]			[193, 194]	[193, 194]				[193, 194]		[193, 194]	
Phantom	[168, 221]	[166]	[221]	[166]		[166, 221]	[168]	[166]	[221]		[166, 221]	[168]

was to solve for both shear and bulk moduli using the algebraic inversion technique, which resulted in a bulk modulus much lower than expected, confirming the poroelastic nature of the brain (compressible solid matrix and incompressible fluid channels) [209]. More recently was proposed an improvement in MR poroelastography acquisition processes allowing to separate solid and fluid contributions to the shear motion field using an inversion recovery sequence adapted to MRE, along with a tailored MR signal modeling [295].

To conclude, **Figure 6** illustrates typical wave maps and elastograms from MRE acquisitions in the liver, breast, heart, and brain. **Table 3** presents an overview of main components constituting MRE investigations, from motion generation techniques to inversion categories described in previous paragraphs.

OPTICAL SHEAR WAVE ELASTOGRAPHY

Elastography based on ultrasonography or MRI has found popular clinical applications facilitated by the implementation of those imaging technologies on clinical systems. These tools can provide images over centimeter to whole-body depth ranges. However, many applications require millimeter-scale spatial resolution images, which can only be made possible using optical means. For example, on the cellular scale, the measurement of mechanical properties requires higher resolutions to focus on the understanding of how cells respond to physical forces. Thus, the use of optical elastography provides an opportunity for microscale imaging and for numerous applications in fundamental research [298].

Within the last 2 decades, developments in this new area of imaging led to multiple scientific advancements at the interface between optics and mechanics, which included biomedical applications in ophthalmology, oncology, and cell mechanics. The following subsections discuss recent developments in cellular and optical elastography, and their applications across biomedical and life sciences.

Cellular Shear Wave Elastography

Tissue elasticity at a microscopic scale is determined by the cell and the extracellular matrix elasticity. Main components of a cell are the membrane, cytoplasm, and cytoskeleton. The latter structure contributes to the cell mechanical stability and characteristics, and to its morphology. An imbalance in the mechanical homeostasis and defect in the cellular

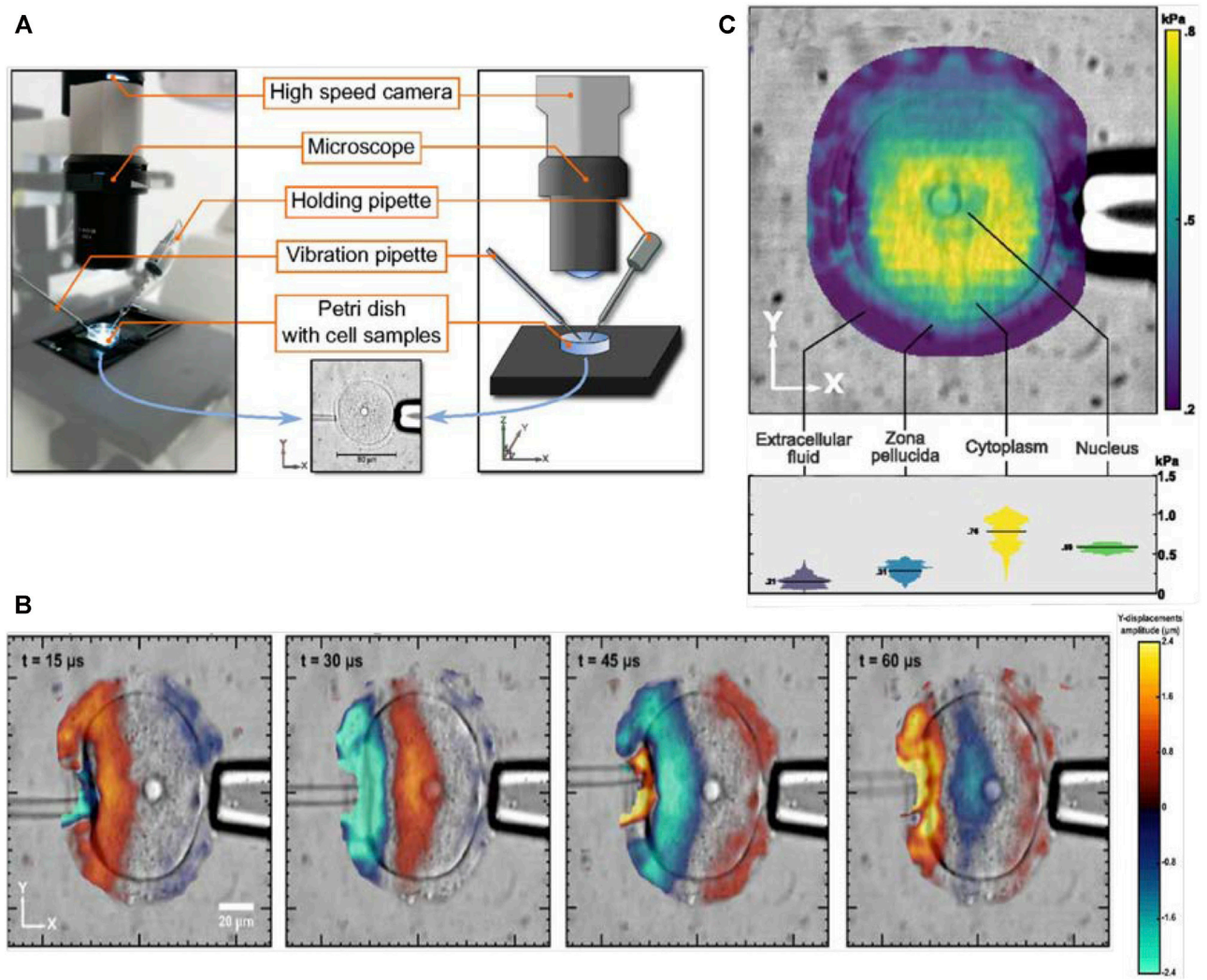

FIGURE 7 | (A) Experimental set up for optical microelastography, **(B)** intracellular displacement map through time, **(C)** elasticity map of the cell into the zona pellucida, cytoplasm, and nucleus. Adapted with permission from [302]. Copyright 2018, National Academy of Sciences.

mechanotransduction can contribute to various human diseases. Therefore, cellular viscoelasticity can be viewed as a biomarker for determining the cellular state [299]. Determining mechanical properties of a cell during different stages of the disease progression could help to develop novel treatments by considering the role of mechanical factors into genetic and drug therapies [300]. As recently reviewed [301], there are several techniques for measuring cell mechanical properties, most of them requiring a mechanical stress (e.g., micropipette aspiration and atomic force microscopy). However, in this review, the focus is on rheological properties assessed using a mechanical stress based on acoustical shear wave propagation.

Grasland-Mongrain et al. [302] developed a novel method called optical microelastography, also labeled as "cell quake elastography". This technique uses a high frequency shear wave excitation and an optical microscope to assess cell elasticity. High frequency shear waves inside the cell are produced by a vibrating micropipette at a wavelength comparable to the cell's size. The wave propagation is captured optically by a high frame rate camera coupled to the microscope. The sampling rate of the camera is selected to avoid shear wave frequency aliasing with sufficient samples per wavelength to allow efficient speckle tracking. The spatial resolution of captured images should also be sufficient to track the shear wave speed from displacement maps (knowing the time elapsed between images). The proof-of-concept in [302] was made by using an ultrasound speckle tracking method adapted to optical images for obtaining displacement maps [303]. A passive elastography algorithm was used as a reconstruction method to obtain shear modulus images [304]. The passive elastography method was inspired by the seismology field [210], so the name "cell quake elastography" for this method. The main advantage of this technology compared with other cell elasticity methods is the time resolution of a few microseconds to

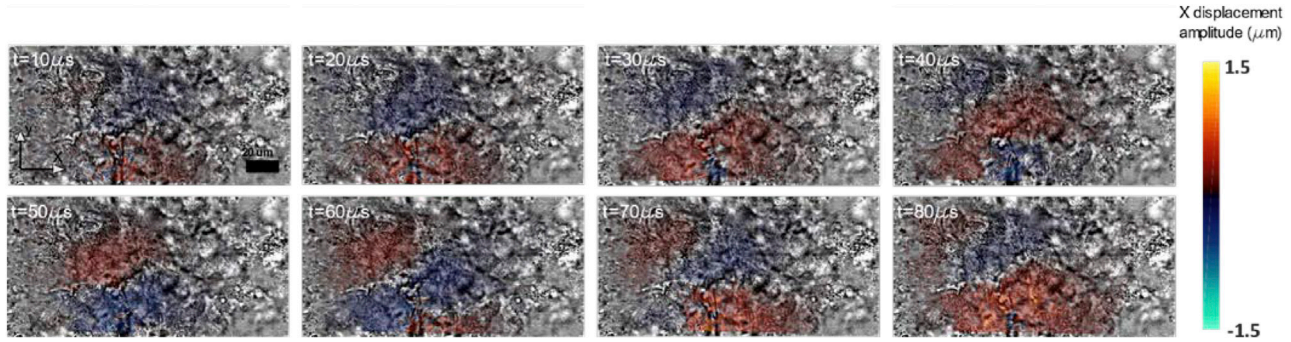

FIGURE 8 | Preliminary results on displacements of the shear wave propagation within adhesive cell clusters of macrophages RAW 264.7.

produce elasticity maps with a good spatial resolution, which may allow studying dynamic cellular processes.

First experiments were performed on mouse oocytes, making a shear wave inside the cell by a 15 kHz vibrating micropipette, and capturing the traveling wave optically at a 200,000 acquisition frame rate [302]. The sensitivity and spatial resolution of the technique allowed to distinguish the shear modulus of different regions/zones of a cell (**Figure 7**). The technique was recently applied on mouse macrophage-like RAW 264.7 cell clusters, Abelson leukemia virus-transformed cell line derived from mice, using a 18 kHz stimulation and a 100,000 frames per second image capturing rate. Shear wave displacement maps at 10 μs intervals are given in **Figure 8**. Future developments should aim at assessing the viscous component of single cells, likely using finite-elements modeling (FEM) reconstruction methods.

Optical Coherence Elastography Imaging

Optical coherence elastography (OCE) is a technique that can non-invasively assess tissue mechanical properties by measuring the localized deformation, strain or shear wave propagation properties inside a sample [305]. In OCE, a stimulation technique is utilized to load the tissue and its response is recorded with an OCT based detection method [306–308]. The high resolution structural images of OCE (1–10 μm *in-vivo*) provides it an advantage over the ultrasound or MRI modality [309], that stretches its potential for micron and submicron imaging of elastic properties of biological tissues. Microstructures of biological tissues can be quantified based on optical scattering properties of the tissue under investigation. OCE holds great potential for diagnosis of many clinical conditions and pathologies, particularly for detection and monitoring of cancers [310], cardiovascular diseases [311], and eye diseases [312].

While optical contrast signals are detected based on differences in two or multiple optical scattering events, the mechanical contrast requires only one scattering event to obtain an OCT signal. Thus, structural inclusions that cannot be detected by OCT can be revealed by OCE if a mechanical contrast exists for the inclusion. The first few studies in OCE development focused on static mechanical contact loading (i.e., no shear wave involved) [313, 314]. Later, the emergence of phase resolved OCT, which is detecting the interferometric phase information from complex OCT signals, enabled the assessment of tissue deformation with a high accuracy for tissue elasticity reconstruction [315–318]. A shear wave stimulus was involved in studies of [316] and [318].

The latest developments include OCE resolution to improve over the range from several microns to hundreds of microns [308, 319, 320]. The lowest range of OCE spatial resolution is similar to the cell quake elastography imaging method described earlier. In comparison, the spatial resolution of ultrasound or MRI elasticity imaging methods remain at a macroscopic level with a typical resolution of hundreds of micrometers to several millimeters, respectively [54, 191]. OCE is a great alternative to traditional elastography methods in terms of spatial resolution, acquisition speed, sub nanometer mechanical displacement sensitivity, but at the cost of a lower penetration depth into the probed tissue than ultrasound or MRI [308]. Additionally, shear wave OCE as a 3D imaging modality may enable its clinical applications in many areas, such as ophthalmology and cardiology using intravascular devices [321–323]. Shear wave based OCE has shown potential for measuring local elasticity changes of mouse brains [324, 325]. Details on these methods are given next.

Systems and Methods

An OCE system has two main components: a loading system that can deform the biological tissue, and an OCT imaging system for detection. Shear wave methods in OCE are relatively in the very early stages of development. Shear waves-based OCE utilize an excitation from a noncontact air-puff or air-coupled ultrasonic probe [326–328], or piezo-transducers (PZT) [320]. In addition, an OCT mechanism is then employed to detect the displacement field of generated shear waves. By monitoring the shear wave propagation in the sample, elasticity, shear wave speed, or the shear modulus can be quantified. Shear wave visualization was performed in tissue mimicking phantoms with phase sensitive optical coherence elastography [329]. Razani et al. [318] were one of the first to measure the shear wave speed and its associated properties with OCT phase maps. They utilized an external acoustic radiation force mechanism for excitation and a swept-source OCT system to acquire phase images. The central wavelength of the laser was 1,310 nm and the bandwidth was

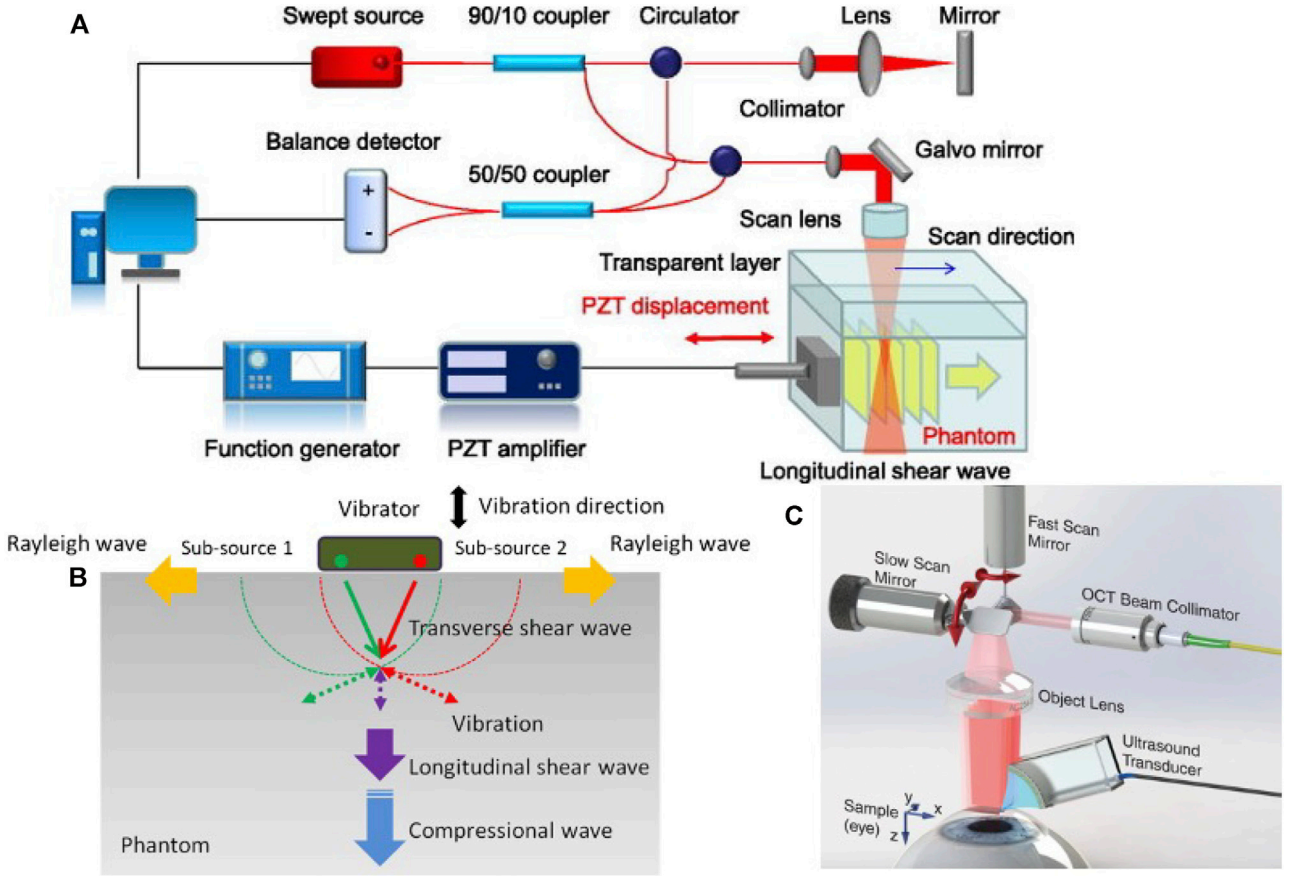

FIGURE 9 | (A) Schematic of the OCE system. The system employs a swept source OCT unit and a PZT excitation unit. The PZT unit induces displacements within the sample, and the OCT unit detects the signals and visualizes the longitudinal shear wave propagation. Reproduced with permission from [330]. Copyright 2017, AIP Publishing. **(B)** A representation of waves generated by the PZT unit: transverse shear waves, longitudinal shear waves, compressional waves, and Rayleigh waves. Reproduced with permission from [331]. Copyright 2017, AIP Publishing. **(C)** Schematic of the acoustic micro-tapping phase sensitive OCT imaging system developed by Ambrozinski et al. Reproduced with permission from [332]. Copyright 2016, Nature Research.

~110 nm. The system could register a lateral resolution of 13 μm in gelatin mixed with titanium dioxide phantoms. Images could be acquired at a depth of 3 mm. Song et al. [320] used a piezoelectric point loading to generate shear waves within samples. More recently, Zhu et al. [330, 331] developed a PZT-based system to induce longitudinal shear waves and they visualized the signals using OCT for the quantified mapping of shear moduli. A brief detail of their technique is presented next.

The OCE system included an OCT imaging unit and a PZT excitation unit, as shown in **Figure 9A**. Elastic waves were induced by a ring PZT actuator driven by a PZT amplifier. The vibrating mechanism of the PZT system could excite three types of waves in the sample under investigation: 1) Rayleigh waves, 2) compressional waves travelling from the top surface to the deep region, and 3) transverse and longitudinal shear waves traveling through the interior of the sample, as shown in **Figure 9B**. Rayleigh waves propagate at the surface of the sample. Compressional waves propagate parallel to the oscillation direction of the vibrator. Transverse shear waves propagate perpendicular to the displacement direction. Additionally, in the near field of the planar vibration source, which contained multiple sub-sources, a longitudinal shear wave much slower than the compressional wave also propagate along the displacement direction. This longitudinal shear wave is present due to the sum contributions of diffracted transverse shear waves [331]. These longitudinal shear waves could be visualized with the attached OCT imaging unit. The OCT system was based on a swept source at a central wavelength of 1,310 nm, and a wavelength tuning range of 141 nm. Axial and lateral resolutions of the employed OCT unit were 7.6 and 17.7 μm, respectively. The PZT unit utilized for excitation was driven by a function generator producing a sine wave cycle with a frequency of 1 kHz. The displacement observed in the near field was close to 10 μm.

As introduced above, noncontact shear wave imaging optical coherence tomography (SWI-OCT) system has been developed using a focused air-puff device for localized tissue deformation [333]. The non-contact mechanical excitation in a sample could be performed with a PZT transducer that was specially designed to launch an US beam through air that was focused onto the

air-medium interface. The reflection of the beam at this interface could produce significant acoustic radiation force toward the sample medium. This induced a transient displacement at the surface, including shear waves. The large difference in acoustic impedances of air and soft tissues could increase the efficiency of the acoustic energy conversion even to the extent of one hundred percent. Ambrozinski et al. [332] developed a non-invasive system that needed transient displacements to be only about 1 μm, and the acoustic pressure only a few kPa, which was within safety limits for clinical applications. This acoustic micro-tapping method had enabled 4D imaging of tissue stiffness by employing a focused air-coupled US to induce mechanical deformations at the boundary of a tissue [332]. A schematic representation of their system is shown in **Figure 9C**. In here, the cornea surface was aligned at the transducer focus and the US radiation push was sent through with a repetition period of 3 ms. The driving signal was having a bandwidth range of 0.95–1.05 MHz. The measured pressure amplitude at the transducer focus was about 7 kPa.

Wang et al. performed a quantitative biomechanical characterization of cardiac muscles and corneas using a noncontact SWI-OCT system [334, 335]. Shear waves had a frequency range of 0–2.5 kHz. This method employed a multi-wave imaging technique, where shear wave measurements in the tissue enabled mapping of the mechanical contrast in elastograms, and the OCT unit enabled improving the imaging resolution from a millimeter scale to a micron scale [334]. The system was capable of simultaneously providing structural images with depth wise maps of the tissue stiffness [335]. Recently, a confocal air-coupled US probe could also be co-focused with a phase-sensitive OCT system to generate elastic waves up to a 4 kHz frequency for quantitative elastography [336]. These noncontact excitation methods have found wide applications in ophthalmology and dermatology [337–339].

Spatial resolution in dynamic shear wave based OCE is governed by temporal and spatial characteristics of mechanical waves rather than optical waves. Hence, the mechanical resolution in dynamic OCE is different from the usual optical resolution of OCT systems [57]. Spatial resolution ideally should match the spatial resolution of the detection system, however, propagating mechanical waves undergo mode conversions at tissue interfaces causing artifacts in the elasticity image. The geometry of the tissue interface and its elasticity contrast can produce complex propagating fields near the tissue boundary affecting both the spatial resolution and contrast of the final reconstructed image [57].

Recent dynamic OCE systems provided elasticity information from local group velocity measurements [321, 330, 339], however, the complex geometry of bounded tissues like the cornea may not reflect a simple relationship between group velocity and elasticity [338]. Dynamic OCE has been successfully utilized in elasticity mapping of the cornea using noncontact excitation methods based on air-puffs and acoustic micro tapping [332, 333, 340–342]. Inversion of moduli from experimental data, especially in the case of bounded and anisotropic tissues such as cornea, is a challenging and complicated process in dynamic elastography. Recently, a nearly-incompressible transverse isotropic (NITI) model addressed this challenge and characterized corneal biomechanics while accounting for corneal microstructure and anisotropy, and presented a more accurate model for cornea shear moduli computation [337]. Viscosity assessment in shear wave OCE is in its early phase of development. Proposed methods used shear wave frequency dispersion [343–346], storage and loss moduli using a rheological model [347], and the elastic wave attenuation [345].

A trade-off in OCE is its reduced depth of field while evolving for higher resolution measurements due to the requirement of higher numerical aperture for such systems. On the other hand, the ability to measure and record depth scans with a single spectral acquisition can be used as an advantageous feature to enable phase-sensitive displacement measurements. Of course, the tissue penetration attained with OCE, although sufficient for numerous applications, is not comparable to ultrasound or MRI elastography methods. Song et al. implemented a beam-steering US as a wave source for shear wave optical coherence elastography of retinal and choroidal tissues within a porcine eyes ball *ex vivo*. Shear wave propagation imaged on a porcine retina by their system is shown in **Figure 10** [323].

Photoacoustic Elastography

Photoacoustic elastography (PAE) research is rapidly growing due to its potential and promising features of clinical interest [348–350]. PAE can exhibit a mechanical contrast in biological tissues while also providing high spatial resolution images and an excellent penetration depth compared to commercially available optical imaging modalities [351]. It has the promise to provide great scalability, ranging from cellular levels to entire body with multiple resolution levels. Recent studies have demonstrated recovery of mechanical properties of biological tissues using PAE [352–355]. Several studies demonstrated computation of elastic properties of soft tissues [354, 356–359]. Nevertheless, clinical translation of PAE is still far way for research studies to accomplish, the development of the PAE technology has shown the potential to be used in life threatening diseases, such as breast and prostate cancers, and brain tumors [350, 360]. Photoacoustic elastography can be used for mapping elastic properties of diseased tissues with highly vascularized structures, such as carcinoma and glioblastoma [351]. Most PAE studies have focused on qualitative imaging and quantitative PAE is still a challenge. Moreover, PAE using propagating shear waves still need to be clearly addressed. A recent study by Wang et al. did develop a PA viscoelasticity technique for quantitative imaging of liver cirrhosis based on a PA shear wave model [359]. This viscoelasticity imaging model was inspired by the acoustic radiation force impulse (ARFI) technique (see *Ultrasound Shear Wave Elastography*). In this model, a laser beam was focused into a tissue that resulted in the tissue thermal expansion and a PA pressure field was generated. The pressure field induced a localized ultrasound impulse similar to ARFI, and subsequently a tissue displacement field could be observed. The study assumed that these forward propagating PA waves could be modeled using shear wave equations.

As a summary of methods addressed in this review, **Table 4** compares photoacoustic elastography with other elastography modalities in term of performance.

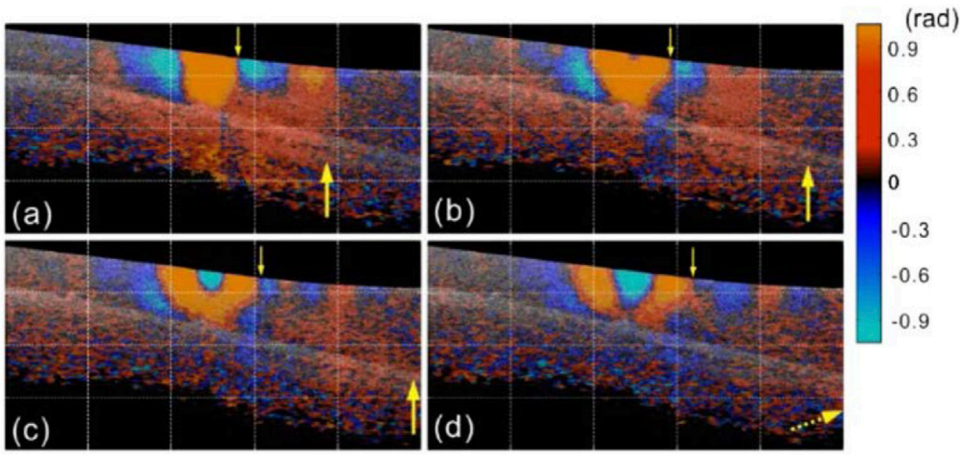

FIGURE 10 | Images of shear wave propagation in a porcine retina generated with a single acoustic radiation force ultrasound push. The images are taken snapshots at **(A)** 0.2, **(B)** 0.25, **(C)** 0.3, and **(D)** 0.35 ms after the push. Lateral scale: 0.5 mm/div; axial (depth) scale: 0.25 mm/div. Reproduced with permission from [323]. Copyright 2015, OSA Publishing.

TABLE 4 | Overview and comparison of various elastography technologies.

Modality\features	Manual palpation	USE	MRE	OCE	PAE
Interrogating mechanism	External assessment by hand	Acoustic waves	Acoustic waves	Usually optical or acoustic waves	Optical waves (near infrared laser)
Detection	Sense of touch	Acoustic waves	Magnetic field gradients	Optical waves (near infrared)	Acoustic waves
Tissue property	Mechanical strain	Acoustic impedance	Tissue nuclear property	Optical absorption	Optical absorption/acoustic impedance
Spatial resolution	Not deterministic	~500 μm	~1 mm (clinical 3T machine) - 500 μm (preclinical 7T machine)	~ μm	~50 μm
Imaging depth	Not deterministic	~ cm(s) (whole body)	~ cm(s) (whole body)	~1 mm	~ cm(s)

USE, ultrasound elastography; MRE, magnetic resonance elastography; OCE, optical coherence elastography; PAE, photoacoustic elastography.

CHALLENGES AND PERSPECTIVES

Ultrasound Shear Wave Elastography

Many notable ultrasound elastography methods have been translated into clinical applications, and adopted by clinicians for diagnosis of several organs, as introduced in *Applications*. A limitation lay in the depth of SW penetration due to attenuation, especially for the diagnosis of liver fibrosis and steatosis, which could result in unsuccessful measurements with large patients or patients with ascites [31]. Note that SW attenuation is a concern for any shear wave elastography method. Consequently, measurements on superficial regions showed a higher success rate, such as the diagnosis of breast lesions and tumors. Another limitation lies in the assumption often used in shear wave elastography; notably considering the tissue as isotropic and homogeneous. Certain tissues such as muscles or tendons do not respect the isotropy hypothesis and are rather considered as anisotropic or transverse isotropic media. To answer this problem, teams have developed stiffness tensors for assessing shear wave propagation and for evaluating mechanical properties in several directions [161, 361], even in three dimensions [162]. Bones, brains, or lungs are parts of the body that can be considered porous and for which the assumption of homogeneity is limited. Poroelasticity based on the estimation of the temporal response of tissues to compression [15, 362–364] is a technique derived from strain elastography. Although a little off topic because it does not use shear waves, its development in the characterization of tumors is promising [364, 365]. Other applications, such as the characterization of muscles, Achilles tendons, the cardiovascular system, and lymph nodes [110, 366–368], have shown good results that reflected the difference between normal and abnormal tissues.

At present, the measurement of the tissue elasticity has dominated the field, and technologies, such as the transient elastography, SSI, ARFI, and comb push ARFs are available on clinical scanners [67, 110, 144, 369–376]. In fact, most manufacturers have today a shear wave elastography package for clinical use, and the spatial resolution of those elastography systems are as good as ultrasound B-mode imaging. However for measurements on more complex tissues, such as anisotropic,

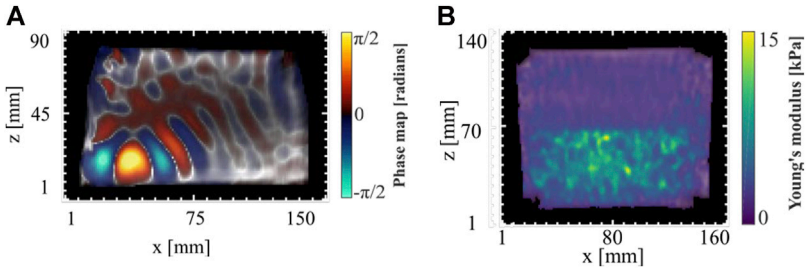

FIGURE 11 | Preliminary results of Lorentz force MRE in gel phantoms. **(A)** Phase map due to the propagation of displacements induced by a Lorentz force. **(B)** Young's modulus map of a heterogeneous phantom constructed from the Lorentz force induced motion.

layered, or near close to interface results should be taken with caution. The characterization of human tissue viscoelasticity without using a rheological model, and studies on viscosity, anisotropy, porosity, and nonlinearity, are important topics in development [23, 51, 377–383]. While those innovations have not yet received clinical approval, further validation with robustness and reproducibility results should allow manufacturers to consider these biomarkers. New applications of SW ultrasound elastography are also in developments. Studies pointed out that the measurement of the elastic property could be used to monitor thermal ablation [374, 384, 385].

Magnetic Resonance Shear Wave Elastography

Magnetic resonance elastography has been proven successful and robust in a broad range of applications, from clinical diagnosis of liver diseases [386] to brain [280], and breast [387] pathologies. However, generalization of MRE in clinics is impacted by the scan time required for the acquisition of complete data sets necessary for accurate reconstruction. Clinical sequences currently acquire one component of the motion field at one frequency, and rely on a 1D direct inversion assuming isotropy, incompressibility, local homogeneity, and pure elasticity. This package is fast and guaranties results. Mechanical solicitation of the tissue under multi-frequency loads may be a first step into the characterization of tissue viscoelastic responses by providing valuable information on the frequency dependent biomechanics in pathological cases [201]. Motion encoding may also reach a limit at high frequencies in the case of oscillating gradients due to peripheral nerve stimulation [388]. The actuation regime also determines the physics to consider for inferring mechanical parameters from experimental datasets [184]. An elegant avenue circumventing the use of external actuators is intrinsic actuation from low frequency heart beats along with poroelastic modeling of the tissue [211]. Along the same lines, natural vibrations in the brain have been exploited using the novel passive elastography technique based on time reversal concepts to quantify the vibration wavelengths, assumed to be related to brain stiffness [210]. A potential solution to shear wave attenuation in soft viscoelastic tissues may be to place motion sources closer to the region of interest. This may be achieved using ultrasound transducers generating an acoustic radiation force impulse (ARFI) along with MRE acquisition [207, 389]. Alternatively, a promising approach that may prove feasible with clinical MRI scanner is Lorentz force elastography for *in situ* actuation at different frequencies [390, 391]. An elasticity reconstruction obtained using a Lorentz force and a clinical MRI scanner is displayed in **Figure 11**, in the case of a gel phantom.

On a similar note, localized motion generation using ARFI has been employed with MRE to measure elasticity changes during high intensity focused ultrasound ablations in *ex-vivo* porcine muscle samples [392]. Such monitoring requires sufficient displacement amplitude [393]. Assessment of stiffness changes due to ablation or percutaneous procedures has been performed both during [394, 395], and separately before and after ablation [396], all cases reporting a stiffness increase after the intervention.

On the acquisition side, significant amount of effort has been put into MR sequence developments to reduce scan time while preserving 3D motion encoding and signal amplitude. Although equipping an MR sequence with bipolar magnetic field gradients prevails, recent implementations took advantage of MR sequence inherent gradients to encode motion, thus keeping the timing shorter than conventional use of MEG [397]. As in any MRI scan, artefacts may occur due to patient motion. Sequence dependent artefacts include and are not restricted to signal loss in GRE sequences due to irregular geometries, and associated magnetic field inhomogeneity and distortion in echo-planar sequences. Specific to MRE, phase wrapping occurs when motion cannot be encoded in the [-π, π] range leading to phase jumps within this range. Three solutions appear and consist in either decreasing the gradient sensitivity, decreasing the motion generator strength, or using a phase unwrapping algorithm. Whilst a weakness of MRE may be viewed as a lack of universal protocol applicable to any organ, its strength resides in the capacity of providing usable data in multiple cases owing to various hardware and MR sequences, and in the availability of physical models to process produced experimental data for stiffness estimation. This technology is still mainly used in the context of clinical research, and additional validations might be required for robust viscosity, porosity, and anisotropy assessments.

Optical Shear Wave Elastography

Cellular Shear Wave Elastography

Although the optical microelastography technique has an unprecedented high temporal resolution with the capability of

producing elasticity images, its spatial resolution is not as good as other rheology methods, such as atomic force microscopy. The spatial resolution of this technique is currently limited to 10 μm, approximately, but it could be improved to resolutions close to optical microscopy (≈1 μm) by utilizing a higher stimulus frequency and by improvements in the reconstruction process. This technique is currently limited to elasticity measurements but viscosity might become available through FEM modeling, or by considering shear wave attenuation [50].

More improvements need to be done beyond solving limitations mentioned above. The mechanical behavior of the cell should be further investigated in a range of frequencies. One remaining difficulty is the absence of good standard rheology method to validate the microelastography technique at frequencies in the kHz range. This makes it difficult to compare results from different techniques on a similar cell type. Other reasons for the lack of concordance of results, obtained with different cell elasticity technologies, were recently addressed [398] and apply to the reported microelastography method. Recent developments might allow using mechanically stable microgel bead to compare different cell elasticity methods [399], which may reduce variability when performing such comparisons at different (non-overlapping) frequencies.

Also, to make these techniques more applicable and practical for biologists, and to promote using cell mechanics as a biomarker, improvements are required for the technique to be automatic, high throughput while being robust, accurate, and sensitive with high time and space resolutions. This might be done by coupling the optical microelastography technique with other methods, such as microfluidics with a high throughput [400, 401].

Optical Coherence Elastography

Higher resolution OCE may face computational challenges due to the fact that the speckle decorrelation length scales with the speckle size [402, 403]. This would reduce the maximum displacement that can be measured between frames. Many studies have made progress to further demonstrate substantial improvements in resolution [404, 405]. High resolution OCE systems can be used to assess mechanical properties of cells and a few preliminary studies have showed this potential [404, 406]. These are relatively new developments and the hope remains that OCE would be able to characterize cell aggregates [305], with penetration depth going up to several hundred microns, whilst maintaining a sub-cellular scale resolution.

There has been several studies on elastogram image reconstruction in OCE by inverse problem approaches [407]. Sridhar et al. [408] used an inverse problem approach to understand how stromal tissues affect the broad spectrum of the viscoelastic response [409], by minimizing the mean squared error between computed and measured displacements. Different methods to constrain the optimization algorithm has been summarized by [410], in the context of ultrasound strain elastography. Basic principles are also applicable to OCE. However, one challenge that often prevails in these scenarios is the optimization of the regularization parameter for efficient reconstruction, especially in the context of *in vivo* experiments.

Another area of interest representing some challenges is the quantitative assessment of tissue viscoelastic properties with OCE. This research is still in its early years acknowledging the fact that the viscosity is not accounted for in the simple approach [411], but hopefully with the development of new models, OCE would be able to convert elastic wave speed and attenuation into quantitative values for clinical diagnosis based on tissue viscoelasticity.

Despite several advancements, very few studies have been done in the area of validation of performance. This would require phantoms that are developed for optics rather than mechanics [305]. Rigorous assessment of sensitivity and specificity for diagnostic applications would be required for translating the method to the clinics.

Photoacoustic Elastography

Photoacoustic elastography imaging is relatively a new development and it still needs to overcome many challenges. The PA signal contrast detected by ultrasound transducers is low due to lower variation in the tissue elasticity distribution in comparison to the optical absorption coefficient. This can potentially be overcome by additionally employing an ultrasound modulation of the laser pulse to provide external mechanical simulation of the tissue [412]. In addition, elasticity can also be estimated from the resonance frequency of the tissue material observed in the measurement of PA signal strength against the operating frequency of the external (ultrasound) mechanical stimulation [412, 413]. Another challenge is the development of quantitative PAE imaging systems, as the first few studies in the field reported only qualitative assessment of elastic properties. However, Hai et al. were the first to develop a quantitative PAE system [414]. It would also be interesting to detect the contrast in the PA signal due to elastic property variation separately from that of other parameters (including the optical absorption coefficient). Grasland-Mongrain et al. generated shear waves in soft tissues in ablative and thermoelastic regimes with a 532 nm Nd:YAG laser [415]. However, it remained a challenge to keep the laser beam energy within safety limits for use in biomedical applications. This can potentially be overcome by use of other types of laser or by emission of the high energy laser beam onto a protective absorbing layer, such as a black sheet, that can cover the tissue externally. In conclusion, PAE is still in the beginning phase of its development compared to ultrasound, MRI or OCT elastography, and there definitely remains scope for many promising improvements to increase its potential for various imaging applications.

AUTHOR CONTRIBUTIONS

HL supervised and structured the review, wrote the introduction and the conclusion, contributed to the section on the generation and detection of shear waves, reviewed, and edited the final document. GF co-supervised and structured the review, wrote the magnetic resonance elastography and the general concepts on shear wave elastography sections, reviewed, and edited the final document. MB wrote the optical coherence elastography imaging and the photoacoustic elastography sections. ZQ wrote the

characterization of tissue viscoelasticity section, and contributed to the generation and detection of shear waves section. SG wrote the cellular shear wave elastography section. LY wrote the viscoelasticity reconstruction section and applications in ultrasound. GB wrote the clinical applications of ultrasound shear wave elastography section. IR contributed to the section on ultrasound shear wave elastography. GC received the invitation to provide this review, contributed to the general supervision of all co-authors, did reviewing of all sections of this document for final approval, and provided editing and funding.

FUNDING

Financial support for this research on shear wave elastography was provided by the Canadian Institutes of Health Research (#273738, #301520, #142334, #95288), Natural Sciences and Engineering Research Council of Canada (#503381, #365656), Fonds de Recherche du Québec (#263591), Fonds de Recherche du Québec sur la Nature et les Technologies (#174387), Cancer Research Society (#19075), and Quebec Bioimaging Network (Strategic Program).

REFERENCES

1. Sarvazyan AP, Skovoroda AR, Emelianov SY, Fowlkes JB, Pipe JG, Adler RS, et al. Biophysical Bases of Elasticity Imaging. *Acoust Imaging* (1995) 21: 223–40. doi:10.1007/978-1-4615-1943-0_23
2. Zhang M, Castaneda B, Wu Z, Nigwekar P, Joseph JV, Rubens DJ, et al. Congruence of Imaging Estimators and Mechanical Measurements of Viscoelastic Properties of Soft Tissues. *Ultrasound Med Biol* (2007) 33(10):1617–31. doi:10.1016/j.ultrasmedbio.2007.04.012
3. Shahmirzadi D, Bruck HA, and Hsieh AH. Measurement of Mechanical Properties of Soft Tissues *In Vitro* under Controlled Tissue Hydration. *Exp Mech* (2012) 53(3):405–14. doi:10.1007/s11340-012-9644-y
4. Estermann S-J, Pahr DH, and Reisinger A. Hyperelastic and Viscoelastic Characterization of Hepatic Tissue under Uniaxial Tension in Time and Frequency Domain. *J Mech Behav Biomed Mater* (2020) 112:104038. doi:10.1016/j.jmbbm.2020.104038
5. Vappou J, Breton E, Choquet P, Goetz C, Willinger R, and Constantinesco A. Magnetic Resonance Elastography Compared with Rotational Rheometry for *In Vitro* Brain Tissue Viscoelasticity Measurement. *Magn Reson Mater Phy* (2007) 20(5):273–8. doi:10.1007/s10334-007-0098-7
6. Klatt D, Friedrich C, Korth Y, Vogt R, Braun J, and Sack I. Viscoelastic Properties of Liver Measured by Oscillatory Rheometry and Multifrequency Magnetic Resonance Elastography. *Biorheology* (2010) 47(2):133–41. doi:10.3233/bir-2010-0565
7. Chatelin S, Oudry J, Périchon N, Sandrin L, Allemann P, Soler L, et al. *In Vivo* liver Tissue Mechanical Properties by Transient Elastography: Comparison with Dynamic Mechanical Analysis. *Biorheology* (2011) 48(2):75–88. doi:10.3233/bir-2011-0584
8. Dittmann F, Hirsch S, Tzschätzsch H, Guo J, Braun J, and Sack I. *In Vivo* wideband Multifrequency MR Elastography of the Human Brain and Liver. *Magn Reson Med* (2016) 76(4):1116–26. doi:10.1002/mrm.26006
9. Lin H, Shen Y, Chen X, Zhu Y, Zheng Y, Zhang X, et al. Viscoelastic Properties of normal Rat Liver Measured by Ultrasound Elastography: Comparison with Oscillatory Rheometry. *Biorheology* (2016) 53(5-6): 193–207. doi:10.3233/BIR-16091
10. Ormachea J, and Parker KJ. Elastography Imaging: the 30 Year Perspective. *Phys Med Biol* (2020) 65:24TR06. doi:10.1088/1361-6560/abca00
11. D Royer, E. Dieulesaint, and SSB Media, editors. *Elastic Waves in Solids I: Free and Guided Propagation*. Springer Science & Business Media (1999).
12. Skovoroda AR, Emelianov SY, Lubinski MA, Sarvazyan AP, and O'Donnell M. Theoretical Analysis and Verification of Ultrasound Displacement and Strain Imaging. *IEEE Trans Ultrason Ferroelect., Freq Contr* (1994) 41(3): 302–13. doi:10.1109/58.285463
13. Sarvazyan AP, Rudenko OV, Swanson SD, Fowlkes JB, and Emelianov SY. Shear Wave Elasticity Imaging: a New Ultrasonic Technology of Medical Diagnostics. *Ultrasound Med Biol* (1998) 24(9):1419–35. doi:10.1016/s0301-5629(98)00110-0
14. Özkaya N, Leger D, Goldsheyder D, and Nordin M. *Fundamentals of Biomechanics: Equilibrium, Motion, and Deformation*. Springer (2016).
15. Konofagou EE, Harrigan TP, Ophir J, and Krouskop TA. Poroelastography: Imaging the Poroelastic Properties of Tissues. *Ultrasound Med Biol* (2001) 27(10):1387–97. doi:10.1016/s0301-5629(01)00433-1
16. Biot MA. Theory of Propagation of Elastic Waves in a Fluid-Saturated Porous Solid. I. Low-Frequency Range. *The J Acoust Soc America* (1956) 28(2): 168–78. doi:10.1121/1.1908239
17. Biot MA. Theory of Propagation of Elastic Waves in a Fluid-Saturated Porous Solid. II. Higher Frequency Range. *J Acoust Soc America* (1956) 28(2):179–91. doi:10.1121/1.1908241
18. Cheng AHD, Badmus T, and Beskos DE. Integral Equation for Dynamic Poroelasticity in Frequency Domain with BEM Solution. *J Eng Mech* (1991) 117(5):1136–57. doi:10.1061/(asce)0733-9399(1991)117:5(1136)
19. Hirsch S, Braun J, and Sack I. *Magnetic Resonance Elastography - Physical Background and Medical Applications*. Wiley VCH (2017).
20. Romano A, Scheel M, Hirsch S, Braun J, and Sack I. *In Vivo* waveguide Elastography of white Matter Tracts in the Human Brain. *Magn Reson Med* (2012) 68(5):1410–22. doi:10.1002/mrm.24141
21. Meyers MA, and Chawla KK. *Mechanical Behavior of Materials*. New York: Cambridge University Press (2008). doi:10.1017/cbo9780511810947
22. Schiessel H, Metzler R, Blumen A, and Nonnenmacher TF. Generalized Viscoelastic Models: Their Fractional Equations with Solutions. *J Phys A: Math Gen* (1995) 28(23):6567–84. doi:10.1088/0305-4470/28/23/012
23. Rus G, Faris IH, Torres J, Callejas A, and Melchor J. Why Are Viscosity and Nonlinearity Bound to Make an Impact in Clinical Elastographic Diagnosis? *Sensors* (2020) 20(8):2379. doi:10.3390/s20082379
24. Qiang B, Brigham JC, Aristizabal S, Greenleaf JF, Zhang X, and Urban MW. Modeling Transversely Isotropic, Viscoelastic, Incompressible Tissue-like Materials with Application in Ultrasound Shear Wave Elastography. *Phys Med Biol* (2015) 60(3):1289–306. doi:10.1088/0031-9155/60/3/1289
25. Greenwood MS, and Bamberger JA. Measurement of Viscosity and Shear Wave Velocity of a Liquid or Slurry for On-Line Process Control. *Ultrasonics* (2002) 39(9):623–30. doi:10.1016/s0041-624x(02)00372-4
26. Madsen EL, Sathoff HJ, and Zagzebski JA. Ultrasonic Shear Wave Properties of Soft Tissues and Tissuelike Materials. *J Acoust Soc America* (1983) 74(5): 1346–55. doi:10.1121/1.390158
27. Kelly P. *Solid Mechanics Part I: An Introduction to Solid Mechanics*. Solid mechanics lecture notes (2013).
28. Schmitt C, Hadj Henni A, and Cloutier G. Characterization of Blood Clot Viscoelasticity by Dynamic Ultrasound Elastography and Modeling of the Rheological Behavior. *J Biomech* (2011) 44(4):622–9. doi:10.1016/j.jbiomech.2010.11.015
29. Serra-Aguila A, Puigoriol-Forcada JM, Reyes G, and Menacho J. Viscoelastic Models Revisited: Characteristics and Interconversion Formulas for Generalized Kelvin-Voigt and Maxwell Models. *Acta Mech Sin* (2019) 35(6):1191–209. doi:10.1007/s10409-019-00895-6
30. Greenleaf JF, Fatemi M, and Insana M. Selected Methods for Imaging Elastic Properties of Biological Tissues. *Annu Rev Biomed Eng* (2003) 5:57–78. doi:10.1146/annurev.bioeng.5.040202.121623
31. Parker KJ, Doyley MM, and Rubens DJ. Corrigendum: Imaging the Elastic Properties of Tissue: the 20 Year Perspective. *Phys Med Biol* (2012) 57(16): 5359–60. doi:10.1088/0031-9155/57/16/5359
32. Chen S, Fatemi M, and Greenleaf JF. Remote Measurement of Material Properties from Radiation Force Induced Vibration of an Embedded Sphere. *J Acoust Soc America* (2002) 112(3):884–9. doi:10.1121/1.1501276
33. Gao L, Parker KJ, Lerner RM, and Levinson SF. Imaging of the Elastic Properties of Tissue-A Review. *Ultrasound Med Biol* (1996) 22(8):959–77. doi:10.1016/s0301-5629(96)00120-2

34. Li SP, Zhao G, and Chen HY. The Relationship between Steady Shear Viscosity and Complex Viscosity. *J dispersion Sci Technol* (2005) 26(4): 415–9. doi:10.1081/dis-200054555
35. Barnes HA, Hutton JF, and Walters K *An Introduction to Rheology*. Elsevier (1989).
36. Ophir J, Alam SK, Garra B, Kallel F, Konofagou E, Krouskop T, et al. Elastography: Ultrasonic Estimation and Imaging of the Elastic Properties of Tissues. *Proc Inst Mech Eng H* (1999) 213(3):203–33. doi:10.1243/0954411991534933
37. Lewandowski R, and Chorążyczewski B. Identification of the Parameters of the Kelvin–Voigt and the Maxwell Fractional Models, Used to Modeling of Viscoelastic Dampers. *Comput Structures* (2010) 88(1-2):1–17. doi:10.1016/j.compstruc.2009.09.001
38. Cheeke JDN *Fundamentals and Applications of Ultrasonic Waves*. CRC Press (2017). doi:10.1201/b12260
39. Lerner RM, Parker KJ, Holen J, Gramiak R, and Waag RC. Sono-elasticity: Medical Elasticity Images Derived from Ultrasound Signals in Mechanically Vibrated Targets. *Acoust Imaging* (1988) 317–27. doi:10.1007/978-1-4613-0725-9_31
40. Yamakoshi Y, Sato J, and Sato T. Ultrasonic Imaging of Internal Vibration of Soft Tissue under Forced Vibration. *IEEE Trans Ultrason Ferroelect., Freq Contr* (1990) 37(2):45–53. doi:10.1109/58.46969
41. Catheline S, Wu F, and Fink M. A Solution to Diffraction Biases in Sonoelasticity: the Acoustic Impulse Technique. *J Acoust Soc America* (1999) 105(5):2941–50. doi:10.1121/1.426907
42. Wu Z, Taylor LS, Rubens DJ, and Parker KJ. Sonoelastographic Imaging of Interference Patterns for Estimation of the Shear Velocity of Homogeneous Biomaterials. *Phys Med Biol* (2004) 49(6):911–22. doi:10.1088/0031-9155/49/6/003
44. Fatemi M, and Greenleaf JF. Ultrasound-stimulated Vibro-Acoustic Spectrography. *Science* (1998) 280(5360):82–5. doi:10.1126/science.280.5360.82
45. Chen S, Fatemi M, and Greenleaf JF. Quantifying Elasticity and Viscosity from Measurement of Shear Wave Speed Dispersion. *J Acoust Soc America* (2004) 115(6):2781–5. doi:10.1121/1.1739480
46. Chen S, Urban MW, Pislaru C, Kinnick R, Zheng Y, Yao A, et al. Shearwave Dispersion Ultrasound Vibrometry (SDUV) for Measuring Tissue Elasticity and Viscosity. *IEEE Trans Ultrason Ferroelectr Freq Control* (2009) 56(1): 55–62. doi:10.1109/TUFFC.2009.1005
47. Bercoff J, Tanter M, and Fink M. Supersonic Shear Imaging: A New Technique for Soft Tissue Elasticity Mapping. *IEEE Trans Ultrason Ferroelect., Freq Contr* (2004) 51(4):396–409. doi:10.1109/tuffc.2004.1295425
48. McAleavey SA, Menon M, and Orszulak J. Shear-modulus Estimation by Application of Spatially-Modulated Impulsive Acoustic Radiation Force. *Ultrason Imaging* (2007) 29(2):87–104. doi:10.1177/016173460702900202
49. Song P, Zhao H, Manduca A, Urban MW, Greenleaf JF, and Chen S. Comb-push Ultrasound Shear Elastography (CUSE): a Novel Method for Two-Dimensional Shear Elasticity Imaging of Soft Tissues. *IEEE Trans Med Imaging* (2012) 31(9):1821–32. doi:10.1109/tmi.2012.2205586
50. Kazemirad S, Bernard S, Hybois S, Tang A, and Cloutier G. Ultrasound Shear Wave Viscoelastography: Model-independent Quantification of the Complex Shear Modulus. *IEEE Trans Ultrason Ferroelect., Freq Contr* (2016) 63(9): 1399–408. doi:10.1109/tuffc.2016.2583785
51. Bhatt M, Moussu MAC, Chayer B, Destrempes F, Gesnik M, Allard L, et al. Reconstruction of Viscosity Maps in Ultrasound Shear Wave Elastography. *IEEE Trans Ultrason Ferroelect., Freq Contr* (2019) 66(6):1065–78. doi:10.1109/tuffc.2019.2908550
52. Sandrin L, Catheline S, and Fink M. Transient Elastography in Biological Tissues. *J Acoust Soc America* (1999) 105(2):1014–5. doi:10.1121/1.425852
53. Sandrin L, Catheline S, Tanter M, Hennequin X, and Fink M. Time-resolved Pulsed Elastography with Ultrafast Ultrasonic Imaging. *Ultrason Imaging* (1999) 21(4):259–72. doi:10.1177/016173469902100402
54. Zemzemi C, Zorgani A, Daunizeau L, Belabhar S, Souchon R, and Catheline S. Super-resolution Limit of Shear-Wave Elastography. *EPL (Europhysics Letters)* (2020) 129(3). doi:10.1209/0295-5075/129/34002
55. Deffieux T, Gennisson J-L, Bercoff J, and Tanter M. On the Effects of Reflected Waves in Transient Shear Wave Elastography. *IEEE Trans Ultrason Ferroelect., Freq Contr* (2011) 58(10):2032–5. doi:10.1109/tuffc.2011.2052
56. Lipman SL, Rouze NC, Palmeri ML, and Nightingale KR. Evaluating the Improvement in Shear Wave Speed Image Quality Using Multidimensional Directional Filters in the Presence of Reflection Artifacts. *IEEE Trans Ultrason Ferroelect., Freq Contr* (2016) 63(8):1049–63. doi:10.1109/tuffc.2016.2558662
57. Kirby MA, Zhou K, Pitre JJ, Gao L, Li DS, Pelivanov IM, et al. Spatial Resolution in Dynamic Optical Coherence Elastography. *J Biomed Opt* (2019) 24(9):1–16. doi:10.1117/1.jbo.24.9.096006
58. Chen X, Shen Y, Zheng Y, Lin H, Guo Y, Zhu Y, et al. Quantification of Liver Viscoelasticity with Acoustic Radiation Force: a Study of Hepatic Fibrosis in a Rat Model. *Ultrasound Med Biol* (2013) 39(11):2091–102. doi:10.1016/j.ultrasmedbio.2013.05.020
59. Gennisson J-L, Deffieux T, Fink M, and Tanter M. Ultrasound Elastography: Principles and Techniques. *Diagn Interv Imaging* (2013) 94(5):487–95. doi:10.1016/j.diii.2013.01.022
60. Nightingale K, McAleavey S, and Trahey G. Shear-wave Generation Using Acoustic Radiation Force: *In Vivo* and *Ex Vivo* Results. *Ultrasound Med Biol* (2003) 29(12):1715–23. doi:10.1016/j.ultrasmedbio.2003.08.008
61. Tang A, Cloutier G, Szeverenyi NM, and Sirlin CB. Ultrasound Elastography and MR Elastography for Assessing Liver Fibrosis: Part 1, Principles and Techniques. *Am J Roentgenology* (2015) 205(1):22–32. doi:10.2214/ajr.15.14552
62. Tang A, Cloutier G, Szeverenyi NM, and Sirlin CB. Ultrasound Elastography and MR Elastography for Assessing Liver Fibrosis: Part 2, Diagnostic Performance, Confounders, and Future Directions. *Am J Roentgenology* (2015) 205(1):33–40. doi:10.2214/ajr.15.14553
63. Sandrin L, Fourquet B, Hasquenoph J-M, Yon S, Fournier C, Mal F, et al. Transient Elastography: a New Noninvasive Method for Assessment of Hepatic Fibrosis. *Ultrasound Med Biol* (2003) 29(12):1705–13. doi:10.1016/j.ultrasmedbio.2003.07.001
64. Arena U, Vizzutti F, Corti G, Ambu S, Stasi C, Bresci S, et al. Acute Viral Hepatitis Increases Liver Stiffness Values Measured by Transient Elastography. *Hepatology* (2007) 47(2):380–4. doi:10.1002/hep.22007
65. Castéra L, Bernard P-H, Le Bail B, Foucher J, Trimoulet P, Merrouche W, et al. Transient Elastography and Biomarkers for Liver Fibrosis Assessment and Follow-Up of Inactive Hepatitis B Carriers. *Aliment Pharmacol Ther* (2011) 33(4):455–65. doi:10.1111/j.1365-2036.2010.04547.x
66. Gennisson J-L, Lerouge S, and Cloutier G. Assessment by Transient Elastography of the Viscoelastic Properties of Blood during Clotting. *Ultrasound Med Biol* (2006) 32(10):1529–37. doi:10.1016/j.ultrasmedbio.2006.06.008
67. Castéra L, Vergniol J, Foucher J, Le Bail B, Chanteloup E, Haaser M, et al. Prospective Comparison of Transient Elastography, Fibrotest, APRI, and Liver Biopsy for the Assessment of Fibrosis in Chronic Hepatitis C. *Gastroenterology* (2005) 128(2):343–50. doi:10.1053/j.gastro.2004.11.018
68. Frulio N, and Trillaud H. Ultrasound Elastography in Liver. *Diagn Interv Imaging* (2013) 94(5):515–34. doi:10.1016/j.diii.2013.02.005
69. Gerber L, Kasper D, Fitting D, Knop V, Vermehren A, Sprinzl K, et al. Assessment of Liver Fibrosis with 2-D Shear Wave Elastography in Comparison to Transient Elastography and Acoustic Radiation Force Impulse Imaging in Patients with Chronic Liver Disease. *Ultrasound Med Biol* (2015) 41(9):2350–9. doi:10.1016/j.ultrasmedbio.2015.04.014
70. Nightingale K. Acoustic Radiation Force Impulse (ARFI) Imaging: A Review. *Curr Med Imaging Rev* (2011) 7(4):328–39. doi:10.2174/157340511798038657
71. Cassinotto C, Boursier J, de Lédinghen V, Lebigot J, Lapuyade B, Cales P, et al. Liver Stiffness in Nonalcoholic Fatty Liver Disease: A Comparison of Supersonic Shear Imaging, FibroScan, and ARFI with Liver Biopsy. *Hepatology* (2016) 63(6):1817–27. doi:10.1002/hep.28394
72. Tanter M, Bercoff J, Athanasiou A, Deffieux T, Gennisson J-L, Montaldo G, et al. Quantitative Assessment of Breast Lesion Viscoelasticity: Initial Clinical Results Using Supersonic Shear Imaging. *Ultrasound Med Biol* (2008) 34(9): 1373–86. doi:10.1016/j.ultrasmedbio.2008.02.002
73. Lee MS, Bae JM, Joo SK, Woo H, Lee DH, Jung YJ, et al. Prospective Comparison Among Transient Elastography, Supersonic Shear Imaging, and

ARFI Imaging for Predicting Fibrosis in Nonalcoholic Fatty Liver Disease. *PLoS One* (2017) 12(11):e0188321. doi:10.1371/journal.pone.0188321
74. Amador C, Urban MW, Chen S, and Greenleaf JF. Loss tangent and Complex Modulus Estimated by Acoustic Radiation Force Creep and Shear Wave Dispersion. *Phys Med Biol* (2012) 57(5):1263–82. doi:10.1088/0031-9155/57/5/1263
75. Rouze NC, Palmeri ML, and Nightingale KR. An Analytic, Fourier Domain Description of Shear Wave Propagation in a Viscoelastic Medium Using Asymmetric Gaussian Sources. *J Acoust Soc America* (2015) 138(2):1012–22. doi:10.1121/1.4927492
76. Chen S, Sanchez W, Callstrom MR, Gorman B, Lewis JT, Sanderson SO, et al. Assessment of Liver Viscoelasticity by Using Shear Waves Induced by Ultrasound Radiation Force. *Radiology* (2013) 266(3):964–70. doi:10.1148/radiol.12120837
77. Muller M, Gennisson J-L, Deffieux T, Tanter M, and Fink M. Quantitative Viscoelasticity Mapping of Human Liver Using Supersonic Shear Imaging: Preliminary *In Vivo* Feasability Study. *Ultrasound Med Biol* (2009) 35(2):219–29. doi:10.1016/j.ultrasmedbio.2008.08.018
78. Kijanka P, and Urban MW. Local Phase Velocity Based Imaging of Viscoelastic Phantoms and Tissues. *IEEE Trans Ultrason Ferroelectr Freq Control* (2021) 68:389. doi:10.1109/TUFFC.2020.2968147
79. Orescanin M, Yue Wang Y, and Insana MF. 3-D FDTD Simulation of Shear Waves for Evaluation of Complex Modulus Imaging. *IEEE Trans Ultrason Ferroelect., Freq Contr* (2011) 58(2):389–98. doi:10.1109/tuffc.2011.1816
80. Montagnon E, Hadj-Henni A, Schmitt C, and Cloutier G. Rheological Assessment of a Polymeric Spherical Structure Using a Three-Dimensional Shear Wave Scattering Model in Dynamic Spectroscopy Elastography. *IEEE Trans Ultrason Ferroelect., Freq Contr* (2014) 61(2):277–87. doi:10.1109/tuffc.2014.6722613
81. Bhatt M, Montagnon E, Destrempes F, Chayer B, Kazemirad S, and Cloutier G. Acoustic Radiation Force Induced Resonance Elastography of Coagulating Blood: Theoretical Viscoelasticity Modeling and *Ex-Vivo* Experimentation. *Phys Med Biol* (2018) 63(6):065018. doi:10.1088/1361-6560/aab46a
82. Bernard S, and Cloutier G. Forward and Inverse Viscoelastic Wave Scattering by Irregular Inclusions for Shear Wave Elastography. *J Acoust Soc America* (2017) 142(4):2346–64. doi:10.1121/1.5007729
83. Ouared A, Kazemirad S, Montagnon E, and Cloutier G. Ultrasound Viscoelasticity Assessment Using an Adaptive Torsional Shear Wave Propagation Method. *Med Phys* (2016) 43(4):1603–14. doi:10.1118/1.4942813
84. Henni AH, Schmitt C, Trop I, and Cloutier G. Shear Wave Induced Resonance Elastography of Spherical Masses with Polarized Torsional Waves. *Appl Phys Lett* (2012) 100(13):1337021–5. doi:10.1063/1.3696300
85. Budelli E, Brum J, Bernal M, Deffieux T, Tanter M, Lema P, et al. A Diffraction Correction for Storage and Loss Moduli Imaging Using Radiation Force Based Elastography. *Phys Med Biol* (2017) 62(1):91–106. doi:10.1088/1361-6560/62/1/91
86. Nenadic IZ, Urban MW, Heng Z, Sanchez W, Morgan PE, Greenleaf JF, et al. Application of Attenuation Measuring Ultrasound Shearwave Elastography in 8 post-transplant Liver Patients. In: IEEE International Ultrasonics Symposium (2014). p. 987–90.
87. Bernard S, Kazemirad S, and Cloutier G. A Frequency-Shift Method to Measure Shear-Wave Attenuation in Soft Tissues. *IEEE Trans Ultrason Ferroelect., Freq Contr* (2017) 64(3):514–24. doi:10.1109/tuffc.2016.2634329
88. Ormachea J, and Parker KJ. Comprehensive Viscoelastic Characterization of Tissues and the Inter-relationship of Shear Wave (Group and Phase) Velocity, Attenuation and Dispersion. *Ultrasound Med Biol* (2020) 46(12):3448–59. doi:10.1016/j.ultrasmedbio.2020.08.023
89. Wang MH, Palmeri ML, Rotemberg VM, Rouze NC, and Nightingale KR. Improving the Robustness of Time-Of-Flight Based Shear Wave Speed Reconstruction Methods Using RANSAC in Human Liver *In Vivo*. *Ultrasound Med Biol* (2010) 36(5):802–13. doi:10.1016/j.ultrasmedbio.2010.02.007
90. Engel AJ, and Bashford GR. A New Method for Shear Wave Speed Estimation in Shear Wave Elastography. *IEEE Trans Ultrason Ferroelect., Freq Contr* (2015) 62(12):2106–14. doi:10.1109/tuffc.2015.007282
91. Rouze NC, Deng Y, Trutna CA, Palmeri ML, and Nightingale KR. Characterization of Viscoelastic Materials Using Group Shear Wave Speeds. *IEEE Trans Ultrason Ferroelect., Freq Contr* (2018) 65(5):780–94. doi:10.1109/tuffc.2018.2815505
92. Shiina T, Nightingale KR, Palmeri ML, Hall TJ, Bamber JC, Barr RG, et al. WFUMB Guidelines and Recommendations for Clinical Use of Ultrasound Elastography: Part 1: Basic Principles and Terminology. *Ultrasound Med Biol* (2015) 41(5):1126–47. doi:10.1016/j.ultrasmedbio.2015.03.009
93. Palmeri ML, Wang MH, Dahl JJ, Frinkley KD, and Nightingale KR. Quantifying Hepatic Shear Modulus *In Vivo* Using Acoustic Radiation Force. *Ultrasound Med Biol* (2008) 34(4):546–58. doi:10.1016/j.ultrasmedbio.2007.10.009
94. Song P, Manduca A, Zhao H, Urban MW, Greenleaf JF, and Chen S. Fast Shear Compounding Using Robust 2-D Shear Wave Speed Calculation and Multi-Directional Filtering. *Ultrasound Med Biol* (2014) 40(6):1343–55. doi:10.1016/j.ultrasmedbio.2013.12.026
95. Liu H-C, Kijanka P, and Urban MW. Four-dimensional (4D) Phase Velocity Optical Coherence Elastography in Heterogeneous Materials and Biological Tissue. *Biomed Opt Express* (2020) 11(7):3795–817. doi:10.1364/boe.394835
96. Deffieux T, Montaldo G, Tanter M, and Fink M. Shear Wave Spectroscopy for *In Vivo* Quantification of Human Soft Tissues Visco-Elasticity. *IEEE Trans Med Imaging* (2009) 28(3):313–22. doi:10.1109/tmi.2008.925077
97. Urban MW, Pislaru C, Nenadic IZ, Kinnick RR, and Greenleaf JF. Measurement of Viscoelastic Properties of *In Vivo* Swine Myocardium Using Lamb Wave Dispersion Ultrasound Vibrometry (LDUV). *IEEE Trans Med Imaging* (2013) 32(2):247–61. doi:10.1109/tmi.2012.2222656
98. Helfenstein-Didier C, Andrade RJ, Brum J, Hug F, Tanter M, Nordez A, et al. In Vivoquantification of the Shear Modulus of the Human Achilles Tendon during Passive Loading Using Shear Wave Dispersion Analysis. *Phys Med Biol* (2016) 61(6):2485–96. doi:10.1088/0031-9155/61/6/2485
99. Ambrozinski L, Packo P, Pieczonka L, Stepinski T, Uhl T, and Staszewski WJ. Identification of Material Properties - Efficient Modelling Approach Based on Guided Wave Propagation and Spatial Multiple Signal Classification. *Struct Control Health Monit* (2015) 22(7):969–83. doi:10.1002/stc.1728
100. Parker KJ, Ormachea J, Will S, and Hah Z. Analysis of Transient Shear Wave in Lossy media. *Ultrasound Med Biol* (2018) 44(7):1504–15. doi:10.1016/j.ultrasmedbio.2018.03.014
101. Bernal M, Nenadic I, Urban MW, and Greenleaf JF. Material Property Estimation for Tubes and Arteries Using Ultrasound Radiation Force and Analysis of Propagating Modes. *J Acoust Soc America* (2011) 129(3):1344–54. doi:10.1121/1.3533735
102. Alleyne D, and Cawley P. A Two-Dimensional Fourier Transform Method for the Measurement of Propagating Multimode Signals. *J Acoust Soc America* (1991) 89(3):1159–68. doi:10.1121/1.400530
103. Nightingale K, Rouze N, Rosenzweig S, Wang M, Abdelmalek M, Guy C, et al. Derivation and Analysis of Viscoelastic Properties in Human Liver: Impact of Frequency on Fibrosis and Steatosis Staging. *IEEE Trans Ultrason Ferroelect., Freq Contr* (2015) 62(1):165–75. doi:10.1109/tuffc.2014.006653
104. Parker KJ, Szabo T, and Holm S. Towards a Consensus on Rheological Models for Elastography in Soft Tissues. *Phys Med Biol* (2019) 64(21):215012. doi:10.1088/1361-6560/ab453d
105. Kijanka P, and Urban MW. Local Phase Velocity Based Imaging: A New Technique Used for Ultrasound Shear Wave Elastography. *IEEE Trans Med Imaging* (2019) 38(4):894–908. doi:10.1109/tmi.2018.2874545
106. Kijanka P, and Urban MW. Fast Local Phase Velocity-Based Imaging: Shear Wave Particle Velocity and Displacement Motion Study. *IEEE Trans Ultrason Ferroelect., Freq Contr* (2020) 67(3):526–37. doi:10.1109/tuffc.2019.2948512
107. Nenadic IZ, Qiang B, Urban MW, Zhao H, Sanchez W, Greenleaf JF, et al. Attenuation Measuring Ultrasound Shearwave Elastography Andin Vivoapplication in post-transplant Liver Patients. *Phys Med Biol* (2016) 62(2):484–500. doi:10.1088/1361-6560/aa4f6f
108. Rouze NC, Deng Y, Palmeri ML, and Nightingale KR. Accounting for the Spatial Observation Window in the 2-D Fourier Transform Analysis of Shear Wave Attenuation. *Ultrasound Med Biol* (2017) 43(10):2500–6. doi:10.1016/j.ultrasmedbio.2017.06.006
109. Gennisson J-L, Deffieux T, Macé E, Montaldo G, Fink M, and Tanter M. Viscoelastic and Anisotropic Mechanical Properties of *In Vivo* Muscle Tissue Assessed by Supersonic Shear Imaging. *Ultrasound Med Biol* (2010) 36(5):789–801. doi:10.1016/j.ultrasmedbio.2010.02.013

110. Brum J, Bernal M, Gennisson JL, and Tanter M. In Vivoevaluation of the Elastic Anisotropy of the Human Achilles Tendon Using Shear Wave Dispersion Analysis. *Phys Med Biol* (2014) 59(3):505–23. doi:10.1088/0031-9155/59/3/505
111. Rouze NC, Wang MH, Palmeri ML, and Nightingale KR. Finite Element Modeling of Impulsive Excitation and Shear Wave Propagation in an Incompressible, Transversely Isotropic Medium. *J Biomech* (2013) 46(16):2761–8. doi:10.1016/j.jbiomech.2013.09.008
112. Chatelin S, Gennisson J-L, Bernal M, Tanter M, and Pernot M. Modelling the Impulse Diffraction Field of Shear Waves in Transverse Isotropic Viscoelastic Medium. *Phys Med Biol* (2015) 60(9):3639–54. doi:10.1088/0031-9155/60/9/3639
113. Quan Y, and Harris JM. Seismic Attenuation Tomography Using the Frequency Shift Method. *Geophysics* (1997) 62(3):895–905. doi:10.1190/1.1444197
114. Dines KA, and Kak AC. Ultrasonic Attenuation Tomography of Soft Tissues. *Ultrason Imaging* (1979) 1(1):16–33. doi:10.1177/016173467900100102
115. Fink M, Hottier F, and Cardoso JF. Ultrasonic Signal Processing for *In Vivo* Attenuation Measurement: Short Time Fourier Analysis. *Ultrason Imaging* (1983) 5(2):117–35. doi:10.1177/016173468300500202
116. Kijanka P, and Urban MW. Two-point Frequency Shift Method for Shear Wave Attenuation Measurement. *IEEE Trans Ultrason Ferroelect., Freq Contr* (2020) 67(3):483–96. doi:10.1109/tuffc.2019.2945620
117. Zaleska-Dorobisz U, Kaczorowski K, Pawluś A, Puchalska A, and Inglot M. Ultrasound Elastography - Review of Techniques and its Clinical Applications. *Adv Clin Exp Med* (2014) 23(4):645–55. doi:10.17219/acem/26301
118. Barr RG. Elastography in Clinical Practice. *Radiologic Clin North America* (2014) 52(6):1145–62. doi:10.1016/j.rcl.2014.07.002
119. Sigrist RMS, Liau J, Kaffas AE, Chammas MC, and Willmann JK. Ultrasound Elastography: Review of Techniques and Clinical Applications. *Theranostics* (2017) 7(5):1303–29. doi:10.7150/thno.18650
120. El-Serag HB. Hepatocellular Carcinoma and Hepatitis C in the United States. *Hepatology* (2002) 36(5B):s74–s83. doi:10.1053/jhep.2002.36807
121. Kose S, Ersan G, Tatar B, Adar P, and Erturk Sengel B. Evaluation of Percutaneous Liver Biopsy Complications in Patients with Chronic Viral Hepatitis. *Eurasian J Med* (2015) 47(3):161–4. doi:10.5152/eurasianjmed.2015.107
122. Bamber J, Cosgrove D, Dietrich C, Fromageau J, Bojunga J, Calliada F, et al. EFSUMB Guidelines and Recommendations on the Clinical Use of Ultrasound Elastography. Part 1: Basic Principles and Technology. *Ultraschall Med* (2013) 34(02):169–84. doi:10.1055/s-0033-1335205
123. Ferraioli G, Tinelli C, Zicchetti M, Above E, Poma G, Di Gregorio M, et al. Reproducibility of Real-Time Shear Wave Elastography in the Evaluation of Liver Elasticity. *Eur J Radiol* (2012) 81(11):3102–6. doi:10.1016/j.ejrad.2012.05.030
124. Ganne-Carrié N, Ziol M, de Ledinghen V, Douvin C, Marcellin P, Castera L, et al. Accuracy of Liver Stiffness Measurement for the Diagnosis of Cirrhosis in Patients with Chronic Liver Diseases. *Hepatology* (2006) 44(6):1511–7. doi:10.1002/hep.21420
125. Nahon P, Kettaneh A, Tengher-Barna I, Ziol M, de Lédinghen V, Douvin C, et al. Assessment of Liver Fibrosis Using Transient Elastography in Patients with Alcoholic Liver Disease. *J Hepatol* (2008) 49(6):1062–8. doi:10.1016/j.jhep.2008.08.011
126. Ferraioli G. Point Shear Wave Elastography Method for Assessing Liver Stiffness. *World J Gastroenterol* (2014) 20(16). doi:10.3748/wjg.v20.i16.4787
127. Millonig G, Friedrich S, Adolf S, Fonouni H, Golriz M, Mehrabi A, et al. Liver Stiffness Is Directly Influenced by central Venous Pressure. *J Hepatol* (2010) 52(2):206–10. doi:10.1016/j.jhep.2009.11.018
128. Millonig G, Reimann FM, Friedrich S, Fonouni H, Mehrabi A, Büchler MW, et al. Extrahepatic Cholestasis Increases Liver Stiffness (FibroScan) Irrespective of Fibrosis. *Hepatology* (2008) 48(5):1718–23. doi:10.1002/hep.22577
129. Takahashi H, Ono N, Eguchi Y, Eguchi T, Kitajima Y, Kawaguchi Y, et al. Evaluation of Acoustic Radiation Force Impulse Elastography for Fibrosis Staging of Chronic Liver Disease: a Pilot Study. *Liver Int* (2010) 30(4):538–45. doi:10.1111/j.1478-3231.2009.02130.x
130. Boursier J, Isselin G, Fouchard-Hubert I, Oberti F, Dib N, Lebigot J, et al. Acoustic Radiation Force Impulse: a New Ultrasonographic Technology for the Widespread Noninvasive Diagnosis of Liver Fibrosis. *Eur J Gastroenterol Hepatol* (2010) 22(9):1074–84. doi:10.1097/meg.0b013e328339e0a1
131. Friedrich-Rust M, Nierhoff J, Lupsor M, Sporea I, Fierbinteanu-Braticevici C, Strobel D, et al. Performance of Acoustic Radiation Force Impulse Imaging for the Staging of Liver Fibrosis: a Pooled Meta-Analysis. *J Viral Hepat* (2012) 19(2):e212–e219. doi:10.1111/j.1365-2893.2011.01537.x
132. Hudson JM, Milot L, Parry C, Williams R, and Burns PN. Inter- and Intra-operator Reliability and Repeatability of Shear Wave Elastography in the Liver: A Study in Healthy Volunteers. *Ultrasound Med Biol* (2013) 39(6):950–5. doi:10.1016/j.ultrasmedbio.2012.12.011
133. Carey E, and Carey WD. Noninvasive Tests for Liver Disease, Fibrosis, and Cirrhosis: Is Liver Biopsy Obsolete? *Cleve Clin J Med* (2010) 77(8):519–27. doi:10.3949/ccjm.77a.09138
134. Ferraioli G, Tinelli C, Dal Bello B, Zicchetti M, Filice G, and Filice C. Accuracy of Real-Time Shear Wave Elastography for Assessing Liver Fibrosis in Chronic Hepatitis C: a Pilot Study. *Hepatology* (2012) 56(6):2125–33. doi:10.1002/hep.25936
135. Dietrich C, Bamber J, Berzigotti A, Bota S, Cantisani V, Castera L, et al. EFSUMB Guidelines and Recommendations on the Clinical Use of Liver Ultrasound Elastography, Update 2017 (Long Version). *Ultraschall Med* (2017) 38(4):e16–e47. doi:10.1055/s-0043-103952
136. Ferraioli G, Wong VW-S, Castera L, Berzigotti A, Sporea I, Dietrich CF, et al. Liver Ultrasound Elastography: An Update to the World Federation for Ultrasound in Medicine and Biology Guidelines and Recommendations. *Ultrasound Med Biol* (2018) 44(12):2419–40. doi:10.1016/j.ultrasmedbio.2018.07.008
137. Barry CT, Mills B, Hah Z, Mooney RA, Ryan CK, Rubens DJ, et al. Shear Wave Dispersion Measures Liver Steatosis. *Ultrasound Med Biol* (2012) 38(2):175–82. doi:10.1016/j.ultrasmedbio.2011.10.019
138. Sugimoto K, Moriyasu F, Oshiro H, Takeuchi H, Yoshimasu Y, Kasai Y, et al. Viscoelasticity Measurement in Rat Livers Using Shear-Wave US Elastography. *Ultrasound Med Biol* (2018) 44(9):2018–24. doi:10.1016/j.ultrasmedbio.2018.05.008
139. Sugimoto K, Moriyasu F, Oshiro H, Takeuchi H, Yoshimasu Y, Kasai Y, et al. Clinical Utilization of Shear Wave Dispersion Imaging in Diffuse Liver Disease. *Ultrasonography* (2020) 39(1):3–10. doi:10.14366/usg.19031
140. Ophir J, Céspedes I, Ponnekanti H, Yazdi Y, and Li X. Elastography: A Quantitative Method for Imaging the Elasticity of Biological Tissues. *Ultrason Imaging* (1991) 13(2):111–34. doi:10.1177/016173469101300201
141. Krouskop TA, Wheeler TM, Kallel F, Garra BS, and Hall T. Elastic Moduli of Breast and Prostate Tissues under Compression. *Ultrason Imaging* (1998) 20(4):260–74. doi:10.1177/016173469802000403
142. Athanasiou A, Tardivon A, Tanter M, Sigal-Zafrani B, Bercoff J, Deffieux T, et al. Breast Lesions: Quantitative Elastography with Supersonic Shear Imaging-Preliminary Results. *Radiology* (2010) 256(1):297–303. doi:10.1148/radiol.10090385
143. Kolb TM, Lichy J, and Newhouse JH. Comparison of the Performance of Screening Mammography, Physical Examination, and Breast US and Evaluation of Factors that Influence Them: an Analysis of 27,825 Patient Evaluations. *Radiology* (2002) 225(1):165–75. doi:10.1148/radiol.2251011667
144. Chiou S-Y, Chou Y-H, Chiou H-J, Wang H-K, Tiu C-M, Tseng L-M, et al. Sonographic Features of Nonpalpable Breast Cancer: A Study Based on Ultrasound-Guided Wire-Localized Surgical Biopsies. *Ultrasound Med Biol* (2006) 32(9):1299–306. doi:10.1016/j.ultrasmedbio.2006.05.018
145. Evans A, Whelehan P, Thomson K, McLean D, Brauer K, Purdie C, et al. Quantitative Shear Wave Ultrasound Elastography: Initial Experience in Solid Breast Masses. *Breast Cancer Res* (2010) 12(6):R104. doi:10.1186/bcr2787
146. Goddi A, Bonardi M, and Alessi S. Breast Elastography: A Literature Review. *J Ultrasound* (2012) 15(3):192–8. doi:10.1016/j.jus.2012.06.009
147. Xue Y, Yao S, Li X, and Zhang H. Benign and Malignant Breast Lesions Identification through the Values Derived from Shear Wave Elastography: Evidence for the Meta-Analysis. *Oncotarget* (2017) 8(51):89173–81. doi:10.18632/oncotarget.21124
148. Berg WA, Cosgrove DO, Doré CJ, Schäfer FKW, Svensson WE, Hooley RJ, et al. Shear-wave Elastography Improves the Specificity of Breast US: the BE1 Multinational Study of 939 Masses. *Radiology* (2012) 262(2):435–49. doi:10.1148/radiol.11110640

149. Lee SH, Chang JM, Kim WH, Bae MS, Seo M, Koo HR, et al. Added Value of Shear-Wave Elastography for Evaluation of Breast Masses Detected with Screening US Imaging. *Radiology* (2014) 273(1):61–9. doi:10.1148/radiol.14132443
150. Lee SH, Chung J, Choi HY, Choi SH, Ryu EB, Ko KH, et al. Evaluation of Screening US-Detected Breast Masses by Combined Use of Elastography and Color Doppler US with B-Mode US in Women with Dense Breasts: A Multicenter Prospective Study. *Radiology* (2017) 285(2):660–9. doi:10.1148/radiol.2017162424
151. Kumar V, Denis M, Gregory A, Bayat M, Mehrmohammadi M, Fazzio R, et al. Viscoelastic Parameters as Discriminators of Breast Masses: Initial Human Study Results. *PLoS One* (2018) 13(10):e0205717. doi:10.1371/journal.pone.0205717
152. Ormachea J, Parker KJ, and Barr RG. An Initial Study of Complete 2D Shear Wave Dispersion Images Using a Reverberant Shear Wave Field. *Phys Med Biol* (2019) 64(14):145009. doi:10.1088/1361-6560/ab2778
153. Nabavizadeh A, Bayat M, Kumar V, Gregory A, Webb J, Alizad A, et al. Viscoelastic Biomarker for Differentiation of Benign and Malignant Breast Lesion in Ultra- Low Frequency Range. *Sci Rep* (2019) 9(1):5737. doi:10.1038/s41598-019-41885-9
154. Athanasiou A, Latorre-Ossa H, Criton A, Tardivon A, Gennisson J-L, and Tanter M. Feasibility of Imaging and Treatment Monitoring of Breast Lesions with Three-Dimensional Shear Wave Elastography. *Ultraschall Med* (2015) 38:51–9. doi:10.1055/s-0034-1398980
155. Jing H, Cheng W, Li Z-Y, Ying L, Wang Q-C, Wu T, et al. Early Evaluation of Relative Changes in Tumor Stiffness by Shear Wave Elastography Predicts the Response to Neoadjuvant Chemotherapy in Patients with Breast Cancer. *J Ultrasound Med* (2016) 35(8):1619–27. doi:10.7863/ultra.15.08052
156. Evans A, Armstrong S, Whelehan P, Thomson K, Rauchhaus P, Purdie C, et al. Can Shear-Wave Elastography Predict Response to Neoadjuvant Chemotherapy in Women with Invasive Breast Cancer? *Br J Cancer* (2013) 109(11):2798–802. doi:10.1038/bjc.2013.660
157. Barr RG, Nakashima K, Amy D, Cosgrove D, Farrokh A, Schafer F, et al. WFUMB Guidelines and Recommendations for Clinical Use of Ultrasound Elastography: Part 2: Breast. *Ultrasound Med Biol* (2015) 41(5):1148–60. doi:10.1016/j.ultrasmedbio.2015.03.008
158. Woo S, Suh CH, Kim SY, Cho JY, and Kim SH. Shear-wave Elastography for Detection of Prostate Cancer: a Systematic Review and Diagnostic Meta-Analysis. *Am J Roentgenology* (2017) 209(4):806–14. doi:10.2214/ajr.17.18056
159. Zhao C-K, and Xu H-X. Ultrasound Elastography of the Thyroid: Principles and Current Status. *Ultrasonography* (2019) 38(2):106–24. doi:10.14366/usg.18037
160. Hoang P, Wallace A, Sugi M, Fleck A, Pershad Y, Dahiya N, et al. Elastography Techniques in the Evaluation of Deep Vein Thrombosis. *Cardiovasc Diagn Ther* (2017) 7(Suppl. 3):S238–S245. doi:10.21037/cdt.2017.10.04
161. Rouze NC, Palmeri ML, and Nightingale KR. Tractable Calculation of the Green's Tensor for Shear Wave Propagation in an Incompressible, Transversely Isotropic Material. *Phys Med Biol* (2020) 65(1):015014. doi:10.1088/1361-6560/ab5c2d
162. Correia M, Deffieux T, Chatelin S, Provost J, Tanter M, and Pernot M. 3D Elastic Tensor Imaging in Weakly Transversely Isotropic Soft Tissues. *Phys Med Biol* (2019) 63(15):155005. doi:10.1088/1361-6560/aacfaf
163. Wang M, Byram B, Palmeri M, Rouze N, and Nightingale K. Imaging Transverse Isotropic Properties of Muscle by Monitoring Acoustic Radiation Force Induced Shear Waves Using a 2-D Matrix Ultrasound Array. *IEEE Trans Med Imaging* (2013) 32(9):1671–84. doi:10.1109/tmi.2013.2262948
164. Miyamoto N, Hirata K, Kanehisa H, and Yoshitake Y. Validity of Measurement of Shear Modulus by Ultrasound Shear Wave Elastography in Human Pennate Muscle. *PLoS One* (2015) 10(4):e0124311. doi:10.1371/journal.pone.0124311
165. Aubry S, Nueffer J-P, Tanter M, Becce F, Vidal C, and Michel F. Viscoelasticity in Achilles Tendonopathy: Quantitative Assessment by Using Real-Time Shear-Wave Elastography. *Radiology* (2015) 274(3):821–9. doi:10.1148/radiol.14140434
166. Muthupillai R, Lomas D, Rossman P, Greenleaf J, Manduca A, and Ehman R. Magnetic Resonance Elastography by Direct Visualization of Propagating Acoustic Strain Waves. *Science* (1995) 269(5232):1854–7. doi:10.1126/science.7569924
167. Kolipaka A, McGee KP, Araoz PA, Glaser KJ, Manduca A, Romano AJ, et al. MR Elastography as a Method for the Assessment of Myocardial Stiffness: Comparison with an Established Pressure-Volume Model in a Left Ventricular Model of the Heart. *Magn Reson Med* (2009) 62(1):135–40. doi:10.1002/mrm.21991
168. Perriñez PR, Kennedy FE, Van Houten EE, Weaver JB, and Paulsen KD. Magnetic Resonance Poroelastography: An Algorithm for Estimating the Mechanical Properties of Fluid-Saturated Soft Tissues. *IEEE Trans Med Imaging* (2010) 29(3):746–55. doi:10.1109/TMI.2009.2035309
169. Mariappan YK, Glaser KJ, Hubmayr RD, Manduca A, Ehman RL, and McGee KP. MR Elastography of Human Lung Parenchyma: Technical Development, Theoretical Modeling and *In Vivo* Validation. *J Magn Reson Imaging* (2011) 33(6):1351–61. doi:10.1002/jmri.22550
170. Kolipaka A, McGee KP, Manduca A, Anavekar N, Ehman RL, and Araoz PA. *In Vivo* assessment of MR Elastography-Derived Effective End-Diastolic Myocardial Stiffness under Different Loading Conditions. *J Magn Reson Imaging* (2011) 33(5):1224–8. doi:10.1002/jmri.22531
171. Yin M, Kolipaka A, Woodrum DA, Glaser KJ, Romano AJ, Manduca A, et al. Hepatic and Splenic Stiffness Augmentation Assessed with MR Elastography in an *In Vivo* Porcine portal Hypertension Model. *J Magn Reson Imaging* (2013) 38(4):809–15. doi:10.1002/jmri.24049
172. Klatt D, Johnson CL, and Magin RL. Simultaneous, Multidirectional Acquisition of Displacement fields in Magnetic Resonance Elastography of the *In Vivo* Human Brain. *J Magn Reson Imaging* (2015) 42(2):297–304. doi:10.1002/jmri.24806
173. Low G, Owen NE, Joubert I, Patterson AJ, Graves MJ, Glaser KJ, et al. Reliability of Magnetic Resonance Elastography Using Multislice Two-Dimensional Spin-echo echo-planar Imaging (SE-EPI) and Three-Dimensional Inversion Reconstruction for Assessing Renal Stiffness. *J Magn Reson Imaging* (2015) 42(3):844–50. doi:10.1002/jmri.24826
174. Numano T, Mizuhara K, Hata J, Washio T, and Homma K. A Simple Method for MR Elastography: A Gradient-echo Type Multi-echo Sequence. *Magn Reson Imaging* (2015) 33(1):31–7. doi:10.1016/j.mri.2014.10.002
175. Fattahi N, Arani A, Perry A, Meyer F, Manduca A, Glaser K, et al. MR Elastography Demonstrates Increased Brain Stiffness in normal Pressure Hydrocephalus. *AJNR Am J Neuroradiol* (2016) 37(3):462–7. doi:10.3174/ajnr.a4560
176. Anderson AT, Van Houten EEW, McGarry MDJ, Paulsen KD, Holtrop JL, Sutton BP, et al. Observation of Direction-dependent Mechanical Properties in the Human Brain with Multi-Excitation MR Elastography. *J Mech Behav Biomed Mater* (2016) 59:538–46. doi:10.1016/j.jmbbm.2016.03.005
177. Klatt D, Hamhaber U, Asbach P, Braun J, and Sack I. Noninvasive Assessment of the Rheological Behavior of Human Organs Using Multifrequency MR Elastography: A Study of Brain and Liver Viscoelasticity. *Phys Med Biol* (2007) 52(24):7281–94. doi:10.1088/0031-9155/52/24/006
178. Asbach P, Klatt D, Hamhaber U, Braun J, Somasundaram R, Hamm B, et al. Assessment of Liver Viscoelasticity Using Multifrequency MR Elastography. *Magn Reson Med* (2008) 60(2):373–9. doi:10.1002/mrm.21636
179. Sack I, Rump J, Elgeti T, Samani A, and Braun J. MR Elastography of the Human Heart: Noninvasive Assessment of Myocardial Elasticity Changes by Shear Wave Amplitude Variations. *Magn Reson Med* (2009) 61(3):668–77. doi:10.1002/mrm.21878
180. Asbach P, Klatt D, Schlosser B, Biermer M, Muche M, Rieger A, et al. Viscoelasticity-based Staging of Hepatic Fibrosis with Multifrequency MR Elastography. *Radiology* (2010) 257(1):80–6. doi:10.1148/radiol.10092489
181. Murphy MC, Huston J, Jack CR, Glaser KJ, Manduca A, Felmlee JP, et al. Decreased Brain Stiffness in Alzheimer's Disease Determined by Magnetic Resonance Elastography. *J Magn Reson Imaging* (2011) 34(3):494–8. doi:10.1002/jmri.22707
182. Streitberger KJ, Sack I, Krefting D, Pfüller C, Braun J, Paul F, et al. Brain Viscoelasticity Alteration in Chronic-Progressive Multiple Sclerosis. *PLoS ONE* (2012) 7(1):e29888. doi:10.1371/journal.pone.0029888
183. Johnson CL, Holtrop JL, McGarry MDJ, Weaver JB, Paulsen KD, Georgiadis JG, et al. 3D Multislab, Multishot Acquisition for Fast, Whole-Brain MR

Elastography with High Signal-To-Noise Efficiency. *Magn Reson Med* (2014) 71(2):477–85. doi:10.1002/mrm.25065
184. McGarry MDJ, Johnson CL, Sutton BP, Georgiadis JG, Van Houten EEW, Pattison AJ, et al. Suitability of Poroelastic and Viscoelastic Mechanical Models for High and Low Frequency MR Elastography. *Med Phys* (2015) 42(2):947–57. doi:10.1118/1.4905048
185. Sinkus R, Tanter M, Xydeas T, Catheline S, Bercoff J, and Fink M. Viscoelastic Shear Properties of *In Vivo* Breast Lesions Measured by MR Elastography. *Magn Reson Imaging* (2005) 23(2):159–65. doi:10.1016/j.mri.2004.11.060
186. Rump J, Klatt D, Braun J, Warmuth C, and Sack I. Fractional Encoding of Harmonic Motions in MR Elastography. *Magn Reson Med* (2007) 57(2): 388–95. doi:10.1002/mrm.21152
187. Green MA, Bilston LE, and Sinkus R. In Vivobrain Viscoelastic Properties Measured by Magnetic Resonance Elastography. *NMR Biomed* (2008) 21(7): 755–64. doi:10.1002/nbm.1254
188. Riek K, Klatt D, Nuzha H, Mueller S, Neumann U, Sack I, et al. Wide-range Dynamic Magnetic Resonance Elastography. *J Biomech* (2011) 44(7):1380–6. doi:10.1016/j.jbiomech.2010.12.031
189. Zhang J, Green MA, Sinkus R, and Bilston LE. Viscoelastic Properties of Human Cerebellum Using Magnetic Resonance Elastography. *J Biomech* (2011) 44(10):1909–13. doi:10.1016/j.jbiomech.2011.04.034
190. Garteiser P, Sahebjavaher RS, Ter Beek LC, Salcudean S, Vilgrain V, Van Beers BE, et al. Rapid Acquisition of Multifrequency, Multislice and Multidirectional MR Elastography Data with a Fractionally Encoded Gradient echo Sequence. *NMR Biomed* (2013) 26(10):1326–35. doi:10.1002/nbm.2958
191. Braun J, Guo J, Lützkendorf R, Stadler J, Papazoglou S, Hirsch S, et al. High-resolution Mechanical Imaging of the Human Brain by Three-Dimensional Multifrequency Magnetic Resonance Elastography at 7T. *NeuroImage* (2014) 90:308–14. doi:10.1016/j.neuroimage.2013.12.032
192. Sahebjavaher RS, Frew S, Bylinskii A, ter Beek L, Garteiser P, Honarvar M, et al. Prostate MR Elastography with Transperineal Electromagnetic Actuation and a Fast Fractionally Encoded Steady-State Gradient echo Sequence. *NMR Biomed* (2014) 27(7):784–94. doi:10.1002/nbm.3118
193. Hirsch S, Guo J, Reiter R, Papazoglou S, Kroencke T, Braun J, et al. MR Elastography of the Liver and the Spleen Using a Piezoelectric Driver, Single-Shot Wave-Field Acquisition, and Multifrequency Dual Parameter Reconstruction. *Magn Reson Med* (2014) 71(1):267–77. doi:10.1002/mrm.24674
194. Tzschätzsch H, Guo J, Dittmann F, Hirsch S, Barnhill E, Jöhrens K, et al. Tomoelastography by Multifrequency Wave Number Recovery from Time-Harmonic Propagating Shear Waves. *Med Image Anal* (2016) 30:1–10. doi:10.1016/j.media.2016.01.001
195. Guo J, Hirsch S, Fehlner A, Papazoglou S, Scheel M, Braun J, et al. Towards an Elastographic Atlas of Brain Anatomy. *PLoS ONE* (2013) 8(8):e71807. doi:10.1371/journal.pone.0071807
196. Strasser J, Haindl MT, Stollberger R, Fazekas F, and Ropele S. Magnetic Resonance Elastography of the Human Brain Using a Multiphase DENSE Acquisition. *Magn Reson Med* (2019) 81(6):3578–87. doi:10.1002/mrm.27672
197. Doyley MM, VanHouten EE, Weaver JB, Poplack S, Duncan L, Kennedy F, et al. Shear Modulus Estimation Using Parallelized Partial Volumetric Reconstruction. *IEEE Trans Med Imaging* (2004) 23(11):1404–16. doi:10.1109/tmi.2004.834624
198. Clayton EH, Garbow JR, and Bayly PV. Frequency-dependent Viscoelastic Parameters of Mouse Brain Tissue Estimated by MR Elastography. *Phys Med Biol* (2011) 56(8):2391–406. doi:10.1088/0031-9155/56/8/005
199. Yin Z, Kearney SP, Magin RL, and Klatt D. Concurrent 3D Acquisition of Diffusion Tensor Imaging and Magnetic Resonance Elastography Displacement Data (DTI-MRE): Theory and *In Vivo* Application. *Magn Reson Med* (2017) 77(1):273–84. doi:10.1002/mrm.26121
200. Papazoglou S, Hirsch S, Braun J, and Sack I. Multifrequency Inversion in Magnetic Resonance Elastography. *Phys Med Biol* (2012) 57(8):2329–46. doi:10.1088/0031-9155/57/8/2329
201. Streitberger KJ, Reiss-Zimmermann M, Freimann FB, Bayerl S, Guo J, Arlt F, et al. High-resolution Mechanical Imaging of Glioblastoma by Multifrequency Magnetic Resonance Elastography. *PLoS ONE* (2014) 9(10):e110588. doi:10.1371/journal.pone.0110588
202. Streitberger K-J, Diederichs G, Guo J, Fehlner A, Hamm B, Braun J, et al. *In Vivo* multifrequency Magnetic Resonance Elastography of the Human Intervertebral Disk. *Magn Reson Med* (2015) 74(5):1380–7. doi:10.1002/mrm.25505
203. Testu J, McGarry MDJ, Dittmann F, Weaver JB, Paulsen KD, Sack I, et al. Viscoelastic Power Law Parameters of *In Vivo* Human Brain Estimated by MR Elastography. *J Mech Behav Biomed Mater* (2017) 74:333–41. doi:10.1016/j.jmbbm.2017.06.027
204. Neumann W, Schad LR, and Zöllner FG. A Novel 3D-Printed Mechanical Actuator Using Centrifugal Force for Magnetic Resonance Elastography. In: 2017 39th Annual International Conference of the IEEE Engineering in Medicine and Biology Society. EMBC (2017). p. 3541–4.
205. Numano T, Kawabata Y, Mizuhara K, Washio T, Nitta N, and Homma K. Magnetic Resonance Elastography Using an Air ball-actuator. *Magn Reson Imaging* (2013) 31(6):939–46. doi:10.1016/j.mri.2013.02.001
206. Runge JH, Hoelzl SH, Sudakova J, Dokumaci AS, Nelissen JL, Guenthner C, et al. A Novel Magnetic Resonance Elastography Transducer Concept Based on a Rotational Eccentric Mass: Preliminary Experiences with the Gravitational Transducer. *Phys Med Biol* (2019) 64(4):045007. doi:10.1088/1361-6560/aaf9f8
207. Wu T, Felmlee JP, Greenleaf JF, Riederer SJ, and Ehman RL. MR Imaging of Shear Waves Generated by Focused Ultrasound. *Magn Reson Med* (2000) 43(1):111–5. doi:10.1002/(sici)1522-2594(200001)43:1<111::aid-mrm13>3.0.co;2-d
208. Weaver JB, Pattison AJ, McGarry MD, Perreard IM, Swienckowski JG, Eskey CJ, et al. Brain Mechanical Property Measurement Using MRE with Intrinsic Activation. *Phys Med Biol* (2012) 57(22):7275–87. doi:10.1088/0031-9155/57/22/7275
209. Hirsch S, Klatt D, Freimann F, Scheel M, Braun J, and Sack I. *In Vivo* measurement of Volumetric Strain in the Human Brain Induced by Arterial Pulsation and Harmonic Waves. *Magn Reson Med* (2013) 70(3):671–83. doi:10.1002/mrm.24499
210. Zorgani A, Souchon R, Dinh A-H, Chapelon J-Y, Ménager J-M, Lounis S, et al. Brain Palpation from Physiological Vibrations Using MRI. *Proc Natl Acad Sci USA* (2015) 112(42):12917–21. doi:10.1073/pnas.1509895112
211. Solamen LM, McGarry MDJ, Fried J, Weaver JB, Lollis SS, and Paulsen KD. Poroelastic Mechanical Properties of the Brain Tissue of normal Pressure Hydrocephalus Patients during Lumbar drain Treatment Using Intrinsic Actuation MR Elastography. *Acad Radiol* (2020) 28(4):457–66. doi:10.1016/j.acra.2020.03.009
212. Guenthner C, and Kozerke S. Encoding and Readout Strategies in Magnetic Resonance Elastography. *NMR Biomed* (2018) 31(10):1–29. doi:10.1002/nbm.3919
213. Hahn EL. Detection of Sea-Water Motion by Nuclear Precession. *J Geophys Res* (1960) 65(2):776–7. doi:10.1029/jz065i002p00776
214. Moran PR. A Flow Velocity Zeugmatographic Interlace for NMR Imaging in Humans. *Magn Reson Imaging* (1982) 1(4):197–203. doi:10.1016/0730-725x(82)90170-9
215. Haacke EM, Brown RW, Thompson MR, and Venkatesan R *Magnetic Resonance Imaging: Physical Principles and Sequence Design*. John Wiley & Sons (2014).
216. Hahn EL. Free Nuclear Induction. *Phys Today* (1953) 6(11):4–9. doi:10.1063/1.3061075
217. Muthupillai R, Rossman PJ, Lomas DJ, Greenleaf JF, Riederer SJ, and Ehman RL. Magnetic Resonance Imaging of Transverse Acoustic Strain Waves. *Magn Reson Med* (1996) 36(2):266–74. doi:10.1002/mrm.1910360214
218. Sinkus R, Daire JL, Van Beers BE, and Vilgrain V. Elasticity Reconstruction: Beyond the assumption of Local Homogeneity. *Comptes Rendus - Mecanique* (2010) 338(7-8):474–9. doi:10.1016/j.crme.2010.07.014
219. Boulet T, Kelso ML, and Othman SF. Microscopic Magnetic Resonance Elastography of Traumatic Brain Injury Model. *J Neurosci Methods* (2011) 201(2):296–306. doi:10.1016/j.jneumeth.2011.08.019
220. Okamoto RJ, Clayton EH, and Bayly PV. Viscoelastic Properties of Soft Gels: Comparison of Magnetic Resonance Elastography and Dynamic Shear Testing in the Shear Wave Regime. *Phys Med Biol* (2011) 56(19): 6379–400. doi:10.1088/0031-9155/56/19/014

221. Yin Z, Magin RL, and Klatt D. Simultaneous MR Elastography and Diffusion Acquisitions: Diffusion-MRE (dMRE). *Magn Reson Med* (2014) 71(5): 1682–8. doi:10.1002/mrm.25180
222. Sack I, McGowan CK, Samani A, Luginbuhl C, Oakden W, and Plewes DB. Observation of Nonlinear Shear Wave Propagation Using Magnetic Resonance Elastography. *Magn Reson Med* (2004) 52(4):842–50. doi:10.1002/mrm.20238
223. Clayton EH, Genin GM, and Bayly PV. Transmission, Attenuation and Reflection of Shear Waves in the Human Brain. *J R Soc Interf* (2012) 9(76): 2899–910. doi:10.1098/rsif.2012.0325
224. Bernstein MA, King KF, and Zhou XJ *Handbook of MRI Pulse Sequences*. Burlington: Academic Press (2004). p. iv.
225. Manduca A, Muthupillai R, Rossman PJ, Greenleaf JF, and Ehman RL. Local Wavelength Estimation for Magnetic Resonance Elastography. *Proc 3rd IEEE Int Conf Image Process* (1996) 3:527–30.
226. Latta P, Gruwel MLH, Debergue P, Matwiy B, Sboto-Frankenstein UN, and Tomanek B. Convertible Pneumatic Actuator for Magnetic Resonance Elastography of the Brain. *Magn Reson Imaging* (2011) 29(1):147–52. doi:10.1016/j.mri.2010.07.014
227. Sack I, Beierbach B, Wuerfel J, Klatt D, Hamhaber U, Papazoglou S, et al. The Impact of Aging and Gender on Brain Viscoelasticity. *NeuroImage* (2009) 46(3):652–7. doi:10.1016/j.neuroimage.2009.02.040
228. Wuerfel J, Paul F, Beierbach B, Hamhaber U, Klatt D, Papazoglou S, et al. MR-elastography Reveals Degradation of Tissue Integrity in Multiple Sclerosis. *NeuroImage* (2010) 49(3):2520–5. doi:10.1016/j.neuroimage.2009.06.018
229. Sack I, Streitberger KJ, Krefting D, Paul F, and Braun J. The Influence of Physiological Aging and Atrophy on Brain Viscoelastic Properties in Humans. *PLoS ONE* (2011) 6(9):e23451. doi:10.1371/journal.pone.0023451
230. Solanas PS, Tse K, Koon V, Ratiney H, Millioz F, Caussy C, et al. Harmonic Wideband Simultaneous Dual-Frequency MR Elastography. *NMR Biomed* (2020) e4442.
231. Gordon-Wylie SW, Solamen LM, McGarry MDJ, Zeng W, VanHouten E, Gilbert G, et al. MR Elastography at 1 Hz of Gelatin Phantoms Using 3D or 4D Acquisition. *J Magn Reson* (2018) 296:112–20. doi:10.1016/j.jmr.2018.08.012
232. Herzka DA, Kotys MS, Sinkus R, Pettigrew RI, and Gharib AM. Magnetic Resonance Elastography in the Liver at 3 Tesla Using a Second Harmonic Approach. *Magn Reson Med* (2009) 62(2):284–91. doi:10.1002/mrm.21956
233. Elgeti T, Steffen IG, Knebel F, Hättasch R, Hamm B, Braun J, et al. Time-resolved Analysis of Left Ventricular Shear Wave Amplitudes in Cardiac Elastography for the Diagnosis of Diastolic Dysfunction. *Invest Radiol* (2016) 51(1):1–6. doi:10.1097/rli.0000000000000198
234. Elgeti T, Knebel F, Hättasch R, Hamm B, Braun J, and Sack I. Shear-wave Amplitudes Measured with Cardiac MR Elastography for Diagnosis of Diastolic Dysfunction. *Radiology* (2014) 271(3):681–7. doi:10.1148/radiol.13131605
235. Rump J, Warmuth C, Braun J, and Sack I. Phase Preparation in Steady-State Free Precession MR Elastography. *Magn Reson Imaging* (2008) 26(2):228–35. doi:10.1016/j.mri.2007.07.009
236. Elgeti T, Tzschätzsch H, Hirsch S, Krefting D, Klatt D, Niendorf T, et al. Vibration-synchronized Magnetic Resonance Imaging for the Detection of Myocardial Elasticity Changes. *Magn Reson Med* (2012) 67(4):919–24. doi:10.1002/mrm.24185
237. Bieri O, Maderwald S, Ladd ME, and Scheffler K. Balanced Alternating Steady-State Elastography. *Magn Reson Med* (2006) 55(2):233–41. doi:10.1002/mrm.20812
238. Klatt D, Asbach P, Rump J, Papazoglou S, Somasundaram R, Modrow J, et al. *In Vivo* determination of Hepatic Stiffness Using Steady-State Free Precession Magnetic Resonance Elastography. *Invest Radiol* (2006) 41(12):841–8. doi:10.1097/01.rli.0000244341.16372.08
239. Doyley MM. Model-based Elastography: A Survey of Approaches to the Inverse Elasticity Problem. *Phys Med Biol* (2012) 57(3):R35–R73. doi:10.1088/0031-9155/57/3/r35
240. Knutsson H, Westin CF, and Granlund G. Local Multiscale Frequency and Bandwidth Estimation. In: International Conference on Image Processing (1994). p. 36–40.
241. Braun J, Buntkowsky G, Bernarding J, Tolxdorff T, and Sack I. Simulation and Analysis of Magnetic Resonance Elastography Wave Images Using Coupled Harmonic Oscillators and Gaussian Local Frequency Estimation. *Magn Reson Imaging* (2001) 19(5):703–13. doi:10.1016/s0730-725x(01)00387-3
242. McGee KP, Lake D, Mariappan Y, Hubmayr RD, Manduca A, Ansell K, et al. Calculation of Shear Stiffness in Noise Dominated Magnetic Resonance Elastography Data Based on Principal Frequency Estimation. *Phys Med Biol* (2011) 56(14):4291–309. doi:10.1088/0031-9155/56/14/006
243. Manduca A, Oliphant TE, Dresner MA, Mahowald JL, Kruse SA, Amromin E, et al. Magnetic Resonance Elastography: Non-invasive Mapping of Tissue Elasticity. *Med Image Anal* (2001) 5(4):237–54. doi:10.1016/s1361-8415(00)00039-6
244. Oliphant TE, Manduca A, Ehman RL, and Greenleaf JF. Complex-valued Stiffness Reconstruction for Magnetic Resonance Elastography by Algebraic Inversion of the Differential Equation. *Magn Reson Med* (2001) 45(2):299–310. doi:10.1002/1522-2594(200102)45:2<299::aid-mrm1039>3.0.co;2-o
245. Manduca A, Lake DS, Kruse SA, and Ehman RL. Spatio-temporal Directional Filtering for Improved Inversion of MR Elastography Images. *Med Image Anal* (2003) 7(4):465–73. doi:10.1016/s1361-8415(03)00038-0
246. Manduca A, Oliphant TE, Dresner MA, Lake DS, Greenleaf JF, and Ehman RL. Comparative Evaluation of Inversion Algorithms for Magnetic Resonance Elastography. In: Proceedings IEEE International Symposium on Biomedical Imaging (2002). p. 997–1000.
247. Sinkus R, Tanter M, Catheline S, Lorenzen J, Kuhl C, Sondermann E, et al. Imaging Anisotropic and Viscous Properties of Breast Tissue by Magnetic Resonance-Elastography. *Magn Reson Med* (2005) 53(2):372–87. doi:10.1002/mrm.20355
248. Reiter R, Majumdar S, Kearney S, Kajdacsy-Balla A, Macias V, Crivellaro S, et al. Prostate Cancer Assessment Using MR Elastography of Fresh Prostatectomy Specimens at 9.4 T. *Magn Reson Med* (2020) 84(1): 396–404. doi:10.1002/mrm.28127
249. Fovargue D, Kozerke S, Sinkus R, and Nordsletten D. Robust MR Elastography Stiffness Quantification Using a Localized Divergence Free Finite Element Reconstruction. *Med Image Anal* (2018) 44:126–42. doi:10.1016/j.media.2017.12.005
250. Antonio Sánchez C, Drapaca CS, Sivaloganathan S, and Vrscay ER. Elastography of Biological Tissue: Direct Inversion Methods that Allow for Local Shear Modulus Variations. In: International Conference Image Analysis and Recognition (2010). p. 195–206. doi:10.1007/978-3-642-13775-4_20
251. Barnhill E, Davies PJ, Ariyurek C, Fehlner A, Braun J, and Sack I. Heterogeneous Multifrequency Direct Inversion (HMDI) for Magnetic Resonance Elastography with Application to a Clinical Brain Exam. *Med Image Anal* (2018) 46:180–8. doi:10.1016/j.media.2018.03.003
252. Babuška I, and Suri M. Locking Effects in the Finite Element Approximation of Elasticity Problems. *Numerische Mathematik* (1992) 62(1):439–63.
253. Park E, and Maniatty AM. Shear Modulus Reconstruction in Dynamic Elastography: Time Harmonic Case. *Phys Med Biol* (2006) 51(15): 3697–721. doi:10.1088/0031-9155/51/15/007
254. Guo Z, You S, Wan X, and Bićanić N. A FEM-Based Direct Method for Material Reconstruction Inverse Problem in Soft Tissue Elastography. *Comput Structures* (2010) 88(23-24):1459–68. doi:10.1016/j.compstruc.2008.06.004
255. Eskandari H, Salcudean SE, Rohling R, and Bell I. Real-time Solution of the Finite Element Inverse Problem of Viscoelasticity. *Inverse Probl* (2011) 27(8): 085002. doi:10.1088/0266-5611/27/8/085002
256. Honarvar M, Sahebjavaher R, Sinkus R, Rohling R, and Salcudean SE. Curl-based Finite Element Reconstruction of the Shear Modulus without Assuming Local Homogeneity: Time Harmonic Case. *IEEE Trans Med Imaging* (2013) 32(12):2189–99. doi:10.1109/tmi.2013.2276060
257. Honarvar M, Rohling R, and Salcudean SE. A Comparison of Direct and Iterative Finite Element Inversion Techniques in Dynamic Elastography. *Phys Med Biol* (2016) 61(8):3026–48. doi:10.1088/0031-9155/61/8/3026
258. Hansen PC. Getting to Business: Discretizations of Linear Inverse Problems. *Discrete Inverse Probl* (2010) 23–51.
259. Kallel F, and Bertrand M. Tissue Elasticity Reconstruction Using Linear Perturbation Method. *IEEE Trans Med Imaging* (1996) 15(3):299–313. doi:10.1109/42.500139

260. Samani A, Bishop J, and Plewes DB. A Constrained Modulus Reconstruction Technique for Breast Cancer Assessment. *IEEE Trans Med Imaging* (2001) 20(9):877–85. doi:10.1109/42.952726
261. Zhang Y, Hall LO, Goldgof DB, and Sarkar S. A Constrained Genetic Approach for Computing Material Property of Elastic Objects. *IEEE Trans Evol Comput* (2006) 10(3):341–57.
262. Oberai AA, Gokhale NH, and Feij o GR. Solution of Inverse Problems in Elasticity Imaging Using the Adjoint Method. *Inverse Probl* (2003) 19(2): 297–313. doi:10.1088/0266-5611/19/2/304
263. Van Houten EEW, Paulsen KD, Miga MI, Kennedy FE, and Weaver JB. An Overlapping Subzone Technique for MR-Based Elastic Property Reconstruction. *Magn Reson Med* (1999) 42(4):779–86. doi:10.1002/(sici)1522-2594(199910)42:4<779::aid-mrm21>3.0.co;2-z
264. McGarry MDJ, Van Houten EEW, Johnson CL, Georgiadis JG, Sutton BP, Weaver JB, et al. Multiresolution MR Elastography Using Nonlinear Inversion. *Med Phys* (2012) 39(10):6388–96. doi:10.1118/1.4754649
265. McGarry MDJ, Van Houten E, Guertler C, Okamoto RJ, Smith DR, Sowinski DR, et al. A Heterogenous, Time Harmonic, Nearly Incompressible Transverse Isotropic Finite Element Brain Simulation Platform for MR Elastography. *Phys Med Biol* (2020) 66. doi:10.1088/1361-6560/ab9a84
266. McGarry MDJ, Van Houten EEW, Perrïez PR, Pattison AJ, Weaver JB, and Paulsen KD. An Octahedral Shear Strain-Based Measure of SNR for 3D MR Elastography. *Phys Med Biol* (2011) 56(13):N153. doi:10.1088/0031-9155/56/13/n02
267. Van Houten EEW, Viviers Dv., McGarry MDJ, Perriñez PR, Perreard II, Weaver JB, et al. Subzone Based Magnetic Resonance Elastography Using a Rayleigh Damped Material Model. *Med Phys* (2011) 38(4):1993–2004. doi:10.1118/1.3557469
268. Van Houten EEW, Doyley MM, Kennedy FE, Paulsen KD, and Weaver JB. A Three-Parameter Mechanical Property Reconstruction Method for MR-Based Elastic Property Imaging. *IEEE Trans Med Imaging* (2005) 24(2): 311–24. doi:10.1109/tmi.2004.842451
269. Van Houten EEW, Weaver JB, Miga MI, Kennedy FE, and Paulsen KD. Elasticity Reconstruction from Experimental MR Displacement Data: Initial Experience with an Overlapping Subzone Finite Element Inversion Process. *Med Phys* (2000) 27(1):101–7. doi:10.1118/1.598861
270. Tan L, McGarry MDJ, Van Houten EEW, Ji M, Solamen L, Weaver JB, et al. Gradient-based Optimization for Poroelastic and Viscoelastic MR Elastography. *IEEE Trans Med Imaging* (2017) 36(1):236–50. doi:10.1109/tmi.2016.2604568
271. Perriñez PR, Kennedy FE, Van Houten EEW, Weaver JB, and Paulsen KD. Modeling of Soft Poroelastic Tissue in Time-Harmonic MR Elastography. *IEEE Trans Biomed Eng* (2009) 56(3):598–608. doi:10.1109/tbme.2008.2009928
272. Solamen LM, McGarry MD, Tan L, Weaver JB, and Paulsen KD. Phantom Evaluations of Nonlinear Inversion MR Elastography. *Phys Med Biol* (2018) 63(14):145021. doi:10.1088/1361-6560/aacb08
273. McGarry M, Van Houten E, Solamen L, Gordon-Wylie S, Weaver J, and Paulsen K. Uniqueness of Poroelastic and Viscoelastic Nonlinear Inversion MR Elastography at Low Frequencies. *Phys Med Biol* (2019) 64(7):075006. doi:10.1088/1361-6560/ab0a7d
274. Singh S, Venkatesh SK, Wang Z, Miller FH, Motosugi U, Low RN, et al. Diagnostic Performance of Magnetic Resonance Elastography in Staging Liver Fibrosis: A Systematic Review and Meta-Analysis of Individual Participant Data. *Clin Gastroenterol Hepatol* (2015) 13(3):440–51.e6. doi:10.1016/j.cgh.2014.09.046
275. Singh S, Venkatesh SK, Loomba R, Wang Z, Sirlin C, Chen J, et al. Magnetic Resonance Elastography for Staging Liver Fibrosis in Non-alcoholic Fatty Liver Disease: a Diagnostic Accuracy Systematic Review and Individual Participant Data Pooled Analysis. *Eur Radiol* (2016) 26(5):1431–40. doi:10.1007/s00330-015-3949-z
276. Huwart L, Peeters F, Sinkus R, Annet L, Salameh N, ter Beek LC, et al. Liver Fibrosis: Non-invasive Assessment with MR Elastography. *NMR Biomed* (2006) 19(2):173–9. doi:10.1002/nbm.1030
277. Huwart L, Sempoux C, Salameh N, Jamart J, Annet L, Sinkus R, et al. Liver Fibrosis: Noninvasive Assessment with MR Elastography versus Aspartate Aminotransferase-To-Platelet Ratio Index. *Radiology* (2007) 245(2):458–66. doi:10.1148/radiol.2452061673
278. Salameh N, Larrat B, Abarca-Quinones J, Pallu S, Dorvillius M, Leclercq I, et al. Early Detection of Steatohepatitis in Fatty Rat Liver by Using MR Elastography. *Radiology* (2009) 253(1):90–7. doi:10.1148/radiol.2523081817
279. Ronot M, Lambert SA, Wagner M, Garteiser P, Doblas S, Albuquerque M, et al. Viscoelastic Parameters for Quantifying Liver Fibrosis: Three-Dimensional Multifrequency MR Elastography Study on Thin Liver Rat Slices. *Plos One* (2014) 9(4):e94679. doi:10.1371/journal.pone.0094679
280. Hiscox LV, Johnson CL, Barnhill E, McGarry MDJ, Huston J, Van Beek EJR, et al. Magnetic Resonance Elastography (MRE) of the Human Brain: Technique, Findings and Clinical Applications. *Phys Med Biol* (2016) 61(24):401–37. doi:10.1088/0031-9155/61/24/r401
281. Hiscox LV, Johnson CL, McGarry MDJ, Perrins M, Littlejohn A, van Beek EJR, et al. High-resolution Magnetic Resonance Elastography Reveals Differences in Subcortical gray Matter Viscoelasticity between Young and Healthy Older Adults. *Neurobiol Aging* (2018) 65:158–67. doi:10.1016/j.neurobiolaging.2018.01.010
282. Hiscox LV, Schwarb H, McGarry MDJ, and Johnson CL. Aging Brain Mechanics: Progress and Promise of Magnetic Resonance Elastography. *NeuroImage* (2021) 232:117889. doi:10.1016/j.neuroimage.2021.117889
283. Schregel K, Nazari N, Nowicki MO, Palotai M, Lawler SE, Sinkus R, et al. Characterization of Glioblastoma in an Orthotopic Mouse Model with Magnetic Resonance Elastography. *NMR Biomed* (2018) 31(10):e3840. doi:10.1002/nbm.3840
284. Fehlner A, Behrens JR, Streitberger K-J, Papazoglou S, Braun J, Bellmann-Strobl J, et al. Higher-resolution MR Elastography Reveals Early Mechanical Signatures of Neuroinflammation in Patients with Clinically Isolated Syndrome. *J Magn Reson Imaging* (2016) 44(1):51–8. doi:10.1002/jmri.25129
285. Schwarb H, Johnson CL, McGarry MDJ, and Cohen NJ. Medial Temporal Lobe Viscoelasticity and Relational Memory Performance. *NeuroImage* (2016) 132:534–41. doi:10.1016/j.neuroimage.2016.02.059
286. Schwarb H, Johnson CL, Daugherty AM, Hillman CH, Kramer AF, Cohen NJ, et al. Aerobic Fitness, Hippocampal Viscoelasticity, and Relational Memory Performance. *NeuroImage* (2017) 153:179–88. doi:10.1016/j.neuroimage.2017.03.061
287. Sandroff BM, Johnson CL, and Motl RW. Exercise Training Effects on Memory and Hippocampal Viscoelasticity in Multiple Sclerosis: a Novel Application of Magnetic Resonance Elastography. *Neuroradiology* (2017) 59(1):61–7. doi:10.1007/s00234-016-1767-x
288. Johnson CL, Schwarb H, Horecka KM, McGarry MDJ, Hillman CH, Kramer AF, et al. Double Dissociation of Structure-Function Relationships in Memory and Fluid Intelligence Observed with Magnetic Resonance Elastography. *NeuroImage* (2018) 171:99–106. doi:10.1016/j.neuroimage.2018.01.007
289. Schwarb H, Johnson CL, Dulas MR, McGarry MDJ, Holtrop JL, Watson PD, et al. Structural and Functional MRI Evidence for Distinct Medial Temporal and Prefrontal Roles in Context-dependent Relational Memory. *J Cogn Neurosci* (2019) 31(12):1857–72. doi:10.1162/jocn_a_01454
290. Hiscox LV, Johnson CL, McGarry MDJ, Schwarb H, van Beek EJR, Roberts N, et al. Hippocampal Viscoelasticity and Episodic Memory Performance in Healthy Older Adults Examined with Magnetic Resonance Elastography. *Brain Imaging Behav* (2020) 14(1):175–85. doi:10.1007/s11682-018-9988-8
291. McIlvain G, Clements RG, Magoon EM, Spielberg JM, Telzer EH, and Johnson CL. Viscoelasticity of Reward and Control Systems in Adolescent Risk Taking. *NeuroImage* (2020) 215:116850. doi:10.1016/j.neuroimage.2020.116850
292. Sinkus R, Lorenzen J, Schrader D, Lorenzen M, Dargatz M, and Holz D. High-resolution Tensor MR Elastography for Breast Tumour Detection. *Phys Med Biol* (2000) 45(6):1649–64. doi:10.1088/0031-9155/45/6/317
293. Qin EC, Sinkus R, Geng G, Cheng S, Green M, Rae CD, et al. Combining MR Elastography and Diffusion Tensor Imaging for the Assessment of Anisotropic Mechanical Properties: A Phantom Study. *J Magn Reson Imaging* (2013) 37(1):217–26. doi:10.1002/jmri.23797
294. Schmidt JL, Tweten DJ, Badachhape AA, Reiter AJ, Okamoto RJ, Garbow JR, et al. Measurement of Anisotropic Mechanical Properties in Porcine Brain white Matter *Ex Vivo* Using Magnetic Resonance Elastography. *J Mech Behav Biomed Mater* (2018) 79:30–7. doi:10.1016/j.jmbbm.2017.11.045
295. Lilaj L, Fischer T, Guo J, Braun J, Sack I, and Hirsch S. Separation of Fluid and Solid Shear Wave fields and Quantification of Coupling Density by Magnetic

Resonance Poroelastography. *Magn Reson Med* (2021) 85(3):1655–68. doi:10.1002/mrm.28507
296. Yin M, Talwalkar JA, Glaser KJ, Manduca A, Grimm RC, Rossman PJ, et al. Assessment of Hepatic Fibrosis with Magnetic Resonance Elastography. *Clin Gastroenterol Hepatol* (2007) 5(10):1207–13. doi:10.1016/j.cgh.2007.06.012
297. Patel BK, Samreen N, Zhou Y, Chen J, Brandt K, Ehman R, et al. MR Elastography of the Breast: Evolution of Technique, Case Examples, and Future Directions. *Clin Breast Cancer* (2021) 21(1):e102–e111. doi:10.1016/j.clbc.2020.08.005
298. Kennedy BF, Wijesinghe P, and Sampson DD. The Emergence of Optical Elastography in Biomedicine. *Nat Photon* (2017) 11(4):215–21. doi:10.1038/nphoton.2017.6
299. Ingber D. Mechanobiology and Diseases of Mechanotransduction. *Ann Med* (2003) 35(8):564–77. doi:10.1080/07853890310016333
300. Di Carlo D. A Mechanical Biomarker of Cell State in Medicine. *J Lab Autom* (2012) 17(1):32–42. doi:10.1177/2211068211431630
301. Akinyi T, Grasland-Mongrain P, Bhatt M, Catheline S, and Cloutier G. Recent Advances in Imaging of Cell Elasticity. *Viscoelasticity and Collective Cell Migration* (2021) 257–96. doi:10.1016/b978-0-12-820310-1.00010-0
302. Grasland-Mongrain P, Zorgani A, Nakagawa S, Bernard S, Paim LG, Fitzharris G, et al. Ultrafast Imaging of Cell Elasticity with Optical Microelastography. *Proc Natl Acad Sci USA* (2018) 115(5):861–6. doi:10.1073/pnas.1713395115
303. Poree J, Garcia D, Chayer B, Ohayon J, and Cloutier G. Noninvasive Vascular Elastography with Plane Strain Incompressibility assumption Using Ultrafast Coherent Compound Plane Wave Imaging. *IEEE Trans Med Imaging* (2015) 34(12):2618–31. doi:10.1109/tmi.2015.2450992
304. Gallot T, Catheline S, Roux P, Brum J, Benech N, and Negreira C. Passive Elastography: Shear-Wave Tomography from Physiological-Noise Correlation in Soft Tissues. *IEEE Trans Ultrason Ferroelect., Freq Contr* (2011) 58(6):1122–6. doi:10.1109/tuffc.2011.1920
305. Larin KV, and Sampson DD. Optical Coherence Elastography - OCT at Work in Tissue Biomechanics [Invited]. *Biomed Opt Express* (2017) 8(2):1172–202. doi:10.1364/BOE.8.001172
306. Liang X, and Boppart SA. Biomechanical Properties of *In Vivo* Human Skin from Dynamic Optical Coherence Elastography. *IEEE Trans Biomed Eng* (2010) 57(4):953–9. doi:10.1109/TBME.2009.2033464
307. Sun C, Standish B, and Yang VX. Optical Coherence Elastography: Current Status and Future Applications. *J Biomed Opt* (2011) 16(4):043001. doi:10.1117/1.3560294
308. Kennedy KM, Ford C, Kennedy BF, Bush MB, and Sampson DD. Analysis of Mechanical Contrast in Optical Coherence Elastography. *J Biomed Opt* (2013) 18(12):121508. doi:10.1117/1.jbo.18.12.121508
309. Yang VXD, Munce N, Pekar J, Gordon ML, Lo S, Marcon NE, et al. Micromachined Array Tip for Multifocus Fiber-Based Optical Coherence Tomography. *Opt Lett* (2004) 29:1754–6. doi:10.1364/ol.29.001754
310. Kennedy BF, McLaughlin RA, Kennedy KM, Chin L, Curatolo A, Tien A, et al. Optical Coherence Micro-elastography: Mechanical-Contrast Imaging of Tissue Microstructure. *Biomed Opt Express* (2014) 5(7):2113–24. doi:10.1364/BOE.5.002113
311. Wang S, Singh M, Tran TT, Leach J, Aglyamov SR, Larina IV, et al. Biomechanical Assessment of Myocardial Infarction Using Optical Coherence Elastography. *Biomed Opt Express* (2018) 9(2):728–42. doi:10.1364/boe.9.000728
312. Qu Y, Ma T, He Y, Zhu J, Dai C, Yu M, et al. Acoustic Radiation Force Optical Coherence Elastography of Corneal Tissue. *IEEE J Select Top Quan Electron.* (2016) 22(3):288–94. doi:10.1109/jstqe.2016.2524618
313. Rogowska J, Patel NA, Fujimoto JG, and Brezinski ME. Optical Coherence Tomographic Elastography Technique for Measuring Deformation and Strain of Atherosclerotic Tissues. *Heart* (2004) 90(5):556–62. doi:10.1136/hrt.2003.016956
314. Chan RC, Chau AH, Karl WC, Nadkarni S, Khalil AS, Iftimia N, et al. OCT-based Arterial Elastography: Robust Estimation Exploiting Tissue Biomechanics. *Opt Express* (2004) 12(19):4558–457. doi:10.1364/opex.12.004558
315. Wang RK, Ma Z, and Kirkpatrick SJ. Tissue Doppler Optical Coherence Elastography for Real Time Strain Rate and Strain Mapping of Soft Tissue. *Appl Phys Lett* (2006) 89(14):144103. doi:10.1063/1.2357854
316. Crecea V, Oldenburg AL, Liang X, Ralston TS, and Boppart SA. Magnetomotive Nanoparticle Transducers for Optical Rheology of Viscoelastic Materials. *Opt Express* (2009) 17(25):23114–22. doi:10.1364/oe.17.023114
317. Li C, Huang Z, and Wang RK. Elastic Properties of Soft Tissue-Mimicking Phantoms Assessed by Combined Use of Laser Ultrasonics and Low Coherence Interferometry. *Opt Express* (2011) 19(11):10153–63. doi:10.1364/oe.19.010153
318. Razani M, Mariampillai A, Sun C, Luk TWH, Yang VXD, and Kolios MC. Feasibility of Optical Coherence Elastography Measurements of Shear Wave Propagation in Homogeneous Tissue Equivalent Phantoms. *Biomed Opt Express* (2012) 3(5):972–80. doi:10.1364/boe.3.000972
319. Nahas A, Bauer M, Roux S, and Boccara AC. 3D Static Elastography at the Micrometer Scale Using Full Field OCT. *Biomed Opt Express* (2013) 4(10):2138–49. doi:10.1364/boe.4.002138
320. Song S, Huang Z, and Wang RK. Tracking Mechanical Wave Propagation within Tissue Using Phase-Sensitive Optical Coherence Tomography: Motion Artifact and its Compensation. *J Biomed Opt* (2013) 18(12):121505. doi:10.1117/1.jbo.18.12.121505
321. Wang S, and Larin KV. Optical Coherence Elastography for Tissue Characterization: a Review. *J Biophoton* (2015) 8(4):279–302. doi:10.1002/jbio.201400108
322. Zhu J, Qi L, Miao Y, Ma T, Dai C, Qu Y, et al. 3D Mapping of Elastic Modulus Using Shear Wave Optical Micro-elastography. *Scientific Rep* (2016) 6(1):1–9. doi:10.1038/srep35499
323. Song S, Le NM, Huang Z, Shen T, and Wang RK. Quantitative Shear-Wave Optical Coherence Elastography with a Programmable Phased Array Ultrasound as the Wave Source. *Opt Lett* (2015) 40(21):5007–10. doi:10.1364/ol.40.005007
324. Zvietcovich F, Ge GR, Mestre H, Giannetto M, Nedergaard M, Rolland JP, et al. Longitudinal Shear Waves for Elastic Characterization of Tissues in Optical Coherence Elastography. *Biomed Opt Express* (2019) 10(7):3699–718. doi:10.1364/BOE.10.003699
325. Nahas A, Tanter M, Nguyen T-M, Chassot J-M, Fink M, and Claude Boccara A. From Supersonic Shear Wave Imaging to Full-Field Optical Coherence Shear Wave Elastography. *J Biomed Opt* (2013) 18(12):121514. doi:10.1117/1.jbo.18.12.121514
326. Zhu J, Qu Y, Ma T, Li R, Du Y, Huang S, et al. Imaging and Characterizing Shear Wave and Shear Modulus under Orthogonal Acoustic Radiation Force Excitation Using OCT Doppler Variance Method. *Opt Lett* (2015) 40(9):2099–102. doi:10.1364/ol.40.002099
327. Nguyen T-M, Song S, Arnal B, Huang Z, O'Donnell M, and Wang RK. Visualizing Ultrasonically Induced Shear Wave Propagation Using Phase-Sensitive Optical Coherence Tomography for Dynamic Elastography. *Opt Lett* (2014) 39(4):838–41. doi:10.1364/ol.39.000838
328. Qi W, Li R, Ma T, Li J, Kirk Shung K, Zhou Q, et al. Resonant Acoustic Radiation Force Optical Coherence Elastography. *Appl Phys Lett* (2013) 103(10):103704. doi:10.1063/1.4820252
329. Nguyen TM, Arnal B, Song S, Huang Z, Wang RK, and O'Donnell M. Shear Wave Elastography Using Amplitude-Modulated Acoustic Radiation Force and Phase-Sensitive Optical Coherence Tomography. *J Biomed Opt* (2015) 20(1):016001. doi:10.1117/1.jbo.20.1.016001
330. Zhu J, Miao Y, Qi L, Qu Y, He Y, Yang Q, et al. Longitudinal Shear Wave Imaging for Elasticity Mapping Using Optical Coherence Elastography. *Appl Phys Lett* (2017) 110(20):201101. doi:10.1063/1.4983292
331. Zhu J, Yu J, Qu Y, He Y, Li Y, Yang Q, et al. Coaxial Excitation Longitudinal Shear Wave Measurement for Quantitative Elasticity Assessment Using Phase-Resolved Optical Coherence Elastography. *Opt Lett* (2018) 43(10):2388–91. doi:10.1364/ol.43.002388
332. Ambrozinski L, Song S, Yoon SJ, Pelivanov I, Li D, Gao L, et al. Acoustic Micro-tapping for Non-contact 4D Imaging of Tissue Elasticity. *Sci Rep* (2016) 6(1):38967. doi:10.1038/srep38967
333. Wang S, and Larin KV. Shear Wave Imaging Optical Coherence Tomography (SWI-OCT) for Ocular Tissue Biomechanics. *Opt Lett* (2014) 39(1):41–4. doi:10.1364/ol.39.000041
334. Wang S, Lopez AL, 3rd, Morikawa Y, Tao G, Li J, Larina IV, et al. Noncontact Quantitative Biomechanical Characterization of Cardiac Muscle Using Shear Wave Imaging Optical Coherence Tomography. *Biomed Opt Express* (2014) 5(7):1980–92. doi:10.1364/BOE.5.001980

335. Wang S, and Larin KV. Noncontact Depth-Resolved Micro-scale Optical Coherence Elastography of the Cornea. *Biomed Opt Express* (2014) 5(11): 3807–21. doi:10.1364/boe.5.003807
336. Zvietcovich F, Nair A, Ambekar YS, Singh M, Aglyamov SR, Twa MD, et al. Confocal Air-Coupled Ultrasonic Optical Coherence Elastography Probe for Quantitative Biomechanics. *Opt Lett* (2020) 45(23):6567–70. doi:10.1364/ol.410593
337. Pitre JJ, Jr., Kirby MA, Li DS, Shen TT, Wang RK, O'Donnell M, et al. Nearly-incompressible Transverse Isotropy (NITI) of Cornea Elasticity: Model and Experiments with Acoustic Micro-tapping OCE. *Sci Rep* (2020) 10(1):12983. doi:10.1038/s41598-020-69909-9
338. Pelivanov I, Gao L, Pitre J, Kirby MA, Song S, Li D, et al. Does Group Velocity Always Reflect Elastic Modulus in Shear Wave Elastography. *J Biomed Opt* (2019) 24(7):076003. doi:10.1117/1.jbo.24.7.076003
339. Kirby MA, Pelivanov I, Song S, Ambrozinski Ł, Yoon SJ, Gao L, et al. Optical Coherence Elastography in Ophthalmology. *J Biomed Opt* (2017) 22(12): 1–28. doi:10.1117/1.jbo.22.12.121720
340. Alonso-Caneiro D, Karnowski K, Kaluzny BJ, Kowalczyk A, and Wojtkowski M. Assessment of Corneal Dynamics with High-Speed Swept Source Optical Coherence Tomography Combined with an Air Puff System. *Opt Express* (2011) 19(15):14188–99. doi:10.1364/oe.19.014188
341. Wang S, Li J, Manapuram RK, Menodiado FM, Ingram DR, Twa MD, et al. Noncontact Measurement of Elasticity for the Detection of Soft-Tissue Tumors Using Phase-Sensitive Optical Coherence Tomography Combined with a Focused Air-Puff System. *Opt Lett* (2012) 37(24):5184–6. doi:10.1364/ol.37.005184
342. Ambrozinski L, Pelivanov I, Song S, Yoon SJ, Li D, Gao L, et al. Air-coupled Acoustic Radiation Force for Non-contact Generation of Broadband Mechanical Waves in Soft media. *Appl Phys Lett* (2016) 109(4):043701. doi:10.1063/1.4959827
343. Ramier A, Tavakol B, and Yun SH. Measuring Mechanical Wave Speed, Dispersion, and Viscoelastic Modulus of the Cornea Using Optical Coherence Elastography. *Opt Express* (2019) 27(12):16635–49. doi:10.1364/OE.27.016635
344. Han Z, Li J, Singh M, Wu C, Liu C-h., Raghunathan R, et al. Optical Coherence Elastography Assessment of Corneal Viscoelasticity with a Modified Rayleigh-Lamb Wave Model. *J Mech Behav Biomed Mater* (2017) 66:87–94. doi:10.1016/j.jmbbm.2016.11.004
345. Jin Z, Zhou Y, Shen M, Wang Y, Lu F, and Zhu D. Assessment of Corneal Viscoelasticity Using Elastic Wave Optical Coherence Elastography. *J Biophotonics* (2020) 13(1):e201960074. doi:10.1002/jbio.201960074
346. Liu HC, Abbasi M, Ding YH, Roy T, Capriotti M, Liu Y, et al. Characterizing Blood Clots Using Acoustic Radiation Force Optical Coherence Elastography and Ultrasound Shear Wave Elastography. *Phys Med Biol* (2021) 66(3): 035013. doi:10.1088/1361-6560/abcb1e
347. Liu HC, Kijanka P, and Urban MW. Acoustic Radiation Force Optical Coherence Elastography for Evaluating Mechanical Properties of Soft Condensed Matters and its Biological Applications. *J Biophotonics* (2020) 13(3):e201960134. doi:10.1002/jbio.201960134
348. Wang LV, and Hu S. Photoacoustic Tomography: *In Vivo* Imaging from Organelles to Organs. *Science* (2012) 335(6075):1458–62. doi:10.1126/science.1216210
349. Hai P, Zhou Y, Liang J, Li C, and Wang LV. Photoacoustic Tomography of Vascular Compliance in Humans. *J Biomed Opt* (2015) 20(12):126008. doi:10.1117/1.jbo.20.12.126008
350. Singh MS, and Thomas A. Photoacoustic Elastography Imaging: a Review. *J Biomed Opt* (2019) 24(4):040902. doi:10.1117/1.jbo.24.4.040902
351. Hai P, Yao J, Li G, Li C, and Wang LV. Photoacoustic Elastography. *Opt Lett* (2016) 41(4):725–8. doi:10.1364/ol.41.000725
352. Gao G, Yang S, and Xing D. Viscoelasticity Imaging of Biological Tissues with Phase-Resolved Photoacoustic Measurement. *Opt Lett* (2011) 36(17):3341–3. doi:10.1364/ol.36.003341
353. Wadamori N. Non-restrained Measurement of Young's Modulus for Soft Tissue Using a Photoacoustic Technique. *Appl Phys Lett* (2014) 105(10): 103707. doi:10.1063/1.4893725
354. Liu Y, and Yuan Z. Multi-spectral Photoacoustic Elasticity Tomography. *Biomed Opt Express* (2016) 7(9):3323–34. doi:10.1364/BOE.7.003323
355. Upputuri PK, and Pramanik M. Recent Advances toward Preclinical and Clinical Translation of Photoacoustic Tomography: a Review. *J Biomed Opt* (2017) 22(4):41006. doi:10.1117/1.JBO.22.4.041006
356. Singh MS, and Jiang H. Elastic Property Attributes to Photoacoustic Signals: an Experimental Phantom Study. *Opt Lett* (2014) 39(13):3970–3. doi:10.1364/OL.39.003970
357. Singh MS, and Jiang H. Ultrasound (US) Transducer of Higher Operating Frequency Detects Photoacoustic (PA) Signals Due to the Contrast in Elastic Property. *AIP Adv* (2016) 6(2):025210. doi:10.1063/1.4942106
358. Zhao Y, Yang S, Chen C, and Xing D. Simultaneous Optical Absorption and Viscoelasticity Imaging Based on Photoacoustic Lock-In Measurement. *Opt Lett* (2014) 39(9):2565–8. doi:10.1364/OL.39.002565
359. Wang Q, Shi Y, Yang F, and Yang S. Quantitative Photoacoustic Elasticity and Viscosity Imaging for Cirrhosis Detection. *Appl Phys Lett* (2018) 112(21): 211902. doi:10.1063/1.5021675
360. Scholz M, Noack V, Pechlivanis I, Engelhardt M, Fricke B, Linstedt U, et al. Vibrography during Tumor Neurosurgery. *J Ultrasound Med* (2005) 24(7): 985–92. doi:10.7863/jum.2005.24.7.985
361. Lee W-N, Larrat B, Pernot M, and Tanter M. Ultrasound Elastic Tensor Imaging: Comparison with MR Diffusion Tensor Imaging in the Myocardium. *Phys Med Biol* (2012) 57(16):5075–95. doi:10.1088/0031-9155/57/16/5075
362. Islam MT, Chaudhry A, Tang S, Tasciotti E, and Righetti R. A New Method for Estimating the Effective Poisson's Ratio in Ultrasound Poroelastography. *IEEE Trans Med Imaging* (2018) 37(5):1178–91. doi:10.1109/tmi.2018.2792437
363. Righetti R, Ophir J, Srinivasan S, and Krouskop TA. The Feasibility of Using Elastography for Imaging the Poisson's Ratio in Porous media. *Ultrasound Med Biol* (2004) 30(2):215–28. doi:10.1016/j.ultrasmedbio.2003.10.022
364. Chaudhry A, Kim N, Unnikrishnan G, Nair S, Reddy JN, and Righetti R. Effect of Interstitial Fluid Pressure on Ultrasound Axial Strain and Axial Shear Strain Elastography. *Ultrason Imaging* (2017) 39(2):137–46. doi:10.1177/0161734616671713
365. Islam MT, Tasciotti E, and Righetti R. Estimation of Vascular Permeability in Irregularly Shaped Cancers Using Ultrasound Poroelastography. *IEEE Trans Biomed Eng* (2020) 67(4):1083–96. doi:10.1109/tbme.2019.2929134
366. Drakonaki EE, Allen GM, and Wilson DJ. Ultrasound Elastography for Musculoskeletal Applications. *Br J Radiol* (2012) 85(1019):1435–45. doi:10.1259/bjr/93042867
367. Bhatia KSS, Cho CCM, Tong CSL, Yuen EHY, and Ahuja AT. Shear Wave Elasticity Imaging of Cervical Lymph Nodes. *Ultrasound Med Biol* (2012) 38(2):195–201. doi:10.1016/j.ultrasmedbio.2011.10.024
368. Strachinaru M, Bosch JG, van Dalen BM, van Gils L, van der Steen AFW, de Jong N, et al. Cardiac Shear Wave Elastography Using a Clinical Ultrasound System. *Ultrasound Med Biol* (2017) 43(8):1596–606. doi:10.1016/j.ultrasmedbio.2017.04.012
369. Zhou J, Zhan W, Chang C, Zhang J, Yang Z, Dong Y, et al. Role of Acoustic Shear Wave Velocity Measurement in Characterization of Breast Lesions. *J Ultrasound Med* (2013) 32(2):285–94. doi:10.7863/jum.2013.32.2.285
370. Palmeri ML, Wang MH, Rouze NC, Abdelmalek MF, Guy CD, Moser B, et al. Noninvasive Evaluation of Hepatic Fibrosis Using Acoustic Radiation Force-Based Shear Stiffness in Patients with Nonalcoholic Fatty Liver Disease. *J Hepatol* (2011) 55(3):666–72. doi:10.1016/j.jhep.2010.12.019
371. Golatta M, Schweitzer-Martin M, Harcos A, Schott S, Gomez C, Stieber A, et al. Evaluation of Virtual Touch Tissue Imaging Quantification, a New Shear Wave Velocity Imaging Method, for Breast Lesion Assessment by Ultrasound. *Biomed Res Int* (2014) 2014:960262. doi:10.1155/2014/960262
372. Deffieux T, Gennisson J-L, Bousquet L, Corouge M, Cosconea S, Amroun D, et al. Investigating Liver Stiffness and Viscosity for Fibrosis, Steatosis and Activity Staging Using Shear Wave Elastography. *J Hepatol* (2015) 62(2): 317–24. doi:10.1016/j.jhep.2014.09.020
373. Castera L, Denis J, Babany G, and Roudot-Thoraval F. Evolving Practices of Non-invasive Markers of Liver Fibrosis in Patients with Chronic Hepatitis C in France: Time for New Guidelines? *J Hepatol* (2007) 46(3):528–9. doi:10.1016/j.jhep.2006.12.002
374. Arnal B, Pernot M, and Tanter M. Monitoring of thermal Ablation Therapy Based on Shear Modulus Changes: Shear Wave Thermometry and Shear

Wave Lesion Imaging. In: 2010 IEEE International Ultrasonics Symposium (2010). p. 1522–5.
375. Tanter M, and Fink M. Ultrafast Imaging in Biomedical Ultrasound. *IEEE Trans Ultrason Ferroelect., Freq Contr* (2014) 61(1):102–19. doi:10.1109/tuffc.2014.2882
376. Song P, Macdonald MC, Behler RH, Lanning JD, Wang MH, Urban MW, et al. Shear Wave Elastography on the GE LOGIQ E9 with Comb-Push Ultrasound Shear Elastography (CUSE) and Time Aligned Sequential Tracking (TAST). In: 2014 IEEE International Ultrasonics Symposium (2014). p. 1101–4.
377. Aristizabal S, Amador Carrascal C, Nenadic IZ, Greenleaf JF, and Urban MW. Application of Acoustoelasticity to Evaluate Nonlinear Modulus in *Ex Vivo* Kidneys. *IEEE Trans Ultrason Ferroelect., Freq Contr* (2018) 65(2):188–200. doi:10.1109/tuffc.2017.2781654
378. Gennisson J-L, and Aristizabal S. Nonlinear Shear Elasticity. In: Ultrasound Elastography for Biomedical Applications and Medicine (2018). p. 451–69. doi:10.1002/9781119021520.ch29
379. Caenen A, Pernot M, Peirlinck M, Mertens L, Swillens A, and Segers P. An In Silico Framework to Analyze the Anisotropic Shear Wave Mechanics in Cardiac Shear Wave Elastography. *Phys Med Biol* (2018) 63(7):075005. doi:10.1088/1361-6560/aaaffe
380. Chen YL, Gao Y, Chang C, Wang F, Zeng W, and Chen JJ. Ultrasound Shear Wave Elastography of Breast Lesions: Correlation of Anisotropy with Clinical and Histopathological Findings. *Cancer Imaging* (2018) 18(1):1–11. doi:10.1186/s40644-018-0144-x
382. Islam MT, Chaudhry A, Unnikrishnan G, Reddy JN, and Righetti R. An Analytical Model of Tumors with Higher Permeability Than Surrounding Tissues for Ultrasound Elastography Imaging. *J Eng Sci Med Diagn Ther* (2018) 1(3):031006. doi:10.1115/1.4040145
383. Islam MT, Reddy JN, and Righetti R. An Analytical Poroelastic Model of a Nonhomogeneous Medium under Creep Compression for Ultrasound Poroelastography Applications—Part I. *J Biomechanical Eng* (2019) 141(6):060902. doi:10.1115/1.4040604
384. Mariani A, Kwiecinski W, Pernot M, Balvay D, Tanter M, Clement O, et al. Real Time Shear Waves Elastography Monitoring of thermal Ablation: *In Vivo* Evaluation in Pig Livers. *J Surg Res* (2014) 188(1):37–43. doi:10.1016/j.jss.2013.12.024
385. Sapin-de Brosses E, Gennisson J-L, Pernot M, Fink M, and Tanter M. Temperature Dependence of the Shear Modulus of Soft Tissues Assessed by Ultrasound. *Phys Med Biol* (2010) 55(6):1701–18. doi:10.1088/0031-9155/55/6/011
386. Venkatesh SK, Yin M, and Ehman RL. Magnetic Resonance Elastography of Liver: Technique, Analysis, and Clinical Applications. *J Magn Reson Imaging* (2013) 37(3):544–55. doi:10.1002/jmri.23731
387. Bohte AE, Nelissen JL, Runge JH, Holub O, Lambert SA, de Graaf L, et al. Breast Magnetic Resonance Elastography: a Review of Clinical Work and Future Perspectives. *NMR Biomed* (2018) 31(10):e3932. doi:10.1002/nbm.3932
388. Davids M, Guérin B, vom Endt A, Schad LR, and Wald LL. Prediction of Peripheral Nerve Stimulation Thresholds of MRI Gradient Coils Using Coupled Electromagnetic and Neurodynamic Simulations. *Magn Reson Med* (2019) 81(1):686–701. doi:10.1002/mrm.27382
389. Souchon R, Salomir R, Beuf O, Milot L, Grenier D, Lyonnet D, et al. Transient MR Elastography (T-MRE) Using Ultrasound Radiation Force: Theory, Safety, and Initial Experiments *In Vitro*. *Magn Reson Med* (2008) 60(4):871–81. doi:10.1002/mrm.21718
390. Grasland-Mongrain P, Souchon R, Cartellier F, Zorgani A, Chapelon JY, Lafon C, et al. Imaging of Shear Waves Induced by Lorentz Force in Soft Tissues. *Phys Rev Lett* (2014) 113(3):1–5. doi:10.1103/physrevlett.113.038101
391. Grasland-Mongrain P, Miller-Jolicoeur E, Tang A, Catheline S, and Cloutier G. Contactless Remote Induction of Shear Waves in Soft Tissues Using a Transcranial Magnetic Stimulation Device. *Phys Med Biol* (2016) 61(6):2582–93. doi:10.1088/0031-9155/61/6/2582
392. Vappou J, Bour P, Marquet F, Ozenne V, and Quesson B. MR-ARFI-based Method for the Quantitative Measurement of Tissue Elasticity: Application for Monitoring HIFU Therapy. *Phys Med Biol* (2018) 63(9):095018. doi:10.1088/1361-6560/aabd0d
393. Yuan L, Glaser KJ, Rouviere O, Gorny KR, Chen S, Manduca A, et al. Preliminary Assessment of One-Dimensional MR Elastography for Use in Monitoring Focused Ultrasound Therapy. *Phys Med Biol* (2007) 52(19):5909–19. doi:10.1088/0031-9155/52/19/012
394. Corbin N, Vappou J, Breton E, Boehler Q, Barbé L, Renaud P, et al. Interventional MR Elastography for MRI-Guided Percutaneous Procedures. *Magn Reson Med* (2016) 75(3):1110–8. doi:10.1002/mrm.25694
395. Chen J, Woodrum DA, Glaser KJ, Murphy MC, Gorny K, and Ehman R. Assessment of *In Vivo* Laser Ablation Using MR Elastography with an Inertial Driver. *Magn Reson Med* (2014) 72(1):59–67. doi:10.1002/mrm.24891
396. Wu T, Felmlee JP, Greenleaf JF, Riederer SJ, and Ehman RL. Assessment of thermal Tissue Ablation with MR Elastography. *Magn Reson Med* (2001) 45(1):80–7. doi:10.1002/1522-2594(200101)45:1<80::aid-mrm1012>3.0.co;2-y
397. Guenthner C, Sethi S, Troelstra M, Gorkum RJH, Gastl M, Sinkus R, et al. Unipolar MR Elastography: Theory, Numerical Analysis and Implementation. *NMR Biomed* (2020) 33(1):e4138. doi:10.1002/nbm.4138
398. Wu P-H, Aroush DR-B, Asnacios A, Chen W-C, Dokukin ME, Doss BL, et al. A Comparison of Methods to Assess Cell Mechanical Properties. *Nat Methods* (2018) 15(7):491–8. doi:10.1038/s41592-018-0015-1
399. Girardo S, Träber N, Wagner K, Cojoc G, Herold C, Goswami R, et al. Standardized Microgel Beads as Elastic Cell Mechanical Probes. *J Mater Chem B* (2018) 6(39):6245–61. doi:10.1039/c8tb01421c
400. Guck J. Some Thoughts on the Future of Cell Mechanics. *Biophys Rev* (2019) 11(5):667–70. doi:10.1007/s12551-019-00597-0
401. Hao Y, Cheng S, Tanaka Y, Hosokawa Y, Yalikun Y, and Li M. Mechanical Properties of Single Cells: Measurement Methods and Applications. *Biotechnol Adv* (2020) 45:107648. doi:10.1016/j.biotechadv.2020.107648
402. Fu J, Pierron F, and Ruiz PD. Elastic Stiffness Characterization Using Three-Dimensional Full-Field Deformation Obtained with Optical Coherence Tomography and Digital Volume Correlation. *J Biomed Opt* (2013) 18(12):121512. doi:10.1117/1.jbo.18.12.121512
403. Chin L, Curatolo A, Kennedy BF, Doyle BJ, Munro PR, McLaughlin RA, et al. Analysis of Image Formation in Optical Coherence Elastography Using a Multiphysics Approach. *Biomed Opt Express* (2014) 5(9):2913–30. doi:10.1364/BOE.5.002913
404. Leroux C-E, Palmier J, Boccara AC, Cappello G, and Monnier S. Elastography of Multicellular Aggregates Submitted to Osmo-Mechanical Stress. *New J Phys* (2015) 17(7):073035. doi:10.1088/1367-2630/17/7/073035
405. Curatolo A, Villiger M, Lorenser D, Wijesinghe P, Fritz A, Kennedy BF, et al. Ultrahigh-resolution Optical Coherence Elastography. *Opt Lett* (2016) 41(1):21–4. doi:10.1364/ol.41.000021
406. Pokharel D, Wijesinghe P, Oenarto V, Lu JF, Sampson DD, Kennedy BF, et al. Deciphering Cell-To-Cell Communication in Acquisition of Cancer Traits: Extracellular Membrane Vesicles Are Regulators of Tissue Biomechanics. *OMICS: A J Integr Biol* (2016) 20(8):462–9. doi:10.1089/omi.2016.0072
407. Karimi R, Zhu T, Bouma BE, and Kaazempur Mofrad MR. Estimation of Nonlinear Mechanical Properties of Vascular Tissues via Elastography. *Cardiovasc Eng* (2008) 8(4):191–202. doi:10.1007/s10558-008-9061-0
408. Sridhar M, Liu J, and Insana MF. Elasticity Imaging of Polymeric media. *J Biomech Eng* (2007) 129(2):259–72. doi:10.1115/1.2540804
409. Banerjee B, Roy D, and Vasu RM. Efficient Implementations of a Pseudodynamical Stochastic Filtering Strategy for Static Elastography. *Med Phys* (2009) 36(8):3470–6. doi:10.1118/1.3158808
410. Le Floc'h S, Ohayon J, Tracqui P, Finet G, Gharib AM, Maurice RL, et al. Vulnerable Atherosclerotic Plaque Elasticity Reconstruction Based on a Segmentation-Driven Optimization Procedure Using Strain Measurements: Theoretical Framework. *IEEE Trans Med Imaging* (2009) 28(7):1126–37. doi:10.1109/tmi.2009.2012852
411. Graff KF *Wave Motion in Elastic Solids*. Courier Corporation (2012).
412. Singh MS, Yalavarthy PK, Vasu RM, and Rajan K. Assessment of Ultrasound Modulation of Near Infrared Light on the Quantification of Scattering Coefficient. *Med Phys* (2010) 37(7):3744–51. doi:10.1118/1.3456441

413. Singh MS, Rajan K, Vasu RM, and Roy D. Quantitative Estimation of Mechanical and Optical Properties from Ultrasound Assisted Optical Tomography Data. *J Biomed Opt* (2012) 17(10):101507. doi:10.1117/1.jbo.17.10.101507
414. Hai P, Zhou Y, Gong L, and Wang LV. Quantitative Photoacoustic Elastography in Humans. *J Biomed Opt* (2016) 21(6):66011. doi:10.1117/1.JBO.21.6.066011
415. Grasland-Mongrain P, Lu Y, Lesage F, Catheline S, and Cloutier G. Generation of Shear Waves by Laser in Soft media in the Ablative and Thermoelastic Regimes. *Appl Phys Lett* (2016) 109(22):1–5. doi:10.1063/1.4968538
416. Ferraioli G, Parekh P, Levitov AB, and Filice C. Shear Wave Elastography for Evaluation of Liver Fibrosis. *J Ultrasound Med* (2014) 33(2):197–203. doi:10.7863/ultra.33.2.197
417. Crombé A, Hurtevent-Labrot G, Asad-Syed M, Palussière J, MacGrogan G, Kind M, et al. Shear-wave Elastography Quantitative Assessment of the Male Breast: Added Value to Distinguish Benign and Malignant Palpable Masses. *Br J Radiol* (2018) 91(1082):20170676. doi:10.1259/bjr.20170676
418. Barr RG, and Zhang Z. Shear-wave Elastography of the Breast: Value of a Quality Measure and Comparison with Strain Elastography. *Radiology* (2015) 275(1):45–53. doi:10.1148/radiol.14132404
419. Cantisani V, Lodise P, Grazhdani H, Mancuso E, Maggini E, Di Rocco G, et al. Ultrasound Elastography in the Evaluation of Thyroid Pathology. Current Status. *Eur J Radiol* (2014) 83(3):420–8. doi:10.1016/j.ejrad.2013.05.008
420. Gu J, Du L, Bai M, Chen H, Jia X, Zhao J, et al. Preliminary Study on the Diagnostic Value of Acoustic Radiation Force Impulse Technology for Differentiating between Benign and Malignant Thyroid Nodules. *J Ultrasound Med* (2012) 31(5):763–71. doi:10.7863/jum.2012.31.5.763
421. Magri F, Chytiris S, Capelli V, Alessi S, Nalon E, Rotondi M, et al. Shear Wave Elastography in the Diagnosis of Thyroid Nodules: Feasibility in the Case of Coexistent Chronic Autoimmune Hashimoto's Thyroiditis. *Clin Endocrinol* (2012) 76(1):137–41. doi:10.1111/j.1365-2265.2011.04170.x
422. Zhan J, Jin J-M, Diao X-H, and Chen Y. Acoustic Radiation Force Impulse Imaging (ARFI) for Differentiation of Benign and Malignant Thyroid Nodules-A Meta-Analysis. *Eur J Radiol* (2015) 84(11):2181–6. doi:10.1016/j.ejrad.2015.07.015
423. Dong F-J, Li M, Jiao Y, Xu JF, Xiong Y, Zhang L, et al. Acoustic Radiation Force Impulse Imaging for Detecting Thyroid Nodules: a Systematic Review and Pooled Meta-Analysis. *Med Ultrason* (2015) 17(2):192–9. doi:10.11152/mu.2013.2066.172.hyr
424. Slapa RZ, Piwowonski A, Jakubowski WS, Bierca J, Szopinski KT, Slowinska-Srzednicka J, et al. Shear Wave Elastography May Add a New Dimension to Ultrasound Evaluation of Thyroid Nodules: Case Series with Comparative Evaluation. *J Thyroid Res* (2012) 2012:657147. doi:10.1155/2012/657147
425. Sebag F, Vaillant-Lombard J, Berbis J, Griset V, Henry JF, Petit P, et al. Shear Wave Elastography: a New Ultrasound Imaging Mode for the Differential Diagnosis of Benign and Malignant Thyroid Nodules. *J Clin Endocrinol Metab* (2010) 95(12):5281–8. doi:10.1210/jc.2010-0766
426. Szczepanek-Parulska E, Woliński K, Stangierski A, Gurgul E, Biczysko M, Majewski P, et al. Comparison of Diagnostic Value of Conventional Ultrasonography and Shear Wave Elastography in the Prediction of Thyroid Lesions Malignancy. *PLoS One* (2013) 8(11):e81532. doi:10.1371/journal.pone.0081532
427. Hu L, He NA, Xie L, Ye X, Liu X, Pei C, et al. Evaluation of the Perinodular Stiffness Potentially Predicts the Malignancy of Thyroid Nodules. *J Ultrasound Med* (2020) 39(11):2183–93. doi:10.1002/jum.15329
428. You J, Chen J, Xiang F, Song Y, Khamis S, Lu C, et al. The Value of Quantitative Shear Wave Elastography in Differentiating the Cervical Lymph Nodes in Patients with Thyroid Nodules. *J Med Ultrason* (2018) 45(2):251–9. doi:10.1007/s10396-017-0819-0
429. Veyrieres J-B, Albarel F, Lombard JV, Berbis J, Sebag F, Oliver C, et al. A Threshold Value in Shear Wave Elastography to Rule Out Malignant Thyroid Nodules: a Reality? *Eur J Radiol* (2012) 81(12):3965–72. doi:10.1016/j.ejrad.2012.09.002
430. Samir AE, Dhyani M, Anvari A, Prescott J, Halpern EF, Faquin WC, et al. Shear-wave Elastography for the Preoperative Risk Stratification of Follicular-Patterned Lesions of the Thyroid: Diagnostic Accuracy and Optimal Measurement Plane. *Radiology* (2015) 277(2):565–73. doi:10.1148/radiol.2015141627
431. Eby SF, Cloud BA, Brandenburg JE, Giambini H, Song P, Chen S, et al. Shear Wave Elastography of Passive Skeletal Muscle Stiffness: Influences of Sex and Age throughout Adulthood. *Clin Biomech* (2015) 30(1):22–7. doi:10.1016/j.clinbiomech.2014.11.011
432. Koo TK, Guo J-Y, Cohen JH, and Parker KJ. Quantifying the Passive Stretching Response of Human Tibialis Anterior Muscle Using Shear Wave Elastography. *Clin Biomech* (2014) 29(1):33–9. doi:10.1016/j.clinbiomech.2013.11.009
434. Cortes DH, Suydam SM, Silbernagel KG, Buchanan TS, and Elliott DM. Continuous Shear Wave Elastography: A New Method to Measure Viscoelastic Properties of Tendons *In Vivo*. *Ultrasound Med Biol* (2015) 41(6):1518–29. doi:10.1016/j.ultrasmedbio.2015.02.001
435. Aubry S, Risson J-R, Kastler A, Barbier-Brion B, Siliman G, Runge M, et al. Biomechanical Properties of the Calcaneal Tendon *In Vivo* Assessed by Transient Shear Wave Elastography. *Skeletal Radiol* (2013) 42(8):1143–50. doi:10.1007/s00256-013-1649-9
436. Chen X-M, Cui L-G, He P, Shen W-W, Qian Y-J, and Wang J-R. Shear Wave Elastographic Characterization of Normal and Torn Achilles Tendons. *J Ultrasound Med* (2013) 32(3):449–55. doi:10.7863/jum.2013.32.3.449
438. Schmitt C, Hadj Henni A, and Cloutier G. Characterization of Blood Clot Viscoelasticity by Dynamic Ultrasound Elastography and Modeling of the Rheological Behavior. *J Biomech* (2011) 44(4):622–9. doi:10.1016/j.jbiomech.2010.11.015
439. Mfoumou E, Tripette J, Blostein M, and Cloutier G. Time-dependent Hardening of Blood Clots Quantitatively Measured *In Vivo* with Shear-Wave Ultrasound Imaging in a Rabbit Model of Venous Thrombosis. *Thromb Res* (2014) 133(2):265–71. doi:10.1016/j.thromres.2013.11.001
440. Mercado-Shekhar KP, Kleven RT, Aponte Rivera H, Lewis R, Karani KB, Vos HJ, et al. Effect of Clot Stiffness on Recombinant Tissue Plasminogen Activator Lytic Susceptibility *In Vitro*. *Ultrasound Med Biol* (2018) 44(12):2710–27. doi:10.1016/j.ultrasmedbio.2018.08.005
441. Zheng X, Ji P, Mao H, and Hu J. A Comparison of Virtual Touch Tissue Quantification and Digital Rectal Examination for Discrimination between Prostate Cancer and Benign Prostatic Hyperplasia. *Radiol Oncol* (2012) 46(1):69–74. doi:10.2478/v10019-011-0026-3
442. Ahmad S, Cao R, Varghese T, Bidaut L, and Nabi G. Transrectal Quantitative Shear Wave Elastography in the Detection and Characterisation of Prostate Cancer. *Surg Endosc* (2013) 27(9):3280–7. doi:10.1007/s00464-013-2906-7
443. Rouvière O, Melodelima C, Hoang Dinh A, Bratan F, Pagnoux G, Sanzalone T, et al. Stiffness of Benign and Malignant Prostate Tissue Measured by Shear-Wave Elastography: a Preliminary Study. *Eur Radiol* (2017) 27(5):1858–66. doi:10.1007/s00330-016-4534-9
444. Boehm K, Salomon G, Beyer B, Schiffmann J, Simonis K, Graefen M, et al. Shear Wave Elastography for Localization of Prostate Cancer Lesions and Assessment of Elasticity Thresholds: Implications for Targeted Biopsies and Active Surveillance Protocols. *J Urol* (2015) 193(3):794–800. doi:10.1016/j.juro.2014.09.100
445. Woo S, Kim SY, Lee MS, Cho JY, and Kim SH. Shear Wave Elastography Assessment in the Prostate: an Intraobserver Reproducibility Study. *Clin Imaging* (2015) 39(3):484–7. doi:10.1016/j.clinimag.2014.11.013

446. Barr RG, Memo R, and Schaub CR. Shear Wave Ultrasound Elastography of the Prostate. *Ultrasound Q* (2012) 28(1):13–20. doi:10.1097/ruq.0b013e318249f594
447. Correas J-M, Tissier A-M, Khairoune A, Vassiliu V, Méjean A, Hélénon O, et al. Prostate Cancer: Diagnostic Performance of Real-Time Shear-Wave Elastography. *Radiology* (2015) 275(1):280–9. doi:10.1148/radiol.14140567
448. Majeed W, Kalra P, and Kolipaka A. Simultaneous Multislice Rapid Magnetic Resonance Elastography of the Liver. *NMR Biomed* (2020) 33(4):1–15. doi:10.1002/nbm.4252

Conflict of Interest: The authors declare that the research was conducted in the absence of any commercial or financial relationships that could be construed as a potential conflict of interest.

GLOSSARY

US ultrasound

MR magnetic resonance

SW shear wave

ARF acoustic radiation force

ARFI acoustic radiation force imaging

SMURF spatially modulated ultrasound radiation force

SSI supersonic shear imaging

TOF time-of-flight

TTP time-to-peak

2D-F two-dimensional Fourier transform

LPVI local phase velocity imaging

AMUSE attenuation-measuring ultrasound shear wave elastography

E Young's modulus

K Bulk modulus

ν Poisson's ratio

$|\mu|$ real shear modulus

G^* magnetic field gradient complex shear modulus

G' shear storage modulus

G'' shear loss modulus

T Stress tensor

S Deformation tensor

λ First Lamé's coefficient

ω angular frequency

v_s shear wave speed

α_s shear wave attenuation

η shear viscosity

B_0 static magnetic field in MRI

T_1 longitudinal magnetisation regrowth time constant

T_2 transverse magnetisation decay time constant due to spin-spin interaction

MRI magnetic resonance imaging

RF radiofrequency

MEGs motion encoding gradients

MRE magnetic resonance elastography

FID free induction decay

EPI echo planar imaging

SE spin echo

GRE gradient recalled echo

LFE local frequency estimation

MDEV multi-frequency dual-elasto-visco inversion

HMDI heterogeneous multifrequency direct inversion

FE finite element

T_{2^*} transverse magnetisation decay time constant due to spin-spin interaction and magnetic field inhomogeneity

TE echo time

TR repetition time

ϕ_p material porosity

p complex time harmonic pressure field

ρ_f pore fluid density

κ hydraulic conductivity

ρ_a apparent mass density

P_0 tissue initial pressure

β thermal expansion coefficient

v_L speed of sound

C_p specific heat capacity at constant pressure

ϵ strain

ϵ_A complex strain amplitude

δ phase delay

μ_a intrinsic absorption coefficient

ϕ spatial resolution of optical fluence

frontiers in Physics

ORIGINAL RESEARCH
published: 22 July 2021
doi: 10.3389/fphy.2021.704878

A Novel Cell Vertex Model Formulation that Distinguishes the Strength of Contraction Forces and Adhesion at Cell Boundaries

Katsuhiko Sato[1]* *and Daiki Umetsu*[2]

[1]Research Institute for Electronic Science, Hokkaido University, Sapporo, Japan, [2]Laboratory for Histogenetic Dynamics, Graduate School of Life Sciences, Tohoku University, Sendai, Japan

The vertex model is a useful mathematical model to describe the dynamics of epithelial cell sheets. However, existing vertex models do not distinguish contraction forces on the cell boundary from adhesion between cells, employing a single parameter to express both. In this paper, we introduce the rest length of the cell boundary and its dynamics into the existing vertex model, giving a novel formulation of the model that treats separately the contraction force and the strength of adhesion between cells. We apply this vertex model to the phenomenon of compartment boundary in the fruit fly pupa, recapturing the observation that increasing the strength of adhesion between cells straightens the compartment boundary, even though contraction forces at cell boundaries remain unchanged. We also discuss possibilities of the novel vertex models by considering the stretching of a cell sheet by external forces.

Keywords: epithelial cells, mathematical model, resting length, contraction force, adhesion strength, turnover rate, cell intercalation

OPEN ACCESS

Edited by:
Karine Guevorkian, UMR168 Unite physico-chimie Curie (PCC), France

Reviewed by:
Carles Blanch-Mercader, UMR168 Unite physico-chimie Curie (PCC), France
Claudia Tanja Mierke, Leipzig University, Germany

***Correspondence:**
Katsuhiko Sato
katsuhiko_sato@es.hokudai.ac.jp

Specialty section:
This article was submitted to Biophysics, a section of the journal Frontiers in Physics

Received: *04 May 2021*
Accepted: *06 July 2021*
Published: *22 July 2021*

Citation:
Sato K and Umetsu D (2021) A Novel Cell Vertex Model Formulation that Distinguishes the Strength of Contraction Forces and Adhesion at Cell Boundaries. Front. Phys. 9:704878. doi: 10.3389/fphy.2021.704878

INTRODUCTION

During embryonic development, epithelial cells form a monolayer sheet that covers the entire embryo. Cells comprising the sheet move drastically, like an active viscoelastic fluid, while maintaining their attachment to adjacent cells. This spontaneous movement of epithelial cells is considered a driving force for morphogenesis of multicellular organisms. Understanding the mechanism of the movement from not only a molecular but also a mechanical point of view is a challenging problem in morphogenesis. Although the molecular mechanism of the movement has come to be relatively well understood [1], its mechanical mechanism is still an ongoing problem.

To approach the mechanical mechanism of the dynamics of the epithelial sheet, a cell-based mathematical model, the vertex model, is often used [2, 3]. In this model, each epithelial cell in the sheet is expressed by a polygon, and the cell configuration within the sheet is completely specified by the positions of the vertices of the polygons. The vertex model can describe various aspects of the epithelial sheet at the cellular level, including mechanical forces generated by each cell and the planar polarities of cells [2, 3]. Indeed, by using the vertex model, important behaviors of the epithelial sheet, such as elongation, bending, and unidirectional movement of the sheet, have been explained from not only a biological but also a mechanical viewpoint [4–7].

Although the existing vertex model is well able to describe important properties of epithelial cell sheets, certain modifications are necessary in order to more precisely describe cell sheet dynamics. One important consideration is the lack of distinction between the contraction forces acting on the

cell boundaries and the adhesion between cells. The existing vertex models consider the contraction forces and the strength of adhesion together and express the strengths of these two factors using a single parameter [8, 9]. However, biologically, contraction and adhesion are regulated by different molecules. For example, contraction forces are generated by actomyosin networks beneath the plasma membrane, whereas adhesion between cells is accomplished by adhesion molecules such as cadherin. Hence, to make the vertex model more useful and to more precisely describe epithelial cell sheet dynamics, it is preferable to modify the existing model to separately treat the forces of contraction and adhesion at the cell boundaries.

In this paper, we provide a novel formulation of the vertex model that introduces a phenomenological variable corresponding to the rest length of a cell boundary. This formulation allows us to treat separately the contraction forces acting on cell boundaries and the effects of adhesion between cells. The vertex model presented here is in accordance with and an extension of the existing vertex model. As an application of the model presented in this paper, we consider a phenomenon observed in the anterior-posterior (AP) compartment boundary in the *Drosophila* pupa [10, 11], in which the AP compartment boundary is straightened not only by an increase in contraction force at this boundary but also by an increase in the strength of adhesion between cells in the posterior region. While it has been demonstrated that the increase in contraction forces at the AP compartment boundary straightens the boundary [10], it has not yet been demonstrated whether the increase in adhesion between posterior cells does likewise. We use the vertex model presented here to show that the increase in adhesion between cells in the posterior region does straighten the AP compartment boundary and explain why the increase in adhesion straightens the boundary. As a second application of the new vertex model, we focus on stretching of the epithelial sheet by an external force. This application illustrates the difference in cell remodeling behavior between existing vertex models and our new model and compares the results predicted by the models with those observed experimentally.

SETUP OF THE VERTEX MODEL

As in existing vertex models, cells comprising an epithelial sheet are represented by polygons. The mechanical forces generated by the cells are expressed by the potential function U:

$$U = \frac{K}{2}\sum_{\text{cell }\alpha}\left(A_\alpha - A_\alpha^{(0)}\right)^2 + \sum_{\langle ij\rangle}\gamma_{ij}\ell_{ij} + \frac{k}{2}\sum_{\langle ij\rangle}\left(\ell_{ij} - \ell_{ij}^{(M)}\right)^2, \quad (1)$$

where A_α is the area of the α^{th} cell, $A_\alpha^{(0)}$ is its preferred value, K and k are positive constants, and ℓ_{ij} is the length of cell boundary ij that connects the i^{th} and j^{th} vertices. The index α includes all cells in the cell sheet, and $\langle ij\rangle$ below the summation symbol implies that index ij includes all cell boundaries in the system. A point of difference of this model compared with previous ones is the third term in **Eq. 1**. The first term in **Eq. 1** represents cytosolic hydrostatic pressure that acts on the cell boundaries. The second term in **Eq. 1** represents the contraction force acting on the cell boundary ij, which comes from the cortical actomyosin network beneath the plasma membrane. In this model, γ_{ij} represents only the strength of the contraction force and does not include the strength of adhesion between cells; the strength of adhesion will be expressed by τ_{ij} in **Eq. 3**. The novel third term in **Eq. 1** represents phenomenological forces acting on cell boundaries, which are introduced by considering the rest length (natural length) of cell boundary ij, denoted by $\ell_{ij}^{(M)}$. The introduction of this last term is based on the following considerations. The cell boundary consists of materials such as membrane, cytoskeleton, and associated components. In our model, we symbolically describe the amount of these cell boundary components by $\ell_{ij}^{(M)}$. Since $\ell_{ij}^{(M)}$ has the dimension of length, this quantity is obtained by dividing the amount of the cell boundary components by some constant having the dimensions of (amount of components)/(length). If the amount of the materials at cell boundary ij is greater than the appropriate amount of the materials for making the boundary with length ℓ_{ij}, the excess of the materials may give rise to repulsive forces by showing the wriggle of membrane. On the other hand, if the amount of material comprising the cell boundary ij is less than the appropriate value for the length ℓ_{ij}, where the distances between the components comprising the cell boundary, such as lipid molecules, are large, an attractive force may arise to return these components to the equilibrium positions. These tendencies of the force on the cell boundary are expressed by the third term in **Eq. 1**. The quantity $\ell_{ij}^{(M)}$ is a variable that evolves with time, as given by **Eq. 3**.

In the previous vertex models [2, 7, 9], there is another term in U, which is a quadratic term of cell perimeter, expressed by $\frac{K_p}{2}\sum_{\text{cell}\alpha}(L_\alpha - L_0)^2$ (see **Supplementary Appendix 1**), where L_α is the perimeter of cell α, and K_p and L_0 are constants. This term serves to express the conservation of the amount of cell membrane, or the effect of quadratic terms of cell perimeter, into the cell sheet dynamics. Our model, however, does not include this term in U, because an equivalent effect is included in **Eq. 3**.

The total mechanical force acting on vertex i is given by $-\partial U/\partial \mathbf{r}_i$, where $\mathbf{r}_i$ is the position of the ith vertex, $\mathbf{r}_i = (x_i, y_i)$. We set up the model such that the positions of all vertices in the sheet move in such a way that the total mechanical force on each vertex must sum to zero at any time, i.e.,

$$-\frac{\partial U}{\partial \mathbf{r}_i} = 0 \quad (2)$$

holds for all vertices i at any time t. This situation corresponds to the case where we consider the cell sheet dynamics on a relatively longer time scale, such as minutes or tens of minutes. For the practical implementation of **Eq. 2**, it is useful to solve $\eta\frac{d\mathbf{r}_i}{dt} = -\frac{\partial U}{\partial \mathbf{r}_i}$ with an extremely small positive value of η. In this implementation, the vertex positions obtained are nearly independent of the value of η, when η is taken to be sufficiently small.

Next, we consider the time evolution equation for $\ell_{ij}^{(M)}$. As mentioned above, the quantity $\ell_{ij}^{(M)}$ corresponds to the amount of

materials comprising cell boundary ij, so that the rate of change in $\ell_{ij}^{(M)}$ is related to the rate of change in the amount of these materials. For example, it depends on the rate of turnover of cell membrane at the boundary, which relates to the frequency of membrane endocytosis [12] and exocytosis at the cell boundary. Hereafter we refer to the ability to change the amount of cell boundary components as the "activity of the cell boundary". In addition, $\ell_{ij}^{(M)}$ tends to approach ℓ_{ij} over time, because if the amount of cell boundary components is not appropriate for length ℓ_{ij}, the amount tries to approach the appropriate value. The speed at which $\ell_{ij}^{(M)}$ approaches ℓ_{ij} may depend on the activity of the cell boundary. Furthermore, the total sum of $\ell_{ij}^{(M)}$ in each cell tends to be conserved over the timescale considered here, because the creation and destruction of components of cell membrane are modest within periods of minutes or several tens of minutes [13]. Considering these properties of the dynamics of cell boundary components, we determine the time evolution equation for $\ell_{ij}^{(M)}$ as

$$\frac{d\ell_{ij}^{(M)}}{dt} = -\frac{1}{\tau_{ij}}\left(\ell_{ij}^{(M)} - \ell_{ij}\right) - \frac{\partial M}{\partial \ell_{ij}^{(M)}}, \tag{3}$$

where τ_{ij} is a relaxation time that expresses the rate of approach of $\ell_{ij}^{(M)}$ to ℓ_{ij}. In this model, τ_{ij} is assumed to depend on the activity of cell boundary ij. M is a function of $\{\ell_{ij}^{(M)}\}$ that expresses the tendency to conserve the sum of $\ell_{ij}^{(M)}$ for each cell, given as

$$M = \frac{k_{pm}}{2}\sum_{\text{cell }\alpha}\left(\left(\sum_{kl\ in\ \text{cell }\alpha}\ell_{kl}^{(M)}\right) - L_{\alpha}^{(0)}\right)^2, \tag{4}$$

where k_{pm} is a positive constant expressing the degree of tendency to conserve the junction rest lengths. $L_{\alpha}^{(0)}$ is a positive constant corresponding to the total amount of cell boundary components in the α^{th} cell. The sign "kl in cell α" under the summation symbol signifies that the sum is taken over all boundaries of cell α.

As stated above, the quantity τ_{ij} in **Eq. 3** expresses the inverse of the rate at which $\ell_{ij}^{(M)}$ approaches ℓ_{ij}. That is, when τ_{ij} is large, $\ell_{ij}^{(M)}$ approaches ℓ_{ij} slowly, and vice versa. Experimental results indicate that the rate of cell membrane turnover can differ from one cell boundary to another, due to planar polarized endocytic activity [14]. In addition, the rate of endocytosis at a cell boundary is related to the degree of adhesion at the boundary [14], i.e., when endocytosis at the cell boundary is frequent, adhesion between the cells sharing the boundary is weakened, and vice versa. Thus, in this model we interpret that the state where τ_{ij} is large is a state at which the adhesion at cell boundary ij is strong, and vice versa. If we accept this setup, we can distinguish contraction force acting on the cell boundary from the strength of adhesion at the boundary, namely, the contraction on cell boundary ij is expressed by γ_{ij} in **Eq. 1** (large γ_{ij} indicating strong contraction on cell boundary ij), while the strength of adhesion at cell boundary ij is expressed by τ_{ij} in **Eq. 3** (large τ_{ij} indicating strong adhesion at this boundary).

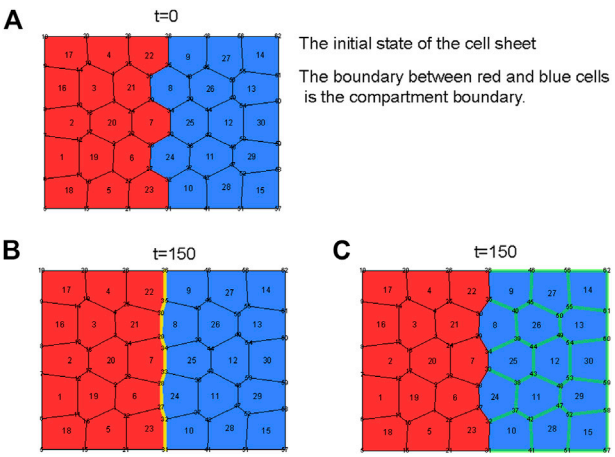

FIGURE 1 | (A) The initial state of the cell sheet. Red and blue cells are anterior and posterior cells, respectively. At the initial state of the sheet, both cells have the same parameters. At time $t = 0$, some parameters are changed. The compartment boundary is the boundary between red and blue cells. **(B)** The final state of the cell sheet when γ_{ij} at the compartment boundary is changed from $\gamma_{ij} = 0.1$(default value) to $\gamma_{ij} = 0.2$ (see **Supplementary Movie 1**). **(C)** The final state of the cell sheet when τ_{PP} at the cell boundary between P cells is changed from $\tau_{PP} = 0.1$ (default value) to $\tau_{PP} = 0.3$ (see **Supplementary Movie 2**). To highlight which cell boundary changed parameters, we colored them yellow **(B)** and green **(C)**. The parameter values used here are $K = 4$, $k = 1$, $A_{\alpha}^{(0)} = 2.2$, $\gamma_{ij} = 0.1$ (default), $k_{pm} = 5$, $\eta = 0.01$, $\tau_{ij} = 0.1$ (default), and $L_{\alpha}^{(0)} = 1.2 \times (2\pi\sqrt{A_{\alpha}^{(0)}/\pi}) = 6.3$. For the units of these parameters see **Supplementary Table 1**.

APPLICATION 1: STRAIGHTENING OF COMPARTMENT BOUNDARY IN DEVELOPING FRUIT FLY PUPA

Numerical Demonstrations that the Increase in τ_{ij} at Boundaries Between P Cells Shortens the Compartment Boundary

As an application of this new vertex model, we treat the phenomenon of compartment boundary straightening in the fruit fly pupa [15]. In this phenomenon, two types of epithelial cells, anterior (A) cells and posterior (P) cells, form two domains in an epithelial sheet, and the two cell domains meet at a boundary called the compartment boundary. For pupal development to progress correctly, the compartment boundary must undergo sufficient straightening. A mechanism that has been considered for the straightening of the compartment boundary is a strengthening of the contraction force on the compartment boundary, which shortens and straightens the compartment boundary. This scenario has been confirmed using the previous vertex model [10]. Recently, however, another mechanism for straightening of the compartment boundary was experimentally demonstrated [11], in which this boundary is straightened by an increase in the strength of adhesion between P cells, with the contraction force on the compartment boundary remaining unchanged. To restore this

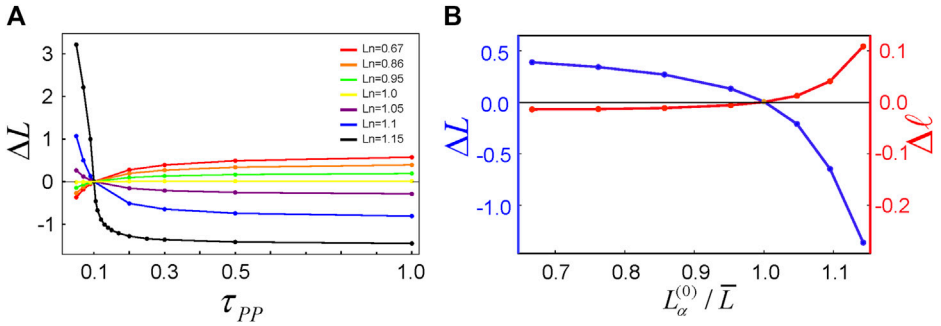

FIGURE 2 | (A) The length difference (ΔL) of the compartment boundary between the initial and final states of the sheet as a function of τ_{PP} and L_n. The quantity L_n is given by $L_\alpha^{(0)}/\bar{L}$. The quantity $\bar{L}$ (=5.56) is the mean perimeter length of P cells in the initial state. **(B)** Plots of ΔL and the mean length difference ($\Delta\ell$) of cell boundaries between P cells as a function of $L_\alpha^{(0)}/\bar{L}$. In this simulation, τ_{PP} was changed from τ_{PP} = 0.1 (default) to τ_{PP} = 0.3 at t=0. The parameter values used here are the same as in **Figure 1**, except for the values of the parameters τ_{PP} and $L_\alpha^{(0)}$. In this simulation τ_{PP} is varied from 0.05 to 1.0, and $L_\alpha^{(0)}$ is varied from 4.4 to 7.6.

phenomenon, we used the new vertex model to try to understand why and how an increase in adhesion between P cells straightens the compartment boundary.

To do this, we set up the situation where a cell sheet consists of two types of cells, A cells (red) and P cells (blue) (**Figure 1A**). We refer to the boundary between the A and P cells as the compartment boundary in this model. As the initial state (t = 0) of the cell sheet, we took the equilibrium state obtained under the condition in which both A and P cells had the same parameters. Then at t = 0, we changed the parameters of interest and observed the length difference (ΔL) of the compartment boundary between the initial state (t = 0) and the final state. Here, the final state is the steady state of the sheet under the new parameter values. If the result of numerical simulation exhibited $\Delta L < 0$, the compartment boundary was shortened and straightened, or vice versa. First, to retrace the previous work [10], we increased the contraction forces (γ_{ij}) at the compartment boundary at t = 0 in our model. The result of numerical simulation showed that $\Delta L < 0$ in response to the increase in γ_{ij} at compartment boundary (**Figure 1B**; **Supplementary Movie 1**). This result is reasonable because the large γ_{ij} (strong contraction) at the compartment boundary pulls the vertices at the compartment boundary closer together, hence shortening and straightening the compartment boundary.

Next, to investigate the effects on ΔL of a change in adhesion strength between cells, we changed the values of τ_{ij} at the cell boundaries between P cells at t = 0. In this simulation, we increased only the adhesion strength, without changing any other cell parameters, such as γ_{ij}. Hereafter, we will use the symbols τ_{PP}, τ_{AP}, and τ_{AA} to refer to the relaxation times (τ_{ij}) at the boundaries between P cells, between A and P cells, and between A cells, respectively. Numerical simulations in which we increased τ_{PP} showed that when $L_\alpha^{(0)}$ in **Eq. 4** was larger than some characteristic value, denoted by $L^{(0)*}$, ΔL became negative, and vice versa (**Figures 2A,B**). The value of the characteristic length $L^{(0)*}$ (=5.55) is close to the mean perimeter length (=5.56) of cells of the system. In our model, $L_\alpha^{(0)}$ denotes the preferred total resting length of a cell, and in reality, it is reasonable to expect $L_\alpha^{(0)}$ to be longer than the perimeter of the cell because laser ablation experiments [16] have demonstrated extension of the cell boundary after cutting of actomyosin networks beneath the plasma membrane. Hence, in our model, it is reasonable to set $L_\alpha^{(0)}$ longer than the mean cell perimeter. Under this setup ($L_\alpha^{(0)} > L^{(0)*}$), the results of numerical simulations in this vertex model coincided with experimental outcomes, i.e., when adhesion between P cells was made stronger than adhesion between other pairs of cells, i.e., $\tau_{PP} > \tau_{AP} = \tau_{AA}$, $\Delta L < 0$ (**Figure 1C**; **Supplementary Movie 2**).

Here a question may arise. Why does the increase in τ_{PP} shorten the compartment boundary? In the case of an increase in γ_{ij} at the compartment boundary, shortening of the compartment boundary is reasonable because the term in U that contains γ_{ij} (**Eq. 1**) makes shortening energetically preferable. However, in the case of a change in τ_{ij}, this parameter represents the relaxation time defined in **Eq. 3** and is not directly related to the potential energy U. Hence, it is not immediately apparent how τ_{PP} affects the length of the compartment boundary. To understand this, we first look at the data given in **Figure 2B**, where the quantity $\Delta\ell$ is the average length change of cell boundaries between P cells that contact the compartment boundary. These data indicate that, with the increase in τ_{PP}, the cell boundaries between P cells became longer ($\Delta\ell$ increases), while the cell boundaries between A and P cells became shorter (ΔL decreases). This result suggests that, if we consider in this model a cell having cell boundaries with different relaxation times τ_{ij}, the cell boundary having a large τ_{ij} would lengthen, while the cell boundary having a small τ_{ij} would shorten. To illustrate this property of the model, in the next subsection we conduct a simple analysis concerning the cell boundary length of a simple cell.

A Simple Analysis to Understand Why the New Vertex Model Lengthens the Cell Boundary with Large τ_{ij}

Let us consider a single cell whose dynamics obey **Eqs. 1–4** and whose shape is kept rectangular, in which the state of the cell is specified only by the quantities characterizing the vertical and

horizontal boundaries of the cell. Let us denote the lengths of vertical and horizontal boundaries of the cell by ℓ_1 and ℓ_2, respectively. All the boundaries of the cell have the same contraction force γ (>0), while the vertical and horizontal cell boundary have different relaxation times, τ_1 and τ_2, respectively. We are concerned with the cell's steady state under these conditions. The potential function U of this cell is given by

$$U = \frac{K}{2}\left(\ell_1\ell_2 - A^{(0)}\right)^2 + 2\gamma(\ell_1 + \ell_2) + k\Big[\left(\ell_1 - \ell_1^{(M)}\right)^2 + \left(\ell_2 - \ell_2^{(M)}\right)^2\Big]. \tag{5}$$

The force balance equations at each boundary are given by $\partial U/\partial\ell_1 = \partial U/\partial\ell_2 = 0$, which gives

$$\begin{aligned}\frac{1}{2}\ell_2 K\left(\ell_1\ell_2 - A^{(0)}\right) + \gamma + k\left(\ell_1 - \ell_1^{(M)}\right) = 0\\ \frac{1}{2}\ell_1 K\left(\ell_1\ell_2 - A^{(0)}\right) + \gamma + k\left(\ell_2 - \ell_2^{(M)}\right) = 0.\end{aligned} \tag{6}$$

In our model, ℓ_1, ℓ_2, $\ell_1^{(M)}$, and $\ell_2^{(M)}$ are independent variables, so $\ell_1^{(M)}$ and $\ell_2^{(M)}$ are not differentiated with ℓ_1 and ℓ_2. The time evolution equations for $\ell_1^{(M)}$ and $\ell_2^{(M)}$ are given by

$$\begin{aligned}\frac{d\ell_1^{(M)}}{dt} = -\frac{1}{\tau_1}\left(\ell_1^{(M)} - \ell_1\right) - \frac{1}{2}\frac{\partial M}{\partial \ell_1^{(M)}}\\ \frac{d\ell_2^{(M)}}{dt} = -\frac{1}{\tau_2}\left(\ell_2^{(M)} - \ell_2\right) - \frac{1}{2}\frac{\partial M}{\partial \ell_1^{(M)}},\end{aligned} \tag{7}$$

where $\ell_1^{(M)}$ and $\ell_2^{(M)}$ are the respective rest lengths of the vertical and horizontal cell boundaries, and M is given by $M = \frac{k_{pm}}{2}\left(2\left(\ell_1^{(M)} + \ell_2^{(M)}\right) - L^{(0)}\right)^2$, where $L^{(0)}$ is the preferred total resting length of this cell. The factor 1/2 in front of $\partial M/\partial\ell_i^{(M)}$ comes from the setup that the shape of this cell is rectangular, where both sides of the cell have the same quantities. To consider the steady state of this cell, we put $d\ell_i^{(M)}/dt = 0$ in **Eq. 7**, to obtain

$$\begin{aligned}-\frac{1}{\tau_1}\left(\ell_1^{(M)} - \ell_1\right) - k_{pm}\left(2\left(\ell_1^{(M)} + \ell_2^{(M)}\right) - L^{(0)}\right) = 0\\ -\frac{1}{\tau_2}\left(\ell_2^{(M)} - \ell_2\right) - k_{pm}\left(2\left(\ell_1^{(M)} + \ell_2^{(M)}\right) - L^{(0)}\right) = 0.\end{aligned} \tag{8}$$

Although we can analytically solve **Eqs. 6**, **8** for the variables, $\ell_1, \ell_2, \ell_1^{(M)}, \ell_2^{(M)}$, the forms of the solution are too complex to extract information about the τ_i-dependence of ℓ_i. Thus, we shall take another approach for this aim. First, we note that the terms $K\left(\ell_1\ell_2 - A^{(0)}\right)/2$ and $k_{pm}\left(2\left(\ell_1^{(M)} + \ell_2^{(M)}\right) - L^{(0)}\right)$ are common to **Eqs. 6**, **8**. Thus, we assign $p = K\left(A^{(0)} - \ell_1\ell_2\right)/2$ and $f = k_{pm}\left(L^{(0)} - 2\left(\ell_1^{(M)} + \ell_2^{(M)}\right)\right)$ and rearrange **Eqs. 6**, **8** to obtain $\ell_1 = \frac{\gamma - \tau_2 kf}{p}$ and $\ell_2 = \frac{\gamma - \tau_1 kf}{p}$. Subtracting ℓ_2 from ℓ_1 gives

$$\ell_1 - \ell_2 = \frac{kf}{p}(\tau_1 - \tau_2). \tag{9}$$

It should be noted here that p is the pressure acting on the cell boundaries, and p is positive when $\gamma > 0$ because contraction forces acting on the cell boundaries tend to shrink these boundaries as well as the area of the cell, $\ell_1\ell_2$, such that $\ell_1\ell_2 < A^{(0)}$. In addition, if $L^{(0)}$ is so large that $L^{(0)} > 2\left(\ell_1^{(M)} + \ell_2^{(M)}\right)$ is the case, f becomes positive. In this case, the magnitude relationship between ℓ_i and τ_i is the same, i.e., when $\tau_1 > \tau_2$, $\ell_1 > \ell_2$, or vice versa (see **Eq. 9**). On the other hand, in the case where $L^{(0)}$ is small enough that $L^{(0)} < 2\left(\ell_1^{(M)} + \ell_2^{(M)}\right)$, the magnitude relationship between ℓ_i and τ_i becomes opposite, i.e., when $\tau_1 > \tau_2$, $\ell_1 < \ell_2$, and vice versa. This consideration suggests that there exists a characteristic value of $L^{(0)}$, denoted by $L^{(0)*}$, at which f becomes zero. Indeed, such a value of $L^{(0)*}$ does exist, which is confirmed analytically. This property of the model appears in **Figures 2A,B**: when $L_\alpha^{(0)} > L^{(0)*}$, the compartment boundary is shortened and straightened, with a large τ_{ij}, and vice versa. That is, P cells in contact with the compartment boundary have different relaxation times, τ_{PP} and τ_{AP}, depending on the side (remembering that the compartment boundary is the boundary between A and P cells). Since we have set $\tau_{PP} > \tau_{AP}$ and $L_\alpha^{(0)} > L^{(0)*}$, the cell boundary between P cells lengthens, and the cell boundary between A and P cells shortens (**Figure 1C**).

While the above analysis is restricted to a case in which the cell shape is rectangular, the relation between ℓ_i and τ_i continues to hold when the cell shape is pentagonal, hexagonal, etc. (see **Supplementary Appendix 2**). In addition, although the preceding analysis concerned the case of a single cell, a similar relation between ℓ_i and τ_i continues to apply in the case of a cell sheet, i.e., when the cell boundary has a longer relaxation time, the cell boundary length tends to become longer.

APPLICATION 2: THE RESPONSE OF THE CELL SHEET WHEN STRETCHED BY EXTERNAL FORCES

In this section, we consider the stretch of a cell sheet by external forces. In the previous vertex models, when the cell sheet is stretched greatly enough by external forces, the sheet necessarily undergoes cell remodeling (**Figures 3A,B**; **Supplementary Movie 3**; the formulation of the previous vertex model is given in **Supplementary Appendix 1**). This behavior originates in two properties of the previous vertex model: 1) cell shape tends to be round, due to the quadratic term $\left(\frac{K_p}{2}\sum_{\text{cell}\alpha}\left(L_\alpha - L_0\right)^2\right)$ in U, and 2) there is no repulsive force between vertices to prevent rounding of the cell. We will explain property 2) in more detail. Consider the case where external forces deform the cell shape well away from the preferred round shape, i.e., an elliptical shape with a large ratio of width to height. In this situation, the cell shape tends to return to roundness due to property 1). As a result, cell remodeling occurs (see **Supplementary Movie 3**). To put it another way, the previous vertex model has no repulsive force between vertices to maintain the cell in an elliptical shape. The present vertex model, on the other hand, has a repulsive force on the cell boundary when $1/\tau_{ij} = 0$ as indicated below. This is the meaning of statement 2). Moreover, experimental results show that even when the cell sheet is stretched greatly enough by external forces, remodeling of the cell configuration does not

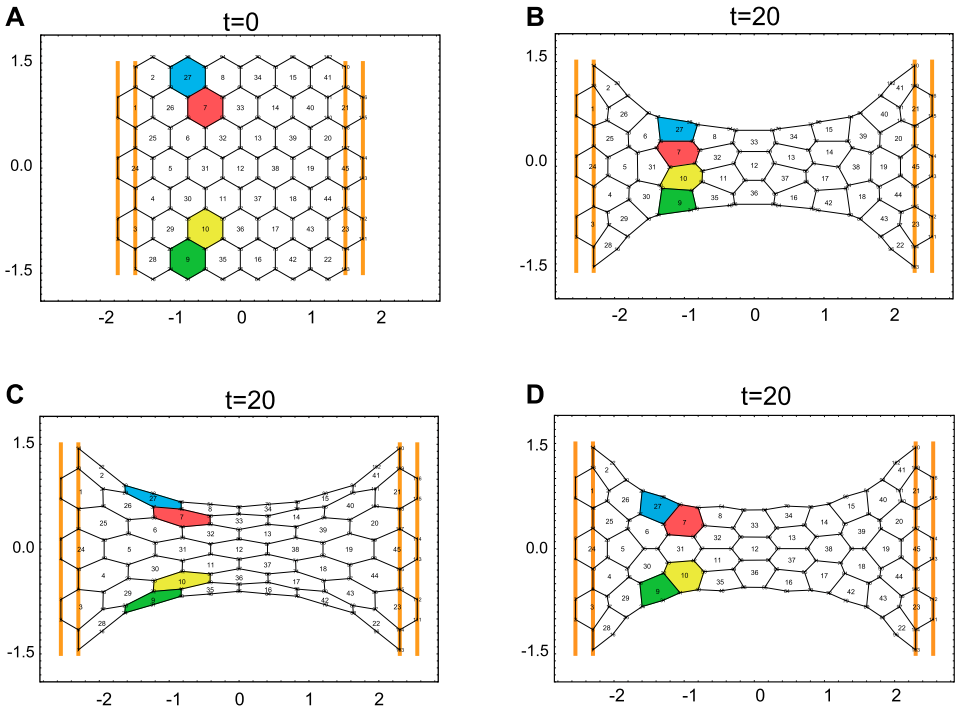

FIGURE 3 | (A) The initial configuration of the cell sheet. At time $t = 0$, the cell sheet begins to be stretched by external forces, which are represented by the orange bars. At these bars, the cell boundaries are fixed, and the bars are shifted with time (for the movement of the bars see **Supplementary Movies 3–5**). **(B)** The final cell configuration of the sheet stretched by external forces. The cell sheet dynamics are implemented by the previous vertex model (see **Supplementary Appendix 1**). The time evolution equation for r_i is given by $\dot{r}_i = -((1/\tilde{\eta}))\partial U/\partial r_i$, where $\tilde{\eta}$ is a constant. The parameter values used here are $K = 1$, $A_\alpha^{(0)} = 0.22$, $\tilde{\gamma}_{ij} = 1.0$. $\tilde{\eta} = 1.0$, $L_0 = 1.65$, and $K_p = 50$. **(C)** The final cell configuration of the sheet stretched by the external forces. The cell sheet dynamics are implemented by the present vertex model. The parameter values used here are $K = 1$, $A_\alpha^{(0)} = 0.22$, $\gamma_{ij} = 1.0$, $\eta = 0.01$, $L_\alpha^{(0)} = 1.65$, $k_{pm} = 50$, $k = 100$, and $1/\tau_{ij} = 0$. **(D)** The final cell configuration of the sheet after being stretched by external forces using the present vertex model with finite $\tau_{ij} = 0.1$. The other parameter values are the same as those in **(C)**.

necessarily occur [17]. The discrepancy between the numerical and experimental results implies the necessity to improve the previous vertex model. In our modified vertex model, in fact, cell remodeling does not necessarily occur when the cell sheet is stretched (**Figure 3C**; **Supplementary Movie 4**), but whether or not remodeling occurs depends upon the parameters of the model. If τ_{ij} in **Eq. 3** is infinitely large, i.e., $1/\tau_{ij}$ is zero, the time evolution equation for $\ell_{ij}^{(M)}$ is decoupled from ℓ_{ij}, and the value of $\ell_{ij}^{(M)}$ is determined by the initial values of $\ell_{ij}^{(M)}$ and $L_\alpha^{(0)}$. That is, $\ell_{ij}^{(M)}$ becomes a constant independent of ℓ_{ij}. In this case, the third term in **Eq. 1** generates a repulsive force between vertices, and the elliptical shape is retained even in the steady state. On the other hand, if the value of τ_{ij} is finite, $\ell_{ij}^{(M)}$ tends to follow ℓ_{ij} according to **Eq. 3**, and repulsive forces coming from the third terms are weakened. Then, the cells eventually undergo remodeling, and each cell becomes round (**Figure 3D** and **Supplementary Movie 2**). The final cell configuration in the new vertex model for finite τ_{ij} is not necessarily the same as that in the former vertex model because the order of cell remodeling affects the final state (see **Supplementary Movies 3, 5**). The speed at which the system approaches the energetically minimum state depends on the value of τ_{ij}; the larger τ_{ij} is, the slower this approach. Thus, τ_{ij} plays a role analogous to a friction coefficient for the relative movement between the ith and jth vertices.

CONCLUSION AND DISCUSSION

In this paper, we provided a novel formulation of the vertex model that separately treats the contraction force on the cell boundary and the strength of adhesion between cells, by considering the resting length of the cell boundary and its dynamics. We applied this vertex model to understanding the straightening of the compartment boundary observed in the fruit fly pupa and showed that the model recaptures compartment boundary straightening in response to an increase in strength of adhesion between P cells. We also used this model to examine the stretching of a cell sheet by external forces and gained insights into cell remodeling resulting from the stretch. This model has the potential to clarify points that were ambiguous in the previous vertex model. One such point is the frictional force exerted on the vertex. In the previous model, the equation for time evolution of vertex positions is obtained by assuming that total mechanical force on the vertex and frictional force on the vertex are balanced. However, the meaning and origin of the frictional force on the

vertex had not yet been well discussed. The present vertex model has the potential to explain the origin and meaning of the frictional force between vertices. Indeed, as mentioned in *Application 2: The Response of the Cell Sheet When Stretched by External Forces*, changes in τ_{ij}in **Eq. 3** change the speed of cell remodeling, and the meaning of $\tau_{ij}$is interpreted through **Eq. 3**. This model could be applicable to the phenomenon [18] where E-cadherin binding protein (p120-catenin) speeds cell intercalation.

Recently, it has been reported that cell intercalation (cell remodeling) in the cell sheet is related to endocytosis at the cell boundary of epithelial cells [12, 14]. In our model, the effect of endocytosis frequency at the cell boundary is represented by τ_{ij} in **Eq. 3**. The present vertex model can be applied to the phenomenon [12] where blocking endocytosis at the cell boundary inhibits cell remodeling. Relaxation time τ_{ij} in **Eq. 3** can be changed when expression levels of molecules associated with endocytosis, such as clathrin, dynamin, and its ortholog, change.

As demonstrated in **Figure 3C**, the cell sheet described by the present vertex model does not necessarily undergo cell intercalation even when the cells are largely deformed by external forces. Similar behaviors of epithelia are sometimes observed in experiments. A representative example of this is the defect in the formation of the tracheal system in the fruit fly embryo [19]. In the control case of the tracheal system, the tube consisting of epithelial cells undergoes cell intercalation and elongates along the long axis of the tube, during which the tip cells of the tube keep pulling the stalk cells toward the direction of the tip cells. The pulling forces of the tip cells were considered to a dominant factor for cell intercalation in the tube. However, expression of some molecules (e.g., Spalt) inhibits cell intercalation, and tube elongation stops at a certain length, even though the tip cells continue to pull the stalk cells [19]. This experimental result implies that for cell intercalation proceeding external forces on the cell sheet are not sufficient and other factors are necessary. We might be able to consider the factors necessary for cell intercalation through the notion of τ_{ij} in **Eq. 3**. As we stated above, molecules that change the turnover rate of cell membrane can change the value of τ_{ij}. It is considered that τ_{ij} closely relates to the strength of adhesion between cell membranes and the turnover rate of the adhesion molecules, which may be checked with the present vertex model and experimental results.

In the morphological study of multicellular organisms, it becomes more important to investigate responses of the cell sheet to external mechanical perturbations [17]; thus, more detailed research on this issue using cell-based mathematical models, such as vertex models, is expected.

DATA AVAILABILITY STATEMENT

The original contributions presented in the study are included in the article/**Supplementary Material**, further inquiries can be directed to the corresponding author.

AUTHOR CONTRIBUTIONS

KS and DU designed the concept of the paper. KS created the model, and performed its numerical simulations and analyses. KS and DU wrote the paper. KS and DU contributed to the review and approval of the paper for publication.

FUNDING

This work was supported by Global Station for Soft Matter at Hokkaido University (KS), the Cooperative Research Program of "NJRC Mater. and Dev." (KS), and MEXT/JSPS KAKENHI Grant Nos. 17H02939 (KS and DU), 20K03871 (KS), 18H01135 (KS), 17K07402 (DU), and 21K06144 (DU).

ACKNOWLEDGMENTS

We would like to thank Y. Ishimoto, M. Nishikawa, T. Shibata, E. Kuranaga, S. Okuda, T. Taguchi, and S. Hayashi for valuable comments and discussions.

SUPPLEMENTARY MATERIAL

The Supplementary Material for this article can be found online at: https://www.frontiersin.org/articles/10.3389/fphy.2021.704878/full#supplementary-material

REFERENCES

1. Friedl P, and Gilmour D. Collective Cell Migration in Morphogenesis, Regeneration and Cancer. *Nat Rev Mol Cel BiolJul* (2009) 10(7):445–57. doi:10.1038/nrm2720
2. Fletcher AG, Osterfield M, Baker RE, and Shvartsman SY. Vertex Models of Epithelial Morphogenesis. *Biophysical J* (2014) 106(11):2291–304. doi:10.1016/j.bpj.2013.11.4498
3. Alt S, Ganguly P, and Salbreux G. Vertex Models: from Cell Mechanics to Tissue Morphogenesis. *Phil Trans R Soc B* (2017) 372(1720):20150520. doi:10.1098/rstb.2015.0520
4. Rauzi M, Verant P, Lecuit T, and Lenne P-F. Nature and Anisotropy of Cortical Forces Orienting Drosophila Tissue Morphogenesis. *Nat Cel Biol.* (2008) 10:1401–10. doi:10.1038/ncb1798
5. Hočevar Brezavšček A, Rauzi M, Leptin M, and Ziherl P. A Model of Epithelial Invagination Driven by Collective Mechanics of Identical Cells. *Biophys J* (2012) 103(5):1069–77. doi:10.1016/j.bpj.2012.07.018
6. Okuda S, Inoue Y, Watanabe T, and Adachi T. Coupling Intercellular Molecular Signalling with Multicellular Deformation for Simulating Three-Dimensional Tissue Morphogenesis. *Interf Focus.* (2015) 5:20140095. doi:10.1098/rsfs.2014.0095
7. Sato K, Hiraiwa T, and Shibata T. Cell Chirality Induces Collective Cell Migration in Epithelial Sheets. *Phys Rev Lett* (2015) 115:188102. doi:10.1103/physrevlett.115.188102

8. Nagai T, and Honda H. A Dynamic Cell Model for the Formation of Epithelial Tissues. *Philosophical Mag B* (2001) 81:699–719. doi:10.1080/13642810108205772
9. Farhadifar R, Röper J-C, Aigouy B, Eaton S, and Jülicher F. The Influence of Cell Mechanics, Cell-Cell Interactions, and Proliferation on Epithelial Packing. *Curr Biol* (2007) 17:2095–104. doi:10.1016/j.cub.2007.11.049
10. Landsberg KP, Farhadifar R, Ranft J, Umetsu D, Widmann TJ, Bittig T, et al. Increased Cell Bond Tension Governs Cell Sorting at the Drosophila Anteroposterior Compartment Boundary. *Curr Biol* (2009) 19:1950–5. doi:10.1016/j.cub.2009.10.021
11. Iijima N, Sato K, Kuranaga E, and Umetsu D. Differential Cell Adhesion Implemented by Drosophila Toll Corrects Local Distortions of the Anterior-Posterior Compartment Boundary. *Nat Commun* (2020) 11(1):6320. doi:10.1038/s41467-020-20118-y
12. Blackie L, Tozluoglu M, Trylinski M, Walther RF, Schweisguth F, Mao Y, et al. A Combination of Notch Signaling, Preferential Adhesion and Endocytosis Induces a Slow Mode of Cell Intercalation in the Drosophila Retina. *Development* 148. (2021). p. 197301. doi:10.1242/dev.197301
13. Kaplan J, and Moskowitz M. Studies on the Turnover of Plasma Membranes in Cultured Mammalian Cells. *Biochim Biophys Acta (Bba) - Biomembranes* (1975) 389(2):306–13. doi:10.1016/0005-2736(75)90323-5
14. Levayer R, Pelissier-Monier A, and Lecuit T. Spatial Regulation of Dia and Myosin-II by RhoGEF2 Controls Initiation of E-Cadherin Endocytosis during Epithelial Morphogenesis. *Nat Cel Biol* (2011) 13(5):529–40. doi:10.1038/ncb2224May
15. Umetsu D, and Dahmann C. Compartment Boundaries. *Fly* (2010) 4(3):241–5. doi:10.4161/fly.4.3.12173
16. Liang X, Michael M, and Gomez G. Measurement of Mechanical Tension at Cell-Cell Junctions Using Two-Photon Laser Ablation. *Bio-protocol* (2016) 6(24):e2068. doi:10.21769/BioProtoc.2068
17. Duda M, Kirkland NJ, Khalilgharibi N, Tozluoglu M, Yuen AC, Carpi N, et al. Polarization of Myosin II Refines Tissue Material Properties to Buffer Mechanical Stress. *Dev Cel* (2019) 48(2):245–60. doi:10.1016/j.devcel.2018.12.020
18. Iyer KV, Piscitello-Gómez R, Paijmans J, Jülicher F, and Eaton S. Epithelial Viscoelasticity Is Regulated by Mechanosensitive E-Cadherin Turnover. *Curr Biol* (2019) 29(4):578–91. doi:10.1016/j.cub.2019.01.021
19. Ribeiro C, Neumann M, and Affolter M. Genetic Control of Cell Intercalation during Tracheal Morphogenesis in Drosophila. *Curr Biol* (2004) 14(24):2197–207. doi:10.1016/j.cub.2004.11.056.11

Conflict of Interest: The authors declare that the research was conducted in the absence of any commercial or financial relationships that could be construed as a potential conflict of interest.

frontiers in Physics

REVIEW
published: 17 August 2021
doi: 10.3389/fphy.2021.666709

Jamming in Embryogenesis and Cancer Progression

*Eliane Blauth, Hans Kubitschke, Pablo Gottheil, Steffen Grosser and Josef A. Käs**

Peter-Debye Institute for Soft Matter Physics, Leipzig University, Leipzig, Germany

The ability of tissues and cells to move and rearrange is central to a broad range of diverse biological processes such as tissue remodeling and rearrangement in embryogenesis, cell migration in wound healing, or cancer progression. These processes are linked to a solid-like to fluid-like transition, also known as unjamming transition, a not rigorously defined framework that describes switching between a stable, resting state and an active, moving state. Various mechanisms, that is, proliferation and motility, are critical drivers for the (un) jamming transition on the cellular scale. However, beyond the scope of these fundamental mechanisms of cells, a unifying understanding remains to be established. During embryogenesis, the proliferation rate of cells is high, and the number density is continuously increasing, which indicates number-density-driven jamming. In contrast, cells have to unjam in tissues that are already densely packed during tumor progression, pointing toward a shape-driven unjamming transition. Here, we review recent investigations of jamming transitions during embryogenesis and cancer progression and pursue the question of how they might be interlinked. We discuss the role of density and shape during the jamming transition and the different biological factors driving it.

Keywords: embryogenesis, cancer, jamming, unjamming, jamming transition, physics of cancer, morphogenesis, glass transition

OPEN ACCESS

Edited by:
Jose J. Munoz,
Universitat Politecnica de Catalunya, Spain

Reviewed by:
Fabio Giavazzi,
University of Milan, Italy
José Rafael Bordin,
Federal University of Pelotas, Brazil
Jennifer A. Mitchel,
Harvard University, United States

****Correspondence:***
Josef A. Käs
jkaes@uni-leipzig.de

Specialty section:
This article was submitted to Biophysics, a section of the journal Frontiers in Physics

Received: *10 February 2021*
Accepted: *24 May 2021*
Published: *17 August 2021*

Citation:
Blauth E, Kubitschke H, Gottheil P, Grosser S and Käs JA (2021) Jamming in Embryogenesis and Cancer Progression. Front. Phys. 9:666709. doi: 10.3389/fphy.2021.666709

1 INTRODUCTION

Spatiotemporal tissue organization is crucial in various biological processes ranging from fundamental shaping of tissues during embryogenesis, tissue fluidization during wound healing, and pathological alterations in diseases like asthma [1–3] and cancer [4–6]. Sculpting biological tissues is a demanding task, from both an (epi)genetic and physical perspective. Typically, there is no external force driving tissue deformation and cellular rearrangement. Instead, the organisms and tissues generate internal forces themselves. A significant ingredient for reshaping tissues is to locally control the flux of cells while remaining in a global structurally stable state. All cells and proto-tissues are in a fluid, viscous regime; however, larger tissues require further mechanical integrity, which a fluid cannot provide.

A solid-like tissue with force and tension percolation can exert forces onto a fluid-like without compromising its structural integrity by the counter-acting forces. Conversely, fluid-like tissues can deform and shear, enabling cells to moving along or through other tissues. Losing cell-cell contacts to one cell and establishing new contacts to new cells is another primary ingredient in reshaping tissues. Without this switching of cellular neighbors, the tissue cannot fundamentally reshape and restructure.

In recent years, observations and theoretical descriptions of sudden fluidization, collective motion arrest, and solidification of tissues elucidated how tissues organize and structure. Local control of viscoelasticity, rigidity, and viscosity is necessary for shaping tissues during embryogenesis [7–10]. On the other hand, it also harbors the risk of failure when tissue does not comply with its intended

viscoelastic properties, for example, diseases like cancer. The current concept toward understanding viscoelastic changes in tissues in the scientific community is that tissues can undergo a rigidity transition, similar to a phase transition. In fluids and solids, physical properties change rapidly at the transition point. Also, sudden changes in viscoelastic properties are seen in biological tissues during embryogenesis and cancer progression.

The leading theoretical framework describing rigidity transitions and sudden collective motion arrest in biological systems is the theory of a jamming transition. Despite the jamming transition is being well-defined in the condensed physics literature [11–13], the biological physics community, however, uses *Jamming* and *Jamming Transition* sometimes a rather descriptive phenomenon for an observed rigidification, solidification, or motion arrest in tissues. Unjamming and jamming transitions are currently interpreted as driving principles for dynamical tissue organization and mechanical integrity [3–6, 10, 14–19]. Here, biological cells are seen as rather densely packed, viscoelastic cells with additional properties, depending on the exact theoretical model, such as motility, adhesion, and cortical tension, as mediators for force generation and tension percolation.

Nonetheless, connecting theory and experimental observation and thus unraveling the fundamental cause of the rigidity transition in biological tissues is still a challenging task [3, 5, 20, 21]. For one, jamming and unjamming and similar theories in biological tissues made significant theoretical advances. Nonetheless, accessible experimental data is sparse; pinpointing exact causes and driving factors is complex.

In this review, we will briefly outline different theoretical interpretations of the jamming phenomena in biological tissues. We cover principles of the rigidity transition of biological systems and discuss recent findings in theory and experiment and disputed views. A key determinant in jamming debated in the scientific community is whether jamming is cell-shape- or cell-density-driven. We focus on embryogenesis and cancer progression and discuss both interpretations from experimental observations. We support jamming as a universal principle in embryogenesis and cancer, albeit the driving factors in both classes differ. We hypothesize that embryogenesis favors density-driven whereas cancer progression favors the cell-shape-induced interpretation of the jamming phenomena. We will outline open questions and investigation into the theory of jamming in biological systems in this review. For some of those, we provide mindful and tentative answers and hypotheses as an incentive for future research. As the accessible experimental data is sparse, we elucidate possible future experiments and possible contributions to deepen our understanding of the jamming phenomenon.

2 SHORT INTRODUCTION TO CELL JAMMING

2.1 Jamming in Colloidal Systems

In passive colloidal or grainy systems, jamming is the transition ranging between gas-, liquid-, solid-, and liquid crystalline-like states controlled by density and temperature [22]. With increasing density, particle motion is more and more constrained by its neighbors. When these systems reach a critical density ρ_c, single-particle motion becomes caged, and the systems become solid-like. However, it is still a matter of debate whether this transition is an actual phase transition.

In the context of this review, it is decisive to understand that the critical parameter in colloid jamming is the particle density ρ or their volume fraction ϕ. The exact value of the critical parameter depends on the dimensionality of the system. Moreover, it can be modulated by external stresses σ. For instance, roundish colloids in three dimensions jam at a volume fraction of around $\phi = 64\%$ [23].

Remarkably, the particle shape can shift the critical parameter in colloid systems. Elongated particles need higher volume fractions to jam than roundish particles [24]—elongated particles have more degrees of freedom and need more neighbors to be constrained. In a colloid system, particle shape is usually simply given; shape-dependent effects play somewhat less of a decisive role. However, cells have highly adaptable shapes, which is one of the main reasons cell shape potentially serves as a control parameter in dense cell systems.

2.2 Jamming in Biological Systems: Density and Shape

Like colloidal systems, the extracellular space and thus the density can control the transition from an unjammed to a jammed state [10]. More extracellular space results in more uncorrelated cellular movement and fluidizes the system. Increasing the density jams the system, and cellular movement becomes confined by neighboring cells [5, 10].

A striking feature of cell systems is that they can considerably tune their number density at high volume fractions close to 100%. The cell number can increase due to proliferation or external pressure. An increase in number density is accompanied by a glass-like slowing down of cell motility in 2D monolayers [14, 25]. Similar behavior was even found in 3D cell aggregates [4, 26]. At first sight, it seems that density is the main driving factor in these systems. However, the question of how cells move at such high volume fractions close to one remains. Hard sphere colloidal jamming happens at much lower volume fractions, for example, $\phi = 0.74$ is the densest packing ratio for hard spheres; however, random packing of spheres will already jam at approx. $\phi = 0.64$ [23]. One key feature of cellular systems is their ability to adapt their shapes. Cells are viscoelastic objects and can deform and actively generate stresses to reshape themselves on the timescale of minutes. Thus, even though they can form confluent layers or 3D cell aggregates with a volume fraction close to 1, they might overcome the jamming constraints of hard spheres by elongating, thereby extending their degrees of freedom.

The concept of shape-dependent unjamming has been strengthened by many experimental studies in the last few years. The slowing-down of cellular motion was associated with more roundish cell shapes in a broad range of systems from 2D monolayers to 3D cell aggregates and primary tumor pieces [1, 3–5, 25, 27, 28]. In densely packed environments, unlike in typical colloidal systems, cells can still move if they elongate and squeeze themselves through narrow spaces (**Figure 1**).

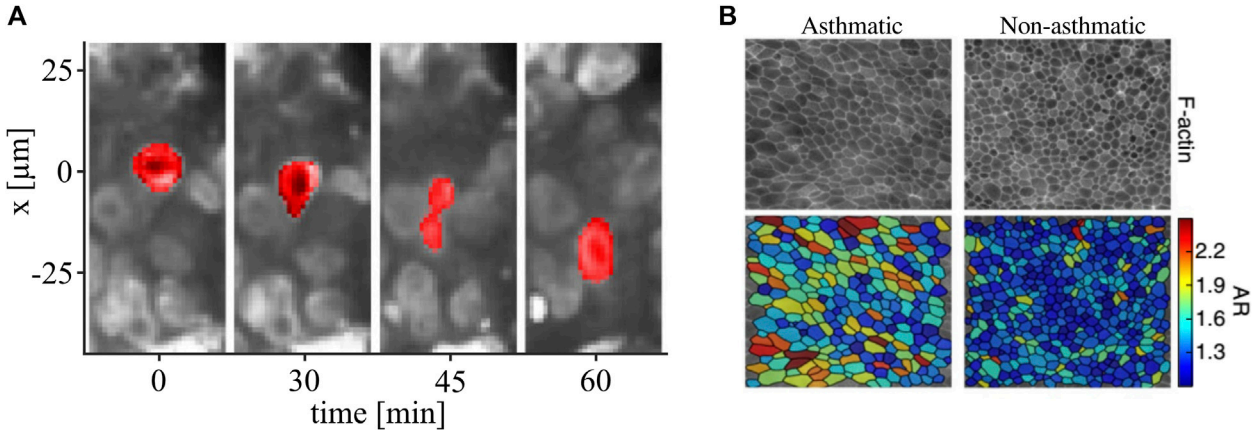

FIGURE 1 | Shape-dependent unjamming. **(A)** Time series of an MDA-MB-436 cancer cell nucleus (red) deforming itself to move through a densely packed three-dimensional cell spheroid. Nuclei are stained with SiR-DNA. From [4]**(B)**, monolayers of cells from asthmatic donors were more motile and had more elongated cells than monolayers of cells from healthy donors. Images were taken and adopted from Atia et al. [28]. Copyright ID 5061921078636.

Atia et al. have found that shape elongation is tied to unjamming across a broad range of biological systems [28]. They empirically find that the shape distributions in biological systems are linked to k-Gamma-distributions found in granular materials. The shape variability increases as the system unjams and decreases when the system approaches the jamming point. This indicates that the jamming transition in living systems is also driven by geometrical constraints similar to inert systems [28].

All of the mentioned studies point toward a significant role of the cell shape as a geometric constraint, thus reducing the system's degrees of freedom leading to jamming transitions. As cells are complex living systems, cellular properties influence the cell shape and thus control the transition.

2.3 The SPV Model as the Paradigmatic Model of Shape-Dependent Jamming

Besides these experimental studies, theoretical models were developed to describe the cell jamming transition. The most influential models are arguably the vertex- and the self-propelled Voronoi (SPV) model, as they predict a density-independent and shape-dependent transition. For this reason, we want to outline the crucial features of both models. The main difference between both models is the way that they obtain the cell shapes. In the vertex model, the tissue is described by a polygonal tiling of space. The Hamiltonian depends on the vertex positions, which correspond to the degrees of freedom. On the other hand, in the SPV model, cell shapes are given by a Voronoi tessellation around the cell positions. Thus, the SPV model has fewer degrees of freedom. Nonetheless, it comes to similar conclusions. Its Hamiltonian is given by the following equation:

$$E = \sum_{i=1}^{N} E_i = \sum_{i=1}^{N} \left[K_A \left(A(r_i) - A_0 \right)^2 + K_P \left(P(r_i) - P_0 \right)^2 \right]. \quad (1)$$

Here, A_i and P_i are the area and perimeter of each cell, their respective moduli $K_{A,i}$ and $K_{P,i}$, and the (theoretical) target values A_0 and P_0. The models assume that the energetically favored perimeter P_0 reflects the competition between cortical tension and cell-cell adhesion, and the target area A_0 accounts for the monolayer's resistance to height fluctuations. In this view, strong cell-cell adhesions and low cortical tension elongate the cells, and the system is driven toward unjamming. In the SPV model, cells can be additionally actively self-propelled. For vanishing self-propulsion, the model predicts a jamming transition for cells with a target shape index $p^* = \frac{P_0^*}{\sqrt{A_0^*}} = 3.81$, which is similar to the vertex model [20].

Increased cellular self-propulsion, which suggests stronger traction forces, pushes the target shape index for the onset of jamming toward more roundish shapes [20]. The prediction of a collective cell motility arrest at a cell shape index of around $p^* = 3.81$ matched the experimental observation in monolayers [3]. Since then, the model has been refined and adapted by introducing, for example, heterogeneity of cell divisions [29, 30]. Chaing et al. also found a shape-dependent transition in a Potts model [31]. We do not want to discuss these in detail as the SPV model serves as a paradigm that explains the mechanism of shape-dependent transitions in dense tissues.

3 JAMMING IN EMBRYOGENESIS

Particularly during the early stages of embryogenesis, tissues are continuously reshaped and restructured, while cells constantly proliferate and differentiate within a single day [32]. Physical cues are guiding morphogenetic rearrangements of tissues with high spatiotemporal precision [33–37]. One key ingredient is local solidification and fluidization of tissue.

In early seminal works, Foty and Steinberg [38, 39] formulated the differential adhesion hypothesis explaining the demixing of different cell types during embryogenesis without relying on intricate biological cues and function. Instead, tissues are treated as liquids with different surface tensions and arrange according to their surface tension, like oil droplets in water. The hypothesis of differential adhesion provided an excellent initial

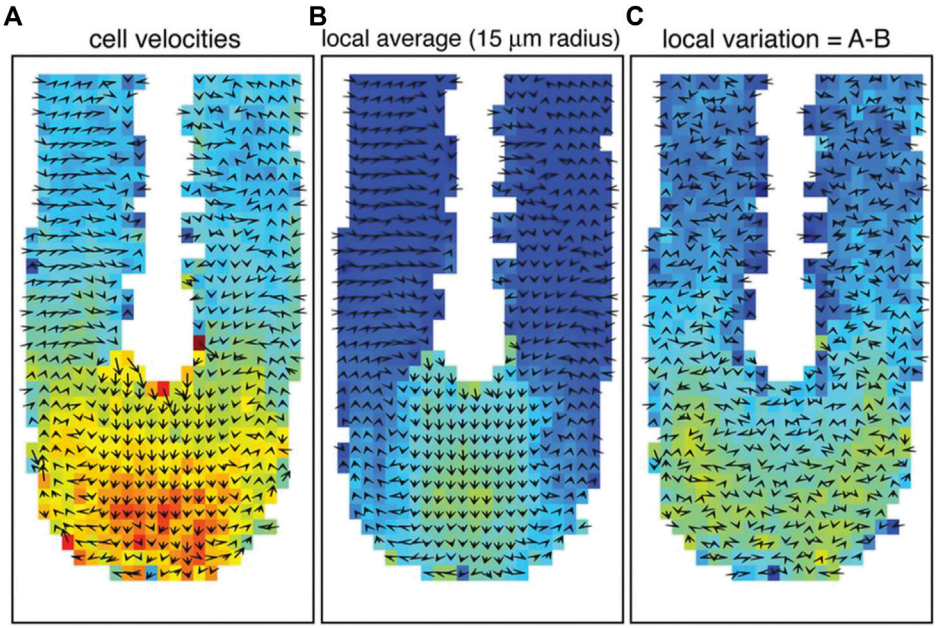

FIGURE 2 | Cell movement and tissue fluidity in the zebrafish tailbud. **(A)** Vector map of cell velocities. **(B)** Local tissue velocity averaged over a 15 µm radius. **(C)** Cell velocity variation from local tissue velocity. The color red represents higher velocities, and arrows indicate the averaged velocity vectors in 2D. The tip of the tailbud displays higher cell velocities, more local rearrangements, and proliferation, indicating an unjammed, fluid-like state. High motility and proliferation are driving factors for unjamming tissues, as verified by Mongera et al. [10]. Images were taken and adopted from Lawton et al. [48], Copyright ID 1096693–1.

explanation of physical guiding principles during embryogenesis [38–43]. However, cellular adhesion strength is not sufficient to fully describe physical actions in embryogenesis and tissue development [44, 45]. In this context, jamming and unjamming were proposed as processes influencing the demixing of cells [45]. Like the differential adhesion hypothesis, the jamming phenomenon is also based on adhesion forces, cell density, and shape.

The vertebrate body axis elongation is an essential step in forming the anteroposterior body axis and a hallmark of animal development [46]. The physical mechanisms that control this process are still not fully understood; however, a study by Mongera et al. showed that it might be driven by localized, mesoscopic jamming and unjamming. During the formation of the vertebrate body axis in zebrafish, the posterior tissue solidifies at the presomitic mesoderm (PSM) while proliferating at the still fluid-like mesodermal progenitor zone (MPZ) [10].

This observation matches previous studies showing a different mode of cell movement during the development of the vertebrate axis [47, 48]. More specifically, the cells in the posterior tip move randomly and individually or fluid-like. At the same time, they become slower and move collectively or instead solidify in the PSM (see **Figure 2**). This corresponds precisely to a jamming transition at the tip of the vertebrate body axis [48].

In this process, the jamming transition is spatiotemporally controlled by the extracellular space regulated by cadherin-dependent cell-cell adhesions [10, 48]. However, it remains unclear whether jamming transitions during embryogenesis are generally density-driven. The solidification along the vertebrate body axis results in unidirectional growth and elongation of the embryo. Supracellular stresses act as mechanical cues for the morphogenetic flow.

Similar to the localized proliferation and (un)jamming during the vertebrate body elongation, tissue jamming and unjamming are also present during branching morphogenesis. In this process, tubular structures are formed from remodeling epithelial or endothelial sheaths, resulting in branched structures such as ducts of the kidney, mammary and salivary glands, or lung tissue [49–51].

Other embryonic processes in which jamming transitions play a role are the ventral furrow formation in *Drosophila* and the early stages of gastrulation [7, 28]. This short overview shows how spatiotemporal control of fluid-like and solid-like tissue states by jamming is essential during tissue morphogenesis.

4 UNJAMMING IN CANCER

In contrast to embryogenesis, cell rearrangements within healthy adult tissues happen only rarely, for example, during wound healing. Still, in some diseases, cells regain the ability to migrate, for instance, metastatic cancer cells. Carcinomas are tumors that develop from epithelial cells. The healthy epithelium separates and protects different organs from each other. It needs to be stable, organized, and mechanically intact against external forces. From a biophysical point of view, bounding epithelium can be seen as a tissue that is in a jammed state. During cancer progression, the cancer cells start to proliferate in an uncontrolled way, grow to a solid tumor, and even migrate through the body. The transition from the stable non-motile

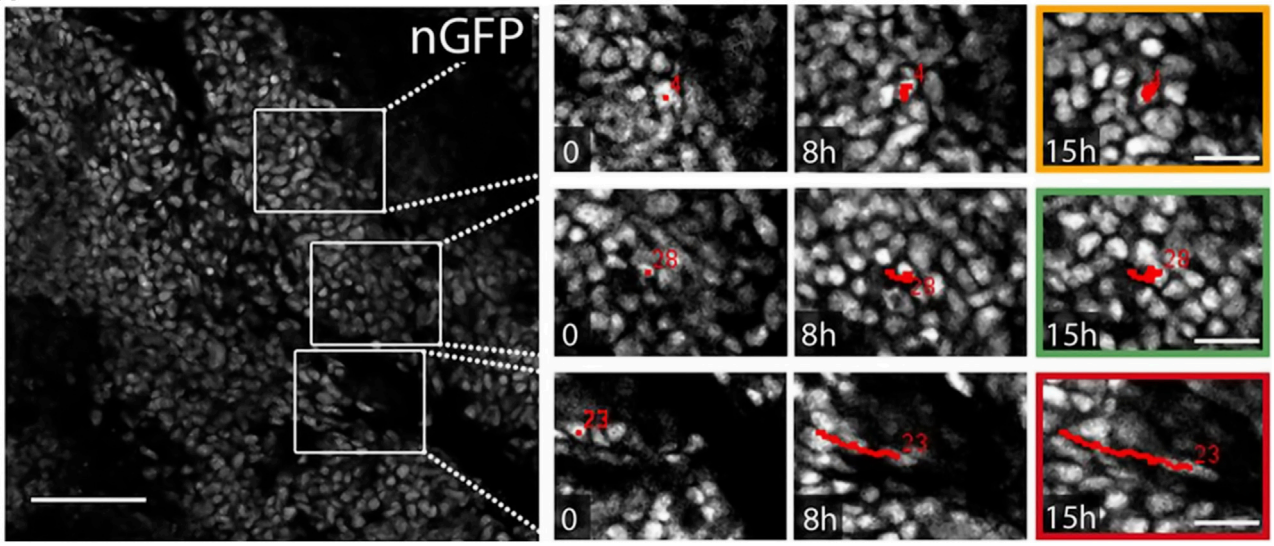

FIGURE 3 | Tumors have jammed and unjammed regions. Cell migration tracks in the core of tumor explants from mice. The *ex vivo* tumor shows jammed regions with resting cells (yellow box) and unjammed regions with moving cells (green and red box). The unjammed areas display different migration dynamics, with high (red) or lower (green) persistence. Red numbers represent the track ID numbers. Nuclei are stained with nuclear-targeting GFP (nGFP). Scale bar 100 μm. Images were taken and adapted from Staneva et al. [55], Copyright ID 1096785–1.

epithelium to an unstructured, partly motile tumor can thus be seen as an unjamming transition.

The idea to link the migration of cancer cells to unjamming has already been proposed some years ago [6]. Particularly, the link between the EMT and unjamming seemed natural because, during EMT, cells detach from the solid tumor and migrate outwards, which resembles the fluidization of the tissue. However, it is still under debate if EMT and unjamming are similar processes. In a 2D model system, inducing partial EMT lead to different structural and dynamical signatures than a pressure-induced unjamming transition [1]. However, deregulation of adherens junctions and downregulation of E-cadherin in epithelial tissues, which is a crucial step during EMT, has been shown to drive invading cells toward a more unjammed state [5]. The biological processes of cancer invasion are heterogeneous, and the cells can adopt different migration modes. The physical concept of unjamming represents a unifying framework that is agnostic of molecular details.

This seems to hold for the pure tumor as well as for the compound of tumor and microenvironment. While the presence of moving cells at the invasive tumor front seems intuitive—most tumors are composed of a proliferation outer rim of cancer cells [52–54]—unjamming appears in the tumor core as well. Recent studies found fluid-like regions with correlated moving cells in tumor explants from humans and mice [4, 55]. This observation is represented in **Figure 3**. Here, the tracks of cancer cells in tumor explants point toward a wide variety of dynamic behavior inside densely packed tumors. This raises the question of the role of jamming and unjamming in the overall tumor stability and shape. Even though uncontrolled proliferation is a hallmark of cancer, both reports conclude that proliferation is not the driving factor for the unjamming transition [4, 55].

Tumors often grow in close vicinity to connective and fatty tissues [56]. While only little is known about the influence of fatty tissue on the unjamming of cancer cells, connective tissue, mainly composed of ECM, has been shown to influence the dynamical behavior of cancer cells. A dilute ECM network can induce a transition to a gas-like state, where cells move individually. Denser networks result in constrained and collective motion and can even block cellular motion [5, 57].

In cancer progression, a crucial determinant in patient survival rate is the occurrence of metastasis. Metastasizing cells can be hypothesized as single unjammed cells escaping a jammed tumorous tissue. The heterogeneous vertex model predicts that single unjammed cells are relatively unlikely, and jamming is a (localized) collective property [30]. For instance, a mixture of one cell type that typically jams and another that stays unjammed would form a globally jammed layer when the mixing ratios of jammed and unjammed cells reach 4:1, thereby trapping the “fluid” unjammed cells in a scaffold of “solid” jammed cells [30, 58]. The encasement of fluid cells by jammed cells results in the percolation of the tension network, which significantly increases the rigidity of the tissue [30]. In essence, soft cells can still form rigid tissues via tension percolation and jamming, thus explaining why rigid tumors contain soft cells [6].

Particularly in the tumor cores, the question of how cells can rearrange in an already densely packed environment, near volume fraction 1, arises. In contrast to embryogenesis, where changes in density have a major role in the dynamical behavior of the cells, the cell shape is a critical parameter in dense tissues. It can be used as a marker for tissue fluidity [4]. In clinical cancer grading, the variance of nuclear shapes and sizes—so-called pleomorphisms [59]—is used as a crucial marker for the

aggressiveness of tumors. The nuclear shape further correlates with the cell shape [4]. A higher grading, which implies more heterogeneous nuclear shapes, means that, statistically, the cell shapes have a higher variability if the correlation is valid for primary tumors. Since cancer cell clusters are amorphous aggregates, higher variances are accompanied by higher average values [28]. Thus, pleomorphism, that is, high variance in nuclear shapes, might be accompanied by higher cell and nuclear shapes in tumors [4, 28]. This circumstance yields a contextual link between conventional clinical cancer grading and the physics of unjamming.

5 CURRENT PROBLEMS IN CELL JAMMING

5.1 Driving Factors of the Unjamming Transition

In real biological systems and models, the number density, the volume fraction, and the cell shapes play a role in the jamming transition. However, cell shapes and densities are not intrinsic properties of cells but result from an interplay of cell-cell adhesion, substrate adhesion, cell activity (such as traction generation or contractile stress), and cell stiffness. Particularly in cancer progression, it is essential to understand which factors shape cells in a dense environment and support migration. From a physical point of view, one can ask, what are the different axes of the jamming phase diagram?

An emerging key feature of more unjammed cell monolayers is strong cell-substrate interaction combined with high traction forces. This has been shown throughout many studies in the last years [3, 25, 60, 61]. Some studies have argued that high substrate traction implies strong cell-cell adhesion to balance and transmit the high intercellular tensile stresses [3, 60, 61]. However, a recent study explicitly tried to disentangle the contributions of cell-cell adhesion and substrate traction, pointing out that the adhesion strength does not change visibly in a more unjammed monolayer [25]. Saraswathibathla et al. even demonstrated that stress fiber alignment and the related traction forces predominantly control the cell shape and, finally, the unjamming transition [25]. A possible explanation for the dominant role of traction forces could be that they are stronger than the forces at the cellular interfaces. Thus, their influence on the cell shapes prevails over cell-cell adhesion and cortical tension effects, which are important control parameters in the SPV model.

In confluent systems without any cell-substrate interaction, for example, three-dimensional cell spheroids, this substrate effect should vanish, and the role of the cell-cell adhesion becomes dominant. The predictions of the 3D-SPV model [62], however, were not confirmed by an experimental study [4]. In fact, cell spheroids built from less adhesive cells were more unjammed, and single cells could move through the spheroid (**Figure 1**), while the more adhesive cells formed jammed spheroids with non-motile cells [4].

In another study that tested the influence of cell-cell adhesion on the dynamics, the authors investigated a non-confluent system by placing cell clusters in a substrate and ECM environment. The strength of cell-cell adhesion clearly influenced cell behavior. Here, a decrease of cell-cell adhesion leads to more individualized and faster cell movement, more elongated cells, and fluidizes the system further (see **Figure 4**) [5]. Additionally, the weaker cell-cell contacts allowed the system to promote unjamming again through a density decrease [5].

In both studies, the authors clearly find an association between unjamming and cell shapes [4, 5], but these were not associated with higher cell-cell adhesion as suggested by the SPV [16, 62].

The question of whether cell-cell adhesion or substrate traction drives the unjamming transition can thus not be clearly answered in general. The role of cell-cell adhesion seems to be more complex than predicted by the SPV model. Some experimental evidence showed that weak adhesion supports unjamming and promotes invasive cell behavior. This behavior fits with the known role of EMT in cancer progression.

5.2 Nuclear Jamming

Cell jamming theories have consistently emphasized cell shapes rather than nucleus shapes because the whole cells are volume-filling

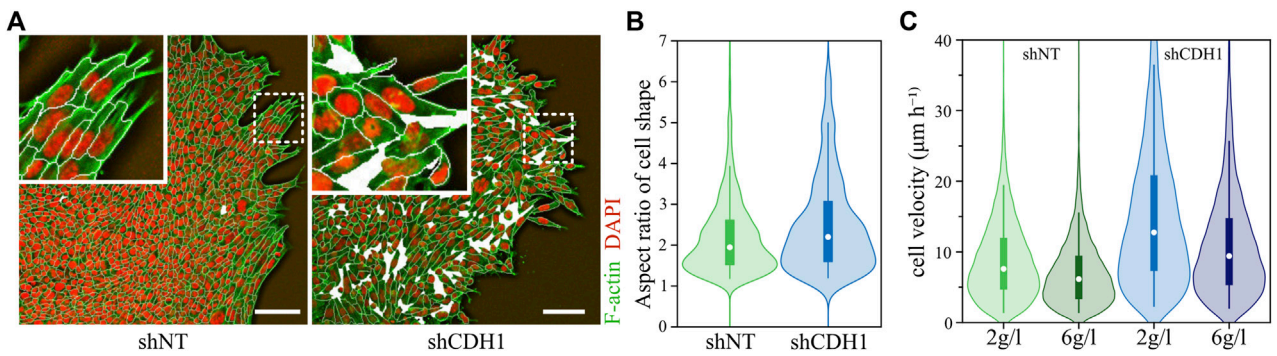

FIGURE 4 | Downregulation of E-cadherin promotes unjamming in migrating cell layer. **(A)** Morphology of wild-type (shNT) and E-cadherin downregulated (shCDH1) cell layers migrating at a collagen interface. The wild-type cell aggregate is almost area-filling and exhibits high spatial correlations for the long axes—the orientation—of the cells. E-Cadherin knockout cell aggregate displays density fluctuations, and cells are randomly aligned. Actin is stained in green (Alexa Fluor 568-conjugated phalloidin), while nuclei are stained in red (DAPI). The white lines visualize a cell segmentation with holes in the tissue represented by white areas. The scale bar represents 100 μm. **(B)** Change of aspect ratio due to loss of E-cadherin. An increase in aspect ratio corresponds to higher shape indices, thus promoting unjamming of tissue. **(C)** Change in cell migration velocity due to downregulated E-cadherin and promoted unjamming. Graphics and data were adopted from Ilina et al. [5].

a tissue – not the nuclei – which is a crucial element in various theories [3, 16, 28]. In other words, cells in dense tissues should be jammed, while nuclei alone would not be jammed, as their volume fraction is much lower. Recent studies, however, suggest that the nucleus might actively be involved.

The role of the nucleus in single-cell migration has been clear for quite a while. The ability of the cell nuclei to squeeze into free spaces was found to be essential for tumor progression [63, 64]. While the cytoplasm of migrating cells can move through pore sizes below 1 μm, this is not the case for the nucleus as it is the stiffest cell organelle [65–67]. The nuclear compressibility and size further limit the single-cell movement through narrow spaces [68–71]. However, the nucleus not only has a limiting effect on cell migration in dense environments. Two recent studies showed that the nucleus itself is mechanosensitive and that nuclear deformation enhances cellular force generation [72, 73]. Moreover, Staneva et al. and Grosser et al. demonstrated that cell nuclei in tumor clusters strongly deform while they move through the tissue (**Figure 1**) [4, 55]. Unjammed regions in tumor samples were characterized by elongated nuclei [4], typically found in elongated cells.

From single-cell movement to primary cancer samples, these observations suggest that the nucleus is actively and passively involved in jamming, potentially adding to the traditional role of nuclei shapes in cancer.

5.3 Motion Arrest or Rigidity Transition

In cell systems, the terms jamming and unjamming are often used loosely. By jamming, some authors refer to collective motion arrest [1, 3, 74] or locally caged behavior [25, 58]. Others call the collective motility arrest glass transition, avoiding the term jamming [14], or simply rigidity transition [16]. In fact, cellular systems exhibit many features typical of glasses, such as an amorphous, disordered structure, a broad range of relaxation time scales, and a flat plateau region of the mean squared displacements on intermediate time scales [14, 20, 61, 75].

A key feature of jamming is that a system that jams actually becomes solid-like. However, the connection between motion arrest and rigidity is not obvious for non-equilibrium systems such as tissues. Tissues are active matter, and various biological and physical mechanisms are intertwined and work simultaneously. They potentially react actively to external stress, for example, by fluidization. Motion, or lack thereof, cannot sufficiently determine jamming and unjamming in tissues in the sense of a true rigidity transition. Fluid-like systems are characterized by stress relaxation, whereas solid-like systems typically show no or only minor stress relaxation. So far, only Serwane and Mongera et al. have provided stress relaxation data in vertebrate body axis formation and connected the data to the jamming phenomenon [10, 76].

An epithelial sheet that moves into a cell-free area could be in a motile but (locally) jammed state. Their neighbors cage cells within the sheet while the whole sheet collectively moves [58, 77]. Conversely, tissues could be in a non-rigid, low tension, unjammed state with only minimal or vacant cell motion insufficient for active neighbor exchange [78]. The relation between rigidity and jamming is of particular interest in cancer development. Recent research has suggested that unjamming is involved in cancer progression. However, tumors are usually harder than their surroundings. Future research has still to connect the dots between hard tumors, soft cells [79], and the role of unjamming in cancer [4–6].

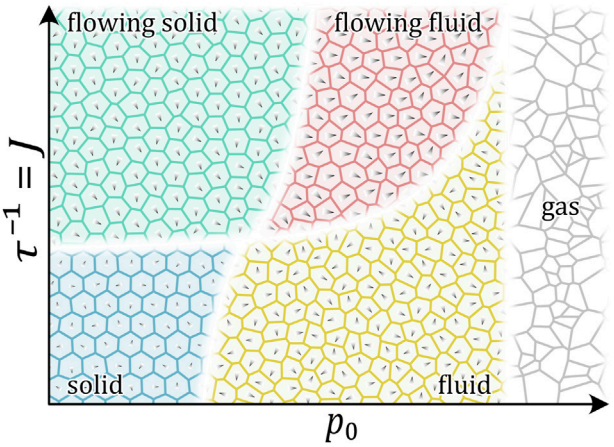

FIGURE 5 | Qualitative phase diagram of 2D cell monolayers at volume fraction close to 1. The phase diagram is based on [61, 75]. Control parameters are the target shape index p_0 and the alignment interaction $J = \tau^{-1}$ with τ being the reorientation time which is the time that cells take to adjust their polarities along the direction of the velocities of the corresponding local environments. The magnitude of the motility v_0 and its direction is indicated as arrows. Tissue approaches hexagonal-like structure for decreasing target shape factor. With increasing alignment interaction, the system displays more long-ranged directed motility. Blue cells in phase space: alignment interactions are minor, and cellular reorientations are governed by rotational diffusion. The target shape index is small yielding roundish cells. Here, cells rarely align with neighborhood velocities and are randomly oriented. The energetically favored shape index is low-yielding hexagonal-like structures. Green cells in phase space: roundish cells and hexagonal-like tissue structures are present induced by a small target shape index. High-velocity correlations yield flowing flocks of solid-like cell aggregates. Red cells in phase space: high-velocity correlations accompanied by elongated cells yield a fluid phase in which aggregates undergo coordinated motion. Yellow cells in phase space: moderate to vanishing alignment interactions and elongated cells yield a fluid phase where cells undergo predominantly random motion. Gray cells in phase space: cell interactions vanish in this phase due to the high target shape index. The cellular system behaves gas-like.

There might be a rather non-physical explanation why the term jamming has become popular. It is because it intuitively expresses the collective, emergent character of this transition—"clearly, jamming is not something that you can do on your own" [80].

5.4 Different Migration Modes of Unjamming

In the literature, the word unjamming is used for various dynamical behavior in biological systems. The observed migration patterns range from the collective motion of sheets or packs [1, 14, 61, 74, 81] to single-cell squeezing events [4, 25], or T1-transitions [82]. These different migration modes can be distinguished by respective characteristic velocity correlation length, migration persistence, or pack size of cooperatively migrating cell clusters.

Cells modify their polarization and migration direction through interaction with surrounding cells [18, 83], which might lead to more collective motion [18, 83]. Theoretical

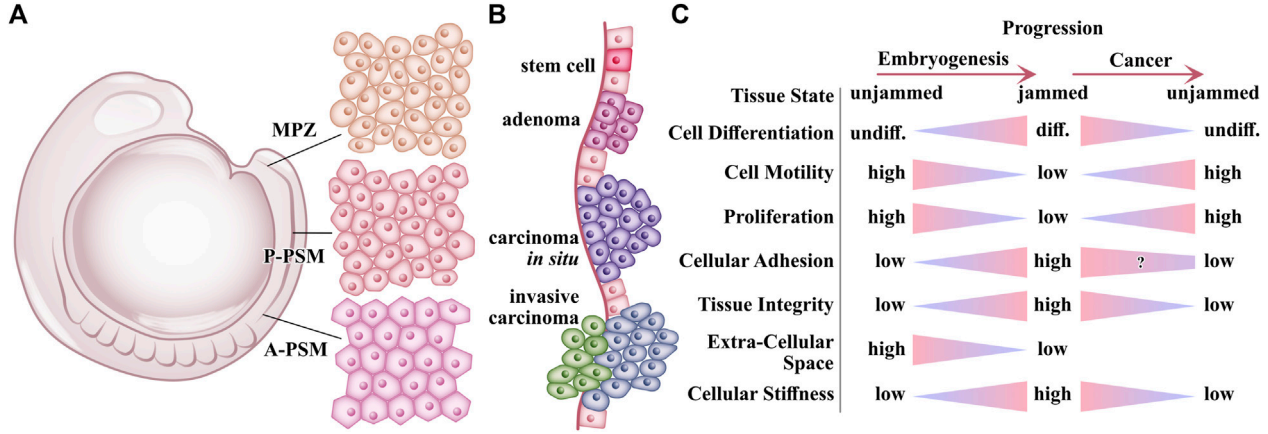

FIGURE 6 | Occurrence of Jamming and unjamming in embryogenesis and cancer. **(A)** Illustration of the lateral view of zebrafish embryo in the 10-somite stage. During periodic rapid elongations at the tail of the embryo, cells from the mesodermal progenitor zone (MPZ) transform to cells of the posterior (P-PSM) presomitic mesoderm and consecutively to anterior presomitic mesoderm (A-PSM). During this transformation, the initial cells of the MPZ slowly decrease the cell motility, filling the voids of the extracellular space, and restructuring their N-cadherin-mediated adhesion with neighboring cells resulting in increased tissue stiffness and integrity [10]. **(B)** Cancer progression during early stages. Growing factors like TGF-β limit the growth of normal epithelium and early-stage tumors resulting in adenomas. After losing growth-inhibitory responsiveness, tumors grow more rapidly, transforming into carcinomas *in situ*. Additional oncogenic mutations are acquired during rapid growth. By chance, tumor cells with specific oncogenic mutations can undergo epithelial-mesenchymal transdifferentiation in response to TGF-β and are becoming more invasive carcinomas [90]. **(C)** Overview of changes on tissue and cellular level during embryogenesis and cancer progression. Various processes and properties which change during embryogenesis are reversed during cancer progression, motivating the hypothesis of cancer being inverse morphogenesis [87, 88, 91].

models take this into account by introducing an additional alignment interaction. The resulting jamming phase diagram contains four distinct phases: solid/jammed, solid flock/flowing solid/active nematics, liquid flock/flowing liquid, and liquid (see **Figure 5**) [61, 75]. These states represent the experimentally observed migration patterns in more detail and show that unjamming can mean different types of motion. This further raises the question of whether the dynamical signature of moving cells can give information about the interaction strength of cells?

This further raises the question of whether the dynamical signature of moving cells can provide information about the interaction strength of cells.

The observed migration modes also resemble the ones seen in active nematic fluids. Self-propelled rods with a higher aspect ratio, similar to elongated mesenchymal cells, display phases of flocking, laning, and isotropic alignment with sharp phase transitions. Furthermore, the flocking motion in active nematics, although collectively moving, is internally, locally jammed [84], which can be observed in biological tissues as well [4, 10]. It should be further noticed that cellular systems might also show mixed jammed/unjammed stated as it is, for example, seen in spheroids embedded in collagen, where the core can be still jammed while the outer shell starts to melt [26, 74].

6 SHAPE- AND DENSITY-DRIVEN JAMMING IN EMBRYOGENESIS AND CANCER

In recent years, it has become clear that rigidity transitions are involved in embryogenesis and diseases. While early studies and modeling approaches had focused on 2D *in vitro* monolayers and 2D models [3, 14, 20, 21], crucial breakthroughs were made by several studies that observed the jamming phenomenon in 3D systems [4, 5, 10, 55, 74]. These studies comprise *in vitro* but also *ex vivo* and *in vivo* systems.

Early experiments pointed to different, even opposing, roles in these processes (see **Figure 6**). Experimentally, jamming-like fluid-to-solid transition accompanied embryogenesis [10, 47, 48, 85]. During embryonic development, cells proliferate quickly and rearrange while they differentiate into specialized cells and form stable, structured organs. The cellular stiffness increases with differentiation [86]. Eventually, proliferation and migration subside, suggesting increasing solidification in the course of embryogenesis. The tissues are in a jammed-like state.

During cancer progression, by contrast, cells de-differentiate. For instance, in cervical cancer, cancer cells de-differentiate and spread from the tissue of origin to tissues of ontogenetic proximity in reverse order to the mature derivatives of the morphogenetic fields [87, 88]. The cancer cell stiffness declines with increasing malignancy [79, 89]. Metastatic cells lose cell-cell adhesion and gain higher motility. This results in a decline in tissue integrity under further tumor growth and cancer cell invasion. These trends suggest a central role of *unjamming* and fluidization in cancer. Several recent studies found this effect in cancer systems [4, 5, 61, 74]. In short, many processes in embryogenesis are reversed in cancer progression, including jamming and unjamming.

Originally, the term jamming was chosen in analogy to colloidal systems that rigidify with increasing density. Cell

number density in epithelial monolayers was the first driver of jamming to be reported [14]. However, observations in an asthma model have suggested cell shape as the central switch between jamming and unjamming [3]. Consequently, the SPV models [16, 20, 62] have become an inspiring driver of research that promoted a new physics: cell-shape-dependent jamming. Several years later, both shape-dependent jamming and density-dependent jamming have experimentally been found [3–5, 10, 28].

However, one can only hypothesize the potentially different roles these two mechanisms play based on the still limited evidence. Rapidly increasing cell density and the maturation and stabilization of cell-cell contacts characterized embryogenesis, solidifying the system. Experimentally, the shrinking volume of extracellular space and increasing adhesion drive jamming during zebrafish development [10] and other systems [7], in line with the global tendencies during embryogenesis. However, shape also plays a role during embryogenesis [28], especially considering 2D-like tissues such as epithelial sheets. Cancer progression and the formation of metastases show an opposing tendency: cancer starts in a dense environment. Tumors grow within an already existing organism against outside homeostatic pressure, resulting in an effective volume constraint. Thus, if cancer progression is accompanied by unjamming, the global environment suggests a more prominent shape-induced unjamming in tumors. In recent years, shape-induced unjamming was found, with several recent studies pointing to shape-dependent unjamming in tumor clusters [4] as well as complex tumor-ECM environments [5] and even asthma [3].

7 CONCLUSION AND OUTLOOK

Observed in embryogenesis and diseases, tissues continuously alter their rigidity and reshape. Solidification of tissues drives embryogenesis, whereas fluidization of cancer cells drives cancer progression, leading to metastasis. Recent findings support the concept of a jamming-like transition as a concept of tissue remodeling of rigidity and fluidity modulation. With this review, we want to shed light on the plurivalent concepts of the jamming phenomenon. While tissue (un)jamming can be induced by different intracellular (E-cadherin, RAB5A, stress fiber alignment) [4, 5, 25, 61, 74] and extracellular mechanisms such as pressure [3, 28], density [5, 10], irradiation [27], or ECM confinements [5], it has turned out to be a remarkable overarching principle that unites processes stemming from a wide variety of cues. Nonetheless, which physical quantity or parameter is the driving factor for jamming and unjamming is still debatable. Given the complexity of the biological matter, it is most likely that more than one parameter should be considered in jamming transitions. Experimental data of embryonic tissues favors cell-density whereas cancer models prefer a shape-induced explanation of the jamming phenomenon. The jamming phenomenon has likely more than one or two sides.

While theoretical models made large advancements in recent years, the experimental data needed for verification or falsification is incomplete. The biological and physical mechanisms of tissues have to be carefully dissected. Reliable quantification of jamming-related quantities is a challenging task.

Future experiments under controlled conditions should further elucidate how stresses in jammed and unjammed tissues relax. These experiments also provide the opportunity to identify (and perhaps quantify) more molecular details involved in stress relaxation in tissue. Cell-cell adhesion generates tension in tissues. Thus, density-driven cell crowding can significantly generate rigidity in tissue as predicted in vertex and SPV models [62, 92]. When the cell density increases, the number, and thus strength of cell-cell contacts increases. At a critical density, sufficient force bridges are generated, the tension network percolates and the tissue undergoes a rigidity transition [30, 93]. The rigidity percolation can also encase fluid-like cells by rigid cells, which significantly increases the rigidity of the tissue [30]. Data of local tissue rigidity current provides the most convincing link to the jamming phenomenon [10, 93] and supports the interpretation of jamming as a density-driven transition as seen in embryogenesis. As the largest and stiffest organelle, the cell nucleus harbors significant potential for the observed rigidity percolation. In models (and experiments), the feedback (loop) between nuclear deformation and cell migration/force generation is not sufficiently investigated. The nucleus and its importance in jamming were only considered in one experiment by Grosser et al. [4]. Cells, however, are mechanosensitive and adapt to the rigidity of their environment [94–96]. Thus, experiments addressing rigidity will have difficulties in dissecting physical aspects from biological aspects. On the other hand, these difficulties are also a large opportunity to link jamming to the molecular origin.

AUTHOR CONTRIBUTIONS

All authors discussed the results and contributed to the final manuscript; provided critical feedback and helped shape the manuscript; and contributed to writing the manuscript.

FUNDING

This project has received funding from the European Research Council (ERC-741350/HoldCancerBack). We acknowledge funding from the European Commission H2020-PHC-2015-two-stage as part of the 'FORCE' project (668039/Imaging the Force of Cancer). We acknowledge support from the German Research Foundation (DFG) and University of Leipzig within the program of Open Access Publishing.

ACKNOWLEDGMENTS

We like to thank Jürgen Lippoldt for fruitful discussions and vital feedback for this manuscript.

REFERENCES

1. Mitchel JA, Das A, O'Sullivan MJ, Stancil IT, DeCamp SJ, Koehler S, et al. In Primary Airway Epithelial Cells, the Unjamming Transition Is Distinct from the Epithelial-To-Mesenchymal Transition. *Nat Commun* (2020) 11:1–14. doi:10.1038/s41467-020-18841-7
2. Park JA, Atia L, Mitchel JA, Fredberg JJ, and Butler JP. Collective Migration and Cell Jamming in Asthma, Cancer and Development. *J Cel Sci* (2016) 129: 3375–83. doi:10.1242/jcs.187922
3. Park JA, Kim JH, Bi D, Mitchel JA, Qazvini NT, Tantisira K, et al. Unjamming and Cell Shape in the Asthmatic Airway Epithelium. *Nat Mater* (2015) 14: 1040–8. doi:10.1038/nmat4357
4. Grosser S, Lippoldt J, Oswald L, Merkel M, Sussman DM, Renner F, et al. Cell and Nucleus Shape as an Indicator of Tissue Fluidity in Carcinoma. *Phys Rev X* (2021) 11:011033. doi:10.1103/PhysRevX.11.011033
5. Ilina O, Gritsenko PG, Syga S, Lippoldt J, La Porta CAM, Chepizhko O, et al. Cell–cell Adhesion and 3D Matrix Confinement Determine Jamming Transitions in Breast Cancer Invasion. *Nat Cel Biol* (2020) 22:1103–15. doi:10.1038/s41556-020-0552-6
6. Oswald L, Grosser S, Smith DM, and Käs JA. Jamming Transitions in Cancer. *J Phys D: Appl Phys* (2017) 50:483001. doi:10.1088/1361-6463/aa8e83
7. Petridou NI, Grigolon S, Salbreux G, Hannezo E, and Heisenberg CP. Fluidization-mediated Tissue Spreading by Mitotic Cell Rounding and Non-canonical Wnt Signalling. *Nat Cel Biol* (2019) 21:169–78. doi:10.1038/s41556-018-0247-4
8. Petridou NI, and Heisenberg CP. Tissue Rheology in Embryonic Organization. *EMBO J* (2019) 38:e102497. doi:10.15252/embj.2019102497
9. Barriga EH, and Mayor R. Adjustable Viscoelasticity Allows for Efficient Collective Cell Migration. *Semin Cel Dev Biol* (2019) 93:55–68. doi:10.1016/j.semcdb.2018.05.027
10. Mongera A, Rowghanian P, Gustafson HJ, Shelton E, Kealhofer DA, Carn EK, et al. A Fluid-To-Solid Jamming Transition Underlies Vertebrate Body axis Elongation. *Nature* (2018) 561:401–5. doi:10.1038/s41586-018-0479-2
11. Berthier L, Flenner E, and Szamel G. Glassy Dynamics in Dense Systems of Active Particles. *J Chem Phys* (2019) 150:200901.
12. Liu AJ, and Nagel SR. The Jamming Transition and the Marginally Jammed Solid. *Annu Rev Condens Matter Phys* (2010) 1:347–69. doi:10.1146/annurev-conmatphys-070909-104045
13. Charbonneau P, Kurchan J, Parisi G, Urbani P, and Zamponi F. Glass and Jamming Transitions: From Exact Results to Finite-Dimensional Descriptions. *Annu Rev Condens Matter Phys* (2017) 8:265–88. doi:10.1146/annurev-conmatphys-031016-025334
14. Angelini TE, Hannezo E, Trepat X, Marquez M, Fredberg JJ, and Weitz DA. Glass-like Dynamics of Collective Cell Migration. *Proc Natl Acad Sci U.S.A* (2011) 108:4714–9. doi:10.1073/pnas.1010059108
15. Bi D, Lopez JH, Schwarz JM, and Manning ML. Energy Barriers and Cell Migration in Densely Packed Tissues. *Soft Matter* (2014) 10:1885–90. doi:10.1039/C3SM52893F
16. Bi D, Lopez JH, Schwarz JM, and Manning ML. A Density-independent Rigidity Transition in Biological Tissues. *Nat Phys* (2015) 11:1074–9. doi:10.1038/nphys3471
17. Farhadifar R, Röper JC, Aigouy B, Eaton S, and Jülicher F. The Influence of Cell Mechanics, Cell-Cell Interactions, and Proliferation on Epithelial Packing. *Curr Biol* (2007) 17:2095–104. doi:10.1016/j.cub.2007.11.049
18. Sadati M, Taheri Qazvini N, Krishnan R, Park CY, and Fredberg JJ. Collective Migration and Cell Jamming. *Differentiation* (2013) 86:121–5. doi:10.1016/j.diff.2013.02.005
19. Schötz EM, Lanio M, Talbot JA, and Manning ML. Glassy Dynamics in Three-Dimensional Embryonic Tissues. *J R Soc Interf* (2013) 10. doi:10.1098/rsif.2013.0726
20. Bi D, Yang X, Marchetti MC, and Manning ML. Motility-Driven Glass and Jamming Transitions in Biological Tissues. *Phys Rev X* (2016) 6:021011. doi:10.1103/PhysRevX.6.021011
21. Garcia S, Hannezo E, Elgeti J, Joanny JF, Silberzan P, and Gov NS. Physics of Active Jamming during Collective Cellular Motion in a Monolayer. *Proc Natl Acad Sci* (2015) 112:15314–9. doi:10.1073/pnas.1510973112
22. Anderson VJ, and Lekkerkerker HNW. Insights into Phase Transition Kinetics from Colloid Science. *Nature* (2002) 416:811–5. doi:10.1038/416811a
23. Song C, Wang P, and Makse HA. A Phase Diagram for Jammed Matter. *Nature* (2008) 453:629–32. doi:10.1038/nature06981
24. Donev A, Cisse I, Sachs D, Variano EA, Stillinger FH, Connelly R, et al. Improving the Density of Jammed Disordered Packings Using Ellipsoids. *Science* (2004) 303:990–3. doi:10.1126/science.1093010
25. Saraswathibhatla A, and Notbohm J. Tractions and Stress Fibers Control Cell Shape and Rearrangements in Collective Cell Migration. *Phys Rev X* (2020) 10: 011016. doi:10.1103/PhysRevX.10.011016
26. Han YL, Pegoraro AF, Li H, Li K, Yuan Y, Xu G, et al. Cell Swelling, Softening and Invasion in a Three-Dimensional Breast Cancer Model. *Nat Phys* (2020) 16:101–8. doi:10.1038/s41567-019-0680-8
27. O'Sullivan MJ, Mitchel JA, Das A, Koehler S, Levine H, Bi D, et al. Irradiation Induces Epithelial Cell Unjamming. *Front Cel Dev Biol* (2020) 8. doi:10.3389/fcell.2020.00021
28. Atia L, Bi D, Sharma Y, Mitchel JA, Gweon B, Koehler A, et al. Geometric Constraints during Epithelial Jamming. *Nat Phys* (2018) 14:613–20. doi:10.1038/s41567-018-0089-9
29. Czajkowski M, Sussman DM, Marchetti MC, and Manning ML. Glassy Dynamics in Models of Confluent Tissue with Mitosis and Apoptosis. *Soft Matter* (2019) 15:9133–49. doi:10.1039/C9SM00916G
30. Li X, Das A, and Bi D. Mechanical Heterogeneity in Tissues Promotes Rigidity and Controls Cellular Invasion. *Phys Rev Lett* (2019) 123:058101. doi:10.1103/PhysRevLett.123.058101
31. Chiang M, and Marenduzzo D. Glass Transitions in the Cellular Potts Model. *EPL* (2016) 116:28009. doi:10.1209/0295-5075/116/28009
32. Briggs JA, Weinreb C, Wagner DE, Megason S, Peshkin L, Kirschner MW, et al. The Dynamics of Gene Expression in Vertebrate Embryogenesis at Single-Cell Resolution. *Science* (2018) 360. doi:10.1126/science.aar5780
33. Keller R, Davidson LA, and Shook DR. How We Are Shaped: The Biomechanics of Gastrulation. *Differentiation* (2003) 71:171–205. doi:10.1046/j.1432-0436.2003.710301.x
34. Adamo L, Naveiras O, Wenzel PL, McKinney-Freeman S, Mack PJ, Gracia-Sancho J, et al. Biomechanical Forces Promote Embryonic Haematopoiesis. *Nature* (2009) 459:1131–5. doi:10.1038/nature08073
35. Responte DJ, Lee JK, Hu JC, and Athanasiou KA. Biomechanics-driven Chondrogenesis: from Embryo to Adult. *FASEB J* (2012) 26:3614. doi:10.1096/fj.12-207241
36. Delile J, Herrmann M, Peyriéras N, and Doursat R. A Cell-Based Computational Model of Early Embryogenesis Coupling Mechanical Behaviour and Gene Regulation. *Nat Commun* (2017) 8:1–10. doi:10.1038/ncomms13929
37. Heisenberg CP, and Bellaïche Y. Forces in Tissue Morphogenesis and Patterning. *Cell* (2013) 153:948–62. doi:10.1016/j.cell.2013.05.008
38. Foty RA, Pfleger CM, Forgacs G, and Steinberg MS. Surface Tensions of Embryonic Tissues Predict Their Mutual Envelopment Behavior. *Development* (1996) 122:1611–20.
39. Steinberg MS. ON THE MECHANISM OF TISSUE RECONSTRUCTION BY DISSOCIATED CELLS, III. FREE ENERGY RELATIONS AND THE REORGANIZATION OF FUSED, HETERONOMIC TISSUE FRAGMENTS. *Proc Natl Acad Sci U.S.A* (1962) 48:1769–76. doi:10.1073/pnas.48.10.1769
40. Steinberg MS. ON THE MECHANISM OF TISSUE RECONSTRUCTION BY DISSOCIATED CELLS, I. POPULATION KINETICS, DIFFERENTIAL ADHESIVENESS, AND THE ABSENCE OF DIRECTED MIGRATION. *Proc Natl Acad Sci U.S.A* (1962) 48:1577–82. doi:10.1073/pnas.48.9.1577
41. Steinberg MS. Reconstruction of Tissues by Dissociated Cells. *Science* (1963) 141:401–8. doi:10.1126/science.141.3579.401
42. Schötz EM, Burdine RD, Jülicher F, Steinberg MS, Heisenberg CP, and Foty RA. Quantitative Differences in Tissue Surface Tension Influence Zebrafish Germ Layer Positioning. *HFSP J* (2008) 2:42–56. doi:10.2976/1.2834817
43. Krens SFG, Veldhuis JH, Barone V, Čapek D, Maître JL, Brodland GW, et al. Interstitial Fluid Osmolarity Modulates the Action of Differential Tissue Surface Tension in Progenitor Cell Segregation during Gastrulation. *Development* (2017) 144:1798–806. doi:10.1242/dev.144964
44. Ninomiya H, David R, Damm EW, Fagotto F, Niessen CM, and Winklbauer R. Cadherin-dependent Differential Cell Adhesion in Xenopus Causes Cell

Sorting *In Vitro* but Not in the Embryo. *J Cel Sci* (2012) 125:8. doi:10.1242/jcs.095315
45. Pawlizak S, Fritsch AW, Grosser S, Ahrens D, Thalheim T, Riedel S, et al. Testing the Differential Adhesion Hypothesis across the Epithelial-Mesenchymal Transition. *New J Phys* (2015) 17:083049. doi:10.1088/1367-2630/17/8/083049
46. Bénazéraf B, and Pourquié O. Formation and Segmentation of the Vertebrate Body axis. *Annu Rev Cel Dev Biol* (2013) 29. doi:10.1146/annurev-cellbio-101011-155703
47. Bénazéraf B, Francois P, Baker RE, Denans N, Little CD, and Pourquié O. A Random Cell Motility Gradient Downstream of FGF Controls Elongation of an Amniote Embryo. *Nature* (2010) 466:248–52. doi:10.1038/nature09151
48. Lawton AK, Nandi A, Stulberg MJ, Dray N, Sneddon MW, Pontius W, et al. Regulated Tissue Fluidity Steers Zebrafish Body Elongation. *Development* (2013) 140:573–82. doi:10.1242/dev.090381
49. Ochoa-Espinosa A, and Affolter M. Branching Morphogenesis: From Cells to Organs and Back. *Cold Spring Harbor Perspect Biol* (2012) 4. doi:10.1101/cshperspect.a008243
50. Spurlin JW, Siedlik MJ, Nerger BA, Pang MF, Jayaraman S, Zhang R, et al. Mesenchymal Proteases and Tissue Fluidity Remodel the Extracellular Matrix during Airway Epithelial Branching in the Embryonic Avian Lung. *Development* (2019) 146. doi:10.1242/dev.175257
51. Varner VD, and Nelson CM. Cellular and Physical Mechanisms of Branching Morphogenesis. *Development* (2014) 141:2750–9. doi:10.1242/dev.104794
52. Jiang Y, Pjesivac-Grbovic J, Cantrell C, and Freyer JP. A Multiscale Model for Avascular Tumor Growth. *Biophys J* (2005) 89:3884–94. doi:10.1529/biophysj.105.060640
53. Nath S, and Devi GR. Three-Dimensional Culture Systems in Cancer Research: Focus on Tumor Spheroid Model. *Pharmacol Ther* (2016) 163:94. doi:10.1016/j.pharmthera.2016.03.013
54. Wallace DI, and Guo X. Properties of Tumor Spheroid Growth Exhibited by Simple Mathematical Models. *Front Oncol* (2013) 3. doi:10.3389/fonc.2013.00051
55. Staneva R, Marjou FE, Barbazan J, Krndija D, Richon S, Clark AG, et al. Cancer Cells in the Tumor Core Exhibit Spatially Coordinated Migration Patterns. *J Cel Sci* (2019) 132. doi:10.1242/jcs.220277
56. Balkwill FR, Capasso M, and Hagemann T. The Tumor Microenvironment at a Glance. *J Cel Sci* (2012) 125:5591–6. doi:10.1242/jcs.116392
57. Mierke CT, Sauer F, Grosser S, Puder S, Fischer T, and Käs JA. The Two Faces of Enhanced Stroma: Stroma Acts as a Tumor Promoter and a Steric Obstacle. *NMR Biomed* (2018) 31:e3831. doi:10.1002/nbm.3831
58. Heine P, Lippoldt J, Reddy GA, Katira P, and Käs JA. Anomalous Cell Sorting Behavior in Mixed Monolayers Discloses Hidden System Complexities. *New J Phys* (2021) 23:043034. doi:10.1088/1367-2630/abf273
59. Elston CW, and Ellis IO. Pathological Prognostic Factors in Breast Cancer. I. The Value of Histological Grade in Breast Cancer: Experience from a Large Study with Long-Term Follow-Up. *Histopathology* (1991) 19:403–10.
60. Bazellières E, Conte V, Elosegui-Artola A, Serra-Picamal X, Bintanel-Morcillo M, Roca-Cusachs P, et al. Control of Cell-Cell Forces and Collective Cell Dynamics by the Intercellular Adhesome. *Nat Cel Biol* (2015) 17:409–20. doi:10.1038/ncb3135
61. Malinverno C, Corallino S, Giavazzi F, Bergert M, Li Q, Leoni M, et al. Endocytic Reawakening of Motility in Jammed Epithelia. *Nat Mater* (2017) 16:587–96. doi:10.1038/nmat4848
62. Merkel M, and Manning ML. A Geometrically Controlled Rigidity Transition in a Model for Confluent 3D Tissues. *New J Phys* (2018) 20:022002. doi:10.1088/1367-2630/aaaa13
63. Weigelin B, Bakker GJ, and Friedl P. Intravital Third Harmonic Generation Microscopy of Collective Melanoma Cell Invasion: Principles of Interface Guidance and Microvesicle Dynamics. *Intravital* (2012) 1:32–43. doi:10.4161/intv.21223
64. Thomas DG, Yenepalli A, Denais CM, Rape A, Beach JR, Wang Y, et al. Non-muscle Myosin IIB Is Critical for Nuclear Translocation during 3D Invasion. *J Cel Biol* (2015) 210:583. doi:10.1083/jcb.201502039
65. Dahl KN, Kahn SM, Wilson KL, and Discher DE. The Nuclear Envelope Lamina Network Has Elasticity and a Compressibility Limit Suggestive of a Molecular Shock Absorber. *J Cel Sci* (2004) 117:4779–86. doi:10.1242/jcs.01357
66. Gerlitz G, and Bustin M. The Role of Chromatin Structure in Cell Migration. *Trends Cel Biol* (2011) 21:6–11. doi:10.1016/j.tcb.2010.09.002
67. Chow KH, Factor RE, and Ullman KS. The Nuclear Envelope Environment and its Cancer Connections. *Nat Rev Cancer* (2012) 12:196–209. doi:10.1038/nrc3219
68. Harada T, Swift J, Irianto J, Shin JW, Spinler KR, Athirasala A, et al. Nuclear Lamin Stiffness Is a Barrier to 3D Migration, but Softness Can Limit Survival. *J Cel Biol* (2014) 204:669–82. doi:10.1083/jcb.201308029
69. Wolf K, Te Lindert M, Krause M, Alexander S, Te Riet J, Willis AL, et al. Physical Limits of Cell Migration: Control by ECM Space and Nuclear Deformation and Tuning by Proteolysis and Traction Force. *J Cel Biol* (2013) 201:1069–84. doi:10.1083/jcb.201210152
70. Davidson PM, Denais C, Bakshi MC, and Lammerding J. Nuclear Deformability Constitutes a Rate-Limiting Step during Cell Migration in 3-D Environments. *Cel. Mol Bioeng* (2014) 7:293–306. doi:10.1007/s12195-014-0342-y
71. Fu Y, Chin LK, Bourouina T, Liu AQ, and VanDongen AMJ. Nuclear Deformation during Breast Cancer Cell Transmigration. *Lab Chip* (2012) 12:3774–8. doi:10.1039/C2LC40477J
72. Lomakin AJ, Cattin CJ, Cuvelier D, Alraies Z, Molina M, Nader GPF, et al. The Nucleus Acts as a Ruler Tailoring Cell Responses to Spatial Constraints. *Science* (2020) 370:eaba2894. doi:10.1126/science.aba2894
73. Venturini V, Pezzano F, Català Castro F, Häkkinen HM, Jiménez-Delgado S, Colomer-Rosell M, et al. The Nucleus Measures Shape Changes for Cellular Proprioception to Control Dynamic Cell Behavior. *Science* (2020) 370:eaba2644. doi:10.1126/science.aba2644
74. Palamidessi A, Malinverno C, Frittoli E, Corallino S, Barbieri E, Sigismund S, et al. Unjamming Overcomes Kinetic and Proliferation Arrest in Terminally Differentiated Cells and Promotes Collective Motility of Carcinoma. *Nat Mater* (2019) 18:1252–63. doi:10.1038/s41563-019-0425-1
75. Giavazzi F, Paoluzzi M, Macchi M, Bi D, Scita G, Manning ML, et al. Flocking Transitions in Confluent Tissues. *Soft Matter* (2018) 14:3471–7. doi:10.1039/C8SM00126J
76. Serwane F, Mongera A, Rowghanian P, Kealhofer DA, Lucio AA, Hockenbery ZM, et al. *In Vivo* quantification of Spatially Varying Mechanical Properties in Developing Tissues. *Nat Methods* (2017) 14:181–6. doi:10.1038/nmeth.4101
77. Nnetu KD, Knorr M, Käs J, and Zink M. The Impact of Jamming on Boundaries of Collectively Moving Weak-Interacting Cells. *New J Phys* (2012) 14:115012. doi:10.1088/1367-2630/14/11/115012
78. Devany J, Sussman DM, Yamamoto T, Manning ML, and Gardel ML. Cell Cycle–dependent Active Stress Drives Epithelia Remodeling. *Proc Natl Acad Sci U.S.A* (2021) 118:e1917853118. doi:10.1073/pnas.1917853118
79. Fritsch A, Höckel M, Kiessling T, Nnetu KD, Wetzel F, Zink M, et al. Are Biomechanical Changes Necessary for Tumour Progression? *Nat Phys* (2010) 6:730–2. doi:10.1038/nphys1800
80. Tambe DT, and Fredberg JJ. And I hope You like Jamming Too. *New J Phys* (2015) 17:091001. doi:10.1088/1367-2630/17/9/091001
81. Kim JH, Pegoraro AF, Das A, Koehler SA, Ujwary SA, Lan B, et al. Unjamming and Collective Migration in MCF10A Breast Cancer Cell Lines. *Biochem Biophys Res Commun* (2020) 521:706–15. doi:10.1016/j.bbrc.2019.10.188
82. Etournay R, Popović M, Merkel M, Nandi A, Blasse C, Aigouy B, et al. *Interplay of Cell Dynamics and Epithelial Tension during Morphogenesis of the Drosophila Pupal wing*. Cambridge, United Kingdom: eLife Sciences Publications, Ltd (2015). doi:10.7554/eLife.07090
83. Friedl P, and Mayor R. Tuning Collective Cell Migration by Cell–Cell Junction Regulation. *Cold Spring Harbor Perspect Biol* (2017) 9. doi:10.1101/cshperspect.a029199
84. Kuan HS, Blackwell R, Hough LE, Glaser MA, and Betterton MD. Hysteresis, Reentrance, and Glassy Dynamics in Systems of Self-Propelled Rods. *Phys Rev E* (2015) 92:060501. doi:10.1103/PhysRevE.92.060501
85. Mongera A, Michaut A, Guillot C, Xiong F, and Pourquié O. Mechanics of Anteroposterior Axis Formation in Vertebrates. *Annu Rev Cel Dev Biol* (2019) 35:259–83. doi:10.1146/annurev-cellbio-100818-125436
86. Pillarisetti A, Desai JP, Ladjal H, Schiffmacher A, Ferreira A, and Keefer CL. Mechanical Phenotyping of Mouse Embryonic Stem Cells: Increase in Stiffness with Differentiation. *Cell. Reprogramming* (2011) 13:371–80. doi:10.1089/cell.2011.0028

87. Höckel M, and Behn U. The Order of Cancer: A Theory of Malignant Progression by Inverse Morphogenesis. *Front Oncol* (2019) 9. doi:10.3389/fonc.2019.00416
88. Kubitschke H, Wolf B, Morawetz E, Horn LC, Aktas B, Behn U, et al. Roadmap to Local Tumour Growth: Insights from Cervical Cancer. *Scientific Rep* 9 (2019) 1–14. doi:10.1038/s41598-019-49182-1
89. Seltmann K, Fritsch AW, Käs JA, and Magin TM. Keratins Significantly Contribute to Cell Stiffness and Impact Invasive Behavior. *Proc Natl Acad Sci U.S.A* (2013) 110:18507–12. doi:10.1073/pnas.1310493110
90. Siegel PM, and Massagué J. Cytostatic and Apoptotic Actions of TGF-β in Homeostasis and Cancer. *Nat Rev Cancer* (2003) 3:807–20. doi:10.1038/nrc1208
91. Höckel M. Morphogenetic fields of Embryonic Development in Locoregional Cancer Spread. *Lancet Oncol* (2015) 16:148–51. doi:10.1016/S1470-2045(14)71028-9
92. Merkel M, Baumgarten K, Tighe BP, and Manning ML. A Minimal-Length Approach Unifies Rigidity in Underconstrained Materials. *Proc Natl Acad Sci U.S.A* (2019) 116:6560–8. doi:10.1073/pnas.1815436116
93. Petridou NI, Corominas-Murtra B, Heisenberg CP, and Hannezo E. Rigidity Percolation Uncovers a Structural Basis for Embryonic Tissue Phase Transitions. *Cell* (2021) 184:1914–28.e19. doi:10.1016/j.cell.2021.02.017
94. Doss BL, Pan M, Gupta M, Grenci G, Mège RM, Lim CT, et al. Cell Response to Substrate Rigidity Is Regulated by Active and Passive Cytoskeletal Stress. *Proc Natl Acad Sci U.S.A* (2020) 117:12817–25. doi:10.1073/pnas.1917555117
95. Gupta M, Doss B, Lim CT, Voituriez R, and Ladoux B. Single Cell Rigidity Sensing: A Complex Relationship between Focal Adhesion Dynamics and Large-Scale Actin Cytoskeleton Remodeling. *Cell Adhes Migration* (2016) 10:554–67. doi:10.1080/19336918.2016.1173800
96. Kamkin A, and Kiseleva I. *Mechanosensitivity In Cells And Tissues*. Gent, Belgium: Academia (2005).

Conflict of Interest: The authors declare that the research was conducted in the absence of any commercial or financial relationships that could be construed as a potential conflict of interest.

Publisher's Note: All claims expressed in this article are solely those of the authors and do not necessarily represent those of their affiliated organizations, or those of the publisher, the editors and the reviewers. Any product that may be evaluated in this article, or claim that may be made by its manufacturer, is not guaranteed or endorsed by the publisher.

frontiers in Physics

ORIGINAL RESEARCH
published: 23 August 2021
doi: 10.3389/fphy.2021.711860

Oscillatory Microrheology, Creep Compliance and Stress Relaxation of Biological Cells Reveal Strong Correlations as Probed by Atomic Force Microscopy

D.A.D. Flormann[1], C. Anton[1], M.O. Pohland[1], Y. Bautz[1], K. Kaub[1,2], E. Terriac[3], T.E. Schäffer[4], J. Rheinlaender[4], A. Janshoff[2], A. Ott[1†] and F. Lautenschläger[1*†]*

[1]Center for Biophysics, Saarland University, Saarbruecken, Germany, [2]Institute of Physical Chemistry, University of Goettingen, Göttingen, Germany, [3]Leibniz Institute for New Materials, Saarbruecken, Germany, [4]Institute of Applied Physics, Eberhard-Karls University Tübingen, Tübingen, Germany

OPEN ACCESS

Edited by:
Ivana Dusan Pajic-Lijakovic,
University of Belgrade, Serbia

Reviewed by:
Bruno Goud,
Centre National de la Recherche Scientifique (CNRS), France
Alfred Nguyen,
University of Münster, Germany

***Correspondence:**
A. Ott
albrecht.ott@physik.uni-saarland.de
F. Lautenschläger
f.lautenschlaeger@physik.uni-saarland.de

[†]These authors have contributed equally to this work

Specialty section:
This article was submitted to Biophysics, a section of the journal Frontiers in Physics

Received: 19 May 2021
Accepted: 09 August 2021
Published: 23 August 2021

Citation:
Flormann DAD, Anton C, Pohland MO, Bautz Y, Kaub K, Terriac E, Schäffer TE, Rheinlaender J, Janshoff A, Ott A and Lautenschläger F (2021) Oscillatory Microrheology, Creep Compliance and Stress Relaxation of Biological Cells Reveal Strong Correlations as Probed by Atomic Force Microscopy. Front. Phys. 9:711860. doi: 10.3389/fphy.2021.711860

The mechanical properties of cells are important for many biological processes, including wound healing, cancers, and embryogenesis. Currently, our understanding of cell mechanical properties remains incomplete. Different techniques have been used to probe different aspects of the mechanical properties of cells, among them microplate rheology, optical tweezers, micropipette aspiration, and magnetic twisting cytometry. These techniques have given rise to different theoretical descriptions, reaching from simple Kelvin-Voigt or Maxwell models to fractional such as power law models, and their combinations. Atomic force microscopy (AFM) is a flexible technique that enables global and local probing of adherent cells. Here, using an AFM, we indented single retinal pigmented epithelium cells adhering to the bottom of a culture dish. The indentation was performed at two locations: above the nucleus, and towards the periphery of the cell. We applied creep compliance, stress relaxation, and oscillatory rheological tests to wild type and drug modified cells. Considering known fractional and semi-fractional descriptions, we found the extracted parameters to correlate. Moreover, the Young's modulus as obtained from the initial indentation strongly correlated with all of the parameters from the applied power-law descriptions. Our study shows that the results from different rheological tests are directly comparable. This can be used in the future, for example, to reduce the number of measurements in planned experiments. Apparently, under these experimental conditions, the cells possess a limited number of degrees of freedom as their rheological properties change.

Keywords: cell mechanics, atomic force microscopy, cell rheology, power-law, microrheology, creep compliance, stress relaxation

INTRODUCTION

The mechanical properties of cells are of great importance in a wide diversity of biological phenomena, which include cell migration [1, 2], cell differentiation [3], cell division [4], embryogenesis, and cancers [5, 6]. To investigate cell mechanics [7], a broad range of techniques have been established. Examples here are seen with beads moved by optical tweezers [8, 9], magnetic twisting cytometry [10, 11], microplate viscometry [12], cell monolayer shearing, and atomic force microscopy (AFM) [13–21]. Comparisons across techniques have revealed strong quantitative differences, even when the same parameter has been probed for the same cell type [22]. Differences in the mechanical state of the cells might be involved here. Such differences can be caused by biochemical signaling; for instance, through specific adhesion to a substrate [19, 21]. Moreover, cells actively react to deformation, which means that their mechanical properties are history dependent [23]. Probing on different time and length scales might result in large differences in cell responses that are accompanied by different mechanical properties. Cell deformation at small scales follows a linear description [46]. In this regime, the validity of a power-law description was found to hold for many different cell types [24]. Large-scale deformation requires a more sophisticated description, taking into account non-linear and history-dependent properties [23]. Accordingly, small-scale cell deformation cannot simply be integrated to obtain the response at larger scales [25].

Here, we used AFM to characterize the viscoelastic properties of living cells in a liquid environment and at physiological temperatures [26]. Depending on the shape of the cantilever used to establish the mechanical contact with the cells, AFM can be used to probe the viscoelastic properties globally [27] or locally [28]. The Hertz-Sneddon model [29] is most commonly used to extract quantitative elastic material properties from AFM measurements. However, this model assumes purely elastic materials, while cells exhibit viscoelastic properties [14, 18–21, 30]. Creep compliance [14, 31], stress relaxation [20, 32], and oscillatory microrheology [17, 18] are standard rheological tests that can been applied with AFM, thereby giving information about both the elastic and the viscous properties of the cells.

Here, we asked whether the tests performed are interdependent, such that the main parameters from these different tests are correlated. For this study, we applied well-known pharmacological agents to alter the cellular cortex, and potentially thereby also altering the mechanical properties of the cells. These drugs have been extensively characterized in other studies. Here, we were not interested in the precise working actions or properties of these drugs; rather, we used them to alter the mechanical properties of the cells to determine whether these changes are reflected by the different rheological tests in ways that are related and that can be understood. In our local probing experiments, we identified correlations and further interrelations between the parameters obtained.

RESULTS

In this study, all of the probing was performed either at the cell nucleus or at the perinucleus. We took the perinucleus as the region between the border of the nucleus and the periphery of the cell (see **Figure 1A** for details). At each location, we performed the different rheological methods, as schematically shown in **Figure 2A**.

From analysis of the force-indentation data during the cantilever approach, the Young's modulus E was determined using the Hertz-Sneddon model (see **Supplementary Figure S1** for an example curve).

In oscillatory microrheology, the complex modulus of the cell (**Figure 2B**, left panel) can be described by a power-law structural damping material model [17, 33, 34]:

$$G^* = G_0\left(1 + i\,tan\left(\alpha\frac{\pi}{2}\right)\right)\left(\frac{f}{f_0}\right)^{\alpha} + i\mu f \tag{1}$$

where G_0 is the shear modulus scaling factor, α is the power-law exponent, which describes the fluidity of the sample, and μ is the (linear) viscosity [18]. f_0 is a frequency scaling factor, assumed to be $f_0 = 1$ Hz. The viscosity related term is known to describe the higher frequency behavior. To demonstrate that the lower frequency range can be described by a single power law, we fitted **Equation 1** without the viscosity term to the data f = 1–10 Hz (**Figure 2B**, dashed curves), yielding $G_0 = 620 \pm 40$ Pa and $\alpha = 0.14 \pm 0.02$. This agrees with the fit including the viscous term ($G_0 = 580 \pm 60$ Pa, $\alpha = 0.17 \pm 0.02$, $\mu = 1.4 \pm 0.1$). We used the model including the viscosity term for the oscillatory microrheology analysis, but a single power law for the two time-domain related methods as described in the following.

We describe the creep compliance of the cell (**Figure 2B**, 2nd left panel) as:

$$J(t) = \frac{1}{E_0}\left(\frac{t}{t_0}\right)^{\beta}, \tag{2}$$

where E_0 is the modulus scaling parameter, which is a measure of the stiffness of the material and equivalent to the apparent Young's modulus of the material at time t_0, which is usually set to $t_0 = 1$ s. The power-law exponent β is a measure of the fluidity of the material, where β ranges from 0 for a purely elastic solid to one for a purely viscous fluid.

We describe the stress relaxation response of the cell (**Figure 2B**, 3rd left panel) by modelling as a thin contractile shell according to:

$$\widetilde{K}_A = K_A\left(\frac{t}{t_0}\right)^{-\gamma}, \tag{3}$$

where K_A is the area compressibility modulus, and γ is the fluidity. The time scaling parameter t_0 is set to $t_0 = 1$ s. However, since a single power law was not sufficient for accurately describing the stress relaxation here (see **Supplementary Figure S2**), we included the cortical tension T_0 as an additional parameter (see *Methods* for details).

More information on the formalism and the extraction of the numerical values from the experiments is included in the Methods section.

Cytoskeletal Perturbation Using Drugs

Here, we only refer to the results from the nuclear region of the cell (**Figures 3A,B**), as the results from probing within the perinuclear regions were similar (**Figures 3C,D**).

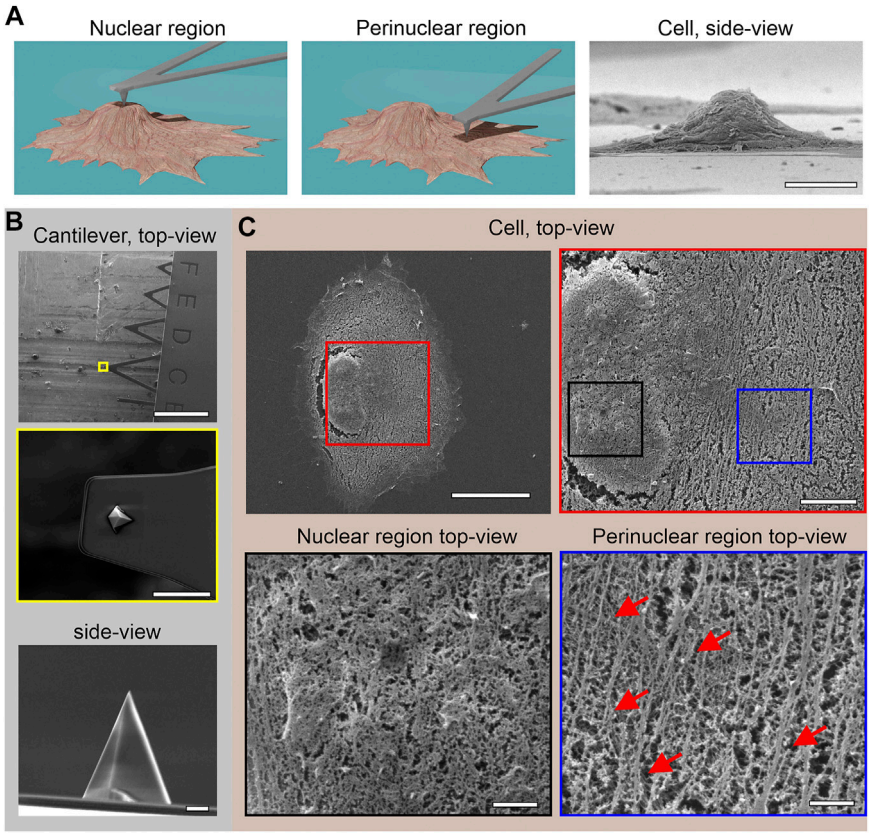

FIGURE 1 | Scanning electron microscopy images. **(A)** Schemes of AFM cantilever positioning at the nuclear **(left)** and perinuclear **(middle)** cell regions, showing also a side-view of a hTERT-RPE1 cell after membrane removal **(right)**. **(B)** Representative images of the AFM cantilever **(top)** and the indenter **(middle, bottom)**. **(C)** A representative hTERT-RPE1 cell after membrane removal at different magnifications (color-coded frames highlight the magnified regions). Arrows, exemplary actin bundles. Scale bars: **(A)**: 10 µm; **(B)** top to bottom: 300 µm, 10 µm, 1 µm; **(C)**: 20 µm **(top left)**, 5 µm **(top right)**, 1 µm (bottom left, black frame), 1 µm (bottom right, blue frame).

The inhibition of nonmuscle myosin II (NM II) using blebbistatin is expected to decrease the pre-stress of the cellular cortex [35]. Here, the addition of blebbistatin had no significant influence (**Figure 3A**), with the exception of an increase in viscosity μ (**Figure 4**). Calyculin A is reported to increase the NM II activity *via* inhibition of PP1 and PP2A [36]. Compared to untreated cells (control), calyculin A resulted in a significant increase in the scaling factor G_0, and a decrease in the power-law exponents α and β (**Figure 3B**). Treatment of the cells with Y-27632 is reported to inhibit Rho-associated protein kinase (ROCK), with downstream effects on cofilin activity, for example [37]. Here, Y-27632 resulted in a decrease in the Young's modulus E, and in the cell viscosity μ, and G_0 and E_0. All of the power-law exponents (i.e., the fluidities) appear to be increased by Y-27632 (**Figure 3B**). According to the literature, CK-666 inhibits the Arp2/3 complex [38], and its application here resulted in a decrease in E_0 and μ (**Figure 3B**). Smifh2 inhibits formin *via* the FH2 domain [39], and it showed very similar effects to CK-666 here; however, in addition, Smifh2 resulted in an increase in β and a decrease in G_0 (**Figure 3B**). Finally, treatment with the actin polymerization inhibitor latrunculin A [40] resulted in an increase in the power-law exponents α and β, while the parameters G_0, E_0, μ, and E decrease concomitantly (**Figure 3B**).

Active Responses of Cells Upon External Mechanical Stimuli

Cells are not just viscoelastic objects, they are viscoelastic objects that can actively respond to external mechanical stimuli [41]. Depending on the cytoskeletal alterations performed, active responses were obtained for 10–50% of the cells (**Figure 3B**, right column), which developed forces ΔF of up to a mean of 200 pN; these were reached within a time interval Δt of 8 s on average (**Supplementary Figures S3B, D**). Typically, the active response (if any) started after a few seconds of force relaxation, and continued until the end of the measurement (after 15 s), as would be expected [42]. Perturbation using various drugs reduced the maximum force per unit time ($\Delta F/\Delta t$) compared to the control (while the majority of cells, as 50–90%, show no active responses; see **Figures 3B,D**). Moreover, drug perturbations enabled cells to reach their maximum active force faster than for the control if they were probed at the

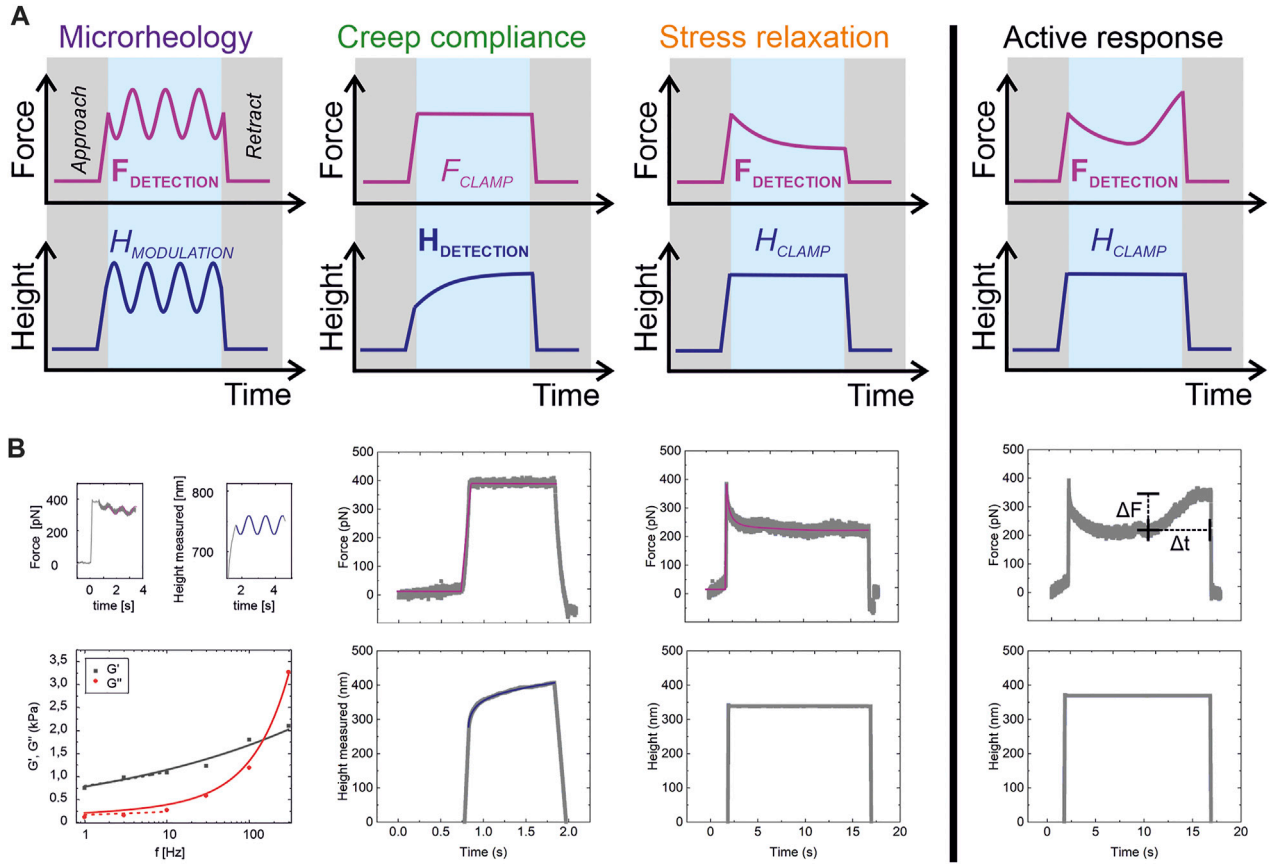

FIGURE 2 | Methods and raw data. **(A)** Overview of the rheological test protocols used in this study, where either force or cell height are imposed, and the other parameters are measured. **(B)** Raw data from the tests in **(A)**. Fits of **Eqs 1**, **6**, **7**, and **10** to data are in color; force (magenta), height (blue). G′ over full frequency range: black line, G′ over 1–10 Hz (approximated with single power law): dashed black line. G″ over full frequency range: red line. G″ over 1–10 Hz (approximated with single power law): dashed red line.

nucleus; however, this was slower than the control if probed at the perinucleus (compare Δt in **Supplementary Figures S3B, D**). This difference can be attributed to the higher cortical tension within the perinucleus that is induced by actin bundles, which were observed for all of the drug treatments (**Figure 1C**). Potentially, these bundles are a reason for the lower active response forces of the perinucleus compared to the nucleus (**Supplementary Figures S3B, D**).

Parameters From Power-Law Descriptions of the Different Rheological Tests Strongly Correlate

As the individual cells presented a large spread in their parameters, we examined the drug-induced changes as illustrated in **Figures 5A–C**. Here, G_0, E_0, and T_0 correlated positively with the Young's modulus E. The power law exponents (i.e., the so-called fluidities α, β, γ) of all of the tests correlated positively (**Figures 5D,E**), as did the scaling factors E_0, K_A, and G_0. The scaling factors and fluidities were inversely correlated, as has been reported previously [20, 43]. T_0, E, and μ correlated positively to the scaling factors (and inversely to the exponents α, β, γ), as shown in **Figures 5D,E**, which suggested universal scaling laws for living cells. **Figure 5G** underlines the correlation of the scaling factors (stiffnesses) and exponents (fluidities) of all three tests in a three dimensional plot.

Parameters are Conserved Over Cell Regions

Statistically, it is likely that correlations will be found even if the parameter set considered is random. To rule out such effects, we repeated the experiments at the perinucleus (i.e., the region between the nucleus and the cell periphery). Almost all of the parameters of creep, stress relaxation, and oscillatory microrheology showed similar results, and we observed the same correlations (**Figures 5D,E**). As the probing of the nucleus and the probing of the perinucleus are independent of each other, we can conclude that the correlations presented are statistically sustainable, as represented by the multiplication of the nuclear and perinuclear Pearson R values (**Figure 5F**). However, the perinuclear region did lead to larger scaling factors for all of the tests (compare **Figures 3B,D**).

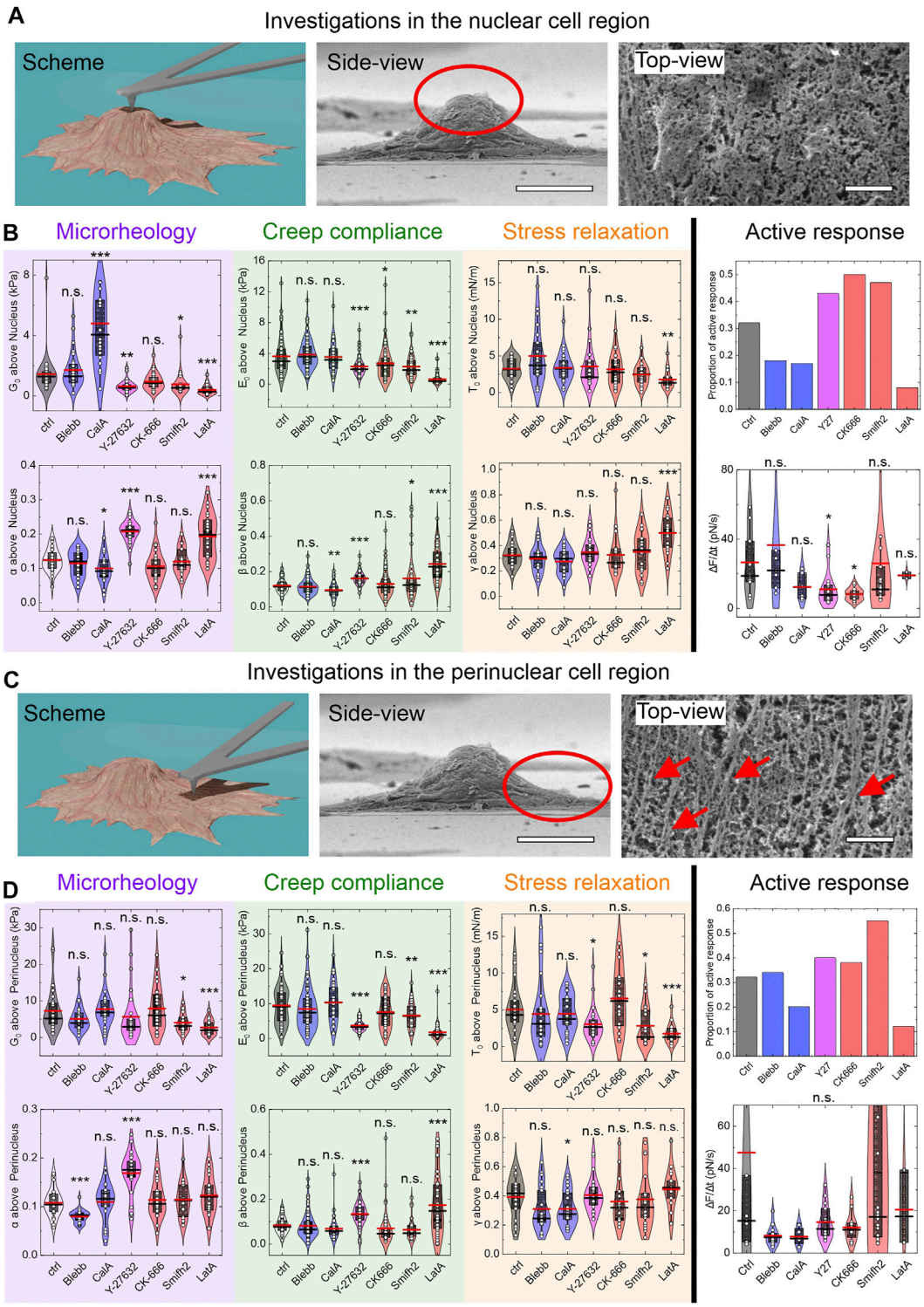

FIGURE 3 | Selected parameters obtained from rheological tests. **(A)** Position of the cantilever. **(B)** Data for control and applied drugs for G_0 and α from microrheology; E_0 and β from the creep compliance; T_0 and γ from stress relaxation and the proportion of cells actively responding during stress relaxation; $\Delta F/\Delta t$ for the active response. **(C, D)** Same as in **(A)** and **(B)**, except for the cantilever positioned at the perinucleus. Arrows, exemplary actin bundles. n. s., $p > 0.05$; *, $p < 0.05$; **, $p < 0.01$; ***, $p < 0.001$ vs. untreated cells (ctrl) (Student's t-tests). Scale bars **(A, C)**: 20 µm (middle images), 1 µm (right images). Cell numbers N apply to all parameters tested by the particular protocol (including **Figure 4** and **Supplementary Figure S3**). Cell numbers N are in the following order: Ctrl, Blebb, CalA, Y-27632, CK-666, Smifh2, LatA. Microrheology **(B)**: N = 28, 28, 20, 29, 29, 24, 26; Microrheology **(D)**: N = 27, 29, 26, 27, 24, 19, 22; Creep compliance **(B)**: N = 53, 86, 38, 51, 63, 45, 40; Creep compliance **(D)**: N = 52, 73, 34, 49, 47, 31, 43; Stress relaxation **(B)**: N = 26, 21, 28, 23, 19, 20, 17; Stress relaxation **(D)**: N = 22, 22, 26, 24, 15, 21, 17; Active response **(B)** for $\Delta F/\Delta t$: N = 9, 7, 7, 16, 16, 18, 2; Active response **(D)** for $\Delta F/\Delta t$: N = 9, 13, 8, 15, 12, 20, 3. The total numbers of cells analyzed for active responses were the same as for stress relaxation.

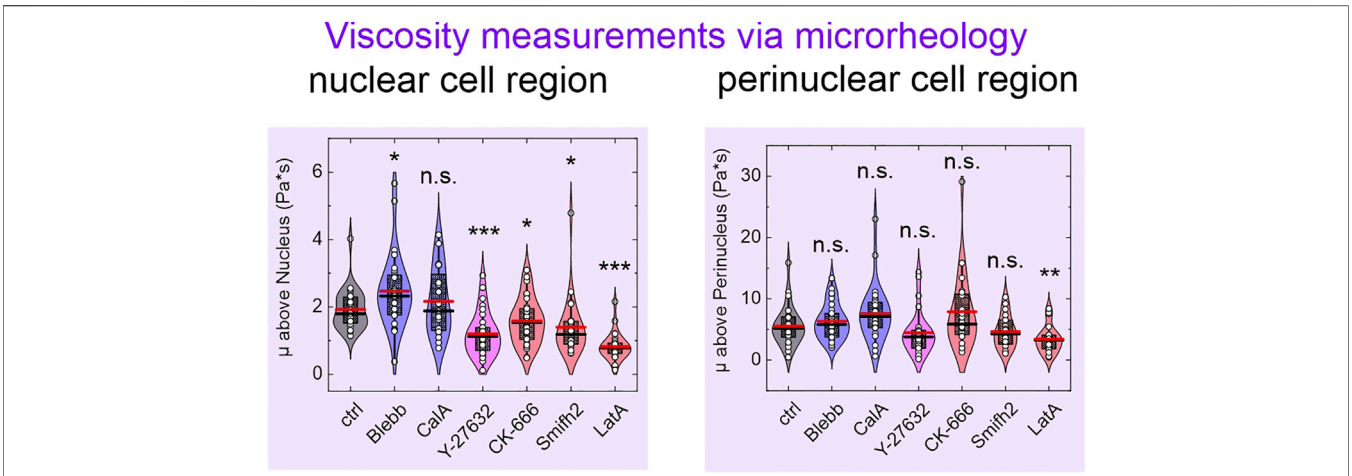

FIGURE 4 | Viscosity μ as an additional parameter obtained from oscillatory microrheology tests at the nucleus and at the perinuclear region.

DISCUSSION

The exponents α, β, and γ from the power-law descriptions above are known as the fluidities, and they were clearly correlated (**Figure 5**). The scaling parameters, E_0, K_A, and G_0 were also correlated. The scaling parameters and fluidities were inversely correlated. This agrees well with earlier studies (see **Supplementary Tables S1–S4**), where the inverse behaviors of the scaling parameters and fluidities have been observed for each test protocol independently [14, 18, 20]. Both creep and stress relaxation are linked to the viscous properties of the cell. At the same time, under the assumption of a linear viscoelastic material and a Poisson ratio of 0.5 that is time or frequency independent (both are usually assumed), the scaling parameters E_0 and $3G_0$ should be identical [33]. This appears to be the case at the nucleus (**Supplementary Figure S4**), but not for the perinucleus. We hypothesize that this is due to the higher cortex tension within the perinucleus [44], which can lead to nonlinear material behavior [43, 45, 46], plasticity [47], or different memory effects in oscillatory microrheology when compared to creep compliance.

We see that the viscosity parameter μ correlated with the above parameters. However, the cortical tension T_0 and the Young's modulus also correlated with the fluidities (and stiffnesses). This might appear surprising, as a viscosity is a-priori independent of a stiffness; however, we have already shown that only very small deformations (i.e., of the order of 10 nm) lead to deformation size independent, "real" elasticities [25, 46]. Although large-scale deformations show in-phase, linear force-deformation relations as expected for a purely elastic body, they must be suspected of being pseudoelastic; i.e., to include a restructuring component [34, 48]. Therefore, if only a single parameter was to be used to follow cell mechanics, it would indeed appear to be justified to use the Hertz-Sneddon model, which considers elastic properties only [49–51].

For the drug-based perturbations, some of the rheological tests were more affected than others (**Figure 3**). In stress relaxation tests, only latrunculin A had significant effects on γ and T_0 (but not on K_A) (**Figure 5**; **Supplementary Figure S3**). The absence of detectable differences upon treatment with the other drugs might appear to contradict reports by others [18, 20]. We hypothesize that the statistically weaker significance of the changes in stress relaxation upon drug treatment as compared to creep and oscillatory microrheology are due to the initial approach at the relatively higher velocity (5 μm/s). Stress relaxation analysis yields different results if a cell is approached at a velocity of 0.5 μm/s [20]. Although, the differences that appear between drug-treated cells and the controls are often too small to be statistically significant, they were again consistently correlated, following a similar pattern to that discussed above. Notably, only for stress relaxation a material model with additional constant term had to be used, which is probably due to the fact that entirely different assumptions are made here (cortical shell model) as compared to the other two methods (viscoelastic half space).

For the oscillatory microrheology, the situation was different from the other two rheological tests. Oscillatory microrheology fixes the timescale of the perturbation according to the applied frequency, while the other tests probe a superposition on many timescales in a single test. This has the advantage that the frequency-dependency of the material response can be measured directly and that the measurement frequency can be adopted to the frequency range of interest [52]. However, time- and frequency-domain data are mathematical equivalents and time-domain data of the cells viscoelastic response can even be directly transformed into the frequency domain [53].

Investigation of the perinuclear region led to larger stiffness-related parameters than at the nuclear region. We hypothesize that this is a result of actin bundles under high tension within the perinucleus, as depicted in **Figure 1** (perinucleus top-view, red arrowheads). This is well reflected by the increased (approximately by a factor of 2) cortical tensions T_0 from nucleus (**Figure 3B**) to perinucleus (**Figure 3D**). Another explanation might be the presence of the substrate, as suggested in the studies by Garcia [54, 55], or local strain stiffening of cytoskeleton as proposed recently [56–58].

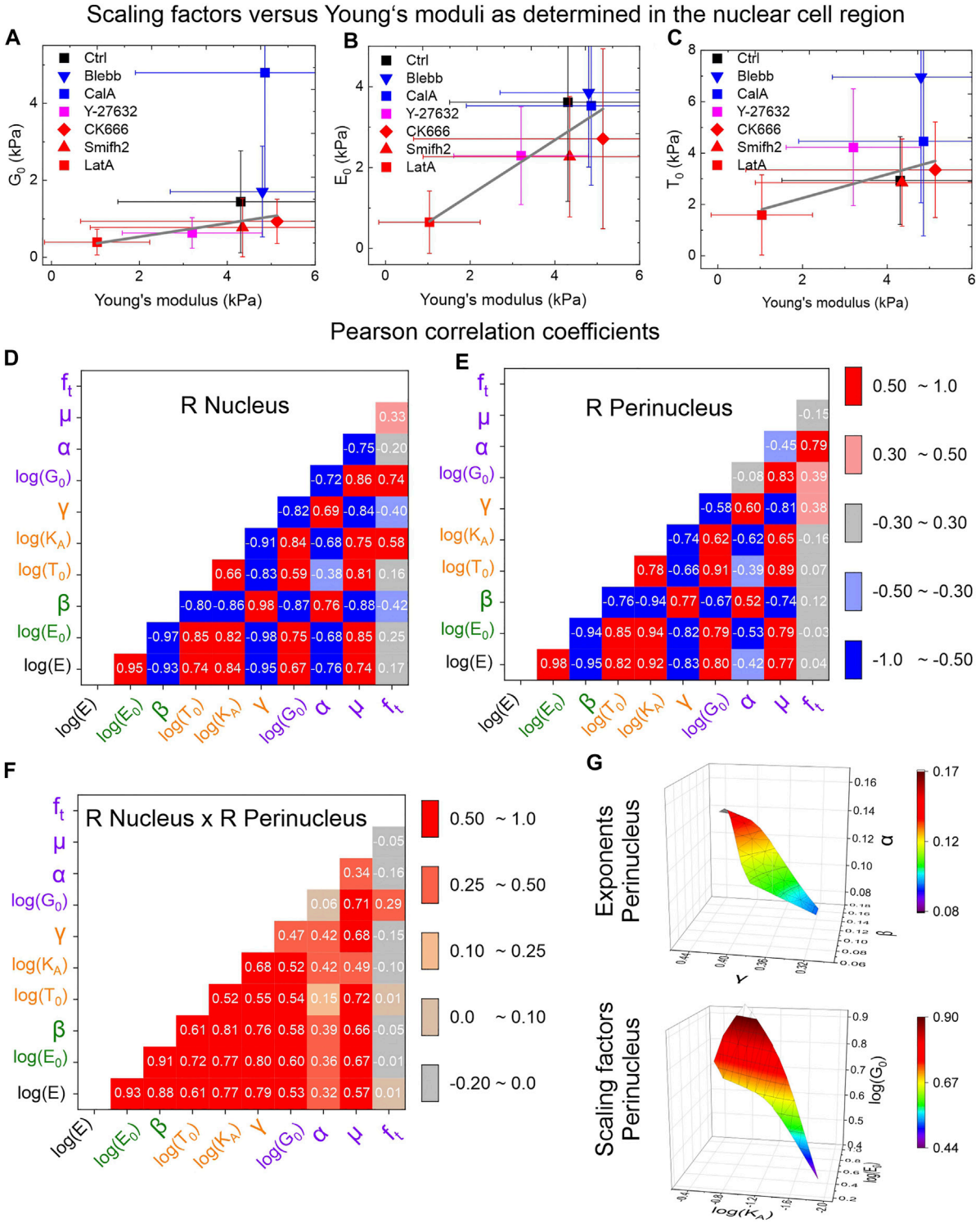

FIGURE 5 | Correlations among all of parameters extracted from the different rheological tests. **(A–C)** Correlation of the Young's modulus to G_0, E_0 and T_0, as determined within the nuclear region of hTERT RPE1-cells; error bars represent standard deviations. Cell numbers N are in the following order: Ctrl, Blebb, CalA, Y-27632, CK-666, Smifh2, LatA: **(A)** N = 81, 114, 58, 80, 92, 69, 66; **(B)** N = 106, 172, 76, 102, 126, 90, 80; **(C)** N = 75, 108, 64, 75, 78, 66, 57. **(D, E)** Correlations among all of the accessible parameters of all of the three rheological tests, as well as the Young's modulus as determined within the nuclear and perinuclear region. **(F)** Multiplication of Pearson R coefficients of each respective pair belonging to nucleus and perinucleus. **(G)** Three dimensional correlations between the scaling factors ("stiffnesses") and exponents ("fluidity") of creep compliance (E_0, β), stress relaxation (K_A, γ) and microrheology (G_0, α); representation of the z-axis corresponds to the color code. Cell numbers N for correlations are based on seven data points each (see **A–C**). Therefore indirectly, each Pearson correlation coefficient between tests in **(D)** and **(E)** is based on typically N = 500–750 single cells (addition of cell numbers for the seven (drug) conditions for two tests).

In conclusion, although different viscoelastic parameters are determined in different rheological tests, these parameters are far from independent. This suggests that cells regulate their mechanical parameters in a way that stiffening cells become less fluid at the same time.

Summary

Here, we show that the investigational methods of stress relaxation, creep compliance, and oscillatory microrheology are interdependent, since the parameter sets used for the description are clearly correlated. We analyzed the force-indentation during the initial approach to cells by Hertz-Sneddon contact mechanics [50, 59]. Although this purely elastic approach neglects viscous properties a priori, it produces a useful description. The Young's modulus of cells is the most commonly determined mechanical parameter in AFM studies. We probed this parameter at a different approach velocity, so that viscous relaxation does not occur during the approach. We do not claim to universally explain the connections between these different rheological tests. A full study would require much more data, which is unfortunately beyond our reach to date, given the combinatorial explosion of multivariate experiments. However, we have shown that the different deformation patterns that were applied using these different methodologies are related, which indicates that the underlying connections here need to be investigated further to be fully understood.

MATERIALS AND METHODS

Cell Culture

All of the experiments were performed with retinal pigmented epithelium cells (hTERT-RPE-1; ATCC, Manassas, VA, United States). The cell culture medium was DMEM/F12 with 1% Glutamax, 1% Pen/Strep and 10% fetal bovine serum (Thermo Fisher Scientific, Waltham, MA, United States). The cells were incubated in cell culture flasks (Cellstar, Greiner Bio-One, Kremsmünster, Austria) at 37°C and 5% CO_2. Before each measurement, low numbers of cells were plated in Petri dishes (FluoroDish, World Precision Instruments, Sarasota, FL, United States), which were incubated overnight at 37°C and 5% CO_2. The cell medium was then replaced with fresh medium with 25 mM Hepes (Sigma-Aldrich, St. Louis, MO, United States). If a pharmacological agent was added, the cells were incubated at 37°C in air for 30 min, or for 10 min for latrunculin A.

Cellular Regions

We investigated two cellular regions within the adhered hTERT-RPE1 cells: the nuclear and perinuclear regions (**Figure 1A**). We defined the nuclear region as the cellular region where the nucleus was identified by brightfield illumination, using the microscopy system specified below. We defined the perinuclear region as the region between the edge of the nucleus and the cell periphery. AFM experiments were always performed within the middle of the two-dimensional projections of those regions, rather than on the edges. As the indentations were less than 10% of the cell height (which corresponds to absolute values in the range of several 100 nm; data not shown), we expected to probe predominantly the viscoelastic properties of the cellular cortex, rather than the nucleus itself, or the substrate the cells were adhered to (35-mm glass bottomed FluorDishes, Ibidi, Germany).

Pharmacological Perturbations

In this study, hTERT-RPE-1 cells were treated with a range of inhibitory drugs. Blebbistatin (20 μM; para-nitroblebbistatin; Optopharma Ltd., Hungary) inhibits nonmuscle myosin II (NM II) [35]. Calyculin A (1 nM; Cayman Chemical, MI, United States) increases cell contractility by increasing NM II activity [36]. Y-27632 (10 μM; Biomol GmbH, Germany) inhibits Rho-associated protein kinase (ROCK), which among other effects, lead to an indirect inhibition of NM II and activation of phospho-cofilin *via* LIMK [37]. CK-666 (100 μM; Abcam, UK) inhibits the actin nucleator Arp 2/3 that is also involved in crosslinking of actin filaments [38]. Smifh2 (10 μM; Sigma-Aldrich, Germany) inhibits the stabilization of actin filaments *via* the formins [39]. Latrunculin A (0.1 μM; Sigma Aldrich, Germany) inhibits polymerization of filamentous actin [40].

AFM: Setup and Measurements

All of the AFM measurements were performed using an atomic force microscope (Nanowizard 3; Bruker, Berlin, Germany) mounted on an optical microscope (Eclipse Ti-U, Nikon, Minato, Tokyo, Japan) and equipped with a PlanFluor 40x/0.6 Ph2 objective (Nikon). The system used lever C of a MLCT cantilever (Bruker, Billerica, MA, United States) with a nominal spring constant of 0.01 N/m, and a four-sided pyramidal tip with half-opening angle of $\theta = 18.75°$ (axis to face) and a nominal tip radius of 20 nm (see **Figure 1B**). A Petri dish heater (Bruker, Berlin, Germany) was used to keep the samples at 37°C during all of the measurements. A built-in camera (ProgRes MFcool, Jenoptik, Jena, Germany) and a motorized precision stage (Bruker, Berlin, Germany) were used to identify single adhered cells. The cantilevers were calibrated using the thermal noise method [60]. Calibration and measurements were controlled with the SPM software (Bruker, Berlin, Germany). At the beginning of each measurement, the cantilever approached the samples with a velocity of 5 μm/s, until a setpoint force of 400 pN was reached. For oscillatory microrheology only, the setpoint force was readjusted after each frequency step. The low approach velocity of 5 μm/s was chosen to avoid the effects of hydrodynamic drag on the cantilever (data not shown). The measured force F was calculated from the measured cantilever deflection d as $F = k^*d$ with spring constant k. The indentation δ was determined from the vertical cantilever position z as $\delta = z—d$ and was set to zero at the contact point. As the approach velocity of the cantilever to the cell might have a significant effect on the outcome of measurements, we chose a fixed approach velocity to keep any possible influence of the approach velocity constant. We stopped as soon as the setpoint force or height was reached to perform either creep, stress relaxation, or oscillatory microrheology tests on these hTERT-RPE1 cells. As these tests probe mainly on much longer timescales than the initial

indentation, they are probably independent of the initial approach, but mainly sensitive to the cell viscoelastic response. That elastic, viscous, and active cell responses have different time scales was shown earlier [12].

To analyze the AFM data, various models are available. A good overview can be found in [61]. The models we used for the data analysis are detailed in the following section.

Young's Modulus

The Young's modulus was analyzed using the Hertz-Sneddon model for four-sided pyramidal indenters, which was described in detail by Bilodeau and co-workers [62]. Here, the force is defined as in **Eq. 4**:

$$F(\delta) = \frac{3}{4}\frac{E}{1-\nu^2}\tan\theta \cdot \delta^2, \tag{4}$$

where E is the Young's modulus, ν is the Poisson's ratio, θ is the half-opening angle of the indenter (axis to face), and δ is the indentation. The Poisson's ratio was taken as $\nu = 0.5$ here, and in all other methods [63–65]. As all of the AFM approach settings were identical for all of the experiments, we could have used any of the approach curves to obtain the Young's modulus. We decided to use the approach curve of the creep compliance for this purpose.

Oscillatory Microrheology

During the AFM oscillatory microrheology measures, the oscillation frequency of the cantilever was varied. In contrast to both of the methods above, oscillatory microrheology determines the glassy transition frequency of cells. By indenting a cell with a cantilever and applying a sinusoidal excitation signal to the Piezo motors, in-phase and an out-of-phase deflection signals of the cantilever are detected [17, 18], which are used to determine the complex shear modulus, as:

$$G^*(\omega) = G'(\omega) + iG''(\omega) = \frac{1-\nu}{3\delta_0 \cdot \tan(\theta)}\frac{F(\omega)}{\delta(\omega)} \tag{5}$$

where G' is the storage modulus, G'' is the loss modulus, i is the complex unit, ω is the angular frequency, ν is the Poisson's ratio (assumed to be 0.5), δ_0 is the initial indentation, and θ is the half opening angle of the indenter. $F(\omega)$ and $\delta(\omega)$ are the Fourier transforms of the force F and the indentation δ. **Eq. 5** can be derived from Hertz-Sneddon contact mechanics for a four-sided pyramidal indenter, as proposed by Alcaraz et al. [17] and corrected by the hydrodynamic drag coefficient, measured as proposed in [16].

In these measurements, the cantilever was oscillated with an amplitude of 15 nm. The frequency was varied from 1 to 300 Hz in five approximately logarithmic steps (as 1, 3, 10, 30, 100, 300 Hz). Before each modulation, the contact force was kept constant at 400 pN for 0.5 s without any modulation. Finally, the cantilever was retracted to its initial position.

Creep Compliance

To characterize the viscoelastic properties of cells, the cell creep behavior can be investigated with the force clamp method, as described by Hecht et al. [14]. After reaching the setpoint force, the cantilever maintains a constant force for a specified time, here chosen to be 1 s, which results in increasing indentation. Subsequently, the cantilever was retracted to its initial position.

The experimental data were analyzed as described previously [14]. Briefly, the analysis assumes that the cell behaves as a power-law material with creep compliance according to **Eq. 2**. The force history $F(t)$ was fit according to:

$$F(t) = F_{\mathrm{Clamp}}\begin{cases} 0 & ; \quad t < t_{\mathrm{C}} \\ \left(\dfrac{t-t_{\mathrm{C}}}{\Delta t_{\mathrm{A}}}\right)^a & ; \quad t_{\mathrm{C}} \le t < t_{\mathrm{C}} + \Delta t_{\mathrm{A}} \\ 1 & ; \quad t_{\mathrm{C}} + \Delta t_{\mathrm{A}} \le t \end{cases}, \tag{6}$$

where F_{Clamp} is the clamp force, t_{C} is the time until the tip first makes contact with the sample, Δt_{A} is the duration of the force increase, and a is the shape parameter, as a free parameter. The measured indentation was then fit with:

$$\begin{aligned}\delta(t) &= \left[C\int_0^t J\left(t-t'\right)\frac{\mathrm{d}F(t')}{\mathrm{d}t'}\mathrm{d}t'\right]^{1/2} \\ &= \left[\frac{C\,F_{\mathrm{Clamp}}}{E_0}\frac{a\,(t-t_{\mathrm{C}})^{a+\beta}}{\Delta t_A^a\, t_0^\beta}\mathrm{B}\left(\frac{\Delta t_{\mathrm{A}}}{t-t_{\mathrm{C}}}; a, \beta+1\right)\right]^{1/2},\end{aligned} \tag{7}$$

where $C = 4(1-\nu^2)/(3\tan\theta)$ is a geometrical pre-factor for a four-sided pyramidal indenter, and B is the incomplete beta function, and E_0 and β are free parameters using the creep response given by **Eq. 2**.

The modulus scaling parameter from the creep compliance and the shear modulus scaling parameter from oscillatory microrheology are related, as indicated by [33], and according to:

$$E_0 = 2(1+\nu)G_0 = 3G_0, \tag{8}$$

which simplifies to $E_0 = 3G_0$ for $\nu = 0.5$ as assumed here [63–65].

Stress Relaxation

Stress relaxation is a method to characterize the viscoelastic properties. As soon as the cantilever reaches the setpoint force, the height of the cantilever is kept constant for 15 s, while the relaxation of the force is measured. Finally, the cantilever retracts to its initial position. The results are to a great extent independent of the AFM feedback-loop [66]. The elastic-viscoelastic-correspondence principle leads to the following expression for the overall tension σ of a shell-like structure with in-plane viscoelasticity:

$$\sigma(t) = T_0 + \int_0^t \widetilde{K}_A(t-\tau)\frac{\partial\alpha(\tau)}{\partial\tau}\mathrm{d}\tau \tag{9}$$

where α is the relative area change, T_0 is the prestress, and $\widetilde{K}_A(t)$ is the stress relaxation response after **Eq. 3**. This hereditary integral can be solved analytically if the generic shape functions are approximated by a polynomial of the indentation depth, as described by Cordes et al. [20]. The forces can be computed from the tension as:

$$f = 2\pi R g(\xi)\sigma(t) \tag{10}$$

where R is the initial radius of the cell when in suspension, $g(\xi)$ is approximated with polynomials.

Statistical Analysis and Data Distribution

Two-sample student's t-tests were used to find significant changes in the fitting parameters after treating the cells with physiological perturbers. To determine whether linear correlations were detectable, the Pearson correlation coefficients (Pearson R) were calculated for every pair of AFM parameters (**Figure 5**).

As the Young's modulus, E_0, T_0, K_A, and G_0 are log-normally distributed (see **Supplementary Table S5** and [14, 20, 67]) as depicted by the shape of all of the relevant violin plots, the Pearson correlation coefficients were calculated for the logarithms of these parameters (**Figure 5**). Nonetheless, and of note, a direct (nonlogarithmic) comparison only minimally altered the Pearson R values (data not shown).

DATA AVAILABILITY STATEMENT

The original contributions presented in the study are included in the article/**Supplementary Material**, further inquiries can be directed to the corresponding authors.

AUTHOR CONTRIBUTIONS

DF, ET, and FL designed the study; DF and FL supervised the study. DF, CA, MP, and YB performed experiments; DF performed, JR and TS helped with creep analysis. AJ provided analyzing software for stress relaxation. JR, AJ, KK, and AO helped with fruitful discussions; DF and AO wrote the manuscript; DF, TS, JR, AJ, AO, and FL revised the manuscript.

FUNDING

DFG, SFB 1027: The Collaborative Research Centre SFB 1027 at the Saarland University in Saarbrücken and Homburg is an interdisciplinary research team that aims to achieve a quantitative understanding of the physical mechanisms at work when biological matter self-organises into complex structures. Such self-organisation allows biological systems to perform dynamic functions including cell migration and polarisation, cell-cell adherence and synaptic transmission, biofilm formation and tissue growth. DFG, SPP1782: Epithelial intercellular junctions as dynamic hubs to integrate forces, signals and cell behavior. Saarland university provides funding for open access publishing.

ACKNOWLEDGMENTS

The authors thank Claude Verdier (Université Grenoble Alpes, Grenoble, France) and Elisabeth Fischer-Friedrich (Technische Universität Dresden, Dresden, Germany) for the fruitful discussions that led to the presented study. For financial support, the authors thank the Leibniz Institute for New Materials (INM, Saarbrücken, Germany), Saarland University (Saarbrücken, Germany) and Deutsche Forschungsgemeinschaft DFG in the framework of the CRC 1027, SPP1782.

SUPPLEMENTARY MATERIAL

The Supplementary Material for this article can be found online at: https://www.frontiersin.org/articles/10.3389/fphy.2021.711860/full#supplementary-material

REFERENCES

1. Viji Babu PK, Rianna C, Belge G, Mirastschijski U, and Radmacher M. Mechanical and Migratory Properties of normal, Scar, and Dupuytren's Fibroblasts. *J Mol Recognit* (2018) 31:e2719. doi:10.1002/jmr.2719
2. Barriga EH, and Mayor R. Adjustable Viscoelasticity Allows for Efficient Collective Cell Migration. *Semin Cel Dev Biol* (2019) 93:55–68. doi:10.1016/j.semcdb.2018.05.027
3. Ekpenyong AE, Whyte G, Chalut K, Pagliara S, Lautenschläger F, Fiddler C, et al. Viscoelastic Properties of Differentiating Blood Cells Are Fate- and Function-dependent. *PLoS One* (2012) 7:e45237. doi:10.1371/journal.pone.0045237
4. Chen YQ, Kuo CY, Wei MT, Wu K, Su PT, Huang CS, et al. Intracellular Viscoelasticity of HeLa Cells during Cell Division Studied by Video Particle-Tracking Microrheology. *J Biomed Opt* (2014) 19:011008. doi:10.1117/1.JBO.19.1.011008
5. Chen M, Zeng J, Ruan W, Zhang Z, Wang Y, Xie S, et al. Examination of the Relationship between Viscoelastic Properties and the Invasion of Ovarian Cancer Cells by Atomic Force Microscopy. *Beilstein J Nanotechnol* (2020) 11:568–82. doi:10.3762/bjnano.11.45
6. Chim YH, Mason LM, Rath N, Olson MF, Tassieri M, and Yin H. A One-step Procedure to Probe the Viscoelastic Properties of Cells by Atomic Force Microscopy. *Sci Rep* (2018) 8:14462. doi:10.1038/s41598-018-32704-8
7. Pullarkat P, Fernández P, and Ott A. Rheological Properties of the Eukaryotic Cell Cytoskeleton. *Phys Rep* (2007) 449:29–53. doi:10.1016/j.physrep.2007.03.002
8. Wei M-T, Zaorski A, Yalcin HC, Wang J, Hallow M, Ghadiali SN, et al. A Comparative Study of Living Cell Micromechanical Properties by Oscillatory Optical Tweezers. *Opt Express* (2008) 16:8594–603. doi:10.1364/oe.16.008594
9. Chan CJ, Ekpenyong AE, Golfier S, Li W, Chalut KJ, Otto O, et al. Myosin II Activity Softens Cells in Suspension. *Biophysical J* (2015) 108:1856–69. doi:10.1016/j.bpj.2015.03.009
10. Puig-de-Morales M, Grabulosa M, Alcaraz J, Mullol J, Maksym GN, Fredberg JJ, et al. Measurement of Cell Microrheology by Magnetic Twisting Cytometry with Frequency Domain Demodulation. *J Appl Physiol* (2001) 91:1152–9. doi:10.1152/jappl.2001.91.3.1152
11. Puig-de-Morales-Marinkovic M, Turner KT, Butler JP, Fredberg JJ, and Suresh S. Viscoelasticity of the Human Red Blood Cell. *Am J Physiology-Cell Physiol* (2007) 293:C597–C605. doi:10.1152/ajpcell.00562.2006
12. Thoumine O, and Ott A. Time Scale Dependent Viscoelastic and Contractile Regimes in Fibroblasts Probed by Microplate Manipulation. *J Cel Sci* (1997) 110:2109–16. doi:10.1242/jcs.110.17.2109

13. Rigato A, Rico F, Eghiaian F, Piel M, and Scheuring S. Atomic Force Microscopy Mechanical Mapping of Micropatterned Cells Shows Adhesion Geometry-dependent Mechanical Response on Local and Global Scales. *ACS Nano* (2015) 9:5846–56. doi:10.1021/acsnano.5b00430
14. Hecht FM, Rheinlaender J, Schierbaum N, Goldmann WH, Fabry B, and Schäffer TE. Imaging Viscoelastic Properties of Live Cells by AFM: Power-Law Rheology on the Nanoscale. *Soft Matter* (2015) 11:4584–91. doi:10.1039/c4sm02718c
15. Abidine Y, Laurent VM, Michel R, Duperray A, and Verdier C. Local Mechanical Properties of Bladder Cancer Cells Measured by AFM as a Signature of Metastatic Potential. *The Eur Phys J Plus* (2015) 130. doi:10.1140/epjp/i2015-15202-6
16. Alcaraz J, Buscemi L, Puig-de-Morales M, Colchero J, Baró A, and Navajas D. Correction of Microrheological Measurements of Soft Samples with Atomic Force Microscopy for the Hydrodynamic Drag on the Cantilever. *Langmuir* (2002) 18:716–21. doi:10.1021/la0110850
17. Alcaraz J, Buscemi L, Grabulosa M, Trepat X, Fabry B, Farré R, et al. Microrheology of Human Lung Epithelial Cells Measured by Atomic Force Microscopy. *Biophysical J* (2003) 84:2071–9. doi:10.1016/s0006-3495(03)75014-0
18. Rother J, Nöding H, Mey I, and Janshoff A. Atomic Force Microscopy-Based Microrheology Reveals Significant Differences in the Viscoelastic Response between Malign and Benign Cell Lines. *Open Biol* (2014) 4:140046. doi:10.1098/rsob.140046
19. Pietuch A, and Janshoff A. Mechanics of Spreading Cells Probed by Atomic Force Microscopy. *Open Biol* (2013) 3:130084. doi:10.1098/rsob.130084
20. Cordes A, Witt H, Gallemí-Pérez A, Brückner B, Grimm F, Vache M, et al. Prestress and Area Compressibility of Actin Cortices Determine the Viscoelastic Response of Living Cells. *Phys Rev Lett* (2020) 125:068101. doi:10.1103/PhysRevLett.125.068101
21. Schierbaum N, Rheinlaender J, and Schäffer TE. Combined Atomic Force Microscopy (AFM) and Traction Force Microscopy (TFM) Reveals a Correlation between Viscoelastic Material Properties and Contractile Prestress of Living Cells. *Soft Matter* (2019) 15:1721–9. doi:10.1039/c8sm01585f
22. Wu P-H, Aroush DR-B, Asnacios A, Chen W-C, Dokukin ME, Doss BL, et al. A Comparison of Methods to Assess Cell Mechanical Properties. *Nat Methods* (2018) 15:491–8. doi:10.1038/s41592-018-0015-1
23. Sander M, Dobicki H, and Ott A. Large Amplitude Oscillatory Shear Rheology of Living Fibroblasts: Path-dependent Steady States. *Biophysical J* (2017) 113:1561–73. doi:10.1016/j.bpj.2017.07.032
24. Hoffman BD, Massiera G, Van Citters KM, and Crocker JC. The Consensus Mechanics of Cultured Mammalian Cells. *Proc Natl Acad Sci* (2006) 103:10259–64. doi:10.1073/pnas.0510348103
25. Fernández P, and Ott A. Single Cell Mechanics: Stress Stiffening and Kinematic Hardening. *Phys Rev Lett* (2008) 100:238102. doi:10.1103/physrevlett.100.238102
26. Gautier HOB, Thompson AJ, Achouri S, Koser DE, Holtzmann K, Moeendarbary E, et al. Atomic Force Microscopy-Based Force Measurements on Animal Cells and Tissues. *Methods Cel Biol* (2015) 125:211–35. doi:10.1016/bs.mcb.2014.10.005
27. Stewart MP, Hodel AW, Spielhofer A, Cattin CJ, Müller DJ, and Helenius J. Wedged AFM-Cantilevers for Parallel Plate Cell Mechanics. *Methods* (2013) 60:186–94. doi:10.1016/j.ymeth.2013.02.015
28. Lekka M. Discrimination between Normal and Cancerous Cells Using AFM. *BioNanoSci.* (2016) 6:65–80. doi:10.1007/s12668-016-0191-3
29. Sneddon IN. The Relation between Load and Penetration in the Axisymmetric Boussinesq Problem for a Punch of Arbitrary Profile. *Int J Eng Sci* (1965) 3:47–57. doi:10.1016/0020-7225(65)90019-4
30. Krieg M, Fläschner G, Alsteens D, Gaub BM, Roos WH, Wuite GJL, et al. Atomic Force Microscopy-Based Mechanobiology. *Nat Rev Phys* (2018) 1:41–57. doi:10.1038/s42254-018-0001-7
31. Braunsmann C, Proksch R, Revenko I, and Schäffer TE. Creep Compliance Mapping by Atomic Force Microscopy. *Polymer* (2014) 55:219–25. doi:10.1016/j.polymer.2013.11.029
32. Ketene AN, Schmelz EM, Roberts PC, and Agah M. The Effects of Cancer Progression on the Viscoelasticity of Ovarian Cell Cytoskeleton Structures. *Nanomedicine: Nanotechnology, Biol Med* (2012) 8:93–102. doi:10.1016/j.nano.2011.05.012
33. Takahashi R, and Okajima T. Comparison between Power-Law Rheological Parameters of Living Cells in Frequency and Time Domains Measured by Atomic Force Microscopy. *Jpn J Appl Phys* (2016) 55:08NB22. doi:10.7567/jjap.55.08nb22
34. Fabry B, Maksym GN, Butler JP, Glogauer M, Navajas D, and Fredberg JJ. Scaling the Microrheology of Living Cells. *Phys Rev Lett* (2001) 87:148102. doi:10.1103/physrevlett.87.148102
35. Kovács M, Tóth J, Hetényi C, Málnási-Csizmadia A, and Sellers JR. Mechanism of Blebbistatin Inhibition of Myosin II. *J Biol Chem* (2004) 279:35557–63. doi:10.1074/jbc.m405319200
36. Fabian L, Troscianczuk J, and Forer A. Calyculin A, an Enhancer of Myosin, Speeds up Anaphase Chromosome Movement. *Cell Chromosome* (2007) 6:1. doi:10.1186/1475-9268-6-1
37. Riento K, and Ridley AJ. Rocks: Multifunctional Kinases in Cell Behaviour. *Nat Rev Mol Cel Biol* (2003) 4:446–56. doi:10.1038/nrm1128
38. Hetrick B, Han MS, Helgeson LA, and Nolen BJ. Small Molecules CK-666 and CK-869 Inhibit Actin-Related Protein 2/3 Complex by Blocking an Activating Conformational Change. *Chem Biol* (2013) 20:701–12. doi:10.1016/j.chembiol.2013.03.019
39. Isogai T, van der Kammen R, and Innocenti M. SMIFH2 Has Effects on Formins and P53 that Perturb the Cell Cytoskeleton. *Sci Rep* (2015) 5:9802. doi:10.1038/srep09802
40. Coué M, Brenner SL, Spector I, and Korn ED. Inhibition of Actin Polymerization by Latrunculin A. *FEBS Lett* (1987) 213:316–8. doi:10.1016/0014-5793(87)81513-2
41. Lomakin AJ, Cattin CJ, Cuvelier D, Alraies Z, Molina M, Nader GPF, et al. The Nucleus Acts as a Ruler Tailoring Cell Responses to Spatial Constraints. *Science* (2020) 370:370. doi:10.1126/science.aba2894
42. Stamenovic D. Chromium Supplements Could Benefit Patients with Type 2 Diabetes. *Nat Rev Endocrinol* (2006) 2:597–8. doi:10.1038/ncpendmet0311
43. Kollmannsberger P, Mierke CT, and Fabry B. Nonlinear Viscoelasticity of Adherent Cells Is Controlled by Cytoskeletal Tension. *Soft Matter* (2011) 7:3127–32. doi:10.1039/c0sm00833h
44. Rheinlaender J, Wirbel H, and Schäffer TE. Spatial Correlation of Cell Stiffness and Traction Forces in Cancer Cells Measured with Combined SICM and TFM. *RSC Adv* (2021) 11:13951–6. doi:10.1039/d1ra01277k
45. Fernández P, Pullarkat PA, and Ott A. A Master Relation Defines the Nonlinear Viscoelasticity of Single Fibroblasts. *Biophysical J* (2006) 90:3796–805. doi:10.1529/biophysj.105.072215
46. Koenderink GH, Dogic Z, Nakamura F, Bendix PM, MacKintosh FC, Hartwig JH, et al. An Active Biopolymer Network Controlled by Molecular Motors. *Proc Natl Acad Sci* (2009) 106:15192–7. doi:10.1073/pnas.0903974106
47. Bonakdar N, Gerum R, Kuhn M, Spörrer M, Lippert A, Schneider W, et al. Mechanical Plasticity of Cells. *Nat Mater* (2016) 15:1090–4. doi:10.1038/nmat4689
48. Stamenović D, Rosenblatt N, Montoya-Zavala M, Matthews BD, Hu S, Suki B, et al. Rheological Behavior of Living Cells Is Timescale-dependent. *Biophys J* (2007) 93:L39–41. doi:10.1529/biophysj.107.116582
49. Haghparast SMA, Kihara T, Shimizu Y, Yuba S, and Miyake J. Actin-based Biomechanical Features of Suspended normal and Cancer Cells. *J Biosci Bioeng* (2013) 116:380–5. doi:10.1016/j.jbiosc.2013.03.003
50. Fritzsche M, Erlenkämper C, Moeendarbary E, Charras G, and Kruse K. Actin Kinetics Shapes Cortical Network Structure and Mechanics. *Sci Adv* (2016) 2:e1501337. doi:10.1126/sciadv.1501337
51. Nguyen AV, Trompetto B, Tan XHM, Scott MB, Hu KH-h., Deeds E, et al. Differential Contributions of Actin and Myosin to the Physical Phenotypes and Invasion of Pancreatic Cancer Cells. *Cel Mol Bioeng* (2020) 13:27–44. doi:10.1007/s12195-019-00603-1
52. Nguyen A, Brandt M, Muenker TM, and Betz T. Multi-oscillation Microrheology via Acoustic Force Spectroscopy Enables Frequency-dependent Measurements on Endothelial Cells at High-Throughput. *Lab Chip* (2021) 21:1929–47. doi:10.1039/d0lc01135e
53. Rheinlaender J, and Schäffer TE. Mapping the Creep Compliance of Living Cells with Scanning Ion Conductance Microscopy Reveals a Subcellular Correlation between Stiffness and Fluidity. *Nanoscale* (2019) 11:6982–9. doi:10.1039/c8nr09428d
54. Benaglia S, Amo CA, and Garcia R. Fast, Quantitative and High Resolution Mapping of Viscoelastic Properties with Bimodal AFM. *Nanoscale* (2019) 11:15289–97. doi:10.1039/c9nr04396a

55. Garcia PD, Guerrero CR, and Garcia R. Nanorheology of Living Cells Measured by AFM-Based Force-Distance Curves. *Nanoscale* (2020) 12: 9133–43. doi:10.1039/c9nr10316c
56. Kurzawa L, Vianay B, Senger F, Vignaud T, Blanchoin L, and Théry M. Dissipation of Contractile Forces: the Missing Piece in Cell Mechanics. *MBoC* (2017) 28:1825–32. doi:10.1091/mbc.e16-09-0672
57. Rheinlaender J, Dimitracopoulos A, Wallmeyer B, Kronenberg NM, Chalut KJ, Gather MC, et al. Cortical Cell Stiffness Is Independent of Substrate Mechanics. *Nat Mater* (2020) 19:1019–25. doi:10.1038/s41563-020-0684-x
58. Vignaud T, Copos C, Leterrier C, Toro-Nahuelpan M, Tseng Q, Mahamid J, et al. Stress Fibres Are Embedded in a Contractile Cortical Network. *Nat Mater* (2021) 20:410–20. doi:10.1038/s41563-020-00825-z
59. Martens JC, and Radmacher M. Softening of the Actin Cytoskeleton by Inhibition of Myosin II. *Pflugers Arch - Eur J Physiol* (2008) 456:95–100. doi:10.1007/s00424-007-0419-8
60. Hutter JL, and Bechhoefer J. Calibration of Atomic-force Microscope Tips. *Rev Scientific Instr* (1993) 64:1868–73. doi:10.1063/1.1143970
61. Bonfanti A, Kaplan JL, Charras G, and Kabla A. Fractional Viscoelastic Models for Power-Law Materials. *Soft Matter* (2020) 16:6002–20. doi:10.1039/d0sm00354a
62. Bilodeau GG. Regular Pyramid Punch Problem. *J Appl Mech* (1992) 59:519–23. doi:10.1115/1.2893754
63. Radmacher M, Fritz M, Kacher CM, Cleveland JP, and Hansma PK. Measuring the Viscoelastic Properties of Human Platelets with the Atomic Force Microscope. *Biophysical J* (1996) 70:556–67. doi:10.1016/s0006-3495(96)79602-9
64. Harris AR, and Charras GT. Experimental Validation of Atomic Force Microscopy-Based Cell Elasticity Measurements. *Nanotechnology* (2011) 22: 345102. doi:10.1088/0957-4484/22/34/345102
65. Guz N, Dokukin M, Kalaparthi V, and Sokolov I. If Cell Mechanics Can Be Described by Elastic Modulus: Study of Different Models and Probes Used in Indentation Experiments. *Biophysical J* (2014) 107:564–75. doi:10.1016/j.bpj.2014.06.033
66. Efremov YM, Okajima T, and Raman A. Measuring Viscoelasticity of Soft Biological Samples Using Atomic Force Microscopy. *Soft Matter* (2020) 16: 64–81. doi:10.1039/c9sm01020c
67. Millet A. A Universal Model for the Log-Normal Distribution of Elasticity in Polymeric Gels and its Relevance to Mechanical Signature of Biological Tissues. *Biology (Basel)* (2021) 10:64. doi:10.3390/biology10010064

Conflict of Interest: The authors declare that the research was conducted in the absence of any commercial or financial relationships that could be construed as a potential conflict of interest.

Publisher's Note: All claims expressed in this article are solely those of the authors and do not necessarily represent those of their affiliated organizations, or those of the publisher, the editors and the reviewers. Any product that may be evaluated in this article, or claim that may be made by its manufacturer, is not guaranteed or endorsed by the publisher.

frontiers in Physiology

ORIGINAL RESEARCH
published: 01 September 2021
doi: 10.3389/fphys.2021.684121

Effects of Lipid Deposition on Viscoelastic Response in Human Hepatic Cell Line HepG2

*Rui Li, Yang Bu, Chendong Yang and Jizeng Wang**

Key Laboratory of Mechanics on Disaster and Environment in Western China, Ministry of Education, College of Civil Engineering and Mechanics, Lanzhou University, Lanzhou, China

Hepatic steatosis is associated with various liver diseases. The main pathological feature of steatosis is the excessive lipid accumulation. Ultrasound has been extensively used for the diagnosis of hepatic steatosis. However, most ultrasound-based non-invasive methods are still not accurate enough for cases with light lipid infiltration. One important reason is that the extent to which lipid infiltration may affect mechanical properties of hepatocytes remains unknown. In this work, we used atomic force microscope and *in vitro* dose-dependent lipid deposition model to detect the quantitative changes of mechanical properties under different degrees of steatosis in a single-cell level. The results show that hepatic cells with lipid deposition can be treated as linear viscoelastic materials with the power law creep compliance and relaxation modulus. Further analysis showed that even slight accumulation of lipid can lead to measurable decrease of stiffness and increased fluidity in liver cells. The accurate detection of viscoelastic properties of hepatocytes and the analysis methods may provide novel insights into hepatic steatosis grading, especially in the very early stage with reversible liver lesion. The application of viscoelasticity index for grading fat deposition might be a new detection indicator in future clinical diagnosis.

Keywords: liver steatosis, viscoelasticity, atomic force microscopy, oleic acid, HepG2 cells

OPEN ACCESS

Edited by:
Ivana Dusan Pajic-Lijakovic, University of Belgrade, Serbia

Reviewed by:
Sebastian Mueller, Heidelberg University, Germany
Guozhu Ye, Institute of Urban Environment (CAS), China

***Correspondence:**
Jizeng Wang
jzwang@lzu.edu.cn

Specialty section:
This article was submitted to Biophysics, a section of the journal Frontiers in Physiology

Received: *22 March 2021*
Accepted: *13 August 2021*
Published: *01 September 2021*

Citation:
Li R, Bu Y, Yang C and Wang J (2021) Effects of Lipid Deposition on Viscoelastic Response in Human Hepatic Cell Line HepG2. Front. Physiol. 12:684121. doi: 10.3389/fphys.2021.684121

INTRODUCTION

Hepatic steatosis is associated with various liver diseases (Sanyal et al., 2010; Hoyles et al., 2018). Some major diseases associated with steatosis include non-alcoholic fatty liver disease (NAFLD) and alcoholic liver disease (ALD) (Seitz et al., 2018; Gu et al., 2019), which are the major chronic liver diseases with a growing incidence every year. In severe cases, NAFLD can lead to liver dysfunction, hepatitis, and cirrhosis. An effective drug that can prevent and treat NAFLD has not been developed. Most patients with NAFLD may have no obvious clinical symptoms (Krawitz and Pyrsopoulos, 2020). Early control and intervention can effectively reverse disease progression. Thus, early diagnosis is highly important for patients with NAFLD.

Pathological diagnosis is the gold standard for confirming steatosis (Castera et al., 2019). This diagnosis procedure is invasive and is only used for the final determination for severe cases. However, early pathological changes usually occur in a certain part of the liver or dispersed in the liver. The recommended size for the biopsy is usually 1.5–3 cm (Rockey et al., 2009). The evaluation of focal lesions by invasive diagnosis is still affected by sampling error. Non-invasive imaging

methods are widely used in clinical practice as alternative to liver biopsy (Lee and Park, 2014), and these methods include ultrasound (US), computed tomography, and magnetic resonance (MR) (Saadeh et al., 2002; Lee et al., 2010; Lee and Park, 2014; Zhang et al., 2014; Petäjä and Yki-Järvinen, 2016). The US diagnosis of hepatic steatosis is the most common imaging method, because it its widely used, safe, and inexpensive (Mazhar et al., 2009). However, US only has a reliable assessment in moderate and severe degree of steatosis ($\geq$30%) but is not accurate for steatosis; it only meets the diagnostic criteria or is within mild degree ($<$20–30%; Dasarathy et al., 2009; Hernaez et al., 2011; Lee and Park, 2014). Therefore, high accuracy is still highly required in the US.

The inaccurate quantification of mild and local steatosis is related to the unclear changes in the mechanical properties of diseased liver tissue and the resolution of image feature recognition. The principle of US imaging method is based on the mechanical wave propagation in elastic media. Its propagation speed and amplitude are affected by the elastic modulus and bulk modulus of the medium. For viscoelastic (incomplete elasticity) media, the mechanical wave attenuates inside, and the attenuation speed is positively related to the viscosity of the medium (Righetti et al., 2002, 2003; Mueller, 2020b). Therefore, the US is an imaging method that is based on the differences in tissue mechanical properties. However, the imaging resolution is affected by input factors, such as wavelength, frequency, and wave constraint width. At present, the resolution of clinical device can only reach the millimeter level. Mild degree steatosis is limited to the lipid deposition in scattered cells, and reaching the resolution of the deposition area is difficult to reach, making US ineffective for the diagnosis of mild cases. The main pathology feature of liver steatosis is the excess lipid accumulation in liver. In mild cases, only local or small amount of lipid deposition is observed in hepatocytes. Therefore, the quantitative characterization of lipid deposition on the mechanical properties of liver tissue is needed for the accurate identification of mild fatty infiltration. How lipid deposition in liver cells affects the mechanical properties is essential for the accurate diagnosis of liver tissue lesions. A significant amount of work has been done in clinical practice through *in vivo* and *ex vivo* studies. Liver stiffness representing solid character has been studied as elastic moduli for years (Mueller and Sandrin, 2010). Yin et al. (2007) showed that steatosis has no effect on the stiffness of liver tissue via MRI measurements. They speculated that the stiffness range of fatty tissue is similar to the normal liver. Thus, the existence of hepatic steatosis in liver tissue has no obvious effect on the shear stiffness. A study measured by transient elastography on patients with ALD showed that steatosis is not related to liver stiffness (Rausch et al., 2016). Mueller (2020a) listed the stiffness of various living tissues quantified by elastography showed that the stiffness of fat tissue is about six times lower than that of the liver. Viscosity is another reference factor, suggesting that fat has an influence on mechanical properties. Barry et al. (2014) proved that fat adds viscosity to mouse livers and human liver samples. They suggested that the viscosity has a potential for steatosis scoring. Zhu et al. (2015) used gelatin-based phantoms containing a different ratio of castor oil to mimic different degrees of steatosis. Their results showed a viscosity increment with the addition of castor oil. However, a prospective clinical study using shear wave elastography found that viscosity has a remarkable effect with fibrosis rather than steatosis (Deffieux et al., 2015). Moreover, fat is a soft material with fluidity that lowers mechanical properties in liver tissue (Karlas and Mueller, 2020), which may help attenuate the harmful effects of mechanical energy generated by impulse waves (Mueller, 2016). Whether steatosis affects the mechanical properties of liver remains to be determined (Mueller et al., 2020).

From a perspective of materials, liver tissue is a composite material containing hepatocyte, hepatic sinusoid, perisinusoidal cells, and tissue matrix. The overall mechanical properties are related to each component as described in the sinusoidal pressure hypothesis (Mueller, 2016). However, only the hepatocytes are mainly affected by fat deposition. Thus, the mechanical properties of single hepatocyte affected by different degrees of fat depositions should be studied to quantitatively describe the relationship between mechanical properties changes of hepatic lobule and fat deposition. Furthermore, a reference value for the diagnostic criteria of fatty liver in precise localization and classifications should be provided.

Many attempts have been focused on the use of atomic force microscopy (AFM) to characterize the mechanical fingerprint of healthy, fibrosis, and malignant liver cells (Braet et al., 2018). Hepatoma cells with different metastasis ability showed disparity in terms of the distribution patterns of Young's modulus (Tian et al., 2015). Differences in elastic modulus are found between normal liver, hepatoma, liver embryonic stem cells (Kim et al., 2013; Sun et al., 2016; Tsikritsis et al., 2016). An AFM topology study showed that the increased surface roughness and reduced cytoskeleton height are associated with curcumin-induced G2/M phase arrest in HepG2 cells (Jiang et al., 2013). These findings demonstrate the advantages of using AFM as a nanoscale measurement tool in capturing the biomechanical characteristics of liver cells. However, living cells are soft materials with rheological properties (Desprat et al., 2005). Hepatocytes are essential for whole-body energy metabolism and synthesis. The biosynthetic reaction is reflected by the composition change of cytoplasm rather than cytoskeletal structure, and this process might be difficult to capture based on transient elastic changes. Cytoplasmic component may not contribute to shear deformation of the cells, but it is highly incompressible. Considering that the cytoplasm is rich in different molecules such as lipids, carbohydrates, and proteins, dynamic changes in cell composition may be reflected in energy dissipation and time-dependent deformations. Our previous work has showed the viscoelastic differences between different cells in the liver (Bu et al., 2019). Therefore, the viscoelastic parameters may be used as indicators to distinguish cells with different lipid depositions.

The human hepatoma cell line HepG2 preserves part of the hepatic cell characteristics, and it has been widely used to study hepatocyte functions (Knowles et al., 1980). In this work, an oleic acid (OA)-induced hepatocyte deposition model with a gradient change was used to simulate intracellular lipid deposition. Following our previous study (Bu et al., 2019), we adopted a

three-parameter power-law-type constitutive relation to fit the experimental measurements, and this method is better than the five-parameter classical spring-dashpot. The combination of the proposed power law expression and AFM indentation measurements on the creep compliance and relaxation modulus will provide a unique way in determining the viscoelastic properties of the HepG2 cells with different lipid deposition levels. Based on this technique, we expect that the experimental results can quantitatively reveal the dependence of viscoelastic properties of cells on their lipid accumulation.

MATERIALS AND METHODS

Cell Lines and Cell Culture

Human hepatoma cell line HepG2 (Cell Bank of the Chinese Academy of Sciences, Shanghai, China) was cultured in Dulbecco's modified Eagle's medium (Gibco, Thermo Fisher Scientific, United States) containing 10% (v/v) fetal bovine serum (Gibco^{TM}, Thermo Fisher Scientific, United States) supplemented with 100 U/ml penicillin and 100 μg/ml streptomycin in an incubator (INE800749L, Memmert, Germany) containing 5% CO_2 at 37°C. Cells in logarithmic growth phase were used in the experiments.

OA/BSA Complex Preparation

The OA/BSA complex solution was prepared as described before (Cousin et al., 2001; Yun et al., 2006). Briefly, 100 mM OA (Sigma-Aldrich, United States) solution was added to 10% fatty acid-free BSA (Solarbio, Beijing, China) stock solution. The mixture was incubated in a water bath for 30 min at 55°C to prepare a 5 mM OA/10% BSA complex. The solution was filter-sterilized through a 0.22-μm syringe filter (Millipore Corporation, Bedford, United States) after cooling to room temperature. The complex was used within 4 weeks.

Proliferation Assay

The proliferation rate was evaluated by 3-(4,5-dimethylthiazol-2-yl)-2,5-diphenyltetrazolium bromide (MTT) assay (Sigma-Aldrich, MO, United States). HepG2 cells were seeded into a 96-well plate (3×10^3 per well; Corning, NY, United States) and cultured for 24 h at 37°C. Then, DMEM containing different concentrations of FFA/BSA complex solution were added. After incubated for 24–72 h, 20 μL of MTT (5 mg/mL) was added to each well and incubated at 37°C for 4 h. The media was then removed, and 150 μL of dimethyl sulfoxide (Sigma-Aldrich, MO, United States) was added to each well to dissolve the crystal. The absorbance was measured at a wavelength of 570 nm by using a microplate reader (Infinite 200 PRO, TECAN, Switzerland).

Oil Red O (ORO) Staining

Lipid droplets in cells were stained with ORO staining kit (Solarbio, Beijing, China). HepG2 cells were seeded on chamber slides. After treatment for 24 h, cells were fixed with 4% buffered paraformaldehyde for 30 min and washed for three times with PBS. The slides were stained according to the manufacturer's instructions. Morphological changes were observed under light microscopy (Olympus, Tokyo, Japan). Positive area was measured using Image J software (Version 1.52, National Institutes of Health, United States). The extent of intracellular oil lipids was measured as described by Cui et al. (2010). ORO was extracted by isopropanol. The absorbance was measured at a wavelength of 405 nm by using a microplate reader (Infinite 200 PRO, TECAN, Switzerland).

Immunofluorescent Staining

HepG2 cells were seeded on chamber slides. After treatment for 24 h, cells were fixed with 4% buffered paraformaldehyde for 30 min and washed thrice with PBS. For the detection of cell apoptosis, nuclei were labeled with Hoechst 33342 at 0.5 mg/mL for 15 min and washed with PBS. For actin cytoskeleton staining, cells were permeabilized with 0.1% Triton X-100 in PBS for 3 min and blocked with 1% BSA. The slides were stained with FITC-labeled Phalloidin (Sigma-Aldrich, MO, United States) for 1 h. Slides were sealed with ProLong glass antifade mountant (Thermo Fisher Scientific, MA, United States) and stored at room temperature for 24 h in the dark. The slides were observed under fluorescence microscope (Olympus, Tokyo, Japan). Fluorescence intensity was measured using Image J software (Version 1.52, National Institutes of Health, United States).

AFM Indentation Assay

The AFM indentation assay and the theoretical model were conducted as previously described (Bu et al., 2019). Cells were seeded and treated in sterilized 35-mm petri dishes. A NanoWizard III AFM (JPK Instruments, Berlin, Germany) was used for the creep measurements of the cells. A silicon nitride AFM cantilever (NovaScan, Chicago, United States) with a polystyrene bead of 4.5 μm diameter was used. The spring constant was 0.01 N/m. The cantilever was approached to the cell at a velocity of 50 μm/s until the preset force was reached. Once a preset force for the creep was reached, the approaching was stopped by controlling the position of cantilever base. The force was kept constant for 10 s, and the cantilever retracted at a velocity of 1 μm/s. Each cell was only approached once. At least 60 individual cells were tested in each group.

Theoretical Model and Data Processing

The hepatic cells are assumed as incompressible linear viscoelastic materials (Costa, 2003), and the stress–strain relationship can be defined through the creep compliance, $J(t)$, which is expressed as follows:

$$\varepsilon_{ij}(t) = \int_0^t J(t-\tau)\frac{d\sigma_{ij}(\tau)}{d\tau}d\tau. \quad (1)$$

Following Bu et al. (2019), we choose the power-law-type creep kernel function as follows:

$$J(t) = \frac{1}{E_0}\left(\frac{t}{\tau_0}\right)^{\beta} \quad (2)$$

where E_0 is the elastic modulus of viscoelastic material at time τ_0, and β characterizes the degree of dissipation or "fluidity" of the material. If β approaches zero, then Equation

(2) degrades into the Hook Law. If β approaches unity, then Equation (2) just corresponds to the Newtown fluid. In the following sections, we set τ_0 to a very small timescale ($\sim 10^{-5}$s), then E_0 represents the instantaneous stiffness of the cell (Kollmannsberger and Fabry, 2011).

In AFM indentation tests, the tip of the AFM probe is considered as rigid sphere indenter, and the cells are treated as a viscoelastic half space. By neglecting the interfacial friction, the Hertz–Sneddon theory (Sneddon, 1965) is adopted to describe the indentation process. The relationship between the indentation depth, δ, and indentation force, P, can be written as (Yang, 1966) follows:

$$\delta^{3/2}(t) = \frac{3}{8\sqrt{R}} \int_0^t J(t-\tau) \frac{dP(t)}{d\tau} d\tau \tag{3}$$

where R is the radius of polystyrene bead.

In our creep experiments, the indentation force can be pre-set as a step function as follows:

$$P(t) = P_0 \mathrm{H}(t) \tag{4}$$

in which P_0 is the amplitude of the loading force, and $\mathrm{H}(t)$ is the so-called Heaviside step function. By submitting Equation (4) into Equation (3), the measured creep function can be obtained as follows:

$$J(t) = \left\langle \frac{8\sqrt{R}}{3P_0} \delta^{3/2}(t) \right\rangle \tag{5}$$

Notably, $J(t)$ in Equation (5) is obtained by performing ensemble average on sufficiently large number of independent experiments.

Figure 1 shows the process of a single-cell indentation. Contact point is defined as the moment when the indenter first contact with the surface of cells, where Z is the vertical height of cantilever base, and Z_0 is the value of Z just at the contact point, d is the cantilever deflection at the location of tip, and d_0 is its value at contact point. Then, the indentation depth δ can be expressed as follows:

$$\delta = Z - Z_0 - (d - d_0) \tag{6}$$

We assume that the cantilever is deformed like a Hookean spring with elastic constant, k. Then the indentation force and cantilever deflection can be related as follows:

$$P = k(d - d_0). \tag{7}$$

where $d' = P_0/k + d_0$. By keeping the indentation force constant, P_0, the creep compliance can be obtained as follows:

$$J(t) = \left\langle \frac{8\sqrt{R}}{3P_0} \left[Z(t) - Z_0 - d_0 - d' \right]^{3/2} \right\rangle \tag{8}$$

Statistical Analysis

All statistical analyses were performed using SPSS 26 (IBM, NY, United States) and GraphPad Prism software 7.0 (GraphPad Software, CA, United States). Data were expressed as means ± standard deviation. Statistical comparisons of the results were carried out using one-way ANOVA followed by the Bonferroni correction. P-value of < 0.05 was considered statistically significant.

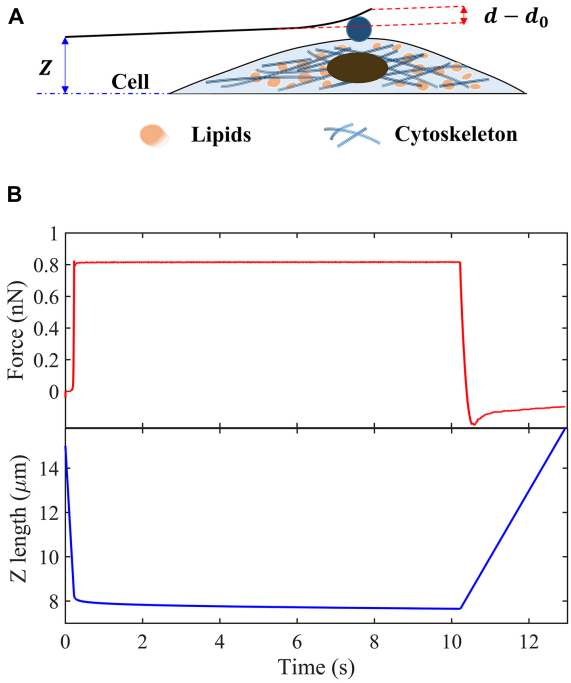

FIGURE 1 | Schematic of creep experiments on living cells. **(A)** Schematic of the indentation experiment. **(B)** Indentation force and Z-position of the cantilever base in the creep measurements.

RESULTS

Toxicity of OA on HepG2 Cells

Cytotoxicity assay was carried out to determine the dose-dependent response of OA on HepG2 cells. As shown in **Figure 2A**, HepG2 cells exposed to OA concentration lower than 1.5 mM did not show proliferation inhibition after 24 h. Cells exposed to 2 and 2.5 mM reduced the viability rate at 24, 48, and 72 h significantly. Hoechst 33342 staining was used to detect apoptosis after 24 h (**Figure 2B**). Mitotic cells were incidentally detected. Cells exposed to OA concentration higher than 1.5 mM showed increased chromatin condensation, nuclear fragmentation, and apoptotic bodies after 24 h. The majority of cells nuclei morphology showed no apparent abnormality under 1.5 mM. Therefore, a concentration lower than 1.5 mM and time of 24 h were chosen as the optimal conditions to observe the dose-dependent effect of HepG2 cell lipid deposit.

OA Increased Lipid Deposition on HepG2 Cells

We performed ORO staining to determine the intracellular lipid deposit for OA-induced lipid accumulation (**Figure 3**). Treatment with OA induced obvious fat deposition in HepG2 cells. The scattered lipid droplet increased the density and size with OA concentration. Considering the excessive deposition of lipids, lipid droplet fused into larger lipid vesicles, or the nuclei were pushed to one side (**Figure 3A**). The positive staining area of ORO staining showed an increase from 0.12% ± 0.02%

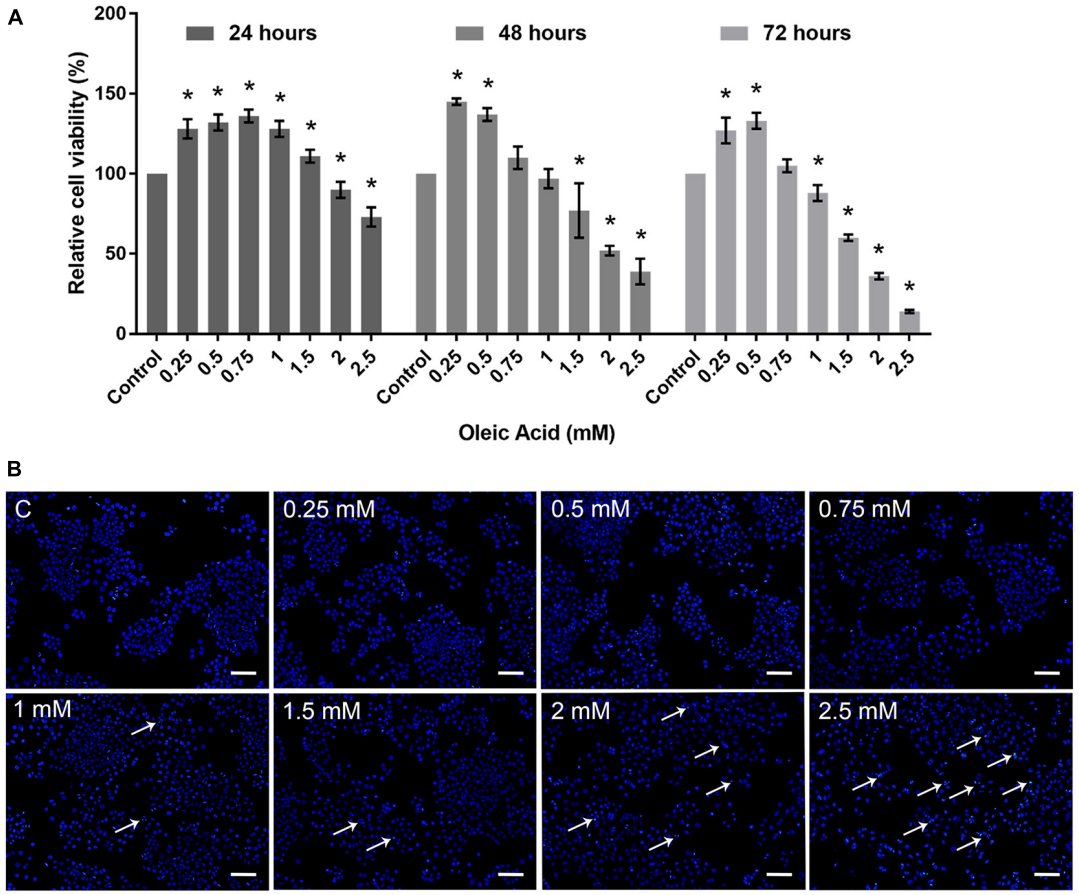

FIGURE 2 | Toxicity of OA on HepG2 cells. **(A)** Proliferation ratio of HepG2 cells treated with different concentrations of OA for 24, 48, and 72 h. **(B)** The evaluation of apoptosis for 24 h. Hoechst 33342 was used to stain the nuclei. Apoptotic cells were indicated by white arrowheads. Images taken at 10 × magnification. Scale bars: 100 μm. Experiments were performed in triplicates in three independent experiments. *$p < 0.05$, compared with the control groups.

to 31.17% ± 1.75% (**Figure 3B**). The extent of ORO staining quantified by spectrophotometry also confirmed that OA could induce different proportions of intracellular lipid deposition (**Figure 3C**). The amount of ORO extracted in the 2 and 2.5 mM groups was reduced compared with the 1.5 mM group, and this phenomenon was related to the decrease in the total cell number. The absorbance was significantly higher than the control group ($p < 0.05$). Therefore, the *in vitro* model of lipid accumulation established by OA can simulate the main characteristics of human fatty liver in a dose-dependent manner for further analysis.

Effects of OA on Actin Cytoskeleton Arrangement

The actin cytoskeleton arrangement was observed by phalloidin staining (**Figure 4**). Each group showed parallel bundles of stress fiber in HepG2 cells (**Figure 4A**). With the increase in concentration, the directional arrangement of the stress fiber remained. The density of actin bundles decreased in the 1.5 mM group, and the nuclei appear as chromatin condensation, suggesting the occurrence of apoptosis. The analysis of fluorescence also showed a weaker intensity in the 1.5 mM group ($p < 0.05$; **Figure 4B**). Therefore, the actin filaments may not show a marked change within a certain concentration of lipid deposition.

Effect of OA on the Viscoelastic Response of HepG2 Cells

Figure 5A shows the average indentation depth of HepG2 cells as a function of time after the given different concentrations of OA. Under the same experimental conditions, the creep compliance increased with OA concentration. The power law model was used to fit the experiment as previously described. Two parameters were obtained, namely, the effective pre-factor compliance ($1/E_0$) at time τ_0, and the power law exponent β. The $1/E_0$ and β-values showed an increased tendency with lipid accumulation (**Figure 5B** and **Table 1**).

DISCUSSION

Steatosis is recognized in multiple liver diseases and characterized by the deposition of fat droplets (Petäjä and Yki-Järvinen, 2016). The diagnosis for steatosis is important for the early prevention

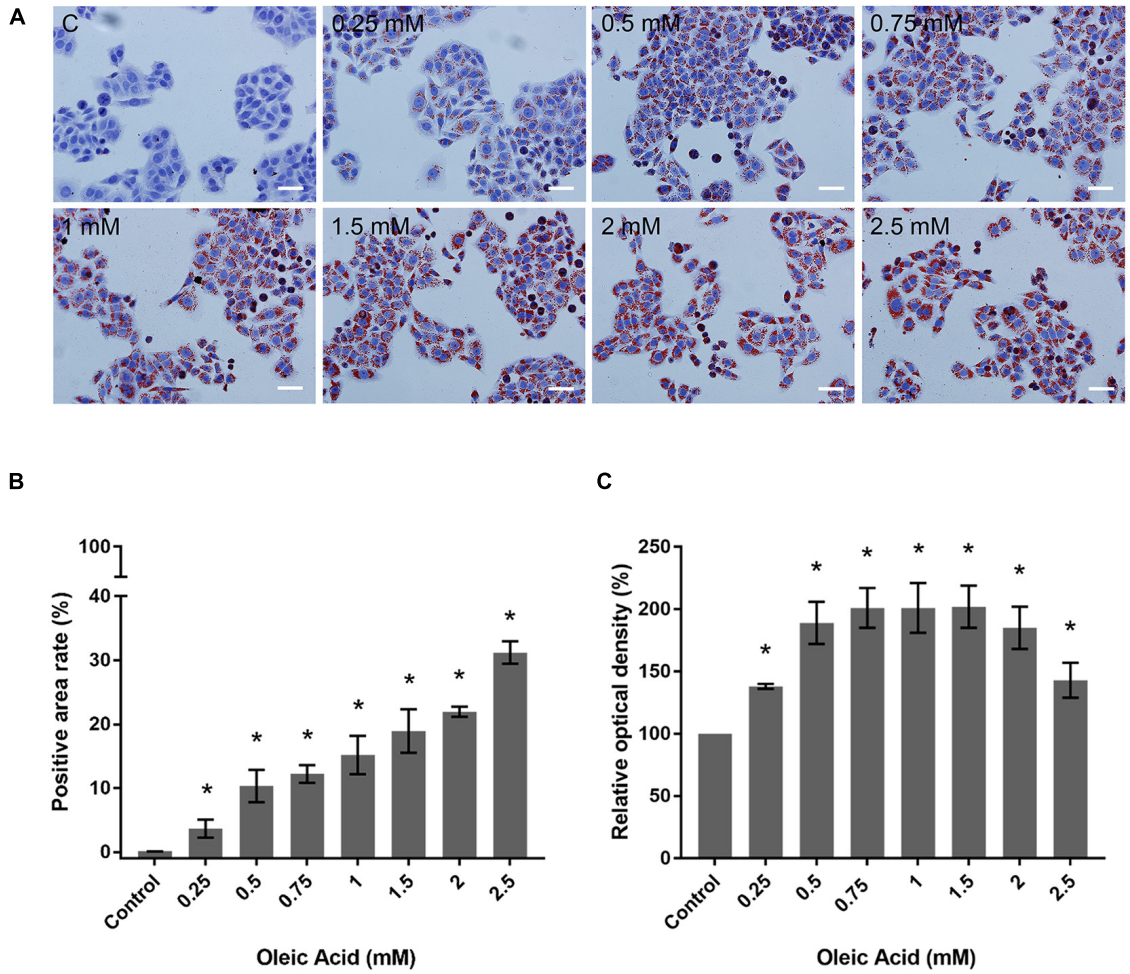

FIGURE 3 | Effects of OA concentration on lipid accumulation in HepG2 cells. **(A)** ORO staining results of HepG2 cells treated with different concentrations of OA for 24 h. Red staining represents lipids. Images taken at 20 × magnification. Scale bars: 50 μm. **(B)** Positive staining area of ORO staining. **(C)** Extent of ORO staining quantified by spectrophotometry. Experiments were performed in triplicates in three independent experiments. $^{*}p < 0.05$, compared with the control groups.

of various liver diseases (Diehl, 2010). In the present work, we used a hepatocyte deposition model with a gradient change to simulate intracellular lipid deposition. In comparison with other fatty acids such as palmitic acid, OA has higher lipid deposition effect and is less damaging (Ricchi et al., 2009). Therefore, OA was selected to amplify lipid deposition and reduce the apoptosis at a certain concentration. The semi-quantitative analysis of ORO staining showed an increased positive area from 3.64 to 19%. The AFM results showed that cell viscoelasticity is obviously concentration-related with lipid accumulation in cells, even when the lipid content is very low. Therefore, viscoelastic parameters can be used to classify light lipid deposition, providing a new insight into the classification of hepatic steatosis, especially in the early stage of the disease.

A significant amount of work has been done in non-invasive diagnostic methods in fatty liver. Yin et al. (2007) demonstrated that softer adipose tissue did not affect the overall stiffness of the liver. The stiffness range of fatty tissue is similar to the normal liver, indicating that the existence of hepatic steatosis in liver tissue does not directly affect the shear stiffness. Barry et al. (2014) found that fat can increase the viscosity of mouse livers, indicating that the viscosity may result in steatosis scoring. Zhu et al. (2015) used gelatin-based phantoms containing different ratios of castor oil to mimic different degrees of steatosis. Their results showed that Young's modulus decreases, whereas viscosity increases with increasing oil ratio (Zhu et al., 2015). The application of fluorescent probe to visualize intracellular viscosity also proved that fatty liver presents significant fluorescence compared with the healthy liver, indicating the high viscosity in fatty tissue (Yin et al., 2019). Although significant progresses have been made on qualitatively characterizing the mechanical properties changes in liver tissue during hepatic steatosis, both analysis methods and quantitative results are very limited for the accurate evaluation of the status of lipid deposition in single cell level. The present results on the changes of softness and fluidity of HepG2 cells clearly show the

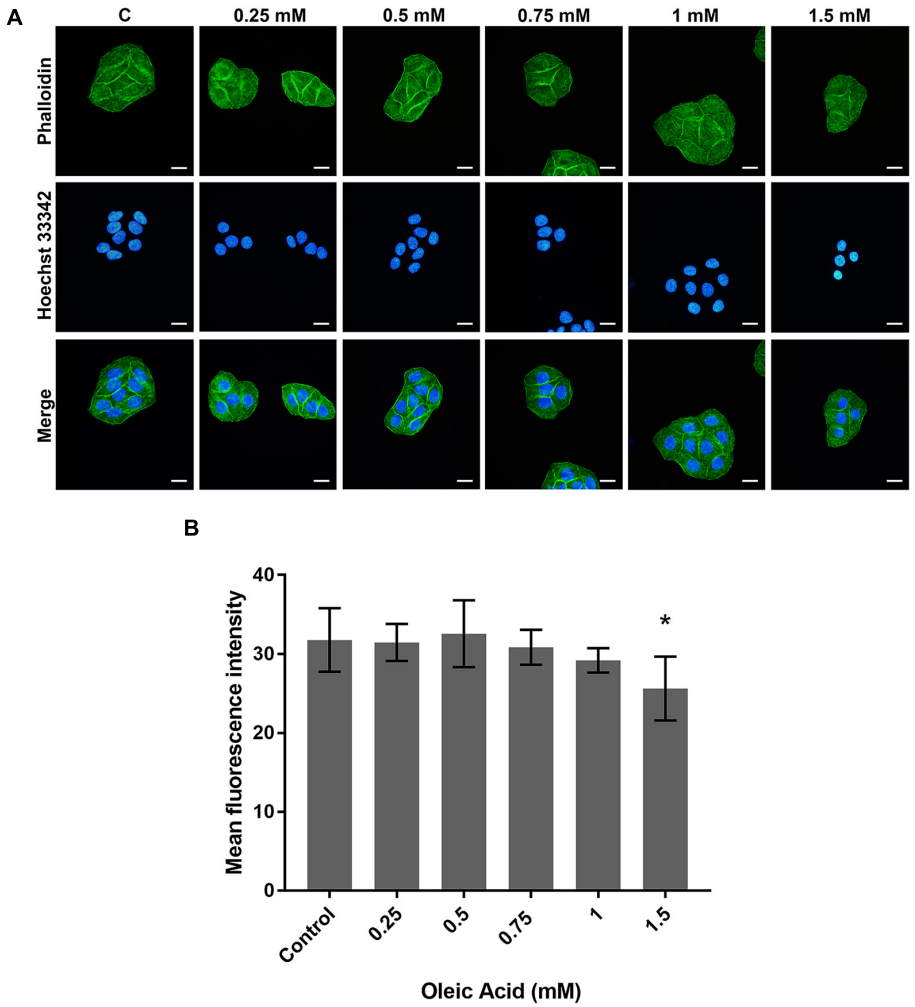

FIGURE 4 | Effects of OA on actin cytoskeleton arrangement for 24 h. **(A)** FITC-labeled Phalloidin was used to stain F-actin. Hoechst 33342 was used to stain nuclei. Images taken at 40 × magnification. Scale bars: 20 μm. **(B)** The mean fluorescence intensity of F-actin. Experiments were performed in triplicates in three independent experiments. *$p < 0.05$, compared with the control groups.

quantitative dependence on lipid deposition. This quantitative rule effectively eliminates the interference of the complexity and uncertainty of the mechanical microenvironment of liver tissue, accurately explains the quantitative relationship between the lipid deposition and the changes of observable mechanical indices during fatty liver disease progression, and provides valuable basis for the clinical diagnosis of this disease in the future.

In addition, as the primary structure to maintain the morphology of cells, studies have focused on the mechanical behavior caused by the remodeling of cytoskeleton (Satcher and Dewey, 1996; Rotsch and Radmacher, 2000; Pegoraro et al., 2017) and confirmed the major contribution of actin filament in cell elasticity (Kim et al., 2013; Grady et al., 2016; Sun et al., 2016). However, apart from cytoskeleton and binding proteins, subcellular organelles and crowding protein in cytoplasm may contribute to the rheology of the cells. These components are directly correlated with physiological and pathological process and hard to be solely defined in terms of elastic parameters. Our results showed that the effect of lipid accumulation on the actin might be limited in a certain degree, while mechanical response changes over time. According to soft glassy rheology theory, the degree of internal disorder in the cell can regulate its rheological behavior. Considering that the power-law constitutive relation is adopted, such a rheological behavior can be reflected by the power-law exponent, β, as shown in Equation (2) (Kollmannsberger and Fabry, 2011; Efremov et al., 2020). The cells behave more fluid-like when β is close to 1 and more solid-like when β approaches 0 (Kollmannsberger and Fabry, 2011). To investigate whether the rheological behavior changes with the intracellular environment, we altered the cellular components by adding lipids. Our results showed that the liver cells tend to be more fluid-like as the lipid concentration increases. The deposition of lipids occupied a limited intracellular space, thus possibly leading to aggravated intracellular crowding. This assumption

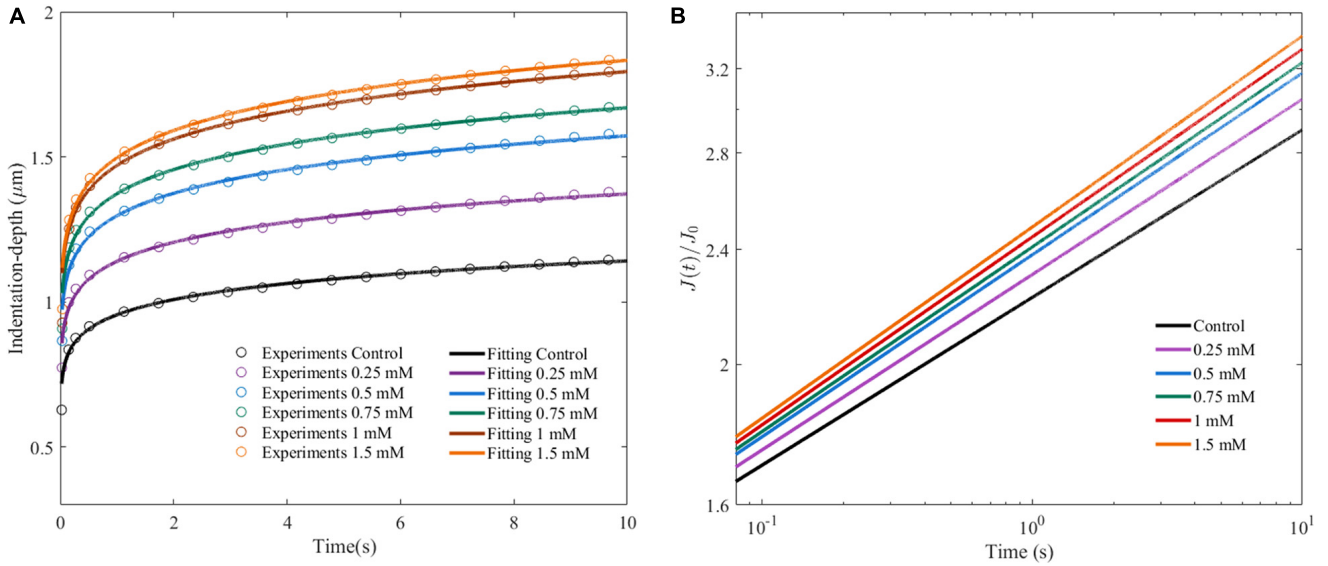

FIGURE 5 | Cell viscoelastic feedback under different concentrations of OA in AFM creep measurements for 24 h. **(A)** Changes of indentation depth as functions of time after treatment of HepG2 cells with different concentrations of OA. The circle marks represent the average of at least 60 indentation tests. Three independent experiments were performed. **(B)** Creep compliance response of HepG2 cells after dimensionless.

matches the experimental trends in which lipid accumulation increased with β.

Our phalloidin staining results revealed that F-actin remained intact within a certain degree of lipid deposition, whereas the values of $1/E_0$ and β increased with increased lipid deposition. Therefore, the contribution of actin cytoskeleton to the increased $1/E_0$ might be limited in our study. The $1/E_0$ value increased when the cytoskeleton remained unchanged possibly because of the proportion competition between the "hard-phase" (cytoskeleton) and the "soft-phase" (lipid) in the cells. As the lipid deposition increases, the "soft-phase" becomes increasingly dominant, resulting in the decrease in stiffness and increase in $1/E_0$. This finding explains the observed $1/E_0$ increase with the OA concentration in a dose-dependent manner. Interestingly, these changes in mechanical properties were mostly caused by the intracellular lipid deposition, rather than the cytoskeleton remodeling, thus providing a new insight into the understanding of the viscoelastic properties of liver cells.

In summary, we discussed the possibility of using viscoelastic feature of single cells to describe the hepatic steatosis. The results showed that the degree of lipid deposition in liver cells was quantitatively correlated with elastic compliance and power-law parameters of the viscoelasticity. The viscoelastic property change in single cells may provide an important potential choice for early hepatic steatosis grading, and the viscoelasticity index might be an accurate detection indicator.

TABLE 1 | Least-square fitting parameters for the power-law model.

Concentration (mM)	$1/E_0$ (Pa^{-1})	τ_0 (s)	β
0	1.49E-03	7.53E-05	0.116
0.25	1.84E-03	7.04E-05	0.121
0.5	2.14E-03	6.63E-05	0.126
0.75	2.26E-03	6.33E-05	0.127
1	2.44E-03	6.29E-05	0.130
1.5	2.45E-03	5.96E-05	0.132

DATA AVAILABILITY STATEMENT

The raw data supporting the conclusions of this article will be made available by the authors, without undue reservation.

AUTHOR CONTRIBUTIONS

JW, RL, and YB conceived the design and wrote the manuscript. JW supervised the study and reviewed the manuscript. RL performed most experiments. RL, YB, and CY analyzed the data. JW and YB contributed to the theoretical analysis. All authors contributed to the article and approved the submitted version.

FUNDING

This work was supported by the National Natural Science Foundation of China (Grant No. 11925204).

ACKNOWLEDGMENTS

We thank the Experimental Center of Stomatology (Lanzhou University).

REFERENCES

Barry, C. T., Hah, Z., Partin, A., Mooney, R. A., Chuang, K. H., Augustine, A., et al. (2014). Mouse liver dispersion for the diagnosis of early-stage fatty liver disease: a 70-sample study. *Ultrasound Med. Biol.* 40, 704–713. doi: 10.1016/j.ultrasmedbio.2013.10.016

Braet, F., Taatjes, D. J., and Wisse, E. (2018). Probing the unseen structure and function of liver cells through atomic force microscopy. *Semin. Cell. Dev. Biol.* 73, 13–30. doi: 10.1016/j.semcdb.2017.07.001

Bu, Y., Li, L., Yang, C., Li, R., and Wang, J. (2019). Measuring viscoelastic properties of living cells. *Acta. Mech. Solida. Sin.* 32, 599–610. doi: 10.1007/s10338-019-00113-7

Castera, L., Friedrich-Rust, M., and Loomba, R. (2019). Noninvasive assessment of liver disease in patients with nonalcoholic fatty liver disease. *Gastroenterology* 156, 1264–1281.e1264. doi: 10.1053/j.gastro.2018.12.036

Costa, K. D. (2003). Single-cell elastography: probing for disease with the atomic force microscope. *Dis. Markers.* 19, 139–154. doi: 10.1155/2004/482680

Cousin, S. P., Hügl, S. R., Wrede, C. E., Kajio, H., Myers, M. G. Jr., and Rhodes, C. J. (2001). Free fatty acid-induced inhibition of glucose and insulin-like growth factor I-induced deoxyribonucleic acid synthesis in the pancreatic beta-cell line INS-1. *Endocrinology* 142, 229–240. doi: 10.1210/endo.142.1.7863

Cui, W., Chen, S. L., and Hu, K. Q. (2010). Quantification and mechanisms of oleic acid-induced steatosis in HepG2 cells. *Am. J. Transl. Res.* 2, 95–104.

Dasarathy, S., Dasarathy, J., Khiyami, A., Joseph, R., Lopez, R., and McCullough, A. J. (2009). Validity of real time ultrasound in the diagnosis of hepatic steatosis: a prospective study. *J. Hepatol.* 51, 1061–1067. doi: 10.1016/j.jhep.2009.09.001

Deffieux, T., Gennisson, J. L., Bousquet, L., Corouge, M., Cosconea, S., Amroun, D., et al. (2015). Investigating liver stiffness and viscosity for fibrosis, steatosis and activity staging using shear wave elastography. *J. Hepatol.* 62, 317–324. doi: 10.1016/j.jhep.2014.09.020

Desprat, N., Richert, A., Simeon, J., and Asnacios, A. (2005). Creep function of a single living cell. *Biophys. J.* 88, 2224–2233. doi: 10.1529/biophysj.104.050278

Diehl, A. M. (2010). Genetic susceptibility to hepatic steatosis. *N. Engl. J. Med.* 362, 1142–1143. doi: 10.1056/NEJMe1000206

Efremov, Y. M., Okajima, T., and Raman, A. (2020). Measuring viscoelasticity of soft biological samples using atomic force microscopy. *Soft. Matter.* 16, 64–81. doi: 10.1039/c9sm01020c

Grady, M. E., Composto, R. J., and Eckmann, D. M. (2016). Cell elasticity with altered cytoskeletal architectures across multiple cell types. *J. Mech. Behav. Biomed. Mater.* 61, 197–207. doi: 10.1016/j.jmbbm.2016.01.022

Gu, J., Liu, S., Du, S., Zhang, Q., Xiao, J., Dong, Q., et al. (2019). Diagnostic value of MRI-PDFF for hepatic steatosis in patients with non-alcoholic fatty liver disease: a meta-analysis. *Eur. Radiol.* 29, 3564–3573. doi: 10.1007/s00330-019-06072-4

Hernaez, R., Lazo, M., Bonekamp, S., Kamel, I., Brancati, F. L., Guallar, E., et al. (2011). Diagnostic accuracy and reliability of ultrasonography for the detection of fatty liver: a meta-analysis. *Hepatology* 54, 1082–1090. doi: 10.1002/hep.24452

Hoyles, L., Fernández-Real, J.-M., Federici, M., Serino, M., Abbott, J., Charpentier, J., et al. (2018). Molecular phenomics and metagenomics of hepatic steatosis in non-diabetic obese women. *Nat. Med.* 24, 1070–1080. doi: 10.1038/s41591-018-0061-3

Jiang, J., Jin, H., Liu, L., Pi, J., Yang, F., and Cai, J. (2013). Curcumin disturbed cell-cycle distribution of HepG2 cells via cytoskeletal arrangement. *Scanning* 35, 253–260. doi: 10.1002/sca.21058

Karlas, T., and Mueller, S. (2020). "Liver steatosis (CAP) as modifier of liver stiffness," in *Liver Elastography: Clinical Use and Interpretation*, ed. S. Mueller (Cham: Springer International Publishing), 459–467.

Kim, Y., Hong, J. W., Kim, J., and Shin, J. H. (2013). Comparative study on the differential mechanical properties of human liver cancer and normal cells. *Anim. Cells Syst.* 17, 170–178. doi: 10.1080/19768354.2013.789452

Knowles, B. B., Howe, C. C., and Aden, D. P. (1980). Human hepatocellular carcinoma cell lines secrete the major plasma proteins and hepatitis B surface antigen. *Science* 209, 497–499. doi: 10.1126/science.6248960

Kollmannsberger, P., and Fabry, B. (2011). Linear and nonlinear rheology of living cells. *Annu. Rev. Mater. Res.* 41, 75–97. doi: 10.1146/annurev-matsci-062910-100351

Krawitz, S., and Pyrsopoulos, N. (2020). "Nonalcoholic fatty liver disease (NAFLD) and nonalcoholic steatohepatitis (NASH)," in *Geriatric Gastroenterology*, eds C. Pitchumoni and T. Dharmarajan (New York, NY: Springer), 1–10.

Lee, S. S., and Park, S. H. (2014). Radiologic evaluation of nonalcoholic fatty liver disease. *World J. Gastroenterol.* 20, 7392–7402. doi: 10.3748/wjg.v20.i23.7392

Lee, S. S., Park, S. H., Kim, H. J., Kim, S. Y., Kim, M.-Y., Kim, D. Y., et al. (2010). Non-invasive assessment of hepatic steatosis: prospective comparison of the accuracy of imaging examinations. *J. Hepatol.* 52, 579–585. doi: 10.1016/j.jhep.2010.01.008

Mazhar, S. M., Shiehmorteza, M., and Sirlin, C. B. (2009). Noninvasive assessment of hepatic steatosis. *Clin. Gastroenterol. Hepatol.* 7, 135–140. doi: 10.1016/j.cgh.2008.11.023

Mueller, S. (2016). Does pressure cause liver cirrhosis? The sinusoidal pressure hypothesis. *World J. Gastroenterol.* 22, 10482–10501. doi: 10.3748/wjg.v22.i48.10482

Mueller, S. (2020a). "Introduction to liver stiffness: a novel parameter for the diagnosis of liver disease," in *Liver Elastography: Clinical Use and Interpretation*, ed. S. Mueller (Cham: Springer International Publishing), 3–9.

Mueller, S. (2020b). "Liver Stiffness and Its Measurement," in *Liver Elastography: Clinical Use and Interpretation*, ed. S. Mueller (Cham: Springer International Publishing), 13–28.

Mueller, S., and Sandrin, L. (2010). Liver stiffness: a novel parameter for the diagnosis of liver disease. *Hepat. Med.* 2, 49–67. doi: 10.2147/hmer.s7394

Mueller, S., Elshaarawy, O., and Piecha, F. (2020). "Future applications and directions of liver stiffness studies," in *Liver Elastography: Clinical Use and Interpretation*, ed. S. Mueller (Cham: Springer International Publishing), 687–693.

Pegoraro, A. F., Janmey, P., and Weitz, D. A. (2017). Mechanical properties of the cytoskeleton and cells. cold spring harb. *Perspect. Biol.* 9:a022038. doi: 10.1101/cshperspect.a022038

Petäjä, E. M., and Yki-Järvinen, H. (2016). Definitions of normal liver fat and the association of insulin sensitivity with acquired and genetic NAFLD-a systematic review. *Int. J. Mol. Sci.* 17:633. doi: 10.3390/ijms17050633

Rausch, V., Peccerella, T., Lackner, C., Yagmur, E., Seitz, H.-K., Longerich, T., et al. (2016). Primary liver injury and delayed resolution of liver stiffness after alcohol detoxification in heavy drinkers with the PNPLA3 variant I148M. *World J. Hepatol.* 8, 1547–1556. doi: 10.4254/wjh.v8.i35.1547

Ricchi, M., Odoardi, M. R., Carulli, L., Anzivino, C., Ballestri, S., Pinetti, A., et al. (2009). Differential effect of oleic and palmitic acid on lipid accumulation and apoptosis in cultured hepatocytes. *J. Gastroenterol. Hepatol.* 24, 830–840. doi: 10.1111/j.1440-1746.2008.05733.x

Righetti, R., Ophir, J., and Ktonas, P. (2002). Axial resolution in elastography. *Ultrasound Med. Biol.* 28, 101–113. doi: 10.1016/S0301-5629(01)00495-1

Righetti, R., Srinivasan, S., and Ophir, J. (2003). Lateral resolution in elastography. *Ultrasound Med. Biol.* 29, 695–704. doi: 10.1016/S0301-5629(03)00028-0

Rockey, D. C., Caldwell, S. H., Goodman, Z. D., Nelson, R. C., and Smith, A. D. (2009). Liver biopsy. *Hepatology* 49, 1017–1044. doi: 10.1002/hep.22742

Rotsch, C., and Radmacher, M. (2000). Drug-induced changes of cytoskeletal structure and mechanics in fibroblasts: an atomic force microscopy study. *Biophys. J.* 78, 520–535. doi: 10.1016/s0006-3495(00)76614-8

Saadeh, S., Younossi, Z. M., Remer, E. M., Gramlich, T., Ong, J. P., Hurley, M., et al. (2002). The utility of radiological imaging in nonalcoholic fatty liver disease. *Gastroenterology* 123, 745–750. doi: 10.1053/gast.2002.35354

Sanyal, A. J., Chalasani, N., Kowdley, K. V., McCullough, A., Diehl, A. M., Bass, N. M., et al. (2010). Pioglitazone, vitamin E, or placebo for nonalcoholic steatohepatitis. *N. Engl. J. Med.* 362, 1675–1685. doi: 10.1056/NEJMoa0907929

Satcher, R. L. Jr., and Dewey, C. F. Jr. (1996). Theoretical estimates of mechanical properties of the endothelial cell cytoskeleton. *Biophys. J.* 71, 109–118. doi: 10.1016/s0006-3495(96)79206-8

Seitz, H. K., Bataller, R., Cortez-Pinto, H., Gao, B., Gual, A., Lackner, C., et al. (2018). Alcoholic liver disease. *Nat. Rev. Dis. Primers* 4:16. doi: 10.1038/s41572-018-0014-7

Sneddon, I. N. (1965). The relation between load and penetration in the axisymmetric boussinesq problem for a punch of arbitrary profile. *Int. J. Eng. Sci.* 3, 47–57. doi: 10.1016/0020-7225(65)90019-4

Sun, J., Luo, Q., Liu, L., Zhang, B., Shi, Y., Ju, Y., et al. (2016). Biomechanical profile of cancer stem-like cells derived from MHCC97H cell lines. *J. Biomech.* 49, 45–52. doi: 10.1016/j.jbiomech.2015.11.007

Tian, M., Li, Y., Liu, W., Jin, L., Jiang, X., Wang, X., et al. (2015). The nanomechanical signature of liver cancer tissues and its molecular origin. *Nanoscale* 7, 12998–13010. doi: 10.1039/c5nr02192h

Tsikritsis, D., Shi, H., Wang, Y., Velugotla, S., Sršeň, V., Elfick, A., et al. (2016). Label-free biomarkers of human embryonic stem cell differentiation to hepatocytes. *Cytometry. A.* 89, 575–584. doi: 10.1002/cyto.a.22875

Yang, W. H. (1966). The contact problem for viscoelastic bodies. *J. Appl. Mech.* 33, 395–401. doi: 10.1115/1.3625055

Yin, J., Peng, M., and Lin, W. (2019). Visualization of mitochondrial viscosity in inflammation, fatty liver, and cancer living mice by a robust fluorescent probe. *Anal. Chem.* 91, 8415–8421. doi: 10.1021/acs.analchem.9b01293

Yin, M., Talwalkar, J. A., Glaser, K. J., Manduca, A., Grimm, R. C., Rossman, P. J., et al. (2007). Assessment of hepatic fibrosis with magnetic resonance elastography. *Clin. Gastroenterol. Hepatol.* 5, 1207–1213.e1202. doi: 10.1016/j.cgh.2007.06.012

Yun, M. R., Lee, J. Y., Park, H. S., Heo, H. J., Park, J. Y., Bae, S. S., et al. (2006). Oleic acid enhances vascular smooth muscle cell proliferation via phosphatidylinositol 3-kinase/Akt signaling pathway. *Pharmacol. Res.* 54, 97–102. doi: 10.1016/j.phrs.2006.03.001

Zhang, B., Ding, F., Chen, T., Xia, L.-H., Qian, J., and Lv, G.-Y. (2014). Ultrasound hepatic/renal ratio and hepatic attenuation rate for quantifying liver fat content. *World J. Gastroenterol.* 20, 17985–17992. doi: 10.3748/wjg.v20.i47.17985

Zhu, Y., Dong, C., Yin, Y., Chen, X., Guo, Y., Zheng, Y., et al. (2015). The role of viscosity estimation for oil-in-gelatin phantom in shear wave based ultrasound elastography. *Ultrasound Med. Biol.* 41, 601–609. doi: 10.1016/j.ultrasmedbio.2014.09.028

Conflict of Interest: The authors declare that the research was conducted in the absence of any commercial or financial relationships that could be construed as a potential conflict of interest.

Publisher's Note: All claims expressed in this article are solely those of the authors and do not necessarily represent those of their affiliated organizations, or those of the publisher, the editors and the reviewers. Any product that may be evaluated in this article, or claim that may be made by its manufacturer, is not guaranteed or endorsed by the publisher.

frontiers in Physics

ORIGINAL RESEARCH
published: 22 September 2021
doi: 10.3389/fphy.2021.744006

Adhesion Percolation Determines Global Deformation Behavior in Biomimetic Emulsions

Lorraine Montel[1], *Iaroslava Golovkova*[1], *Silvia Grigolon*[1], *Elie Wandersman*[1], *Alexis M. Prevost*[1], *Thibault Bertrand*[2]* and *Lea-Laetitia Pontani*[1]*

[1]Sorbonne Université, CNRS, Institut de Biologie Paris-Seine (IBPS), Laboratoire Jean Perrin (LJP), Paris, France, [2]Department of Mathematics, Imperial College London, London, United Kingdom

Characterizing the mechanical properties of tissues is key for the understanding of fundamental biological processes such as morphogenesis or tumor progression. In particular, the intercellular adhesion forces, mediated by transmembrane proteins like cadherins, are expected to control the topology and viscoelastic behavior of tissues under mechanical stress. In order to understand the influence of adhesion in tissues, we use biomimetic emulsions in which droplets mimic cells and adhere to each other through specific bonds. Here, we tune both the binding energy of the adhesive inter-droplets contacts as well as the fraction of contacts that are adhesive, thereby defining a so-called adhesiveness. Our experimental results show that adhesion prevents the emergence of local order in emulsions even at high packing fractions by preventing energetically costly droplet rearrangements. By studying the deformation of droplets within packings with different average adhesiveness values, we reveal the existence of a threshold value of adhesiveness above which all droplets in a packing are deformed as adhesive ones irrespective of their local adhesive properties. We show that this critical adhesiveness coincides with the threshold for percolation of adhesive structures throughout the tissue. From a biological point of view, this indicates that only a fraction of adhesive cells would be sufficient to tune the global mechanical properties of a tissue, which would be critical during processes such as morphogenesis.

Keywords: viscoelasticity, biomimetic emulsions, adhesion, biological tissues, deformation, percolation, topology

OPEN ACCESS

Edited by:
Jose J Munoz,
Universitat Politecnica de Catalunya, Spain

Reviewed by:
Francois Sicard,
University College London, United Kingdom
Morgan Chabanon,
CentraleSupélec, France

***Correspondence:**
Lea-Laetitia Pontani
lea-laetitia.pontani@sorbonne-universite.fr
Thibault Bertrand
t.bertrand@imperial.ac.uk

Specialty section:
This article was submitted to Biophysics, a section of the journal Frontiers in Physics

Received: *19 July 2021*
Accepted: *07 September 2021*
Published: *22 September 2021*

Citation:
Montel L, Golovkova I, Grigolon S, Wandersman E, Prevost AM, Bertrand T and Pontani L-L (2021) Adhesion Percolation Determines Global Deformation Behavior in Biomimetic Emulsions. Front. Phys. 9:744006. doi: 10.3389/fphy.2021.744006

1 INTRODUCTION

The macroscopic response of tissues is characterized by an elastic response at short timescales and a plastic one at long timescales, during which cells undergo rearrangements [1]. Deciphering the mechanical properties of tissues will help gain a better understanding of key biological processes including morphogenesis [2], wound healing [3] or cancer invasion [4]. Indeed, previous studies showed that proper embryo development requires a precise spatiotemporal tuning of the viscoelastic properties of the tissue [2, 5]. In particular, spatiotemporal changes in material characteristics like elastic modulus, yield strength or viscosity can strongly affect morphogenetic processes like tissue spreading or body axis elongation [6–9]. In addition to the regulation of force generation in tissues, regulating material properties thus offers a mechanism for controlling morphogenesis.

At the scale of the tissue, this viscoelastic behavior depends on the physical properties of the individual cells as well as on their adhesive properties through cadherin homophilic interactions.

Moreover, cells respond to an applied force through mechanotransduction processes [10], thus providing a feedback loop between the exerted forces and the mechanical properties of the tissue. The viscoelastic response of a tissue is therefore controlled by both biochemical pathways [11–13] and biomechanical processes [14], relying on the interplay between forces at the scale of single cells [15, 16] and cell-cell adhesion [17, 18]. In order to deepen our understanding of these complex processes, it is thus important to characterize the properties of biological tissues from a materials standpoint and to decipher the role of intercellular adhesion on the tissues properties. Further, changes in tissue properties can be fast and drastic, whereby a small change in properties at the cellular scale can lead to large changes in the macroscopic properties of the tissue. Recent approaches have therefore tackled the study of tissue mechanics by using the language and tools of phase transitions to highlight potential unifying principles.

The idea that the mechanics of tissues can be understood within the framework of a jamming or a rigidity transition scenario is now widely accepted [19–23]. For inert materials, the phase behavior of particulate systems is primarily controlled by the particle or droplet volume fraction ρ. Indeed, above a critical volume fraction ρ_c, a disordered solid develops a non-zero yield stress below which the material responds elastically and above which it flows plastically [24–28]. The distance to the jamming point ($\rho - \rho_c$) generically governs the mechanical response of these disordered systems [24, 26, 29–31]. Recently, the existence of a connection between jamming and geometry spanning both inert particulate systems and living systems was conjectured [22]. Like in jamming for inert particles, jamming in epithelial tissues was linked to caging by immediate neighbors, propagating force chains and cooperative cellular dynamics. For instance, *in vitro* epithelial monolayers were shown to display density-dependent glassy dynamics [32–35]. Further, a recent study argued that the zebrafish blastoderm morphogenesis is governed by a tissue rigidity phase transition which is successfully predicted by a rigidity percolation theory on the basis of the local cell connectivity network [23].

Intercellular adhesion was shown to be one of the key components of jamming in biological tissues during development, highlighting the role of adhesion on tissue rigidity [8, 23]. The maturation and strengthening of cell-cell and cell-substrate adhesions has thus been shown to lead to the jamming of amorphous configurations in confluent epithelial tissues [34]. Moreover, computational models of confluent tissues based on the active vertex model class also display rigidity transitions controlled by cellular motility properties on the one hand, and the balance between intercellular adhesion and cortical tension on the other hand [36–38]. Likewise, adhesion was shown to stabilize higher order vertices in cell tilings, which in turn is linked to the fluid-to-solid transition of the tissue [39].

However, a quantitative approach to decipher the role of adhesion on the rigidity or jamming of tissues is difficult to reach since the binding energy between cells is not readily accessible. Moreover, the topological properties of tissues cannot generically be tuned independently of other parameters. The development of computational or biomimetic approaches is thus useful to study the role of adhesion on the structure and mechanics of biological tissues in a quantitative manner. The effect of attractive interactions in model soft matter systems has been probed experimentally and through simulations; it has been shown to drastically change the nature of the jamming transition [40–43]. For instance, normal attraction forces have been shown to stabilize structures below isostaticity in granular packings, leading to a higher compactivity [40, 44]. Furthermore, attractive emulsions have been shown to display soft gel-like elastic structures capable of sustaining stresses below isostaticity [45–48]. Finally, a recent computational model also highlighted the crucial role of tension fluctuations for tissue rigidity transitions [49], by using a framework derived from deformable particle approaches [50, 51] and explicitly introducing adhesion between the cells.

In this context, biomimetic emulsions have been developed to reproduce *in vitro* the mechanical and adhesive properties of cells in tissues [52]. These systems have shed light on the importance of compressive forces for adhesion growth within tissues and can serve as a general platform to study surface interactions through biological proteins [53]. More recently they have also probed the elasto-plastic response of tissues under mechanical stress [54] and revealed a global polarizing effect of adhesion in elongating tissues [55].

In this work, we use biomimetic emulsions in order to probe the influence of adhesion on the structure and droplet deformations in static 2D packings. We use different types of binders between the droplets, which allows us to tune not only the binding energy between the droplets, but also the number of adhesive contacts one droplet can establish with its neighbors, by varying the proportion of droplets carrying complementary binders in the emulsion. Inspired by Ref. [56], we characterize packings via their *adhesiveness*. Interestingly, we find that adhesion impairs local crystalline order even in emulsions at high packing fractions, suggesting that the presence of adhesion patches hinders emulsion remodelling, in agreement with our previous work [55]. We also show that an increased binding energy or an increased proportion of adhesive contacts in the packing lead to an increase in droplets deformation as a function of their local packing fraction. However, for any given experimental condition, i.e., one type of binder and a fixed proportion of complementary droplets, all the droplets in the packings exhibit the same deformation level independently of their local adhesive neighborhood. We relate this property to a threshold adhesiveness above which the adhesive contacts between droplets form a percolating network in the emulsion. From a biological standpoint, this suggests that tuning the adhesive properties of only a fraction of the cells could affect the global mechanical behavior of a tissue.

2 MATERIALS AND METHODS

2.1 Emulsion Preparation

An oil-in-water emulsion stabilized by Sodium Dodecyl Sulfate (SDS, Sigma Aldrich) was first prepared by emulsifying silicone

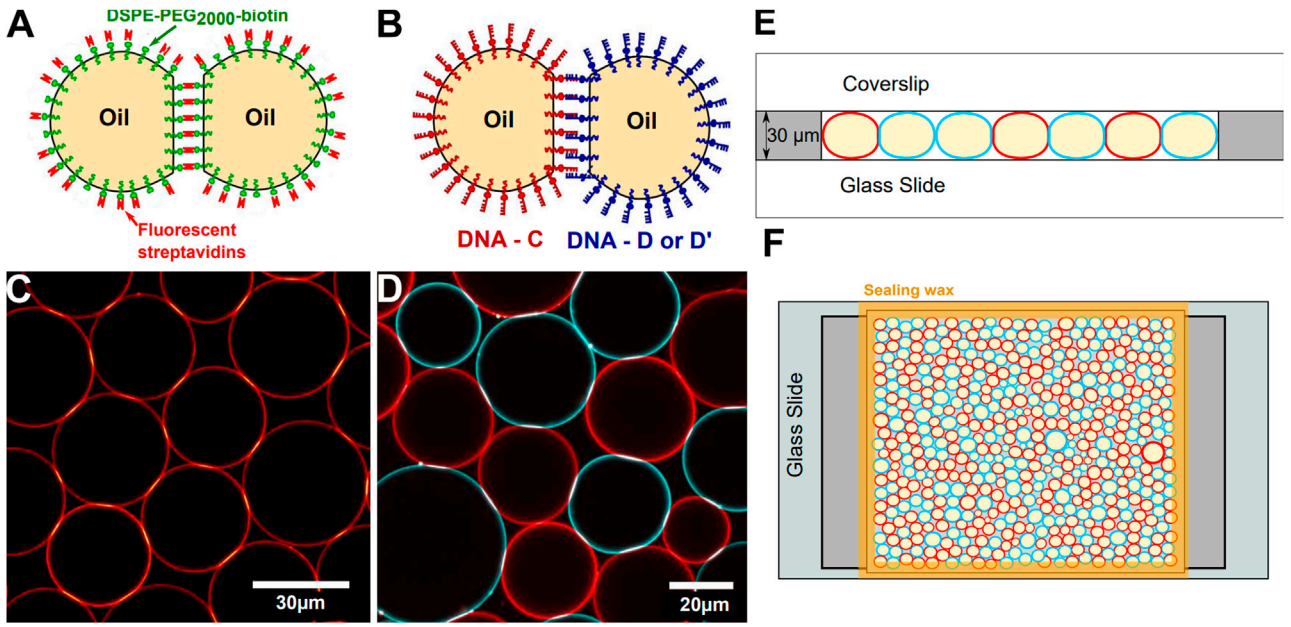

FIGURE 1 | *Experimental setup*—Sketch of adhesive droplets functionalized with streptavidin **(A)** or DNA binders **(B)**. **(C)** Confocal image of a 2D packing of droplets stabilized with fluorescent streptavidin. **(D)** Confocal image of a 2D packing of droplets functionalized with C and D DNA sequences labelled respectively with Alexa Fluor-555 (red) and -488 (blue) streptavidins. In **(C, D)**, brighter patches at droplet-droplet junctions denote adhesion patches enriched in fluorescent binders. **(E)** Side-view of the experimental chamber, **(F)** Sketch of a top view of the experimental chamber containing a packing of complementary DNA-functionalized droplets.

oil (50 cSt, Sigma Aldrich) in a 10 mM SDS solution, using a pressure emulsifier as described in [54]. The droplets stabilization was then modified by replacing the SDS with a mixture of egg L-α-phosphatidylcholine (EPC) lipids and DSPE-PEG(2000)-biotin lipids from Avanti Polar Lipids, at a mass ratio of 9:1, using the protocol described in [55]. At the end of this stabilization process, we obtain an emulsion of phospholipid-stabilized droplets in a 10 mM Tris, pH = 7.2 ± 0.2, 1 mM SDS buffer (referred thereafter as TS buffer) and we let it cream for the functionalization steps. The resulting droplets exhibit a mean diameter of 33µm, with an 18% polydispersity (see **Supplementary Figure S1** for the size distribution).

2.1.1 Streptavidin Functionalization

In order to graft streptavidin onto the biotinylated lipids distributed on the droplets surface, 7.1 µL of Alexa Fluor 555-conjugated (Invitrogen) was added to 193 µL TS buffer and 50 µL of creamed biotinylated emulsion. The droplets were incubated during 1 hour at room temperature in the dark, and mixed gently once every 10 minutes in order to re-suspend the creamed emulsion. After incubation, the emulsion was washed by removing the 200 µL of aqueous lower phase, and subsequently adding 200 µL of TS buffer. This washing step is repeated 3 times to remove all unbound streptavidins that could remain in the water phase, leaving an emulsion of droplets partially covered with fluorescent streptavidin (see **Figures 1A,C**). In order to induce adhesion between the droplets, the TS buffer is replaced by a buffer supplemented in Magnesium (10 mM Tris, 1 mM SDS, 2mM MgCl2, pH = 7.2), hereafter named TM2S buffer.

2.1.2 DNA Functionalization

DNA-functionalized droplets were prepared as described in [57] (see **Figures 1B,D**). DNA sequences consisted in a non-sticky biotinylated 49 base pairs (bp)-long backbone followed by an 11 bp-long sticky end. The 49 bp-long backbone can be hybridized with its complementary sequence (CS) to create a rigid double-stranded backbone. We used three complementary sticky ends:

C: 5′ *GGA TGA AGA TG*A GCA TTA CTT TCC GTC CCG AGA GAC CTA ACT GAC ACG CTT CCC ATC GCT A Biotin-3′

D: 5′ *CAT CTT CAT CC*A GCA TTA CTT TCC GTC CCG AGA GAC CTA ACT GAC ACG CTT CCC ATC GCT A Biotin-3′

D′: Biotin-5′ AGC ATT ACT TTC CGT CCC GAG AGA CCT AAC TGA CAC GCT TCC CAT CGC TA*C ATC TTC ATC C* 3′

CS: TAG CGA TGG GAA GCG TGT CAG TTA GGT CTC TCG GGA CGG AAA GTA ATG C.

The C sequence complements both D and D′ (see slanted parts of the sequences for C/D and C/D′ complementarity), as sketched in **Figure 1B**.

In order to functionalize the droplets, the DNA sequences C, D or D′ were first hybridized with their complementary backbone CS: 113 pmol of CS and 113 pmol of C, D or D′ were incubated together in 200 µL of 10 mM Tris, 1 mM SDS, and either 4 mM or 2 mM MgCl2 buffer (TM4S or TM2S buffer), for 45 min at room temperature. These proportions were chosen so that DNA strands and streptavidins are in 1:1 proportions and the streptavidin-DNA complexes occupy theoretically at most one fourth of the total droplet surface. Note that only three

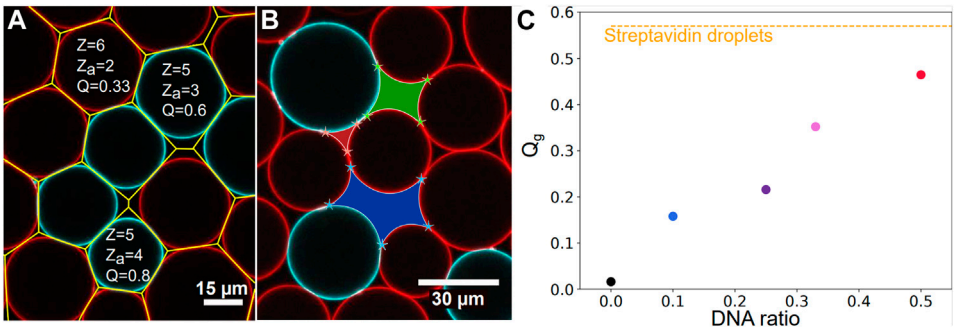

FIGURE 2 | *Image analysis*—**(A)** Surface Voronoi analysis (yellow lines) of a packing of complementary droplets coated with C (red droplets) and D (blue droplets) DNA sequences. Local coordination, number of adhesive contact and the resulting adhesiveness are given as an example for three droplets in the packing. The number of adhesive contacts z_a is here given by the number of surrounding droplets exhibiting a complementary color to the central droplet and a local increase in fluorescence at the contact site with the central droplet. **(B)** Illustration of void analysis displaying a 3-sided (red), a 4-sided (green) and a 5-sided (blue) void in a DNA droplets packing. **(C)** Global adhesiveness Q_g calculated over all droplets in all images acquired as a function of the chosen ratio of complementary DNA droplets. Q_g grows as the ratio is increased from 1:9 to 1:1. The global adhesiveness calculated for the streptavidin packings Q_g = 57% is shown with the yellow dashed line.

experiments were carried out with the TM4S buffer. However, none of the experimental measurement differed between 2 and 4 mM MgCl2. Only the kinetics of streptavidin patches formation was impacted. Patches were formed in both cases well below the 45 min incubation before observation. Therefore, we pool together all experiments carried out with 2 and 4 mM MgCl2 magnesium for a given ratio of droplets functionalized with complementary DNA strands.

Fluorescent streptavidin was then added to the DNA sequences. To do so, 7.1 µg of Alexa-488 streptavidin or Alexa-555 streptavidin at 1 mg/ml was added to the solution, and incubated during 1 h at room temperature in the dark to combine with the biotinylated end of the DNA sequences. The C sequence was associated to the Alexa-555 streptavidin and the D sequence to the Alexa-488 streptavidin, as shown in **Figure 1D**.

Finally, 207 µL of the DNA solution was added to 50 µL of creamed biotinylated droplets, and incubated for 1 hour at room temperature in the dark, with a gentle agitation every 10 min to re-suspend the droplets. These proportions were chosen so that DNA strands and streptavidin are in 1:1 proportions, and the streptavidin-DNA complexes occupy theoretically at most one fourth of the droplet total surface. After the final incubation, the droplets are rinsed with the same buffer 3 times as described above. Immediately before the experiment, the two populations of complementary DNA droplets are mixed together (see **Figure 1D**).

2.2 Experimental Set-Up

The experimental chamber for 2D packings is made with a glass slide and a coverslip separated by two lateral 30 µm high adhesive spacers (polymethylmethacrilate -PMMA-film, Goodfellow) as illustrated in **Figure 1E,F**. A solution of 0.5 mg/ml casein (β-casein from bovine milk, Sigma Aldrich) is first injected inside the chamber to prevent non-specific interactions between the droplets and the walls of the chamber and left aside for 15 min. The chamber is then rinsed with water and dried under nitrogen.

For all droplet types, the functionalized emulsion is resuspended in a water/glycerol solution (60:40 v:v), with the same composition as the desired buffer: TS buffer for non-adhesive streptavidin covered droplets, TM2S for adhesive streptavidin droplets, TM4S or TM2S for adhesive DNA droplets. The use of glycerol in the continuous phase ensures that the optical index of the water phase better matches that of the silicone oil in order to improve droplet edges visualization. This emulsion (≈10 µL) is then injected in the chamber which is subsequently sealed with hot wax (Dental Sticky Wax from Kerr). We then acquire 2D fluorescence images of the droplet packings through spinning-disk confocal microscopy (Spinning Disc Xlight V2, Gataca systems), using a ×20 objective.

2.3 Image Analysis

2.3.1 Image Segmentation and Shape Measurements

Raw images are segmented using Ilastik [58], as illustrated in **Supplementary Figure S2B**. Segmented images are then skeletonized to obtain a binary image of the contour of droplets and a surface Voronoi tesselation is performed on the segmented images with Fiji (see **Figure 2A** and **Supplementary Figure S2C**). All subsequent image analysis are performed with the Sci-kit image Python module. At this stage, the size and circularity $4\pi a/p^2$ are calculated for all binarized objects, with p the perimeter and a the projected surface of the identified objects. We detect two kinds of objects: voids (typical area 25µm^2, typical circularity 0.45) and droplets (typical area 700µm^2, typical circularity 0.9). Only the objects with an area larger than 253 µm^2, (i.e., a radius r > 9µm, the size of our smallest droplets) and a circularity larger than 0.67 are classified as droplets. Droplets whose Voronoi cell touch the border of the image are also excluded from the analysis.

We next calculate the shape parameter $\mathcal{A} = \frac{p^2}{4\pi a}$ for each droplet in the packing. In order to smooth out the roughness due to pixelation of the images, the perimeter of the droplets is computed using the method described in [55]. Briefly, a Savitzky-Golay filter is applied to the contour to smooth it out, then the contour is locally approximated with osculating circles, as

illustrated in **Supplementary Figure S2G, S3**. This contour is then used to compute the perimeter and area of the droplet. Finally, the local packing fraction ρ_l is computed for each droplet as the ratio between the droplet area a and the corresponding Voronoi cell area.

2.3.2 Neighborhood and Adhesion Patches Measurements

The Region Adjacency Graph [59] module from the Sci-kit image Python package [60] was used to determine the neighborhood properties in the packing, as illustrated in **Supplementary Figure S2D**. In particular, for a given droplet, the number of neighbors n refers to adjacent Voronoi cells. Within those neighbors, a number of droplets are in direct contact with the central one, thus defining its number of contacts z, i.e., its coordination number (see **Supplementary Material** for more details).

For every droplet-droplet contact, we detect the presence of an adhesion patch by comparing the fluorescence intensity in the contact to the one on the free surface of the droplet. For two droplets of the same color, we identify a binding patch if the fluorescence intensity at the droplet-droplet contact is at least twice larger than the intensity on the free surface (for more details, see **Supplementary Material** and **Supplementary Figure S4**). Moreover, we only consider patches that are larger than $1\,\mu m^2$ in order to exclude artifacts such as small protein aggregates (see **Supplementary Figure S2F** for an example of detected patches and aggregates). For DNA complementary droplets of different colors, the fluorescence intensity in the patch is not additive. We identify a binding patch when the intensity in the patch is 1.5 times larger than the intensity on the free surface for each color. This threshold was chosen using the intensity histogram of the image, and adjusted by trial and error to match the patches detected by eye, as is explained in more details in section 2.4 of the **Supplementary Material**.

The local adhesiveness of a droplet Q_l is defined as the ratio between its number of contacts displaying an adhesive patch z_a and its total number of contacts with the surrounding droplets z (see two examples in **Figure 2A**).

2.3.3 Void Measurements

Regions discarded from the droplet analysis are the void areas between droplets. We excluded all the voids touching the border of the images from the analysis. For each void, we counted the number of corners detected with a Harris corner detector [61], and assumed that the number of corners was equal to the number of sides of the voids, as shown in **Figure 2B**. Then for each image, we measured the packing fraction (as the total area fraction of the droplets on the image), and the probability of a void having n sides on the image.

2.4 Experimental Conditions

Two-dimensional packings of droplets were prepared as described in the Materials and Methods section. Six distinct experimental conditions were explored in order to tune the number of adhesive droplet-droplet contacts in the packings. To do so, we used droplets coated with streptavidin or DNA complementary strands and, in the latter case, explored a range of ratios for the droplets carrying each strand of DNA. For each condition, we calculated the resulting global adhesiveness Q_g by averaging the local adhesiveness of all droplets in all images corresponding to a given experimental setting (for instance one given ratio of complementary DNA droplets).

Packings of non-adhesive droplets were prepared by using streptavidin coated droplets in the absence of the salts necessary to trigger adhesion (in the so-called TS buffer). In the absence of salt, it was shown that compression could lead to biotin-streptavidin-biotin patches between droplet surfaces over the timescale of hours [52, 55]. To avoid this effect in the case of control experiments, we imaged the samples immediately after they were formed, which indeed yielded a close to zero adhesiveness (Q_g = 2%). To complement these control experiments, we also prepared packings of DNA coated droplets in which only one strand was introduced, namely the C strand. In the absence of a complementary strand to hybridize with, these emulsions also displayed a zero adhesiveness (see **Figure 2C**). As a result, these experiments were pooled together and labelled as *repulsive* packings [52, 55]. Adhesive emulsions were prepared with two distinct strategies. First, we used streptavidin biotin adhesion between the droplets in order to maximize the number of potentially adhesive contacts between the droplets. Second, we used droplets coated with complementary strands of DNA such that only a fraction of the contacts on average can form an adhesion [57]. For streptavidin driven adhesion, the droplets were incubated for 90 min in TM2S buffer in the observation chamber, allowing adhesive patches to form between contacting droplets. We refer to these conditions as *Streptavidin droplets* experiments in the following. The adhesiveness of these emulsions was measured to be Q_g = 57%, as shown on **Figure 2C**. Note that the adhesiveness does not reach 100%, meaning that not all contacts are adhesive. This is due to the fact that the number of available streptavidins or biotins to form patches can differ from one droplet to the other, and may not allow to form patches with all contacting droplets. Moreover, as binders may cluster inside the adhesive patches, a droplet can run out of binders to form additional patches with the other contacting droplets, which could account for the limited adhesiveness in these packings.

In addition to this, partially adhesive droplets experiments were prepared by using various proportions of droplets functionalized with complementary DNA strands. Two distinct sets of complementary strands were used: C/D or C/D' (see Materials and Methods). Since both pairs of DNA strands display the same number of complementary bases, they have the same binding energy of about 26 k_BT [62]. The experiments carried out with C/D or C/D' strands were thus pooled together. The complementary droplets were mixed together immediately before injection in the chamber in proportions ranging from 1:9 (for instance 1.5 µL of C emulsion mixed with 13.5 µL of D emulsion), to 1:3, 1:2 and 1:1. The 1:1 DNA experiment had a mean adhesiveness of 46% as seen on **Figure 2C**, and is labelled *DNA droplets* in **Figures 3**, **4**. The resulting global adhesiveness Q_g in the packings for the different

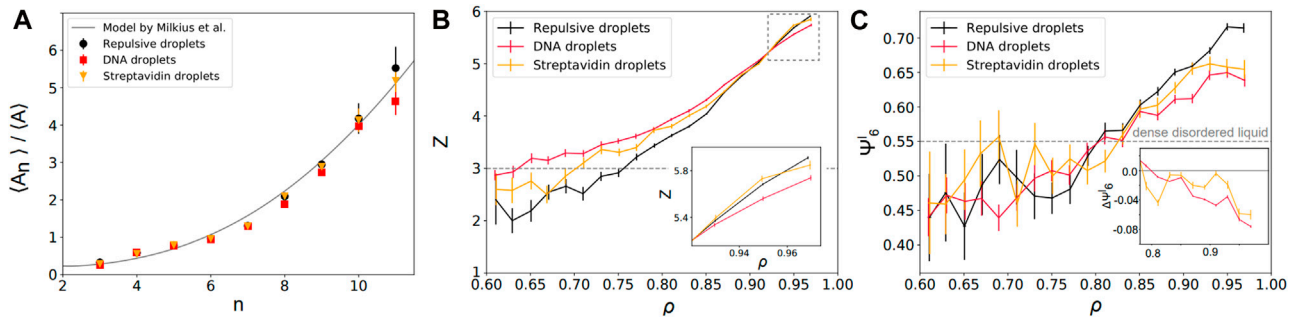

FIGURE 3 | *Local structural properties of static packings*—**(A)** Average area of the Voronoi cells as a function of their number of neighbors n. Repulsive (black disks) and adhesive emulsions (DNA: red squares; streptavidin: yellow triangles) agree with the theoretical predictions of a granocentric model (black line) [70]. **(B)** Mean local droplet coordination number z as a function of their local packing fractions for repulsive (black) and adhesive packings (DNA: red; streptavidin: yellow). Inset: zoom at high packing fractions near confluence. **(C)** Mean local bond orientational order ψ_6^l in the emulsions as a function of the local packing fraction in repulsive emulsions (black), DNA functionalized (red) and streptavidin-biotin functionalized emulsions (yellow). The local bond orientational order does not increase as much in adhesive emulsions at high packing fractions. Inset: Difference between adhesive droplets (DNA functionnalized in red, streptavidin-biotin functionnalized in yellow) and the repulsive droplets: $\Delta\psi_6^l(\rho) = \psi_6^l(\rho)_{\text{adhesive}} - \psi_6^l(\rho)_{\text{repulsive}}$.

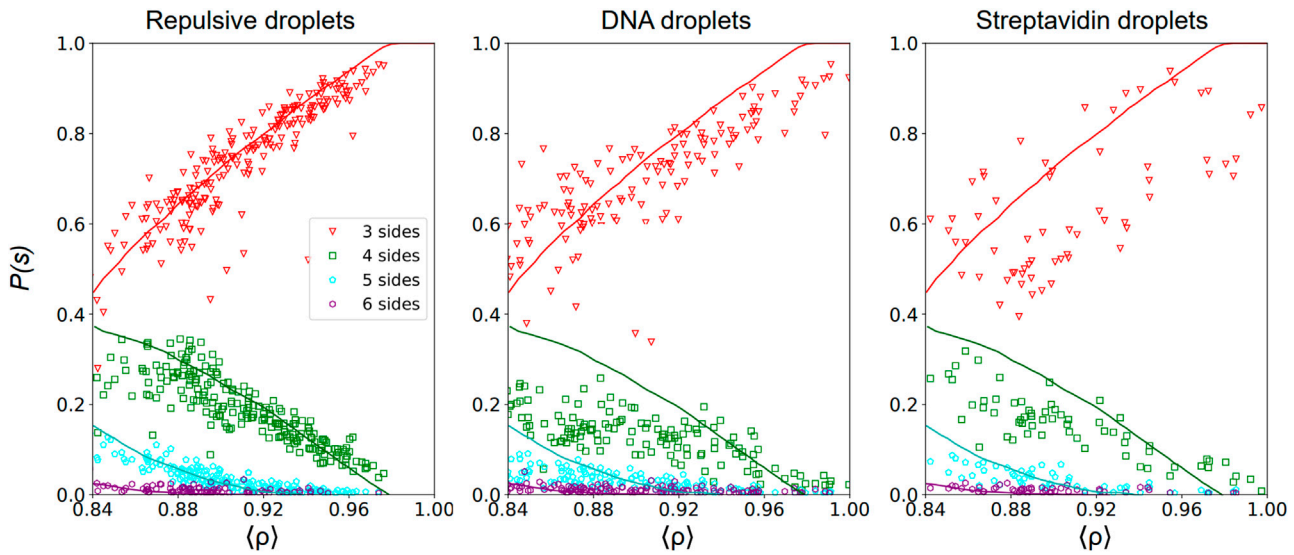

FIGURE 4 | *Topology of the voids*—Probability $P(s)$ to have a void with s sides with s = 3 (red triangles), 4 (green squares), 5 (cyan pentagons) and 6 (purple hexagons) as a function of the packing fraction $\langle\rho\rangle$ calculated as in **Eq. 1** in 2D Packing images of repulsive emulsions **(left)**, DNA emulsions **(center)** and streptavidin emulsions **(right)**. The void probability is normalized such that $\sum_s P_s(\rho) = 1$ at each packing fraction. We superimpose on our experimental data results of numerical simulations of jammed packings in a deformable particle model introduced in [51].

proportions of complementary droplets is shown in **Figure 2C**. The Q_l cumulative distribution for each global adhesiveness Q_g is available on **Supplementary Figure S5**.

After sample preparation and injection in the microfluidic chamber, fluorescent images were acquired at various locations in the sample. Each captured region of interest contains ~ 200–300 droplets. After image analysis, we obtain for each droplet i its area a_i and the area of its associated Voronoi cell A_i^v; this provides us information about its local packing fraction $\rho_i = a_i/A_i^v$. We also extract for each droplet its number of contacts (or coordination) z_i (see Materials and Methods) and neighbors n_i.

3 RESULTS

3.1 Structural Properties of Static Packings

Isotropically compressed systems composed of repulsive and frictionless particles, such as emulsions, typically jam and develop a non-zero yield stress at a critical packing fraction $\rho_c \approx 0.84$ [24, 63, 64]. For $\rho < \rho_c$, the particles have an insufficient number of interparticle contacts for the packing to be mechanically stable. At the jamming onset, Maxwell's criterion dictates that the average coordination in 2D disordered packings of repulsive spheres be given by $z_c = 4$; in other words, the packing develops a connected interparticle contact network which is

exactly isostatic at the critical point ρ_c [24, 63, 65, 66]. If the system is further compressed to $\rho > \rho_c$, the average coordination is expected to increase. We first study how the coordination number grows with the packing for adhesive and non-adhesive packings. To do so, we look at each image independently and measure their average coordination and packing fraction, given respectively by $\langle z \rangle = N^{-1}\sum_{i=1}^{N} z_i$ and

$$\langle \rho \rangle = \frac{\sum_{i=1}^{N} a_i}{\sum_{i=1}^{N} A_i^v}. \quad (1)$$

where the sum runs over the number of droplets which sit entirely in the frame. We compare the data obtained for non-adhesive packings with the two most adhesive conditions: streptavidin packings (corresponding to $Q_g = 0.57$) and DNA packings with a 1:1 ratio (corresponding to $Q_g = 0.46$). As seen in **Supplementary Figure S7**, the average coordination increases with the global packing fraction and our data is in agreement with recently developed models of deformable particles (in which droplets are deformable but cannot overlap, see **Supplementary Material**). Note that in this representation, adhesive and repulsive conditions overlap above the jamming onset, which does not allow us to test the effect of adhesion for the packing of deformable particles.

3.2 Local structural Properties of Static Packings

We then study the local structural properties of static packings. In particular, we look at the local neighborhood properties of particles in the framework of the granocentric model [67–69]. According to this model, random packings of frictionless spheres can be described locally by the assembly of nearest neighbors around a central particle. After filling the available solid angle around it, one randomly chooses which of those neighbors are in contact with the central particle. The granocentric point of view thus reduces the complexity of understanding the global structure of packings to a local stochastic process.

We first examine the relationship between the area of the Voronoi cell associated to each droplet and its number of neighbors n (i.e., the number of faces of the Voronoi cell). Qualitatively, one expects that larger droplets can accommodate a higher number of neighbors around them. In our experiments, we find that the average area $\langle A_n \rangle$ of cells with n neighbors normalized by the average area over all cells $\langle A \rangle$ increases nonlinearly with the number of neighbors n (see **Figure 3A**) as was previously observed for soap foams and emulsions in 3D (in which one instead considers the volume of the Voronoi cells) [71]. Strikingly, we find that all adhesion conditions follow the same law and are in agreement with previous extensions of the granocentric model in 2D [70]. This independence with respect to adhesion hints at the fact that repulsive and adhesive emulsions pave space the same way, i.e., their Voronoi cells have the same number of *neighbors* for a given size. Rather, the difference between repulsive and adhesive emulsions is to be found in the statistics of their number of *contacts* which is the local parameter that should be sensitive to interdroplet adhesion.

To study this in further detail, we measure the coordination of each droplet z (i.e., its number of contacts) as a function of its local packing fraction ρ. We find that adhesive droplets maintain a higher coordination than repulsive droplets at low packing fractions ($\rho < \rho_c$), see **Figure 3B**. In fact, DNA emulsions exhibit local coordination numbers that are located above the value of 3, corresponding to the minimum z for local mechanical stability, far below jamming. This is in agreement with previous observations on packings of attractive droplets in which voids were stabilized with attraction, leading to mechanically stable structures below the jamming transition [40]. At high local packing fraction $\rho \sim 1$, the coordination of repulsive droplets converges to $z = 6$. Indeed, compression is accompanied by structural rearrangements in these packings of non-adhesive droplets. While polydisperse emulsions are fully disordered close to jamming, local crystalline order is expected to emerge under compression. This will lead to locally hexagonal lattices associated to a coordination $z = 6$ in 2D. In contrast, we can observe a slight deficit in coordination in strongly adhesive emulsions when ρ approaches 1 (see inset for DNA functionalized droplets in **Figure 3B**). Qualitatively, this observation is in agreement with the fact that adhesion impairs one degree of freedom in the system. This might also explain why the effect is only visible for DNA bonds that have a higher binding energy of $\approx 26 k_B T$ [62] than streptavidin-biotin bonds associated with $\approx 15 k_B T$ [72, 73]. Indeed, while adhesion patches between droplets can move freely on their surface [57], their rupture is energetically costly which hinders the reorganizations that are leading to local ordering of the system.

To further quantify the emergence of local order in our emulsions, we measure the positional order in our packings as a function of adhesion. To do so, we calculate the bond orientational order parameter ψ_6 which measures hexagonal crystalline order [74, 75]. The local bond orientational order is given by

$$\psi_6^l = \frac{1}{n_k}\left|\sum_{j=1}^{n_k} e^{6i\theta_{kj}}\right| \quad (2)$$

where n_k is the number of neighbors of drop k. The angles θ_{kj} are defined as the angle between the vector joining the centers of droplet k and one of its Voronoi neighbors j and an axis of reference. Here, we focus on the local definition of the bond orientational order as polydispersity would prevent any long-range crystalline order. Indeed, in a polycrystalline system, one potentially observes large values of ψ_6^l even though the global bond orientational order can be very low.

In **Figure 3C**, we represent the average ψ_6^l as a function of the local packing fraction. We observe a characteristic increase of the local bond orientational order corresponding to the fact that compression above the jamming threshold promotes local crystalline order through structural rearrangements. Furthermore, the difference between the ψ_6^l calculated for repulsive and adhesive conditions above jamming is always negative and decreasing with increasing ρ, as illustrated in the inset in **Figure 3C**. In other words, adhesion hinders local crystalline order even at high packing fraction. As adhesion

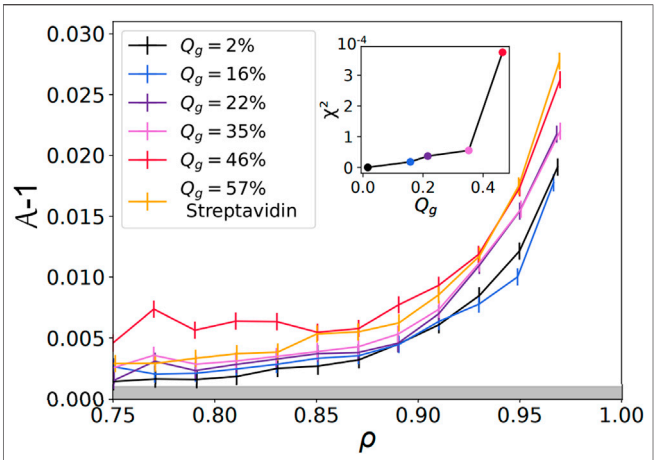

FIGURE 5 | *Shape factor as a function of the packing fraction* — $\mathcal{A}-1$ calculated for each droplet as a function of its local packing fraction ρ for all experimental conditions. Inset: χ^2 calculated between the curve obtained for non-adhesive emulsions (black curve) and the curves obtained for DNA droplets at various ratios. The curves are growing increasingly further away from the black curve as Q_g is increased from 16 to 46%. The grey box represents a lower bound on the values of $\mathcal{A}-1$ which we can measure.

patches move freely on the surface of the droplets, strong adhesion patches only allow structural rearrangements which do not necessitate interdroplet contact breaking. As stresses in the adhesive packings can not be released as efficiently by structural rearrangements, we expect droplet deformation to be significantly higher in adhesive emulsions.

3.3 Void Statistics

To characterize fully the local topology of the packings, we further study the structure of the voids between droplets as a function of the mean packing fraction $\langle\rho\rangle$ above jamming in each image. From our image segmentation, we can extract the void space and characterize the topology of the voids by counting their number of edges.

In **Figure 4**, we represent the probability $P(s)$ to have a void with s sides in repulsive, DNA and streptavidin emulsions as a function of the global packing fraction calculated in each acquired image. For repulsive packings, we observe that the probabilities of three- and 4-sided voids are similar near the jamming onset ρ_c, and greatly exceed the probability of having 5- or 6-sided voids. As the packing fraction increases, structural rearrangements lead to a strong increase of the probability of 3-sided voids while the probability of finding any other type of voids decreases, which is consistent with the emergence of hexagonal order at higher packing fractions. In **Figure 4**, we show quantitative agreement between our experimental data for repulsive emulsions and results of numerical simulations of jammed packings in a deformable particle model [51]. Instead, analysis results for adhesive packings (both DNA and streptavidin droplets) deviate from the numerical results of this purely repulsive model. All distributions are flatter in both cases and the proportion of 3-sided voids are consistently lower than the theoretical curve derived for repulsive packings at high packing fractions. This is again consistent with the idea that adhesion prevents local ordering upon compression in such emulsion packings, or in other terms that droplets have less freedom to rearrange. This would lead in turn to more constrained void topologies as evidenced by distributions that are less sensitive to the packing fraction.

3.4 Local Deformations and Adhesion

We next study the deformation of the droplets as a function of their local packing fraction. To do so, we measure the shape parameter $\mathcal{A}=\frac{p^2}{4\pi a}$ of each droplet in the packings (see Materials and Methods). The presence of adhesion patches should induce additional deformations, i.e., higher values of $\mathcal{A}$, by locally flattening the contact area between contacting droplets. As shown in **Figure 5**, when plotting $\mathcal{A}-1$ against the local packing fraction, we observe that the curve corresponding to repulsive emulsions (black curve) is located below the highest 2 DNA conditions and streptavidin curves. Moreover, for DNA experiments, an increase in global adhesiveness induces an increase in deformation for a given packing fraction. This trend is evidenced by calculating the least-squares measure χ^2 between the repulsive emulsion curve and all DNA experiment curves as a function of their calculated global adhesiveness (see inset in **Figure 5** and **Supplementary Material**). This simple way of quantifying the spacing between experimental curves highlights the increase of deformation with increasing average adhesiveness.

Finally, the curve corresponding to streptavidin experiments, at $Q_g = 57\%$, is located below the highest DNA curve at $Q_g = 46\%$. This shift can be explained by the difference in binding energy between these two types of binders. Indeed, a biotin-streptavidin bond is associated with an energy gain of about $\approx 15 k_B T$, while a sticky DNA sequence of 11 base pairs is estimated to yield $\approx 26 k_B T$. As the size of an adhesion patch between two droplets is set by the balance between the binding energy gain upon adhesion versus the elastic cost due to surface deformation, higher binding energies per bond could lead to larger patches and higher values of $\mathcal{A}$, explaining why DNA emulsions are significantly more deformed than streptavidin ones at comparable global adhesiveness.

Surprisingly, the trend is very different if one looks at *local* droplet adhesiveness Q_l within one experimental condition, i.e., one given Q_g. Indeed, we sorted all the droplets in one given condition as a function of their local adhesiveness and pooled them in bins of local adhesiveness Q_l. For each bin, one can plot again the evolution of their shape factor as a function of the local packing fraction. Strikingly, one can see with this representation that the curves overlap independently of their Q_l, as evidenced both for DNA and streptavidin emulsions in **Figures 6A–C**. This observation is again quantified by a calculation of the χ^2 value between the control curve and all other ones at higher local adhesiveness (see **Supplementary Figure S6**). We conclude from this analysis that the droplets cannot be separated from each other as a function of their local adhesiveness Q_l within a given experimental condition (associated to a given Q_g). In other words, this means that the non-adhesive droplets within adhesive packings display the same

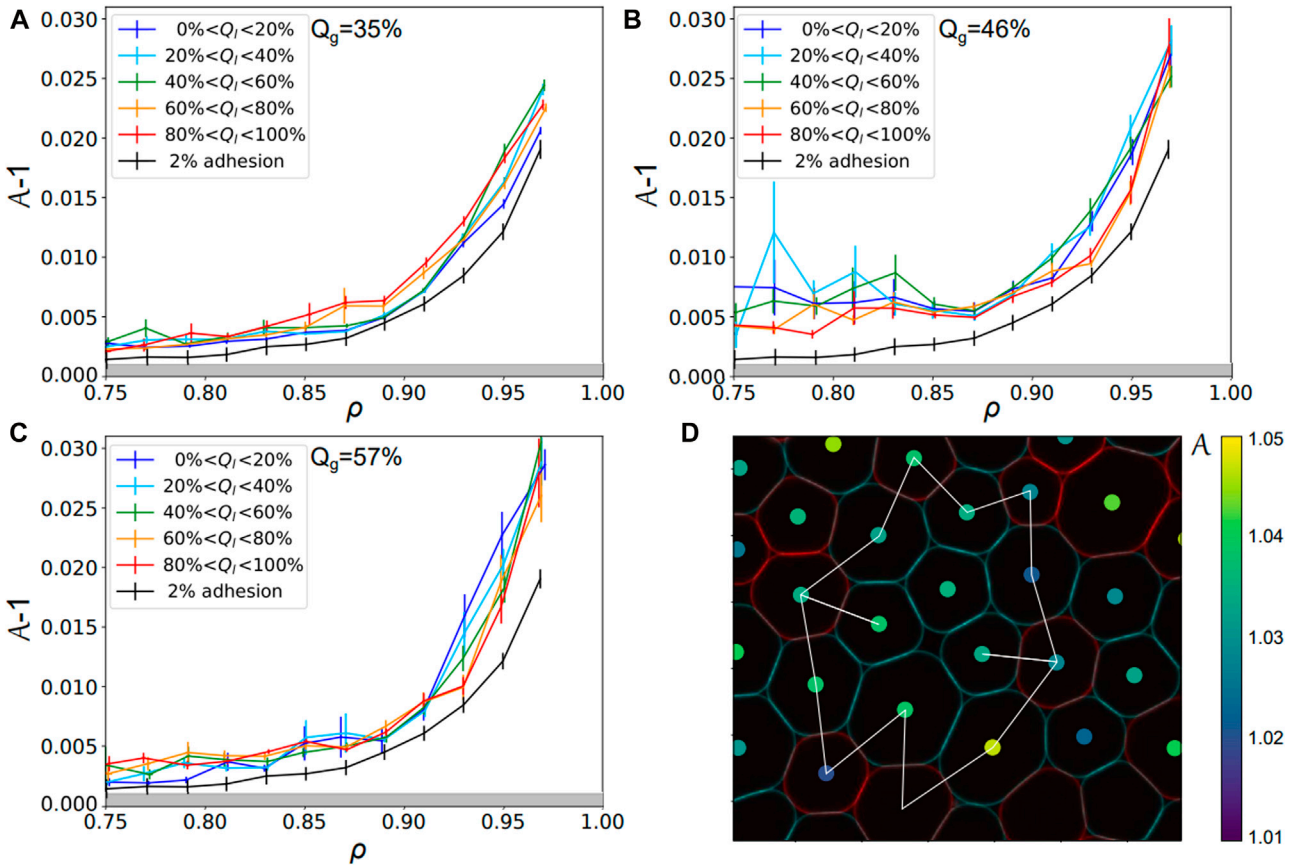

FIGURE 6 | *Droplets local adhesiveness for various global adhesion conditions*—Shape factor $\mathcal{A} - 1$ as a function of local packing fraction plotted for different bins of local adhesiveness Q_l in DNA packings yielding a global adhesiveness $Q_g = 35\%$ **(A)**, $Q_g = 46\%$ **(B)**, and in streptavidin packings yielding $Q_g = 57\%$ **(C)**. **(D)** Confocal image of a DNA complementary droplets packing ($Q_g = 46\%$) in which a central (blue) droplet exhibits first neighbors of the same color (blue), and therefore has a local adhesiveness of 0. However, one can draw a continuous ring of adhesive contacts in farther droplets by drawing a path of contacts between red and blue droplets. Image size: 219.6 μm × 184.3 μm.

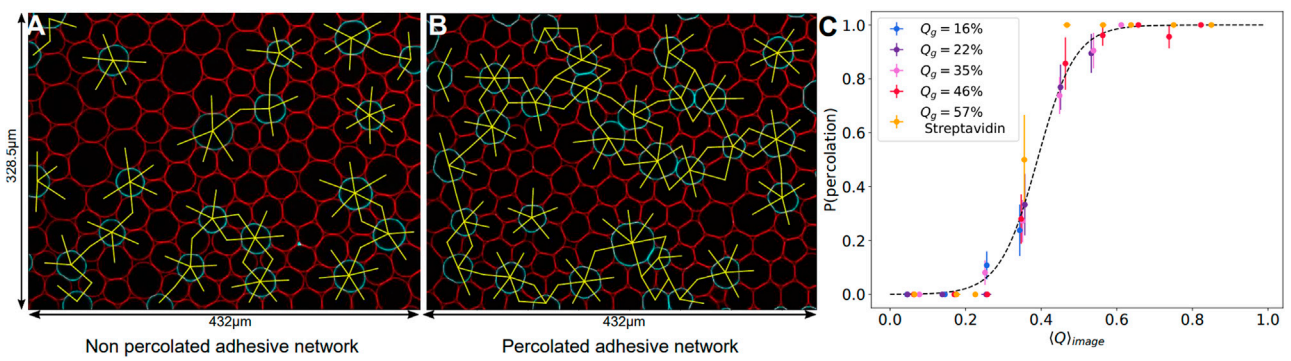

FIGURE 7 | *Adhesive contact percolation*—**(A, B)** Example images of adhesive networks for DNA droplets, with connections between adhesive droplets in yellow. If there is no continuous path between opposite borders, the network is non percolated **(A)**, if a path exists, the network is percolated **(B)**. Image sizes: 432 μm × 328.5 μm. **(C)** Probability of percolation in networks of adhesive droplets. The probability of forming a continuous adhesive path between two opposite borders of each image is plotted against the mean adhesiveness $\langle Q \rangle_{image}$ calculated in the corresponding image. All experimental conditions collapse on the same curve and can be fitted by a sigmoid of equation $[1 + e^{-20(x-0.39)}]^{-1}$ (black dashed line).

behavior as the whole packing independently of their local binding topology. Qualitatively, if a non-adhesive droplet is caged by a ring of adhesive ones, one can understand how the contraction of this adhesive ring will automatically induce deformations in the central droplet, as illustrated in **Figure 6D**.

Therefore, a continuous cage of adhesive droplets should be sufficient to induce deformation on all the non-adhesive droplets enclosed in that chain. Conversely, if adhesive contacts are too sparse, individual non-adhesive droplets will not *feel* the adhesion. In order to quantify this effect, we measured the percolation of adhesive contacts within all emulsions. We defined the adhesive network as the network formed by contacts displaying an adhesive patch. For each image, we check the existence of a path along the adhesive network going from any droplets on one border to any droplet on the opposite border of the image, as shown in **Figures 7A,B**. If at least one such path exists between two opposite borders, the network on the image is classified as percolated. We then measure the average adhesiveness in each of these images and plot the probability of percolation as a function of the image adhesiveness for all experimental conditions. We find that, independently of the Q_g value, all points superimpose onto a master curve showing a sharp transition between packings with non percolating and percolating conditions (see **Figure 7C**). We thus argue that the mechanical properties and local structure of our packings are controlled by a percolation transition for adhesive contacts. We fit the experimental points by a sigmoid function and obtain a critical value of 0.39 for the global adhesiveness above which packings are percolated, which coincides with the value at which the deformation curve significantly deviated from the repulsive case (see inset of **Figure 5**).

4 DISCUSSION

In recent years, approaches borrowed from soft matter have led to the introduction of new frameworks to decipher the physical ingredients at the origin of important biological processes. For instance, recent studies have highlighted the importance of a precise regulation of the mechanical properties of tissues for the shaping of organs during morphogenesis [2, 5–9]. In this context, cell-cell adhesion has been identified as a key parameter in the control of the viscoelastic behavior of tissues. Cellular adhesion is expected to impact the mechanical properties of tissues at multiple levels; indeed, it can tune the topology of cellular tilings [36, 38–40], but also modify their elasto-plastic response under perturbation [54, 55].

Here, we have developed a simplified approach to probe the role of adhesion on the local structure and rigidity of cellular monolayers based on the study of static 2D packings of biomimetic emulsions. In particular, we mimic cellular tissues by using functionalized droplets with controllable adhesion properties. The use of different types of binders between the functionalized droplets allows us to control not only the binding energy between the droplets, but also to tune the structure of the network of adhesive contacts in the 2D packings, by varying the proportion of droplets carrying complementary binders in the emulsion.

The strength of the interdroplet adhesion depends on both the binding energy and the density of binders in the adhesion patches. We calculate the density of binders in the adhesive patches by using a force balance model [76]. To do so, we focused on configurations below the jamming transitions to approximate each droplet as a portion of a sphere and a flat region corresponding to the contact area (**Supplementary Figure S8**). Imposing the force balance equation in the system, i.e., considering the droplets at a stationary state in mechanical equilibrium, we obtained an expression for the average binder density $\rho_{link} = \frac{2\gamma}{E_b}\left[1-\sqrt{1-(\frac{R_c}{R})^2}\right]$, where γ is the surface tension at the oil-water interface, E_b is the binding energy per bond, R_c is the radius of the adhesive patch and R is the radius of the droplets (see details in **Supplementary Material**). We find the values of R_c through the image analysis of the bonds between uncompressed droplets below jamming. By using $E_b = 15k_BT$ and $R_c = (3.9 \pm 0.15)$ μm for streptavidin-biotin bonds, and $E_b = 26k_BT$ and $R_c = (4 \pm 0.05)$ μm for DNA bonds, $\gamma = 10$ mN/m, and $R = 15$ μm, we obtained $\rho_{link} = (10{,}874 \pm 859)\mu m^{-2}$ for streptavidin-biotin patches and $\rho_{link} = (6{,}728 \pm 171)\mu m^{-2}$ for DNA patches as estimates for the binder densities in the two different conditions. These numbers are in remarkable agreement with values reported for the adhesion zones between cells in epithelial tissues [77], which further validates the relevance of our biomimetic approach. Moreover, the difference between the densities of streptavidin-biotin and DNA bonds may arise from entropic effects. Indeed, this model does not take into account the entropic cost of binders hybridization between opposing surfaces inside a patch. Since this energetic cost depends directly on the rotational contraints of the molecules upon binding [57, 78], it should be different for the two types of binders that have different geometries. This highlights the importance of not only the binding energy but also the structural properties of the molecules that are responsible for cell-cell or cell-matrix adhesion in tissues. For instance, cadherins can exhibit large differences in their binding topology depending on biochemical processes [79], which should have significant effects on the mechanics of the tissue as a whole.

Besides differences in the intercellular interaction potential, in such particulate systems the mechanical response directly depends on its structure in the framework of the jamming transition. We therefore studied the impact of adhesion on the structural properties of static packings. Below jamming, we observed that adhesive droplets form more locally stable structures by having a higher number of contacting neighbors than in the repulsive case, remaining above isostaticity far below the jamming volume fraction for repulsive systems. This is consistent with existing literature showing that adhesive emulsions can exhibit a finite elastic modulus below jamming [43, 48]. Conversely, packings with strong interdroplet adhesion reveal a deficit in droplet coordination number and lower bond orientational order parameter when approaching confluence. We argue that this is due to the fact that adhesion prevents local crystalline order by preventing droplet rearrangements which would require breaking adhesive bonds. By preventing ordering,

adhesion can have an impact on the response of compressed emulsions under stress as higher crystalline order in particulate materials has been shown to promote large rearrangements along disclination planes when subjected to shear [55, 80, 81].

Rearrangements in jammed packings participate in the release of stored elastic energy; as adhesion prevents these rearrangements, it is then not surprising that adhesion would promote higher droplet deformation in compressed emulsions. We confirm this intuition and show more specifically that the deformation level in adhesive emulsions is controlled by a percolation transition. Indeed, we observed that percolation of the network formed by adhesive contacts in the packing sets the level of deformation for all droplets, independently of their local environment. More precisely, we found that 40% of adhesive contacts are sufficient to induce a global change in the deformation level of all droplets in the assembly. Qualitatively, percolated networks of adhesive interdroplet contacts promotes local caging of droplets surrounded by strong adhesion rings. Droplets in these cages will thus display the same level of deformation as surrounding droplets with high adhesiveness independently of their own adhesiveness.

Going back to biological tissues, our observation means that the upregulation of adhesion in a small number of cells could induce large global changes in the tissue through mechanosensitive pathways. We argue that the tissue rigidity transition, which is key to fundamental morphogenetic processes, can thus take place with only a low fraction of adhesive contacts between the cells given that their spatial distribution ensures percolation of the adhesive contacts network. Interestingly, a recent study argues that a rigidity percolation transition similar to ours controls the mechanical properties of the zebrafish blastoderm throughout morphogenesis but also across experimental perturbations of cell fate, division, contractility and adhesion [23]. Akin to our observation, it was shown that cell-cell adhesion defines the cell connectivity which in turn, modulates the tissue rigidity. In particular, small changes in cell-cell adhesion were linked to drastic and abrupt changes in tissue viscosity. Overall, this is all consistent with the idea that being close to the rigidity percolation critical point allows a tissue to change its material properties rapidly and drastically [82].

In conclusion, our work explores the physics of jamming and rigidity percolation in tissues from two perspectives. First, from a granular point of view, the structural properties of the packings are controlled by the packing fraction. In this context, we confirm here that adhesion stabilize packings at densities below the jamming onset for repulsive systems. In that sense, the jamming onset (understood as the critical density at which the packing acquires a non zero yield stress) should be defined at a lower threshold packing fraction in the presence of adhesion. Importantly, we further show that long range collective effects control the deformation of individual droplets in our system. We argue here that this observation can be understood in the context of the transition to percolation of the adhesive contacts network. Our work thus paves the way for a redefinition of the jamming phase diagram for tissues, in which the axis related to the intercellular adhesion energy (or the packing fraction) could be replaced by a measurement that combines this value with the spatial arrangement of the adhesive interfaces.

DATA AVAILABILITY STATEMENT

The raw data supporting the conclusions of this article will be made available by the authors, without undue reservation.

AUTHOR CONTRIBUTIONS

L-LP conceived the project, LM and IG performed experiments, TB and SG performed theoretical modelling, LM and TB performed data analysis. L-LP, TB, and LM wrote the original draft, SG, EW, and AP reviewed and edited the manuscript. All authors participated to scientific discussions on the results and commented on the manuscript.

FUNDING

L-LP acknowledges financial support from Agence Nationale de la Recherche (BOAT, ANR-17-CE30-0001) and from Emergence(s) Ville de Paris.

ACKNOWLEDGMENTS

The authors thank Corey S. O'Hern for sharing the numerical data shown in **Figure 4**, as well as Jacques Fattaccioli for letting us use his pressure emulsifier.

SUPPLEMENTARY MATERIAL

The Supplementary Material for this article can be found online at: https://www.frontiersin.org/articles/10.3389/fphy.2021.744006/full#supplementary-material

REFERENCES

1. Marmottant P, Mgharbel A, Käfer J, Audren B, Rieu J-P, Vial J-C, et al. The Role of Fluctuations and Stress on the Effective Viscosity of Cell Aggregates. *Proc Natl Acad Sci* (2009) 106:17271–5. doi:10.1073/pnas.0902085106
2. Forgacs G, Foty RA, Shafrir Y, and Steinberg MS. Viscoelastic Properties of Living Embryonic Tissues: a Quantitative Study. *Biophysical J* (1998) 74: 2227–34. doi:10.1016/S0006-3495(98)77932-9
3. Barriga EH, and Mayor R. Adjustable Viscoelasticity Allows for Efficient Collective Cell Migration. *Semin Cel Developmental Biol* (2019) 93:55–68. doi:10.1016/j.semcdb.2018.05.027

4. Streitberger K-J, Lilaj L, Schrank F, Braun J, Hoffmann K-T, Reiss-Zimmermann M, et al. How Tissue Fluidity Influences Brain Tumor Progression. *Proc Natl Acad Sci USA* (2020) 117:128–34. doi:10.1073/pnas.1913511116
5. Petridou NI, and Heisenberg CP. Tissue Rheology in Embryonic Organization. *EMBO J* (2019) 38:e102497. doi:10.15252/embj.2019102497
6. Morita H, Grigolon S, Bock M, Krens SFG, Salbreux G, and Heisenberg C-P. The Physical Basis of Coordinated Tissue Spreading in Zebrafish Gastrulation. *Developmental Cel* (2017) 40:354–66. doi:10.15252/embj.2019102497
7. Barriga EH, Franze K, Charras G, and Mayor R. Tissue Stiffening Coordinates Morphogenesis by Triggering Collective Cell Migration *In Vivo*. *Nature* (2018) 554:523–7. doi:10.1038/nature25742
8. Mongera A, Rowghanian P, Gustafson HJ, Shelton E, Kealhofer DA, Carn EK, et al. A Fluid-To-Solid Jamming Transition Underlies Vertebrate Body axis Elongation. *Nature* (2018) 561:401–5. doi:10.1038/s41586-018-0479-2
9. Petridou NI, Grigolon S, Salbreux G, Hannezo E, and Heisenberg C-P. Fluidization-mediated Tissue Spreading by Mitotic Cell Rounding and Non-canonical Wnt Signalling. *Nat Cel Biol* (2019) 21:169–78. doi:10.1038/s41556-018-0247-4
10. Farge E. Mechanotransduction in Development. *Curr Top Dev Biol* (2011) 95:243–65. doi:10.1016/B978-0-12-385065-2.00008-6
11. Kutejova E, Briscoe J, and Kicheva A. Temporal Dynamics of Patterning by Morphogen Gradients. *Curr Opin Genet Development* (2009) 19:315–22. doi:10.1016/j.gde.2009.05.004
12. Meinhardt H. Models for the Generation and Interpretation of Gradients. *Cold Spring Harbor Perspect Biol* (2009) 1:a001362. doi:10.1101/cshperspect.a001362
13. Wartlick O, Kicheva A, and González-Gaitán M. Morphogen Gradient Formation. *Cold Spring Harb Perspect Biol* (2009) 1:a001255. 10.1101/cshperspect.a001255.
14. Ladoux B, and Mège R-M. Mechanobiology of Collective Cell Behaviours. *Nat Rev Mol Cel Biol* (2017) 18:743–57. doi:10.1038/nrm.2017.98
15. Mammoto T, Mammoto A, and Ingber DE. Mechanobiology and Developmental Control. *Annu Rev Cel Dev. Biol* (2013) 29:27–61. doi:10.1146/annurev-cellbio-101512-122340
16. Heisenberg C-P, and Bellaïche Y. Forces in Tissue Morphogenesis and Patterning. *Cell* (2013) 153:948–62. doi:10.1016/j.cell.2013.05.008
17. Barone V, and Heisenberg C-P. Cell Adhesion in Embryo Morphogenesis. *Curr Opin Cel Biol* (2012) 24:148–53. doi:10.1016/j.ceb.2011.11.006
18. Foty RA, and Steinberg MS. Differential Adhesion in Model Systems. *Wires Dev Biol* (2013) 2:631–45. doi:10.1002/wdev.104
19. Sadati M, Taheri Qazvini N, Krishnan R, Park CY, and Fredberg JJ. Collective Migration and Cell Jamming. *Differentiation* (2013) 86:121–5. doi:10.1016/j.diff.2013.02.005
20. Nnetu KD, Knorr M, Käs J, and Zink M. The Impact of Jamming on Boundaries of Collectively Moving Weak-Interacting Cells. *New J Phys* (2012) 14:115012. doi:10.1088/1367-2630/14/11/115012
21. Oswald L, Grosser S, Smith DM, and Käs JA. Jamming Transitions in Cancer. *J Phys D: Appl Phys* (2017) 50:483001. doi:10.1088/1361-6463/aa8e83
22. Atia L, Bi D, Sharma Y, Mitchel JA, Gweon B, DeCamp SSJ, et al. Geometric Constraints during Epithelial Jamming. *Nat Phys* (2018) 14:613–20. doi:10.1038/s41567-018-0089-9
23. Petridou NI, Corominas-Murtra B, Heisenberg C-P, and Hannezo E. Rigidity Percolation Uncovers a Structural Basis for Embryonic Tissue Phase Transitions. *Cell* (2021) 184:1914–28. doi:10.1016/j.cell.2021.02.017
24. O'Hern CS, Silbert LE, Liu AJ, and Nagel SR. Jamming at Zero Temperature and Zero Applied Stress: The Epitome of Disorder. *Phys Rev E* (2003) 68:011306. doi:10.1103/PhysRevE.68.011306
25. Cates ME, Wittmer JP, Bouchaud J-P, and Claudin P. Jamming, Force Chains, and Fragile Matter. *Phys Rev Lett* (1998) 81:1841–4. doi:10.1103/PhysRevLett.81.1841
26. Olsson P, and Teitel S. Critical Scaling of Shear Viscosity at the Jamming Transition. *Phys Rev Lett* (2007) 99:178001. doi:10.1103/PhysRevLett.99.178001
27. Goyon J, Colin A, Ovarlez G, Ajdari A, and Bocquet L. Spatial Cooperativity in Soft Glassy Flows. *Nature* (2008) 454:84–7. doi:10.1038/nature07026
28. Chen DTN, Wen Q, Janmey PA, Crocker JC, and Yodh AG. Rheology of Soft Materials. *Annu Rev Condens Matter Phys* (2010) 1:301–22.
29. O'Hern CS, Langer SA, Liu AJ, and Nagel SR. Random Packings of Frictionless Particles. *Phys Rev Lett* (2002) 88:075507. doi:10.1103/PhysRevLett.88.075507
30. Ellenbroek WG, Somfai E, van Hecke M, and van Saarloos W. Critical Scaling in Linear Response of Frictionless Granular Packings Near Jamming. *Phys Rev Lett* (2006) 97:258001. doi:10.1103/PhysRevLett.97.258001
31. Majmudar TS, Sperl M, Luding S, and Behringer RP. Jamming Transition in Granular Systems. *Phys Rev Lett* (2007) 98:058001. doi:10.1103/PhysRevLett.98.058001
32. Angelini TE, Hannezo E, Trepat X, Marquez M, Fredberg JJ, and Weitz DA. Glass-like Dynamics of Collective Cell Migration. *Proc Natl Acad Sci* (2011) 108:4714–9. doi:10.1073/pnas.1010059108
33. Basan M, Elgeti J, Hannezo E, Rappel W-J, and Levine H. Alignment of Cellular Motility Forces with Tissue Flow as a Mechanism for Efficient Wound Healing. *Proc Natl Acad Sci* (2013) 110:2452–9. doi:10.1073/pnas.1219937110
34. Garcia S, Hannezo E, Elgeti J, Joanny J-F, Silberzan P, and Gov NS. Physics of Active Jamming during Collective Cellular Motion in a Monolayer. *Proc Natl Acad Sci USA* (2015) 112:15314–9. doi:10.1073/pnas.1510973112
35. Sepúlveda N, Petitjean L, Cochet O, Grasland-Mongrain E, Silberzan P, and Hakim V. Collective Cell Motion in an Epithelial Sheet Can Be Quantitatively Described by a Stochastic Interacting Particle Model. *Plos Comput Biol* (2013) 9:e1002944–12. doi:10.1371/journal.pcbi.1002944
36. Bi D, Lopez JH, Schwarz JM, and Manning ML. A Density-independent Rigidity Transition in Biological Tissues. *Nat Phys* (2015) 11:1074–9. doi:10.1038/nphys3471
37. Bi D, Yang X, Marchetti MC, and Manning ML. Motility-driven Glass and Jamming Transitions in Biological Tissues. *Phys Rev X* (2016) 6. doi:10.1103/PhysRevX.6.021011
38. Merkel M, and Manning ML. A Geometrically Controlled Rigidity Transition in a Model for Confluent 3d Tissues. *New J Phys* (2018) 20:022002. doi:10.1088/1367-2630/aaaa13
39. Yan L, and Bi D. Multicellular Rosettes Drive Fluid-Solid Transition in Epithelial Tissues. *Phys Rev X* (2019) 9:011029. doi:10.1103/PhysRevX.9.011029
40. Jorjadze I, Pontani L-L, Newhall KA, and Brujic J. Attractive Emulsion Droplets Probe the Phase Diagram of Jammed Granular Matter. *Proc Natl Acad Sci* (2011) 108:4286–91. doi:10.1073/pnas.1017716108
41. Trappe V, Prasad V, Cipelletti L, Segre PN, and Weitz DA. Jamming Phase Diagram for Attractive Particles. *Nature* (2001) 411:772–5. doi:10.1038/35081021
42. Lois G, Blawzdziewicz J, and O'Hern CS. Jamming Transition and New Percolation Universality Classes in Particulate Systems with Attraction. *Phys Rev Lett* (2008) 100:028001. doi:10.1103/PhysRevLett.100.028001
43. Koeze DJ, and Tighe BP. Sticky Matters: Jamming and Rigid Cluster Statistics with Attractive Particle Interactions. *Phys Rev Lett* (2018) 121:188002. doi:10.1103/PhysRevLett.121.188002
44. Henkes S, van Hecke M, and van Saarloos W. Critical Jamming of Frictional Grains in the Generalized Isostaticity Picture. *Epl* (2010) 90:14003. doi:10.1209/0295-5075/90/14003
45. Bécu L, Manneville S, and Colin A. Yielding and Flow in Adhesive and Nonadhesive Concentrated Emulsions. *Phys Rev Lett* (2006) 96:138302. doi:10.1103/PhysRevLett.96.138302
46. Bibette J, Mason TG, Gang H, Weitz DA, and Poulin P. Structure of Adhesive Emulsions. *Langmuir* (1993) 9:3352–6. doi:10.1021/la00036a006
47. Poulin P, Bibette J, and Weitz DA. From Colloidal Aggregation to Spinodal Decomposition in Sticky Emulsions. *Eur Phys J B* (1999) 7:277–81. doi:10.1007/s100510050614
48. Datta SS, Gerrard DD, Rhodes TS, Mason TG, and Weitz DA. Rheology of Attractive Emulsions. *Phys Rev E* (2011) 84:041404. doi:10.1103/PhysRevE.84.041404
49. Kim S, Pochitaloff M, Stooke-Vaughan GA, and Campàs O. Embryonic Tissues as Active Foams. *Nat Phys* (2021) 17:859–66. doi:10.1038/s41567-021-01215-1
50. Boromand A, Signoriello A, Ye F, O'Hern CS, and Shattuck MD. Jamming of Deformable Polygons. *Phys Rev Lett* (2018) 121:248003. doi:10.1103/PhysRevLett.121.248003

51. Boromand A, Signoriello A, Lowensohn J, Orellana CS, Weeks ER, Ye F, et al.The Role of Deformability in Determining the Structural and Mechanical Properties of Bubbles and Emulsions. *Soft Matter* (2019) 15:5854–65. doi:10.1039/C9SM00775J
52. Pontani L-L, Jorjadze I, Viasnoff V, and Brujic J. Biomimetic Emulsions Reveal the Effect of Mechanical Forces on Cell-Cell Adhesion. *Proc Natl Acad Sci* (2012) 109:9839–44. doi:10.1073/pnas.1201499109
53. Pontani L-L, Jorjadze I, and Brujic J. Cis and Trans Cooperativity of E-Cadherin Mediates Adhesion in Biomimetic Lipid Droplets. *Biophysical J* (2016) 110:391–9. doi:10.1016/j.bpj.2015.11.3514
54. Golovkova I, Montel L, Wandersman E, Bertrand T, Prevost AM, and Pontani L-L. Depletion Attraction Impairs the Plasticity of Emulsions Flowing in a Constriction. *Soft Matter* (2020) 16:3294–302. doi:10.1039/c9sm02343g
55. Golovkova I, Montel L, Pan F, Wandersman E, Prevost AM, Bertrand T, et al.Adhesion as a Trigger of Droplet Polarization in Flowing Emulsions. *Soft Matter* (2021) 17:3820–8. doi:10.1039/D1SM00097G
56. Pawlizak S, Fritsch AW, Grosser S, Ahrens D, Thalheim T, Riedel S, et al. Testing the Differential Adhesion Hypothesis across the Epithelial–mesenchymal Transition. *New J Phys* (2015) 17:083049. doi:10.1088/1367-2630/17/8/083049
57. Feng L, Pontani L-L, Dreyfus R, Chaikin P, and Brujic J. Specificity, Flexibility and Valence of Dna Bonds Guide Emulsion Architecture. *Soft Matter* (2013) 9: 9816. doi:10.1039/c3sm51586a
58. Berg S, Kutra D, Kroeger T, Straehle CN, Kausler BX, Haubold C, et al. Ilastik: Interactive Machine Learning for (Bio)image Analysis. *Nat Methods* (2019) 16: 1226–32. doi:10.1038/s41592-019-0582-9
59. Tremeau A, and Colantoni P. Regions Adjacency Graph Applied to Color Image Segmentation. *IEEE Trans Image Process* (2000) 9:735–44. 10.1109/83.841950.
60. Van der Walt S, Schönberger JL, Nunez-Iglesias J, Boulogne F, Warner JD, Yager N, et al. Scikit-Image: Image Processing in python. *PeerJ* (2014) 2:e453. doi:10.7717/peerj.453
61. Harris CG, and Stephens M. A Combined Corner and Edge Detector. *Alvey Vis Conf (Citeseer)* (1988) 15:10–5244. doi:10.5244/c.2.23
62. Rogers WB. A Mean-Field Model of Linker-Mediated Colloidal Interactions. *J Chem Phys* (2020) 153:124901. doi:10.1063/5.0020578
63. van Hecke M. Jamming of Soft Particles: Geometry, Mechanics, Scaling and Isostaticity. *J Phys Condens Matter* (2009) 22:033101. doi:10.1088/0953-8984/22/3/033101
64. Mason TG, Bibette J, and Weitz DA. Elasticity of Compressed Emulsions. *Phys Rev Lett* (1995) 75:2051–4. doi:10.1103/PhysRevLett.75.2051
65. Liu AJ, and Nagel SR. The Jamming Transition and the Marginally Jammed Solid. *Annu Rev Condens Matter Phys* (2010) 1:347–69.
66. Maxwell JC. L. On the Calculation of the Equilibrium and Stiffness of Frames. *Lond Edinb Dublin Philosophical Mag J Sci* (1864) 27:294–9. doi:10.1080/14786446408643668
67. Clusel M, Corwin EI, Siemens AON, and Brujić J. A 'granocentric' Model for Random Packing of Jammed Emulsions. *Nature* (2009) 460:611–5. doi:10.1038/nature08158
68. Corwin EI, Clusel M, Siemens AON, and Brujić J. Model for Random Packing of Polydisperse Frictionless Spheres. *Soft Matter* (2010) 6:2949–59. doi:10.1039/C000984A
69. Newhall KA, Jorjadze I, Vanden-Eijnden E, and Brujic J. A Statistical Mechanics Framework Captures the Packing of Monodisperse Particles. *Soft Matter* (2011) 7:11518–25. doi:10.1039/C1SM06243C
70. Miklius MP, and Hilgenfeldt S. Analytical Results for Size-Topology Correlations in 2d Disk and Cellular Packings. *Phys Rev Lett* (2012) 108: 015502. doi:10.1103/PhysRevLett.108.015502
71. Newhall KA, Pontani LL, Jorjadze I, Hilgenfeldt S, and Brujic J. Size-topology Relations in Packings of Grains, Emulsions, Foams, and Biological Cells. *Phys Rev Lett* (2012) 108:268001. doi:10.1103/PhysRevLett.108.268001
72. Walker SA, Chiruvolu S, Zasadzinski JA, Schmitt F-J, and Israelachvlli JN. Controlled Multi-Stage Self-Assembly of Vesicles. *MRS Proc* (1994) 372: 95–100. doi:10.1557/proc-372-95
73. General IJ, Dragomirova R, and Meirovitch H. Absolute Free Energy of Binding of Avidin/Biotin, Revisited. *J Phys Chem B* (2012) 116:6628–36. doi:10.1021/JP212276M
74. Steinhardt PJ, Nelson DR, and Ronchetti M. Bond-orientational Order in Liquids and Glasses. *Phys Rev B* (1983) 28:784–805. doi:10.1103/PhysRevB.28.784
75. Schreck CF, O'Hern CS, and Silbert LE. Tuning Jammed Frictionless Disk Packings from Isostatic to Hyperstatic. *Phys Rev E Stat Nonlin Soft Matter Phys* (2011) 84:011305
76. Maître J-L, Berthoumieux H, Krens SFG, Salbreux G, Jülicher F, Paluch E, et al.Adhesion Functions in Cell Sorting by Mechanically Coupling the Cortices of Adhering Cells. *Science* (2012) 338:253–6. doi:10.1126/science.1225399
77. Miyaguchi K.Ultrastructure of the Zonula Adherens Revealed by Rapid-Freeze Deep-Etching. *J Struct Biol* (2000) 132:169–78. doi:10.1006/JSBI.2000.4244
78. Dreyfus R, Leunissen ME, Sha R, Tkachenko AV, Seeman NC, Pine DJ, et al.Simple Quantitative Model for the Reversible Association of Dna Coated Colloids. *Phys Rev Lett* (2009) 102:048301. doi:10.1103/PhysRevLett.102.048301
79. Leckband D, and Prakasam A. Mechanism and Dynamics of Cadherin Adhesion. *Annu Rev Biomed Eng* (2006) 8:259–87. doi:10.1146/annurev.bioeng.8.061505.095753
80. Gai Y, Leong CM, Cai W, and Tang SKY. Spatiotemporal Periodicity of Dislocation Dynamics in a Two-Dimensional Microfluidic crystal Flowing in a Tapered Channel. *Proc Natl Acad Sci USA* (2016) 113:12082–7. doi:10.1073/pnas.1606601113
81. Zaiser M. Scale Invariance in Plastic Flow of Crystalline Solids. *Adv Phys* (2006) 55:185–245. doi:10.1080/00018730600583514
82. Krotov D, Dubuis JO, Gregor T, and Bialek W. Morphogenesis at Criticality. *Proc Natl Acad Sci USA* (2014) 111:3683–8. doi:10.1073/pnas.1324186111

Conflict of Interest: The authors declare that the research was conducted in the absence of any commercial or financial relationships that could be construed as a potential conflict of interest.

Publisher's Note: All claims expressed in this article are solely those of the authors and do not necessarily represent those of their affiliated organizations, or those of the publisher, the editors and the reviewers. Any product that may be evaluated in this article, or claim that may be made by its manufacturer, is not guaranteed or endorsed by the publisher.

Advantages of publishing in Frontiers

OPEN ACCESS
Articles are free to read for greatest visibility and readership

FAST PUBLICATION
Around 90 days from submission to decision

HIGH QUALITY PEER-REVIEW
Rigorous, collaborative, and constructive peer-review

TRANSPARENT PEER-REVIEW
Editors and reviewers acknowledged by name on published articles

Frontiers
Avenue du Tribunal-Fédéral 34
1005 Lausanne | Switzerland

Visit us: www.frontiersin.org
Contact us: frontiersin.org/about/contact

REPRODUCIBILITY OF RESEARCH
Support open data and methods to enhance research reproducibility

DIGITAL PUBLISHING
Articles designed for optimal readership across devices

FOLLOW US
@frontiersin

IMPACT METRICS
Advanced article metrics track visibility across digital media

EXTENSIVE PROMOTION
Marketing and promotion of impactful research

LOOP RESEARCH NETWORK
Our network increases your article's readership